METALLURGICAL AND MECHANICAL MODELLING OF TI-6AL-4V FOR WELDING APPLICATIONS

by

MATTEO VILLA

A thesis submitted to the University of Birmingham

for the degree of

DOCTOR OF PHILOSOPHY

School of Engineering and Physical Sciences

Department of Metallurgy and Materials

University of Birmingham

March 2016

UNIVERSITY OF
BIRMINGHAM

University of Birmingham Research Archive

e-theses repository

This unpublished thesis/dissertation is copyright of the author and/or third parties. The intellectual property rights of the author or third parties in respect of this work are as defined by The Copyright Designs and Patents Act 1988 or as modified by any successor legislation.

Any use made of information contained in this thesis/dissertation must be in accordance with that legislation and must be properly acknowledged. Further distribution or reproduction in any format is prohibited without the permission of the copyright holder.

Abstract

Complex heat treatments and manufacturing processes such as welding involve a wide range of temperatures and temperature rates, affecting the microstructure of the material and its properties. In this work, a diffusion based approach to model growth and shrinkage of precipitates in the alpha + beta field of Ti-6Al-4V alloys is established. Experimental heat treatments were used to validate the numerical predictions of the model for lamellar shrinkage, whilst data from literature have been used to evaluate the numerical model for the growth of equiaxed microstructures. The agreement between measurements and numerical predictions was found to be very good. Experimentally-based approaches were used both to describe the growth of alpha lamellae and martensitic needles while cooling down from temperatures above the beta transus, and beta grain growth for temperatures remaining above the beta transus. Such models were coded in the commercial FE software Visual-Weld for the prediction of microstructure evolution during welding simulations. Experimental welding tests were carried out to validate the predictions. The metallurgical models developed were linked with a mechanical physically based model to predict the flow properties and the initial implementation of the coupled models in Visual-Weld is discussed.

Acknowledgements

I am sincerely grateful to my supervisors Dr Mark Ward and Professor Jeffery Brooks for the support and guidance they gave me throughout my PhD. This work would have not been possible without their help.

ESI group, sponsor of my project, gave me also a great technical support and I cannot forget to thank Dr Frédéric Boitout and Dr Rajab Said for their assistance.

I would like to thank also Professor Roger Reed as he offered to me the opportunity for this PhD.

Thanks to Dr Hector Basoalto for the time spent together, even if I was not under his supervision.

Thanks to Dr Richard Turner and Dr Hang Wang for the helpful conversations we had.

Last but not least, thanks to my girlfriend Nicoletta for the support during these years.

Contents

1 Introduction and objectives **1**

2 Literature review **6**

2.1 Introduction 6

2.2 Welding 7

2.2.1 Introduction 7

2.2.2 Classical approach of computational welding mechanics 8

2.2.3 Heat sources 10

2.3 Ti-6Al-4V 18

2.3.1 Introduction 18

2.3.2 Classification 19

2.3.3 Thermo-mechanical data 20

2.3.4 Phases and common microstructures obtainable 26

2.3.5 Phases evolution 30

2.3.5.1 Heating 30

2.3.5.2 Cooling 30

2.3.5.3 Martensitic transformation 35

2.3.6 Morphological and mechanical modelling 36

2.3.6.1 Introduction on the relation between mechanical behaviour and material morphology 36

2.3.6.2 Modelling of the equiaxed and lamellar alpha phase evolution . . . 42
2.3.6.3 Modelling of the beta grains evolution . . . 44
2.3.6.4 Modelling of the mechanical behaviour in relation to the morphology . . . 46
2.4 Welding of Ti-6Al-4V . . . 51
2.4.1 Modelling of welding on Ti-6Al-4V coupling metallurgical and mechanical behaviour of the material . . . 57
2.4.2 Visual-Weld multi-phase code . . . 58
2.4.3 Summary . . . 59
2.5 Surrogate models . . . 61

3 Characterization 64

3.1 Introduction . . . 64
3.2 Project plan . . . 65
3.3 Preliminary FE model . . . 65
3.4 Gleeble tests . . . 73
3.4.1 Microstructural analysis - procedure . . . 81
3.4.2 Microanalysis - technique . . . 86
3.4.3 Heating rate effect on lamellar microstructure . . . 88
3.4.4 Cooling rate effect on lamellar and martensitic microstructures . . . 97
3.4.5 Growth of nucleated lamellae in the $\alpha + \beta$ field . . . 98
3.4.6 β transus . . . 108
3.4.7 β grain growth . . . 112
3.5 Welding tests. . . . 113
3.5.1 Temperature measurements . . . 120
3.5.1.1 Plates with equiaxed microstructure . . . 120
3.5.1.2 Plates with lamellar microstructure . . . 122

3.5.2 Microstructures . . . 122
3.5.2.1 Plates with equiaxed microstructure . . . 122
3.5.2.2 Plates with lamellar microstructure . . . 141
3.5.3 Chemical analysis . . . 152
3.5.3.1 Plates with equiaxed microstructure . . . 152
3.5.3.2 Plates with lamellar microstructure . . . 152
3.5.4 Deformation measurement . . . 157
3.6 Summary . . . 157
3.6.1 Heating rate . . . 157
3.6.2 Cooling rate . . . 159
3.6.3 Welding tests . . . 160

4 Numerical modelling 161

4.1 Introduction . . . 161
4.2 Alpha + Beta field . . . 162
4.2.1 Spherical particles . . . 165
4.2.1.1 Growth . . . 165
4.2.1.2 Shrinkage . . . 168
4.2.2 Lamellar particles . . . 168
4.2.2.1 Growth . . . 168
4.2.2.2 Shrinkage . . . 171
4.2.3 Input data . . . 171
4.2.4 Results and discussion . . . 175
4.2.4.1 Interdiffusion coefficient . . . 175
4.2.4.2 Spherical precipitates growth . . . 176
4.2.4.3 Lamellar precipitates dissolution . . . 188
4.3 Beta grain growth. . . . 193
4.3.1 Results and discussion . . . 197
4.4 Lamellae nucleation . . . 199

4.4.1 Results and discussion . . . 199
4.5 Martensitic model . . . 201
4.5.1 Results and discussion . . . 203
4.6 Welding simulations . . . 203
4.6.1 Workpieces and operative conditions . . . 204
4.6.2 Thermal material properties . . . 204
4.6.3 Model mesh . . . 205
4.6.4 Boundary conditions . . . 207
4.6.5 Weld pool shape . . . 210
4.6.5.1 Equiaxed microstructure . . . 210
4.6.5.2 Lamellar microstructure . . . 212
4.6.6 Implementation in Visual-Weld . . . 216
4.6.7 Thermal comparison with experiments . . . 219
4.6.7.1 Equiaxed microstructure . . . 219
4.6.7.2 Lamellar microstructure . . . 220
4.6.8 Microstructure comparison with experiments . . . 224
4.6.8.1 Equiaxed microstructure . . . 224
4.6.8.2 Lamellar microstructure . . . 228
4.7 Mechanical model . . . 238
4.8 Summary . . . 243
4.8.1 Diffusion based model . . . 243
4.8.2 Experimentally based models . . . 244
4.8.3 Welding models . . . 245
4.8.4 Mechanical model . . . 245

5 Summary 247

6 Conclusions 263

7 Future work 265

A Gleeble numerical model 282

B Montages 292

B.1 Heating rate 5 °C/s . . . 293

B.2 Heating rate 50 °C/s . . . 297

B.3 Heating rate 500 °C/s . . . 299

C Contact in welding 301

C.1 Welding jig . . . 301

C.2 Numerical modelling . . . 302

C.2.1 Chewing gum + contact elements (low preloads) . . . 305

C.2.2 Chewing gum + contact spring elements (high preloads) . . . 305

C.2.3 Preliminary results . . . 306

C.3 Conclusions . . . 309

D Weld sequence optimization 311

D.1 Introduction . . . 311

D.2 Overview . . . 312

D.3 DOE algorithm . . . 315

D.4 Surrogate model . . . 325

D.5 Conclusions . . . 328

E Mechanical model 332

List of Figures

1.1 Representative chart of the percentage of titanium alloys usage in the Boeing 787 Dreamliner [1, 2] 4

1.2 5 axis laser welding of a titanium duct for aerospace [3] 5

2.1 Welding processes ranked according to heat source intensity, where d/w is the depth/width ratio of the weld pool, efficiency represents the amount of energy actually used to melt the material instead of preheating the surrounding, HAZ size is the heat affected zone size, interaction is the interaction time between heat source and material, max speed is the maximum speed allowed by the welding process and cost is the capital cost of the equipment[4] 9

2.2 Couplings in welding: the dominant ones are shown with bold lines, the secondary ones are shown with thin lines [5]. 9

2.3 Schematic representation and description of the density power distribution of the Gaussian [6], Double ellipsoidal [7], TDC [8] and MTDC heat sources [8] used to describe the heat distribution in FE analysis of welding processes. Each heat source is suitable to describe a particular welding processes, which is described in the 4^{th} column 12

2.4 Schematic representation and description of the density power distribution of the nail head heat source [9] used to describe the heat distribution in FE analysis of high energy density welding processes 13

2.5 Graph showing an example of power density distribution obtained adopting a double ellipsoidal heat source model (figure 2.3). In particular half of the front section of the heat source is shown (symmetry plane x-y) 14

2.6 Numerical weld pool shape and temperature distribution obtained in [9] for a laser welding process on AISI304 adopting a nail head shape heat source 16

2.7 Comparison between the cross sections of the weld pool measured by experiments and numerical models in a fusion welding process. Top row: different welding pool shapes obtained experimentally changing the welding speed and keeping the power input constant. In the 2^{nd}, 3^{rd}, 4^{th} rows starting from the top, shapes of the weld pool obtained for different values of the total power input (P_t), fictitious conductivities ($\lambda_{T\,effe}$) and Peclet number at the initial time ($Pe(0)$) set as parameters for the nail head heat source [9] 17

2.8 Graph of the Ti-6Al-4V density as a function of temperature obtained from Mills [10] and the commercial software JMatPro 21

2.9 Graph of the Ti-6Al-4V specific heat as a function of temperature obtained from different sources: Basak [11], Boyer [12], CEA [13], University of Birmingham [14], RVTP [10] e the commercial software JMatPro 22

2.10 Graph of the Ti-6Al-4V thermal conductivity as a function of the temperature obtained from Boivineau [15], University of Birmingham [14], RVTP [10] and thr commercial software JMatPro data 23

2.11 Mean typical values of linear expansion for Ti-6Al-4V as reported in [12] . 24

2.12 Range values of Young's modulus as a function of the temperature for Ti-6Al-4V and others titanium alloys [12] 25

2.13 Young's modulus, Poisson's ratio and Shear modulus at different quenching temperatures for Ti-6Al-4V [12] 25

2.14 Schematic pseudo-binary diagram of Ti-6Al-4V [13] 26

2.15 Indicative microstructures obtainable by cooling down Ti-6Al-4V in three different media (furnace, air and water) after soaking (time not reported in source) at different temperatures (650 °C, 800 °C, 850 °C and 1050 °C) [12] 27

2.16 Micrographs of Ti-6Al-4V showing coarse lamellar structure (left) and a fine lamellar structure (right) of α-phase obtained starting from a full β structure and applying a slow and moderate cooling respectively [16] . . . 28

2.17 Micrographs of Ti-6Al-4V showing a α' martensitic structure obtained from a full β structure and applying a water quenching (left); equiaxed microstructure (right) [16] 29

2.18 Micrograph of Ti-6Al-4V showing a duplex structure constituted by α grains surrounded by transformed β obtained by a water quenching from the α+β domain [17] 29

2.19 Graphs showing for a Ti-6Al-4V alloy a) temperature start (T_p) and finish (T_k) of β transformation as a function of the heating rate, calculated and measured experimentally by dilatometer; b) degree of transformation of β phase (p) as a function of temperature and heating rate for the same Ti-6Al[18] 31

2.20 Graph of the equilibrium β fraction as a function of temperature obtained by Thermocalc for a Ti-6Al-4V alloy with the composition showed in table 2.2 [19] 31

2.21 Graph of the fraction of phase constituents after quenching as a function of the temperature for a Ti-6Al-4V alloy [12] 32

2.22 Two different TTT diagrams found in literature: a) TTT diagram obtained keeping Ti-6Al-4V specimens at 1025 °C for 30 minutes then quenching [20]; b) TTT diagram obtained after a solution annealing at 1020 °C then quenching to reaction temperature [21] 33

2.23 Continuous Cooling Transformation diagram for Ti-6Al-4V, cooling from 1030 °C [22] 33

2.24 Continuous Cooling Transformation diagram for Ti-6Al-4V, cooling from 1020 °C [23] 34

2.25 a) Calculated rate parameter k as a function of the temperature for equation 2.1; b) experimental and calculated degrees of β to α transformed as a function of the temperature and cooling rate applying the JMA approach for a Ti-6Al-4V alloy[24] 35

2.26 Trend of the yield strength 0.2 % and ultimate stress in relation to the platelet thickness measured in [25] and reported in table 2.3 and table 2.4 . 38

2.27 Graph showing the evolution of the platelet thickness reported in table 2.5 as a function of the peak temperature at which the Ti-6Al-4V alloy was water quenched. The data points relative to the "heat treated" material show that the alpha platelet dissolve with increasing the temperature [26] . 40

2.28 α lath thickness distribution as a function of the depth from the surface of the Ti-6Al-4V specimen tested in [27]. Material far from is subjected to slower cooling rates which allow growth of the α lath 41

2.29 Ultimate tensile strength as a function of the α lath thickness measured in a Ti-6Al-4V Widmanstätten structure [28] 42

2.30 Graph comparing experimental data with model predictions of the effect of cooling rate and size distribution on the variation of the total volume fraction of the alpha phase in Ti-6Al-4V, cooling down from 955 °C [29] . . 43

2.31 Graphs showing measured and predicted variation of the volume fraction of primary equiaxed, lamellar and total alpha as a function of temperature and cooling rates from 982 °C in Ti-6Al-4V [30] 45

2.32 Numerical beta grain size predictions obtained using equation 2.6 vs experimental measurements as a function of temperature for a Ti-6Al-4V alloy. PM makes reference to a rolled plate from 16 to 5 mm whilst SM refers to a rolled plate from 16 to 2 mm, both plates had the same chemical composition. Heating rate of 5 and 50 K/s have been tested 46

2.33 True stress-true strain curves obtained from Ti-6Al-4V hot compression tests at 815 °C and strain rates of 0.001, 0.1, 1.0 s^{-1} with microstructures having 3 different platelet thickness (reported in table 2.6) [31] 48

2.34 Average fusion zone and heat affected zone widths as a function of welding speed and specific heat input in a laser welding process of Ti-6Al-4V [32] . 52

2.35 Micrographs showing different microstructures obtained in a Nd-YAG laser welding process joining a 1mm thick Ti-6Al-4V plate ($2.5kW$, $7.5mm/min$). (b) fusion zone - acicular α' martensite, (c)(d) heat affected zone - acicular α' + primary α, (e)(f) bulk material - $\alpha + \beta$ microstructure [33] 53

2.36 Graphs showing the mean values of the fusion zone hardness as function (a) of the welding speed at different laser powers, (b) of the specific heat input measured after laser welding of Ti-6Al-4V. Error bars indicate 80% confidence limits [32] 54

2.37 Comparison of simulation and experimental (hole-drilling) residual stresses measured after a CO2 laser weld of Ti-6Al-4V at a maximum power of 3 kW. The welding plate size is $200\,mm \times 100\,mm \times 4\,mm$ with heat input of 115.7 J/mm in (a) and (b), 162.0 J/mm in (c) and (d) [34] 55

2.38 Hardness measured using Nd-YAG laser on a Ti-6Al-4V sheet 1.6mm thick. (a) location of microidentations, (b) hardness profile observed over the weld cross section ($0.8\,kW$, $17\,mm/s$) [32] 55

2.39 Micrographs showing: a) the microstructure developed in a Ti-6Al-4V plate after electron beam welding process, it is possible to notice the coarse grains developed in the fusion zone; b) a detail of the acicular colony structure developed in the fusion zone, within the prior beta grains [35] 56

2.40 Anatomy of surrogate modelling: model estimation + model appraisal. The former provides an estimate of function f while the latter forecasts the associated error [36] 62

2.41 Key stages of the surrogate-based modelling approach [37] 63

3.1 Project plan 66

3.2 Graph showing the Ti-6Al-4V thermal conductivity data used to run a preliminary FE welding simulation test 67

3.3 Graph showing the Ti-6Al-4V specific heat data used to run a preliminary FE welding simulation test 68

3.4 Graph showing the Ti-6Al-4V density data used to run a preliminary FE welding simulation test 69

3.5 Temperature distribution obtained by a numerical simulation of a laser welding process on a Ti-6Al-4V plate using the commercial software VisualWeld. The inner black border highlights the fusion zone (temperature higher than $1650°C$) whilst the outer one highlights the area where $T_{\beta\,transus} < T < T_{fusion}$ 71

3.6 Cross section of the figure 3.5, starting from the centre of the weld pool (weldline), point where the maximum temperature during the simulation is measured, 6 other points have been sampled progressively farther from the weldline (0.28, 0.62, 0.8, 1.23, 2.0, 2.6 mm), they are highlighted by red dots. Fusion zone and area where $T_{\beta\,transus} < T < T_{fusion}$ are delimited by black contours 72

3.7 Graph of the temperature trends measured on some of the points reported in figure 3.6, values measured at 0.28 and 0.62 mm from the weldline have been omitted for clarity 72

3.8 Graph of the temperature rate trend measured on some of the points reported in figure 3.6, values measured at 0.28 and 0.62 mm from the weldline have been omitted for clarity, the curve relative at 2.6 mm lies almost on the x axis 73

3.9 Graph of the trend of temperatures (suffix "T" in the legend) and temperature rates (suffix "T.r." in the legend) measured in some of the points shown in 3.6 have been reported in the same graph to highlight the possible thermal conditions the material is subjected on during a welding process, at different distances from the weldline. In particular, temperatures below the Ti-6Al-4V melting temperature and temperature rates corresponding to temperatures close to the beta transus temperature are shown 74

3.10 Point sampled for the evaluation of the strains and strain rates the material is subjected on during the welding simulation 74

3.11 Graph of the equivalent Von Mises strain measured in the points showed in figure 3.10 75

3.12 Graph of the equivalent Von Mises strain rates measured in the points showed in figure 3.10 of the numerical model. In a) it is possible to see that the maximum values registered are in correspondence of the weldline, where there are the highest gradient of temperature; at distances from the weldline greater than 0.8 mm the strain rates are so small respect the y-scale that the relative curves lie on the x axis. In b) it is possible to see how after about 10 s the strain rates tend to converge toward zero, with points farther from the weldline subjected to variations of strains higher than points close to the weldline 76

3.13 Tensile Gleeble specimens geometry. TC1, TC2 and TC3 represent the location of the thermocouples fixed on the specimens. Dimensions are in mm 77

3.14 Compressive Gleeble specimen geometry. Dimensions are in mm 77

3.15 Photograph of the assembly used for tension tests carried out by using the testing system Gleeble 3500 80

3.16 Photograph of the assembly used for compression tests carried out by using the testing system Gleeble 3500 80

3.17 From the top to the bottom: a) optical microscope micrograph showing beta grains manually highlighted; b) beta grains thresholded; c) ellipses inscribed in the beta grain shapes 84

3.18 BEI micrograph showing the microstructure of the received Ti-6Al-4V. Alpha lamellae are represented by the darker areas, since they have lower atomic weight. The thin white walls bounding the lamellae represent the beta phase, with higher atomic weight 85

3.19 BEI micrograph showing ellipses inscribed to the lamellae of figure 3.18 . 86

3.20 Monte Carlo simulation of electron scattering due to the interaction between an electron beam, different materials and acceleration voltage [38] 88

3.21 BEI microhraphs showing representative microstructures obtained from all the samples tested at the heating rate of 5 °C/s to different peak temperatures and water quenched. As a comparison, the original microstructure of the material as received is also shown. The specimens heated up to temperatures equal or higher than 976 °C and water quenched do not show anymore the original lamellar morphology, but martensitic microstructure 91

3.22 BEI micrographs showing representative microstructures obtained from each sample heated up at 50 °C/s to different peak temperatures and water quenched. Specimens heated up till temperatures equal or higher than 982 °C have martensitic microstructure instead of the original lamellae one . . 92

3.23 BEI micrographs showing representative microstructures obtained from each sample heated up at 500 °C/s till different peak temperatures and water quenched. Specimens heated up till temperatures higher than 1020 °C have martensitic microstructure instead of the original lamellae one . . 93

3.24 Graphs showing the heating rate effect on the dissolution of lamellae (a), growth of beta boundaries (b) and alpha volume fraction (c) as a function of the peak temperature reached during the heating tests 94

3.25 Same results shown in figure 3.24 but plotted as a function of time. The duration ratio between the fastest and the slowest heat treatment is 1/100 95

3.26 Graphs showing the variation of the lamellae aspect ratio as a function of (a) peak temperature and (b) time at different heating rates. In general, as the reaction proceeds, the lamellae reduce their thickness (figure 3.24 and 3.25) thus their aspect ratio increases 96

3.27 Graphs showing the cooling rate effect on lamellae growth as a function of the temperature from which the cooling started (a), cooling rate effect on lamellae beta boundaries growth as a function of the temperature from which the cooling started (b) 99

3.28 Graphs showing the cooling rate effect on lamellae growth as a function of the beta grain size (a), cooling rate effect on lamellae beta boundaries growth as a function of the beta grain size (b) 100

3.29 BEI micrographs showing an example of sample microstructures obtained cooling down at 5 °C/s (a) and 50 °C/s (b) from the beta field. The first one has a microstructure entirely lamellar, whilst in the second one martensite has started to form 101

3.30 BEI micrographs showing an example of sample microstructures obtained cooling down at 100 °C/s (a) and 300 °C/s (b) from the beta field. The martensitic needles become progressively thicker as the cooling rate increases (see also micrographs in figure 3.29) 102

3.31 Graphs showing the cooling rate effect on the martensitic needles mean thickness as a function of the peak temperature from which the cooling started (a) and as a function of cooling rate (b). The data points shown in graph (b), considering the error bars, can be interpolated by a straight line, suggesting that a logarithmic function can well describe the needles thickness as a function of the cooling rate (see also graph in figure 4.28) . 103

3.32 Graph showing the amount of the alpha phase volume fraction formed in Ti-6Al-4V when the material is cooled down with different cooling rates starting from temperatures above the beta transus temperature (same data points of figure 3.31) 104

3.33 BEI micrograph showing an example of a microstructure obtained in the α + β field. Lamellar microstructure embedded in martensite obtained after holding in the α + β field and then quenching 106

3.34 Graphs showing growth of alpha lamellae in the $\alpha + \beta$ field, cooling down from the β field at different cooling rates and soaking for 0, 10 and 20 seconds then water quenching the samples. Data points with arrows represent samples of 6mm diameter, the other ones represent samples of 12 mm diameter 107

3.35 Optical micrograph image of the sample soaked at 960 °C for the determination of the beta transus temperature. Parent alpha is still present thus beta transus has not been passed 109

3.36 Optical micrograph of the sample soaked at 970 °C for the determination of the beta transus temperature. Parent alpha is still present thus beta transus has not been passed 109

3.37 Optical micrograph of the sample soaked at 980 °C for the determination of the beta transus temperature. Beta grains can be observed along the entire section: the beta transus temperature has been passed 110

3.38 BEI micrograph of the samples tested at 960 °C for the determination of the beta transus temperature. Parent alpha lamellae can be observed, meaning the beta transus temperature has not been passed 110

3.39 BEI micrograph of the samples tested at 970 °C for the determination of the beta transus temperature. Parent alpha lamellae can be observed, meaning the beta transus temperature has not been passed 111

3.40 BEI micrograph of the sample tested at 980 °C for the determination of the beta transus temperature. No parent alpha lamellae can be observed as in figure 3.38-a and b, meaning the beta transus temperature has been passed 111

3.41 Beta grains measurements as a function of the peak temperature and heating rate a), beta grains measurements as a function of the time and heating rate b). 113

3.42 Drawing of the hole positions machined to keep in place the thermocouples during welding tests. In the top face of the plates a series of holes at different distances from the weld line have been machined, in the bottom face the holes are at two different distances but with different depths . . . 117

3.43 Photograph of Ti-6Al-4V plate showing how the thermocouples were kept in place by twisting two wires around them and the specimens 118

3.44 Photographs showing a) the jig used to fix the plates during welding tests and b) the assembly placed in the welding chamber to operate in inert atmosphere 119

3.45 Photograph of a Ti-6Al-4V plate after welding 120

3.46 Cropped photographs of the Ti-6Al-4V plate 5 mm thick, with equiaxed microstructure, after welding tests - detail of the welding area. In this case 100% power was used at two different speeds, 2 m/min and 1.5 m/min. a) Top view. b) Bottom view 121

3.47 Graphs showing the temperatures measured at different distances from the weldline, for the welding test conducted on a Ti-6Al-4V plate 5.8 mm thick with initial equiaxed microstructure, using as operative parameters 100% power and 2 m/min as welding speed. The bottom chart shows a zoom on a time scale of 100 seconds 123

3.48 Graphs showing the temperatures measured at different distances from the weldline, for the welding test conducted on a Ti-6Al-4V plate 5.8 mm thick with initial equiaxed microstructure, using as operative parameters 100% power and 1.5 m/min as welding speed. The bottom chart shows a zoom on a time scale of 100 seconds 124

3.49 Graphs showing the temperatures measured at different distances from the weldline, for the welding test conducted on a Ti-6Al-4V plate 2mm thick with initial equiaxed microstructure, using as operative parameters 60% power and 2.0 m/min as welding speed. The bottom chart shows a zoom on a time scale of 100 seconds 125

3.50 Graph showing the temperatures measured at different distances from the weldline, for the welding test conducted on a Ti-6Al-4V plate 3.75 mm thick with initial lamellar microstructure, using as operative parameters 70% power and 2.0 m/min as welding speed. The bottom chart shows a zoom on a time scale of 100 seconds 126

3.51 Graphs showing the temperatures measured at different distances from the weldline, for the welding test conducted on a Ti-6Al-4V plate 3.06 mm thick with initial lamellar microstructure, using as operative parameters 70% power and 2.0 m/min as welding speed. The bottom chart shows a zoom on a time scale from 110 to 150 seconds 127

3.52 Montages for the Ti-6Al-4V plate 5.8 mm thick tested and the hardness indentations, material with initial equiaxed microstructure. a) weld carried out at 2 m/min 100% power; b) weld carried out at 1.5 m/min at 100% power. The "0" point shows the first hardness measurement referenced in figure 3.54 and corresponds to the weld centreline 129

3.53 Montage of the Ti-6Al-4V plate 2 mm thick, material with initial equiaxed microstructure. 2 m/min 60% power. The "0" point shows the first hardness measurement referenced in figure 3.55 130

3.54 Micro hardness measurements for the Ti-6Al-4V plate 5mm thick with initial equiaxed microstructure. a) weld carried out at 2 m/min 100% power; b) weld carried out at 1.5 m/min at 100% power. The triangle makes reference to the indent in the HAZ/bulk material interface, represented by a triangle also in figure 3.52. Distance 0 corresponds to the "0" point in figure 3.52 131

3.55 Micro hardness measurements of the Ti-6Al-4V plate 2 mm thick with initial equiaxed microstructure. 2 m/min 60% power. The triangle makes reference to the indent in the HAZ/bulk material interface, represented by a triangle also in figure 3.53. Distance 0 corresponds to the "0" point in figure 3.53 132

3.56 High magnification BEI micrographs of the microstructure developed in the fusion zone of the Ti-6Al-4V plates with equiaxed microstructure welded. a) 5 mm thick plate welded at 2 m/min, 100% power; b) 5 mm thick plate welded at 1.5 m/min, 100% power; c) 2 mm thick plate welded at 2 m/min 60% power 133

3.57 BEI micrographs obtained observing the Ti-6Al-4V plate 5mm thick with initial equiaxed microstructure welded at 2 m/min 100% power. Making reference to the row of indentations of figure 3.52-a and considering as 1^{st} point the first indent starting from the centre of the weld pool: a) 1^{st} point, b) 6^{th} point, c) 8^{th} point, d) 9^{th} point, e) 11^{th} point, f) 13^{th} point 135

3.58 BEI micrographs obtained observing the Ti-6Al-4V plate 5mm thick with initial equiaxed microstructure welded at 1.5 m/min 100% power. Making reference to the row of indentations of figure 3.52-b and considering as 1^{st} point the first indent starting from the centre of the weld pool: a) 1^{st} point, b) 6^{th} point, c) 8^{th} point, d) 10^{th} point, e) 12^{th} point, f) 15^{th} point 136

3.59 BEI micrographs obtained observing the Ti-6Al-4V plate 2mm thick with initial equiaxed microstructure welded at 2.0 m/min 60% power. Making reference to the row of indentations of figure 3.53 and considering as 1^{st} point the first indent starting from the centre of the weld pool: a) 1^{st} point 1, b) 3^{rd} point, c) 5^{th} point, d) 7^{th} point 137

3.60 Graphs showing a) lamellae thickness and b) spherical alpha radius as a function of the distance in the Ti-6Al-4V plate 5mm thick with initial equiaxed microstructure welded at 2.0 m/min and 100% power. The distance makes reference to the ruler reported in the micrographs 138

3.61 Graphs showing a) lamellae thickness and b) spherical alpha radius as a function of the distance in the Ti-6Al-4V plate 5mm thick with initial equiaxed microstructure welded at 1.5 m/min and 100% power. The distance makes reference to the ruler reported in the pictures 139

3.62 Graphs showing a) lamellae thickness and b) spherical alpha radius as a function of the distance in the Ti-6Al-4V plate 2mm thick with initial equiaxed microstructure welded at 2.0 m/min and 60% power. The distance makes reference to the ruler reported in the pictures 140

3.63 Montages of the Ti-6Al-4V plates 3.75 mm (a) and 3.06 mm (b) thick with initial lamellar microstructure welded at 2.0 m/min 70% power. The specimens have been characterized by microhardness. The "0" point shows the first hardness measurement referenced in figure 3.64 and corresponds to the weld centreline 142

3.64 Micro hardness measurements graphs of the Ti-6Al-4V plate 3.75 mm (a) and 3.06 mm (b) thick. In both cases the welding operative parameters were set at 2 m/min and 70% power. The triangle makes reference to the indent in the HAZ/bulk material interface, represented by a triangle also in pictures 3.63 144

3.65 High magnification BEI micrographs of the microstructure developed in the fusion zone of the Ti-6Al-4V plates with initial lamellar microstructure welded. a) 3.75 mm thick plate welded at 2 m/min, 70% power; b) 3.06 mm thick plate welded at 2 m/min, 70% power 145

3.66 BEI micrographs of the Ti-6Al-4V plate 3.75mm thick with initial lamellar microstructure welded at 2 m/min 70% power. Making reference to the row of indentations of figure 3.63-a and considering as 1^{st} point the first indent starting from the centre of the weld pool: a) 1^{st} point, b) 3^{rd} point, c) 4^{th} point, d) 6^{th} point, e) 8^{th} point, f) 10^{th} point 146

3.67 BEI micrographs of the Ti-6Al-4V plate 3.06mm thick with initial lamellar microstructure welded at 2 m/min 70% power. Making reference to the row of indentations of figure 3.63-b and considering as 1^{st} point the first indent starting from the centre of the weld pool: a) 1^{st} point, b) 3^{rd} point, c) 4^{th} point, d) 6^{th} point, e) 8^{th} point, f) 11^{th} point 147

3.68 Graphs showing a) the lamellae thickness of the original microstructure and b) the thickness of new lamellae nucleated during welding of the Ti-6Al-4V plate with initial lamellar microstructure 3.75 mm thick welded at 2.0 m/min and 70% power. The distance makes reference to the ruler reported in the pictures 148

3.69 Graph showing the needles thickness of the martensitic microstructure formed during welding of the Ti-6Al-4V plate with initial lamellar microstructure 3.75 mm thick welded at 2.0 m/min and 70% power. The distance makes reference to the ruler reported in the picture 149

3.70 Graphs showing a) the lamellae thickness of the original microstructure and b) the thickness of new lamellae nucleated during welding of the Ti-6Al-4V plate with initial lamellar microstructure 3.06 mm thick welded at 2.0 m/min and 70% power. The distance makes reference to the ruler reported in the pictures 150

3.71 Graph showing the needle thickness of the martensitic microstructure formed during welding of the Ti-6Al-4V plate with initial lamellar microstructure 3.06 mm thick welded at 2.0 m/min and 70% power. The distance makes reference to the ruler reported in the picture 151

3.72 Graphs showing the wt% of Al and V as a function of the distance from the weldline (figure 3.60 and figure 3.61) for the Ti-6Al-4V plates 5 mm thick with initial equiaxed microstructure. a) Plate welded at 2.0 m/min and 70% power, b) plate welded at 1.5 m/min and 100% power. For some points the errors bars are so small that they are not visible. The orange dotted line indicates where the original microstructure of the material dissolves but it is possible to notice still a local segregation related to the initial phases distribution 153

3.73 Graph showing the wt% of Al and V as a function of the distance from the weldline (figure 3.62), starting from the first indent in the centre of the weld pool, for the Ti-6Al-4V plate 2 mm thick with initial equiaxed microstructure. The orange dotted line indicates where the original microstructure of the material dissolves but it is possible to notice still a local segregation related to the initial phases distribution 154

3.74 Graphs showing the wt% of Al and V as a function of the distance from the weldline (figure 3.68 and figure 3.70) for the Ti-6Al-4V plates 3.75 mm a) and 3.06 mm b) thick with initial lamellar microstructure. For some points the errors bars are so small that are not visible. The orange dotted line indicates where the original microstructure of the material dissolves but it is possible to notice still a local segregation related to the initial phases distribution 156

3.75 Deformation of the Ti-6Al-4V plates with initial lamellar morphology, before and after welding. The deformation shown is relative to the longitudinal centre line of the plates in their bottom side. The graph a) shows the deformation of the plate 3.75 mm thick, whilst the graph b) shows the deformation of the plate 3.06 mm thick 158

4.1 Schematic representation of the concentration field during growth a) and shrinkage b) [39] 165

4.2 Graph showing the parameter λ as a function of Ω of equations 4.6 and 4.8 166

4.3 Graph showing the influence of the lamellar aspect ratio to the volume fraction predictions for a Ti-6Al-4V alloy with an initial mean lamellae thickness of 3.0 μm, subjected to a hypothetical heating rate of 60 °C/s, . 169

4.4 Graph showing delta (δ) as a function of omega (Ω) and aspect ratio gamma (Γ) of equation 4.18 170

4.5 Gibbs free energy calculated both by a simplified equation for a Ti-Al-V ternary system and using the actual composition by the Thermocalc database 173

4.6 Ti-6Al-4V intrinsic diffusion coefficients for Vanadium, Aluminium and Titanium and interdiffusion coefficients considering either Al as diffusing element (Al interdiffusion) or Vanadium (V interdiffusion) 176

4.7 Comparison of the equiaxed particle growth results obtained with or without shrinkage, and with diffusion controlled by either Al or V. Cooling from $955°C$ at cooling rate of $11°C/min$. Equiaxed microstructure 179

4.8 Comparison between numerical (Al vs V diffusing elements) and experimental data [40] for a heat treatment consisting of a cooling at $11°C/min$ starting from $955°C$. Equiaxed microstructure with initial spherical particle size $4.5\,\mu m$ 180

4.9 Comparison between numerical (Al vs V diffusing elements) and experimental data [40] for a heat treatment consisting of a cooling at $11°C/min$ starting from $955°C$. Equiaxed microstructure with initial spherical particle size $4.5\,\mu m$ 181

4.10 Comparison between numerical (Al vs V diffusing elements) and experimental data [40] for a heat treatment consisting of a cooling at $11°C/min$ starting from $955°C$. Equiaxed microstructure with initial spherical particle size $4.5\,\mu m$ 182

4.11 Comparison between the different growth kinetics of an equiaxed microstructure resulting from an initial different spherical particle size. Soaking temperature $955°C$ then cooling at $11°C/min$. Vanadium considered as diffusing element 183

4.12 Lambda as a function of temperature considering Aluminium as the diffusing element. Heat treatment consisting of a cooling at $11°C/min$ starting from a soaking temperature of $955°C$. Equiaxed microstructure with initial spherical particle size $4.5\,\mu m$ 183

4.13 Lambda as a function of temperature considering Vanadium as diffusing element. Heat treatment consisting of a cooling at $11°C/min$ starting from a soaking temperature of $955°C$. Equiaxed microstructure with initial spherical particle size $4.5\,\mu m$ 184

4.14 Matrix Vanadium concentration for the growth of spherical alpha precipitate as a function of the time and distance from the particle interface (initial particle radius $4.5\,\mu m$) for the heat treatment consisting of cooling at $42°C/min$ starting from $955\,°C$ (case of figure 4.9) 184

4.15 Vanadium concentration in the matrix as a function of the distance from the precipitate interface at 1 and 13 seconds (figure a and figure b respectively) from the beginning of the heat treatment reported in figure 4.14, corresponding respectively to 954 °C and 945.9 °C 185

4.16 Vanadium concentration in the matrix as a function of the distance from the precipitate interface at 15 and 17 (figure a and figure b respectively) seconds from the beginning of the heat treatment reported in figure 4.14, corresponding respectively to 944.5 °C and 943 °C. It is possible to notice the inversion of the Vanadium concentration field that makes the precipitate grow after an initial dissolution 186

4.17 Vanadium concentration in the matrix as a function of the distance from the precipitate interface at 100 and 364 (figure a and figure b respectively) seconds from the beginning of the heat treatment reported in figure 4.14, corresponding respectively to 885 °C and 700 °C 187

4.18 Lamellar microstructure comparisons between the numerical model considering Vanadium as diffusing element and the experimental measurements at the heating rate of 5 °C/s. a) Lamellae thickness, b) volume fraction lamellar microstructure 190

4.19 Lamellar microstructure comparisons between the numerical model considering Vanadium as diffusing element and the experimental measurements at the heating rate of 50 °C/s. a) Lamellae thickness, b) volume fraction lamellar microstructure 191

4.20 Lamellar microstructure comparisons between the numerical model considering Vanadium as diffusing element and the experimental measurements at the heating rate of 500 °C/s. a) Lamellae thickness, b) volume fraction lamellar microstructure 192

4.21 Beta grain dimension data used for the calculation of the grain growth equation parameters. They are the same as figure 3.41 with estimated points at 1600 °C 194

4.22 Comparison between experimental data and numerical model prediction of the beta grain growth at different heating rates 195

4.23 Beta transus temperature predictions as a function of the heating rate and chemical composition 197
4.24 Beta grain growth predictions as a function of temperature and heating rates 198
4.25 Graph showing the experimental data compared to the predictions obtained applying the equation 4.48 200
4.26 Lamellae thickness predicted as a function of the cooling rate and beta grain radius 201
4.27 Martensitic phase fraction as a function of cooling rate. Comparison between model predictions and experimental data 202
4.28 Needle thickness as a function of the cooling rate. Experimental data (points) and interpolating function (green line) 203
4.29 Graph showing the Ti-6Al-4V thermal conductivity as a function of temperature used for the numerical simulations in Visual-Weld 205
4.30 Graph showing the Ti-6Al-4V specific heat as a function of the temperature used for the numerical simulations in Visual-Weld. Since the variation of this dimension, in correspondence of the liquidus temperature, was too high for the numerical convergence of the numerical simulations, the latent heat of melting has been spread out on a wider range of temperatures 206
4.31 Graph showing the Ti-6Al-4V density as a function of the temperature used for the numerical simulations in Visual-Weld 207
4.32 Mesh used for the welding simulations in Visual-Weld, made of 201,520 quad linear elements 208
4.33 Zoom close to the weld trajectory (green line) of the mesh shown in figure 4.32. Along the thickness, close to the weld line, 24 elements have been used, passing then progressively to 6 going farther from it 208
4.34 Convection coefficient as a function of the difference of temperature between the workpiece and ambient temperature assumed at 20 ^{o}C (private communication from prof Jeffery Brooks) 209

4.35 Experimental (top) and numerical (bottom) weld pool fusion zones for the Ti-6Al-4V plate with initial equiaxed microstructure 2.00 mm thick, welded with a speed of 2 m/min and 60% power ($2.4\,kW$). The fusion zone is bounded in the micrograph by blue lines. In the FE model, the grey colour shows locations where the maximum temperature during the welding simulation passed 1650 °C (melting temperature), representing thus the fusion zone. In the micrograph, depths and widths used for the fitting of the numerical heat source parameters are shown 211

4.36 Comparison of the weld pool shape between numerical and experiment results of the Ti-6Al-4V plate 2 mm thick with initial equiaxed microstructure (figure 4.35). Only one half is shown as the shape of the weld pool is assumed to be symmetric 212

4.37 Experimental (top) and numerical (bottom) weld pool fusion zones for the Ti-6Al-4V plate with lamellar microstructure 3.76 mm thick, welded with a speed of 2 m/min and 70% power ($2.8\,kW$). The fusion zone is bounded in the micrograph by blue lines. In the FE model, the grey colour shows locations where the maximum temperature during the welding simulation passed 1650 °C (melting temperature), represents thus the fusion zone. In the micrograph, depths and widths used for the fitting of the numerical heat source parameters are shown. At half depth of the weld pool, also the beta grains around the heat affected zone are highlighted 213

4.38 Comparison of the weld pool shape between numerical and experiment results of the Ti-6Al-4V plate 3.76 mm thick with lamellar microstructure (figure 4.37). Only one half is shown as the shape of the weld pool is assumed to be symmetric 214

4.39 Experimental (top) and numerical (bottom) weld pool fusion zones for the Ti-6Al-4V plate with lamellar microstructure 3.06 mm thick, welded with a speed of 2 m/min and 70% power (2.8 kW). The fusion zone is bounded in the micrograph by blue lines. In the FE model, the grey colour shows locations where the maximum temperature during the welding simulation passed 1650 °C (melting temperature), and represents the fusion zone of the numerical model. In the micrograph (top), depths and widths used for the fitting of the numerical heat source parameters are shown. At half depth of the weld pool, also the beta grains around the heat affected zone are highlighted 215

4.40 Comparison of the weld pool shape between numerical and experiment results of the Ti-6Al-4V plate 3.06 mm thick with lamellar microstructure (figure 4.39). Only one half is shown as the shape of the weld pool is assumed to be symmetric 216

4.41 Comprehensive numerical model flow chart for the description of the microstructure evolution in welding simulations 217

4.42 Diffusion based model flow chart for the description of the alpha particle growth/shrinkage 218

4.43 Comparison between experimental measured temperatures and numerical results, for the Ti-6Al-4V plate with initial equiaxed microstructure and 2.00 mm thick. In a) and b) the same trends are reported but with different x scales. The different lines make reference to the temperatures measured at a series of distances from the weld line, in the experimental and numerical case 221

4.44 Comparison between experimental measured temperatures and numerical ones, for the Ti-6Al-4V plate with initial lamellar microstructure and 3.76 mm thick. In a) and b) the same trends are reported but with different x scales. The different lines make reference to the temperatures measured at a series of distances from the weld line, in the experimental and numerical case 222

4.45 Comparison between experimental measured temperatures and numerical ones, for the Ti-6Al-4V plate with initial lamellar microstructure and 3.06 mm thick. In a) and b) the same trends are reported but with different x scales. The different lines make reference to the temperatures measured at a series of distances from the weld line, in the experimental and numerical case 223

4.46 Ti-6Al-4V plate 2.0 mm thick with initial equiaxed microstructure. Comparison between the mean alpha equiaxed radius predicted by the numerical model and the one experimentally measured for different distances from the weld line 225

4.47 Ti-6Al-4V plate 2.0 mm thick with initial equiaxed microstructure. Comparison between the mean martensitic needle thickness predicted by the numerical model and the one experimentally measured for different distances from the weld line 225

4.48 Ti-6Al-4V plate 2.0 mm thick with initial equiaxed microstructure. Comparison between the mean beta grain radius predicted by the numerical model and the one experimentally measured for different distances from the weld line 226

4.49 Ti-6Al-4V plate 2.0 mm thick with initial equiaxed microstructure. Comparison between the equiaxed phase proportion predicted by the numerical model and the one experimentally measured for different distances from the weld line 227

4.50 Ti-6Al-4V plate 2.0 mm thick with initial equiaxed microstructure. Comparison between the martensitic phase predicted by the numerical model and the one experimentally measured for different distances from the weld line 227

4.51 Ti-6Al-4V plate 2.0 mm thick with initial equiaxed microstructure. Comparison between the beta phase proportion predicted by the numerical model and the one experimentally measured for different distances from the weld line 228

4.52 Ti-6Al-4V plates with initial lamellar microstructure, a) 3.75 mm thick and b) 3.06 mm thick. Comparison between the mean alpha lamellae thickness predicted by the numerical model and the one experimentally measured for different distances from the weld line 229

4.53 Ti-6Al-4V plates with initial lamellar microstructure, a) 3.75 mm thick and b) 3.06 mm thick. Comparison between the mean martensitic needles thickness predicted by the numerical model and the one experimentally measured for different distances from the weld line 231

4.54 Ti-6Al-4V plates with initial lamellar microstructure, a) 3.75 mm thick and b) 3.06 mm thick. Comparison between the mean beta grain dimension in the HAZ zone predicted by the numerical model and the one experimentally measured for different distances from the weld line 233

4.55 Beta grain distribution in the location around 0.8 mm far from the weld line for the Ti-6Al-4V plate with initial lamellar microstructure and 3.75 mm thick 234

4.56 Beta transus temperature and nucleation beta grains temperature as a function of the heating used for welding simulations of Ti-6Al-4V. The x axis represents the heating rate $\frac{dT}{dt}$ 235

4.57 Ti-6Al-4V plates with initial lamellar microstructure, a) 3.75 mm thick and b) 3.06 mm thick. Comparison between the alpha lamellar phase proportion predicted by the numerical model and the one experimentally measured for different distances from the weld line 236

4.58 Ti-6Al-4V plates with initial lamellar microstructure, a) 3.75 mm thick and b) 3.06 mm thick. Comparison between the martensitic phase proprtion predicted by the numerical model and the one experimentally measured for different distances from the weld line 237

4.59 Ti-6Al-4V plates with initial lamellar microstructure, a) 3.75 mm thick and b) 3.06 mm thick. Comparison between the beta phase proportion predicted by the numerical model and the one experimentally measured for different distances from the weld line 238

4.60 Temperature and phase proportions used as input data for the prediction of the stress-strain curve shown in figure 4.62. In this figure the first 30 seconds of data obtained from a welding simulation with a total duration of 800 seconds are shown, to highlight the area of the chart where variations of phase proportions occur 241

4.61 Temperature and and particle sizes used as input for the prediction of the stress-strain curve shown in figure 4.62. In this figure the first 30 seconds of data obtained from a welding simulation with a total duration of 800 seconds are shown, to highlight the area of the chart where variations of particle sizes occur 242

4.62 Stress-strain curve predicted by the mechanical model for the temperature, phase proportions and particle sizes shown in figure 4.60, 4.61 and strain rate of 0.001 s^{-1}. The section relative to the first 30 seconds of computation covers strains up to 0.007 243

5.1 Experimental (top) and numerical (centre) weld pool fusion zones for the 2 mm thick Ti-6Al-4V plate with initial equiaxed microstructure, welded with a speed of 2 m/min and 60% power (plate 1 in table 5.1). The fusion zone is bounded in the micrograph by blue lines whilst it is identified by the grey color in the FE model (see figure 4.36 for dimensional comparison). The bottom picture shows the α equiaxed phase proportion obtained for the same section of material, at the end of the FE simulation 253

5.2 β phase proportion (top), martensitic phase proportion (centre) and radius [μm] of the α equiaxed microstructure (bottom) obtained running the FE welding simulation with conditions described in figure 5.1 (plate 1 in table 5.1) 254

5.3 Martensitic needles thickness [μm] (top) and beta grain radius [μm] obtained running the FE welding simulation with conditions described in figure 5.1 (plate 1 in table 5.1) 255

5.4 Experimental (top) and numerical (centre) weld pool fusion zones for the 3.76 mm thick Ti-6Al-4V plate with initial lamellar microstructure, welded with a speed of 2.0 m/min and 70% power (plate 2 in table 5.1). The fusion zone is bounded in the micrograph by blue lines whilst it is identified by the grey color in the FE model (see figure 4.38 for dimensional comparison). The bottom picture shows the β phase proportion obtained for the same section of material, at the end of the FE simulation 256

5.5 Lamellar α phase proportion (top), martensitic phase proportion (centre) and lamellar thickness [μm] of the alpha lamellar microstructure (bottom) obtained running the FE welding simulation with conditions described in figure 5.4 (plate 2 in table 5.1) 257

5.6 Martensitic needles thickness [μm] (top) and beta grain radius [μm] obtained running the FE welding simulation with conditions described in figure 5.4 (plate 2 in table 5.1) 258

5.7 Experimental (top) and numerical (centre) weld pool fusion zones for the 3.06 mm thick Ti-6Al-4V plate with initial lamellar microstructure, welded with a speed of 2.0 m/min and 70% power (plate 3 in table 5.1). The fusion zone is bounded in the micrograph by blue lines whilst it is identified by the grey color in the FE model (see figure 4.40 for dimensional comparison). The bottom picture shows the β phase proportion obtained for the same section of material, at the end of the FE simulation 259

5.8 Lamellar α phase proportion (top), martensitic phase proportion (centre) and lamellar thickness $[\mu m]$ of the alpha lamellar microstructure (bottom) obtained running the FE welding simulation with conditions described in figure 5.7 (plate 3 in table 5.1) 260

5.9 Martensitic needles thickness $[\mu m]$ (top) and beta grain radius $[\mu m]$ obtained running the FE welding simulation with conditions described in figure 5.7 (plate 3 in table 5.1) 261

A.1 DEFORM a) tensile numerical model and b) compression numerical model 283

A.2 To evaluate the temperature distribution across the thickness of the Ti-6Al-4V tensile samples, points in two different sections were sampled. P1, P2 and P3 were sampled in the centre of the sample and P4, P5 and P6 were sampled at 8 mm far from the centre 285

A.3 To evaluate the temperature distribution along the longitudinal direction of Ti-6Al-4V tensile samples, points from P1 to P19 were sampled 285

A.4 Temperature trends along the thickness of the Ti-6Al-4V tensile Gleeble samples, applying a voltage potential of 1V (a) and 2V (b). Temperatures relative to the points P1, P2 and P3 are all in the upper group of lines, vice versa for points P4, P5 and P6. See figure A.2 for locations of the points P1, P2, P3, P4, P5 and P6 286

A.5 Temperature trends along the longitudinal direction of the Ti-6Al-4V tensile Gleeble samples, applying a voltage potential of 1V (a) and 2V (b). The trends are not symmetrical because of a not a perfectly symmetrical mesh. See figure A.3 for location of the sampled points: distance 0 is relative to the point P1 287

A.6 Modelled temperature trends across the thickness of the Ti-6Al-4V tensile Gleeble samples, during cooling. Temperatures relative to the points P1, P2 and P3 are all in the upper group of lines, vice versa for points P4, P5 and P6. See figure A.2 for locations of the points P1, P2, P3, P4, P5 and P6 289

A.7 Section view of the Gleeble compression model. To evaluate the temperature distribution across the thickness of the tensile samples, the points P1, P2 and P3 were sampled in the centre of the sample 290

A.8 Modelled temperature distribution across the thickness of the compression sample. The points at which the temperatures make reference are the ones shown in figure A.7 290

A.9 Longitudinal temperature distribution in the modelled numerical compression sample 291

B.1 Montage of the sections taken at the optical microscope for the sample tested at a heating rate of 5 °C/s till 1260 °C then water quenched. The irregular surface close to the vertical hole is due to the spot welding of thermocouples in that area 293

B.2 Montage of the sections taken at the optical microscope for the sample tested at a heating rate of 5 °C/s till 1188 °C then water quenched 294

B.3 Montage of the sections taken at the optical microscope for the sample tested at a heating rate of 5 °C/s till 996 °C then water quenched. At this peak temperature, and magnification, the original morphology is not visible anymore (figure B.4) as beta grains have taken is place 295

B.4 Montage of the sections taken at the optical microscope for the sample tested at a heating rate of 5 °C/s till 996 °C then water quenched. At this peak temperature the original morphology is still visible, with elongated parent beta grains where lamellae are grown 296

B.5 Montage of the sections taken at the optical microscope for the sample tested at a heating rate of 50 °C/s till 1240 °C then water quenched 297

B.6 Montage of the sections taken at the optical microscope for the sample tested at a heating rate of 50 °C/s till 1160 °C then water quenched 298

B.7 Montage of the sections taken at the optical microscope for the sample tested at a heating rate of 500 °C/s till 1164 °C then water quenched . . . 299

B.8 Montage of the sections taken at the optical microscope for the sample tested at a heating rate of 500 °C/s till 1123 °C then water quenched . . . 300

C.1 Welding assembly designed for displacement measurements during and after a welding test. The two pictures show views from two opposite sides. 303

C.2 Chewing gum + contact elements adopted to model the contact of two butts to be welded 306

C.3 Chewing gum + contact spring elements adopted to model the contact of two butts to be welded. The spring contact elements are represented by blue lines connecting the sides of the chewing gum section 307

C.4 Model used for the first numerical investigation on the response of the different techniques adopted to model the contact of the butts 308

C.5 Displacements sampled in the right side of the model shown in figure C.4. Type 6 represents the nomenclature for spring contact elements used in Visual-Weld whilst “Cont” is for contact elements. The blue data are relative to the case where the junction is not modelled 308

C.6 Displacements sampled in the centre of the model shown in figure C.4. "Type 6" represents the nomenclature for spring contact elements used in Visual-Weld whilst "Contact" is for contact elements. At 100 seconds the right side of the model is unclamped 309

D.1 Drawing of the model considered for the weld sequence optimization study 312

D.2 Mesh of the model studied for the weld sequence optimization. The 4 sub-welds constituent the weld sequence to be optimized are shown. For each of them it is possible to choose the direction, clockwise direction is identified by the positive sign vice versa for the anti-clockwise direction 313

D.3 Model mesh. The area where the number of elements is not changed during the mesh sensitivity study is highlighted by the red square 315

D.4 Section view of figure D.3: in the right side of the red line the mesh density is kept constant whilst in the left side the number of elements through the thickness of the body is changed for the mesh sensitivity study 316

D.5 Point sampled for the mechanical analysis. The coordinate system used for the displacement measurement is shown in the bottom left side 317

D.6 Mesh sensitivity study: displacements along X-Y-Z directions measured in the point highlighted in figure D.5 changing the number of elements through the thickness (figure D.4) 318

D.7 Mesh sensitivity study: zoom of the chart reported in figure D.6 319

D.8 Mesh sensitivity study. Light blue rhombus represent the trend of the displacement along the z coordinate at 250 s as a function of the number of elements through the thickness. Red squares represent the difference percentage between the various displacements, referred to the value registered for the case with 2 elements through the thickness 320

D.9 Flow chart of the 1^{st} algorithm 322

D.10 First screen shot of the DOE algorithm used to get an initial list of sequences to analyse, in particular this case would be useful to study the system shown in figure D.2 . In the red rectangle, the number of occurences for the weld shown at the left side of each row, for each position withn the sequences, is reported 323

D.11 Second screen shoot of the DOE algorithm. In the black rectangle, the couples of all the welds formed within the list of sequences suggested by the DOE algorithm if figure D.10 is shown D.10 324

D.12 Displacement measured along Y direction for the sequence -3,2,1,4 in the point shown in figure D.5 325

D.13 Flow chart of the 3^{rd} algorithm 329

D.14 Screen shoot of the program for the calculation of the distortion using the surrogate model 330

D.15 Results obtained doing a FE analysis for the sequence suggested by the program reported in figure D.14 330

E.1 Dislocations glide until they find an obstacle. At this point they climb it until they can return to their gliding direction 333

E.2 The backstress allows the stress calculated at the interface between particle-matrix to be related to the stress applied to the matrix or to the particle . 337

List of Tables

2.1 a) Classification of U.S. technical Titanium multicomponent alloys [12]; b) British technical commercial alloys [12] 19

2.2 Nominal composition of a Ti-6Al-4V ELI and chemical composition of the relative α and β phases measured by micro probe analysis in [19] 20

2.3 Microstructural parameters measured for different cooling rates applied to the same initial structure of Ti-6Al-4V, after soak at 1050 $^{\circ}C$. From left to right: cooling rate and microstructure obtained, mean β-prior grain size, mean α Widmanstätten plates thickness and mean α Widmanstätten colonies size [25] 38

2.4 Strength measured for the different platelet thickness described in table 2.3 [25] 38

2.5 Mean platelet thickness (μm) at different hot working conditions (temperatures and strain rates) of a Ti-6Al-4V alloy. Numbers in parentheses represent the thickness of the martensitic platelet. Values under "P" column are referred to the platelet thickness formed before the quenching following the hot deformation process (compression at strain rates of 0.05 s^{-1}, 0.1 s^{-1}, 0.5 s^{-1} and 1.0 s^{-1}), values under column "S" are platelet thicknesses formed after the quenching following the hot deformation process. Under the column "Heat-treated" the mean values of the platelet thickness obtained without hot deformation processing are reported [26] 40

2.6 Platelet thickness measured for three different Ti-6Al-4V microstructures (A: 1040°C/1h + water quench; B: 1065°C/5min+940°C/5min+815°C/15min + air cool; C: 1040 °C/1h+ furnace cool to T_{amb}+970 °C/4h+ furnace cool to T_{amb}) at 815, 900 and 955 °C [31] 48

2.7 Morphological characterization of the microstructure obtained in the fusion zone of an electron beam process on a Ti-6Al-4V plate of 2.3 mm thickness [35] 54

2.8 Microstructural parameters measured in EB and TIG welding processes of a Ti-6Al-4V 6mm thick plate, "GB" is for grain boundary [41] 56

3.1 Welding operative parameters used for welding tests. Ti-6l-4V plates with two different initial microstructures and different thicknesses were welded, using welding speeds of 2.0 or 1.5 m/min. The welding input power was set as percentage of the maximum power (4 kW) of the welding machine used 114

4.1 Parameters obtained from the current work by fitting equation 4.39 to the experimental results shown in figure 3.41 194

5.1 Welding test parameters used to run FE welding simulations. Experimental welding tests with the same conditions were carried out to validate the numerical models (chapter 3). Ti-6l-4V plates with two different initial microstructures, chemical compositions and different thicknesses were welded, using a welding speed of 2.0 m/min. The welding input power was set as percentage of the maximum power (4 kW) of the welding machine used . . 252

D.1 Example of a minimum number of sequences for a case of 4 welds in which it is possible to choose only one direction (+). The two condition "all welds coupled with all other welds" and "good distribution of every weld in every position" are satisfied 317

D.2 Results obtained running a FE analysis on the list of sequences shown in figure D.10. Starting from the first column on the left the following information is reported: the sequence analyzed, the Δdisplacement measured for each weld into the sequence and due to the cooling and finally the final deformation obtained by the algebraic sum of the previous contributions. Saving the table as format "csv", these data can be readable by the 3^{rd} algorithm 326

Nomenclature

A	Constant in the beta grain growth equation
B	Constant in the beta grain growth equation
C_0	Overall solute concentration
C_α	Concentration in the alpha phase
C	Solute concentration
C_I	Solute concentration in the matrix-particle interface at the matrix side
C_M	Solute concentration in the matrix
C_P	Solute concentration in the matrix-particle interface at the particle side
d_0	Initial diameter
D_A^*	Intrinsic diffusivity of element A
D_{Al}^β	Intrinsic diffusivity of Aluminium in the beta phase
D_B^*	Intrinsic diffusivity of element B
D	Diffusion coefficient
d	Diameter
D_V^β	Intrinsic diffusivity of Vanadium in the beta phase

E Activation energy in the JMA equation for isochronal conditions

f_i Fraction of i-phase

f_α Alpha phase fraction

$f_{\alpha 0}$ Initial alpha phase fraction

G^0 Gibbs free energy of a mechanical mixture of the constituents of the phase

$G0_x^{BCC}$ Gibbs free energy of the pure element x in the BCC phase

G Gibbs free energy

G^{ideal} Entropy of mixing for an indeal solution

G^{xs} Excess Gibbs free energy

J Constant in the JMA equation for isochronal conditions

k_0 Pre-exponential factor in the JMA equation for isochronal conditions

k_i Coefficient dependent on the temperature, composition of parent phase, and grain size for the calculation of the fraction of i-phase f_i

k_s Hall-Petch constant

m_i Coefficient dependent on the type of phase transformation and grain growth, for the calculation of the fraction of i-phase f_i

L Lorentz number

l Platelet thickness

M Taylor factor

n Constant in the grain growth equation

$\overline{P_i}$ Equilibrium phase proportion of phase i

$P_{j\to i}$ Phase proportion in the transformation from phase j to i

p Exponential constant in the JMA equation for isochronal conditions

Q Activation energy

R_0 Initial radius

F Thermodynamic correction factor

R Radius

r Radius considered in the calculation

S_0 Initial lamellae thickness

s Constant in the JMA equation form used in Visual-Weld

t_i^* Fictitious time

$T_{\beta\phi}$ Beta transus temperature at a specific temperature rate ϕ

$\dot{T}$ Temperature derivative respect the time

T_f Finish temperature

TR Shift time constant in the JMA equation form used in Visual-Weld

T_i Starting temperature

T_{Ms} Start temperature of martensitic transformation

T Temperature

t Time

V_e Equivalent volume lamellae

X_A mol fraction of the element A

X_B mol fraction of the element B

x x position along the lamellae thickness considered in the calculation

y_a Volume fraction of the material that can be converted to martensite

X Ellipsoid half length minor axis

Y Ellipsoid half length major axis

y Volume fraction of martensite

D_{Ti}^{β} Intrinsic diffusivity of Titanium in the beta phase

α Alpha phase

β Beta phase

δ Dimensionless parameter in the lamellar growth equation

ΔT_{β} Variation of the beta transus temperature respect a reference alloy

Δt Delta time

Γ Aspect ratio lamellae

κ Constant in the Koistinen equation

λ_T Thermal conductivity

λ Parameter related to the supersaturation in the diffusion based model

Ω Supersaturation

Φ Temperature rate

ρ_{el} Electrical resistivity

$\overline{\sigma_{ss}}$ Steady state stress

$\Delta\overline{\sigma_h}$ Softening term due to the deformation heating

$\overline{\sigma_p}$ Peak stress

τ_0 Friction lattice stress

Υ Gas constant

CHAPTER 1

Introduction and objectives

Titanium and titanium alloys are excellent candidates for high performance applications; e.g. many aerospace structures —airframes, skin, and engine components— have benefited from the introduction of Titanium (figure 1.1), where the reduced weight and increased performance permit lower fuel consumption and emissions, factors which are becoming increasingly important [42]. Besides the choice of the right alloy, an important aspect of the manufacturing process is the selection of the method for joining pieces of material. Welding can produce components that are lighter and have better cost and structural integrity than other methods can (e.g. rivetting) [43], in particular high energy welding processes, such as laser beam welding (LBW) and electron beam welding (EBW), offer shorter part-cycles time (3 times faster) and better overall assembled part quality (smaller distortions, repeatability) than conventional welding processes (e.g. TIG, MIG, spot welding). Their capability to focus onto a small area a beam with high energy density allows the surface of the material to be brought quickly to the melting temperature, reducing the interaction time between beam and material, thus decreasing the heat introduced into the component which will produce a narrow heat affected zone and small deformations. Though high energy welding processes have generally a higher capital cost than conventional welding processes, they represent a competitive choice in sectors where requirements of high quality and productivity (e.g. aerospace and automotive, figure 1.2)

balance the initial higher investment [44, 45, 46]. Nevertheless, in order to produce a welded joint with excellent properties, it can be necessary to consider fields including mechanics, metallurgy and fluid dynamics to investigate and optimize the process.

The equations describing these phenomena, and the behaviour of many materials, are so complex that simple analytical solutions are typically insufficient to predict the behaviour of a welding process with sufficient accuracy to ensure the performance of the resulting joint [43]. In particular, the mechanical properties of materials are typically strongly dependent upon their microstructure, and the ways in which microstructure changes in response to temperature and time are often complex. The need for more accurate solutions is being met by methods such as those in which a structure is broken down into smaller elements in which the governing equations are then solved numerically. Finite element methods are an example of this, and their increasing use over the past 50 years, helped by increasing computer power, gives users the chance to deeply analyse welding and other processes. One of the finite element (FE) software codes for the simulation of welding processes is "Visual-Weld", in which the default model of microstructural development is based on routines originally developed for steels [47, 48, 49, 50]. These microstructural predictions are then used to calculate the mechanical properties of the material which are then used in the elasto visco plastic models describing the weld behaviour. Despite this widespread use, it will be shown in this work that the numerical approaches currently used for the modelling of fusion welds in e.g. alpha-beta alloy Ti-6Al-4V have significant limitations. For a more accurate prediction of the mechanical behaviour of a Titanium alloy, in particular for the description of the variation of the strength of the material (which allows numerical simulations to predict the deformation of the component welded), besides the distribution of phases, it is necessary to predict also the morphology of the microstructures developed during the process (i.e. dimensions of spherical, lamellar and acicular particles). Moreover, it will be shown that using numerical physically based approaches, instead of conventional experimental ones, the model developed will be much more robust, self-adapting to different chemical compositions and initial micro-

structures of Ti-6Al-4V, not needing any fitting parameter. Such models, even if based on more complex equations and thus requiring higher efforts for their development, will not require additional experiments for their calibration when new initial conditions of the material have to be investigated, saving additional costs and time to the final user. As a disadvantage, more complex equations will require longer computational times.

Therefore the aim of this project is to develop improved methods for numerical modelling, by finite element analysis, of the metallurgical and mechanical behaviour of Ti-6Al-4V when subjected to a high energy density welding process. In particular the current multiphase code of Visual-Weld will be examined and if necessary extended, focusing on the description and prediction of the different morphologies of microstructure obtainable in the material and relating them to their stress-strain relationships. The industrial nature of Visual-Weld has to be maintained, in particular the code developed has to return results in reasonable running times and the user must be able both to set up a FE welding simulation without a background in metallurgy and to check the results by using the graphical interface of the software. The project will be focused on: a) describing the evolution of the geometry of the microstructural particles, using a diffusion-based approach where possible or a more empirical method when the complexity of the process makes this necessary; b) describing the strength of the material by dislocation-based approaches dependent on the microstructure from (a). To the best knowledge of the author, the work available in literature on modelling of microstructural evolution in Ti-6Al-4V at this fundamental level is currently centred on forging, with significantly different thermal and mechanical working conditions from welding processes. For validation, a comparison will be made between numerical and experimental results of high energy density welding processes on Ti-6Al-4V plates of different thicknesses, with different thermal loads. The welding experiments will be carried out by using a LBW machine (Trumpf TLC1005) available in University of Birmingham.

Along the main project some minor tasks associated with welding, but not directly related to the material modelling, have been carried out. These topics are:

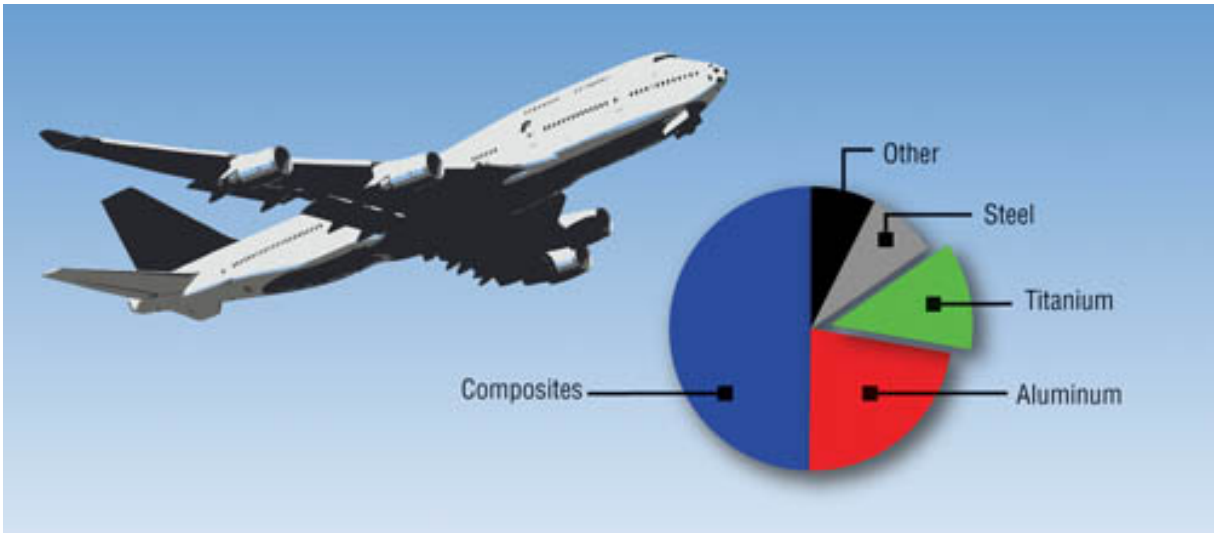

Figure 1.1.: Representative chart of the percentage of titanium alloys usage in the Boeing 787 Dreamliner [1, 2]

(1) How the condition of contact in a butt-joint weld should be modelled numerically, and whether the choice of representation significantly affects the accuracy of the model.

(2) How to most effectively predict the final properties (e.g. distortion at a point) from a sequence of welds. This is extremely computationally expensive, as typically there are many possible orders in which the welds could be done. Therefore a method for predicting the outcomes of some sequences without having to do full models of every welding stage would be extremely valuable.

In the author's opinion, they could present starting points for future research work, deserving a mention in the appendices.

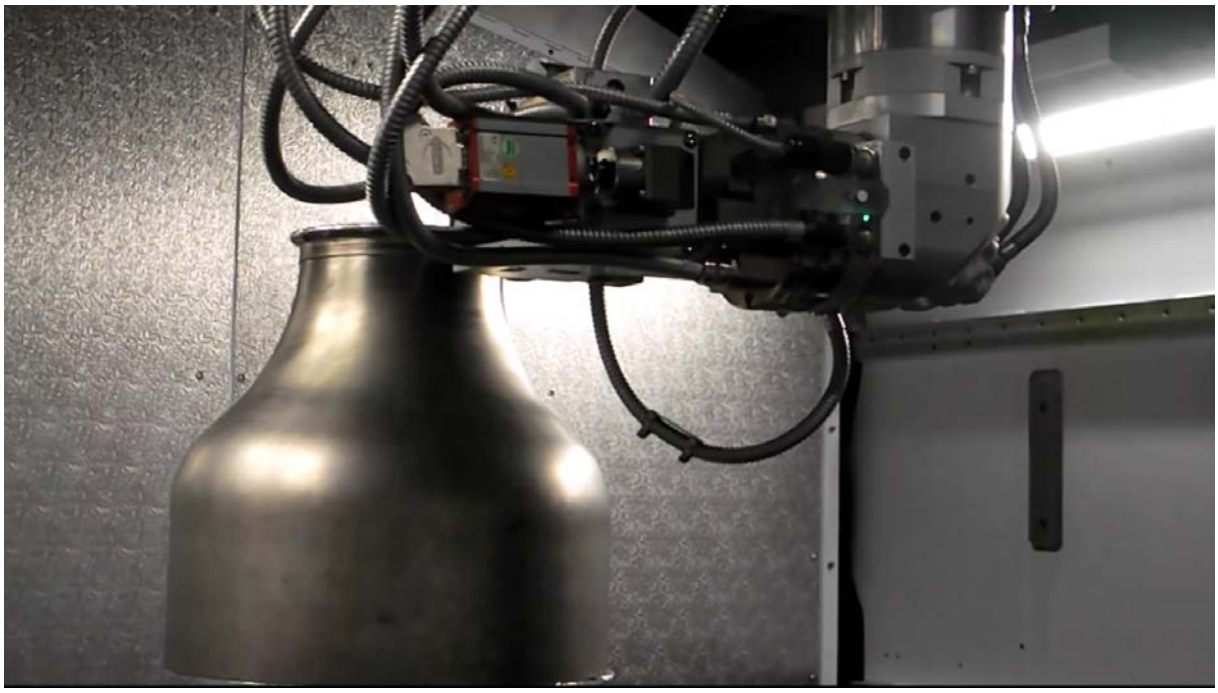

Figure 1.2.: 5 axis laser welding of a titanium duct for aerospace [3]

CHAPTER 2

Literature review

2.1 Introduction

The literature review, after a short introduction on the classification of the welding processes, making a comparison between all of them, identifies the problems of the numerical computation of such processes.

The classical approach of computational welding mechanics is then introduced, as solution adopted in this project, such to simplify the description of certain physical aspects on which the present work is not focused on.

By the classical approach of computation welding mechanics, the welding torch is simplified by a fictitious heat source, calibrated on the thermal profile experimentally measured during a welding process. In this regard, the most relevant solutions found in literature, to numerically schematise the heat source, are reviewed.

Successively, the attention is moved to the constitutive phases and microstructural morphology evolution of Ti-6Al-4V during heating and cooling, the two thermal loads characterizing a welding process. The current literature work to numerically model the metallurgical behaviour of the material is then investigated.

Finally, the most interesting approaches to describe the strength of Ti-6Al-4V are reviewed, putting major attention on the dislocation based ones, where the mechanical

response is directly related to the microstructural morphology of the material.

The chapter ends mentioning surrogate models techniques, adopted to optimize weld sequences, problem investigated in the first year of the PhD and discussed in appendix D.

2.2 Welding

2.2.1 Introduction

Welding processes, identified as processes of permanent junction of two workpieces, are subdivided in two main families:

- autogenous when the butts of the parts are joined by direct melting
- non autogenous when an additional filler material is used.

Welding processes can also be classified by the intensity of the heat source used, as done for some of them in figure 2.1 [4]. For a list of all the welding processes see [51]. This ordering permits to understand the main characteristics of the high energy density fusion welding processes, precisely electron beam and laser beam, in relation to the other ones:

- very high penetration measured as the ratio of depth to width (d/w) given by a very high intensity of the heat source; this allows both a smaller melted volume of material to get the same penetration of other welding processes and higher welding speeds;
- high efficiency and small heat affected zone, resulting in a stronger weld and lower post-weld distortions;
- high capital cost of the equipment, roughly proportional to the intensity of the heat source.

EBW needs to operate under vacuum to control accurately the beam of electrons, contrarely to laser beam welding, which can operate in atmosphere except for special requirements due to the material to be welded (e.g. avoid oxidation). Generally, as reported in [52, 53], electron beam welding is preferred with respect to laser beam welding when:

- the completed assembly must be sealed with internal components under vacuum;
- weld penetrations exceed 1/2", as LBW cannot usually reach deeper penetrations;
- the material is challenging to initiate laser coupling (e.g. material with high refraction);
- when the weld must not be exposed to atmospheric conditions until it has cooled to an acceptable temperature.

Laser beam welding is instead preferred when:

- generation of X-rays is not desired (e.g. added capital cost for protections);
- shorter cycles times are required (EBW requires to have the chamber under vacuum, this produces waiting times not encountered in LBW);
- big components have to be welded (EBW is limited by the size of the vacuum chamber).

High energy density fusion welding processes, in general, are characterized by reaching in a zone of the material fused, the boiling temperature, generating the so-called "key hole". From a point of view of this work, this phenomenon is not taken in consideration (major details in the next section), but it gives the idea of which temperatures and gradient of temperatures affect the material.

2.2.2 Classical approach of computational welding mechanics

Effects of welding processes on materials are very complicated to study and model, they are sensitive to the close coupling between heat transfer, microstructure evolution and thermal stress analysis (figure 2.2) moreover, a complete description of many of them, should take in consideration also the magneto-hydrodynamics of the arc and the fluid flow of the weld pool, phenomena extremely complex to solve [54].

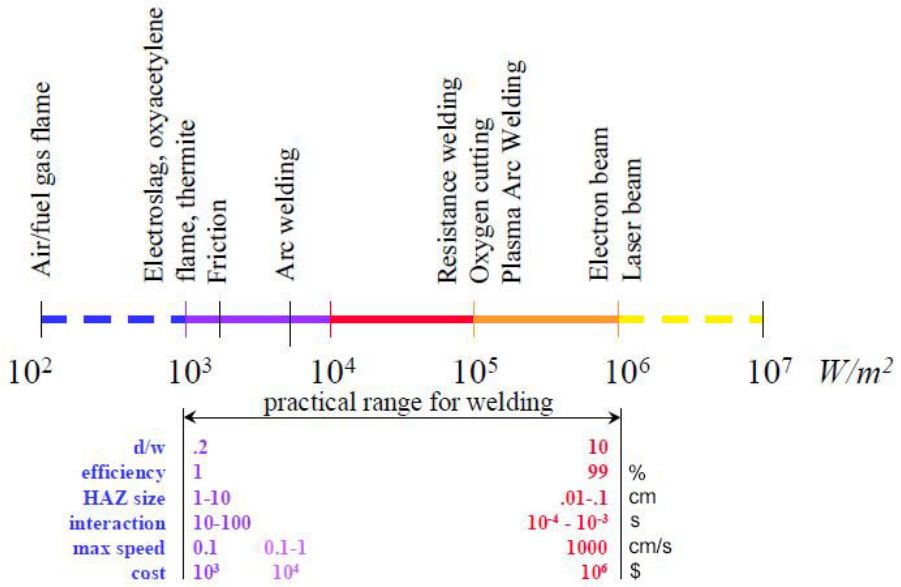

Figure 2.1.: Welding processes ranked according to heat source intensity, where d/w is the depth/width ratio of the weld pool, efficiency represents the amount of energy actually used to melt the material instead of preheating the surrounding, HAZ size is the heat affected zone size, interaction is the interaction time between heat source and material, max speed is the maximum speed allowed by the welding process and cost is the capital cost of the equipment[4]

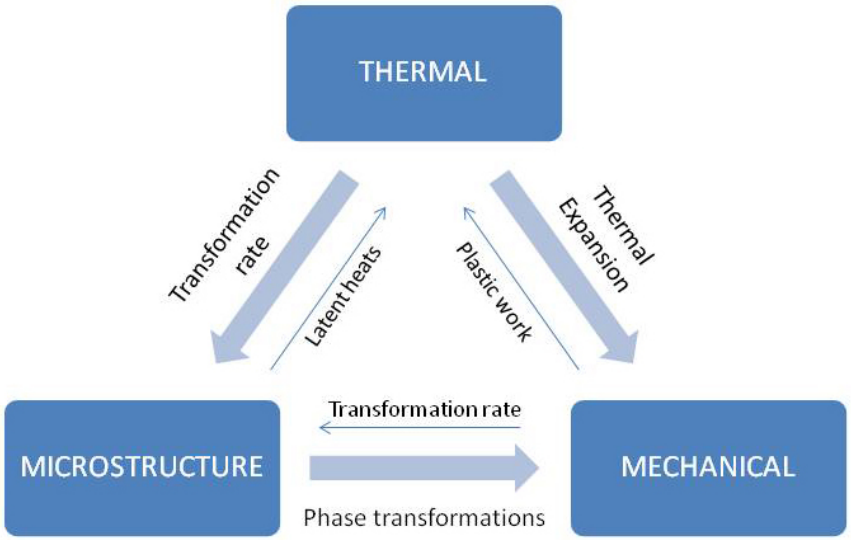

Figure 2.2.: Couplings in welding: the dominant ones are shown with bold lines, the secondary ones are shown with thin lines [5].

Since the aim of the present work is to describe and code numerically the effects generated by the heat source of a fusion welding process on the microstructure and residual stresses of the material, all phenomena related to the arc weld and fluid dynamics of the melted material, are schematised following the classical approach of computational welding mechanics. In this approach, once the thermal properties of the material are known, the heat input of the numerical model is calibrated using experiments, in general setting a simplified heat source to have the same cross-section geometry of the fusion zone in the numerical model (area where the temperature is higher than the T_{fusion} of the material) as in the experimental test (microstructural analysis). It is possible to further validate the numerical model through comparing the predicted temperature and experimentally measured temperatures using thermocouples positioned along the component [55]. This approach permits to get the same thermal load on the material between a hypothetical workpiece welded and its corresponded numerical model, as long as the measurements are sufficiently accurate, avoiding to describe the complexity of phenomena out of the aim of this work, as previously mentioned.

2.2.3 Heat sources

By the previous paragraph, a classical approach of computational welding mechanics needs:

- a prior knowledge of the weld pool shape and thermal properties of the material, thus reducing the predictive nature of the thermal solution;
- the description of the heat input by a schematised shape and distribution of the heat flux.

Regarding the first point, the shape of the weld pool is determined by experiments, essentially sectioning perpendicularly to the welding trajectory the material welded.

Depending on the welding process to be modelled, but also following a progressive development the research field of heat sources has met, different types of heat sources can

be listed from literature. Hereinafter follows a brief analysis of:

- Gaussian heat source [6];
- double ellipsoidal [7], optimized also to take into account arc deflection problems caused by different kind of interference [56];
- three-dimensional conical (TDC) [8];
- modified three-dimensional conical (MTDC) [8];
- nail head shape [9].

Figure 2.3 and 2.4 have been created to give a quick comparison between all of them, showing the heat distribution they describe and reporting indicatively the best kind of welding process they are suitable for.

A Gaussian heat source, represented by an axial symmetrical heat flux with a Gaussian distribution, is used in [6] to simulate gas tungsten arc welding (GTAW) of lead. The calculated penetration depths are in good agreement with the experimental data for low power levels ($325\,W$ and $650\,W$), whilst it becomes poor for higher power inputs ($2000\,W$) of the heat source. For the authors, this is because the heat source model is not able to take in account the effect of the fluid motion in the weld pool at high temperatures. Since this is one of the intrinsic limits of the classical approach of computational welding mechanics, it is believed that, a distribution of the heat also along the thickness of the work piece, instead of just on the top surface, would have been able to better describe the shape of high depth weld pools. This kind of heat source has been developed in the following years.

Goldak et al., in [7], proposed a double ellipsoidal three-dimensional heat source model, demonstrating the improved capability to analyse the thermal history of deep penetration welds like gas metal arc welding (GMAW), respect a two-dimensional Gaussian heat source. In this model, a Gaussian distribution of the heat is spread across a three-dimensional double ellipsoidal shape, along the thickness of the work piece (figure 2.3).

Type of heat source	Schematic representation	Description	Suitable for
Gaussian	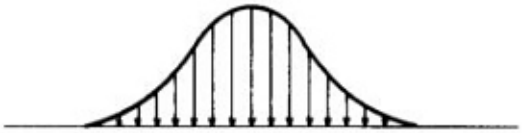	2D axial symmetrical heat flux (W/m^2) with Gaussian distribution	Surface treatments and shallow penetration arc welding
Double ellipsoidal	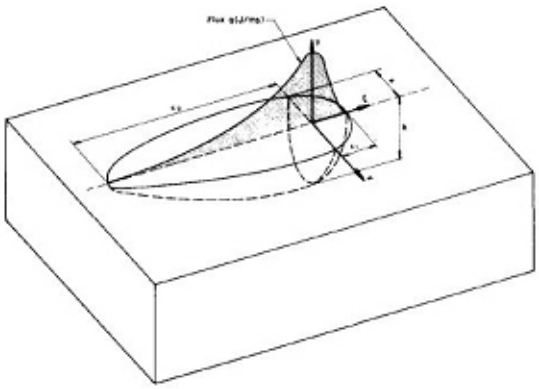	Volumetric heat source (W/m^3) constituted by 2 ellipsoids	Deep penetration welds as TIG but not for high density welding process
Three-dimensional conical (TDC)	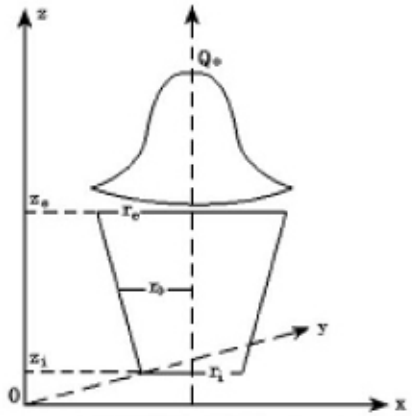	Volumetric heat source (W/m^3). Applies to every plane perpendicular to z-axis a Gaussian heat sources with different distribution parameters and the same central maximum value along the thickness of the work piece	High-density energy welding processes where a keyhole is typically generated
Modified three-dimensional conical (MTDC)	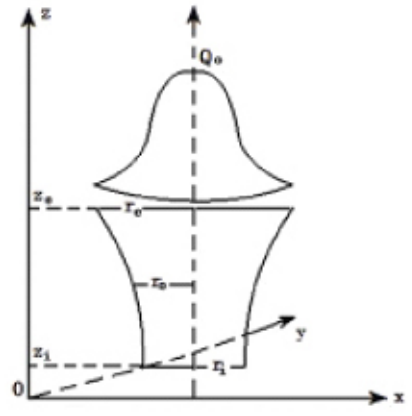	Improves the TDC model with a non-linear decay of the heat intensity along z-axis instead of a linear one	Same of TDC

Figure 2.3.: Schematic representation and description of the density power distribution of the Gaussian [6], Double ellipsoidal [7], TDC [8] and MTDC heat sources [8] used to describe the heat distribution in FE analysis of welding processes. Each heat source is suitable to describe a particular welding processes, which is described in the 4^{th} column

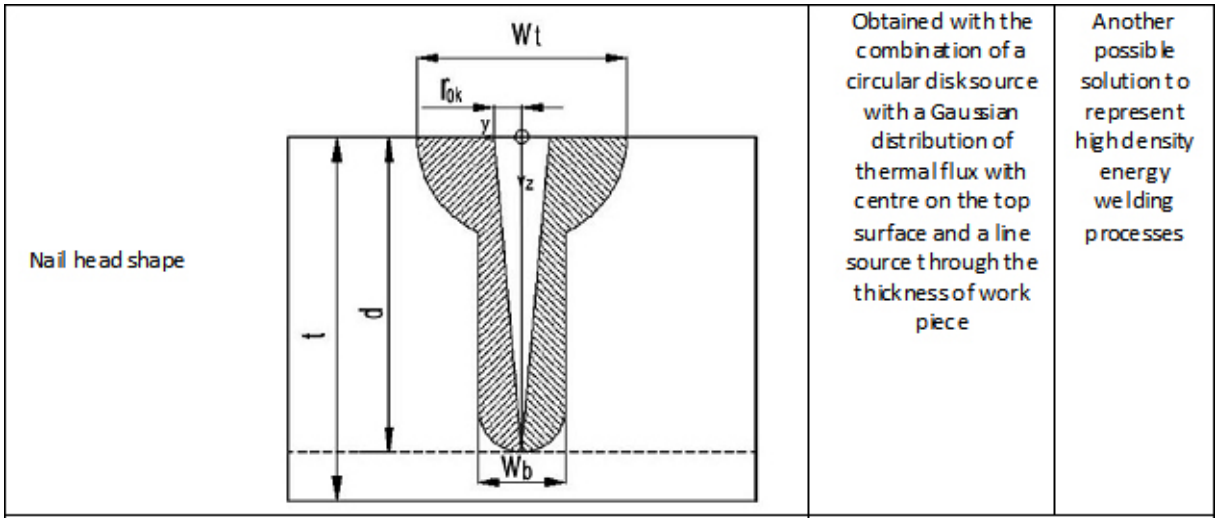

Figure 2.4.: Schematic representation and description of the density power distribution of the nail head heat source [9] used to describe the heat distribution in FE analysis of high energy density welding processes

However, when high energy density welding processes, with high ratio of the weld penetration to width want to be modelled, this heat source still shows limitations, not being able to describe the sharp weld pool shape in the opposite side to the application of the heat source. This is related to the exponential nature of the equation used for this model, that gives a rounded power distribution along the thickness of the workpiece.

Figure 2.5 shows an example of the power density distribution obtained coding a double ellipsoidal heat source in the commercial software package Matlab. For clarity, only a quarter of the heat source is shown. This picture shows clearly how high energy values are localized very close to the surface (y=0), with very rounded shapes as the depth increases (y<0).

For high energy density welding processes, TDC, MTDC or nail head heat sources have been used with better results. These models, as shown in figures 2.3 and 2.4, have in common the idea to describe higher power density distribution along the depth of the component welded, contrarily to the ones previously described.

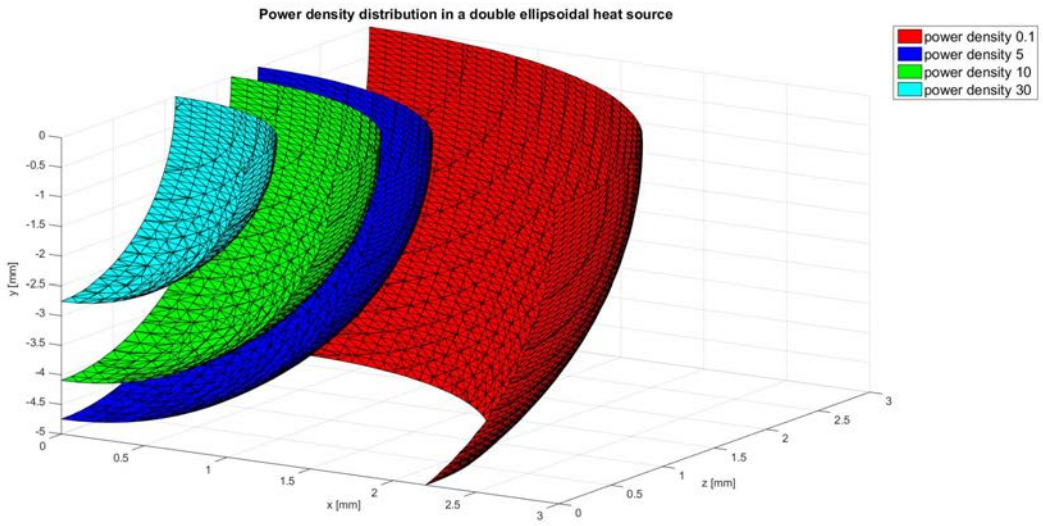

Figure 2.5.: Graph showing an example of power density distribution obtained adopting a double ellipsoidal heat source model (figure 2.3). In particular half of the front section of the heat source is shown (symmetry plane x-y)

In [57] a TDC and a Gaussian heat sources have been compared modelling a laser spot welding process. A good matching with experimental results has been obtained using the TDC heat source whilst, as expected, the Gaussian one was unable to describe accurately the thermal profile of the real heat source when high depths of the weld pool were measured.

A MTDC heat source can still improve the capacity to describe the real temperature profile in the weld pool of a high energy density welding process when a "bugle-like" weld pool shape is obtained, as [8] shows for a plasma arc weld process.

In [9] a nail head shape heat source, constituted by a circular disk and a line heat sources, has been used to describe a conical weld pool shape with a swelling at the top (figure 2.7) obtained in a laser welding process. In this last case, the mathematical description of the heat source becomes more physically based respect the other cases mentioned: instead to use just geometrical parameters to distribute the heat source along different shapes, some terms typical of the heat conduction have been adopted, like the Peclet number, used in the form $Pe = \frac{vr_k}{2k}$ (v uni-axial velocity of the heat source, r_k radius of the line heat source, k thermal diffusivity of the material) and a fictitious thermal conductivity

($\lambda_{T\,effe} = \delta\lambda_{T\,liq}$). The fictitious thermal conductivity $\lambda_{T\,effe}$ has been used to relate the thermal conductivity of the liquid metal ($\lambda_{T\,liq}$) to the speed of the heat source, by a user defined coefficient (δ).

For all the cases above mentioned, it is important to remember the salient characteristic - and limit - of the classical approach of the computational welding mechanics. Making reference again to the work presented in [9], where a laser fusion welding process has been modelled (figure 2.6 and 2.7), and a relatively quite complicated heat source shape has been adopted, can be noticed how the parameters of the model have been adapted by direct comparison with the fusion zone measured by micrographs. Changing the actual operative welding parameters like the welding speed, the shape of the real weld pool may change (figure 2.7 a-b-c-d, top row), inducing to find a new set of parameters for the heat source, to match again the geometry of the real weld pool to the numerical one. Looking at figure 2.7, sometimes, like for the case shown in column a), good matching has been obtained, sometimes, like in case c) and d), the top of the weld pool has been approximated badly. This underlines again how by this approach (section 2.2.2), the temperature gradient measured in the numerical model is not an effect of a prediction, but of an adjustment of the heat source parameters, such to fit the weld pool shape measured experimentally, sometimes accepting a good compromise.

In conclusion, some guidelines for the choice of the right heat source shape can be identified, but the final decision is especially related to the geometry of the weld pool measured experimentally, in particular the transverse cross section, since it is not possible to get a complete longitudinal cross section of the weld pool. The modeller can then decide case by case the best heat source [58], in relation also to the complexity of the model desired. In general, for a high energy density welding process, where a simple conical profile of the weld pool is observed, a TDC heat source is the simplest model to use; for curved profiles of the weld pool section, in relation to the shape observed, a MTDC or a nail head shape heat sources can be adopted.

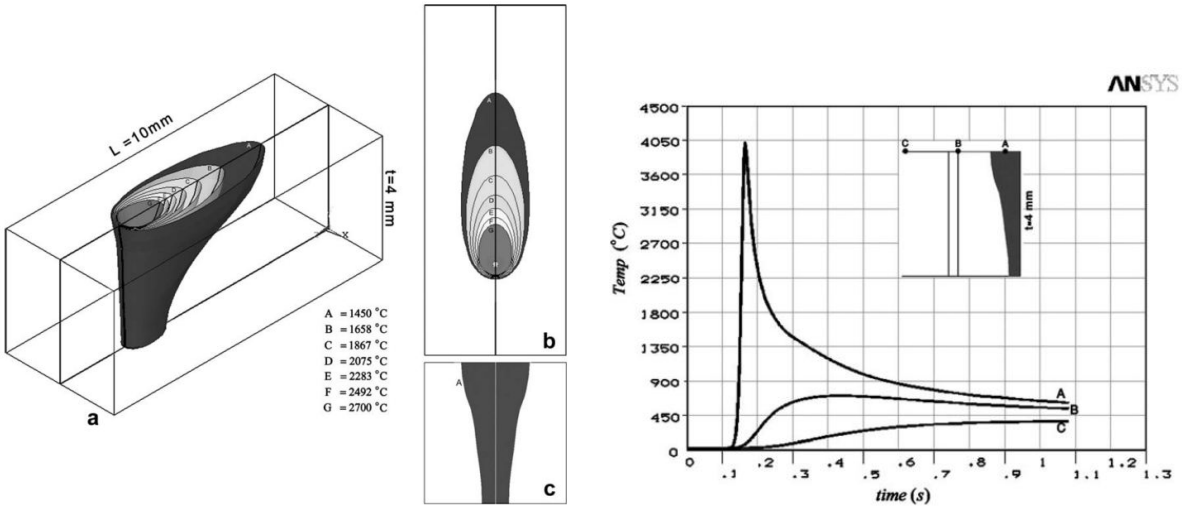

Figure 2.6.: Numerical weld pool shape and temperature distribution obtained in [9] for a laser welding process on AISI304 adopting a nail head shape heat source

All the heat sources described can be adopted and modified in the commercial software package Visual-Weld used in this work. This software implements as default the double ellipsoidal and the TDC models, for the usage of a MTDC or a nail head heat source it is necessary to write user sub routines.

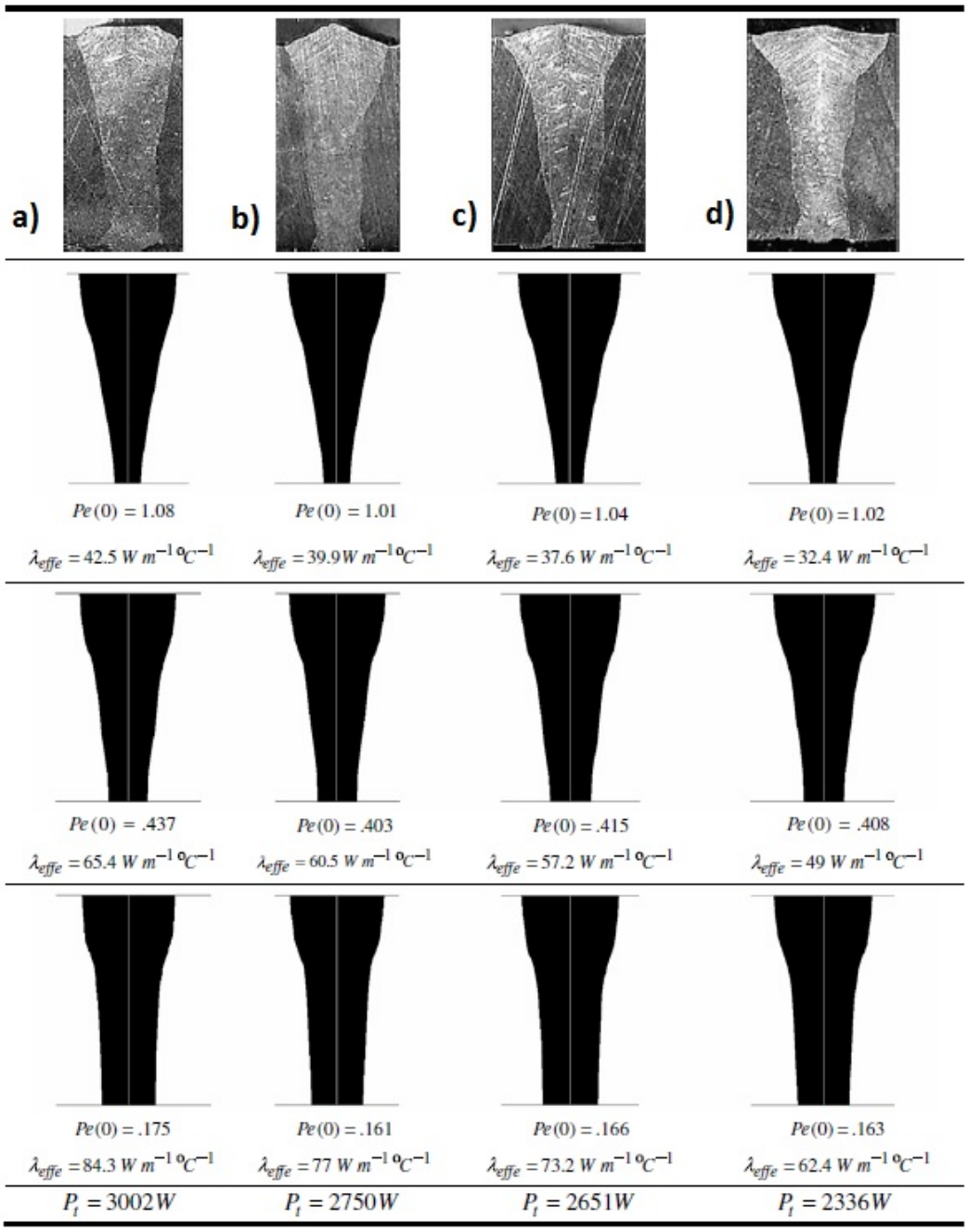

Figure 2.7.: Comparison between the cross sections of the weld pool measured by experiments and numerical models in a fusion welding process. Top row: different welding pool shapes obtained experimentally changing the welding speed and keeping the power input constant. In the 2^{nd}, 3^{rd}, 4^{th} rows starting from the top, shapes of the weld pool obtained for different values of the total power input (P_t), fictitious conductivities ($\lambda_{T\,effe}$) and Peclet number at the initial time ($Pe(0)$) set as parameters for the nail head heat source [9]

2.3 Ti-6Al-4V

2.3.1 Introduction

Ti-6Al-4V belongs to the family of titanium alloys. Although a higher cost than competing materials, titanium alloys use, permits high operative temperature (Al, Ni, steel alloys replacement), galvanic composite compatibility (Al replacement), corrosion resistance (Al and low alloys steels replacement) together with weight saving (steel replacement) [42], all aspects very important in competitive technological fields.

Pure titanium undergoes an allotropic transformation from hcp (α-phase) to bcc (β-phase) as its temperature raises above 882.5 °C [12].

In titanium alloys, the single-phase α and single-phase β regions are not in contact in the phase diagram as they are in pure titanium; they are instead separated by a two phase α + β region whose width increases with increasing solute concentration. The temperature at which the alloys pass from the α + β region to the single phase β region is called beta transus temperature.

Based on these considerations, alloys of titanium are classified as "α", "β" and "α + β", based on the composition of the alloy and the resultant predominant room temperature constituent phase(s). Within the last category are the subclasses “near-α” and “near-β”, referring to alloys whose compositions place them near the α/(α + β) or (α + β)/β phase boundaries [12]. In table 2.1 some common titanium alloys are reported, grouped by family membership.

a)

Composition, wt%	Classification
Ti-5Al-2.5Sn	α
Ti-8Al-1Mo-1V	Near-α
Ti-6Al-2Sn-4Zr-2Mo	Near-α
Ti-6Al-4V	α+β
Ti-6Al-6V-2Sn	α+β
Ti-3Al-2.5V	α+β
Ti-6Al-2Sn-4Zr-6Mo	Near-β
Ti-5Al-2Sn-2Zr-4Cr-4Mo	Near-β
Ti-10V-2Fe-3Al	Near-β
Ti-13V-11Cr-3Al	β
Ti-15V-3Cr-3Al-3Sn	β
Ti-3Al-8V-6Cr-4Mo-4Zr	β
Ti-8Mo-8V-2Fe-3Al	β
Ti-11.5Mo-6Zr-4.5Sn	β

b)

Designation	Composition, wt%
IMI 318	Ti-6Al-4V
IMI 550	Ti-4Al-4Mo-2Sn-0.5Si
IMI 679	Ti-11Sn-1Mo-5Zr-2.25Al-0.25Si
IMI 680	Ti-11Sn-4Mo-2.25Al-0.25Si
IMI 685	Ti-6Al-5Zr-0.5Mo-0.3Si
IMI 829	Ti-5.5Al-3.5Sn-3Zr-1Nb-0.3Mo-0.3Si
IMI 834	Ti-5.5Al-4Sn-4Zr-1Nb-0.3Mo-0.5Si

Table 2.1.: a) Classification of U.S. technical Titanium multicomponent alloys [12]; b) British technical commercial alloys [12]

2.3.2 Classification

In the α+β family of titanium alloys, certainly the Ti-6A1-4V is the most widely used. Designed primarily for high strength at low to moderate temperatures, Ti-6Al-4V has a high specific strength, stability at temperatures up to 400 °C and a good corrosion resistance but the cost continues to be an inhibitive factor if the previous mentioned characteristics are not critical.

Ti-6Al-4V is produced in many different formulations, depending on the application, the oxygen may vary from 0.08% to more than 0.2% (by weight), the nitrogen can be adjusted up to 0.05 %, the aluminium content may reach 6.75 % and the vanadium content may reach 4.5 %. The higher the content of these elements, particularly oxygen and nitrogen, the higher the strength and the lower the ductility, fracture toughness, stress corrosion resistance and resistance against crack growth [12]. Ti-6Al-4V is available in ELI (extra-low interstitial) grades with high damage tolerance properties.

Ti-6Al-4V can acquire a large variety of microstructures, depending on the heat treatment it is subjected to and content of interstitials elements, in turn, chemical composition and thermal history of the base material influence thermal and mechanical properties [59].

Aluminium, Oxygen and Nitrogen are α-stabilizer as they rise the temperature at which the material develops 100 % of β phase; Vanadium, instead, is called β-stabilizer as it has

	Al	V	Fe	Ti
Nominal composition	6.2	4.0	0.17	92.5
β phase	2.92±0.11	15.43±0.86	1.32±0.11	80.7±0.70
α phase	6.73±0.33	1.42±0.73	0.04±0.02	91.2±0.47

Table 2.2.: Nominal composition of a Ti-6Al-4V ELI and chemical composition of the relative α and β phases measured by micro probe analysis in [19]

the opposite effect of the α-stabilizer. An example of the composition of the two phases in a Ti–6Al–4V ELI is reported in table 2.2.

In the following paragraphs, the different phases and microstructures obtainable in Ti-6Al-4V as a function of temperature and cooling rates are defined schematically, underlining the different mechanical properties that these could return. Possible relations that permit to describe the strength of the material based on the microstructural features of the material are then discussed. Before, some thermo-mechanical numerical data found in literature or received by University of Birmingham during collaborations with external businesses are listed; some of these data will be used for preliminary numerical simulations presented in chapter 3.

2.3.3 Thermo-mechanical data

In this paragraph the main thermal and mechanical properties found in literature are shown, both to give a further classification to the material and to see a first variability of certain dimensions in function of the different thermo-mechanical history and/or chemical composition of the material.

The literature data are also compared with the data returned from the commercial software JMatPro for a representative Ti-6Al-4V chemical composition chosen as (in weight percent): 6.4 Al, 4.2 V, 0.14 Fe, 0.19 O, 0.016 C, 0.004 H, 0.005 N, balance Ti.

- **Melting temperature.** Nominal value $1650 - 1660 \pm 15$ °C [12].
- **Boiling temperature.** $3260 - 3285$ °C [13].
- **Beta transus temperature.** For a standard Ti-6Al-4V is 995 ± 15 °C, ELI grade

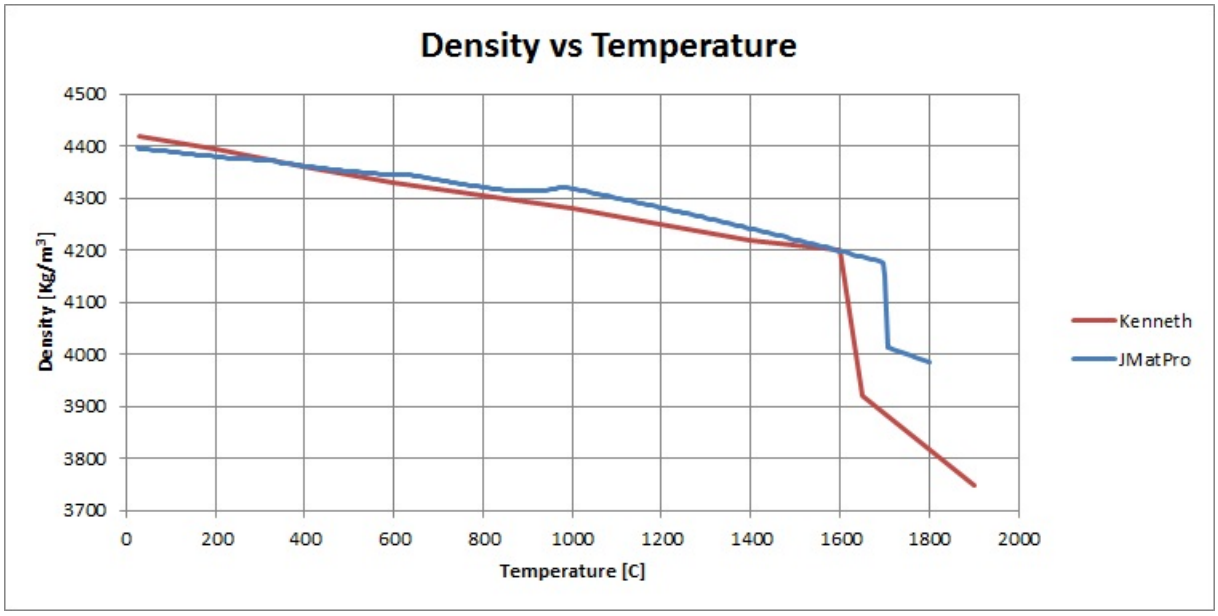

Figure 2.8.: Graph of the Ti-6Al-4V density as a function of temperature obtained from Mills [10] and the commercial software JMatPro

975 ± 15 °C [12].

- **Solidus temperature.** Nominal value 1605 ± 15 °C [12].
- **Martensite start.** 800 °C [12].
- **Density.** Figure 2.8. Data on the original material conditions have not been found. Trends between the two sources agree well except for the temperature at which the step in correspondence of the liquidus temperature is noticed. This can be related to the different chemical composition, measuring technique adopted and interpolation code. As shown in figure 2.8, [10] does not report any variation in the linear trend the density has where a phase change is expected (around 990 °C), this due to the simplified equations form used to represent this dimension as a function of temperature.
- **Specific heat.** The specific heats at constant pressure (cp) and at constant volume (cv) are nearly identical (within 3%), it depends on composition and heat treatment; this is one of the cause generating the differences noticed in the data extracted by

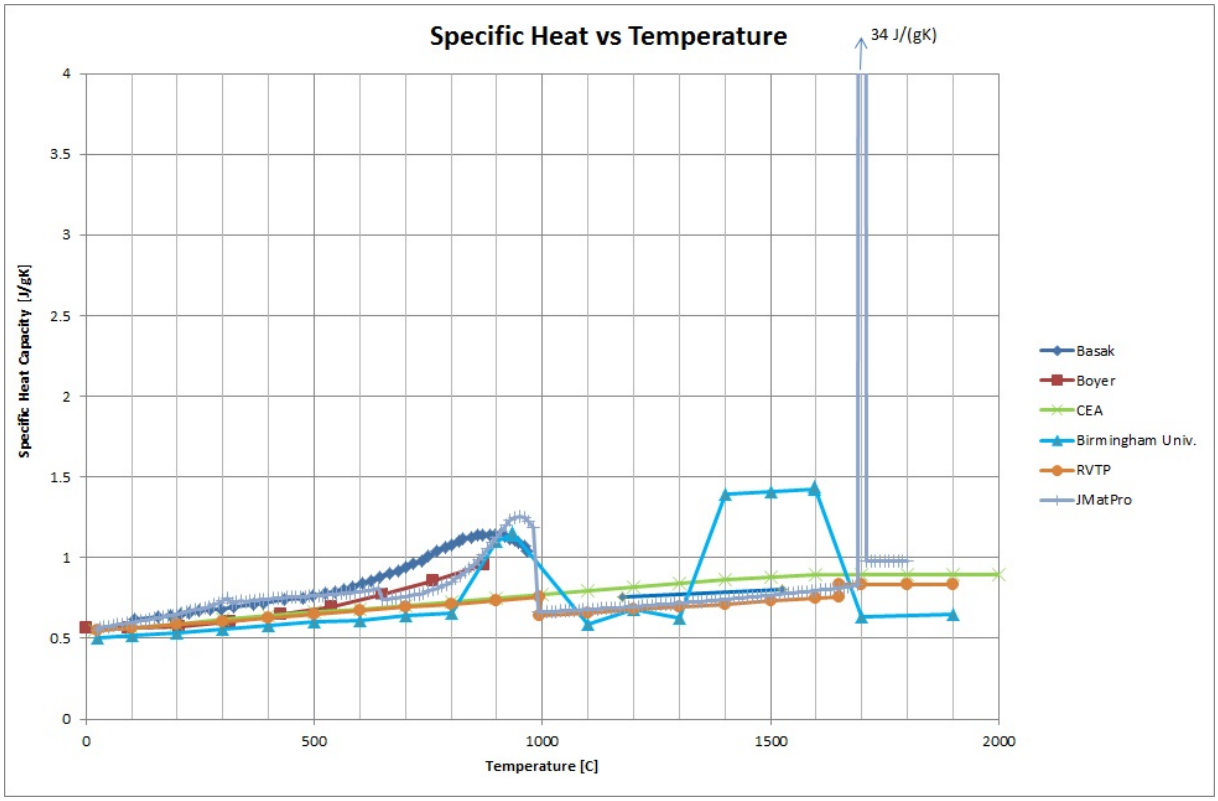

Figure 2.9.: Graph of the Ti-6Al-4V specific heat as a function of temperature obtained from different sources: Basak [11], Boyer [12], CEA [13], University of Birmingham [14], RVTP [10] e the commercial software JMatPro

different sources (figure 2.9). The curves identified as "CEA" and "RVTP" do not show almost any peak in correspondence of temperatures where phase transformations are expected, probably due to missing data in those ranges. No information on the measurement technique has been found. The Basak's data [11], obtained by pulsing heat technique, are the closest to the JMatPro one, even if no information is given around liquidus temperature.

- **Thermal conductivity.** Hereinafter the trend for this physical quantity in function of the temperature obtained in [15] is described. It has been obtained applying the Wiedemann-Franz law, hence indirectly measuring the electrical resistivity in function of the temperature applying the following formula:

$$\lambda_T(T) = \frac{LT}{\rho_{el}(T)}$$

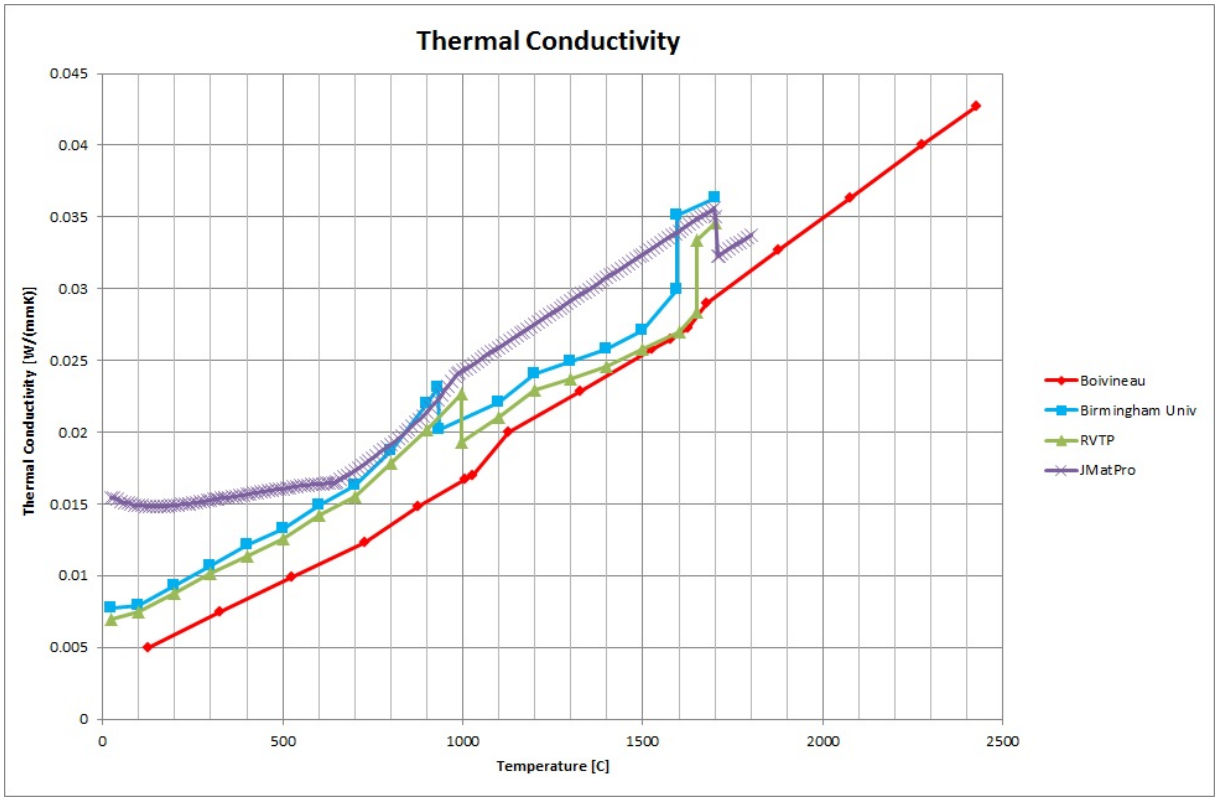

Figure 2.10.: Graph of the Ti-6Al-4V thermal conductivity as a function of the temperature obtained from Boivineau [15], University of Birmingham [14], RVTP [10] and thr commercial software JMatPro data

where L is the Lorentz number, i.e., $L = 2.45 \cdot 10^{-8} V^2 K^{-2}$, ρ_{el} is the electrical resistivity.

The linear fit for the β phase is found to be

$$\lambda_T = -0.32 + 1.46 \cdot 10^{-2} T \text{ with } 1400 < T < 1850\ K$$

$$\lambda_T = -6.66 + 1.83 \cdot 10^{-2} T \text{ with } 1950 < T < 2700\ K$$

where λ_T is in $W \cdot m^{-1} \cdot K^{-1}$and T is in K.

In figure 2.10 others values found in literature are reported.

- **Thermal expansion.** Typical values are reported in the table 2.11.

- **Young modulus.** In [12] typical values at ambient temperature are given in the range from 100 to 130 GPa . Figure 2.12 shows trends of the Young's modulus as a function of the temperature for different Titanium alloys. At temperatures higher

Temperature interval		Linear expansion coefficient	
°C	°F	10^{-6}/°C	10^{-6}/°F
0-100	32-212	9.0	5.0
20-100	70-212	8.6	4.8
20-200	70-400	9.0	5.0
0-315	32-600	9.5	5.3
20-315	70-600	9.2	5.1
20-425	70-800	9.4	5.2
0-540	32-1000	10.1	5.6
20-540	70-1000	9.5	5.3
20-650	70-1200	9.7	5.4
0-650	0-1200	10.6	5.9
0-815	0-1500	11.0	6.1

Source: RMI Co., and *Metals Handbook*, Vol 2, 10th ed.

Figure 2.11.: Mean typical values of linear expansion for Ti-6Al-4V as reported in [12]

than 200 ^{o}C, for Ti-6Al-4V, it is possible to notice the different trend in case the material is texture free or not.

- **Poisson's ratio.** At ambient temperature $\alpha + \beta$ microstructures have a value of 0.27, martensitic microstructures (α' and α") have a value around 0.35, in figure 2.13 the influence of the quenching temperature on the elastic properties of the material is reported [12].

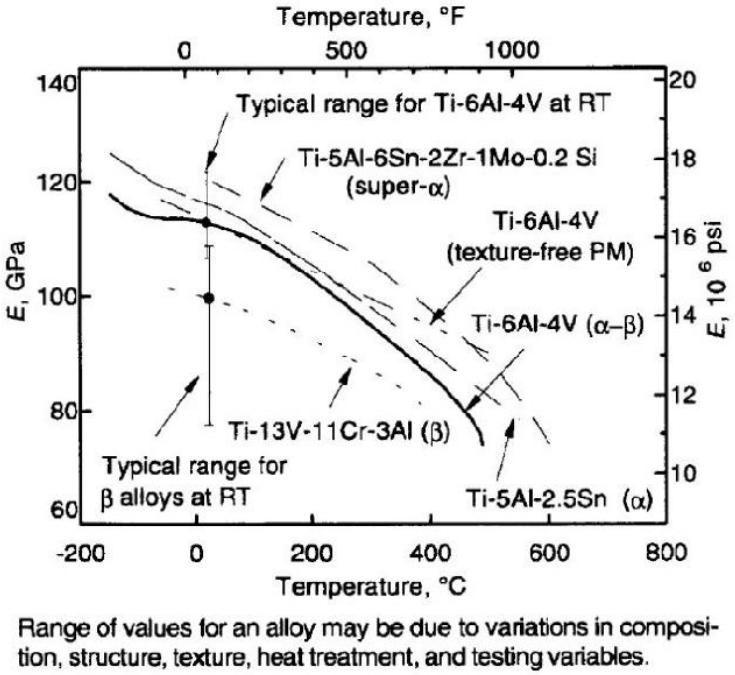

Figure 2.12.: Range values of Young's modulus as a function of the temperature for Ti-6Al-4V and others titanium alloys [12]

Condition	Young's modulus, E GPa	Poisson's ratio	Shear modulus, G GPa
RT	114.0	0.272	44.8
550 °C STQ	113.0	0.274	44.3
600 °C STQ	111.3	0.275	43.6
700 °C STQ	109.0	0.270	42.9
750 °C STQ	108.2	0.267	42.7
800 °C STQ	107.9	0.265	42.6
850 °C STQ	109.1	0.318	41.4
900 °C STQ	110.4	0.370	40.3
950 °C STQ	111.6	0.360	41.0
1000 °C STQ	111.8	0.352	41.3
1050 °C STQ	113.0	0.351	41.8
1100 °C STQ	112.8	0.350	41.8
1150 °C STQ	113.0	0.351	41.8
1200 °C STQ	113.3	0.352	41.9

Alloy as sintered had composition in weight % of Al: 6.2, C: 0.02, Cl:0.12, Fe: 0.18, N: 0.016, Na: 0.10, O: 0.24, V: 4.1. Materials were solution treated at temperatures indicated and water quenched. RT = as sintered, slow cooled. Source: Personal communication, Y.T. Lee, OLR, Institut für Werkstoff-Forschung, Cologne, 1989

Figure 2.13.: Young's modulus, Poisson's ratio and Shear modulus at different quenching temperatures for Ti-6Al-4V [12]

2.3.4 Phases and common microstructures obtainable

To have a first indicative idea of which phases are present, in equilibrium conditions (and not in case of martensite) at different temperatures, a pseudo-binary phase diagram for Ti-6Al-4V is shown in figure 2.14.

Above the β transus temperature the material has 100% β phase, below this temperature first α nuclei start to nucleate if the material is cooled down or the last α precipitates completely dissolve if the material is heated up.

Indicative start and finish temperature of the martensitic transformation (metastable form of the material) are represented respectively as Ms and Mf. If the material is cooled down through these temperatures at a sufficient fast cooling rate, possible existent beta phase transforms to martensite.

The crystallographic structures of the two principal phases of the material are hexagonal close packet for α phase and body centred cubic for β phase.

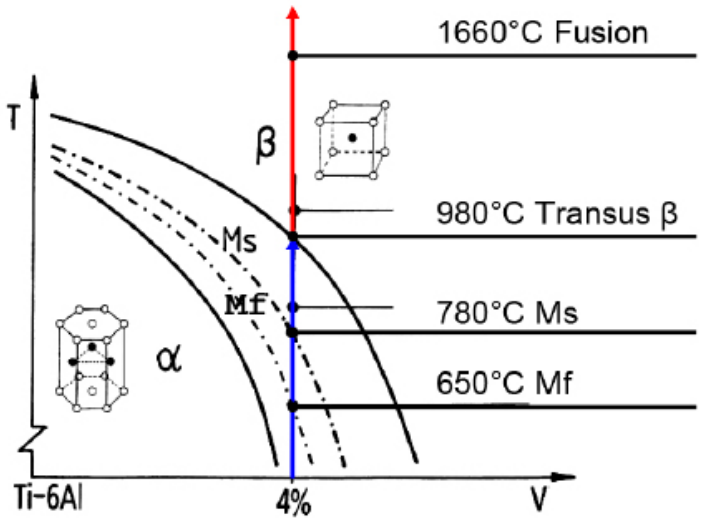

Figure 2.14.: Schematic pseudo-binary diagram of Ti-6Al-4V [13]

Subjecting Ti-6Al-4V to different thermal cycles, its microstructure assumes different morphologies due to complex phenomena driving the solidification, like release of latent heat of fusion, interaction with impurities, variable chemical composition in time and

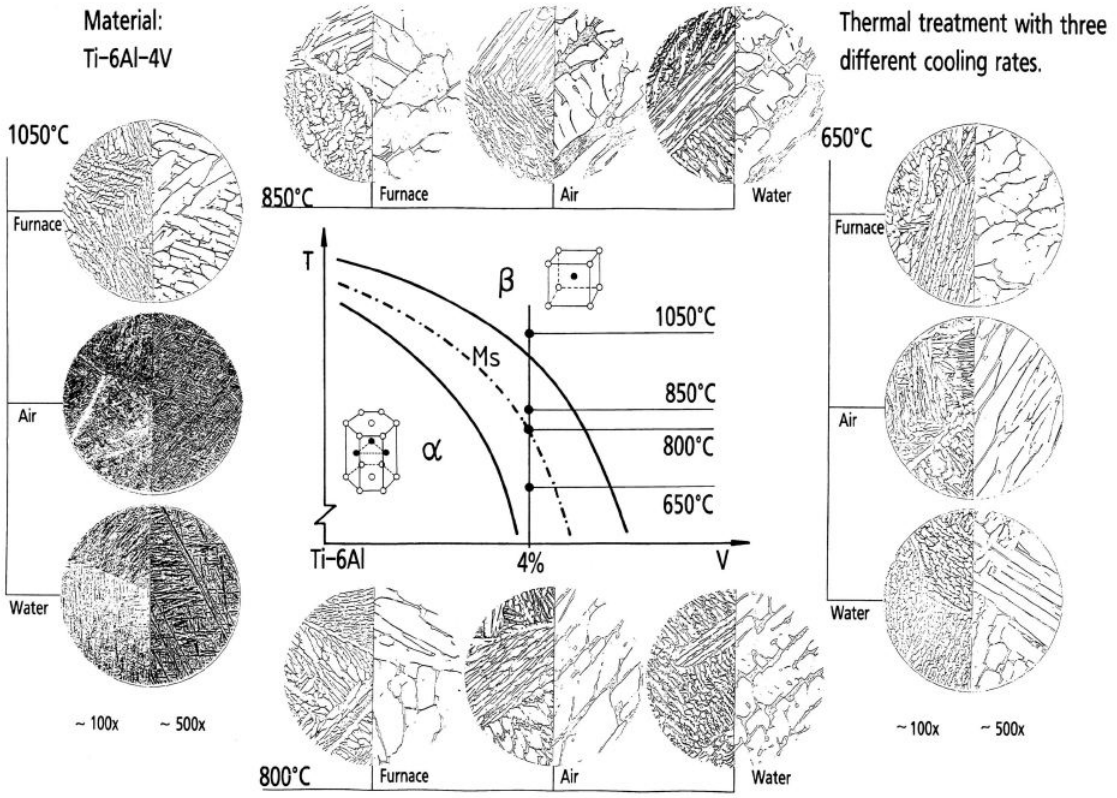

Figure 2.15.: Indicative microstructures obtainable by cooling down Ti-6Al-4V in three different media (furnace, air and water) after soaking (time not reported in source) at different temperatures (650 °C, 800 °C, 850 °C and 1050 °C) [12]

space, mobility of the atoms, different growth rates in relation to the packing factors, convection, etc. [60].

Some of the most significant microstructures obtainable in Ti-6Al-4V are reported in figure 2.15 and described hereinafter.

- *Lamellar structures* can result in a fairly coarse plates often referred as plate-like alpha (figure 2.16), when the material is subjected to slow cooling (e.g. in furnace $15\,K/min$). By higher cooling rates, like air cooling, the microstructure results in a fine needle-like alpha phase referred as acicular alpha. Certain intermediate cooling rates develop Widmanstätten structures (basket-weave) [12].

- M*artensite* (α') is another needle-like α structure with hexagonal close packed lattice, it is obtained by quenching from above 900 °C and it has an acicular or sometimes

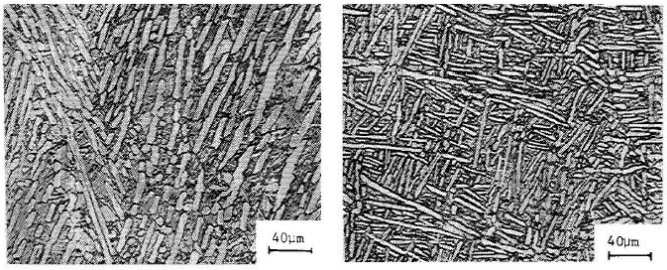

Figure 2.16.: Micrographs of Ti-6Al-4V showing coarse lamellar structure (left) and a fine lamellar structure (right) of α-phase obtained starting from a full β structure and applying a slow and moderate cooling respectively [16]

fine-lamellar microstructure (figure 2.17). It is related crystallographically to the alpha phase and has similar lattice parameters [12].

- *Orthorhombic martensite* (α") is a rather soft martensite that forms during quenching of beta phase with 10±2 wt% vanadium, from temperatures between 750 and 900 °C. The α" martensite can also form as a stress-induced product by straining metastable beta [12].

- *Equiaxed microstructures* (figure 2.17) are obtained by extensive mechanical working of the the material in the α + β phase field, breaking up the the lamellar alpha [12].

- *Ti_3Al precipitation* (α_2) has been experimentally verified in alloys containing less than 0.2% oxygen and it occurs at aging temperatures from 500 to 600 °C when oxygen concentrations (still within specification limits for Ti-6Al-4V) are increased [12].

- A *bimodal morphology or duplex* (figure 2.18) is formed of α phase grains in a β phase matrix. A typical heat treatment by which obtains it, is annealing 1 h at 955°C following water quenching and aging at 600 °C. This microstructure is quite often characteristic of commercial products like plates [12].

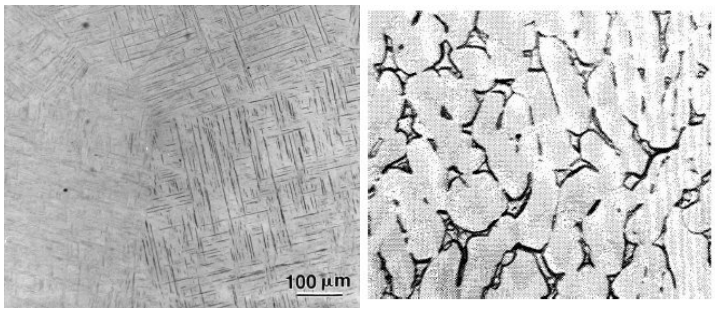

Figure 2.17.: Micrographs of Ti-6Al-4V showing a α' martensitic structure obtained from a full β structure and applying a water quenching (left); equiaxed microstructure (right) [16]

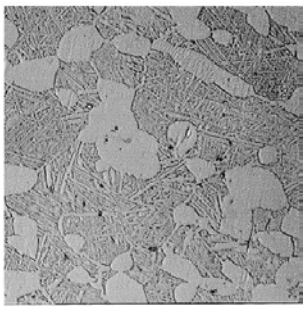

Figure 2.18.: Micrograph of Ti-6Al-4V showing a duplex structure constituted by α grains surrounded by transformed β obtained by a water quenching from the α+β domain [17]

2.3.5 Phases evolution

2.3.5.1 Heating

During heating, the α + β structure existent at ambient temperature gradually changes: initially, transformed β phase grows by diffusional migration of α +β interface toward the increase of β phase then, when the temperature is high enough, α phase starts to transform to β phase too. Depending mainly on the heating rate, but also on the initial microstructure, phases distribution and composition, the fraction of the α phase becomes null in a range of temperatures more or less close to the β transus that the material would show in equilibrium conditions.

In figure 2.19, an example of the heating rate effect on the beta transus temperature shifting, is reported for a Ti-6Al-4V with an initial lamellar α structure and 10% β phase, percentage of the principal alloying elements: 6.2% Al 4.5% V [18]: heating up the material at 100 K/s rather than 0.01 K/s shifts up the beta transus temperature of about 50 K. The beta phase proportion evolution for the heating rate of 0.01 K/s seems to be in reasonable good agreement with the Thermocalc data obtained for equilibrium conditions reported in [19] and shown in figure 2.20. As the heating rate rises, the beta transus shifts toward higher and higher values (T_p) as well as the temperature at which first growth of beta phase is registered (T_k).

From experimental measurements of the beta transus temperature as a function of heating rates, the beta transus temperature trend for unknown heating rates has been predicted by applying the phenomenological Johnson-Mehl-Avrami equation (JMA) [61]. This approach has been adopted is this project and will be deepened in section 4.3, relative to the beta grain growth prediction.

2.3.5.2 Cooling

Cooling Ti-6Al-4V, based on the type of cooling the material is subjected on, β phase is transformed primarily in lamellar α phase or martensitic α' phase. In [12] the phase

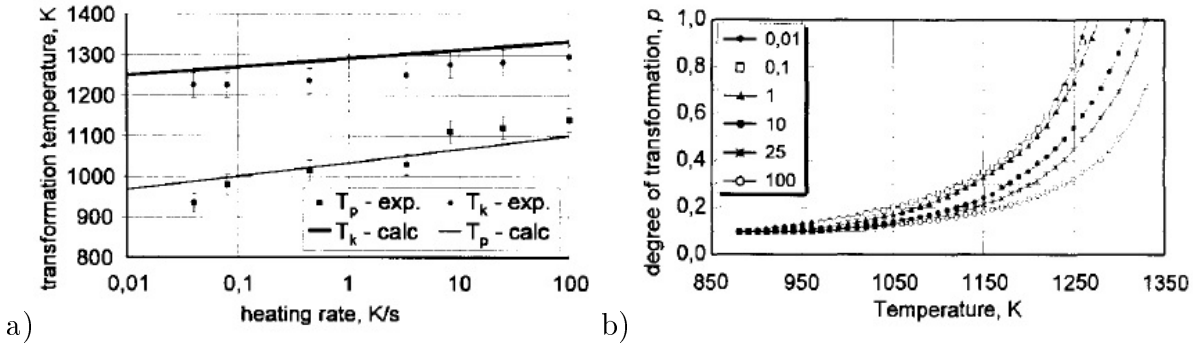

Figure 2.19.: Graphs showing for a Ti-6Al-4V alloy a) temperature start (T_p) and finish (T_k) of β transformation as a function of the heating rate, calculated and measured experimentally by dilatometer; b) degree of transformation of β phase (p) as a function of temperature and heating rate for the same Ti-6Al[18]

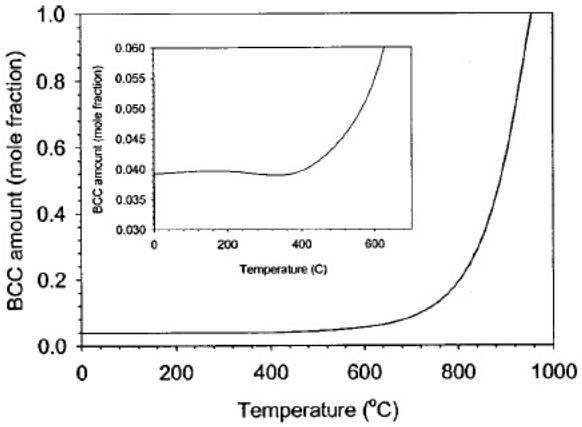

Figure 2.20.: Graph of the equilibrium β fraction as a function of temperature obtained by Thermocalc for a Ti-6Al-4V alloy with the composition showed in table 2.2 [19]

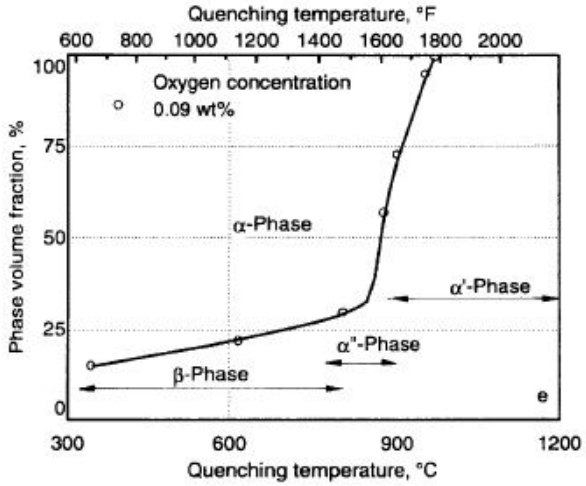

Figure 2.21.: Graph of the fraction of phase constituents after quenching as a function of the temperature for a Ti-6Al-4V alloy [12]

volume fractions obtainable after quenching from different temperatures have been investigated and well reassumed in the figure 2.21. In case of isothermal treatment, Time-Temperature-Transformation (T-T-T) diagrams are probably the best charts to make reference to. Examples are reported in figure 2.22, where two T-T-T diagrams for Ti-6Al-4V are reported, respectively keeping for 30 minutes the temperature of 1025 °C (a) and 1020 °C (b) (over β transus), then rapidly cooling until a specified temperature, that is kept constant throughout the course of the reaction.

Contrarily to the T-T-T curves, continuous cooling transformation (C-C-T) curves, are widely used to describe the phases evolution during a constant cooling rate. In works like [24, 62, 63], the modelling of the phases evolution during cooling in Ti-6Al-4V has been described successfully using these charts. Examples of C-C-T diagrams are reported in figure 2.23 and 2.24, obtained respectively after an annealing at 1030 °C for 30 minutes [22] and after an annealing at 1020 °C of Ti-6Al-4V [23].

As above mentioned, in [24, 62, 64] the phases evolution in Ti-6Al-4V have been numerically described making reference to CCT curves. In general, the models are primarily based on the Johnson-Mehl-Avrami equation (JMA) [47, 48, 49], initially studied for isothermal cases and then adapted to more generic thermal conditions. The procedure used is describing the CCT curves by the sum of small, consecutive isothermal steps referred

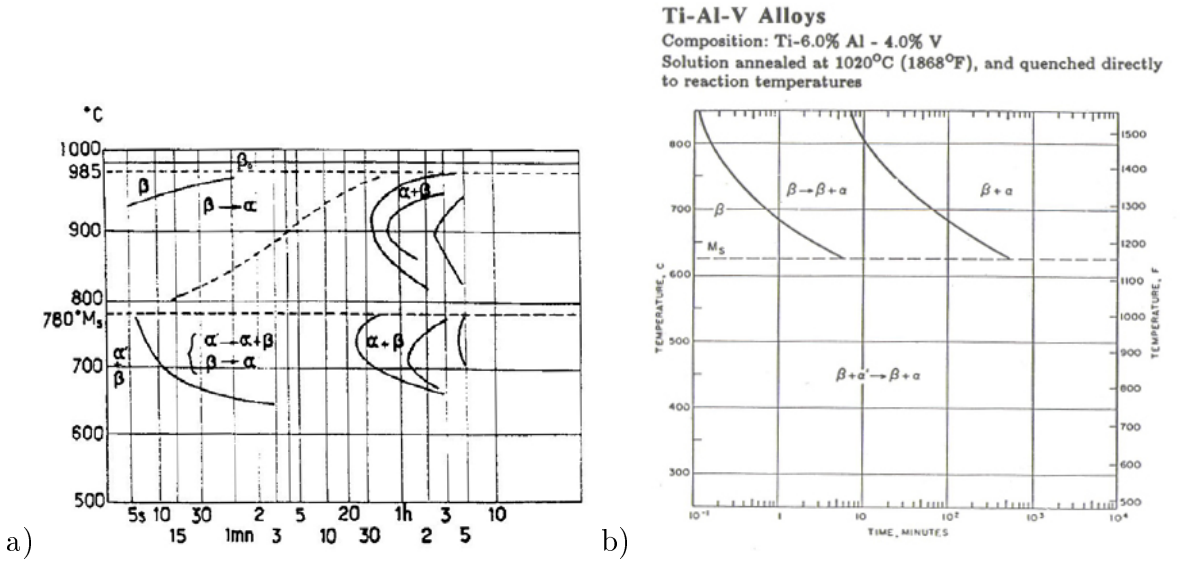

Figure 2.22.: Two different TTT diagrams found in literature: a) TTT diagram obtained keeping Ti-6Al-4V specimens at 1025 °C for 30 minutes then quenching [20]; b) TTT diagram obtained after a solution annealing at 1020 °C then quenching to reaction temperature [21]

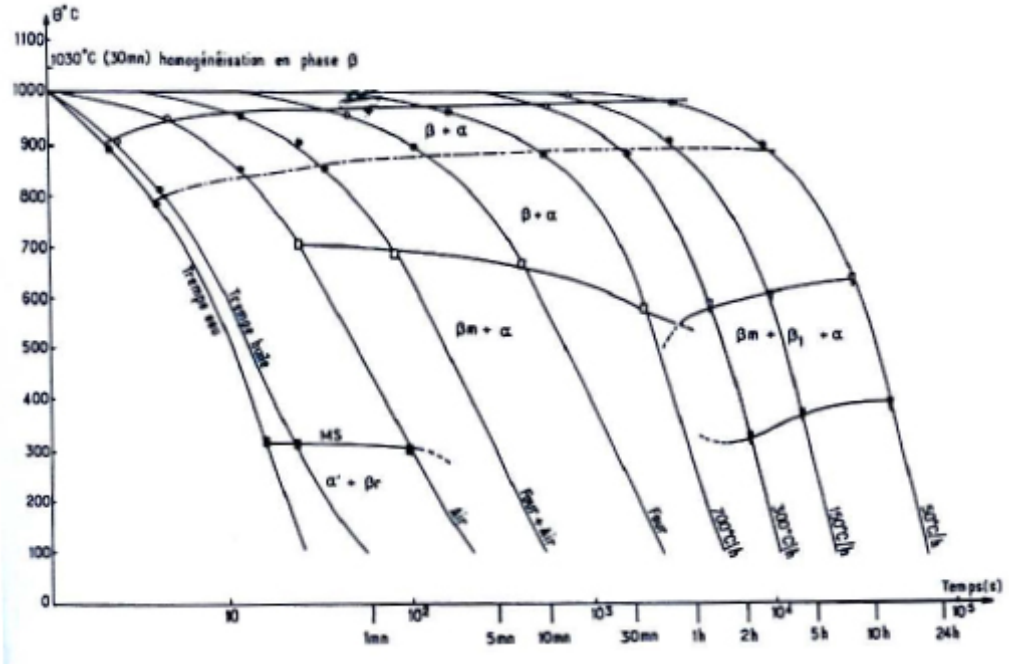

Figure 2.23.: Continuous Cooling Transformation diagram for Ti-6Al-4V, cooling from 1030 °C [22]

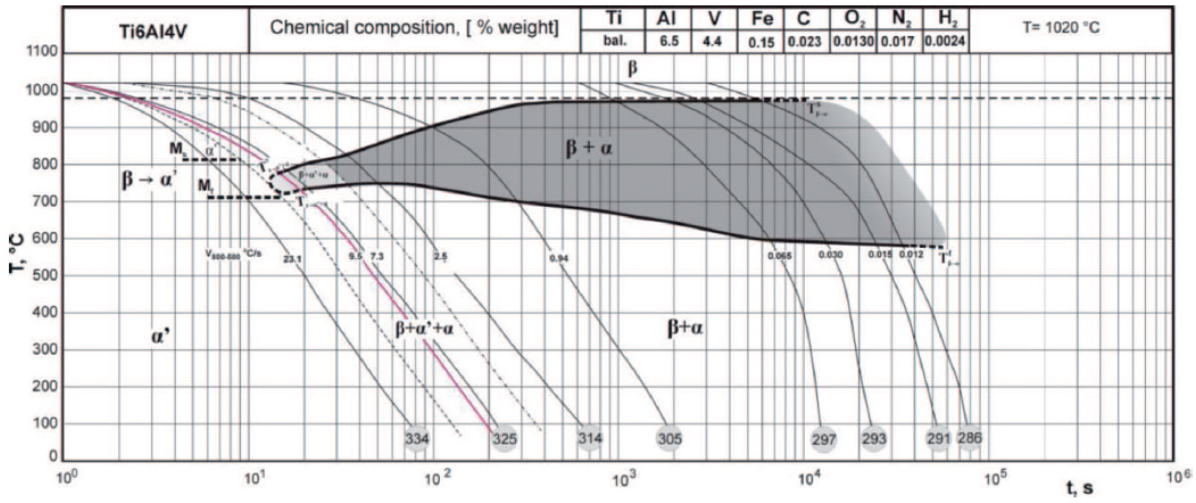

Figure 2.24.: Continuous Cooling Transformation diagram for Ti-6Al-4V, cooling from 1020 °C [23]

to fictitious times (t^*) at which a fraction of phase (f_i) would be transformed if the whole transformation were at an isothermal temperature T_i, in particular, as reported in [24]:

$$f_i = 1 - \exp(-k_i \cdot (t_i^* + \Delta t)^{m_i}) \tag{2.1}$$

where

$$t_i^* = \sqrt[m_i]{\frac{\ln(1 - f_{i-1})}{-k_i}} \tag{2.2}$$

with k is a coefficient dependent on the temperature, composition of parent phase, and grain size; m is a coefficient dependent on the type of phase transformation and grain growth; t_i^* the isothermal time, Δt the length of the steps in which the transformation has been divided. The solution to these equations has been found:

- keeping n constant, since the authors affirm this is reasonable for most transformations over appreciable temperature ranges and that its value should be changed only when the growth geometry changes;
- writing an optimization program for the determination of the best values of k.

In figure 2.25 results obtained in [24] are shown, in particular the coefficient k in function

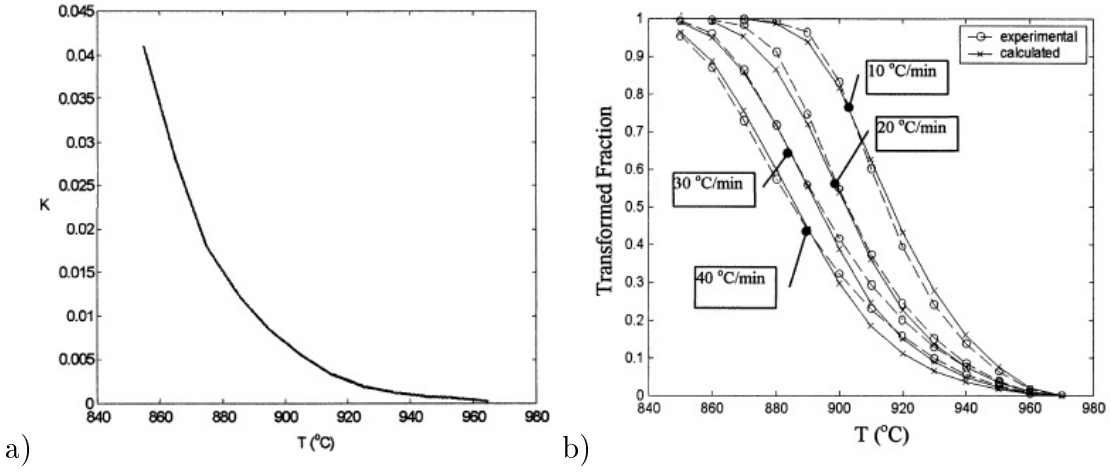

a) b)

Figure 2.25.: a) Calculated rate parameter k as a function of the temperature for equation 2.1; b) experimental and calculated degrees of β to α transformed as a function of the temperature and cooling rate applying the JMA approach for a Ti-6Al-4V alloy[24]

of the temperature, and the comparison between numerical and experimental results about the amount of β to α phase transformed in function of the temperature at different cooling rates.

In [62] this method has been implemented in a numerical code to predict phases distribution in a laser deposition process of Ti-6Al-4V.

This approach can be used in the same way also to describe continuous heating transformations, in fact, the finite element commercial Visual-Weld software adopts this idea both for cooling and heating heat treatments.

2.3.5.3 Martensitic transformation

The kinetics of martensitic transformation takes place without diffusion and the progress of the transformation is independent by the cooling rate.

For steels, Koistinen [65] suggests an empirical relationship between the reduction of temperature below M_s (start temperature of martensitic transformation) and the amount of martensite formed:

$$y = y_a \left\{1 - \exp\left[-\kappa \left\langle T_{Ms} - T \right\rangle\right]\right\} \tag{2.3}$$

The equation 2.3 can therefore represent the progress of the martensitic reaction and it is valid for all cooling rates and the parameters are:

y = volume fraction of martensite

y_a = volume fraction of the material that can be converted

κ = constant, equal to 0.011 K^{-1} for most steels

$\langle x \rangle$ = max (x, 0)

T_{Ms} = temperature of martensite start

T = temperature

The majority of people working on the prediction of the evolution of a tempering process, also for Ti-6Al-4V, use equation 2.3 [63, 62].

2.3.6 Morphological and mechanical modelling

2.3.6.1 Introduction on the relation between mechanical behaviour and material morphology

As it has been shown in section 2.3.4, the morphology of the material after a thermal treatment can appear equiaxed, plate-like, Widmanstätten, acicular or martensitic, each with own characteristics and variable geometrical parameters.

Understanding the microstructural evolution as a function of the heat treatments becomes particularly important when the mechanical behaviour of Ti-6Al-4V wants to be described, since directly related to the evolution of some of the morphological features of the microstructure.

From an experimental point of view, methods for a rapid characterization of the microstructural features have been presented in the last few years [27, 28], getting information of: Widmanstätten α laths thickness and volume fraction, colony size, width of grain boundary α, β grain size, mean edge length of α laths, volume fraction of basket-weave

structure, mean globular α grain size, volume fraction of globularized α, width of transformed β laths and volume fraction of transformed β.

It is then theoretically possible to keep trace of all the properties of the microstructure experimentally, actually, limiting factors like facilities, time available and complexity of the material microstructure could prevent some measurements.

From a numerical point of view, modelling all the morphological features and dimensions described would result a hard challenge. Since this work is focussed in the description of the mechanical strength of the material, the most meaningful morphological characteristics affecting this material property will be investigated, such to reduce both the amount of modelling and the computational cost required.

From [25, 31, 66] it is clear how the platelet thickness of α lamellae has an important effect on the plastic flow and fatigue life of the material, showing how thinner lamellae return a higher plastic flow stress but also a reduced resistance to fatigue.

One of the main factors influencing the platelet dimension is the cooling rate the material is subjected to. In [25] specimens kept at 1050 $°C$ (over β transus) for 1 hour then cooled at different rates (0.23, 0.81, 3.40, 5.10 $°C$) show Widmanstätten structure, except for the highest cooling rate where martensite is formed. The microstructural parameters measured in [25] are summarised in table 2.3. It can be observed that the β-prior grain, α platelet and α colony sizes, decrease progressively with the increasing of the cooling rate, this because the available time for growth decreases. Within this study, some tensile tests have been carried out (table 2.4), showing as the yield stress increases with the decreasing of the laths thickness: passing from 7 to 12 μm of the platelet thickness, a variation of about 10 % of the Yield strength is registered. The martensitic structure, obtained by a relatively low cooling rate (figure 2.24), seems to have a small effect with respect to the Widmanstätten structure with the smallest platelet thickness, except on the capacity of the material to elongate, increasing hence the brittleness. A chart that relates the alpha plate size reported in the table 2.3 and the strength of the material reported in table 2.4 is shown in figure 2.26.

Microstructures	Grain size (μm)	α-plate size (μm)	Colony size (μm)
Widmanstätten 0.23 K s^{-1}	675 ± 15	12 ± 1	230 ± 9
Widmanstätten 0.81 K s^{-1}	501 ± 12	10 ± 1	190 ± 11
Widmanstätten 3.40 K s^{-1}	390 ± 15	7 ± 2	188 ± 16
Martensite 5.10 K s^{-1}	376 ± 15	–	–

Table 2.3.: Microstructural parameters measured for different cooling rates applied to the same initial structure of Ti-6Al-4V, after soak at 1050 °C. From left to right: cooling rate and microstructure obtained, mean β-prior grain size, mean α Widmanstätten plates thickness and mean α Widmanstätten colonies size [25]

Microstructures	Proportional limit (MPa)	Yield strength 0.2% (MPa)	Ultimate strength (MPa)	%Elong
Mill annealed	837 ± 18	986 ± 28	1050 ± 29	14 ± 2
Widmanstätten 0.23 K s^{-1}	560 ± 7	821 ± 18	954 ± 18	7 ± 1
Widmanstätten 0.81 K s^{-1}	567 ± 10	860 ± 13	992 ± 28	8 ± 1
Widmanstätten 3.40 K s^{-1}	573 ± 8	890 ± 20	1020 ± 19	8 ± 1
Martensite 5.10 K s^{-1}	588 ± 8	894 ± 8	1080 ± 38	4 ± 1

Table 2.4.: Strength measured for the different platelet thickness described in table 2.3 [25]

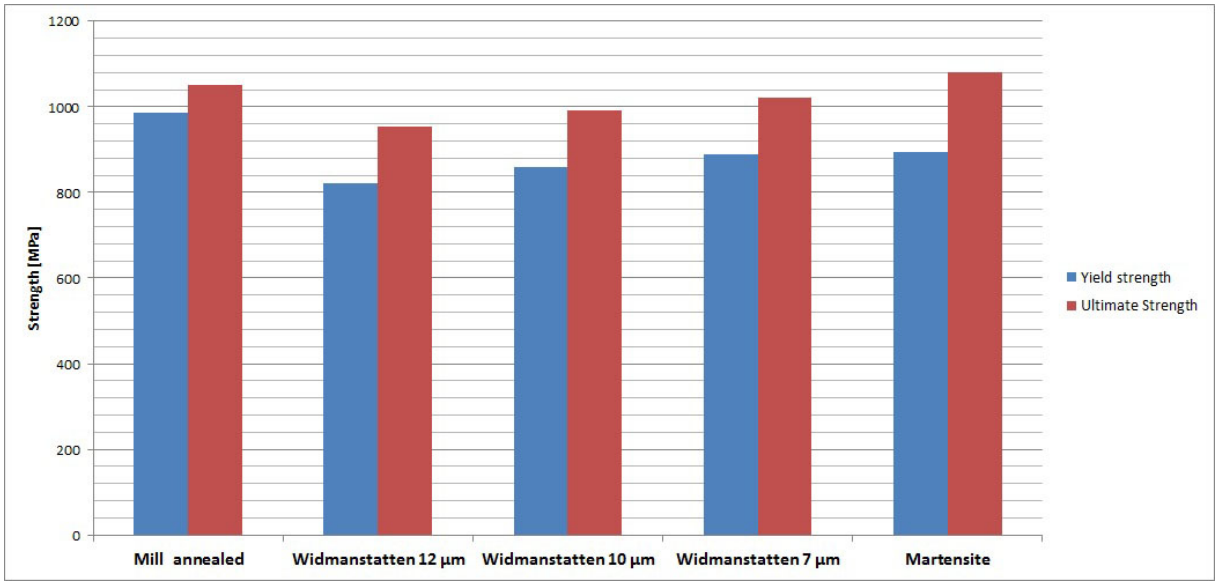

Figure 2.26.: Trend of the yield strength 0.2 % and ultimate stress in relation to the platelet thickness measured in [25] and reported in table 2.3 and table 2.4

Another factor affecting the microstructure and the particle dimensions is the temperature at which the material before being cooled after a heat treatment is. In [26] samples β-solution treated, forged and recrystallized just below β-transus, have been heated at five temperatures: 850, 900, 950, 1000 and 1050 $°C$ then quenched in water (hence same cooling rate, different initial temperatures). The average thickness of the α and martensitic platelet after these heat treatments have been measured and reported in table 2.5 under the column "P" (the column "S" reports the dimensions of the platelets after different compression tests and successive quenching) and figure 2.27. In this case, it is possible to see how the initial platelet dimension determines if shrinkage or growth occurs, driven by the equilibrium lamellar dimension the material would have at the different temperatures. At 950 $°C$ the platelet dimensions seem to converge to the same value. Even if the authors report a high thickness variance of the prior platelets from grain to grain, within the same sample and even from area to area in one grain, the trends seem to be in good agreement. The value reported at 1000 °C is not significant since representative of new nucleated lamellae as the beta transus temperature was overpassed. The effect of the cooling rate can be appreciated also comparing the results obtained in [25] (table 2.4) with the ones in [26] (table 2.5): cooling rates of 0.23, 0.81 and 3.40 °C/s returned respectively a mean platelet thickness of 12, 10 and 7 μm, whilst water quenching (>100 °C/s) returned platelet thicknesses below 4 μm.

As the thermal history affects the dimension of the platelet, a different dimensional particle distribution along the material can be seen as a function of the rate of the heat dissipated through the workpiece, as demonstrated in [27]: it is significant the example of $10 - 15\%$ of variability measured in the lath thickness along the depth - few microns - of the specimen investigated (figure 2.28).

The dispersion of the lamellae width, is reflected in the dispersion of the strength of the material, as shown in [28], where the ultimate tensile strength and yield strength are put in relation with the Widmanstätten α-lath thickness. In figure 2.29 the ultimate tensile strength is plotted as a function of the α lath thickness of the Widmanstätten structure

T (°C)	Strain rate $\dot{\varepsilon}$ (s^{-1})									
	Heat-treated		0.05		0.1		0.5		1.0	
	P	S	P	S	P	S	P	S	P	S
850	4.0	0.8	3.8	0.8	2.2	1.0	3.0	0.8	2.0	0.9
900	3.6	0.6	2.9	0.9	2.7	0.9	2.7	0.9	2.4	0.9
950	2.2	1.0	2.7	0.9	2.8	0.9	2.6	0.8	2.1	0.9
1000	3.2	(1.3)	–	(1.4)	–	(1.4)	–	(1.3)	–	(1.4)
1050	–	(1.4)	–	(1.4)	–	(1.4)	–	(1.4)	–	(1.4)

Table 2.5.: Mean platelet thickness (μm) at different hot working conditions (temperatures and strain rates) of a Ti-6Al-4V alloy. Numbers in parentheses represent the thickness of the martensitic platelet. Values under "P" column are referred to the platelet thickness formed before the quenching following the hot deformation process (compression at strain rates of $0.05s^{-1}$, $0.1s^{-1}$, $0.5s^{-1}$ and $1.0s^{-1}$), values under column "S" are platelet thicknesses formed after the quenching following the hot deformation process. Under the column "Heat-treated" the mean values of the platelet thickness obtained without hot deformation processing are reported [26]

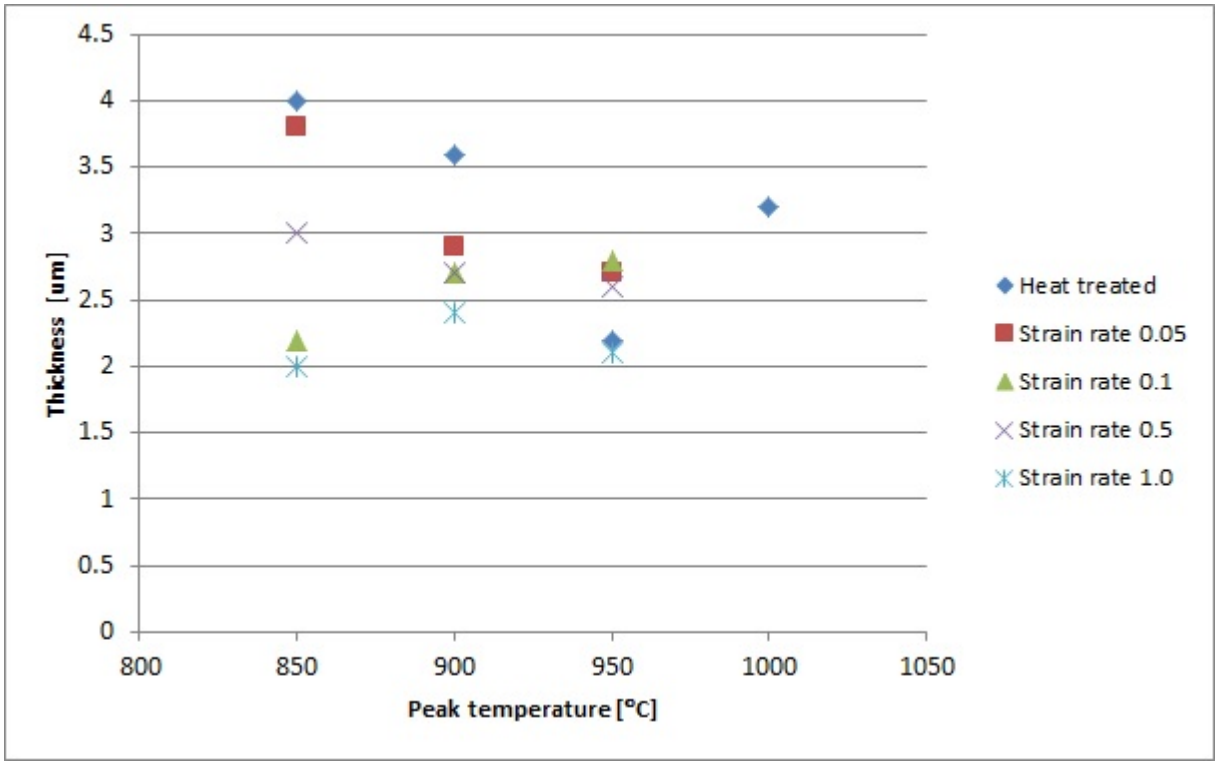

Figure 2.27.: Graph showing the evolution of the platelet thickness reported in table 2.5 as a function of the peak temperature at which the Ti-6Al-4V alloy was water quenched. The data points relative to the "heat treated" material show that the alpha platelet dissolve with increasing the temperature [26]

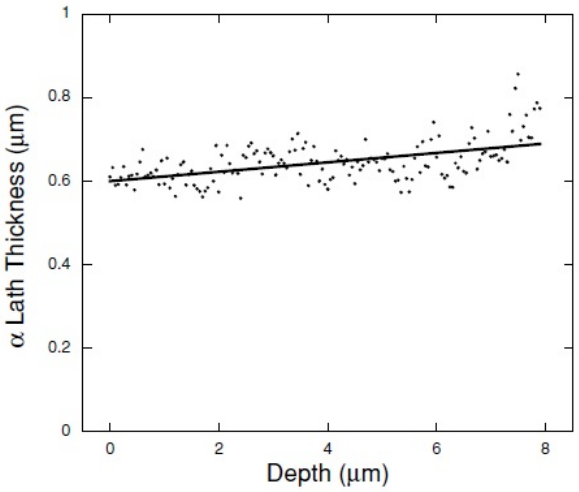

Figure 2.28.: α lath thickness distribution as a function of the depth from the surface of the Ti-6Al-4V specimen tested in [27]. Material far from is subjected to slower cooling rates which allow growth of the α lath

under examination and as it can be noticed, a variation of the lamellae thickness of about 1 μm brings a variation of the ultimate strength of about 10 %.

Further evidence of the impact of the platelet thickness on the strength of the material will be given in section 2.3.6.4: in particular table 2.6 and figure 2.33, from work presented in [31], show the variation of the true stress true strain curves obtained from hot compression tests, with three different platelet dimensions, at strain rates of 1.0, 0.1 and 0.001 s^{-1}. Increased strength of the material was observed with thinner lamellae, and as the strain rate was increased, the effect of the platelet dimension was more pronounced.

It is evident from this paragraph the strong relationship between morphological features of the Ti-6Al-4V microstructure and its strength, in particular, in case of Widmanstätten and martensitic structures, the thickness of the particles represents an important factor.

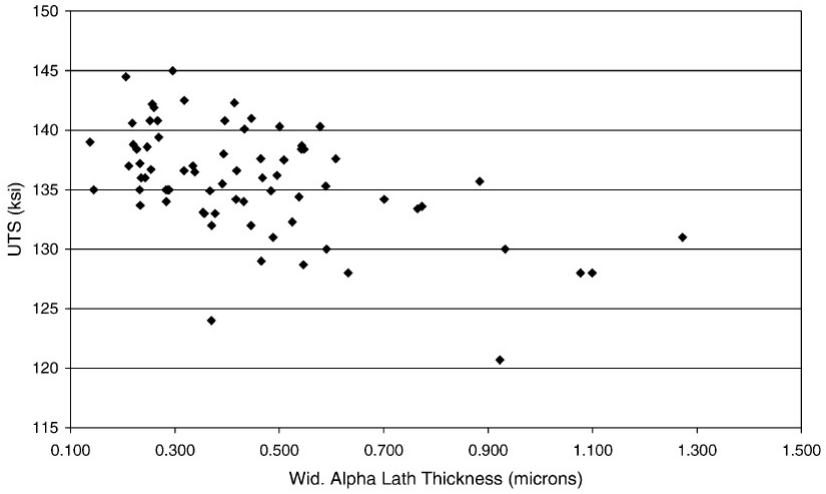

Figure 2.29.: Ultimate tensile strength as a function of the α lath thickness measured in a Ti-6Al-4V Widmanstätten structure [28]

2.3.6.2 Modelling of the equiaxed and lamellar alpha phase evolution

The previous section showed the relation between the variation of the microstructural morphology and the mechanical behaviour of Ti-6Al-4V, suggesting the necessity to develop numerical models to describe the microstructure evolution of the material. Literature work investigating numerical approaches in this regard will be thus reviewed in this and the following section.

Work based on the description of the diffusion process driving the growth/shrinkage of the particles has been carried out on equiaxed and lamellar structures that, in a welded material, can both be present or developed.

A microstructural model for the prediction of the evolution of the equiaxed morphology in Ti-6Al-4V has been developed in [40] then expanded in [29] adopting the approach presented in [39]. A spherical particle growth diffusion model has been used to analyse how different primary-alpha particles of various sizes behave during cool-down from a peak temperature. A classic one-dimensional diffusion problem for a spherical particle of radius R has been adopted as reference model, described by:

$$\frac{dR}{dt} = 2\lambda^2 D/R \tag{2.4}$$

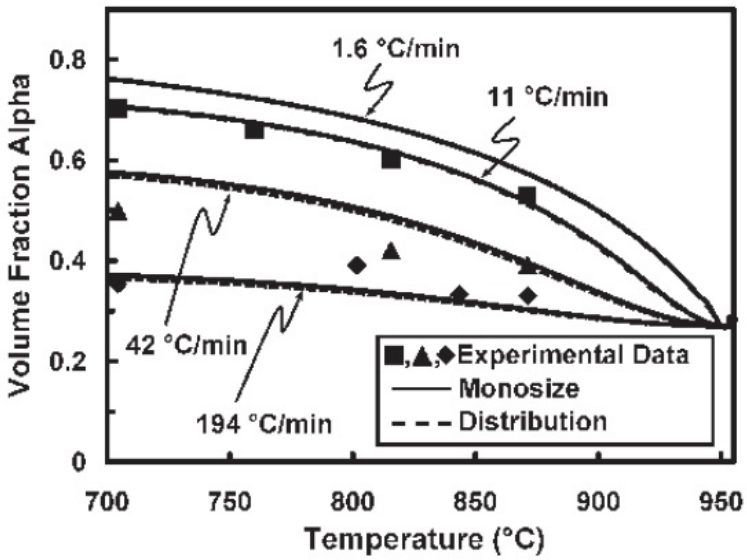

Figure 2.30.: Graph comparing experimental data with model predictions of the effect of cooling rate and size distribution on the variation of the total volume fraction of the alpha phase in Ti-6Al-4V, cooling down from 955 °C [29]

where R is the particle radius in function of time t, D is the diffusion coefficient and λ is a parameter related to the supersaturation Ω which in turn is related to the ratio between the solute concentration in the matrix side and in the precipitate side. The determination of the single parameters of the equation 2.4, explained in [29], permitted good numerical predictions for heat treatments consistent of a soaking at 955 °C and cooling rates at 1.6, 11, 42, 194 °C/min, considering both a distribution of different sizes of the alpha particles and a mono-size distribution. The work shows an essentially identical behaviour between the two different distributions of particles and agreement with experimental results (figure 2.30) about the prediction of the alpha volume fraction evolution. Another result showed in [29] is the tendency of the particles with larger size to grow more rapidly than the ones with bigger size, emphasizing this trend as the cooling rate becomes smaller and smaller.

The single particle diffusion approach presented in [40] has been also used in [30] to describe the growth of platelet thickness, approximating lamellae as ellipsoids, as originally developed in [67] and applied in [68, 69, 70]. Instead to use a more complicated 2-dimensional approach as it should be necessary to describe the growth of precipitates with elongated shape (e.g. lamellar shape), the approach, considering to describe grow

of precipitates already nucleated and impinged, assumes constant aspect ratio of the precipitates allowing to treat the problem as one-dimensional. In [30], Ti-6Al-4V specimens tested at temperatures of 971 and 982 °C and cooling rates of 11 and 42 °C/min, show growth trends in good agreements with the numerical predictions, underlining also the slower lamellar alpha volume fraction growth than the spherical particles, the behaviour being justified by the larger equivalent radius of the platelets when the ellipsoid geometry is converted to an equivalent spherical shape (see equation 2.4). In [30], both the spherical and oblate spheroidal solutions have been used, as the material microstructure presented both of them, and comparisons between numerical model and experimental tests seemed to return trends in agreement (figure 2.31).

Regarding the dissolution, apparently in literature there is no work on Ti-6Al-4V, nevertheless the same approach adopted for the equiaxed growth has been investigated also for shrinkage in [39].

It seems instead, there is no solution in literature to the ellipsoidal approach applied to the dissolution. The most interesting literature work found is relative to the description of this phenomenon by the dissolution of an one-dimensional plate. This idea has been used in [71] for modelling of Aluminium alloys but also in [72] for TiAl alloys. In particular in the last work, one-dimensional lengthening has been coupled with the one-dimensional thickening, switching from the first type of growth to the second, when mechanical impingement of lamellae was identified.

The current work will be carried out following the idea suggested in the works above presented, trying to describe both for heating and cooling the evolution of the particles dimensions when the temperature does not go above beta transus.

2.3.6.3 Modelling of the beta grains evolution

To model numerically the beta grain growth, the phenomenological expression shown in equation 2.5 has been adopted to describe growth during preheating for temperatures close to β-transus [66], for short times [73] and for continuous heating during beta annealing

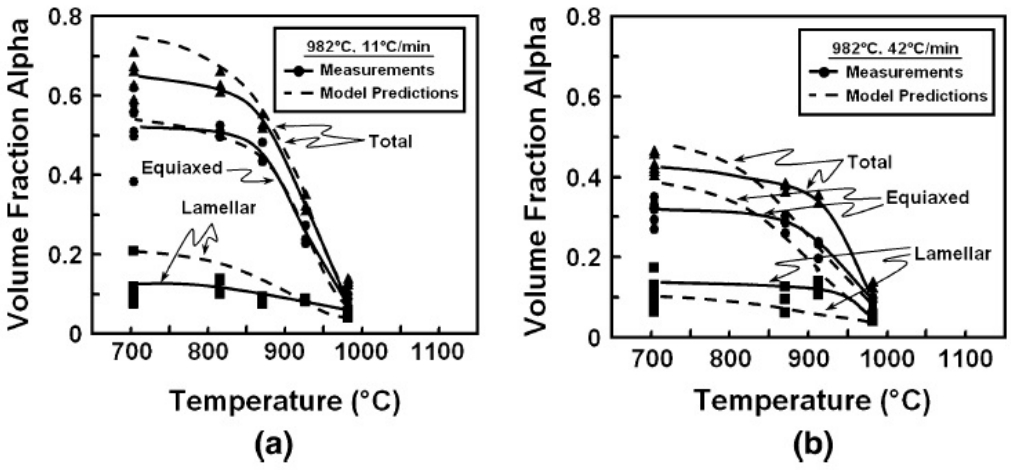

Figure 2.31.: Graphs showing measured and predicted variation of the volume fraction of primary equiaxed, lamellar and total alpha as a function of temperature and cooling rates from 982 °C in Ti-6Al-4V [30]

[74].

$$d^n - d_0^n = A \times t \times \exp(-Q/\Upsilon T) \tag{2.5}$$

where d = final grain size (μm), d_0= starting grain size (μm), t = time (s), Q = activation energy for grain growth (J/mol), Υ = gas constant (8.314 J/(mol*K)), T = temperature (K) and A and n material specific constants.

Of particular interest is the approach shown in [74] since analysing continuous heat treatments. In this work, the equation 2.5 has been converted in differential form, where the grain size (d) is a function of the initial and final temperature (T_i and T_f) of the heat treatment, the temperature rate ($\dot{T}$), the initial grain size (d_0) and the material coefficients (n, A, Q) that are assumed to be independent of temperature:

$$d^n - d_0^n = \frac{A\Upsilon}{\dot{T}Q} \times \left\{ \left[T_f^2 \exp\left(-\frac{Q}{\Upsilon T_f}\right)\right] - \left[T_i^2 \exp\left(-\frac{Q}{\Upsilon T_i}\right)\right] \right\} \tag{2.6}$$

Comparisons between experiments and numerical predictions were made for heating rates of 5 K/s and 50 K/s with good matching for temperatures below 1200 °C at the fastest heating rate and temperatures below 1150 °C for the heating rate of 5 K/s. Above

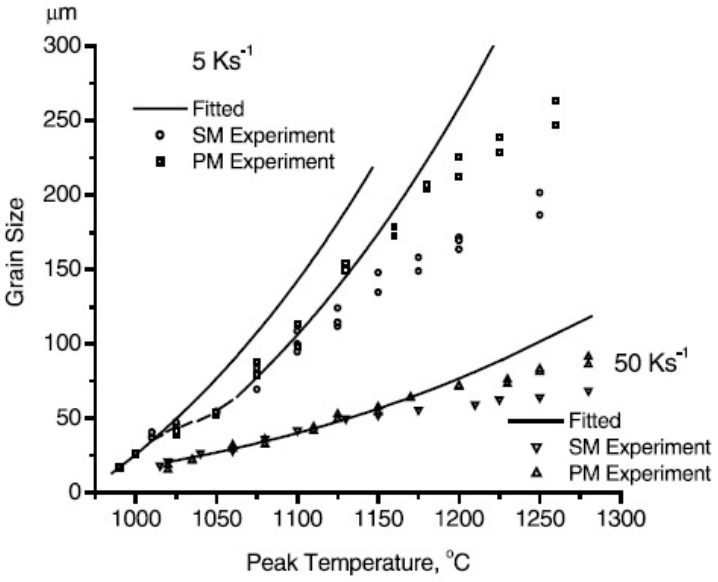

Figure 2.32.: Numerical beta grain size predictions obtained using equation 2.6 vs experimental measurements as a function of temperature for a Ti-6Al-4V alloy. PM makes reference to a rolled plate from 16 to 5 mm whilst SM refers to a rolled plate from 16 to 2 mm, both plates had the same chemical composition. Heating rate of 5 and 50 K/s have been tested

these temperatures, the authors claimed that discontinuous growth attributed to texture affect made numerical predictions more difficult (figure 2.32).

2.3.6.4 Modelling of the mechanical behaviour in relation to the morphology

As stated in section 2.3.6.1, a relation between strength and morphology of the material is evident and different works to establish a mechanism underlying the coupling between plastic flow and microstructure phenomena of Ti-6Al-4V have been carried out. In general, different levels of approximation of the phenomena are used, affecting the precision of the prediction but also the range of validity of the model and the time of elaboration to get the final result. This last aspect, considering the noticeable time that a welding simulation could take, for the number and the intrinsic complexity of the phenomena involved, will be an important weighting factor in the elaboration of the final mechanical model of the project.

Besides works based on phenomenological models like for example [75], where a modified

Norton-Hoff law has been used to describe the material behaviour within $T_{amb} - 1,000\,°C$ and $5 \times 10^{-4} - 5 \times 10^{-2}\ s^{-1}$ as strain rates and [76], where a Johnson-Cook law with temperature dependent parameters and able to describe strain softening has been used for the description of mechanical stresses in cutting processes (strain rates evaluated $1 - 10,000\,s^{-1}$), some more physically-based model have been developed too. Hereinafter, some works sorted by increasing complexity are presented; common denominator is the reference to the particles size of the microstructure for the determination of the strength of the material.

In [31] the effect of the platelet thickness on plastic flow has been studied. Specimens with three different microstructures, all colonies alpha but with different thickness of the platelets (table 2.6), including a martensitic structure, have been subjected to hot compression tests at different temperatures (815, 900, 955 °C) at a strain rates of 0.001, 0.01, 0.1, 1 or $10\,s^{-1}$(e.g. figure 2.33). For the higher strain rates (0.1, 1.0, $10.0\,s^{-1}$) where the Hall-Petch phenomenon (dislocations pileup/slip) is shown and for the temperatures of 815 and 900 °C, where the alpha volume fraction is greater than 0.5, the peak stress measured in the hot compression tests has been expressed as sum of the single crystal resolved shear stress and the Hall Petch effect, multiplied by the Taylor factor:

$$\overline{\sigma_p} = M(\tau_0 + k_s l^{-1/2}) \tag{2.7}$$

where M is the Taylor factor for specific alpha-phase texture (here taken equal to 3), τ_0 is the friction lattice stress, k_s the Hall-Petch constant and l the platelet thickness.

The work demonstrated also the dependence of the flow softening encountered during the tests by the loss of the Hall-Petch strengthening, finding good agreement by expressing the steady state stress as:

$$\overline{\sigma_{ss}} = M\tau_0 - \Delta\overline{\sigma_h} \tag{2.8}$$

where $\Delta\overline{\sigma_h}$ represents the softening due to the deformation heating.

Microstructure	ℓ (µm) at:		
	815°C	900°C	955°C
A	0.40	0.67	0.81
B	1.03	1.07	0.84
C	8.34	6.35	4.41

Table 2.6.: Platelet thickness measured for three different Ti-6Al-4V microstructures (A: 1040 °C/1h + water quench; B: 1065 °C/5min+940 °C/5min+815 °C/15min + air cool; C: 1040 °C/1h+ furnace cool to T_{amb}+970 °C/4h+ furnace cool to T_{amb}) at 815, 900 and 955 °C [31]

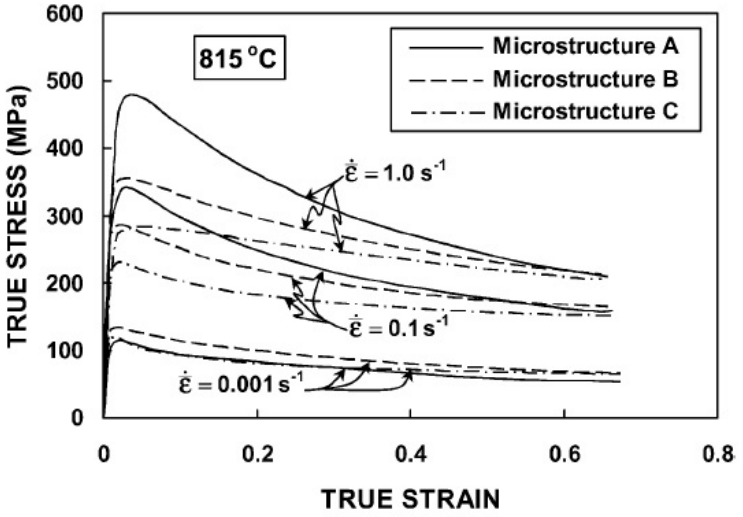

Figure 2.33.: True stress-true strain curves obtained from Ti-6Al-4V hot compression tests at 815 °C and strain rates of 0.001, 0.1, 1.0 s^{-1} with microstructures having 3 different platelet thickness (reported in table 2.6) [31]

A second order effect on the softening of the material seems to derive from its crystallographic texture, as stated in [77], where its effect has been studied both for colony alpha and globular alpha microstructures, strengthening the thesis of the same author, in [31], where the main effect of this phenomenon was attributed to the loosing of the Hall-Petch strengthening.

In [78, 79] a constitutive model to describe the physics of the deformation between 100 and 1400K and strain rates between 10^{-3} and $10s^{-1}$has been presented, using as reference, results obtained by compression tests on an initial equiaxed duplex microstructure. The total stress was decomposed for temperatures below $1230K$ in a thermally activated and an athermal stress: the first contribute described by the superposition of a term related to the interaction of dislocations with impurity atoms (C, N, H and O) and Ti_3Al_2 precipitates (over 800 K Ti_3Al_2 precipitates dissolve and only the contribution of impurity atoms remain) and one related to the interaction of dislocations with Aluminium solute atoms; the second term described by the sum of the Hall-Petch factor and a contribution related to the dislocation density evolution. Recrystallization and grain growth have not been taken in to consideration since during the experimental tests they were not noticed. For temperatures above $1230K$ the total stress has been described instead by only a thermally produced interaction of dislocation with Al atoms in solid solution. A modified rule of mixture in the α+β domain has been used to take in to account the contribution of each phase.

In [80] the material behaviour at high temperatures (715 - 900 °C) of Ti-6Al-4V with 3 different thickness of lamellar structure ($\approx 1\mu m$, $\approx 4\mu m$, $\approx 8\mu m$) has been described successfully using an inelastic-deformation equation, proposed originally in [81], referred to the grain matrix deformation for low deformations ($\epsilon \approx 0.5$), together with grain boundary sliding for high deformations ($\epsilon \approx 1.2$). The grain-matrix deformation in turn, has been described by phenomena due to dislocation glide and dislocation climb. Each effect, has been represented by an equation whose different parameters have been obtained by non-linear regression with the experimental data.

For low strains ($\epsilon \approx 0.5$), the stress-strain rate experimental data of tests at 715 and 815 °C have been well described by the dislocation glide equation, whilst at 900 °C and for strain rates $\dot{\epsilon} \leq 10^{-3}s^{-1}$, the addition of the contribution due to dislocation climb has been necessary to get a good match with the data of the experimental tests. An inversion of the stress-strain rate curve trends has been highlighted in relation to the effect of the platelet thickness, passing from low to high strain rates: at high strain rates small platelets gave higher flow stresses and vice versa for small strain rates, justifying in this last case, a thermal activated contribution typical of creep: thinner platelets, having a higher surface for diffusion with the alpha-beta interface can deform easier.

At high strains ($\epsilon \approx 1.2$), the stress-strain rates curves have been described by grain boundary sliding, checked also experimentally, and dislocation glide contributes.

In [82] a set of dislocation density based constitutive equations for each phase of the alloy have been used to describe the behaviours of Ti-6Al-4V and IMI834, putting also in relation the interaction of the evolution of the phases within the alloys. Since the work has been carried out for high temperatures and in a well defined range (800 - 1100 $°C$), the authors justified with a low impact on the predictions the following simplifications: a) α-phase isotropic; b) neglecting of the twinning phenomenon whose contribution is already decreased by the presence of a high percentage of aluminium in Ti-6Al-4V and c) keeping constant the strain rate sensitivity factor for each constituent phase. The model takes in consideration solution strengthening, Hall-Petch effect, dislocation interaction and dynamic recrystallization, involving a high number of equations whose parameters have been determined by the use of a genetic algorithm. The work reproduced successfully many features of the hot-working of two-phase titanium alloys, like stress and strain partitioning between α and β phases, dependence of flow stress on temperature, strain rate and alloying elements.

As it can be seen, proceeding toward models more and more complicated, the authors delimited the range of validity of the solutions to smaller amplitudes, this can be justified by a simple consideration: the higher is the number of phenomena taken in considera-

tion the lower is the chance they are always valid, unless right corrections are taken in consideration.

In all cases the parameters of the equations, determined initially by fitting with experimental data, has shown good results and capability to predict the strength of the material for the different conditions studied.

In conclusion, it can be stated that for this work a dislocation based approach will be preferred, considering the material as isotropic, and describing the strength of the material as constituted by different contributions, in relation to the working temperature: for high temperatures, where the volume of β phase is higher than 50% (about at 1230 K), stress will be considered mainly thermal, for lower temperatures, a thermal plus an athermal effect related to the strain hardening will be take in account. Recrystallization and plastic transformation induced by strain will not be considered since short times and relatively small strains are involved in welding process. Effect of texture will be considered as having a second order effect hence negligible.

2.4 Welding of Ti-6Al-4V

In this section the effect of welding processes on the microstructure and mechanical properties of the material has been investigated. Several works have studied experimentally the microstructure and/or mechanical properties of Ti–6Al–4V in fusion welding processes at different operative parameters [83, 34, 33, 32]. Some significant results are reported in figures 2.34 - 2.37 - 2.38 - 2.36.

In general, the smaller the heat introduced per unit volume of material, the smaller the dimensions of the fusion and heat affected zones (FZ and HAZ respectively). Figures 2.34 b) and d) confirms this trend for a laser welding process.

Within the FZ and HAZ, the typical microstructures obtainable in a high energy density welding process are shown in figure 2.35. Since the cooling rates in this areas are quite high, the initial $\alpha+\beta$ microstructure results in mainly acicular α' in the FZ and in acicular and lamellar α in the HAZ.

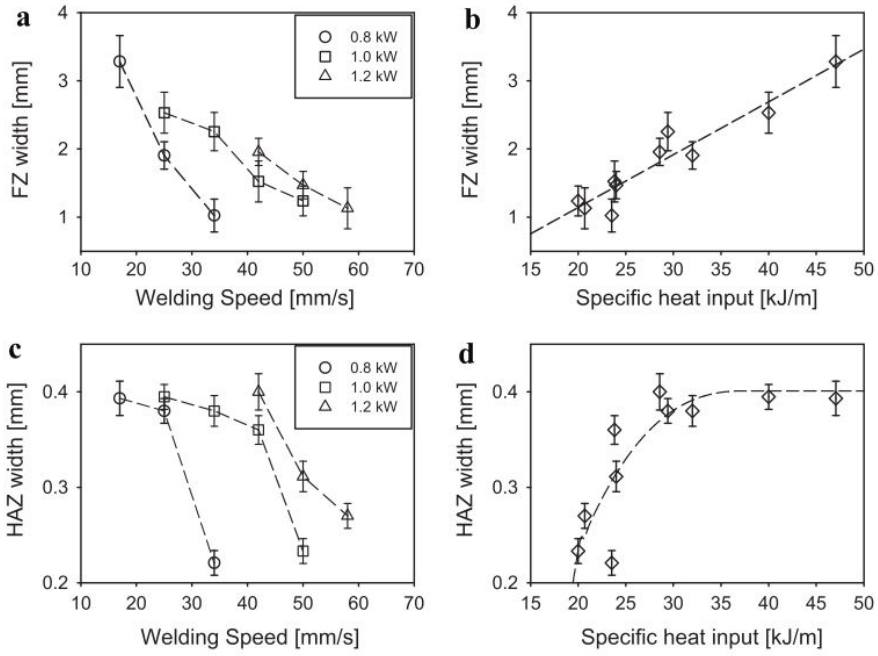

Figure 2.34.: Average fusion zone and heat affected zone widths as a function of welding speed and specific heat input in a laser welding process of Ti-6Al-4V [32]

The acicular α' microstructure has, as shown in figure 2.38, a higher hardness than the base material and, the smaller the needles thickness (e.g. due to higher welding speeds and relative higher cooling rates), the higher is the material hardness (figure 2.36).

The effect of the heat source is reflected also in an introduction of residual stresses in the material, as shown in figure 2.37, where by the hole-drilling technique, in proximity of the weld line, tensile stresses due to the melting, solidification and contraction of the material have been measured both in transversal and longitudinal direction.

Interlamellar spacing and a plate size of the Widmanstätten structure have been measured in [35], in a single and double pass electron beam welding process. The characterized microstructure is summarized in table 2.7. The application of the second pass lower the cooling rate, leading to a decreasing in the nucleation rate and an increasing in the growth of the α lamellae. Relating this information with the structural effect described in paragraph 2.3.6.4, it is clear how quite different mechanical behaviours of the material will occur in different regions affected (or not) by a welding process.

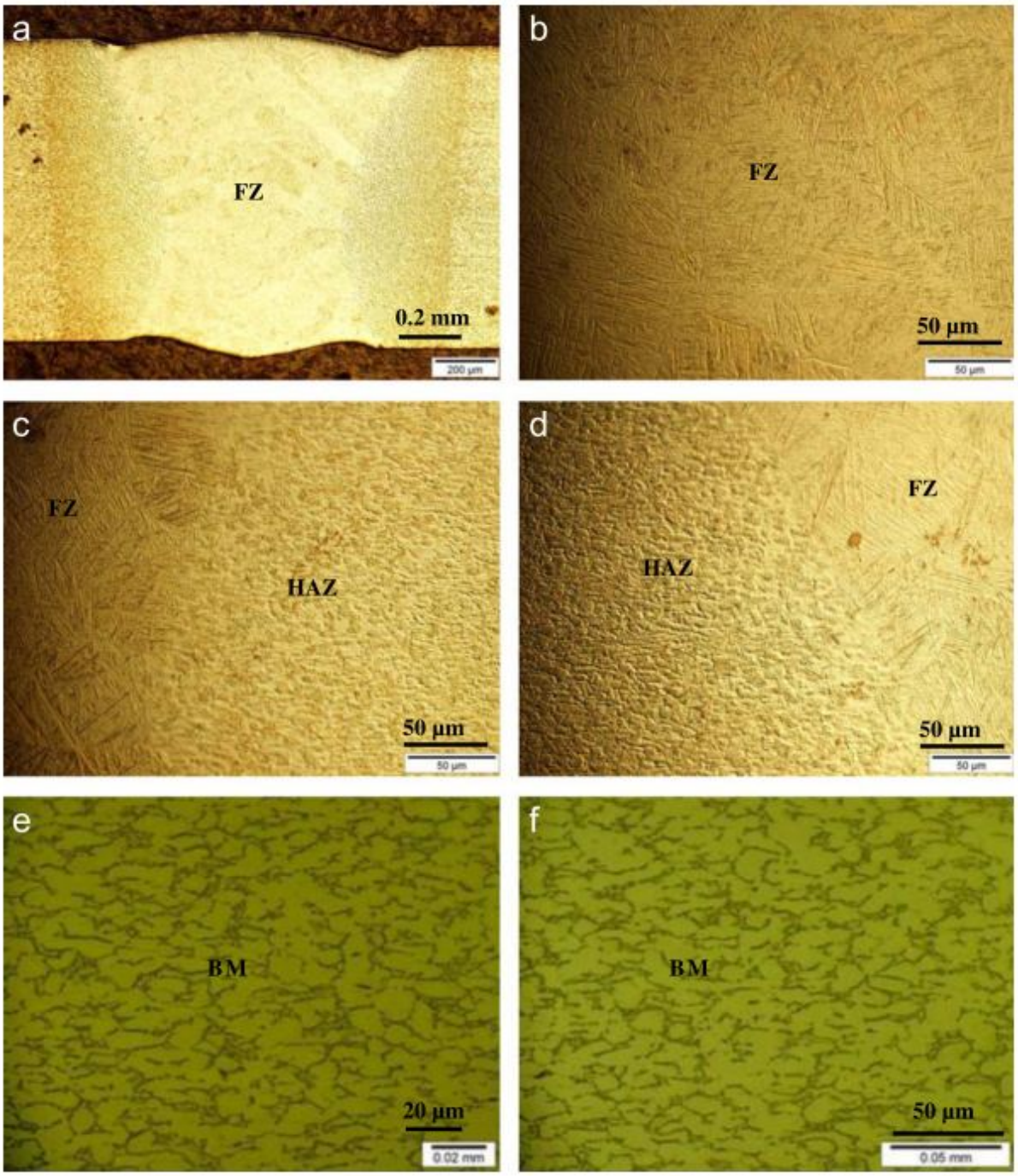

Figure 2.35.: Micrographs showing different microstructures obtained in a Nd-YAG laser welding process joining a 1mm thick Ti-6Al-4V plate ($2.5kW$, $7.5mm/min$). (b) fusion zone - acicular α' martensite, (c)(d) heat affected zone - acicular α' + primary α, (e)(f) bulk material - $\alpha + \beta$ microstructure [33]

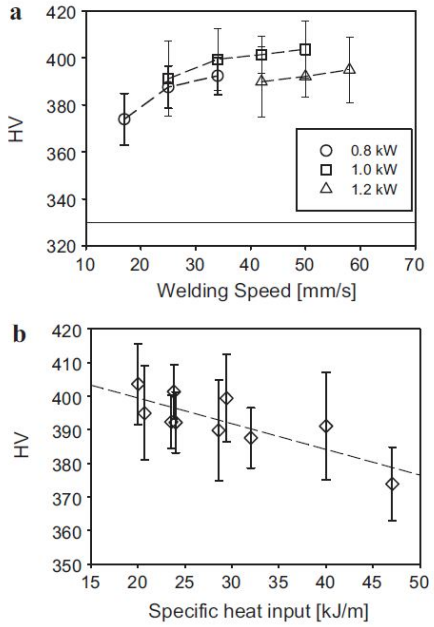

Figure 2.36.: Graphs showing the mean values of the fusion zone hardness as function (a) of the welding speed at different laser powers, (b) of the specific heat input measured after laser welding of Ti-6Al-4V. Error bars indicate 80% confidence limits [32]

Characteristics of Ti–6Al–4V weldment	1 pass EBW	2 passes EBW
	2.3 mm plate	2.3 mm plate
Prior-β grain size (μm)	186	214
Interlamellar spacing (μm)	1.83±0.15	2.35±0.11
α platelet size (μm)	0.93±0.12	1.22±0.15
Grain boundary α (μm)	1.21±0.18	1.54±0.21
Microhardness (HV)	357±5	349±6

Table 2.7.: Morphological characterization of the microstructure obtained in the fusion zone of an electron beam process on a Ti-6Al-4V plate of 2.3 mm thickness [35]

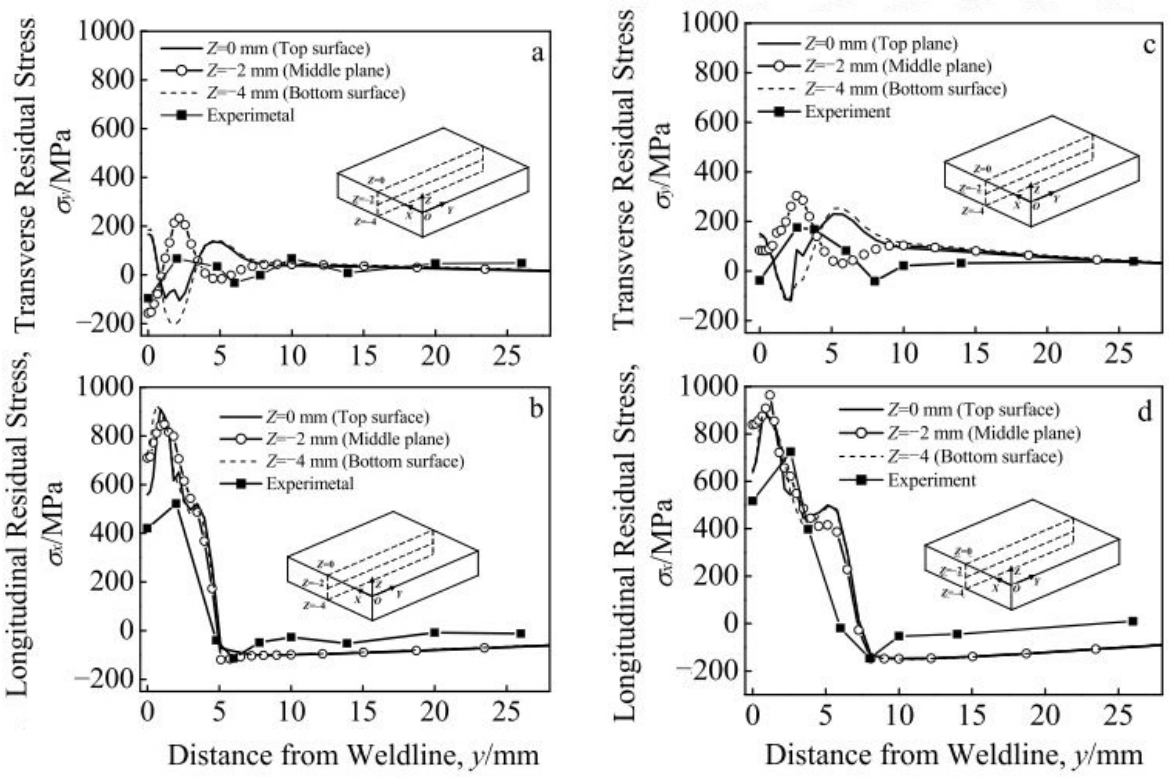

Figure 2.37.: Comparison of simulation and experimental (hole-drilling) residual stresses measured after a CO2 laser weld of Ti-6Al-4V at a maximum power of 3 kW. The welding plate size is $200\,mm \times 100\,mm \times 4\,mm$ with heat input of $115.7\,J/mm$ in (a) and (b), $162.0\,J/mm$ in (c) and (d) [34]

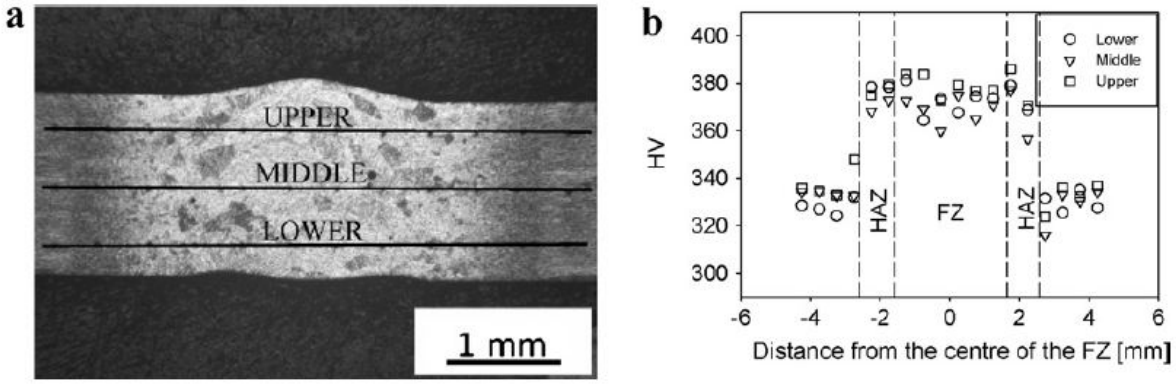

Figure 2.38.: Hardness measured using Nd-YAG laser on a Ti-6Al-4V sheet 1.6mm thick. (a) location of microidentations, (b) hardness profile observed over the weld cross section ($0.8\,kW,\ 17\,mm/s$) [32]

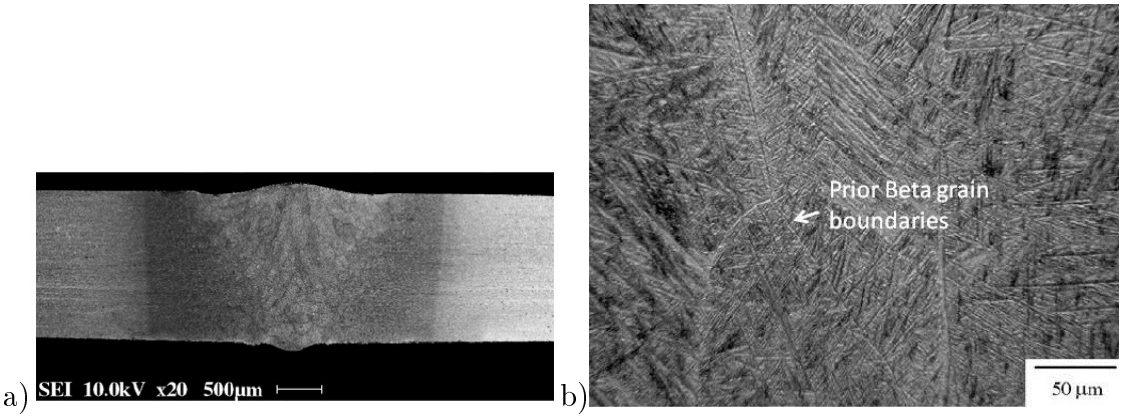

Figure 2.39.: Micrographs showing: a) the microstructure developed in a Ti-6Al-4V plate after electron beam welding process, it is possible to notice the coarse grains developed in the fusion zone; b) a detail of the acicular colony structure developed in the fusion zone, within the prior beta grains [35]

Specimen	Densification[a] (%)	Prior β grain size (µm)	Colony size (µm)	GB α phase width (µm)	α Platelet width (µm)	β Phase width (µm)
Base metal	99.7	840	384	8.6	3.6	0.35
TIG weld	99.7	895	18.1	3.7	1.5	0.08
EB weld	99.3	819	9.9	2.4	1.1	0.05

Table 2.8.: Microstructural parameters measured in EB and TIG welding processes of a Ti-6Al-4V 6mm thick plate, "GB" is for grain boundary [41]

In [41], where the fatigue life resistance of a Ti-6Al-4V 6mm thick plate subjected to TIG and EB welding process is studied, the effect of microstructural parameters are investigated (table 2.8) experimentally. Alpha platelet, grain boundary alpha phase and prior beta grains are larger in TIG compared to EB because of the slower cooling induced during this process; although the latter results in higher tensile and yield stresses, the formation of larger micro-pores induced by this process returns a lower resistance to high cycle fatigue [41].

Comparing results shown in table 2.7 (column 1 pass) and 2.8 (row EB weld), referred to two different thickness of plates (2.3 and 6 mm respectively), it is possible to notice a variation of about 20% in the thickness of the platelet, prior β grain 8 times larger and grain boundary alpha doubled, main cause of this could be the different thickness of the workpieces that results in different cooling rates of the materials and thus different times available for grain growth.

Results presented above show how the microstructure of the material is greatly affected by thermal history of the material hence, by the operative parameters of the welding process. Within the same kind of morphology of the microstructure (e.g. lamellar in the fusion zone, equiaxed far from the fusion zone), there can be differences in the dimension of the particles, that cause a different mechanical behaviour of the material, as discussed previously. Aim of this work would be to catch these variations.

2.4.1 Modelling of welding on Ti-6Al-4V coupling metallurgical and mechanical behaviour of the material

Even though, as demonstrated previously in this chapter, the morphology of the microstructure in Ti-6Al-4V represents an important factor in the determination of the material strength, in literature, to the best knowledge of the author, it is not possible to find any work on the modelling of welding processes coupling morphology and mechanical behaviour of Ti-6Al-4V. The past work is all based on the description of phases evolution by the JMA equation (2.3.5) and, based on phases proportion, the strength of the material is determined by a rule of mixture. The most meaningful works found in literature are listed below.

In [63] the mechanical behaviour of the material, under a laser assisted process, has been described as a function of the α, β distribution, each as a function only of the temperature at a specific time and position, and α' by the equation 2.3. A mixture rule has been used to compose the contribution of each phase, where the total strain was decomposed in elastic strain, viscoplastic strain, thermal strain and phase transformation strain. Deflections measured at some points of the numerical and experimental model were compared, showing an error on the prediction within $20 - 40\,\%$.

In [64] the distribution of phases, in a laser forming process, was predicted referring to the solution proposed in the previously mentioned work in [24] (see equations 2.1, 2.2) and the flow behaviour was calculated by a rule of mixture between the stresses of the single phases, considering the alpha phase as only equiaxed. The authors showed an

improvement in the deformation prediction of a weld on plate for the case where phases transformation was used even though it is believed that a simple rule of mixture to describe the strength of the material in the $\alpha + \beta$ field is not correct, as shown also in [79] where an exponential rule of mixture has been adopted. A comparison with experimental data has been done regarding the prediction of the bending of the work piece, showing good agreement; validation on the residual stresses has not been carried out, in this area probably the model would have shown its limits.

2.4.2 Visual-Weld multi-phase code

The commercial software Visual-Weld is currently being used to simulate the welding process. The diffusional phase transformation model provided by Visual-Weld is based on the Johnson-Mehl-Avrami equation (described also in section 2.3.5), with the limitations mentioned previously. The form of the equation to which the software makes reference is the following one:

$$P_{j \to i} = \overline{P_i} \left\{ 1 - \exp \left[\left(-\frac{t}{TR} \right)^s \right] \right\} \tag{2.9}$$

where:

$P_{j \to i}$ is the actual phase proportion in the transformation from the phase j to i - e.g. to get the phase fraction of i at time t, the value of the phase fraction j at time $t - \Delta t$ will be multiplied by $P_{j \to i}$ and added to the value of P_i at time $t - \Delta t$

$\overline{P_i}$ is the equilibrium phase proportion of phase i at the temperature under examination

t is the time

TR is a shift time constant for the phase i

s is a parameter related to the shape of the particles and the state of the reaction, relative to the phase i

The parameters TR, n and $\overline{P_i}$ are loaded in Visual-Weld in tabular form as a function of the temperature. The parameters are determined by fitting of equation 2.9 to CCT curves.

The martensitic reaction is described by equation 2.3 and it is attributed to only one specific transformation of phase j to i (e.g. β to α') that, during cooling, once the "M_s" temperature has been passed, starts following an exponential law. This reaction has precedence on reactions specified by the equation 2.9 hence, for a hypothetical cooling reaction from the "beta" field, if the thermal conditions are satisfied, "beta" is transformed to martensite following equation 2.3 then, if there is a residual difference between $P_{\beta\to\alpha}$ (eq. 2.9) and y (eq. 2.3) the relative amount of "beta" is transformed to "alpha" phase.

The main problem encountered by this process, besides the limits explained in the previous paragraphs, due to the opportunity to work only on phase fractions, is the impossibility to activate different set of parameters as a function of the starting temperature of the reaction: e.g. a cooling reaction for a specific phase is defined by a unique set of tabular data that, for instance, could be fine for a transformation that starts from the beta field but not for a transformation that starts from the α+β field.

2.4.3 Summary

In conclusion to this section, about the metallurgical and mechanical modeling of Ti-6Al-4V subjected to a high energy density welding process, it can be stated that currently there is not much work in literature and moreover, it is all based on the description of the phase fraction evolution to describe the strength of the material.

It is believed that this approach, even though correct for steels, does not work correctly for titanium alloys, where the main factor in determining the plastic flow of the material is primarily the microstructure morphology, in particular the dimension of spherical and lamellar particles. This probably explains the lack of works in literature and their approximate ability to predict residual stresses in the material.

Another limiting factor of the approach used is that usually the description of the phase fraction evolution is carried out using exponential laws like the JMA equation, making reference to specific initial states of the material, for example a full β structure for cooling transformations and, by fitting to experimental data like CCT curves, the parameters

of the equation are found. This is an approximation that does not permit a correct description of what happens in the material starting from a different initial condition (e.g. α with a specific dimension of the grains + β).

This project will be based on a diffusional approach to describe the evolution of the particle dimensions, spherical and lamellar, during heating and cooling to describe in a high energy density welding process the mechanical behaviour of the material as affected by the morphological properties of the microstructure. Different works present in the literature have been shown based on this idea, to describe the metallurgical and mechanical behaviour of Ti-6Al-4V, but not applied to welding processes, hence this will be the main challenge and innovation represented by this work.

Regarding the description of the martensitic transformation an empirical law, like the one described in the paragraph 2.3.5.3, will be used to describe this diffusionless process, relating the acicular structure dimension to the cooling rate. In the literature, in fact, other solutions to this idea have not been found besides the phase field approach, which is too complex for this project, that aims to be based on relatively simply equations to avoid excessively long run times of the numerical simulations.

2.5 Surrogate models

Surrogate models are approximation models constructed using a data-driven, bottom-up approach. The exact, inner working of the system under evaluation is assumed not to be known (or even understood) and just the input-output behaviour is considered important. The aim of these models is to describe the response of a system by the initial evaluation of a limited number of intelligently chosen cases, doing predictions and eventually self-improving results.

A surrogate model is an engineering method that can be useful when:

- an outcome of interest cannot be easily directly measured, so a model of the outcome is used instead;
- routine tasks such as design optimization, design space exploration, sensitivity analysis and what-if analysis become impossible since they require thousands or even millions of simulation evaluations.

With reference to figure 2.40, surrogate modelling can be seen as a non-linear inverse problem for which one aims to determine a continuous function (f) of a set of design variables from a limited amount of available data (f_1). The available data f_1 can represent exact evaluations of the function f or noisy observations and in general cannot carry sufficient information to uniquely identify f. Thus, surrogate modelling deals with the twin problems of: (a) constructing a model $\hat{f}$ from the available data f_1 (model estimation), and (b) assessing the errors ε attached to it (model appraisal). A general description of the anatomy of inverse problems can be found in [36].

To construct a surrogate model it is necessary to pass through four major steps, as summarized in [37] and in the figure 2.41:

1. DOE: the design of experiment is the sampling plan in design variable space. The key question in this step is how to assess the goodness of such designs, considering

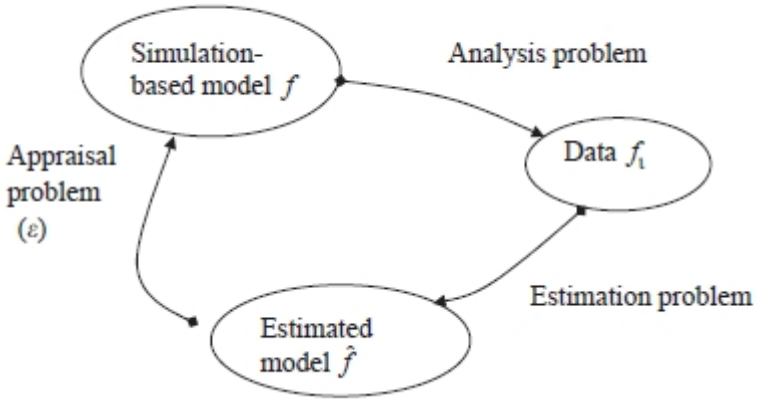

Figure 2.40.: Anatomy of surrogate modelling: model estimation + model appraisal. The former provides an estimate of function f while the latter forecasts the associated error [36]

the number of samples is severely limited by the computational expense of each sample;

2. Numerical simulations at selected locations. Here, the computationally expensive model is executed for all the values of the input variables in the DOE specified in the previous step;

3. Construction of surrogate model. Two questions are of interest in this step: (a) what surrogate model(s) should we use (model selection) and, (b) how do we find the corresponding parameters (model identification)?

4. Model validation. This step has the purpose of establishing the predictive capabilities of the surrogate model away from the available data (generalization error).

Different model estimation and model appraisal components of the prediction have been shown to be effective in the context of surrogate based analysis and optimization (SBAO) (see for example [84] [85][86]), namely polynomial regression (PRG), Gaussian radial basis functions (GRF), and (ordinary) Kriging (KRG) as described in [87].

The scientific challenge of surrogate modelling is the generation of a surrogate that is as accurate as possible, using as few simulation evaluations as possible.

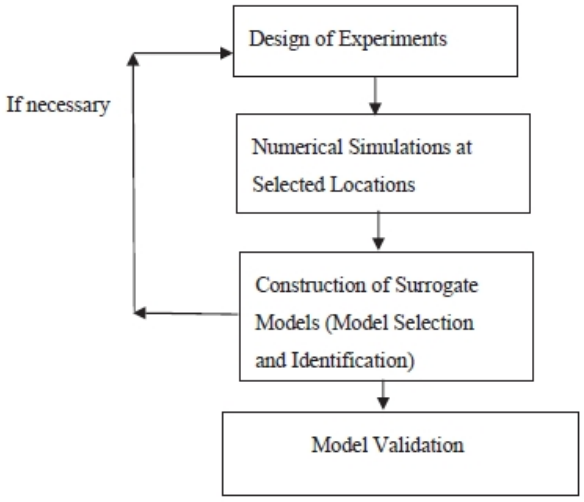

Figure 2.41.: Key stages of the surrogate-based modelling approach [37]

SBAO has been shown to be an effective approach for the design of computationally expensive models such as those found in aerospace systems, involving aerodynamics, structures, and propulsion, among other disciplines. For example, SBAO has been applied to rotor blade design and optimization [88], airfoil shape optimization [89], supersonic turbine [90], and injectors [91].

CHAPTER 3

Characterization

3.1 Introduction

The experimental characterization of this work is focussed on:

- the study of the microstructure evolution of a Ti-6Al-4V alloy when subjected to heat treatments of heating or cooling at a constant temperature rate, trying to investigate some of the thermal loads involved in a welding process, both to validate the numerical models and to get some data for the parameters fitting of the experimentally based equations
- running some welding tests to validate the numerical welding simulation predictions made by coding the models described in chapter 4, in particular comparing particle dimensions, phase proportions at different distances from the weld line.

The thermal treatments were decided by running a representative initial FE welding simulation (section 3.3), by which thermal gradients along the material were captured and used as reference to understand the data needed to characterize and study the microstructure evolution of Ti-6Al-4V in welding processes.

Unfortunately, the thermal loads the material is subjected to during a welding process are so extreme that a compromise with the limitations of the test instruments had to be accepted.

3.2 Project plan

To better understand the relation between the experimental work presented in this chapter and the numerical models described in chapter 4, a scheme of the project plan is shown in figure 3.1. By this figure, also the relationship between the metallurgical and mechanical numerical models is highlighted.

3.3 Preliminary FE model

A preliminary numerical simulation of a laser welding process on a Ti-6Al-4V plate was carried out using the commercial software Visual-Weld to get an indication of the thermal conditions that the material is subjected to.

The parameters of the model were taken from previous work found in literature as a reference [33] where a laser beam with a constant power of 2.5 kW was used to make welding tests on Ti-6Al-4V plates of 1 and 2 mm thickness at different speeds (75, 100, 125, 150 mm/s). In this preliminary model a welding speed of 100 mm/s was assumed for a Ti-6Al-4V plate $80 \times 60 \times 2\, mm^3$. With this geometry the weldline crossed the plate in 0.6 s. The duration of the simulation was 600 s, to ensure a complete cooling of the model.

A three dimensional conical heat source model was used (section 2.2.3) setting the upper and lower diameters of the cone equal to the upper and lower width of the weld pool measured experimentally in [33].

The thermal properties of the material used have been reported in the graphs shown in figure 3.2, 3.3 and 3.4. As the aim of this simulation was not to simulate precisely the thermal flow in the material, but to get an idea of the magnitude of the thermal loads involved during the process, the thermal properties were considered constant above 1500 °C to avoid convergences problems due to the very high value the specific heat has in correspondence of the melting temperature.

In figure 3.5 the distribution of the temperature along the workpiece is shown during

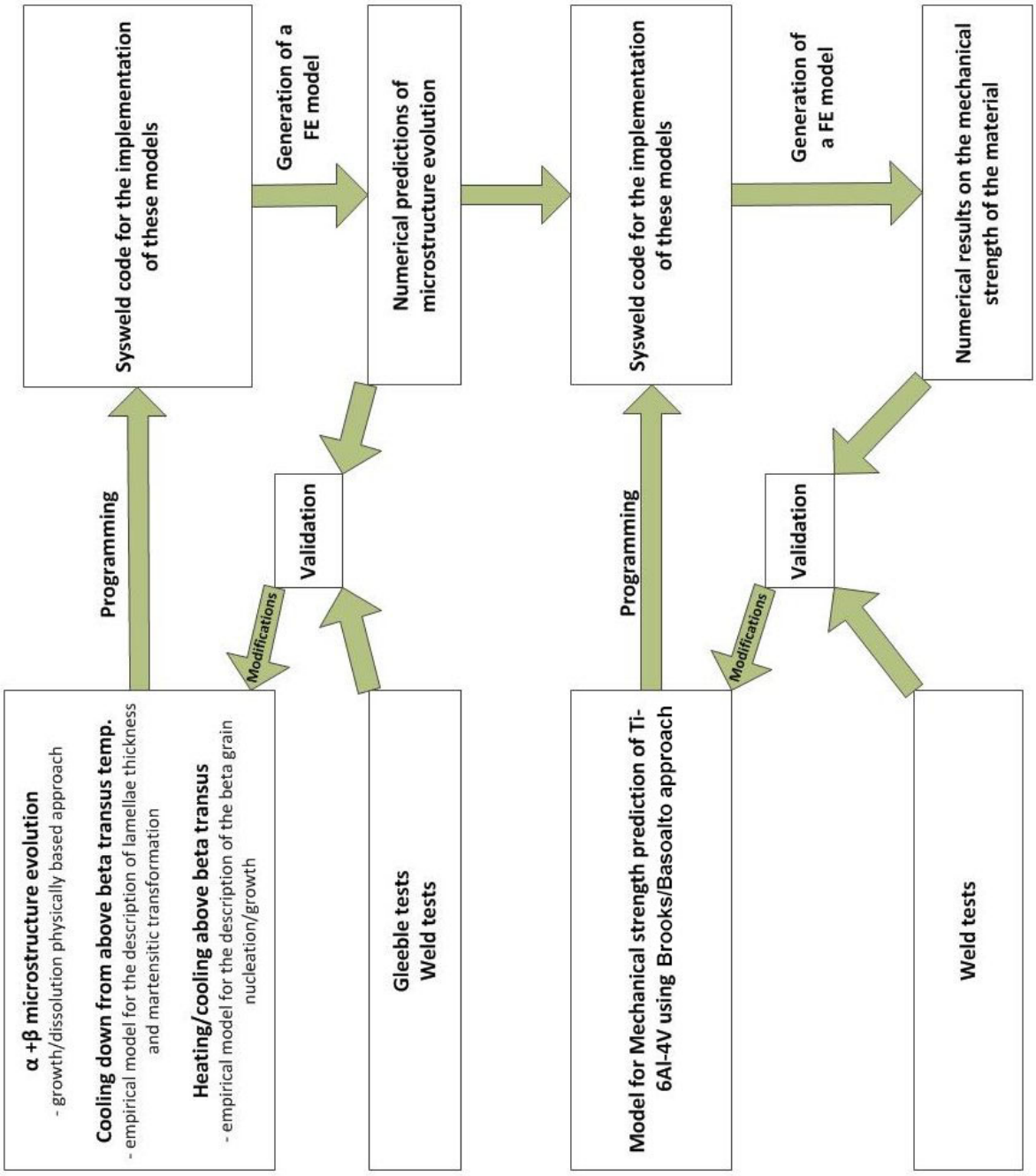

Figure 3.1.: Project plan

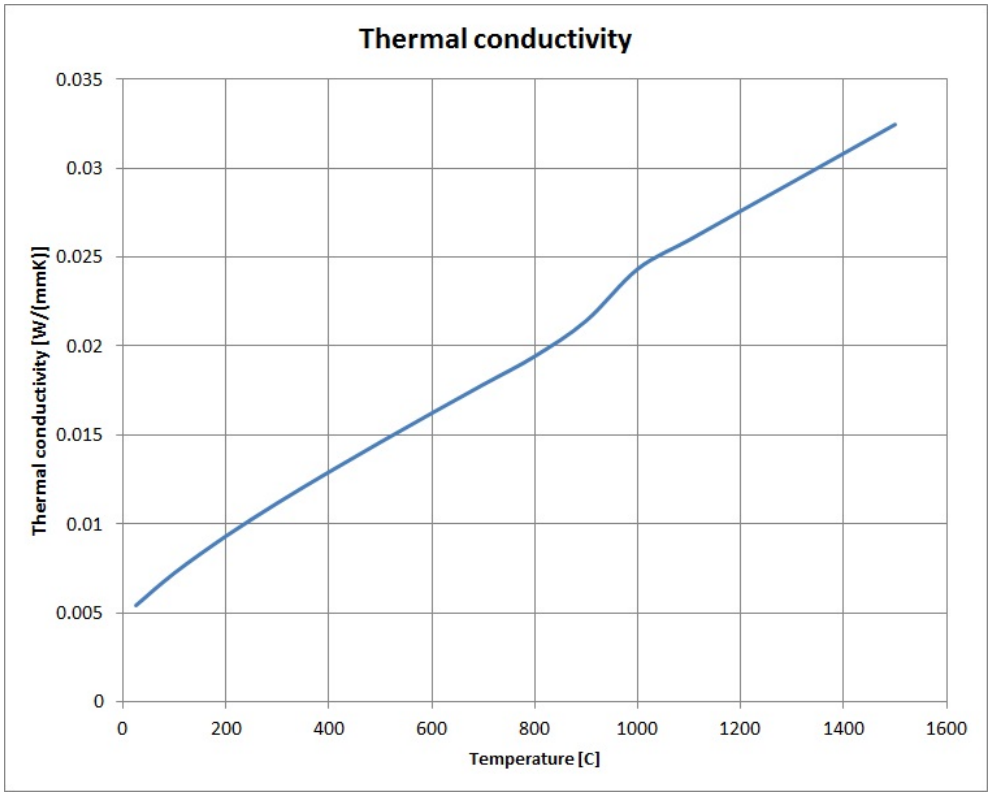

Figure 3.2.: Graph showing the Ti-6Al-4V thermal conductivity data used to run a preliminary FE welding simulation test

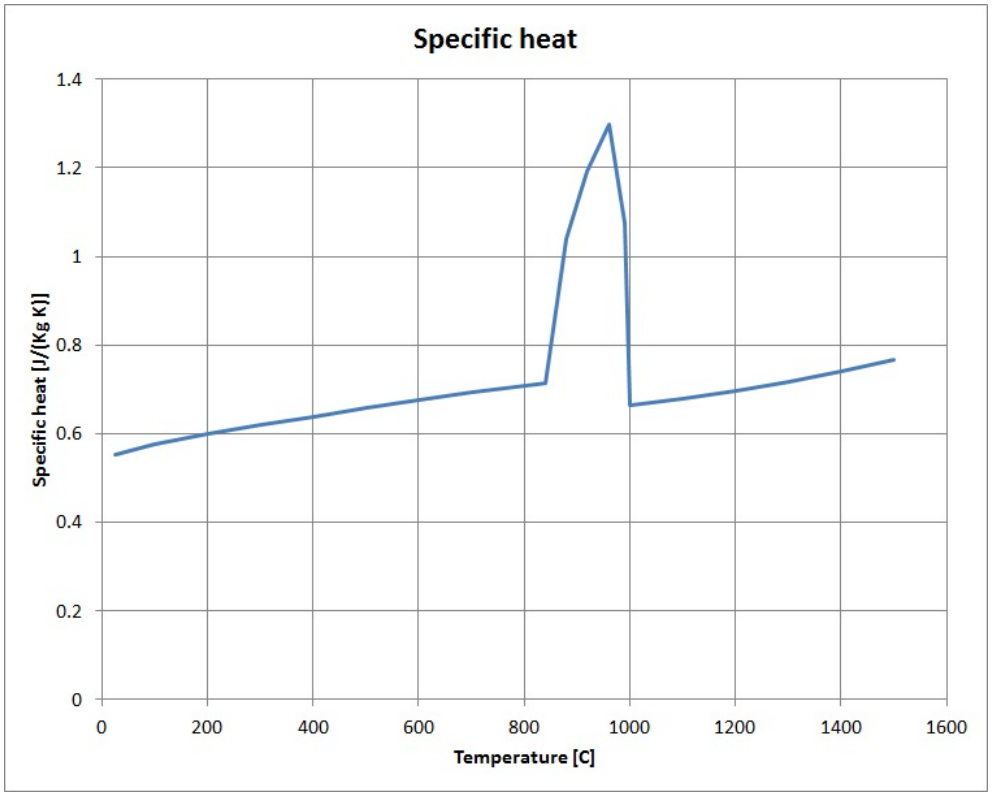

Figure 3.3.: Graph showing the Ti-6Al-4V specific heat data used to run a preliminary FE welding simulation test

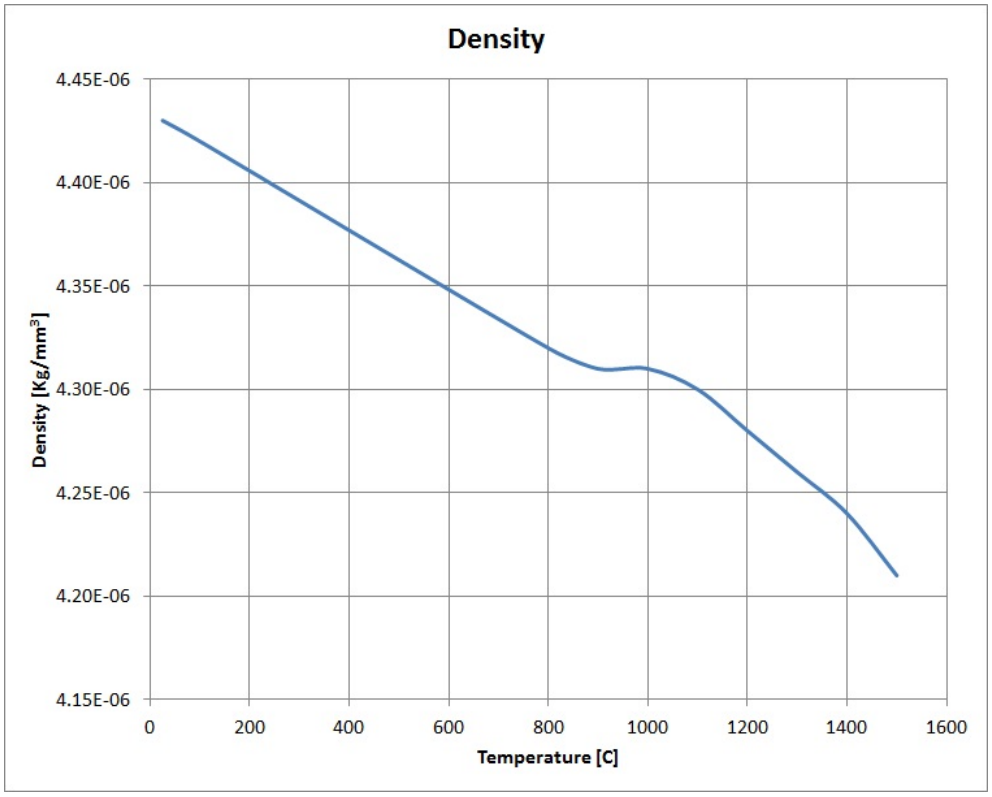

Figure 3.4.: Graph showing the Ti-6Al-4V density data used to run a preliminary FE welding simulation test

the welding process, at a time when a steady state condition of the weld pool has been reached. The fusion zone and the area where $T_{\beta\,transus} < T < T_{fusion}$ are highlighted by black contours.

In figure 3.6 a cross section of the weld pool is shown together with the points where the temperature has been sampled during the simulation. Graphs in figure 3.7 and 3.8 show trends of temperatures and heating/cooling rates sampled at the points showed in figure 3.6, the x-scales have been reduced to put emphasis on the highest variations. It can be seen there are very high gradients of temperatures along the workpiece as functions of both space and time, that subject the material to a great range of different thermal conditions.

The graph in figure 3.9 shows the first second of the simulation is considered reporting, in the same chart, both the trends of temperatures and their rates as a function of time. The maximum temperature is reported to be at 1600 $°C$ at approximately the solidus for the material in equilibrium conditions; considering the effect of the supercooling this value can be moved considerably toward lower values [19]. As a first approximation, the points where the temperature decreases passing through the β transus and then 700 °C at rates higher than $\sim$ 20 $°C/s$ (figure 2.24), will develop a full martensitic structure. At a distance typically between 0.8 and 1.23 mm the maximum temperature goes under 1000$°C$ and the corresponding cooling rates are about $1,800°C/s$: these values were taken in consideration for the definition of the experimental tests.

Similarly, to gain an idea of the strains and strain rates the material could be subjected to during welding, a mechanical simulation was also run. The points sampled for this evaluation are represented in figure 3.10, they were chosen in an attempt to measure within the area where the maximum equivalent Von Mises strains were predicted to be.

In figure 3.11 and 3.12 the equivalent Von Mises strains and strain rates predicted are reported. The maximum value of strain is 0.2 mm/mm, whilst the higher values of strain rates, measured when the temperature of the material is still very high, are such that probably part of the real material is still molten, are considered to be $\sim$ 10 s^{-1}.

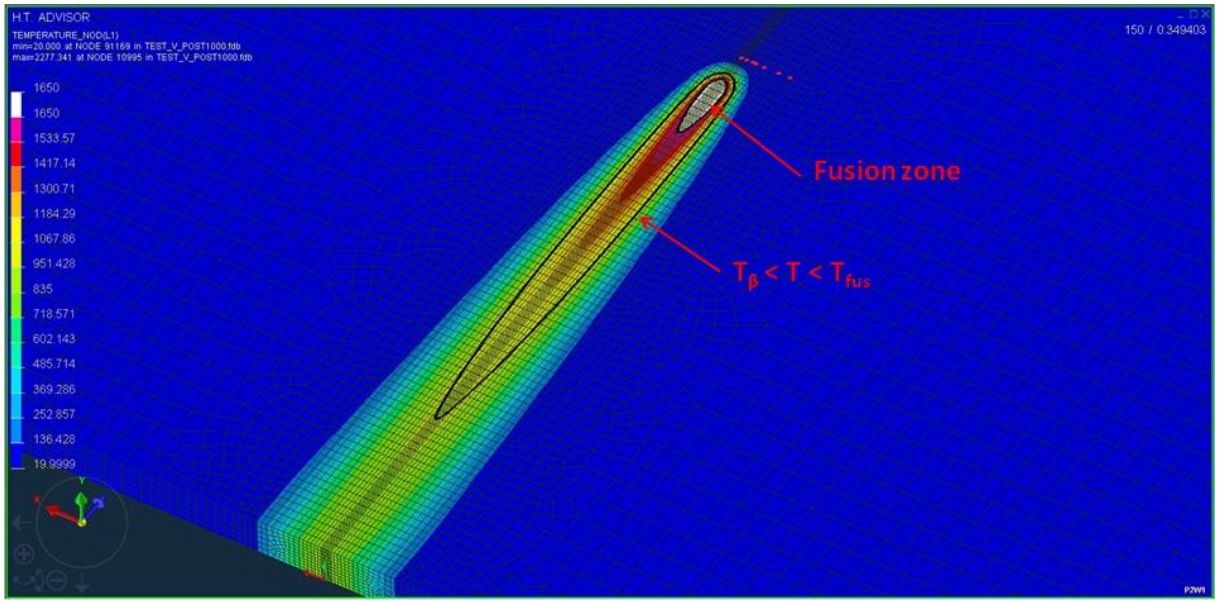

Figure 3.5.: Temperature distribution obtained by a numerical simulation of a laser welding process on a Ti-6Al-4V plate using the commercial software Visual-Weld. The inner black border highlights the fusion zone (temperature higher than 1650°C) whilst the outer one highlights the area where $T_{\beta\, transus} < T < T_{fusion}$

Looking at figure 3.12-b, where the strain rates after the application of the heat source are highlighted, a minimum value of $10^{-4}\ s^{-1}$ can be considered for future evaluations, lower values are not considered to be relevant to the timings involved in a welding process.

As shown by the charts in this section, the thermal loads on the material during a welding process are represented by such high values that, in term of experimental characterization, the temperature and temperature rate limits were established by the testing machine used. In particular it was not allowed to keep temperatures higher than 1300 ^{o}C for few minutes to avoid damage to the specimen holders, the fastest heating rate at which a sample was successfully tested was 500 ^{o}C/s whilst, at 1000 ^{o}C/s, the testing machine showed limits controlling the temperature, melting the material. The maximum constant cooling rate obtained till ambient temperature by water quenching was 300 ^{o}C/s.

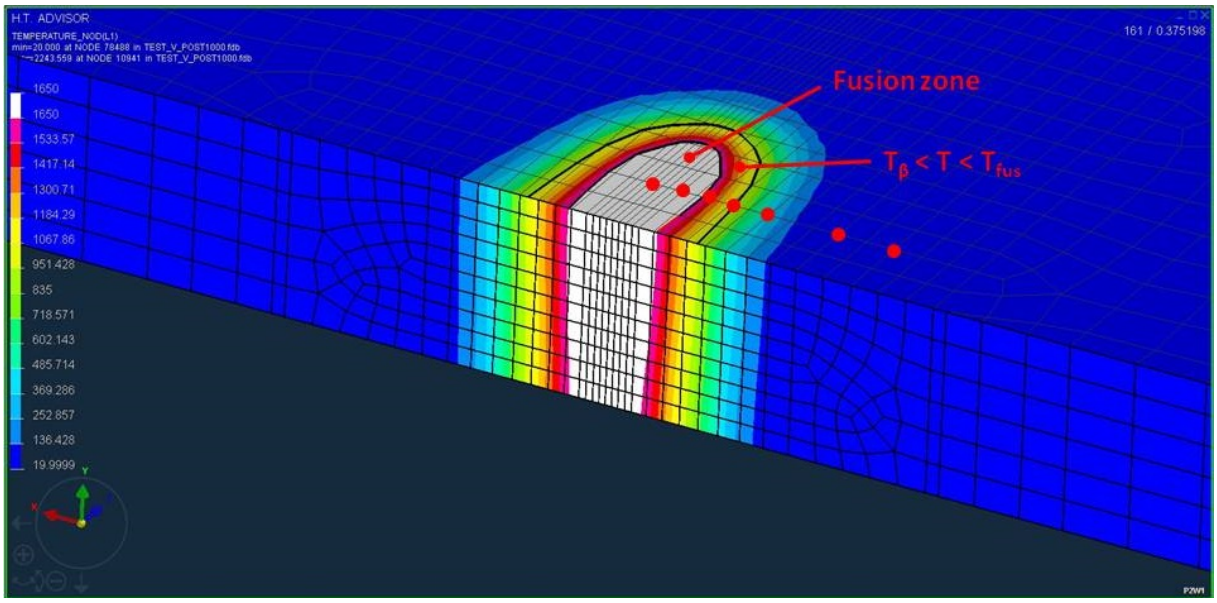

Figure 3.6.: Cross section of the figure 3.5, starting from the centre of the weld pool (weldline), point where the maximum temperature during the simulation is measured, 6 other points have been sampled progressively farther from the weldline (0.28, 0.62, 0.8, 1.23, 2.0, 2.6 mm), they are highlighted by red dots. Fusion zone and area where $T_{\beta\, transus} < T < T_{fusion}$ are delimited by black contours

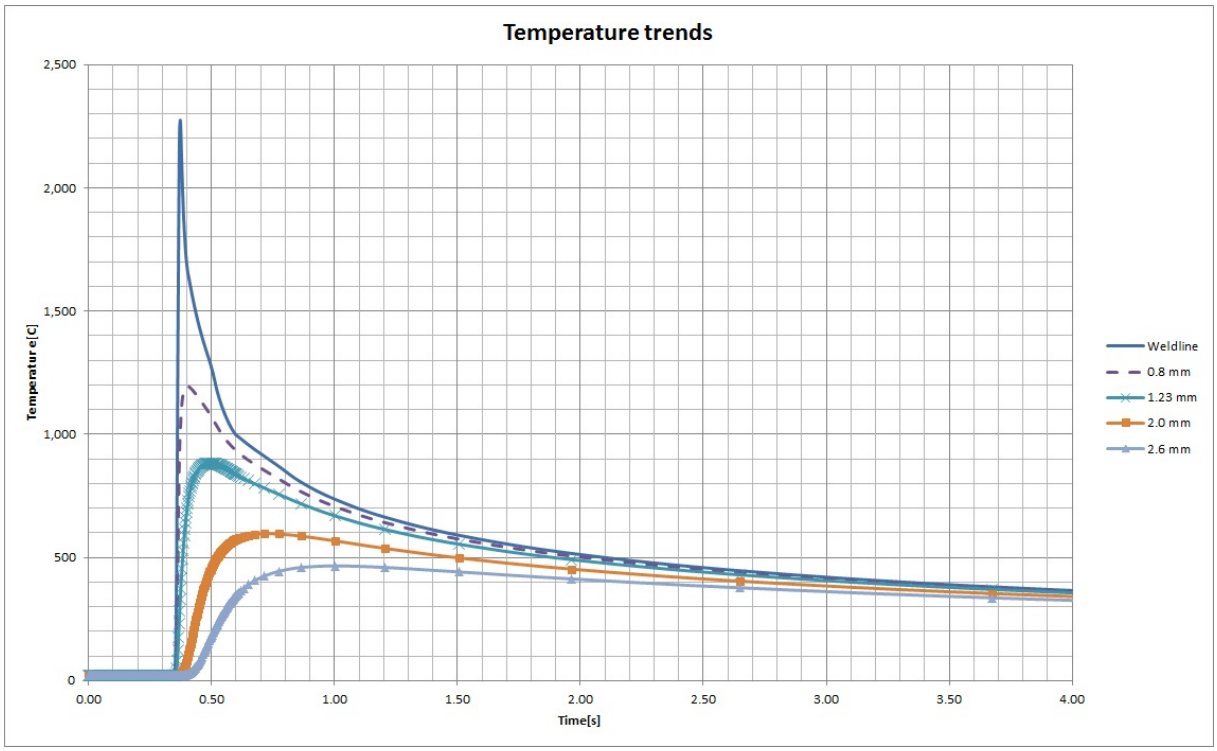

Figure 3.7.: Graph of the temperature trends measured on some of the points reported in figure 3.6, values measured at 0.28 and 0.62 mm from the weldline have been omitted for clarity

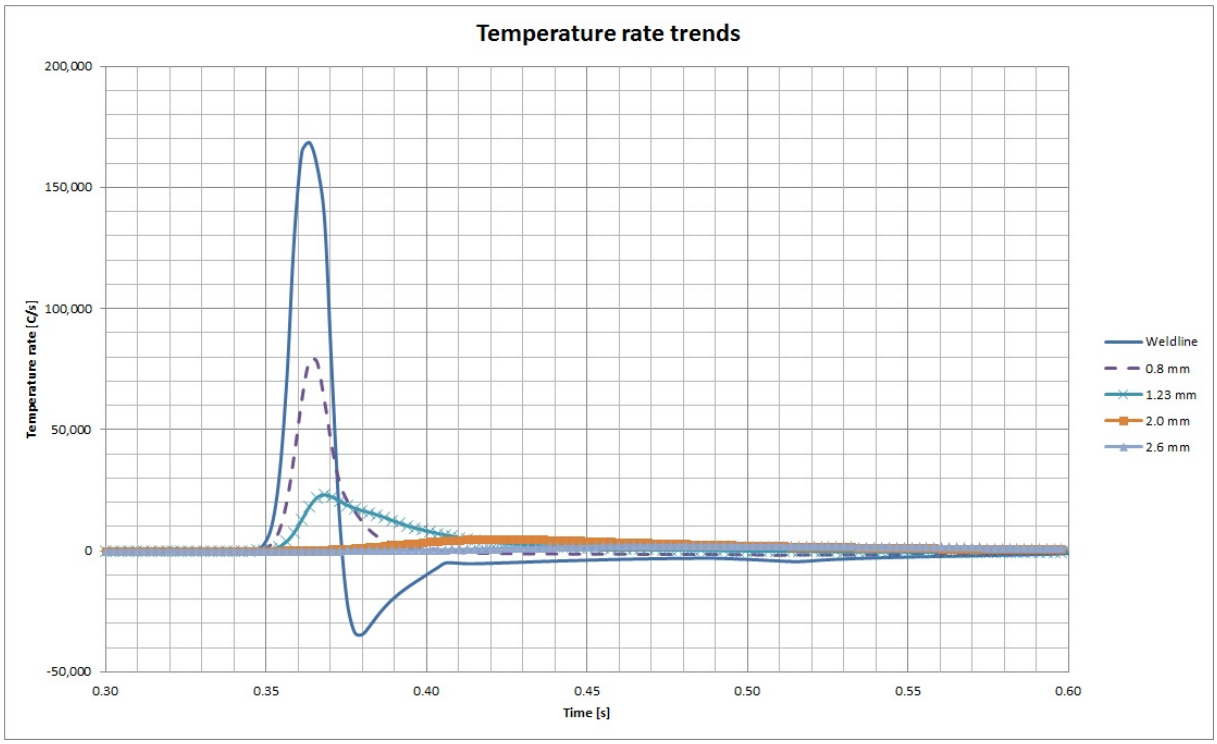

Figure 3.8.: Graph of the temperature rate trend measured on some of the points reported in figure 3.6, values measured at 0.28 and 0.62 mm from the weldline have been omitted for clarity, the curve relative at 2.6 mm lies almost on the x axis

3.4 Gleeble tests

The microstructural evolution of Ti-6Al-4V has been studied using the fully integrated digital closed loop control thermal and mechanical testing system Gleeble 3500, produced by Dynamic System Inc. This machine allows a compressive or tensile loading on a specimen, whilst a controlled current is applied through it. By the Joule effect, the component tested can then be heated following pre specified heat ramps and then cooling can be applied using natural air cooling, forced air cooling or water quenching. Also during cooling the current flowing through the component can be controlled, thus allowing specified cooling rates to be imposed.

Two different types of specimens have been used, according to the requirements for fast ($> 5\ ^{\circ}C/s$) or slow heating rates ($\leq 5\ ^{\circ}C/s$). For high heating rates, tensile specimens (figure 3.13) have been used, since in this mode it was possible to have better electrical

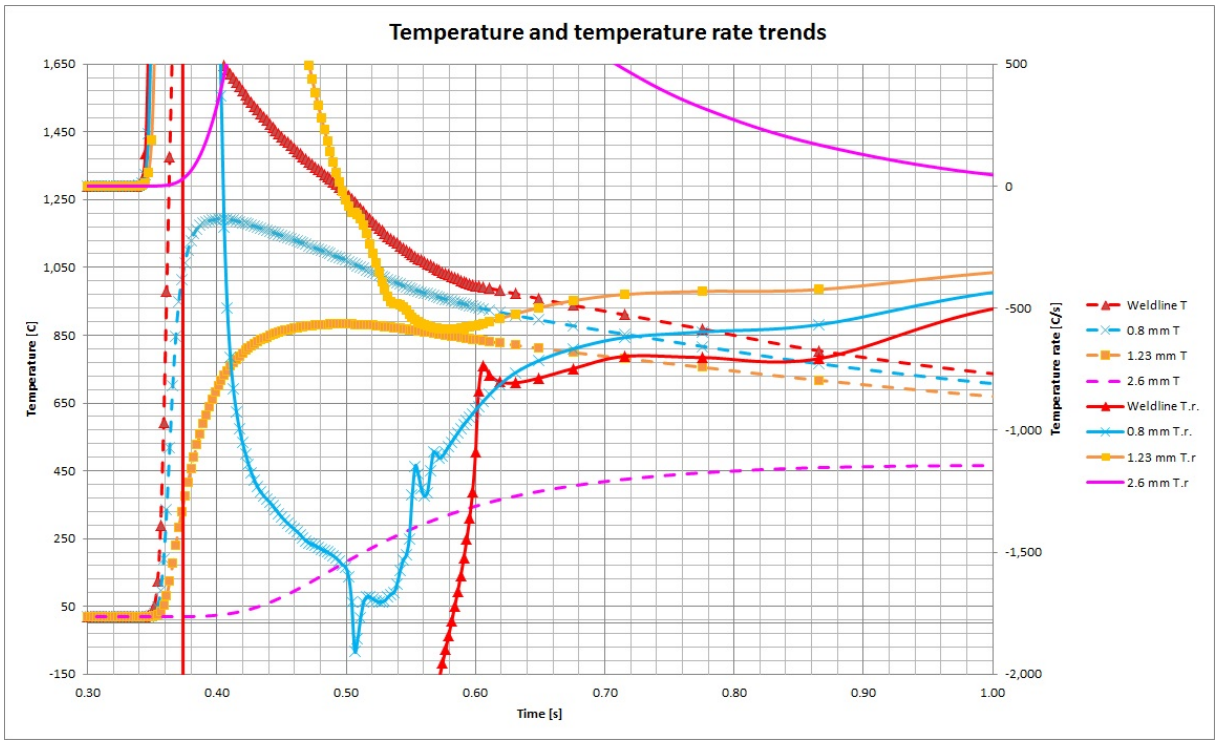

Figure 3.9.: Graph of the trend of temperatures (suffix "T" in the legend) and temperature rates (suffix "T.r." in the legend) measured in some of the points shown in 3.6 have been reported in the same graph to highlight the possible thermal conditions the material is subjected on during a welding process, at different distances from the weldline. In particular, temperatures below the Ti-6Al-4V melting temperature and temperature rates corresponding to temperatures close to the beta transus temperature are shown

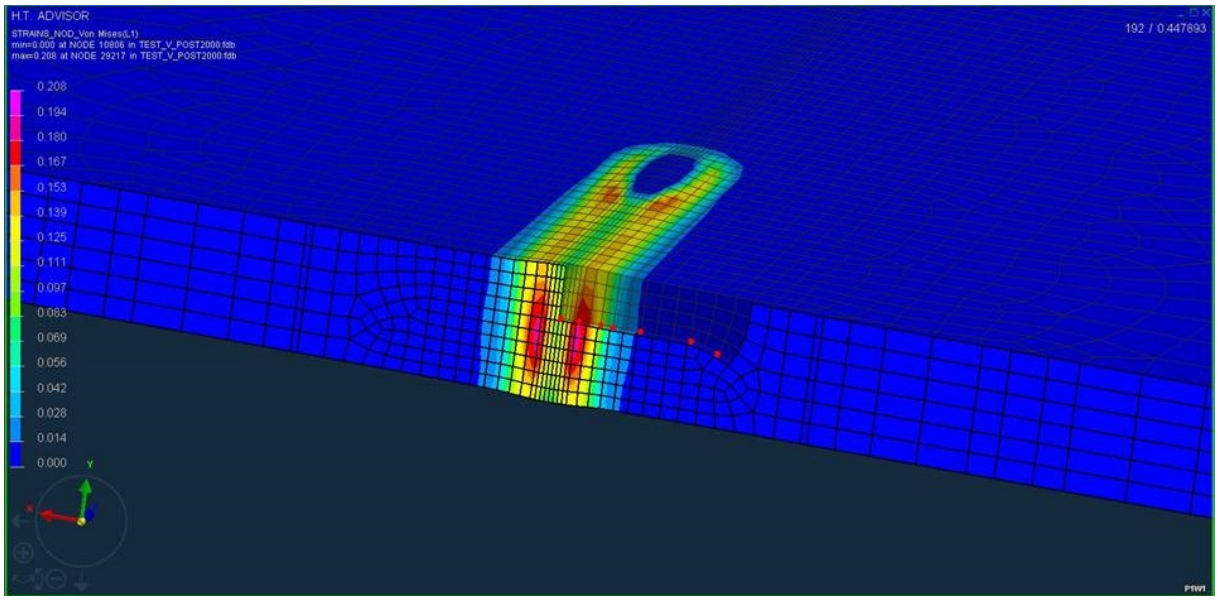

Figure 3.10.: Point sampled for the evaluation of the strains and strain rates the material is subjected on during the welding simulation

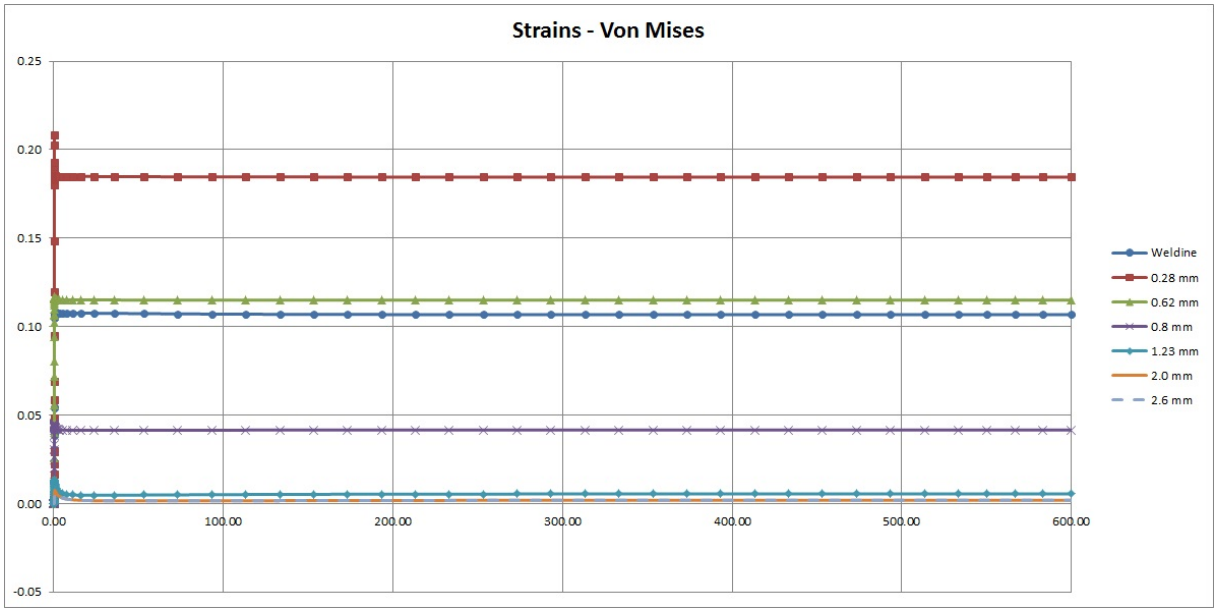

Figure 3.11.: Graph of the equivalent Von Mises strain measured in the points showed in figure 3.10

contact and smaller cross-sectioned area thus allowing a quicker control of the temperature of the sample. For slow heating rates, compressive specimens have been used (figure 3.14), firstly because they were less expensive, having a simpler geometry. Secondly, their dimension was not bounded by the geometry of the tensile jigs, allowing them to be machined with a larger diameter. A wider section area was particularly important for tests conducted at temperatures higher than the beta transus temperature and with soaking, to ensure there were sufficient beta grains to be measured for microstructural analysis. In these conditions, in fact, the beta grain dimensions tends towards order of millimetres.

Both kinds of specimens have been machined from a 16 mm Ti-6Al-4V thick plate, supplied by Ti-Tek ltd., with chemical composition in weight percent Al 5.75, V 3.96, Fe 0.07, H 0.00445, N 0.013, O 0.11, Ti bal.

To let the Gleeble machine control the temperature, at which the samples were subjected during the tests, a thermocouple had to be used to measure the temperature at a point of interest in the specimen. Usually, the thermocouple is connected to the mid point of the specimen using whichever technique is considered appropriate; in this regard, several

a)

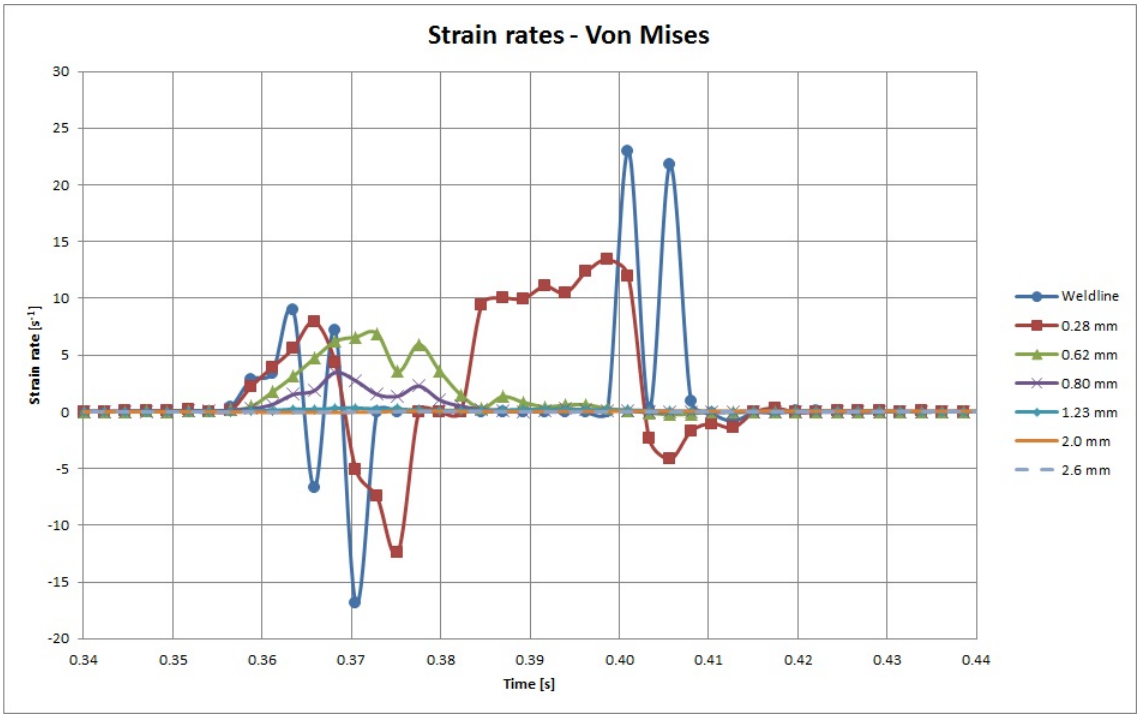

b)

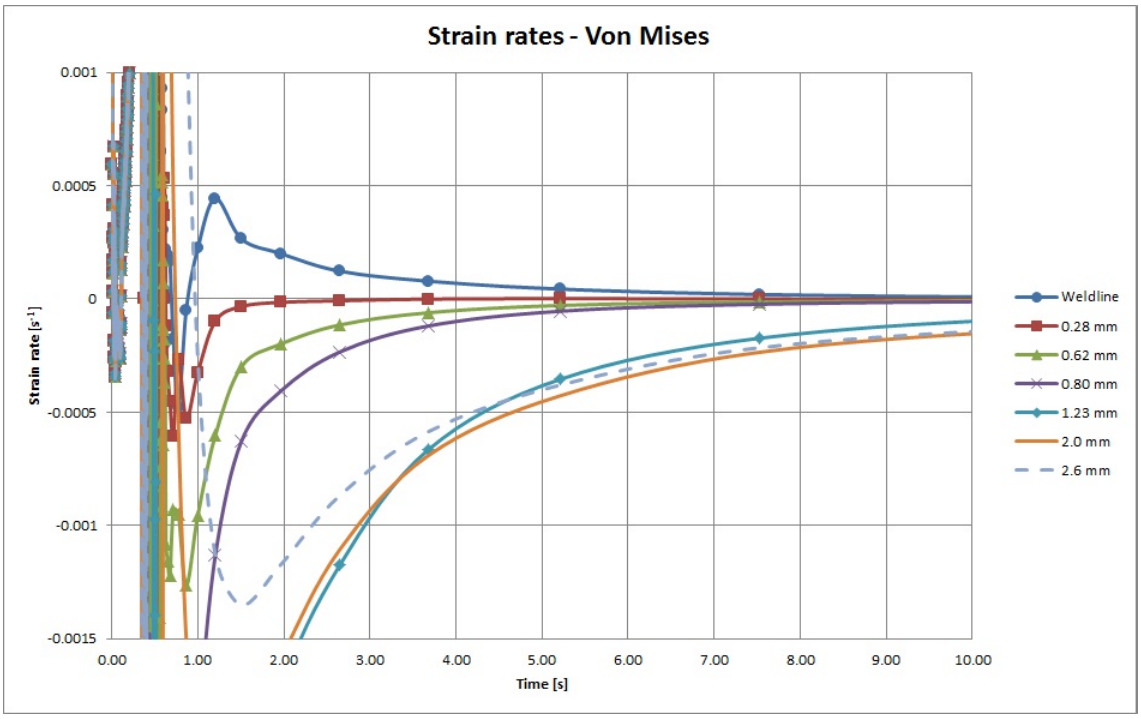

Figure 3.12.: Graph of the equivalent Von Mises strain rates measured in the points showed in figure 3.10 of the numerical model. In a) it is possible to see that the maximum values registered are in correspondence of the weldline, where there are the highest gradient of temperature; at distances from the weldline greater than $0.8mm$ the strain rates are so small respect the y-scale that the relative curves lie on the x axis. In b) it is possible to see how after about $10\,s$ the strain rates tend to converge toward zero, with points farther from the weldline subjected to variations of strains higher than points close to the weldline

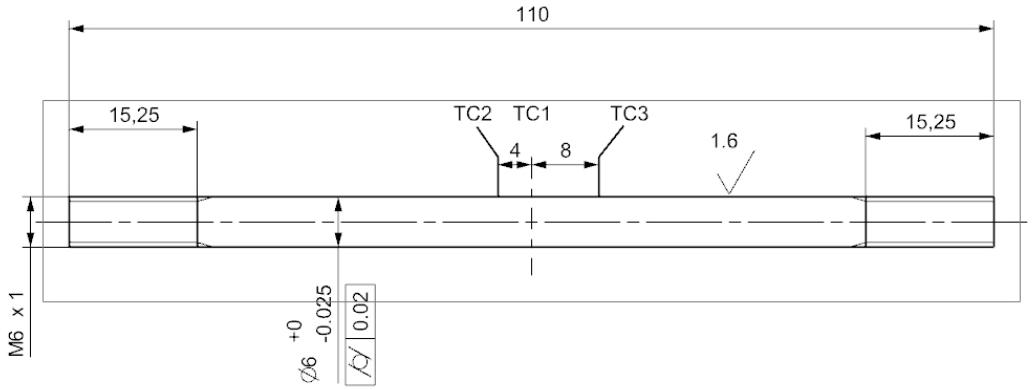

Figure 3.13.: Tensile Gleeble specimens geometry. TC1, TC2 and TC3 represent the location of the thermocouples fixed on the specimens. Dimensions are in mm

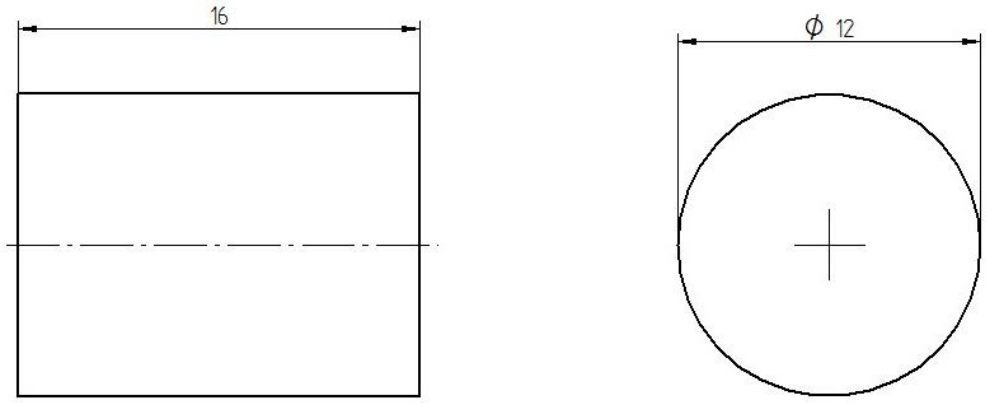

Figure 3.14.: Compressive Gleeble specimen geometry. Dimensions are in mm

problems have been encountered.

The best way to get the quickest response time from a thermocouple is to spot-weld it directly on the component to be measured. This ensures there are no further thermal resistances between the surface measured and the thermocouple, while not modifying the actual temperature measured and minimising delay due to the rise time of the measurement system.

The most common type of thermocouple for this purpose, is the type K, since they can operate at relatively high temperatures (1350°C max for short term) and they are cheaper than other types. Unfortunately, the junction between Titanium and the thermocouple materials (Nickel-Chromium for + wire and Nickel-Aluminum for - wire) seems to lose strength at temperatures around 950 °C, breaking the junction. The cause of this phenomenon could be explained by a possible eutectic transformation taking place at around 940-980 °C, between the binary system Ti-Ni, depending on the specific chemical composition of the junction formed [92]. As a first solution to the problem, holes were drilled in the specimens, then sheathed thermocouples type K were inserted, avoiding the necessity to keep the sensors in position by spot welding. Besides a possible lower response time of this solution, that would have been checked if really important for the testing conditions used, the temperature read by the Gleeble machine was different from the value obtained using a National Instrument acquisition box. This shift in temperature was a function of the length of the thermocouple wires, probably due to poor design, low input impedance, of the Gleeble acquisition instrumentation: sensors longer than about 30 cm introduced there temperature shifts. Since it was not possible to find sheathed thermocouples shorter than 50 cm on the market, and considering also the unknown response time, bare type B thermocouple wires were tried. These thermocouples (Platinum-30% Rhodium for + wire and Platinum-6% Rhodium for - wire), able to work to relatively high temperatures (max 1820 °C) did not show any junction trouble as encountered when the type K was spot welded to Titanium. The downside of using this kind of thermocouple is, besides a higher cost, the inability to work at temperatures below 60 °C, since the voltage re-

turned becomes almost constant. For the purpose of these experiments, the limitation of the minimum temperature was not a problem, since the material microstructure is not affected by temperatures below 500 °C, for the heat treatment timings considered. The higher cost was compensated by the certainty to get the best response time possible and to avoid detachment of the junction at temperatures around 980 °C.

The only problem given by the type B thermocouples, when coupled with the acquisition instrumentation of the Gleeble, was a noisy signal, due to the low voltage returned by the sensors, which was sensitive to other ambient signals. To solve this problem, ferrite inductors were placed around each thermocouple wire, damping down the noise. In conclusion, type B thermocouples have been the thermocouple type used for these experiments, solving the potential possible problems related to using the type K ones.

To control the temperature in compression tests, a type B thermocouple was spot welded in the middle of the length of each component (figure 3.16).

In the tensile specimens, another two type B thermocouples were spot welded on each specimen, at about 4 mm and 8 mm from the middle, respectively one on the right side and one on the left side (figure 3.13). It was then possible to control the temperature at three different positions of each specimen and, since the temperature along the length of the component has a parabolic trend, with a peak in the centre, three different peak temperatures could be tested for each sample. A photograph of the assembly used is shown in figure 3.15.

FE analysis has been carried out to assess any size effects and to ensure the samples did not have a too high temperature gradient through their thickness, so there would be no significant difference of temperature between the one measured by thermocouples spot welded on the specimens surface and that in the centre (appendix A). This numerical analysis did not attempt to be a full physical representation of the Gleeble tests but to give an indicative guideline on the temperature gradient that could be expected along the thickness of the components.

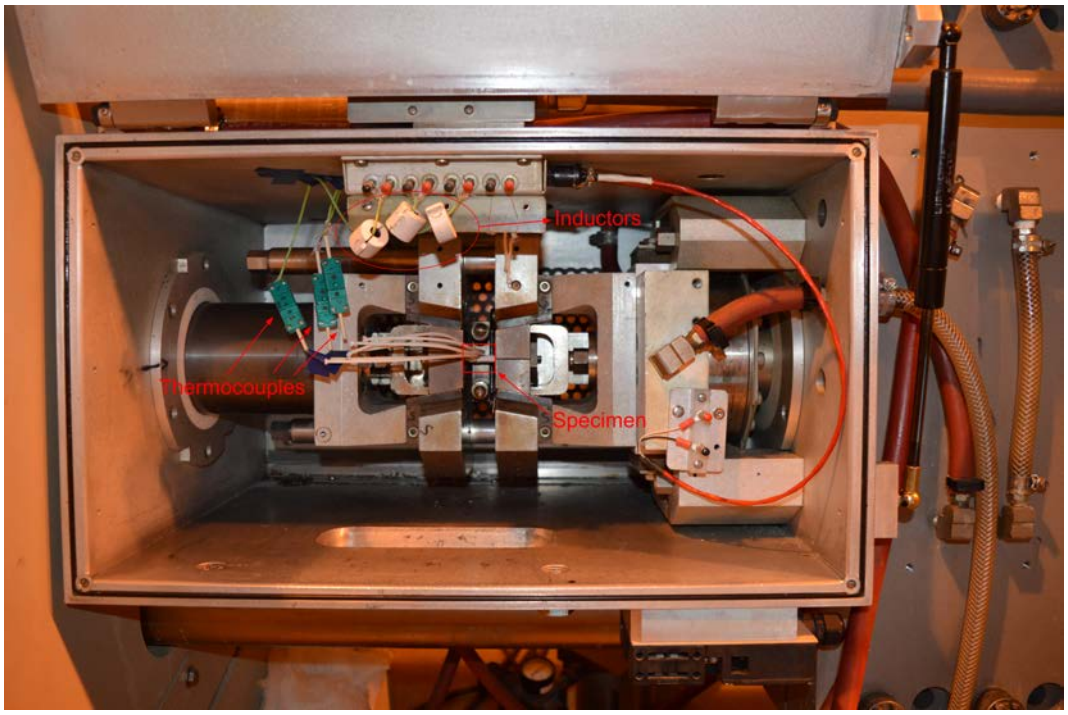

Figure 3.15.: Photograph of the assembly used for tension tests carried out by using the testing system Gleeble 3500

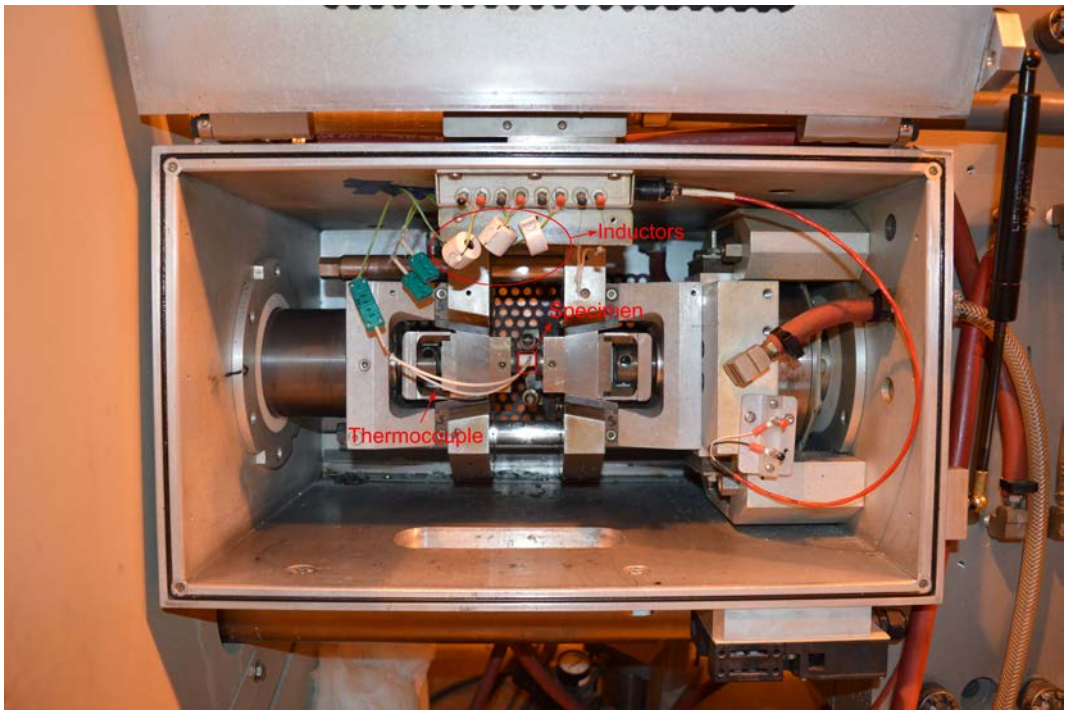

Figure 3.16.: Photograph of the assembly used for compression tests carried out by using the testing system Gleeble 3500

3.4.1 Microstructural analysis - procedure

After each test, the samples were sectioned in correspondence with the thermocouple positions, polished, etched in 2% HF and 10% HNO_3 solution and analysed with:

- optical microscopy using a Zeiss Axioskop 2 MAT mot microscope with software AxioVision v 4.6.3.0
- back scattered electron imaging (BEI) using an Oxford Instruments XL30 ESEM EG

Using optical microscopy, montages of the entire section of each sample were composed, and the beta grain dimensions measured.

From BEI, the thickness of lamellar microstructure, grain boundary and volume fraction of alpha and beta phases were estimated using the open source image processing software ImageJ. In general, alpha phase features were identified by darker colours since containing lighter elements (more Aluminium, atomic mass 26.9 g/mol), vice versa for beta features (more Vanadium, atomic mass 50.94 g/mol).

For the estimation of the dimensions of beta grains, the following procedure has been adopted:

1. Identification of the grain boundaries by manually highlighting their boundaries drawing black or white lines (figure 3.17-a).
2. Thresholding of the image (figure 3.17-b).
3. Using an ImageJ routine, ellipses were inscribed as best as possible in each beta grain, such that the area of each ellipse was equivalent to the grain being evaluated (figure 3.17-c).
4. For each ellipse, a fictitious oblate ellipsoid volume was calculated, using the two smaller principal axis of the ellipsoid as the length of the minor axis of the ellipse, while the major axis of the ellipsoid was equivalent to the major axis of the ellipse.

5. The mean value of the distribution of ellipsoid volumes was calculated and used as a representative value of the beta grain size obtained from the heat treatment considered.

6. For each ellipsoid an equivalent sphere in volume was calculated and the relative radius used as representative of the beta grain size distribution, thus simplifying the particle geometry into spheres.

To estimate the evolution of the lamellae dimensions of the original microstructure of the material tested (figure 3.18), ellipses were manually inscribed, to make the major axis coincident with the length of the lamellae, and the minor axis coincident with the thickest section of the lamellae considered (figure 3.19). From the mean of the minor axis distribution, the mean lamellae thickness was calculated; by the ratio of the mean major and minor axis, the aspect ratio was estimated. In this work, for the study of the lamellae dimension evolution, only the lamellae colonies appearing with sharper boundaries and slimmer shapes have been considered. This aimed to reduce the effect of the random inclination of the sectioning plane used in studying the microstructure of the material. Colonies sectioned not perpendicularly to their longitudinal direction, would appear with wider and darker boundaries but also with an overall larger lamellae thickness. Thus, from this consideration, the choice of evaluating colonies with well defined boundaries would in general end up assessing colonies with a thinner lamellae thickness and hence gives an underestimate.

In the literature, a common procedure adopted for lamellae thickness measurement, consists of collecting a series of intercept readings by rotating a grid of parallel lines at many angular steps, till a complete rotation of 360° has occurred [30, 28]. The mean length of all the intersections of this grid, for each angular step, with each lamellae, multiplied by a factor 1.5 and inverted, would return the hypothetical true mean value of the lamellae measured. This approach conflicted with the aim of the present work, where both lamellae thickness and aspect ratio had to be measured. The intercept approach would have returned only the thickness lamellae estimation. Moreover, a software solution to automate

the intercept measurements was necessary to reduce the working time, but probably it would still have needed a huge interaction from the user, in particular if, for consistency, the same approach was used for the thickness measurement of lamellae nucleated during cooling, where martensitic needles were also developed in the microstructure, introducing significant errors in the measurements on the lamellar microstructure.

To estimate the thickness of the lamellae beta boundaries, a set of perpendicular lines to the sides of the grain boundaries were traced, and from their length distribution, the mean grain boundary thickness was computed.

The volume fraction was estimated by thresholding pictures on the the grey scale of the beta phase, that is represented by a whiter colour in BEI pictures.

For the estimation of the thickness of new lamellae nucleated during heat treatments involving cooling, lines perpendicular to the longitudinal direction of the lamellae were traced, from one side to the other of each lamellae.

All the values measured have been collected and their trend plotted in charts, reporting when more measurements were involved, the error bar shown represent the standard deviation.

The as received microstructure of the material used for the Gleeble tests was lamellar, as shown in figure 3.18.

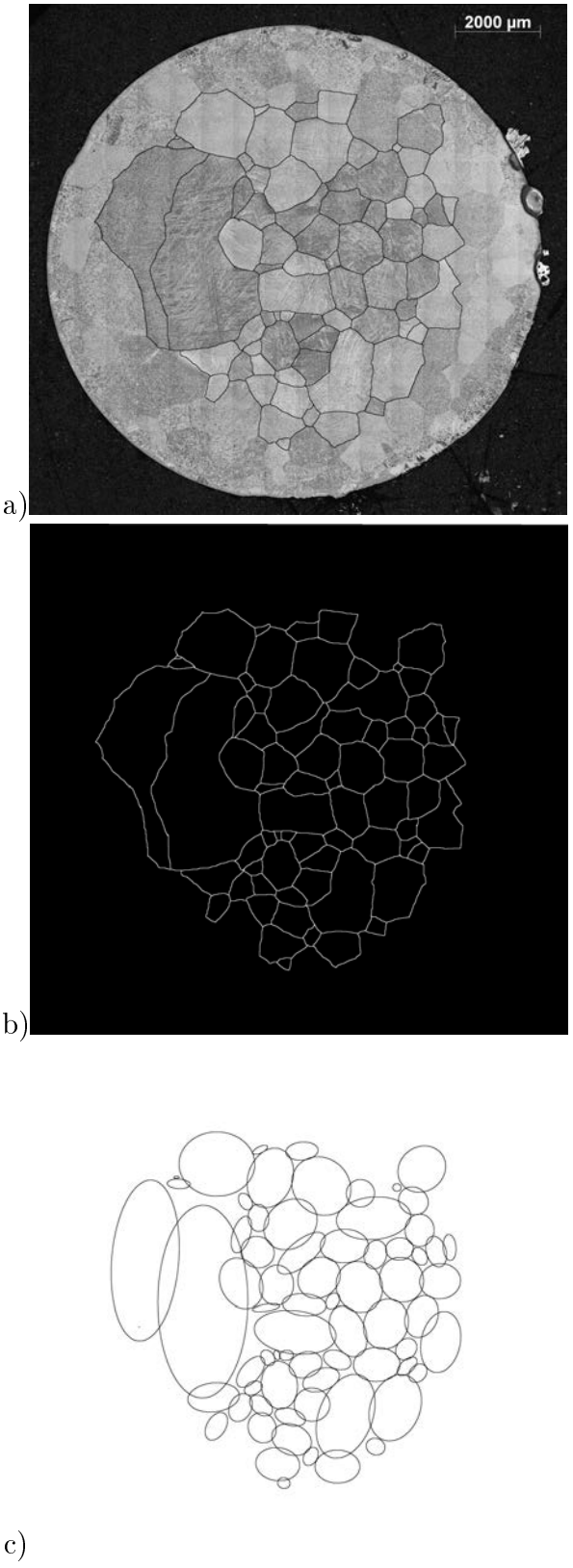

Figure 3.17.: From the top to the bottom: a) optical microscope micrograph showing beta grains manually highlighted; b) beta grains thresholded; c) ellipses inscribed in the beta grain shapes

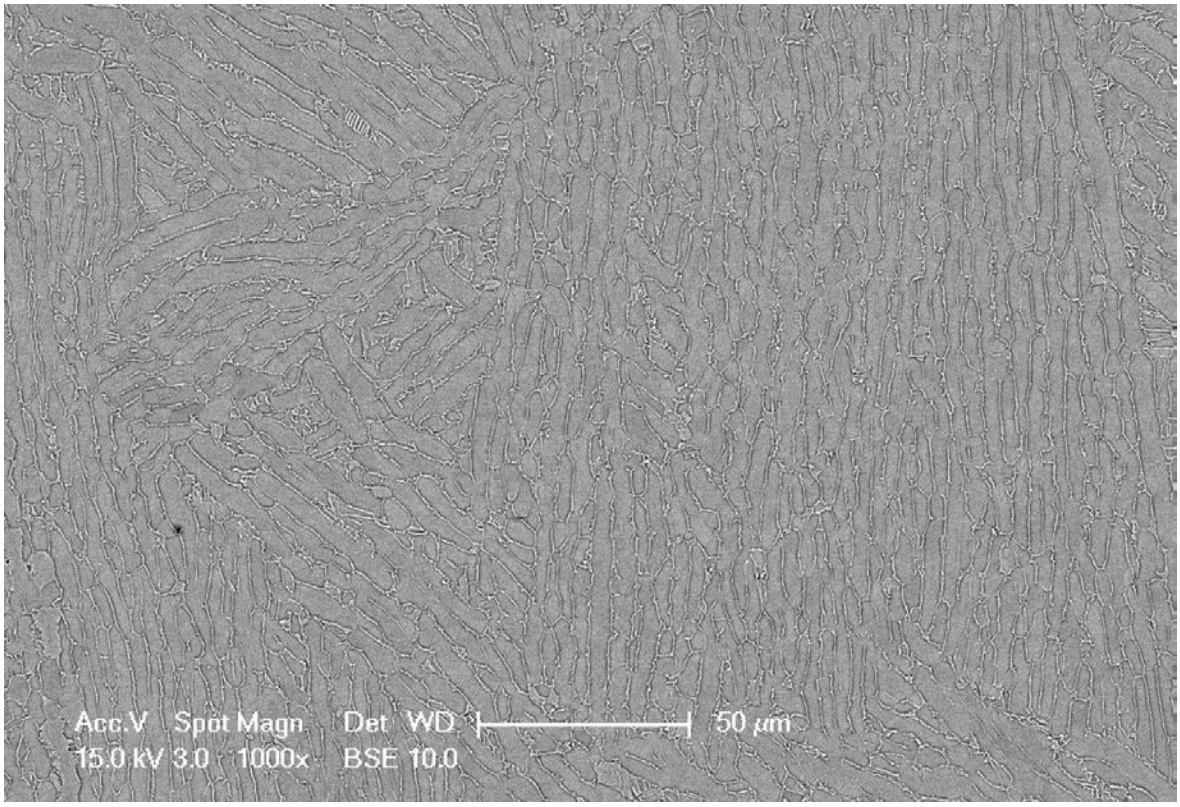

Figure 3.18.: BEI micrograph showing the microstructure of the received Ti-6Al-4V. Alpha lamellae are represented by the darker areas, since they have lower atomic weight. The thin white walls bounding the lamellae represent the beta phase, with higher atomic weight

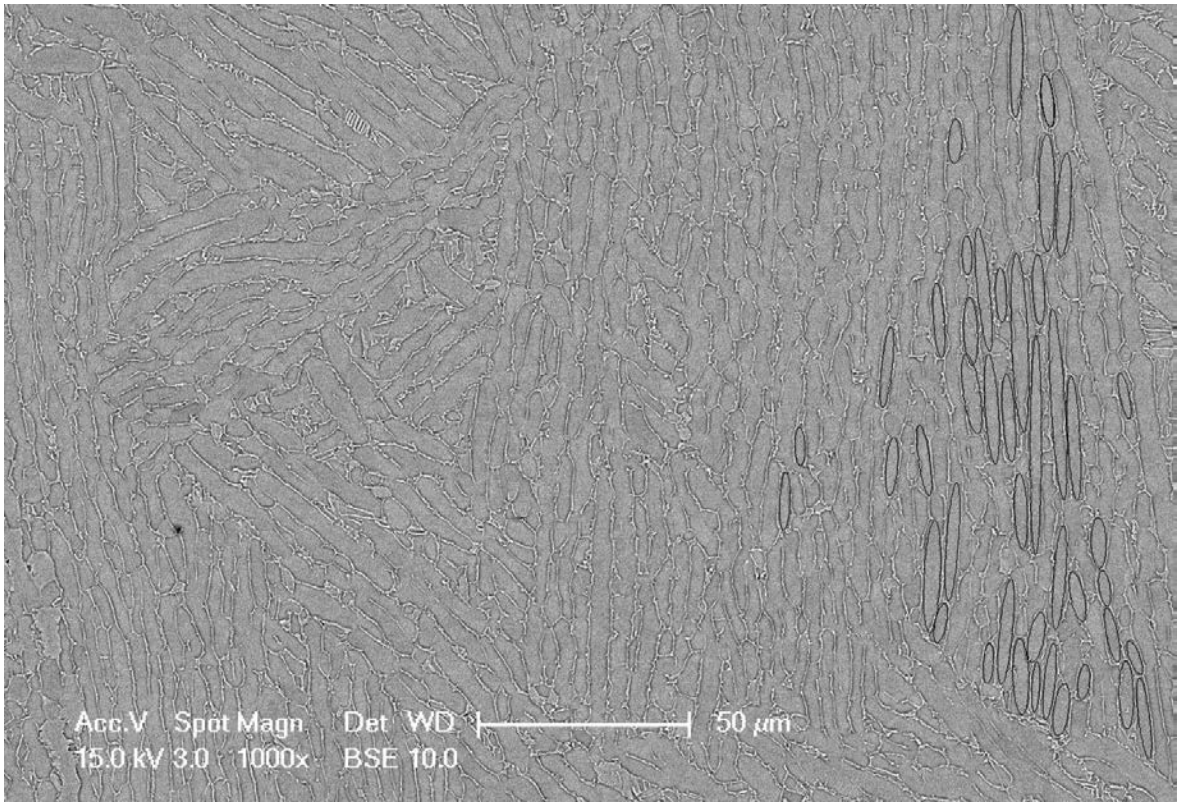

Figure 3.19.: BEI micrograph showing ellipses inscribed to the lamellae of figure 3.18

3.4.2 Microanalysis - technique

When necessary, to study the chemical composition of samples, in particular to analyse its variation in function of position or thermal treatments, energy dispersive spectroscopy (EDS) analysis was adopted by using the Oxford Instrument XL30 ESEM EG coupled with the Oxford Instrument Inca software version 4.15.

The technique is based on the physical interaction between the microscope electrons beam and the electrons of the material studied. When an electron of the beam hits an electron of an atom of the material, this last escapes from its shell producing a vacancy. If the vacancy is filled from a higher level orbital, an x-ray characteristic of that energy transition is produced. Since energy levels are different for each elements of the periodic table, the x-rays emitted can be related to the specific element generating it. In particular, the EDS detector converts the energy of each individual x-ray into a voltage signal of proportional size.

The interactions produced between the electron beam and the material analysed can be represented by a pear shape interaction volume located beneath the sample surface hit by the beam (figure 3.20). This shape is function of the atomic number and crystallographic structure of the material but also of the power of the beam used. As the atomic structure of the atoms constituent the material is denser, the pear shape interaction volume will have a smaller penetration and width as well as the power of the beam decreases.

To get in a relatively short time (minutes) a significant interaction volume from EDS analysis to identify properly the chemical composition of the area investigated, in a material like the one studied in this work an acceleration voltage of 15 kV - 20 kV was needed, thus expecting interaction volumes of $1 - 2\,\mu m^3$.

Considering sometimes the dimension of the particles investigated was fractions of microns, the chemical compositions reported in this chapter is, as already said, indicative of the mean composition of the area investigated but not the actual composition of particles/phases.

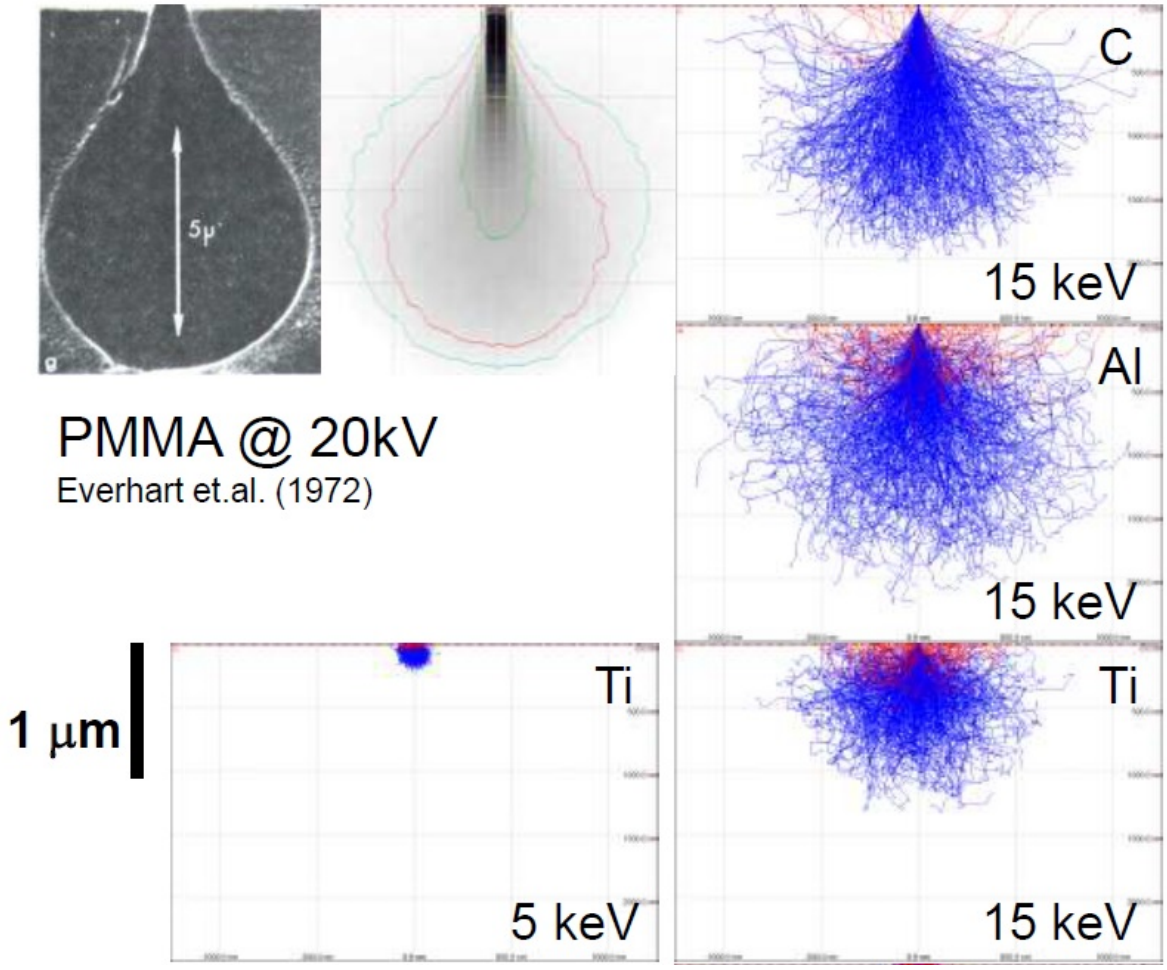

Figure 3.20.: Monte Carlo simulation of electron scattering due to the interaction between an electron beam, different materials and acceleration voltage [38]

3.4.3 Heating rate effect on lamellar microstructure

For the study of the effect of different heating rates on the dissolution of the original lamellar microstructure of the material, and possible formation of beta grains when the beta transus temperature was passed, tensile specimens were used (figure 3.13). Three different heating rates (5, 50 and 500 $°C/s$) have been tested, bringing the specimens to different peak temperatures and then water quenching them.

Representative microstructures, taken from each tested sample, are reported in figure 3.21 for heating rates of 5 °C/s, figure 3.22 for heating rates of 50 °C/s and figure 3.23 for heating rates of 500 °C/s. Looking at the micrographs, going toward higher temperatures, from the right to left and from bottom row to the top, it is possible to notice dissolution of

the alpha phase lamellae (dark grey shapes) whilst the beta phase grows (white matrix). When the lamellae are no longer recognizable, and needles appear, we can say the material passed the beta transus temperature during the heat treatment. This can be deduced in the micrographs due to the appearance of thin, long, white needles, formed by water quenching from a temperature above the beta transus temperature.

Making reference to the figures 3.21, 3.22 and 3.23, the beta transus can be located between 915 °C and 976 °C for the heating rate of 5 °C/s; between 966 °C and 982 °C for the heating rate of 50 °C/s and between 1020 °C and 1123 °C for the heating rate of 500 °C/s.

The beta transus temperature, as the heating rate increases, shifts towards higher values. This is due to the kinetics of the diffusion process, that requires a certain amount of time to let the metallurgical transformations occur. Moreover, in a quasi steady state process, as the temperature rises, the original lamellae would dissolve, until a temperature where they completely disappear, leaving the beta phase. In fast metallurgical reactions, like the ones taken in consideration in this work, the time for a complete dissolution of the lamellae is not sufficient: the lamellae thickness, at temperatures close to the beta transus temperature, is still quite large and the change of crystallographic structure from HCP to BCC occurs before their complete dissolution. This also means that the concentration field of the constituent elements in the different phases, does not have time to change to get the equilibrium concentration at a specific temperature. This is particularly visible in micrographs where the temperature is slightly above the beta transus temperature and the white and dark fields associated with the original concentration of the constituent elements in the lamellar morphology can be still noticed. For example, in figure 3.21, for the heat treatments with peak temperature of 976 °C and 1000 °C, besides the needles, is possible to see an inhomogeneous background with darker and whiter areas, due to remnants memory of the elemental distribution in the lamellar microstructure.

In section B.1, B.2 and B.3 optical microscope montages of the entire cross sections of each sample tested are shown, in which it is possible to appreciate the disappearance of

the original lamellar microstructure and the growth of the beta grains as the temperature increases.

Graphs in figure 3.24 show the results of the image analysis conducted on the samples tested, whose microstructures are shown in micrographs of figures 3.21, 3.22 and 3.23.

As the heating rate increases, the alpha lamellae dissolution and beta phase growth tend to shift toward higher and higher temperatures as well as the alpha volume fraction. This is due to the limited speed of the diffusion kinetics, as already discussed.

The progressive reduction of time available for the diffusion process can be visualised by plotting the same data shown in the graph of figure 3.24 as a function of time (graph in figure 3.25). The heat treatment durations between the fastest heating rate (500 °C/s) and the slowest (5 °C/s) go from 180 seconds to 2 seconds. Thus the diffusing process at the fastest heating rate has 1/100 of the time to occur with respect to the slowest heat treatment.

Graphs in figure 3.26 shows the evolution of the lamellae aspect ratio as a function of the peak temperature and time. As the heat treatment advances and the temperature increases, the lamellae thickness reduces and, as consequence, the aspect ratio progressively increases.

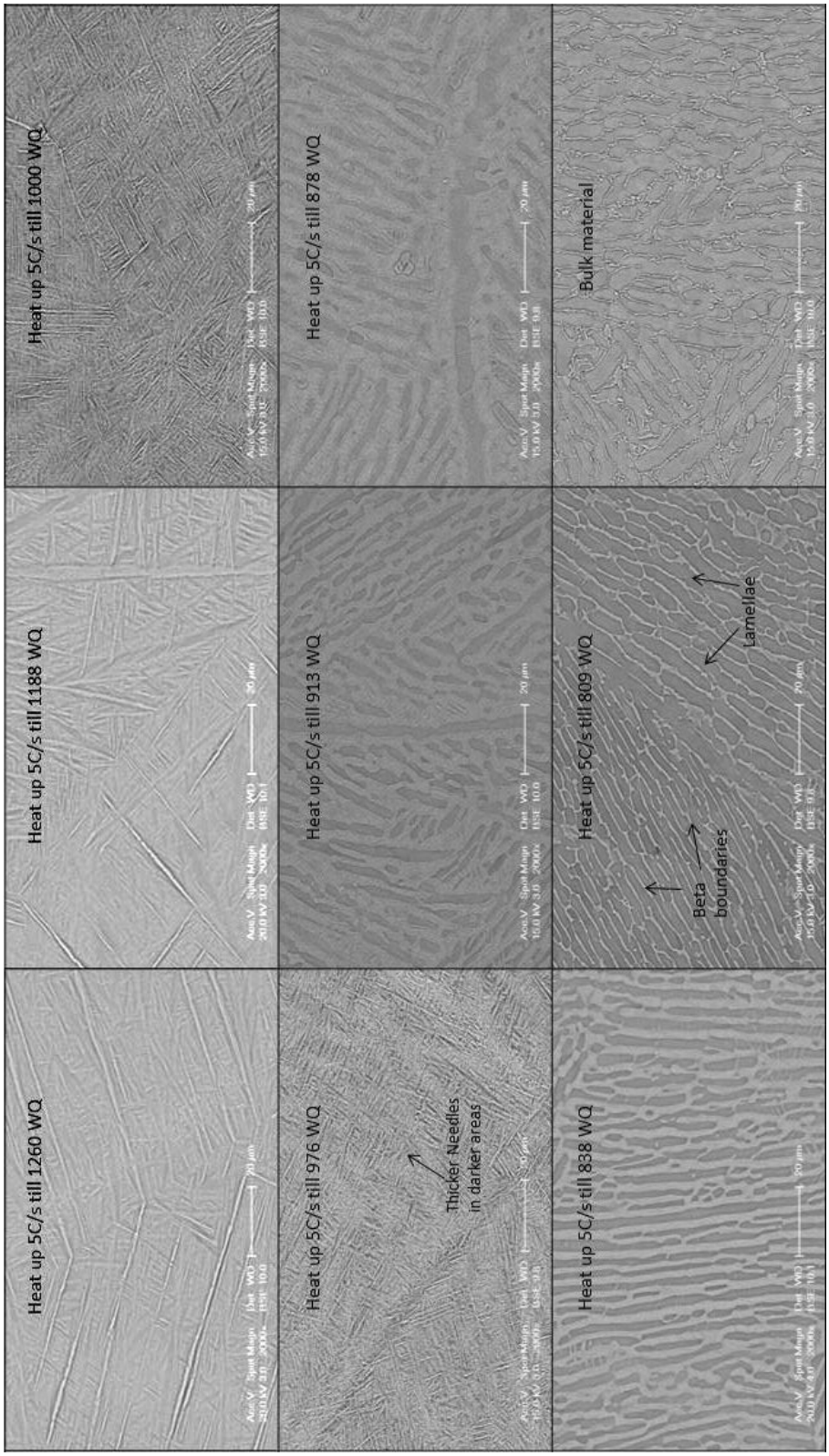

Figure 3.21.: BEI microhraphs showing representative microstructures obtained from all the samples tested at the heating rate of 5 °C/s to different peak temperatures and water quenched. As a comparison, the original microstructure of the material as received is also shown. The specimens heated up to temperatures equal or higher than 976 °C and water quenched do not show anymore the original lamellar morphology, but martensitic microstructure

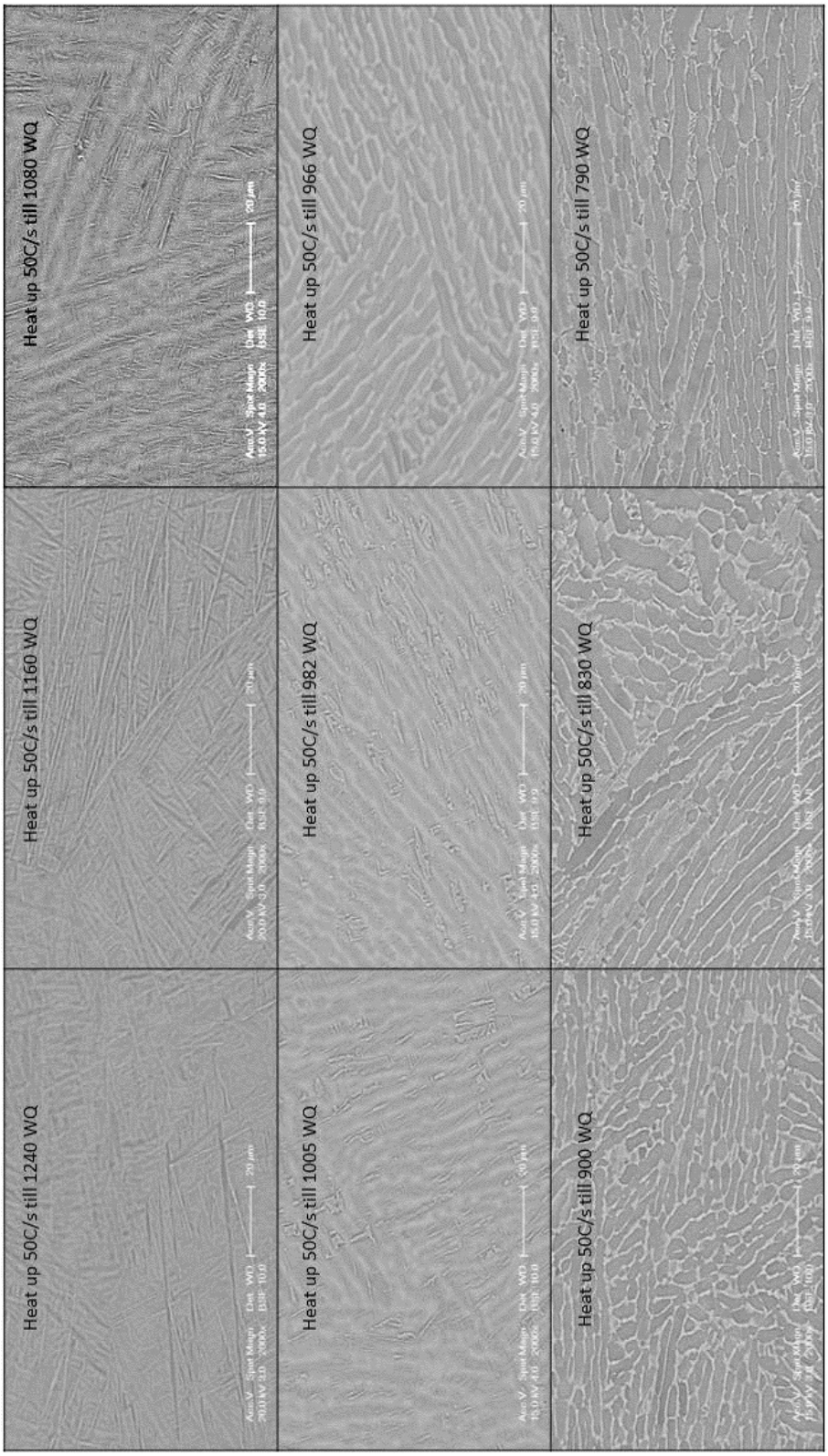

Figure 3.22.: BEI micrographs showing representative microstructures obtained from each sample heated up at 50 °C/s to different peak temperatures and water quenched. Specimens heated up till temperatures equal or higher than 982 °C have martensitic microstructure instead of the original lamellae one

Figure 3.23.: BEI micrographs showing representative microstructures obtained from each sample heated up at 500 °C/s till different peak temperatures and water quenched. Specimens heated up till temperatures higher than 1020 °C have martensitic microstructure instead of the original lamellae one

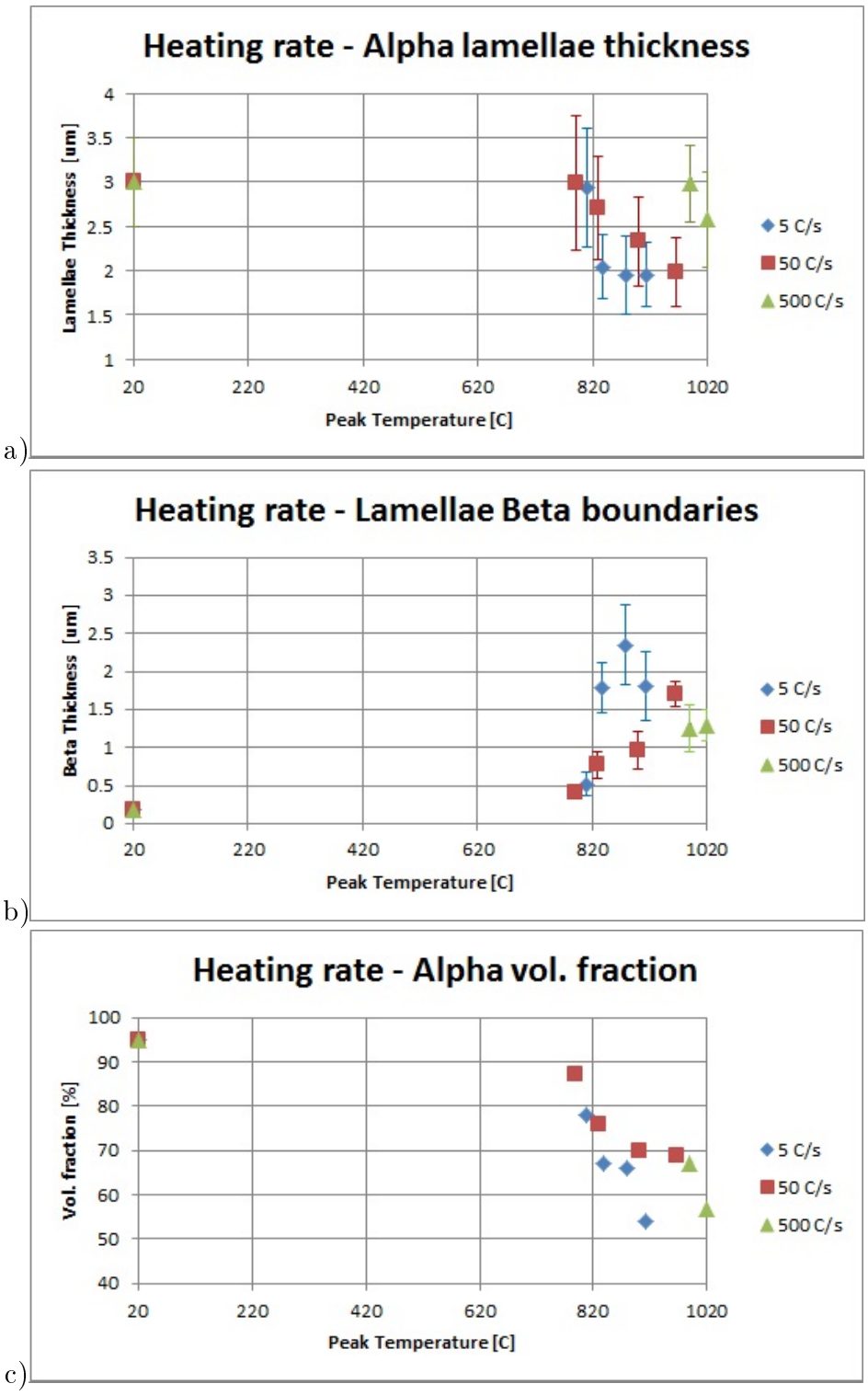

Figure 3.24.: Graphs showing the heating rate effect on the dissolution of lamellae (a), growth of beta boundaries (b) and alpha volume fraction (c) as a function of the peak temperature reached during the heating tests

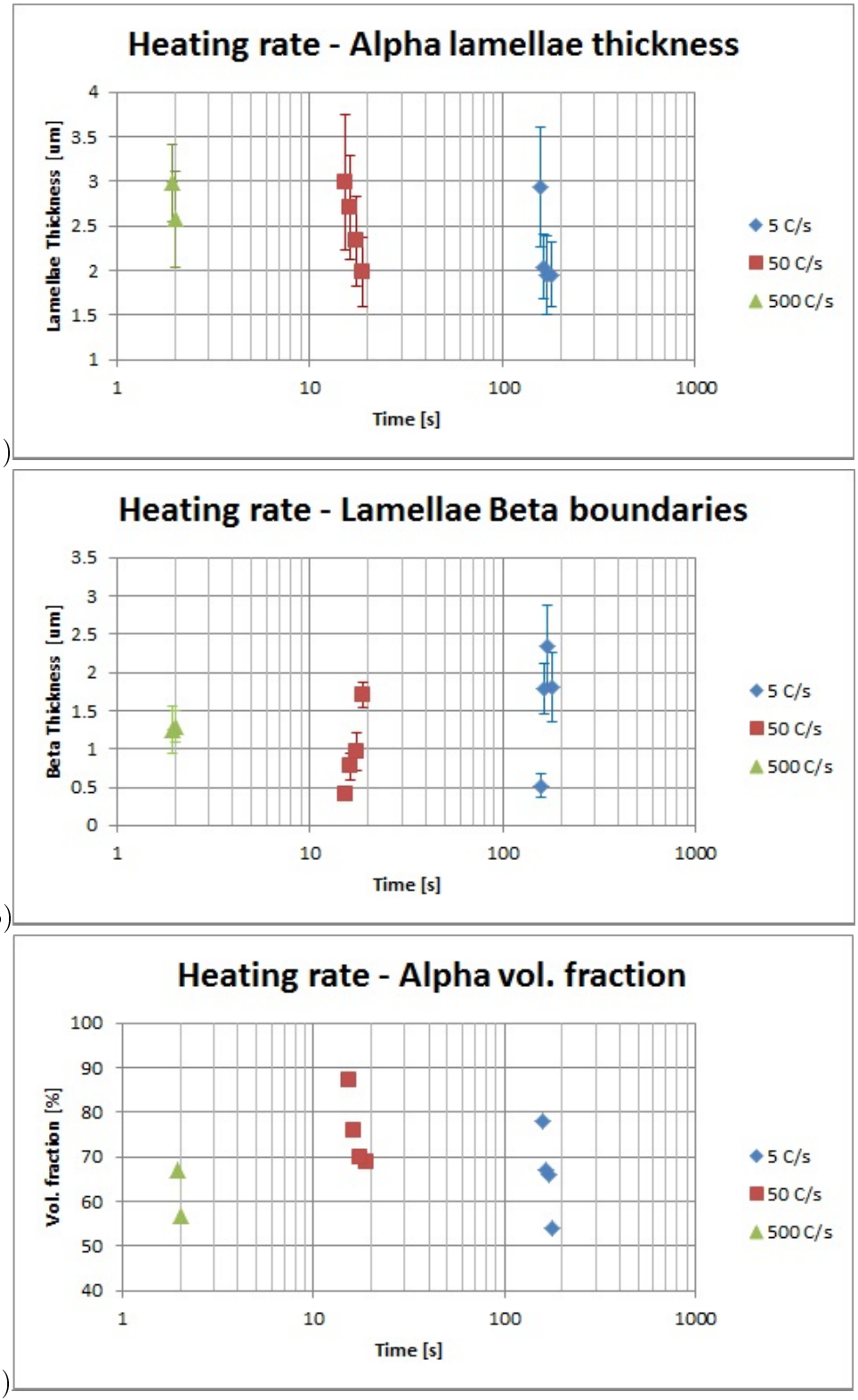

Figure 3.25.: Same results shown in figure 3.24 but plotted as a function of time. The duration ratio between the fastest and the slowest heat treatment is 1/100

a)

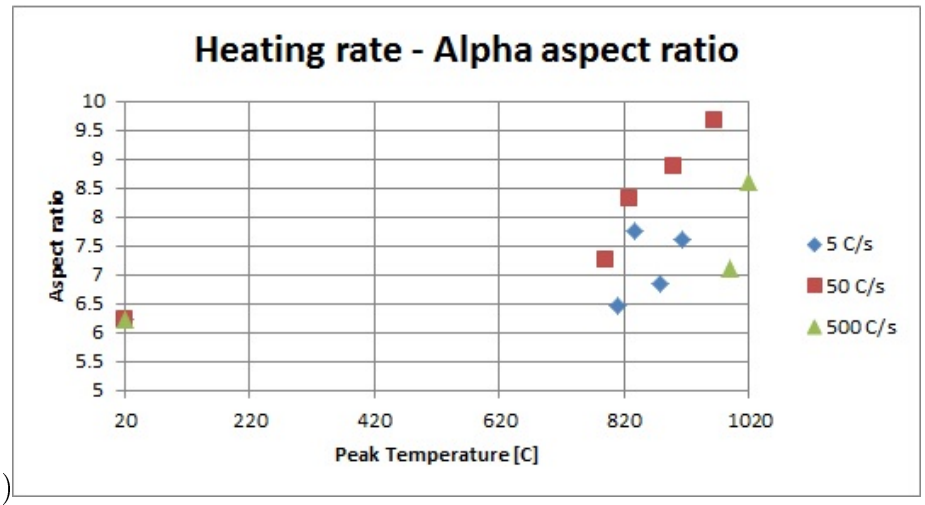

b)

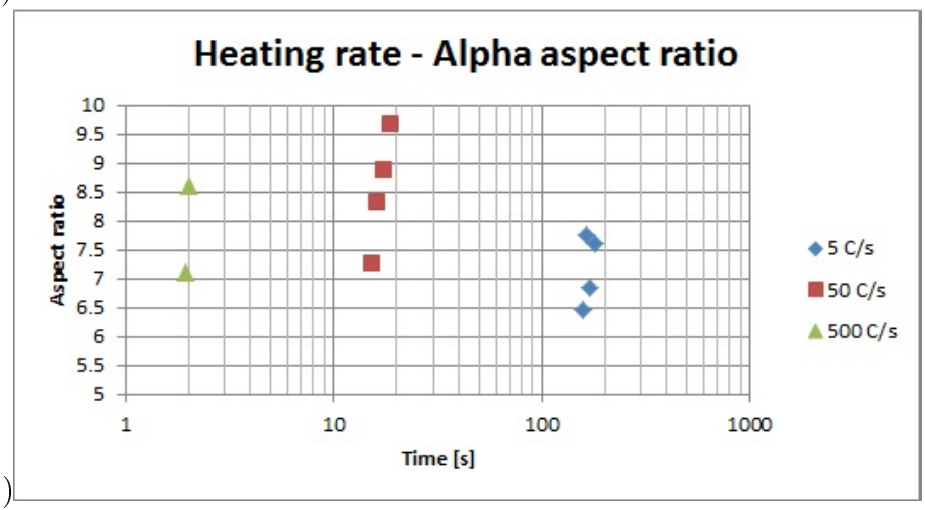

Figure 3.26.: Graphs showing the variation of the lamellae aspect ratio as a function of (a) peak temperature and (b) time at different heating rates. In general, as the reaction proceeds, the lamellae reduce their thickness (figure 3.24 and 3.25) thus their aspect ratio increases

3.4.4 Cooling rate effect on lamellar and martensitic microstructures

For the study of the cooling rate effect on the lamellae growth, during continuous cooling from the beta field, either Gleeble compression or tensile tests have been conducted, based on the availability of the specimens and cooling rates required.

Graphs reporting trends of the data obtained are shown in figure 3.27, where the data measured are reported as a function of the peak temperature from which the cooling started.

Even though the number of data points is not very high to obtain precise trends, it seems that the cooling rate from a specific temperature to ambient temperature does not have a well defined effect on the lamellae thickness, while the starting temperature at which the heat treatment happens is more important. This effect can be attributed to the different beta grain size in which the lamellae grow: the larger the beta grains, the higher is the probability to have a wider distance between nucleated lamellae, that can grow without chemically/mechanically impinging on each other. To accurately verify this hypothesis, another series of thermal tests should be carried out, testing for each cooling rate a wider range of different starting temperatures/beta grain sizes. The relation between beta grain dimension and lamellae thickness seems to be supported in literature, even if not much work seems to be published about this relationship [72].

By plotting the data acquired for the lamellae thickness as a function of the beta grain size where lamellae grew (graphs in figure 3.28), this hypothesis seems to be supported. As a first consideration the lamellae thickness seems really to not be related to the cooling rate in continuous cooling heat treatments, if this statement was not true, at faster cooling rates it would have been possible to observe thinner lamellae because of the shorter growth time. A second consideration is that the thickest lamellae are measured for the fastest cooling rate (300 °C/s), where the beta grains were noticeably larger than the ones at the slower cooling rates (5 °C/s and 50 °C/s). Moreover, looking at the data relative to the cooling rate of 100 °C/s, where a set of points with different beta grains has been collected, the relationship between peak temperature/dimension of the beta grains and

lamellae thickness is very clear. A last consideration can be made for the inter lamellae beta phase as a function of the beta grains dimension, where the beta phase thickens as the beta grains grow, such that the spacing between each lamella is driven by the beta grain size where they nucleate. This further supports the original hypothesis.

The microstructures developed by the different cooling rates, besides differing in the lamellar microstructure, in particular lamellae thickness, presented a higher amount of martensite and thicker martensitic needles as the cooling rate increased (micrographs in figures 3.29 and 3.30 and graphs in figure 3.31 and 3.32). Significantly graph 3.31-b shows a logarithmic relation between needle thickness and the cooling rate used to bring the samples from the tested temperature to the ambient one.

Since the volume fraction measurement of the alpha and martensitic phases was very difficult to carry out, due to the overlapping of the alpha lamellae and martensitic needles, the graph reported in figure 3.32 should be taken as a qualitative indication only. A partial martensitic microstructure at cooling rates of 300 °C/s seems to confirm Ahmed and Rack in [93], where a cooling rate of 500 °C/s is claimed to be necessary to have a microstructure completely transformed to martensite.

Regarding the observation of lamellar alpha even at 300 °C/s, reported in this work, TEM investigations would be required to better classify it. In [93], the α microstructure present at cooling rates faster than 20 °C/s, following TEM study, was classified as a second α morphology, with a heavily dislocated internal substructure and the same hexagonal crystal structure as martensite. Since there was no time for this kind of investigation, the lamellae noticed by SEM were all classified as of the same typology.

3.4.5 Growth of nucleated lamellae in the $\alpha + \beta$ field

To study the isothermal growth of lamellae in the $\alpha + \beta$ field, nucleated by cooling down from the beta field, three series of tests have been carried out. Each of them consist of cooling down samples from the beta field at either 5, 25 or 50 °C/s to different temperatures below the beta transus temperature, then water quenching directly or soaking for 10

a)

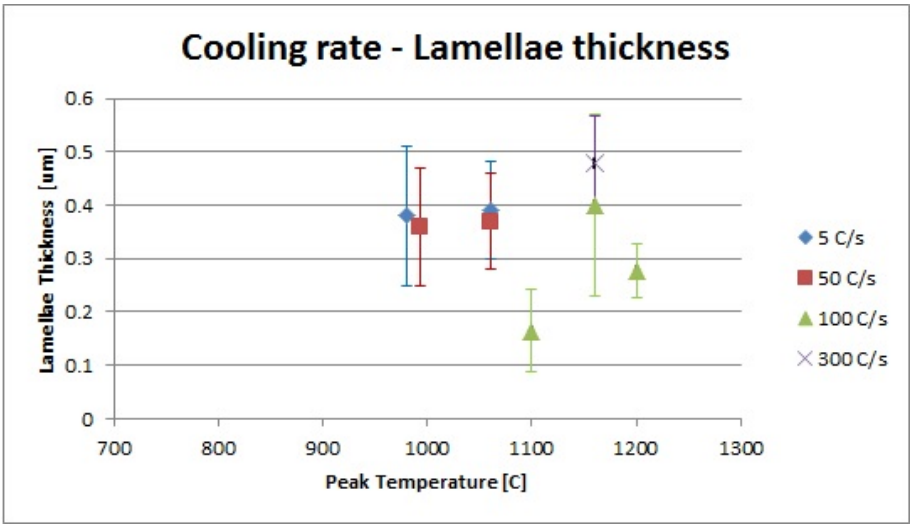

b)

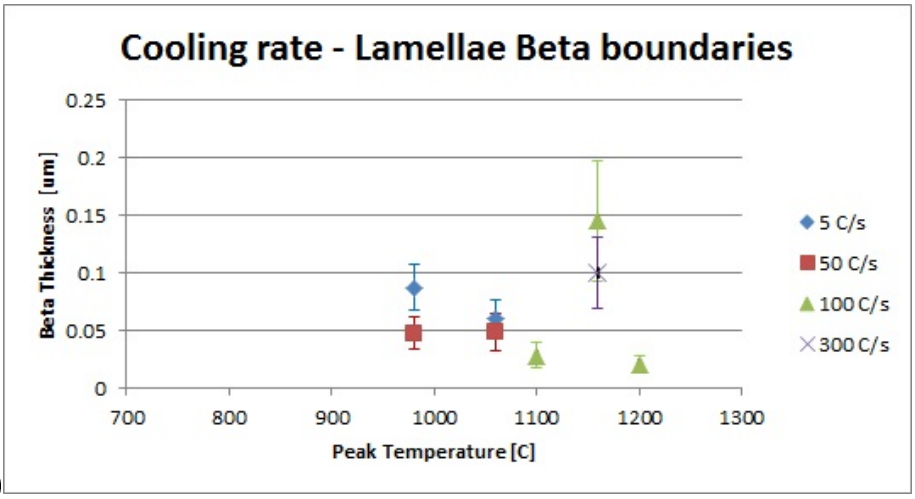

Figure 3.27.: Graphs showing the cooling rate effect on lamellae growth as a function of the temperature from which the cooling started (a), cooling rate effect on lamellae beta boundaries growth as a function of the temperature from which the cooling started (b)

a)

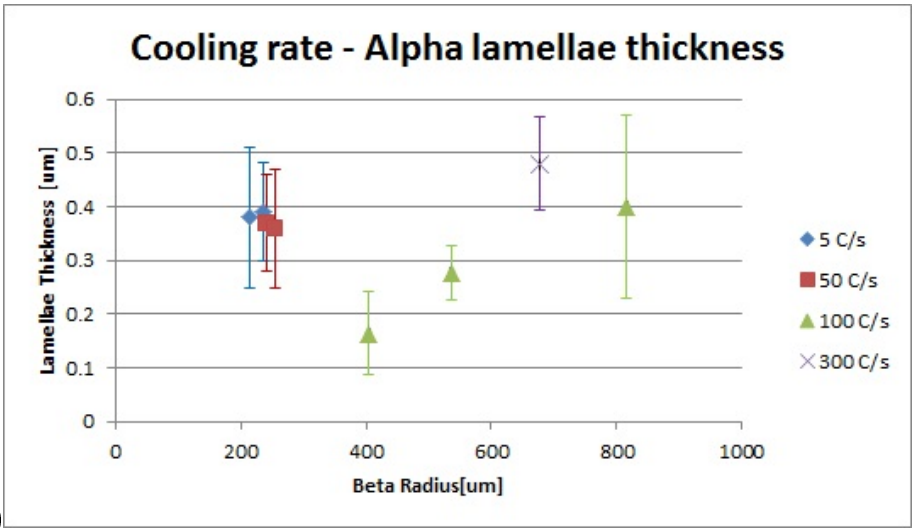

b)

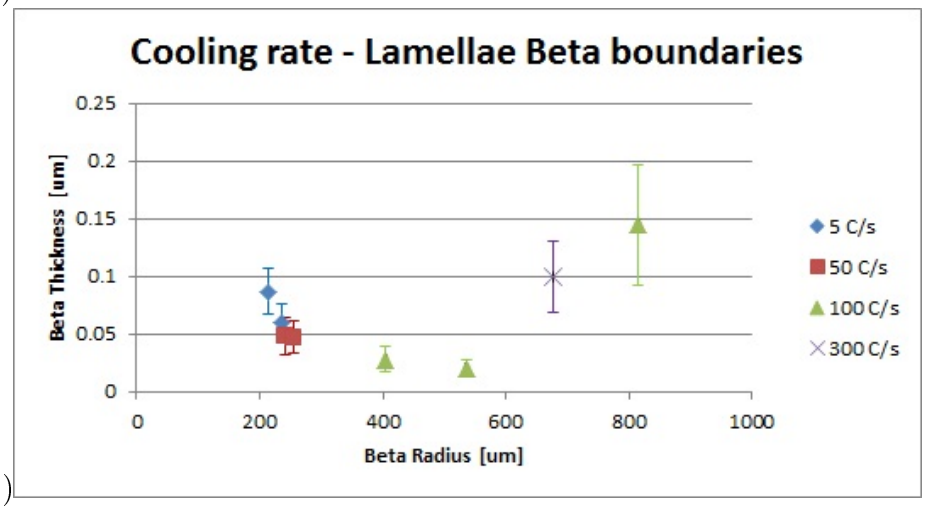

Figure 3.28.: Graphs showing the cooling rate effect on lamellae growth as a function of the beta grain size (a), cooling rate effect on lamellae beta boundaries growth as a function of the beta grain size (b)

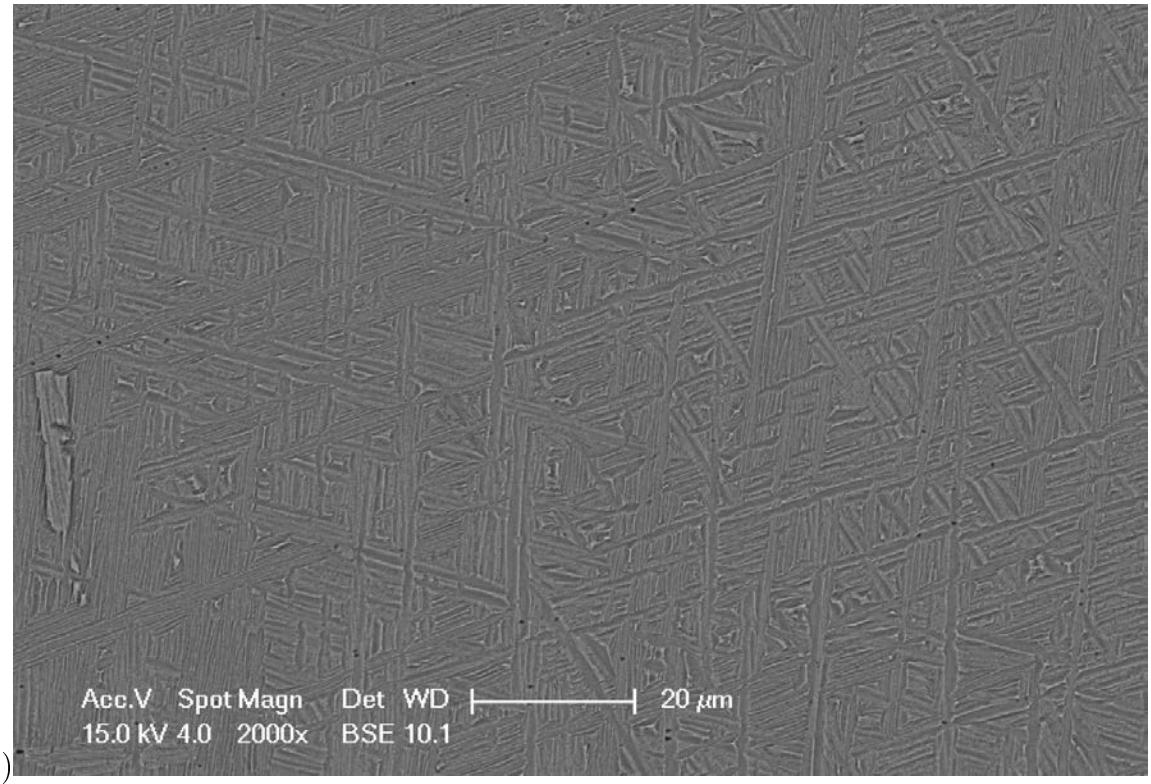

a)

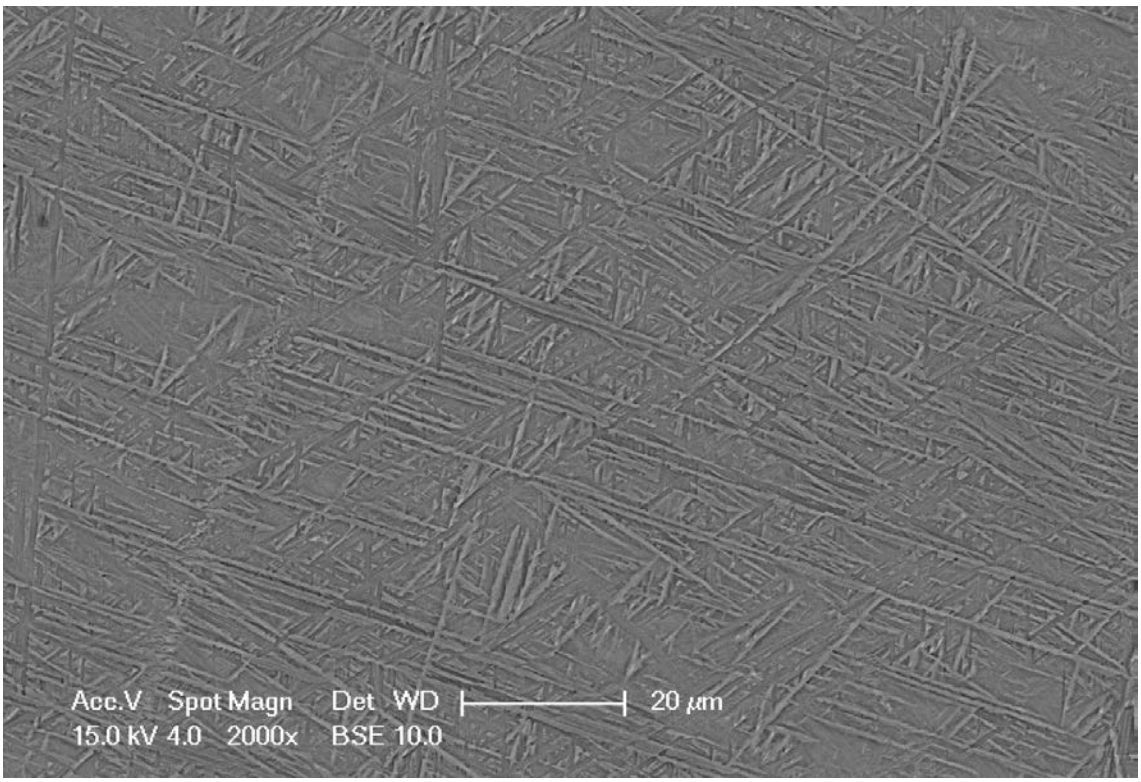

b)

Figure 3.29.: BEI micrographs showing an example of sample microstructures obtained cooling down at 5 °C/s (a) and 50 °C/s (b) from the beta field. The first one has a microstructure entirely lamellar, whilst in the second one martensite has started to form

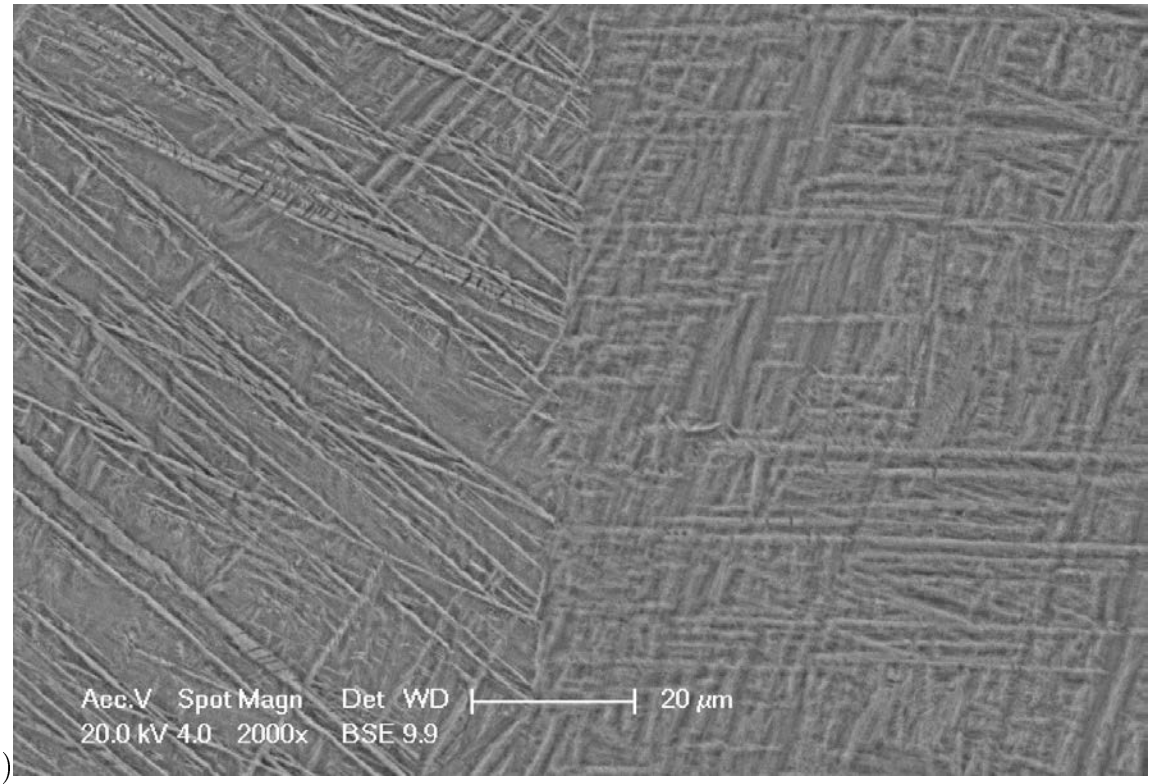

a)

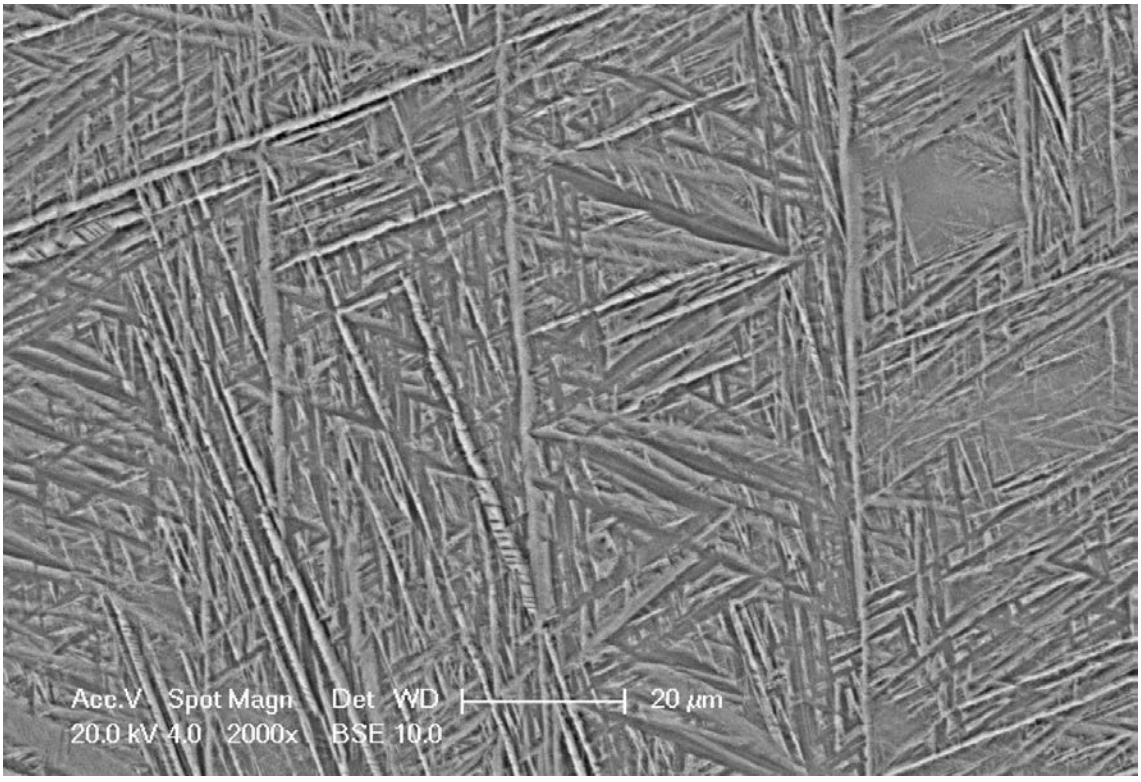

b)

Figure 3.30.: BEI micrographs showing an example of sample microstructures obtained cooling down at 100 °C/s (a) and 300 °C/s (b) from the beta field. The martensitic needles become progressively thicker as the cooling rate increases (see also micrographs in figure 3.29)

a)

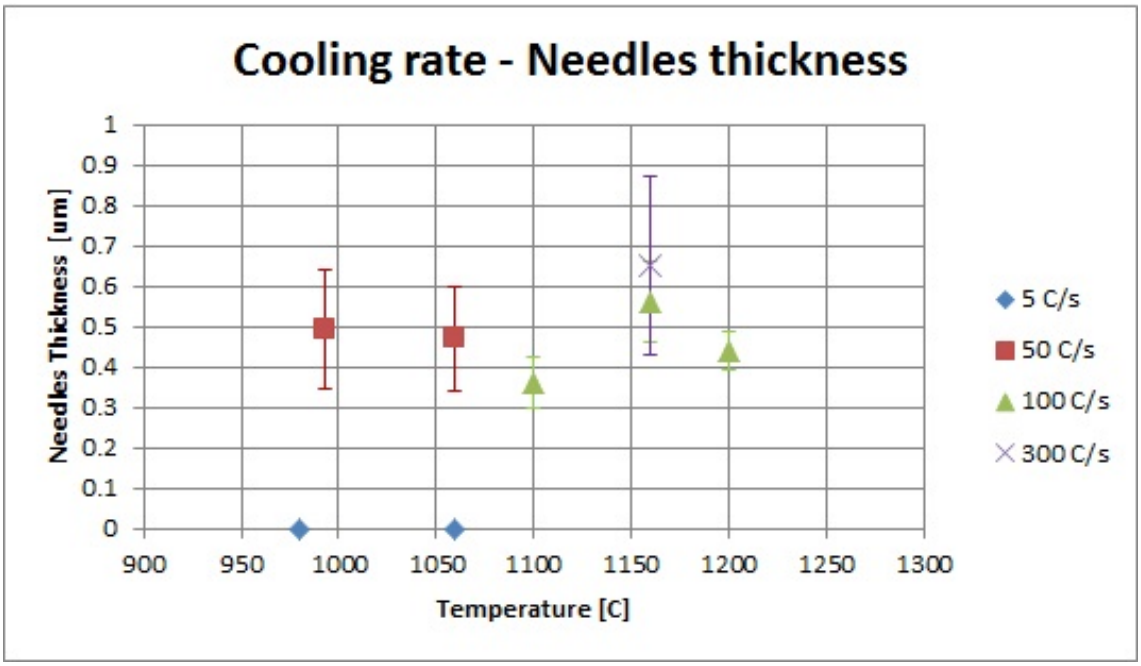

b)

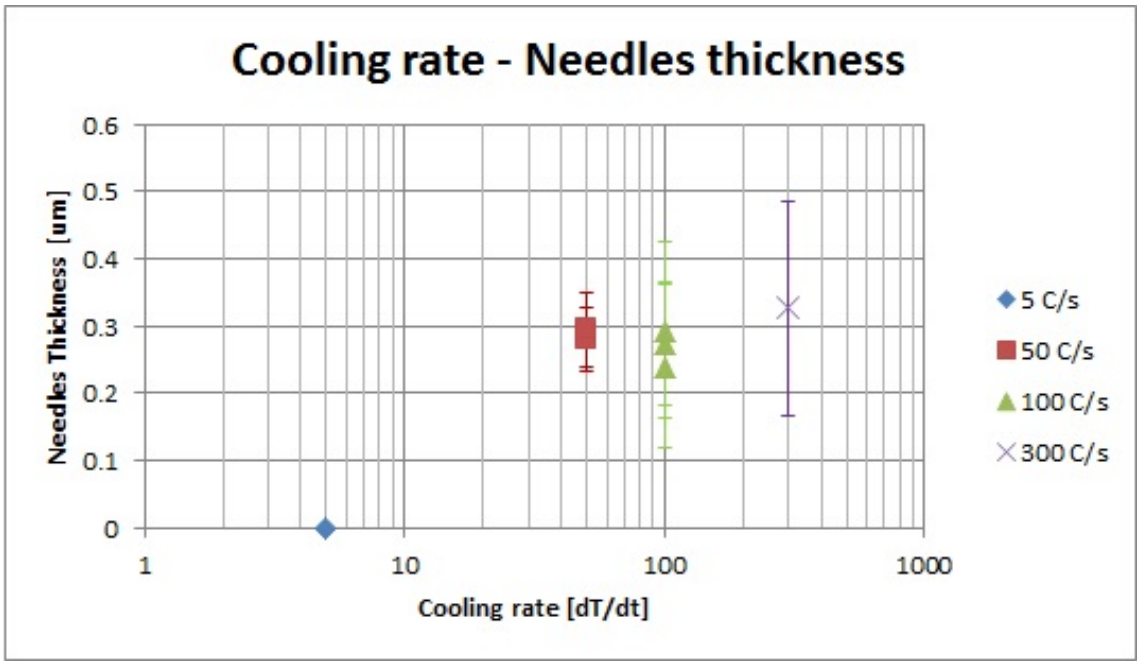

Figure 3.31.: Graphs showing the cooling rate effect on the martensitic needles mean thickness as a function of the peak temperature from which the cooling started (a) and as a function of cooling rate (b). The data points shown in graph (b), considering the error bars, can be interpolated by a straight line, suggesting that a logarithmic function can well describe the needles thickness as a function of the cooling rate (see also graph in figure 4.28)

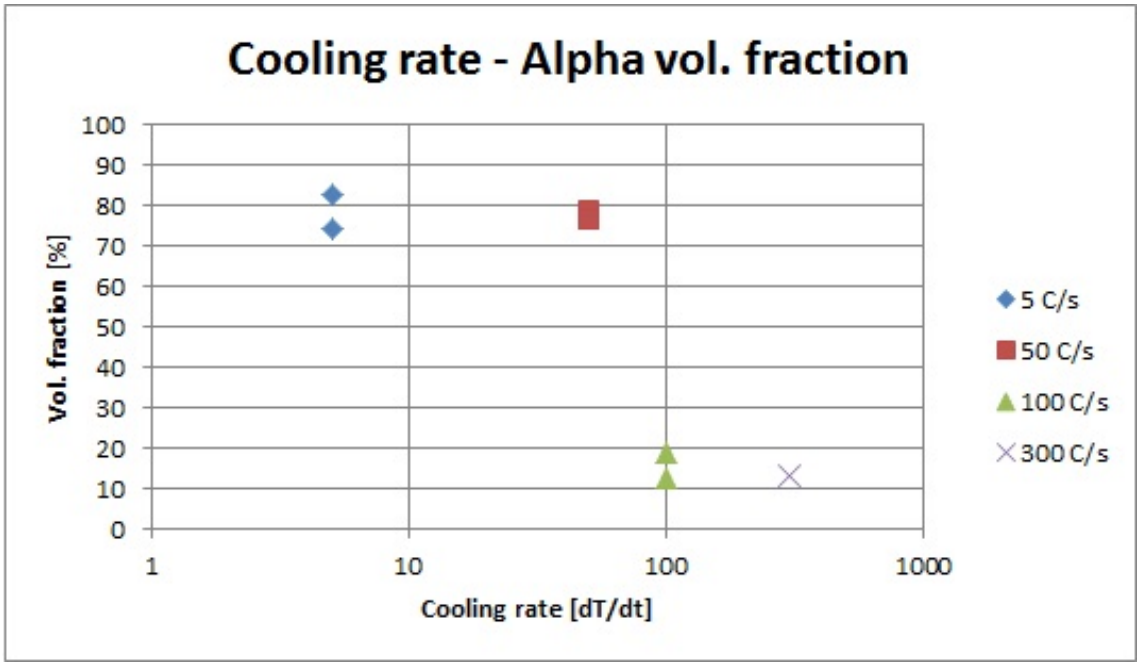

Figure 3.32.: Graph showing the amount of the alpha phase volume fraction formed in Ti-6Al-4V when the material is cooled down with different cooling rates starting from temperatures above the beta transus temperature (same data points of figure 3.31)

or 20 seconds then water quenching. Since the investigation of all the possible combinations of temperatures, cooling rates and soaking times would have required an extensive study, some combinations have been omitted.

This work was undertaken mainly to assess the feasibility of differentiating between the alpha formed on cooling through the transus and the martensite produced on quenching. Although experimentally difficult, this is feasible, giving the possibility of quantifying the alpha phase formation in the alpha-beta phase field which is needed for predicting the mechanical properties.

Measurement of the lamellae thickness for these particular tests was particularly arduous. Due to the particular heat treatment carried out (figure 2.24), a mixture of martensite and alpha lamellar microstructures was obtained, returning complicated BEI images to be studied. The amount of alpha lamellae recognizable per specimens was also very low, which resulted in a poor sample population for calculating the means and standard deviations (micrograph in figure 3.33). A further complication resulted from the use of tensile

or compression specimens, with a different section area. From the considerations in section 3.4.4, the thickness of the lamellae could be affected by a different sample size and this could modify the real trend of the particle dissolution or growth.

With the previous considerations in mind, an indicative analysis of the trends obtained from the measurements conducted (graphs in figure 3.34) is now described, giving particular attention to the heat treatments with more data points.

A first observation comparing the results coming out from cooling down at 5 °C/s and 50 °C/s to the same temperature in the α+β field, at time zero, is the very similar lamellar thickness obtained. Also, it seems there is a clear relation between the cooling time and the thicknesses of the lamellae: the lower the temperature at which the soaking starts, the thicker are the lamellae developed.

In general the tendency for all the cases seems to be a slow growth as the soaking time in the $\alpha + \beta$ field becomes longer. For 50 °C/s the growth seems more pronounced at 20 s, but the low number of lamellae sampled per test and the different sample diameters introduced uncertainty that, in the author's opinion, should be resolved by conducting a wider campaign of tests.

With so few data points and the different specimen dimensions exact conclusions from this part of the work cannot be done. As for the observation in section 3.4.4, approximately the same lamellae thickness would be expected at time 0 for all the cooling rates and, considering the different sample sections, this still seems reasonable. For the first 10 seconds it also seems that lamellae do not have the time to grow considerably, even though at 20 seconds it seems that growth is more appreciable.

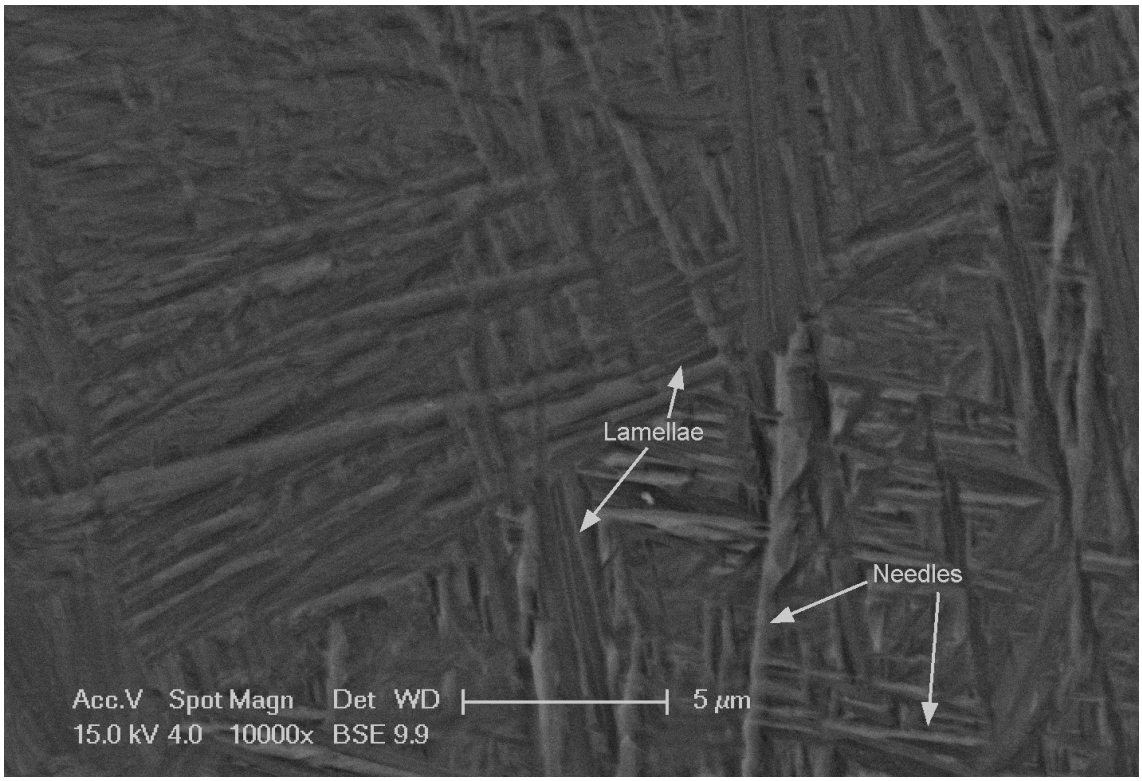

Figure 3.33.: BEI micrograph showing an example of a microstructure obtained in the α + β field. Lamellar microstructure embedded in martensite obtained after holding in the α + β field and then quenching

a)

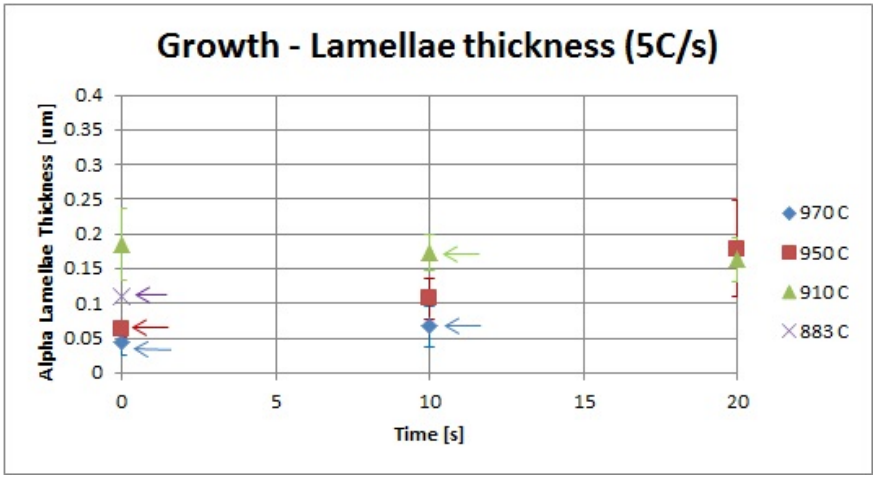

b)

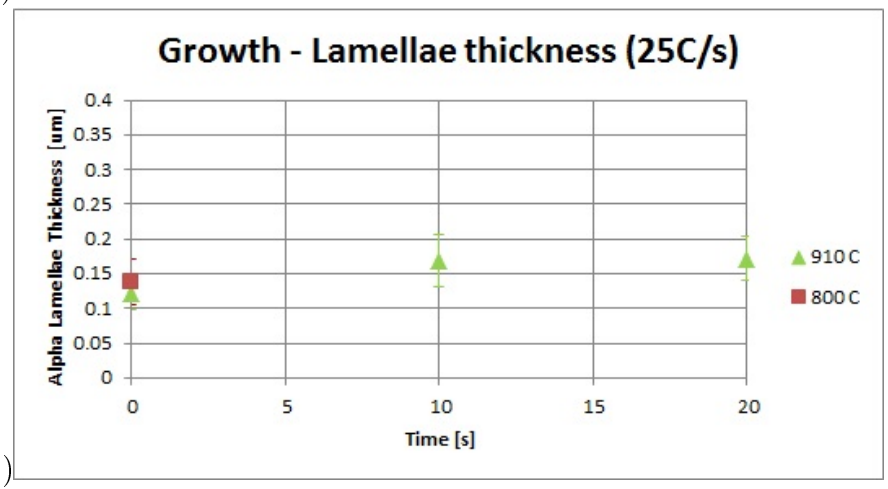

c)

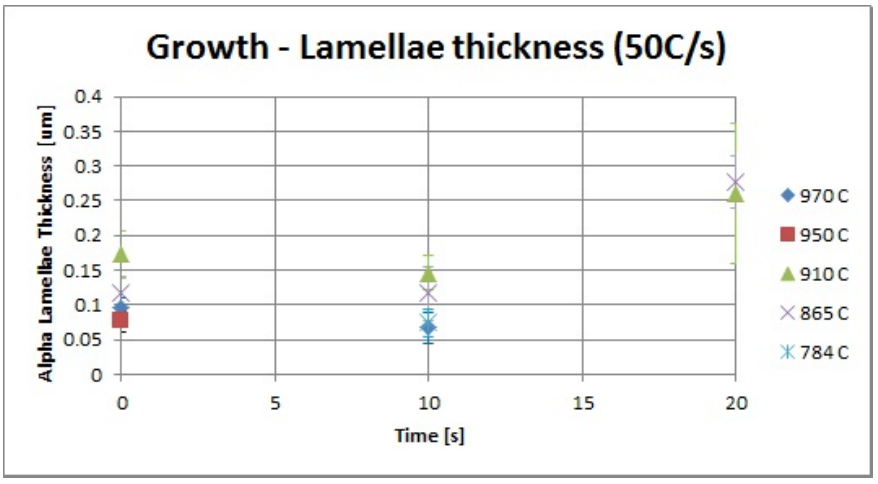

Figure 3.34.: Graphs showing growth of alpha lamellae in the $\alpha+\beta$ field, cooling down from the β field at different cooling rates and soaking for 0, 10 and 20 seconds then water quenching the samples. Data points with arrows represent samples of 6mm diameter, the other ones represent samples of 12 mm diameter

3.4.6 β transus

The beta transus temperature of the Titanium alloy used for the metallurgical study (see section 3.4), has been established by soaking small cubic specimen $10 \times 15 \times 2\,mm^3$ in a furnace for at least 20 minutes, at temperatures around the nominal beta transus, based on the results obtained from heating up the material at 5 °C/s. This heating rate was the slowest tested and thus was considered to be the closest to the response of the material at isothermal conditions. The samples, glass coated before the heat treatment to reduce the oxygen pick up at high temperatures, after soaking were water quenched to freeze the microstructure.

The temperature was acquired from a thermocouple type K placed in contact with the samples and controlled by a National Instrument acquisition box connected to a personal computer, enabling temperature measurement in real time. The furnace temperature was then manually set by small temperature steps, controlling each time the actual temperature on the surface of the specimens.

The temperatures tested were 960 °C, 970 °C and 980 °C. To establish between which range of temperatures the beta transus was located, optical microscopy and BEI investigations were carried out, by checking if any primary alpha lamellae were still not dissolved.

In micrographs shown in figure 3.35, 3.36 and 3.37 optical microscope pictures are shown, respectively a) for 960 °C, b) for 970 °C and c) for 980 °C.

In micrographs shown in figures 3.38, 3.39 and 3.40, in the same order of the previous figures, a BEI image for each sample is shown. It is possible to see how at 980 °C the microstructure was completely transformed to beta, since no parent lamellae can be spotted and only martensite is observed.

The beta transus temperature can thus be estimated to be within 980 °C and 970 °C. Using also results obtained from heating rates at 5 °C/s (micrographs in figure 3.21), the beta transus temperature can be approximately assumed to be at 973 °C, as this is the mean value between the two closest temperatures at which microstructures have been studied and at which it is possible to see still parent material (970 °C) and only beta

transformed phase (976 °C).

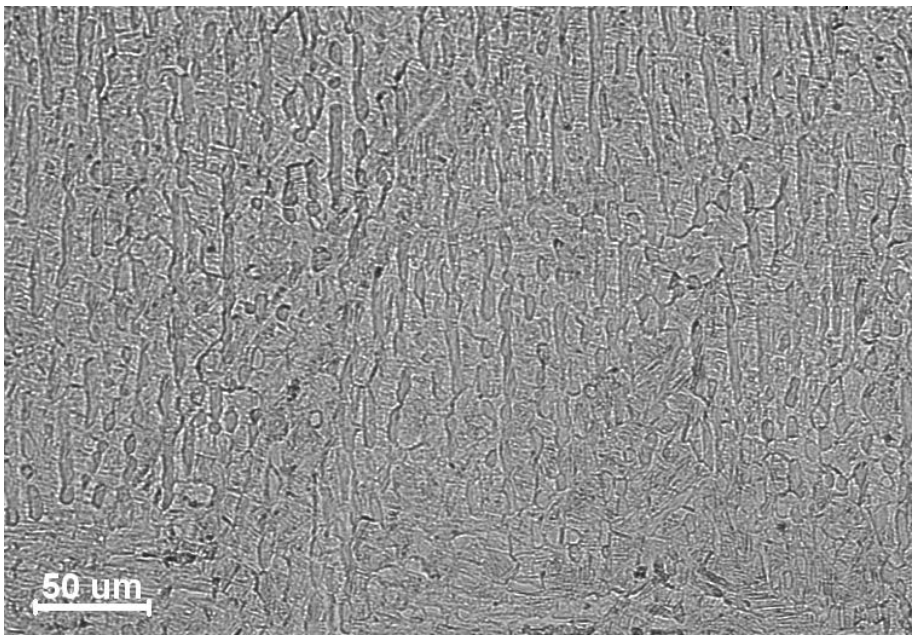

Figure 3.35.: Optical micrograph image of the sample soaked at 960 °C for the determination of the beta transus temperature. Parent alpha is still present thus beta transus has not been passed

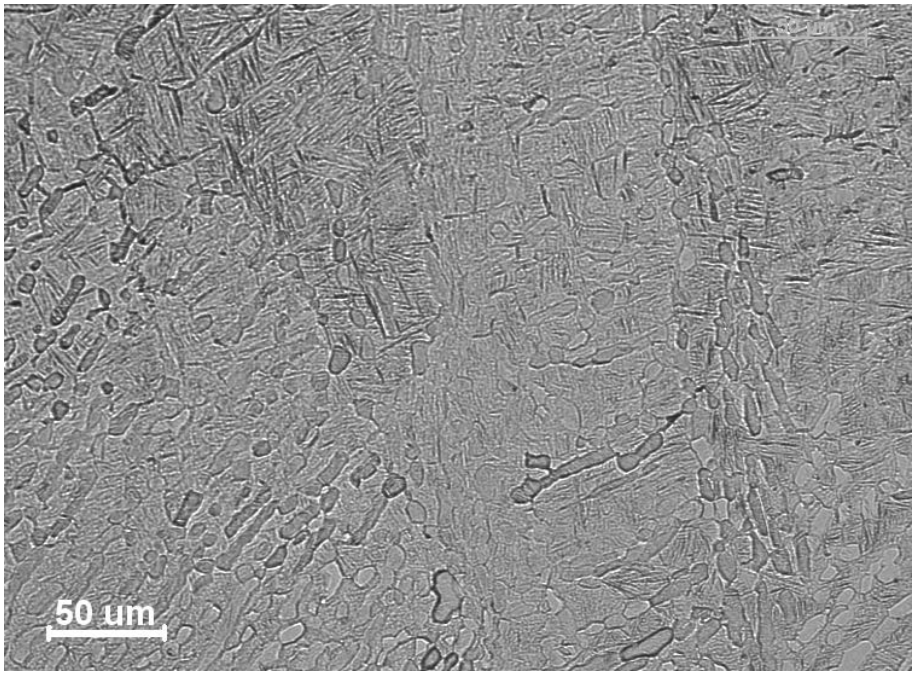

Figure 3.36.: Optical micrograph of the sample soaked at 970 °C for the determination of the beta transus temperature. Parent alpha is still present thus beta transus has not been passed

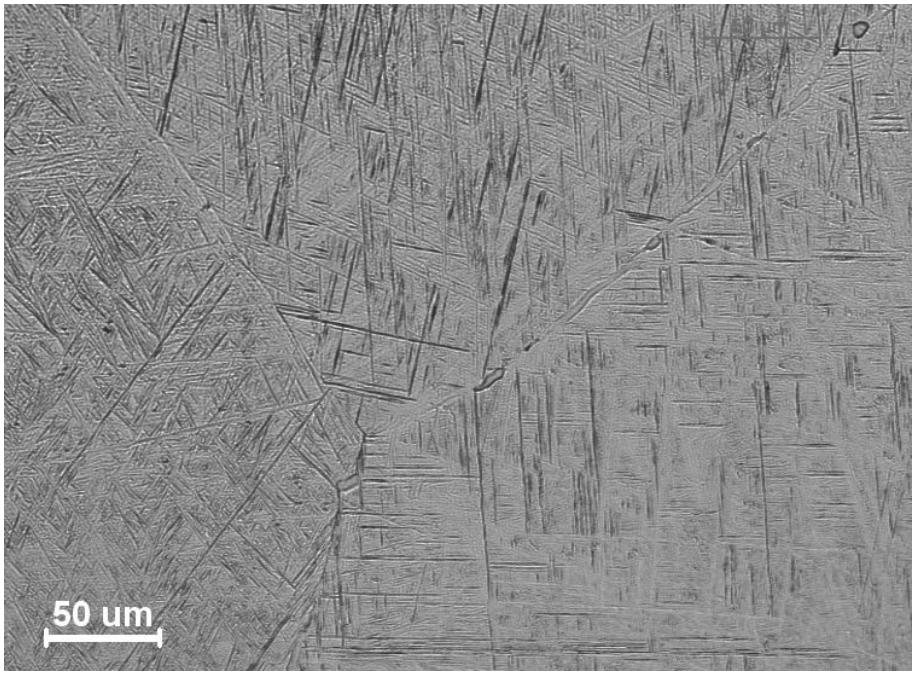

Figure 3.37.: Optical micrograph of the sample soaked at 980 °C for the determination of the beta transus temperature. Beta grains can be observed along the entire section: the beta transus temperature has been passed

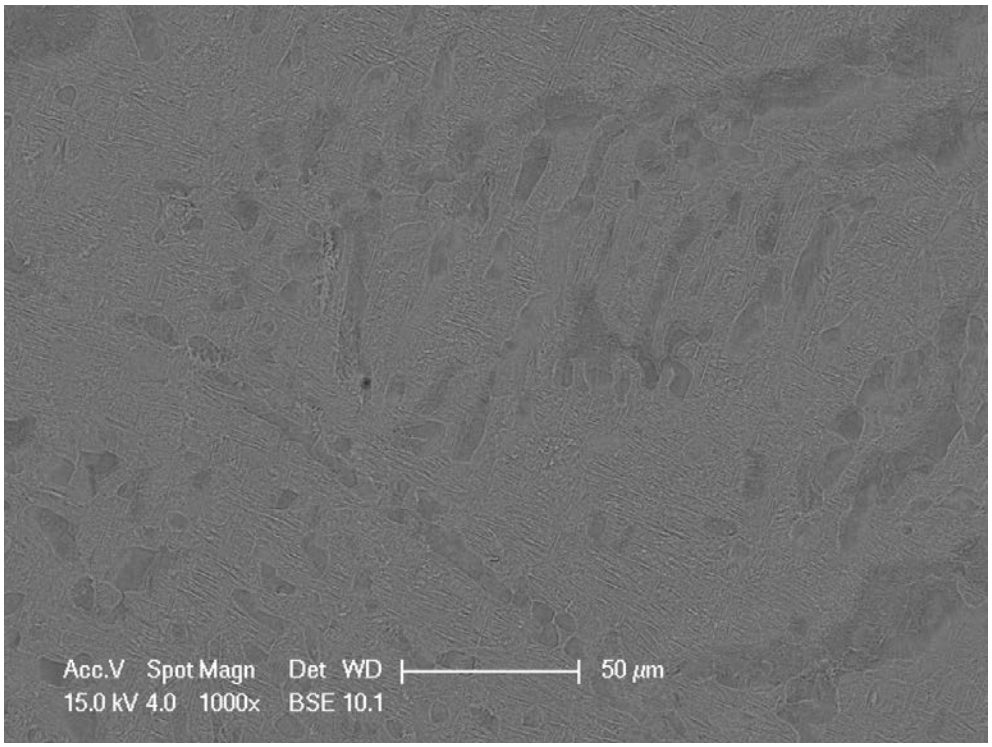

Figure 3.38.: BEI micrograph of the samples tested at 960 °C for the determination of the beta transus temperature. Parent alpha lamellae can be observed, meaning the beta transus temperature has not been passed

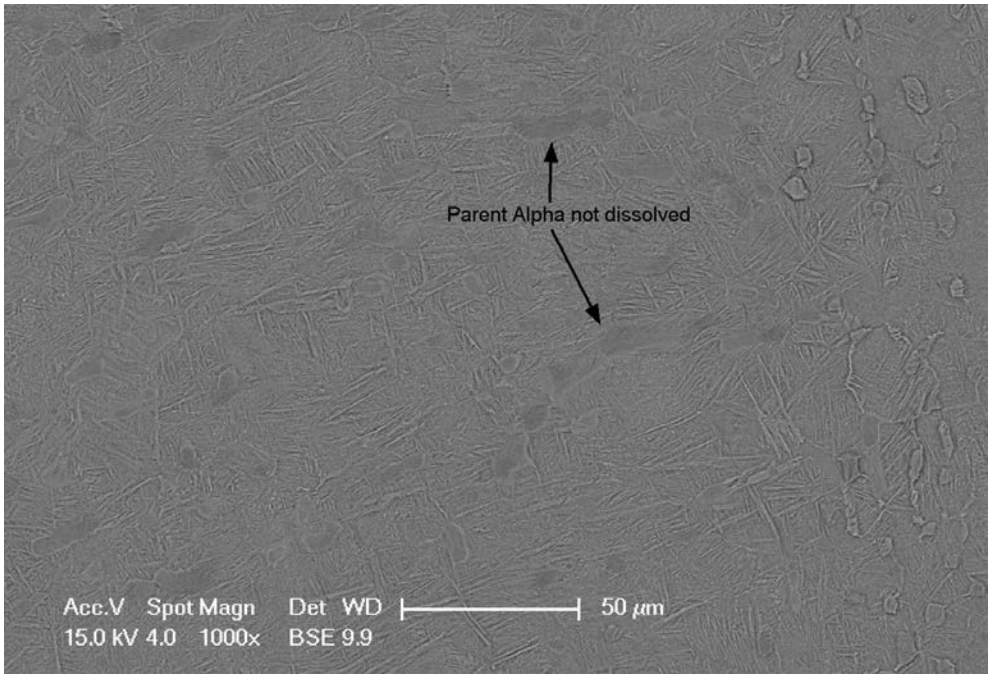

Figure 3.39.: BEI micrograph of the samples tested at 970 °C for the determination of the beta transus temperature. Parent alpha lamellae can be observed, meaning the beta transus temperature has not been passed

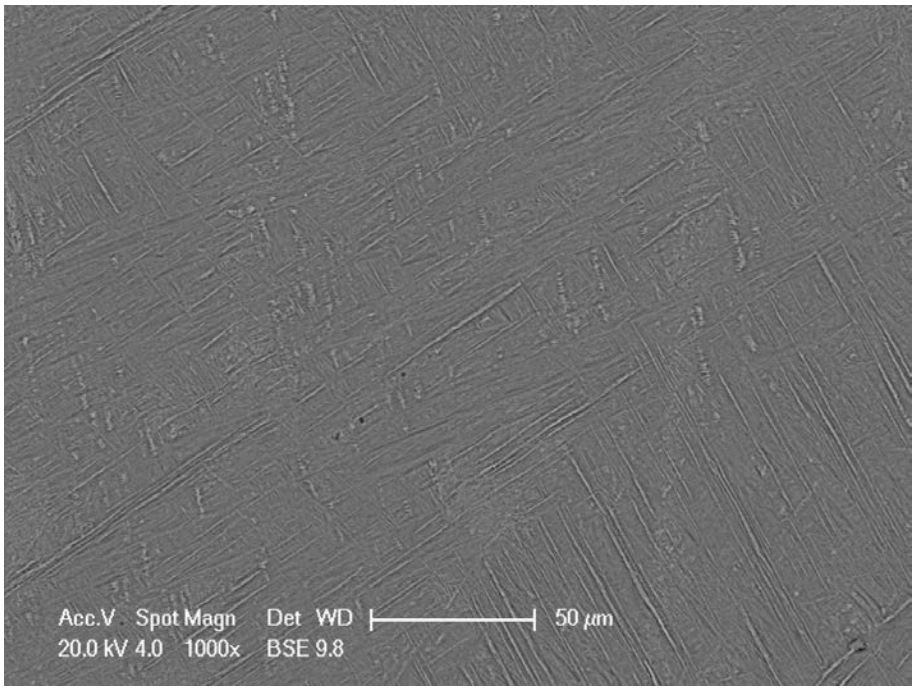

Figure 3.40.: BEI micrograph of the sample tested at 980 °C for the determination of the beta transus temperature. No parent alpha lamellae can be observed as in figure 3.38-a and b, meaning the beta transus temperature has been passed

3.4.7 β grain growth

As described at the beginning of the chapter, beta grain dimensions have been measured, in particular for the specimens tested at different heating rates, to understand and try to get an analytical expression to describe their growth evolution.

The experimental results obtained are shown in graphs of figure 3.41, where the beta grain dimension is reported both as a function of temperature and time for the three heating rates tested (5, 50 and 500 °C/s).

As it can be noticed (figure 3.41), at the fastest heating rate the beta grain dimension remains almost constant, limited by the short time the heat treatment required to reach the test temperatures set. At the intermediate heating rate of 50 °C/s instead, comparing at the same peak temperature, the kinetic of the diffusion process driving the grain growth seems instead to occur in timings long enough to return beta grain dimensions similar to the ones obtained for the slowest heating rate (5 °C/s).

The asymptotic trends registered in these tests (figure 3.41-a) are in agreement with the ones reported in literature [74] and they can be attributed to the beta grain growth coarsening [94]. Moreover, a slower growth rate can be supported also by a progressive homogenization of the chemical field as the growth proceeds in non equilibrium conditions.

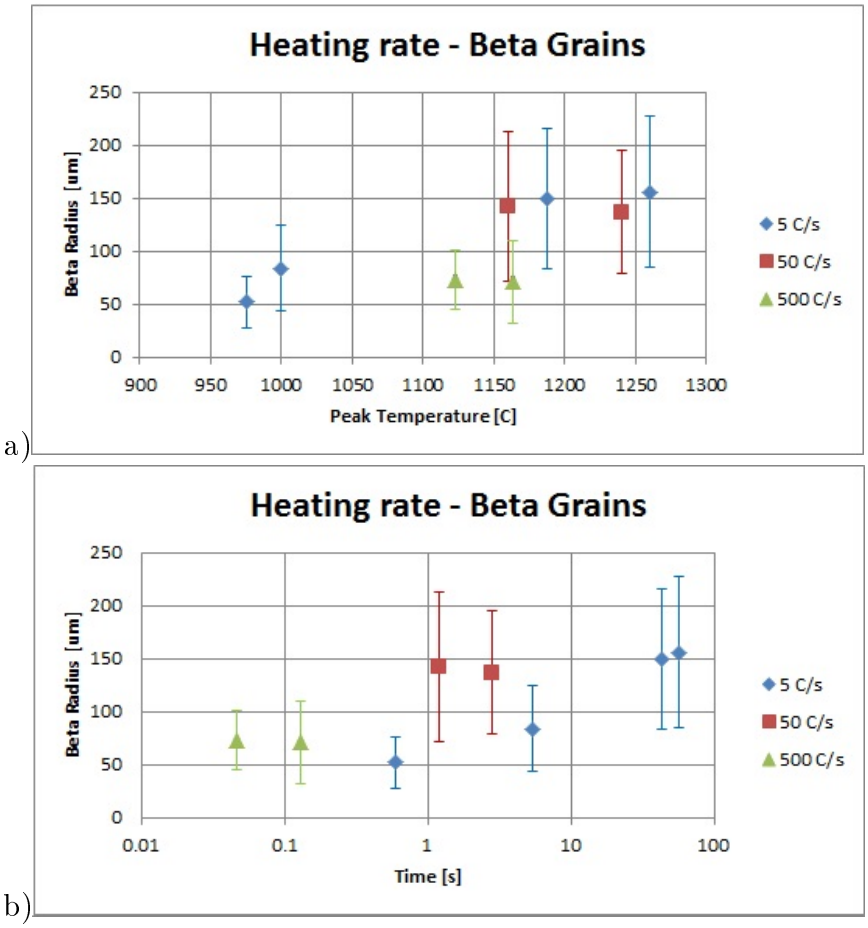

Figure 3.41.: Beta grains measurements as a function of the peak temperature and heating rate a), beta grains measurements as a function of the time and heating rate b).

3.5 Welding tests

For the study of the microstructures obtained in laser welding of Ti-6Al-4V, and for the application and validation of the numerical model developed in this work, a series of laser welding tests on Ti-6Al-4V plates with either an initial equiaxed or lamellar morphologies have been carried out.

The Titanium plates with equiaxed morphology had dimensions a) $51.62 \times 149 \times 5.80 mm^3$ with a measured composition in weight percent of Al 6.05, V 3.99, Fe 0.19, H 0.00314, N 0.005, O 0.18, Ti bal and b) $46.95 \times 151.5 \times 2.00\, mm^3$ with a measured composition in weight percent of Al 5.82, V 4.00, Fe 0.06, H 0.00963, N 0.010, O 0.063, Ti bal.

Microstructure	Thickness of the plate [mm]	Power [%]	Welding speed [m/min]
Equiaxed	5.80	100	2.0 - 1.5
Equiaxed	2.00	60	2.0
Lamellar	3.75	70	2.0
Lamellar	3.06	70	2.0

Table 3.1.: Welding operative parameters used for welding tests. Ti-6l-4V plates with two different initial microstructures and different thicknesses were welded, using welding speeds of 2.0 or 1.5 m/min. The welding input power was set as percentage of the maximum power (4 kW) of the welding machine used

The Ti-6Al-4V plates with lamellar morphology had dimension $47.30 \times 136.96 \times 3.75 mm^3$ and $47.31 \times 137.05 \times 3.06 mm^3$ and they were made of a grade 5 Ti-6Al-4V with a measured composition in weight percent of Al 5.75, V 3.96, Fe 0.07, H 0.00445, N 0.013, O 0.11, Ti bal.

Two thickness have been used for the tests, with different welding parameters. The power was set as a percentage of 4 kW, as this was the maximum power of the machine. Regarding the equiaxed microstructure, for the 2.00 mm thick plate, a power of 60% was used whilst, for the 5.80 mm thick one, a power of 100% was set. For the plates with an initial lamellar microstructure, a power of 70% was used. As explained in paragraph 2.2.2, the determination of the actual power going through the plates is beyond the aims of the current work: thus for the data reported it will be make reference to the percentage set in the machine rather than an actual power value.

The welding machine used for the welding tests was a Trumpf TLC1005.

The welding speeds tested for the plates with equiaxed microstructure were 1.5 m/min and 2.0 m/min for the plate 5.80 mm thick and 2.0 m/min for the plate 2.00 mm thick. The plates with lamellar microstructure were instead welded with a speed of 2.0 m/min (see table 3.1).

The nozzle of the welding machine was set at a distance of 6.8 mm from the top surface of the plates.

Since temperature profiles along the component are needed to set the heat source of the numerical model correctly (section 2.2.2), the plates tested were machined to locate

the thermocouples. Holes were drilled at different distances from the weld line, and thermocouples were placed in them.

Sheathed thermocouples type K were adopted for the following considerations:

- a high number of thermocouples had to be used to get a good understanding of the different temperature gradients along the component: with spot welding, there was a high risk that some sensors would have disconnected while the plates were being prepared for welding. In such a case, the component had to be removed from the jig and brought again to the spot welder. By locating the thermocouples in place with holes, they could be quickly repositioned if some of them came out;

- initially, some welding tests were run with the thermocouples fixed in the holes with either glue or cement. Using glue, where the thermocouples were close enough to the weld heat source, it burnt modifying the temperature readings and also significantly changing the shape of the weld pool. Instead, although the cement did not burn, it changed the weld pool shape by absorbing in a different manner the heat flux respect the workpiece material. A change in the weld pool shape would affect the real thermal profile developed by the welding process, thus preventing the acquisition of reliable information for the numerical model;

- bare wires could not be located in the holes, since the thermocouple wires needed to be bent so as to not touch the nozzle of the welding machine. Moreover by bending, the bare wires touched the upper edge of the holes and since the temperature measured by thermocouples is where the first electrical junction between the sensor wires is formed, the temperature actually measured in this case, would have been from the hole upper edge;

- type B thermocouples would have allowed measurements at higher temperatures but with the temperature rising so high close to the weld pool it was not possible to place the sensor in positions where they could still measure temperature above

1400 °C (type K max temperature), but less than 1600 °C, without them moving out of position when liquid was formed.

For each welding test of the plates with an equiaxed morphology, 14 thermocouples were used, to measure seven different distances from the weld trajectory in one face, and to study the thermal profile of the weld pool using the other seven thermocouples at two distances very close to the weld pool and at different depths (figure 3.42). To save material, each plate was used for 2 welding tests, while ensuring that the distance between the welds was large enough to prevent any effect on the microstructures from the thermal load. In figure 3.43 a photograph of a plate ready to be welded is shown. All the thermocouples were kept in position by twisting a wire around them and the plate. In figure 3.44 a photograph of the assembly used to fix the plates for the welding tests is also shown.

The plates in the welding machine were fixed using a jig designed previously (appendix C), leaving one side free and clamping the other one as shown in figure 3.44-a. A ceramic plate was placed below the specimens to protect the vice on which the jig was mounted, in case of a full penetrating weld.

Because Titanium is very sensible to oxidation, all the instrumentation had to be placed in a chamber to operate in inert atmosphere (Argon) (photograph in figure 3.44-b).

The surfaces of the plates were cleaned with Acetone before each welding tests, to remove any grease or dirt which could affect the quality of the weld.

To measure the chamber temperature close to the specimens during welding, a further thermocouple was placed at about 2 cm below the bottom surface of the plate.

After having run the first weld, the plate was removed from the jig, cleaned with Acetone (figure 3.45) and another 14 thermocouples were placed to measure temperatures for the second welding test.

An example of how a welding plate looked at the end of the welding tests is shown in figure 3.46.

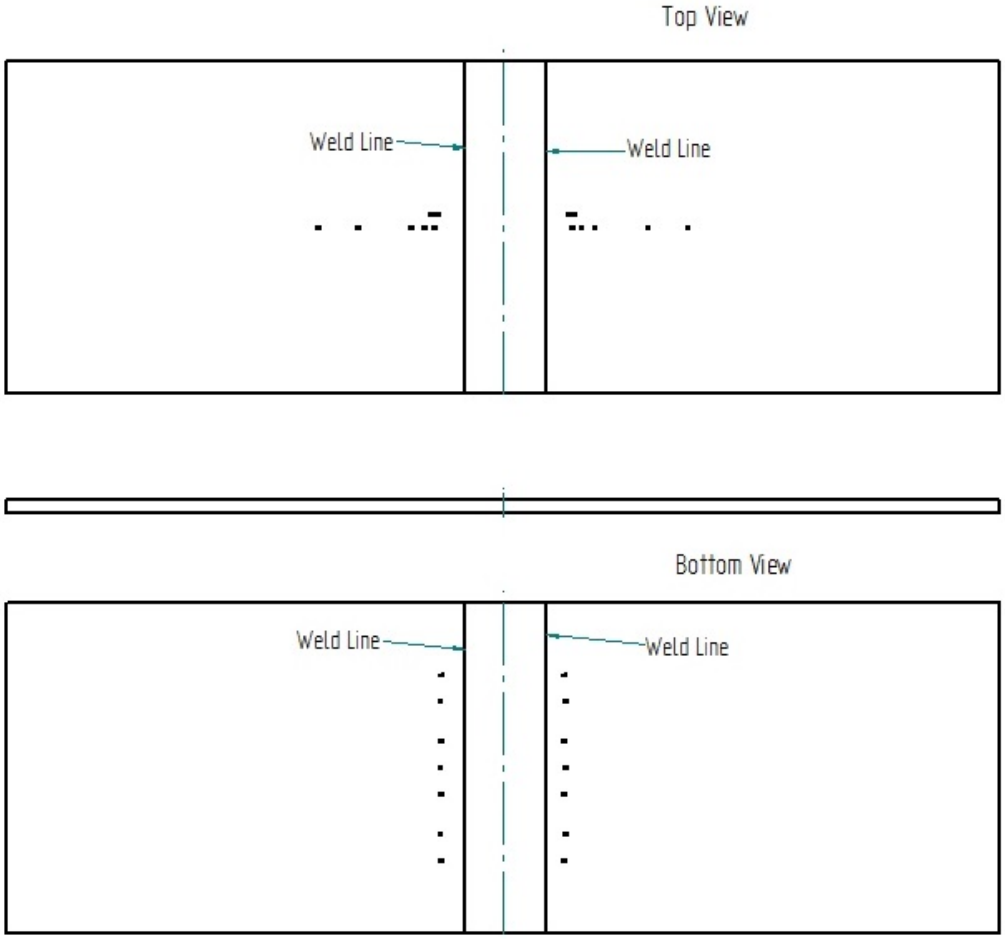

Figure 3.42.: Drawing of the hole positions machined to keep in place the thermocouples during welding tests. In the top face of the plates a series of holes at different distances from the weld line have been machined, in the bottom face the holes are at two different distances but with different depths

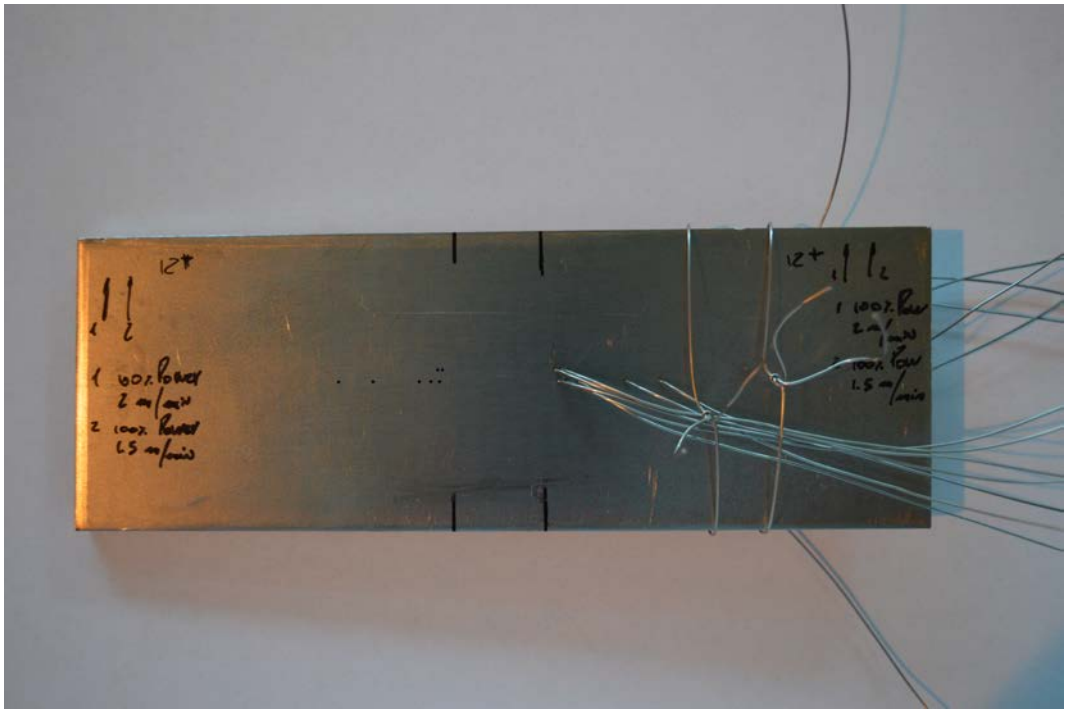

Figure 3.43.: Photograph of Ti-6Al-4V plate showing how the thermocouples were kept in place by twisting two wires around them and the specimens

Unfortunately, not all the thermocouples worked satisfactorily during the tests, thus reducing the actual number of measurements available. Moreover, the row of thermocouples located very close to the weld pool, returned values not in agreement with values expected from their position and depth, suggesting a high sensitivity of the measurements to slightly different positions to the ones planned, caused by movements of the thermocouples tip. Without any fixing technique to keep the thermocouples in position in the holes, small movements were unavoidable and this could be the explanation for the problem.

Welding tests on plates with an initial lamellar morphology were carried out a second time to measure distortion before and after welding, for the validation of the mechanical model. For this purpose, each plate was welded only once, avoiding superimposition of the effects of two welds on the distortion of the components. The temperature measurements were carried out by using only the set of holes in the top surface of each plate tested (figure

a)

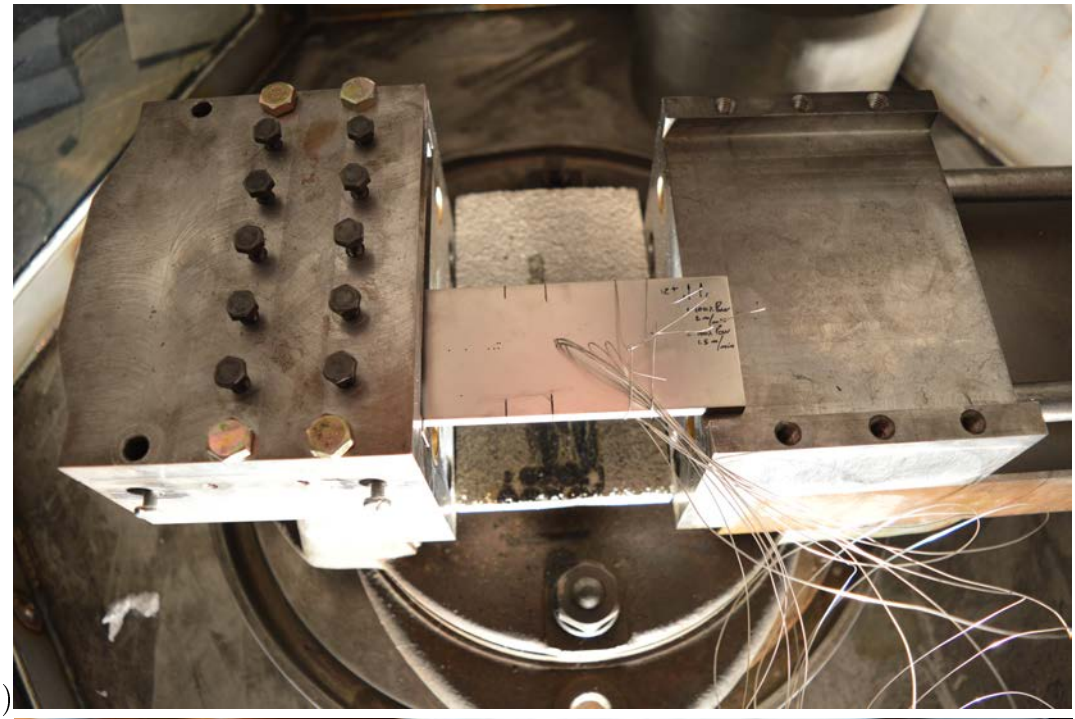

b)

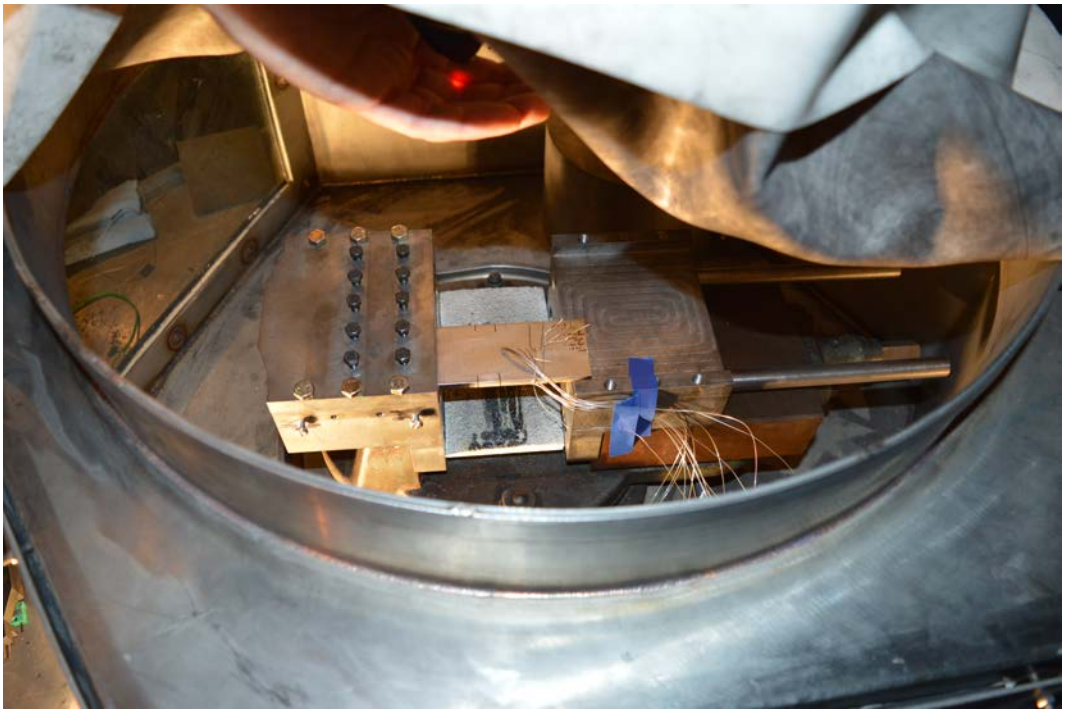

Figure 3.44.: Photographs showing a) the jig used to fix the plates during welding tests and b) the assembly placed in the welding chamber to operate in inert atmosphere

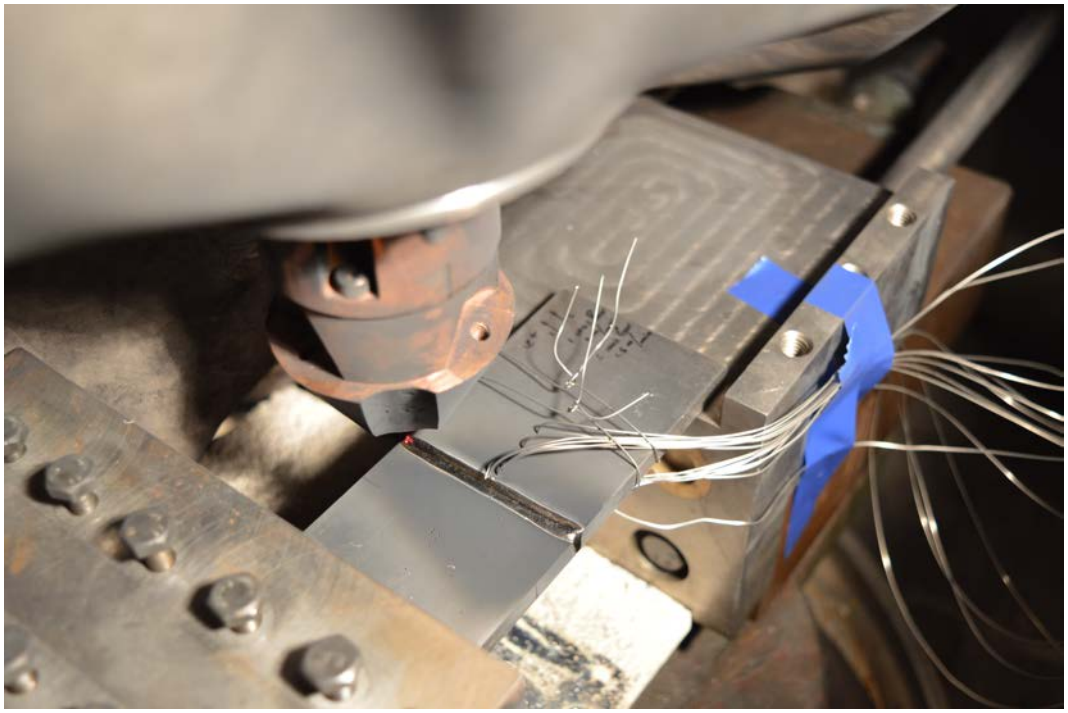

Figure 3.45.: Photograph of a Ti-6Al-4V plate after welding

3.42). This decision was because a) from previous welding tests, the set of holes in the bottom surface did not return reliable results and b) at the time of the tests, the access to the welding chamber was changed, only allowing a maximum of 5 thermocouples.

3.5.1 Temperature measurements

3.5.1.1 Plates with equiaxed microstructure

In the graphs of figure 3.47 and 3.48 results of the welding conducted on a 5.8 mm plate using as operative parameters 100% power and 2 m/min and 1.5 m/min respectively are shown. The time at which the temperature rises does not correspond to the actual time needed by the laser to heat up the thermocouples from the starting of the welding test. The acquisition was launched some seconds before starting the experiments to check if the acquisition system worked correctly.

In the graph of figure 3.49 results of welding tests on a 2mm thick plate with a 2 m/min welding speed are shown.

Results shown in this section are all relative to the plates having an original microstruc-

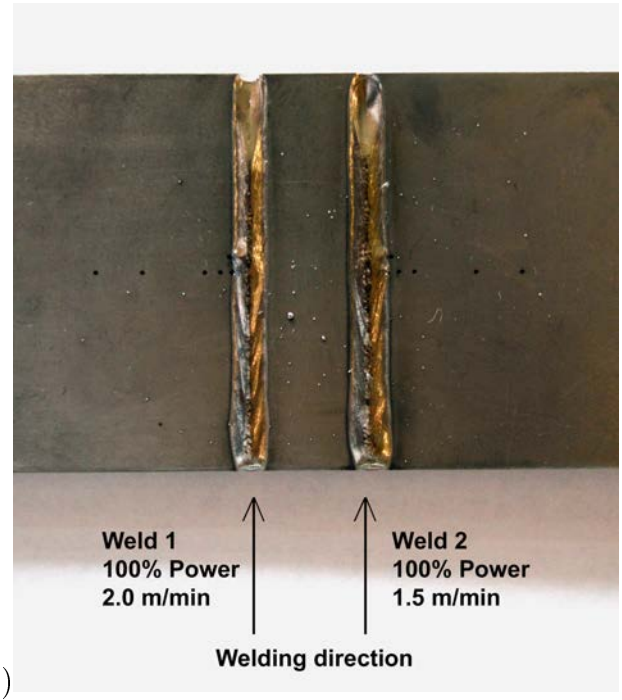

a)

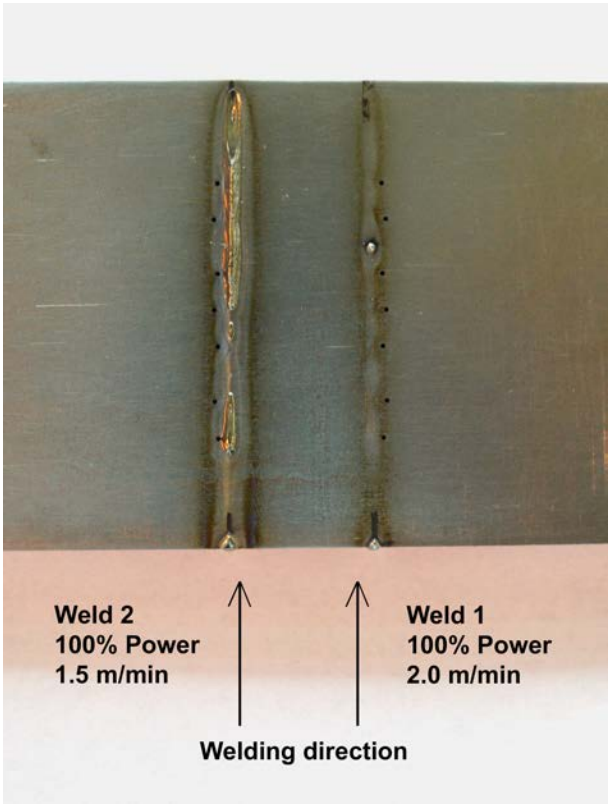

b)

Figure 3.46.: Cropped photographs of the Ti-6Al-4V plate 5 mm thick, with equiaxed microstructure, after welding tests - detail of the welding area. In this case 100% power was used at two different speeds, 2 m/min and 1.5 m/min. a) Top view. b) Bottom view

ture with an equiaxed morphology.

3.5.1.2 Plates with lamellar microstructure

In the graph of figure 3.50 results are shown of the welding conducted on a 3.75 mm plate using operative parameters of 70% power and 2 m/min. The time at which the temperature rises does not correspond to the actual time needed by the laser to heat up the thermocouples, since as before the acquisition was started earlier to check if the acquisition system worked properly.

In the graph of figure 3.51 results of welding tests on a 3.06 mm thick plate at 2 m/min as weld speed are shown.

Results shown in this section are all relative to the plates having as original microstructure equiaxed morphology.

3.5.2 Microstructures

To study the microstructures obtained from the welding processes described previously, a series of micro indentations using a hardness machine allowed both the measurement of the hardness of the material in different locations and to have a position reference at which to take BEI images.

3.5.2.1 Plates with equiaxed microstructure

In figure 3.52 and 3.53 the montages of the micrographs shown correspond with the weld zones of the plates tested.

It can be noticed that, at higher speed, the energy going through the plate per unit time is less, thus giving rise to less penetration. Some porosity is also present, due probably to the formation of gas bubbles. The holes used to fix the thermocouples are also visible and,

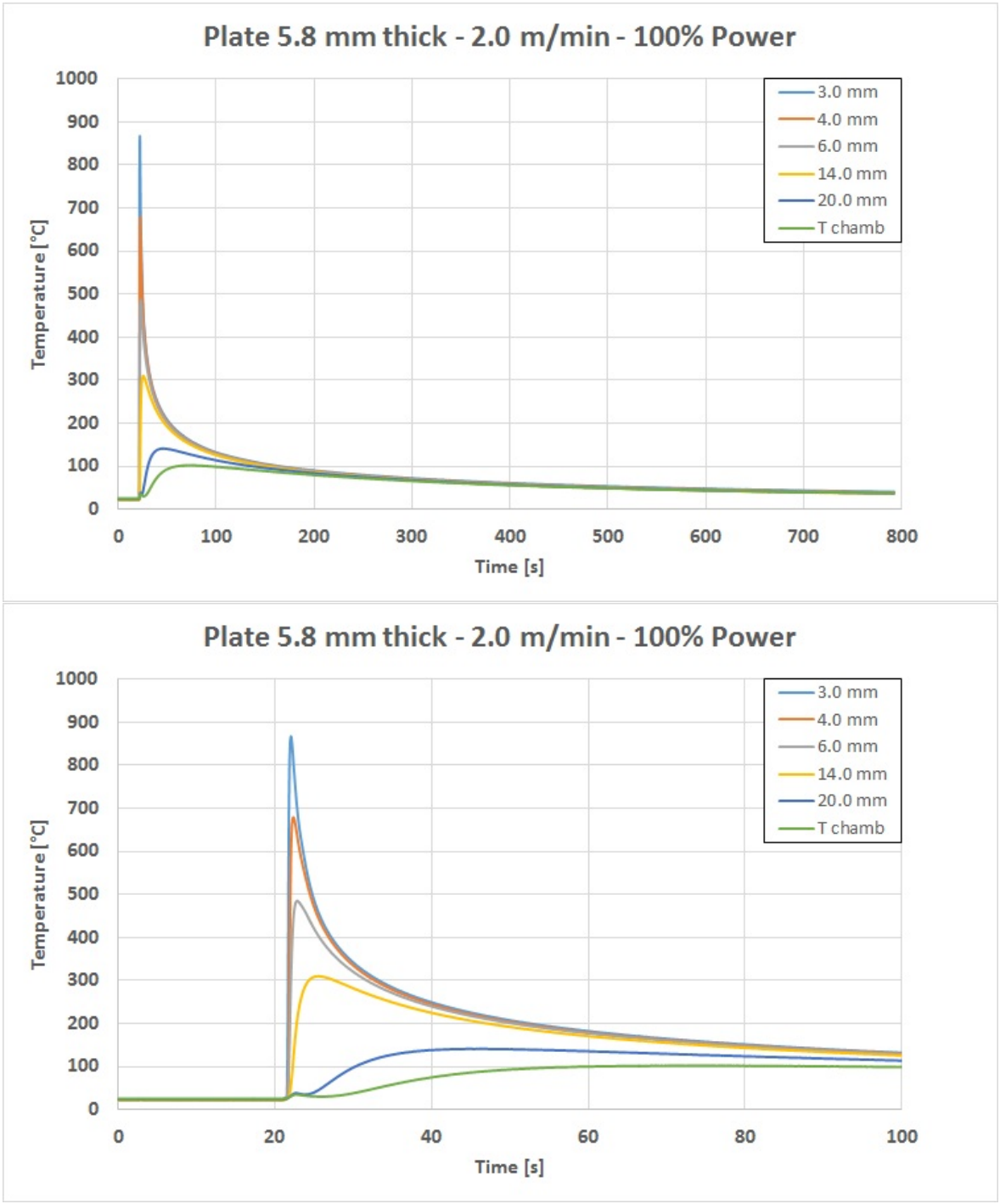

Figure 3.47.: Graphs showing the temperatures measured at different distances from the weldline, for the welding test conducted on a Ti-6Al-4V plate 5.8 mm thick with initial equiaxed microstructure, using as operative parameters 100% power and 2 m/min as welding speed. The bottom chart shows a zoom on a time scale of 100 seconds

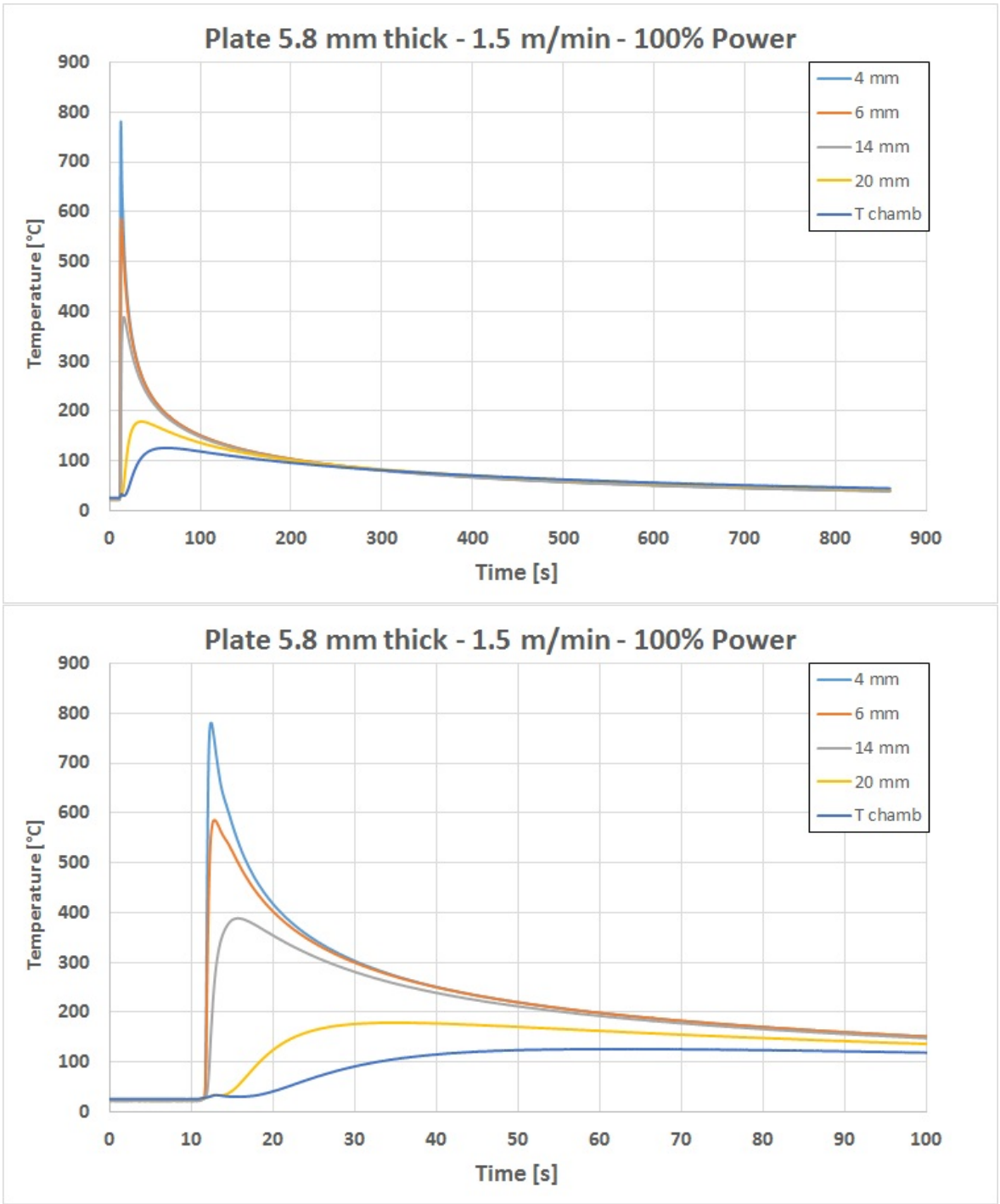

Figure 3.48.: Graphs showing the temperatures measured at different distances from the weldline, for the welding test conducted on a Ti-6Al-4V plate 5.8 mm thick with initial equiaxed microstructure, using as operative parameters 100% power and 1.5 m/min as welding speed. The bottom chart shows a zoom on a time scale of 100 seconds

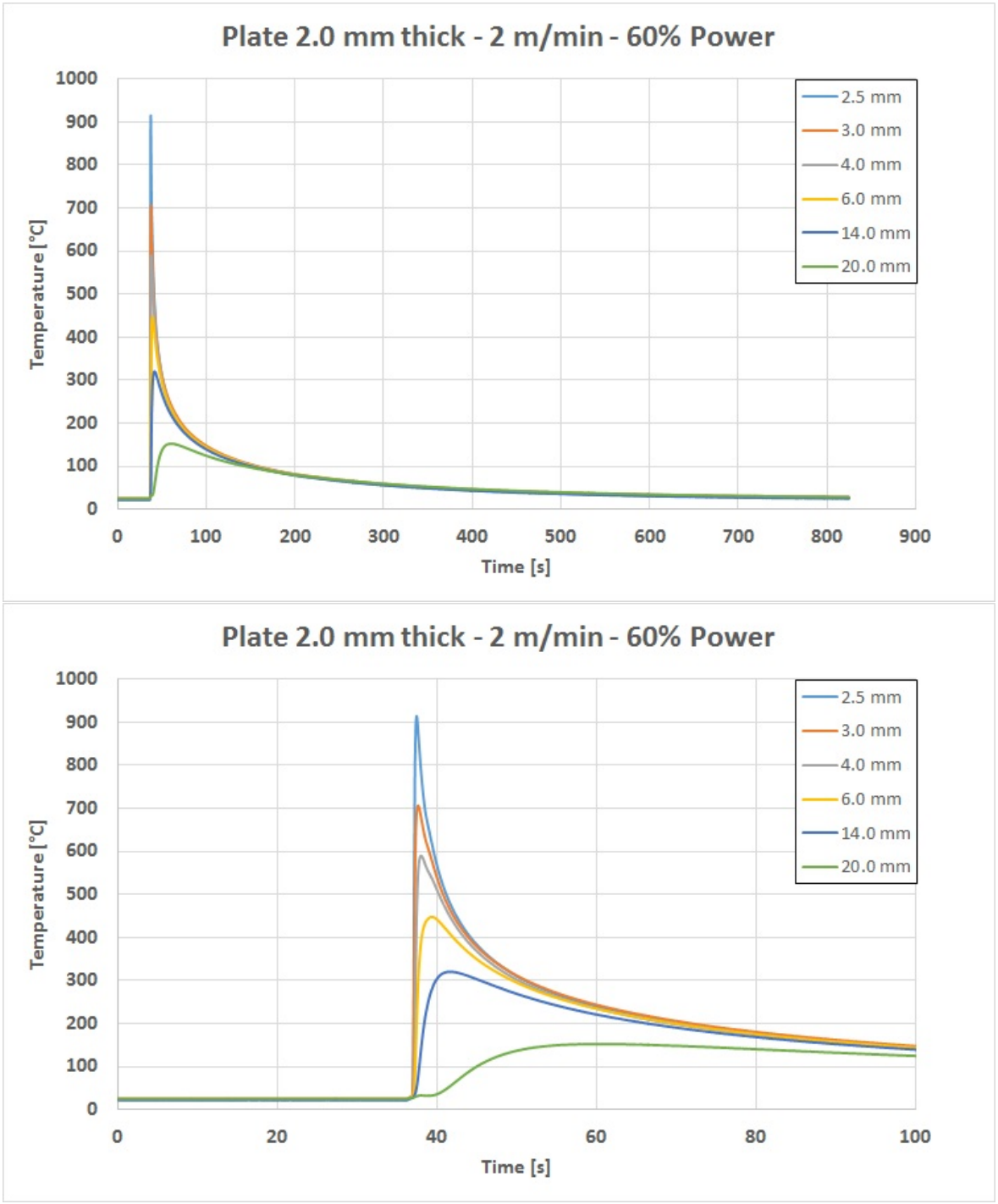

Figure 3.49.: Graphs showing the temperatures measured at different distances from the weldline, for the welding test conducted on a Ti-6Al-4V plate 2mm thick with initial equiaxed microstructure, using as operative parameters 60% power and 2.0 m/min as welding speed. The bottom chart shows a zoom on a time scale of 100 seconds

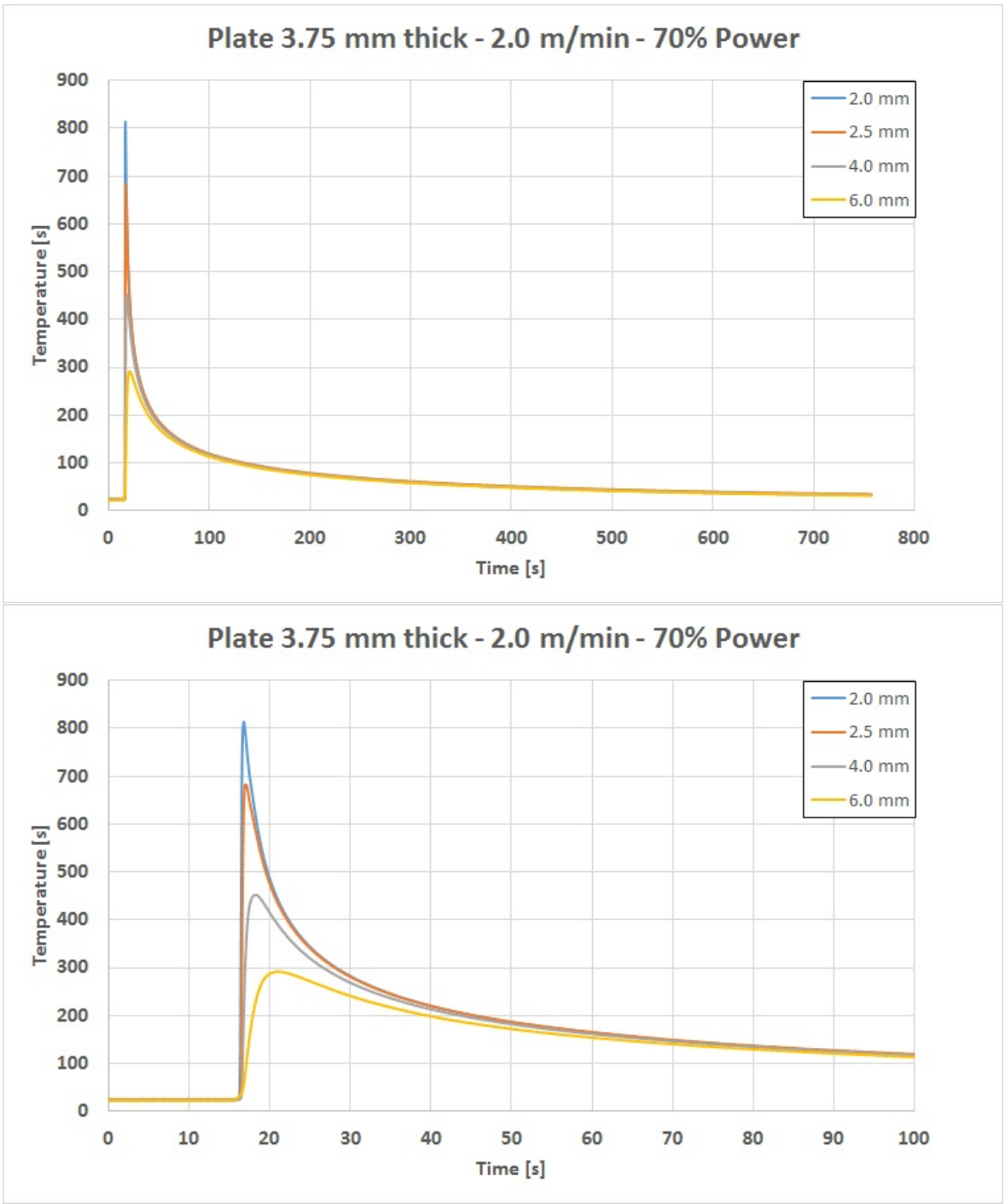

Figure 3.50.: Graph showing the temperatures measured at different distances from the weldline, for the welding test conducted on a Ti-6Al-4V plate 3.75 mm thick with initial lamellar microstructure, using as operative parameters 70% power and 2.0 m/min as welding speed. The bottom chart shows a zoom on a time scale of 100 seconds

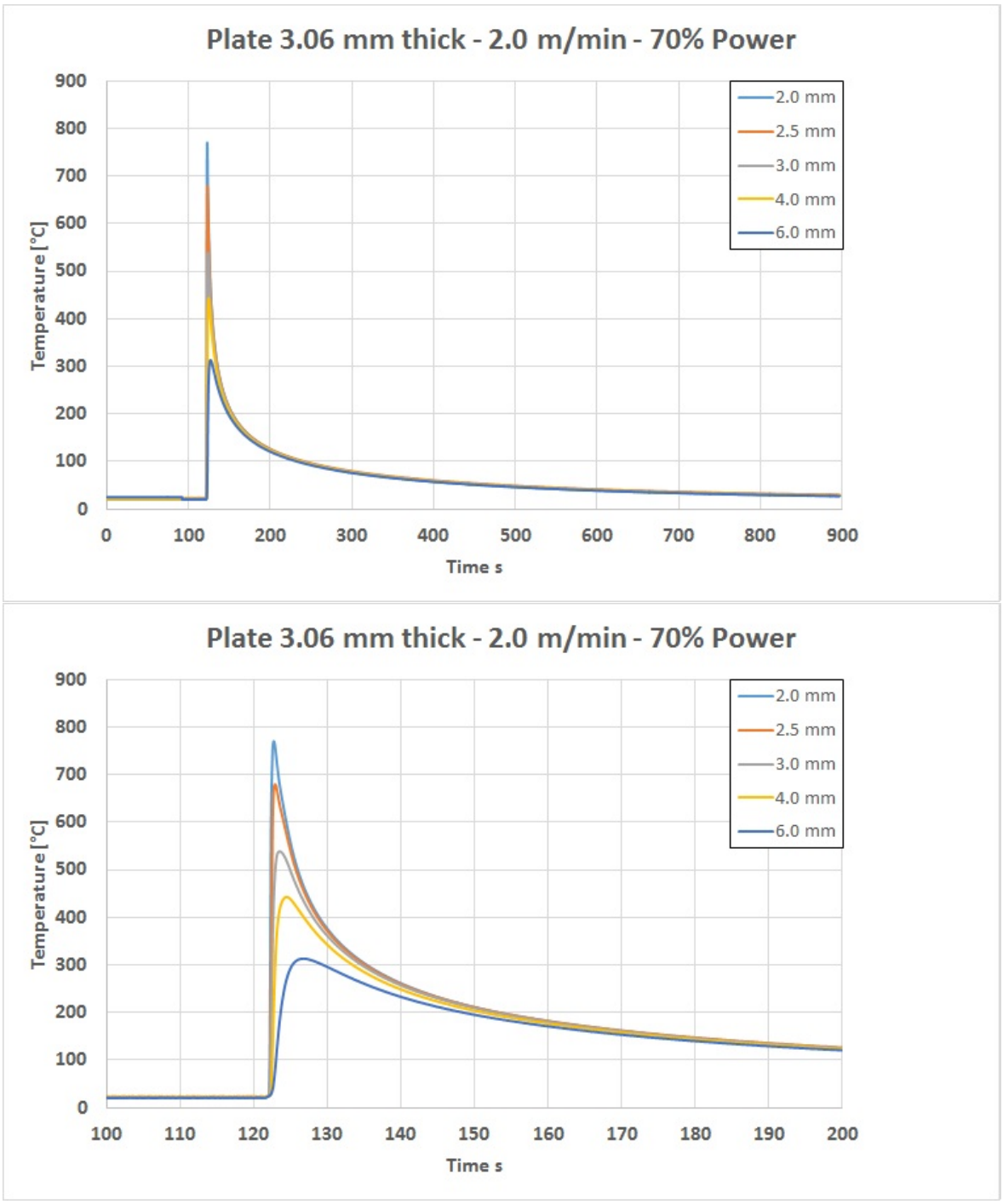

Figure 3.51.: Graphs showing the temperatures measured at different distances from the weldline, for the welding test conducted on a Ti-6Al-4V plate 3.06 mm thick with initial lamellar microstructure, using as operative parameters 70% power and 2.0 m/min as welding speed. The bottom chart shows a zoom on a time scale from 110 to 150 seconds

from the micrograph of figure 3.52-b), the influence of these holes on the shape of the weld pool can be seen by comparing its right side to the left one. Micro hardness measurements and BEI images were taken on the opposite side to where the thermocouples were placed.

A prior beta columnar morphology can be observed in the centre of all the microstructures shown, with an orientation going from the heat affected zone, where the first beta nuclei formed from colder material, toward the centre where the hottest part of the material is. These columnar grains, looking in the centre line of the weld pool, are also oriented toward the colder side: in the upper side they grow going upward, in the bottom side they grow downward. In the centre the elongated beta columnar microstructure becomes more equiaxed.

In the micrograph of figure 3.53, is also possible to observe how the hole where a thermocouple was placed, is deformed under the load induced by bending the thermocouples wires (figure 3.43) that, at high temperatures, become high enough to plastically deform the material. It is also possible to deduce, from the deformation of the hole, how the tip of the thermocouple was not in the deepest position possible, potentially justifying the inconsistent measurements described previously (section 3.5).

The hardness measurements for the samples shown in figures 3.52 and 3.53 are reported in the graphs of figures 3.54 and 3.55. The weld centreline point at which the measurements start is shown as "0", the indents then go progressively at steps of 0.2 mm, farther from the centre.

As expected from the literature (figure 2.38), the hardness of the material is higher in the fusion zone than the bulk, since a martensitic microstructure is developed during cooling from the welding process. It is also interesting to point out the oscillation of the hardness in the fusion zone, particularly noticed in figure 3.54-b, indicating regions with different properties, due probably to the grain orientation effect.

The 5 mm plate welded at a speed of 2 m/min seems to have a slightly higher hardness in the fusion zone than the plate 5 mm thick but welded at a speed of 1.5 m/min. This is probably due to the faster cooling of the material being welded with a faster speed,

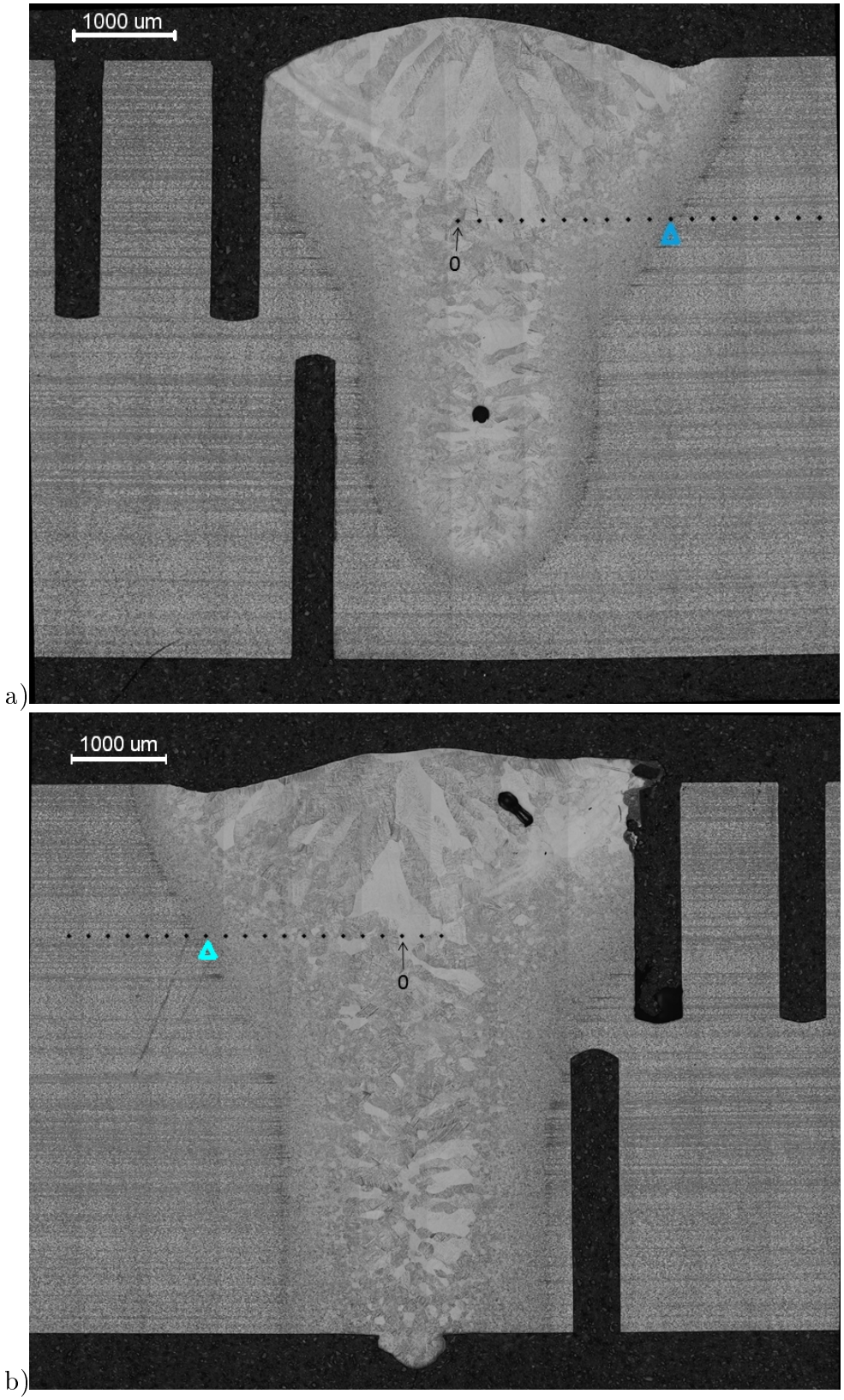

Figure 3.52.: Montages for the Ti-6Al-4V plate 5.8 mm thick tested and the hardness indentations, material with initial equiaxed microstructure. a) weld carried out at 2 m/min 100% power; b) weld carried out at 1.5 m/min at 100% power. The "0" point shows the first hardness measurement referenced in figure 3.54 and corresponds to the weld centreline

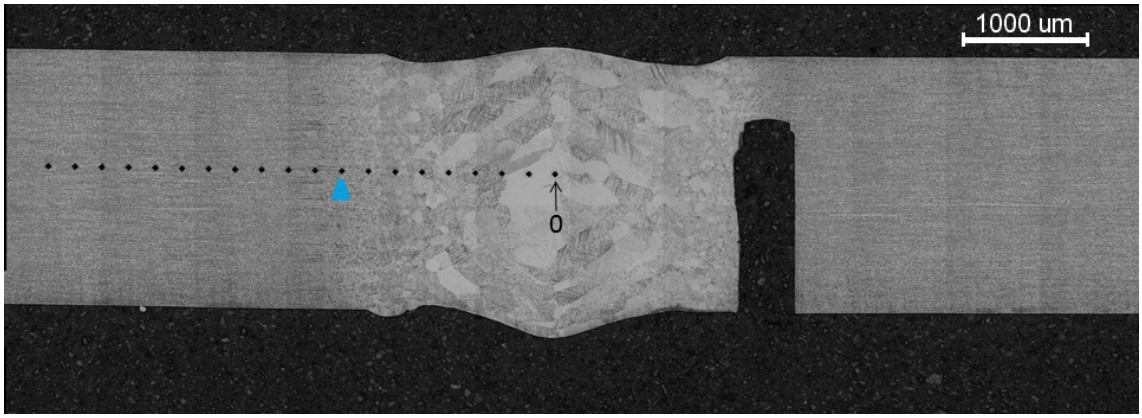

Figure 3.53.: Montage of the Ti-6Al-4V plate 2 mm thick, material with initial equiaxed microstructure. 2 m/min 60% power. The "0" point shows the first hardness measurement referenced in figure 3.55

thus developing a fully martensitic structure, whilst the material welded at 1.5 m/min had both martensite and lamellar microstructures (figures 3.56-a and 3.56-b) in the fusion zone .

Even though the geometry and thermal load were different, the 2 mm thick plate shows a hardness in the fusion zone similar to the 5 mm plate welded at 1.5 m/min, comparing the microstructures in the fusion zone of these two samples, it is possible to observe similarities in the presence of both lamellar and martensitic structures (figure 3.56-b and 3.56-c). Measurement of the lamellae thickness, shown later in the chapter (figure 3.61-a and figure 3.62-a), will confirm the similarity in the lamellae thickness. This highlights the strict relationship between microstructural features shape and mechanical response of the material.

A further observation that can be done for all the samples, regards the drop in hardness close to the interface between the bulk and the heat affected material, which is due probably to the release of local residual stresses in the parent microstructure. In this narrow area it could be supposed that the heating induced by the welding process is such as bring the temperature to values sufficient for annealing but not high enough to generate harder lamellar or martensitic microstructures.

BEI images of the microstructure observed after welding, for some of the points shown in

a)

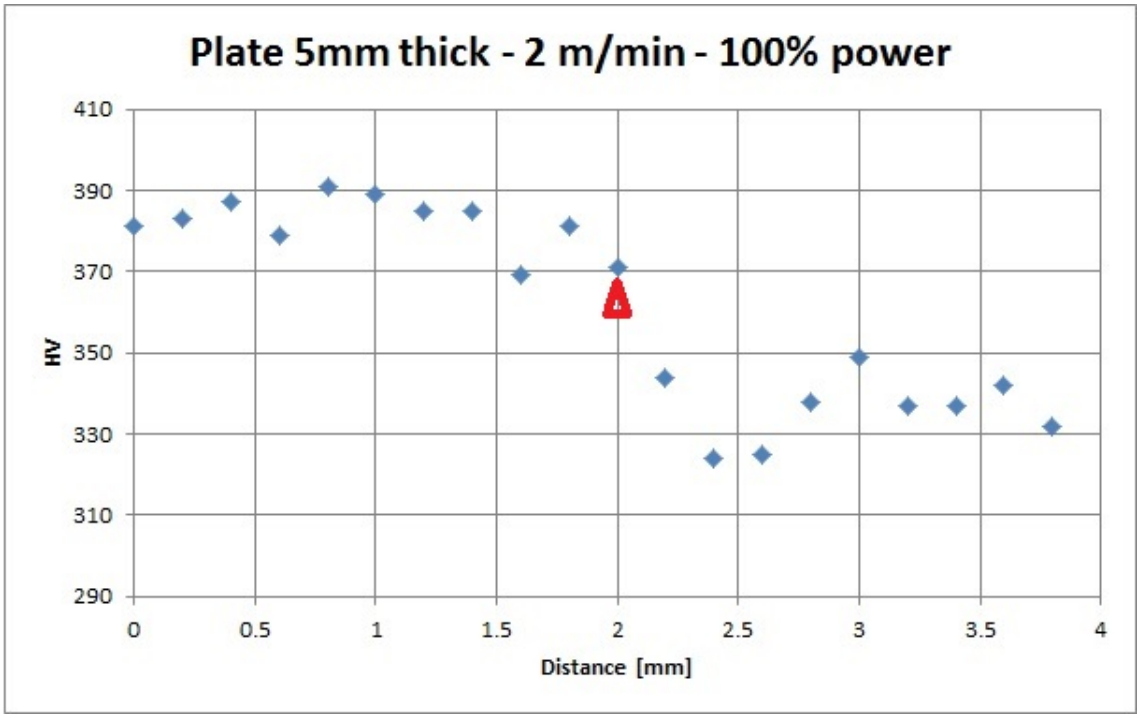

b)

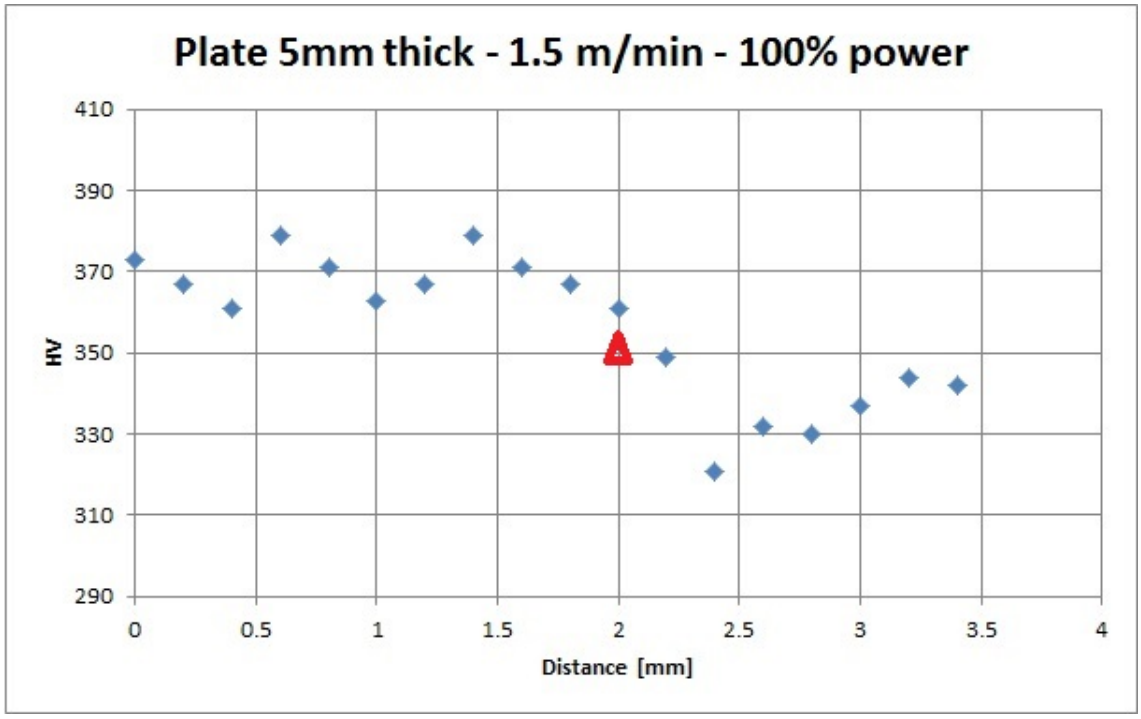

Figure 3.54.: Micro hardness measurements for the Ti-6Al-4V plate 5mm thick with initial equiaxed microstructure. a) weld carried out at 2 m/min 100% power; b) weld carried out at 1.5 m/min at 100% power. The triangle makes reference to the indent in the HAZ/bulk material interface, represented by a triangle also in figure 3.52. Distance 0 corresponds to the "0" point in figure 3.52

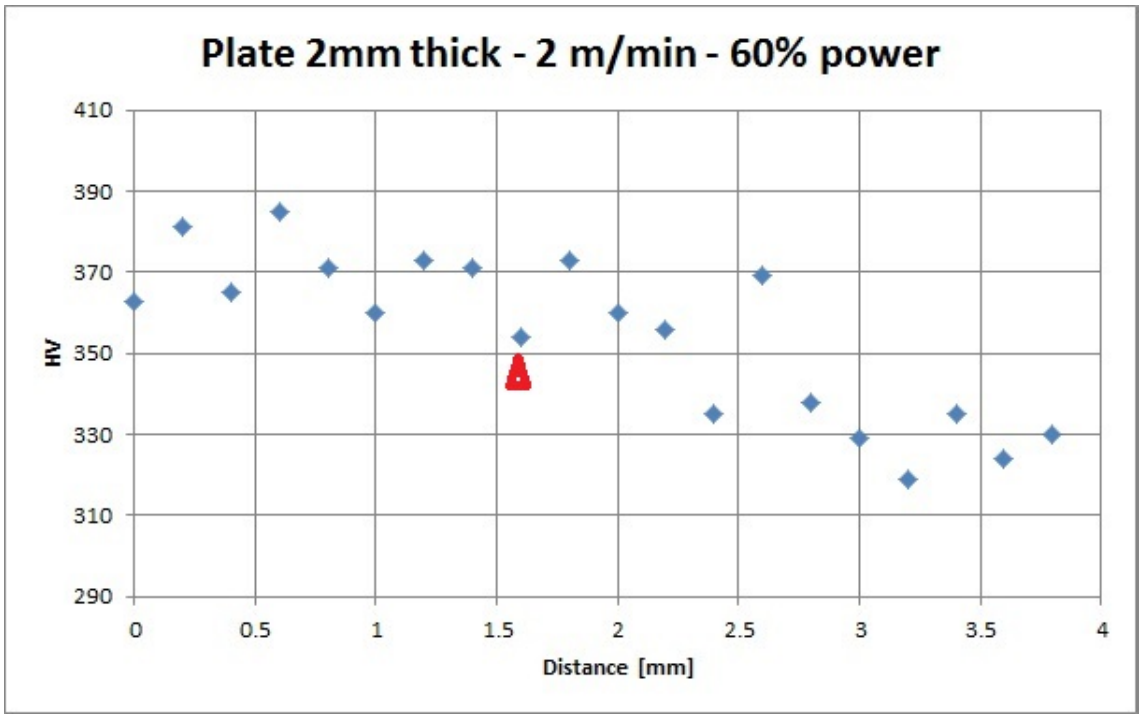

Figure 3.55.: Micro hardness measurements of the Ti-6Al-4V plate 2 mm thick with initial equiaxed microstructure. 2 m/min 60% power. The triangle makes reference to the indent in the HAZ/bulk material interface, represented by a triangle also in figure 3.53. Distance 0 corresponds to the "0" point in figure 3.53

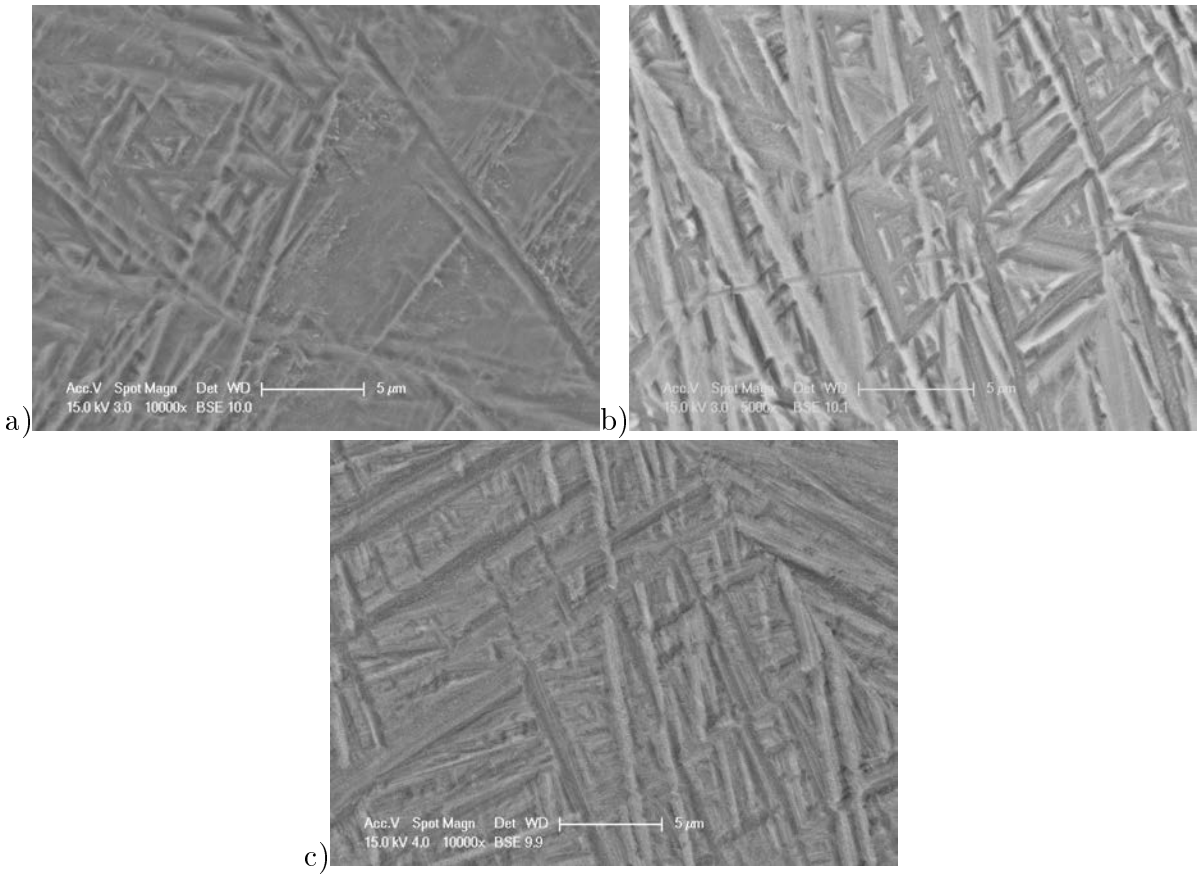

Figure 3.56.: High magnification BEI micrographs of the microstructure developed in the fusion zone of the Ti-6Al-4V plates with equiaxed microstructure welded. a) 5 mm thick plate welded at 2 m/min, 100% power; b) 5 mm thick plate welded at 1.5 m/min, 100% power; c) 2 mm thick plate welded at 2 m/min 60% power

figure 3.52 and 3.53 are reported (micrographs in figure 3.57, 3.58 and 3.59) and analysed.

Looking at the micrographs it is possible to observe the original beta particles (e.g. white small spots in figure 3.57-f) dissolving gradually going toward the fusion zone and being still visible at points where already new beta grains are nucleated and very close to the liquid interface (e.g. figure 3.57-b) . This shows how Vanadium, which segregates to the beta precipitates diffuses through the matrix slower than Aluminium and, non coincidentally, this element is considered the controlling diffusing element in the numerical model. Also, some residual local segregation related to the parent equiaxed alpha precipitates are still noticeable where martensite is already present (e.g. figure 3.57-c), indicating that even if the overall tendency of the crystallographic structure of the material is to switch from HCP to BCC, the diffusing elements are limited in their movement speed by the diffusion process.

Comparing figures 3.58 c) and a) it is possible to observe that going progressively toward the centre of the weld pool, the beta grains become larger presumably as the maximum temperature reached during the welding is higher (section 3.5.1). The length of the transformed beta needles also increases as the beta grains grow.

In the graphs of figure 3.60, 3.61 and 3.62 the thickness of the lamellae and the radius of the spherical alpha precipitates are reported as a function of the distance from the centre of the weld pool. Going progressively toward the centre of the weld pool, the original equiaxed microstructure evolves progressively, giving rise to the lamellar microstructure originating from the beta phase. The thickness of the lamellae nucleated increases toward the centre of the weld pool (e.g. in figure 3.60 from 1.8 to 0 mm), probably due to the increasing size of the beta grains where they nucleate, associated with the higher temperature at which the material is subjected.

As observed previously, the lamellae thickness of the 5 mm thick plate welded at 1.5 m/min is similar to the lamellae thickness developed in the 2 mm plate welded at 2.0 m/min, this resulted, as shown in figure 3.54-b and 3.55, in a similar hardness measurement to that in the fusion zone.

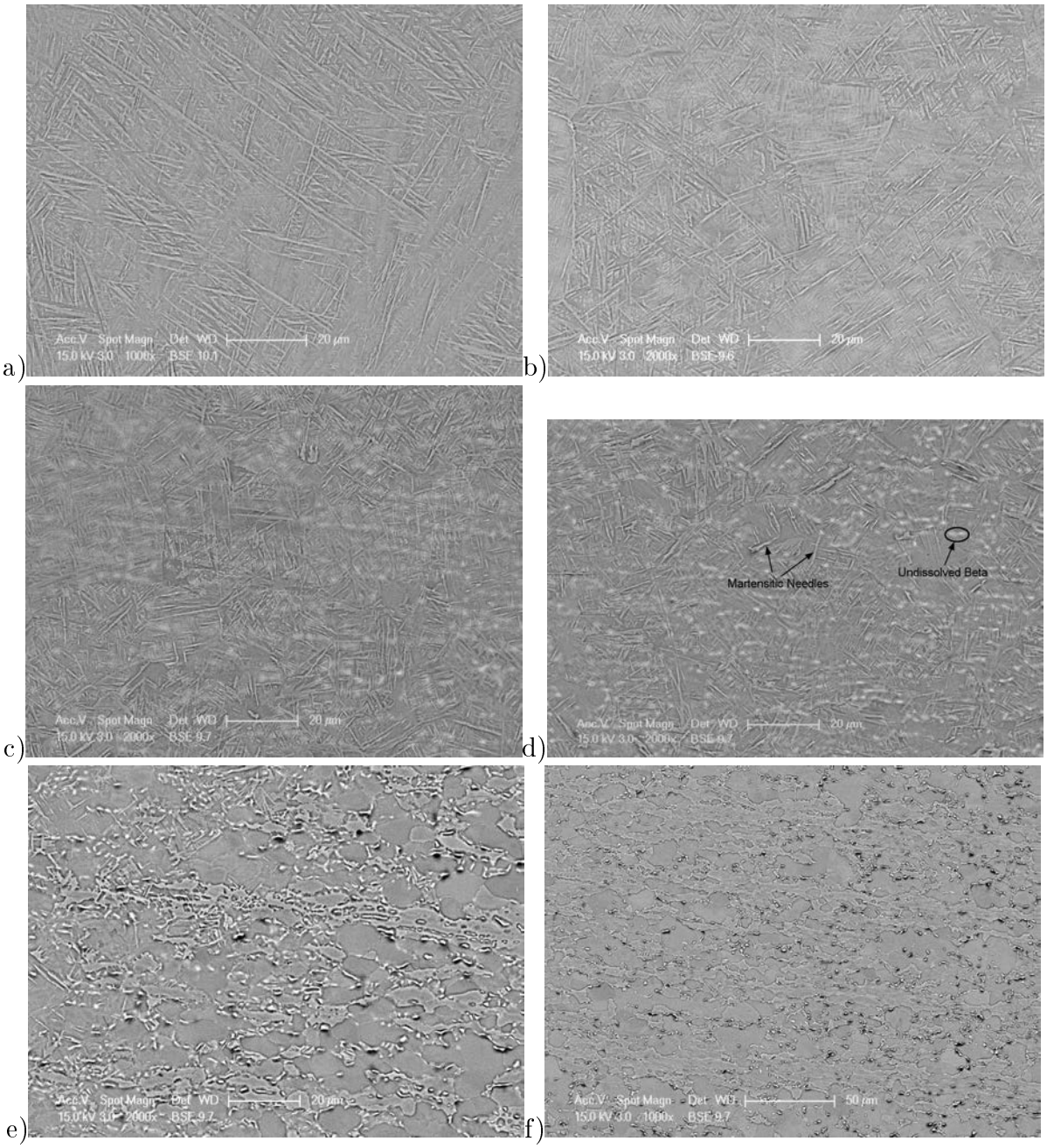

Figure 3.57.: BEI micrographs obtained observing the Ti-6Al-4V plate 5mm thick with initial equiaxed microstructure welded at 2 m/min 100% power. Making reference to the row of indentations of figure 3.52-a and considering as 1^{st} point the first indent starting from the centre of the weld pool: a) 1^{st} point, b) 6^{th} point, c) 8^{th} point, d) 9^{th} point, e) 11^{th} point, f) 13^{th} point

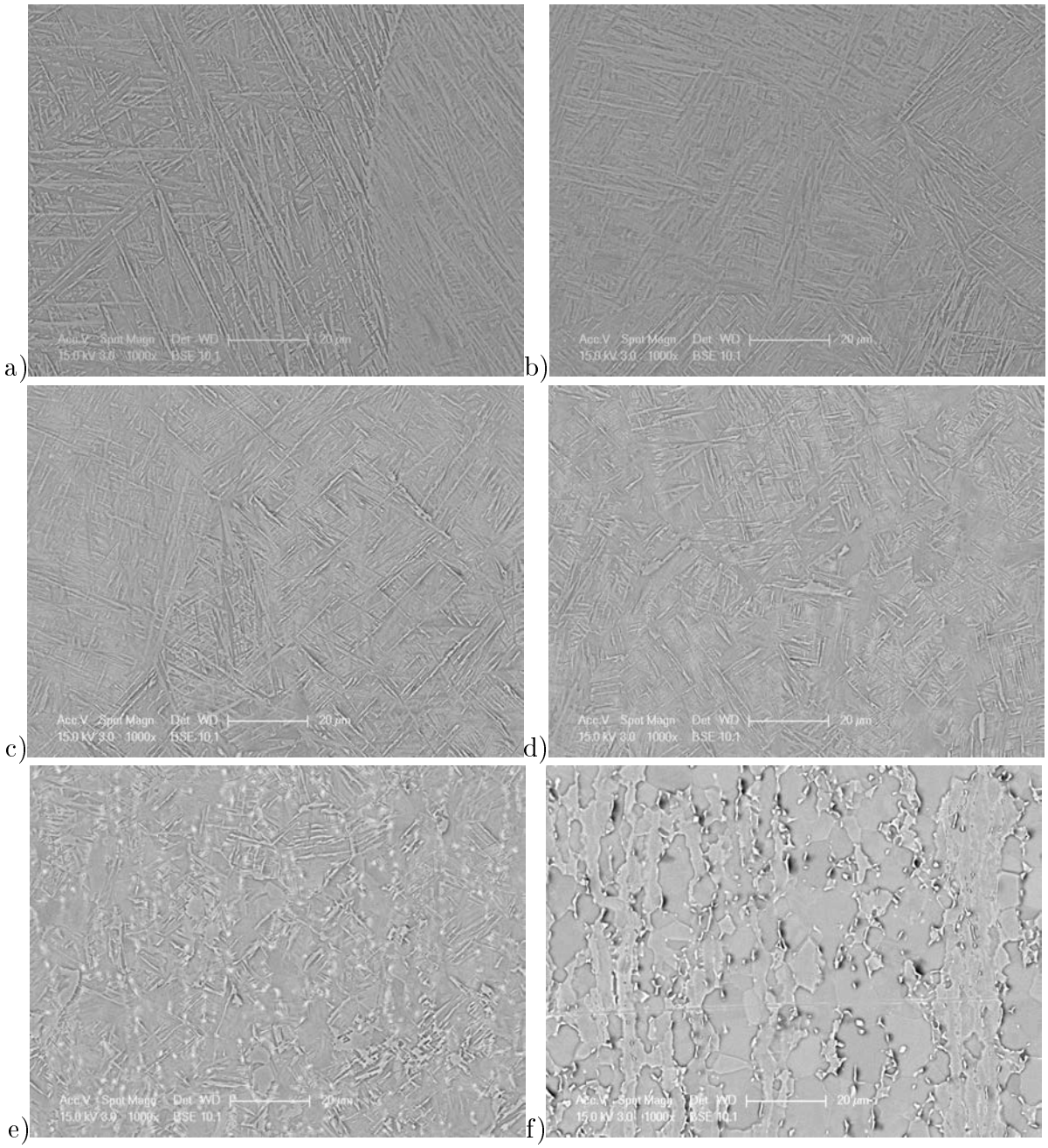

Figure 3.58.: BEI micrographs obtained observing the Ti-6Al-4V plate 5mm thick with initial equiaxed microstructure welded at 1.5 m/min 100% power. Making reference to the row of indentations of figure 3.52-b and considering as 1^{st} point the first indent starting from the centre of the weld pool: a) 1^{st} point, b) 6^{th} point, c) 8^{th} point, d) 10^{th} point, e) 12^{th} point, f) 15^{th} point

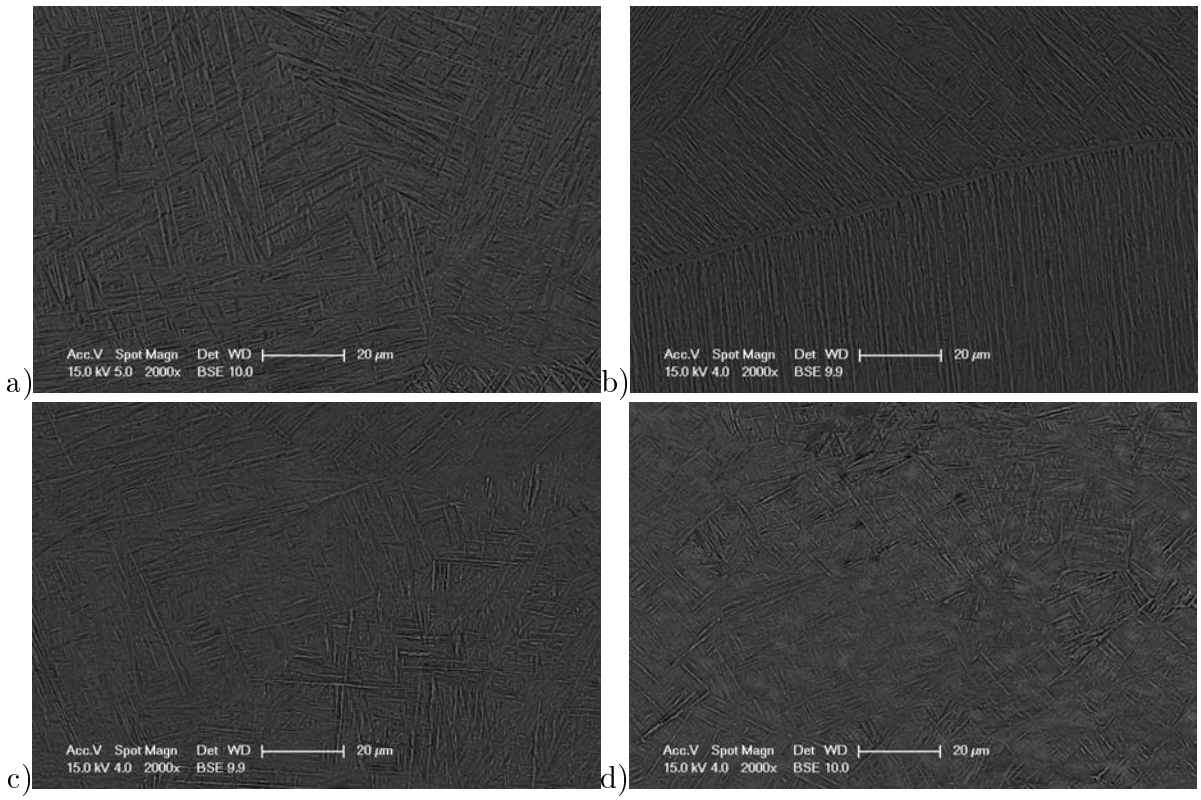

Figure 3.59.: BEI micrographs obtained observing the Ti-6Al-4V plate 2mm thick with initial equiaxed microstructure welded at 2.0 m/min 60% power. Making reference to the row of indentations of figure 3.53 and considering as 1^{st} point the first indent starting from the centre of the weld pool: a) 1^{st} point 1, b) 3^{rd} point, c) 5^{th} point, d) 7^{th} point

a)

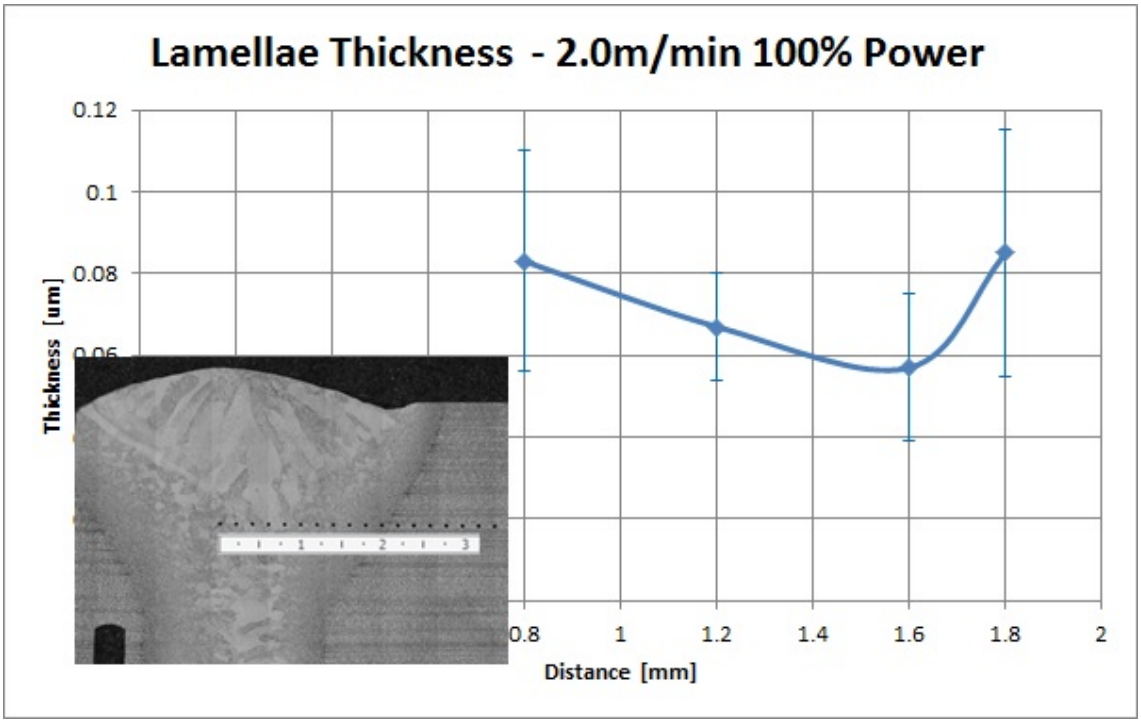

b)

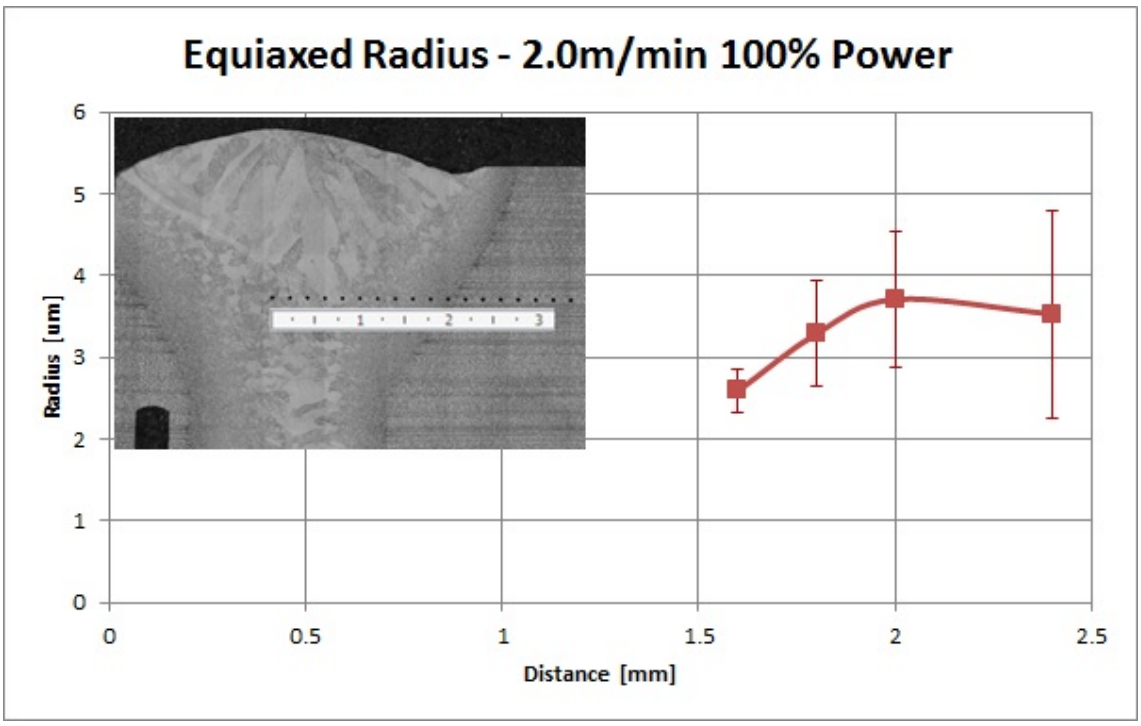

Figure 3.60.: Graphs showing a) lamellae thickness and b) spherical alpha radius as a function of the distance in the Ti-6Al-4V plate 5mm thick with initial equiaxed microstructure welded at 2.0 m/min and 100% power. The distance makes reference to the ruler reported in the micrographs

a)

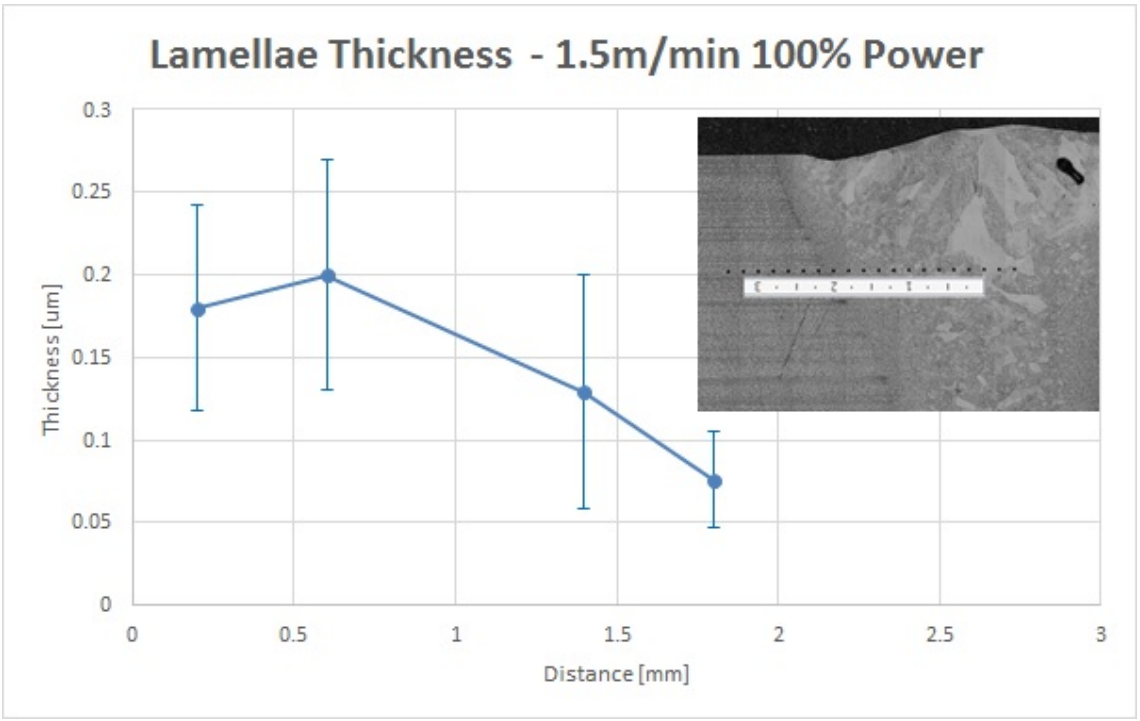

b)

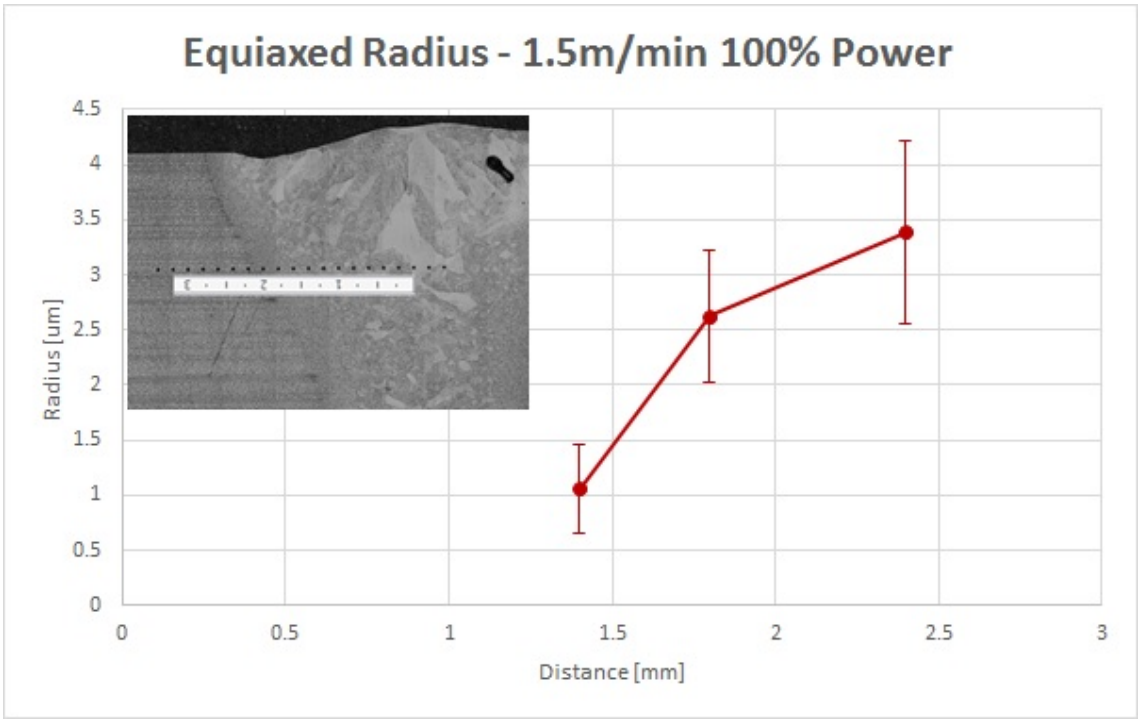

Figure 3.61.: Graphs showing a) lamellae thickness and b) spherical alpha radius as a function of the distance in the Ti-6Al-4V plate 5mm thick with initial equiaxed microstructure welded at 1.5 m/min and 100% power. The distance makes reference to the ruler reported in the pictures

a)

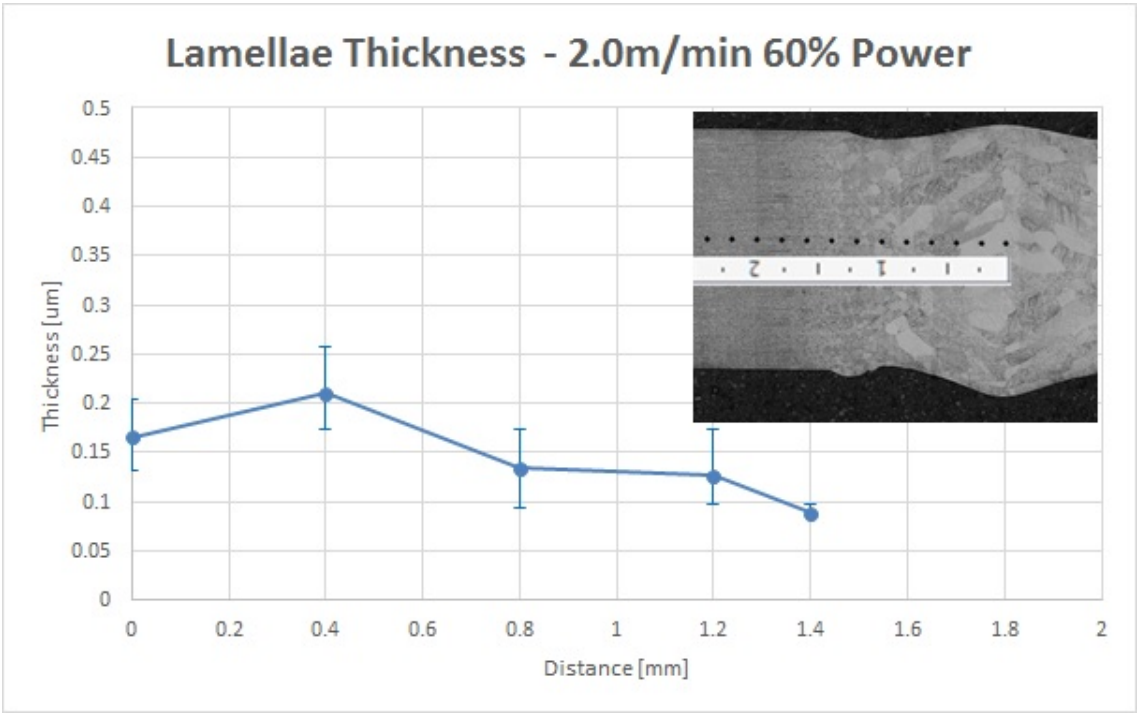

b)

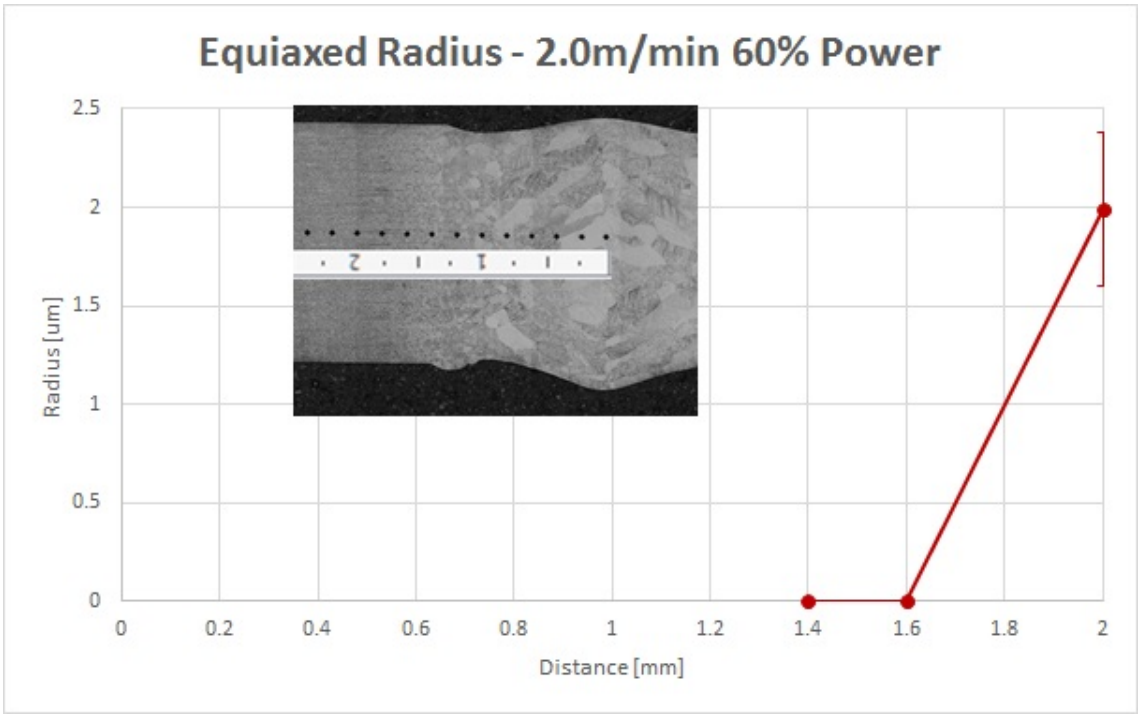

Figure 3.62.: Graphs showing a) lamellae thickness and b) spherical alpha radius as a function of the distance in the Ti-6Al-4V plate 2mm thick with initial equiaxed microstructure welded at 2.0 m/min and 60% power. The distance makes reference to the ruler reported in the pictures

3.5.2.2 Plates with lamellar microstructure

In figure 3.63 the montages corresponding with the welded zones of the plates tested with an initial lamellar microstructure are shown.

The two tests were different only in the plates thickness, since the operative parameters were kept the same: 2.0 m/min as welding speed and 70% as power.

The resulting weld pool shapes were very similar with a classical hourglass shape.

The observations of the paragraph 3.5.2.1 in relation to the beta columnar morphology observed in the centre of pictures are still valid for these cases.

The hardness measurements for the samples shown in figure 3.63 are reported in figure 3.64. The starting point at which the measurements begin is again at the centre and is shown as "0", then go progressively at steps of 0.2 mm farther from the weld line.

As already observed previously, the material is harder in the fusion zone than the bulk, because of the martensitic microstructure developed. Comparing with the results obtained in section 3.5.2.2, the hardness values measured in the weld pool are very similar ($\sim$ 370 HV), whilst in the bulk material there is a difference, with the plates with equiaxed microstructure having a higher hardness (330-340 HV) than the material with the lamellar microstructure (300-310 HV). From these data the chemical composition can be supposed to have a relatively low impact on the hardness, as where the material melts, releasing the residual stresses induced by the manufacturing processes, no relevant variation of the hardness has been measured in all the plates tested even though the chemical compositions of the plates in section 3.5.2.1 and 3.5.2.2 are different. In the bulk material instead, appreciable differences in hardness measurement have been encountered, suggesting that the different microstructures give rise to the variation in hardness, together with, probably, a different mechanical response of the two material microstructural morphologies tested.

The two plates shown in figure 3.64 are characterized by approximatively the same hardness, suggesting their difference in thickness is within the range that does not cause a significant variation in the gradient of temperatures in the specimens during the welding process, or develop substantially different microstructures with a different mechanical

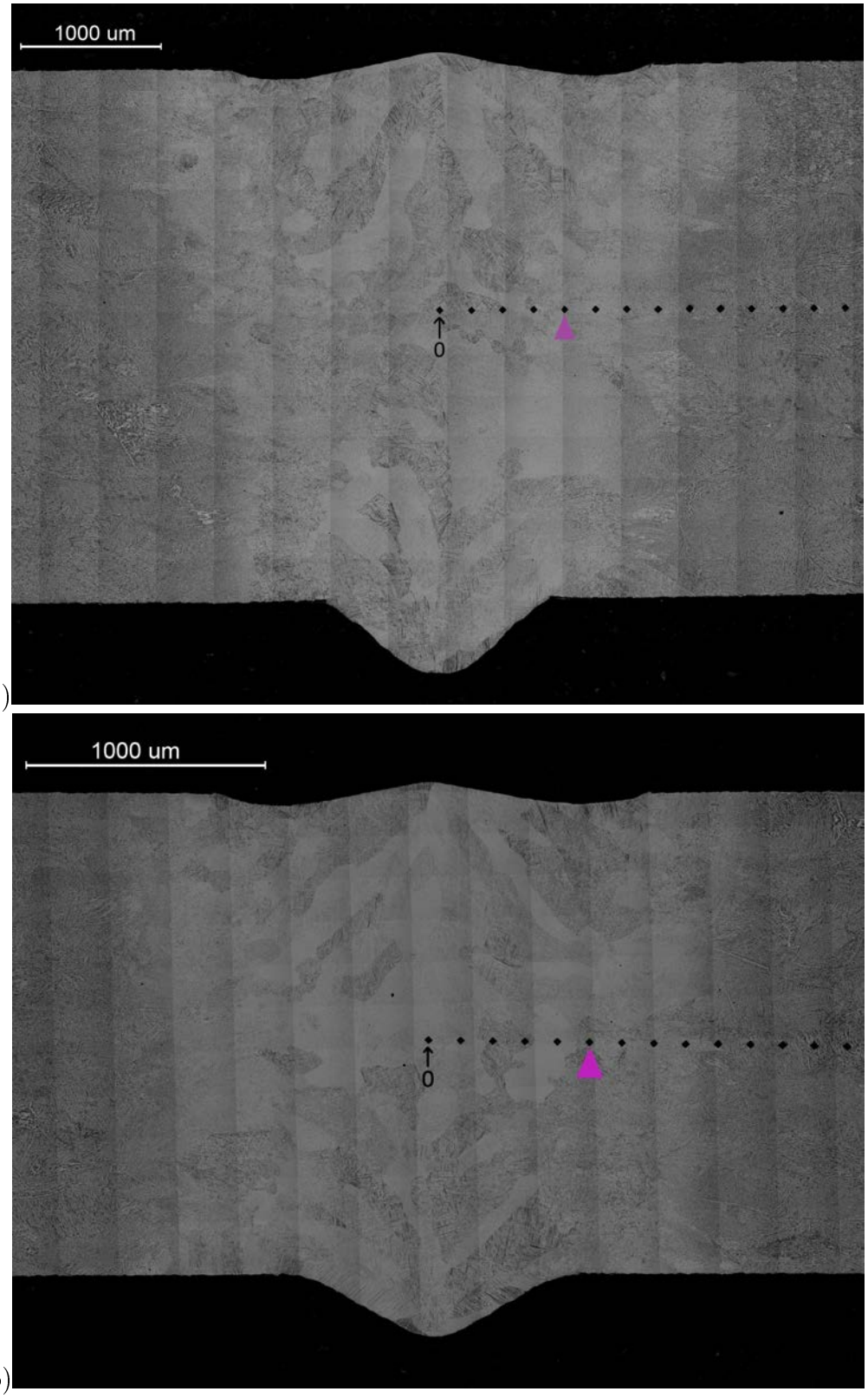

Figure 3.63.: Montages of the Ti-6Al-4V plates 3.75 mm (a) and 3.06 mm (b) thick with initial lamellar microstructure welded at 2.0 m/min 70% power. The specimens have been characterized by microhardness. The "0" point shows the first hardness measurement referenced in figure 3.64 and corresponds to the weld centreline

response. As it is shown in the high magnification BEI images reported in figure 3.65, the microstructure is very similar at the centre of the fusion zone.

The hardness similarity of the parent material in the two plates, where the weld heat source did not affect the material, is explained by the fact that the samples were machined from the same plate, thus have the same initial microstructure.

BEI images of the microstructure observed after welding, for some of the points shown in figure 3.63, are reported in figure 3.66 and figure 3.67 and hereinafter analysed.

Starting from the furthest locations from the application of the heat source, it is possible to observe the gradual dissolution of the original lamellar microstructure, with the white beta boundaries thickening and the dark alpha areas thinning. In locations where the temperature reaches the beta transus and above on subsequent cooling, new lamellae start to nucleate and grow (figure 3.66-e and 3.67-f) and martensitic needles form (figure 3.66-d and figure 3.67-d).

As already observed in the previous section, the speed of the welding process imposes insufficient time to allow homogenization of the different chemical species in the constituent alpha and beta phases and, in locations where the temperature should be such as to have only beta phase, it is still possible to observe local segregations, as seen in the whiter and darker areas in figure 3.66-c and 3.67-c, representing positions very close to the fusion zone of the weld pool.

In figures 3.68 and 3.70 the alpha lamellae thicknesses measured for both plates are reported, whilst in figure 3.69 and 3.71 the martensitic needles thickness is shown.

As expected, the lamellae thickness of the original microstructure tends to become smaller moving toward the higher temperatures present closer to the centre of the weld pool.

The nucleated lamellae thickness seems to be susceptible to the thickness of the plate, as the thicker plate returns thicker nucleated lamellae, due probably to the slight slower heat loss through the specimens (figure 3.50 and 3.51).

The needles thickness seem to be around the same values for both plates as probably

a)

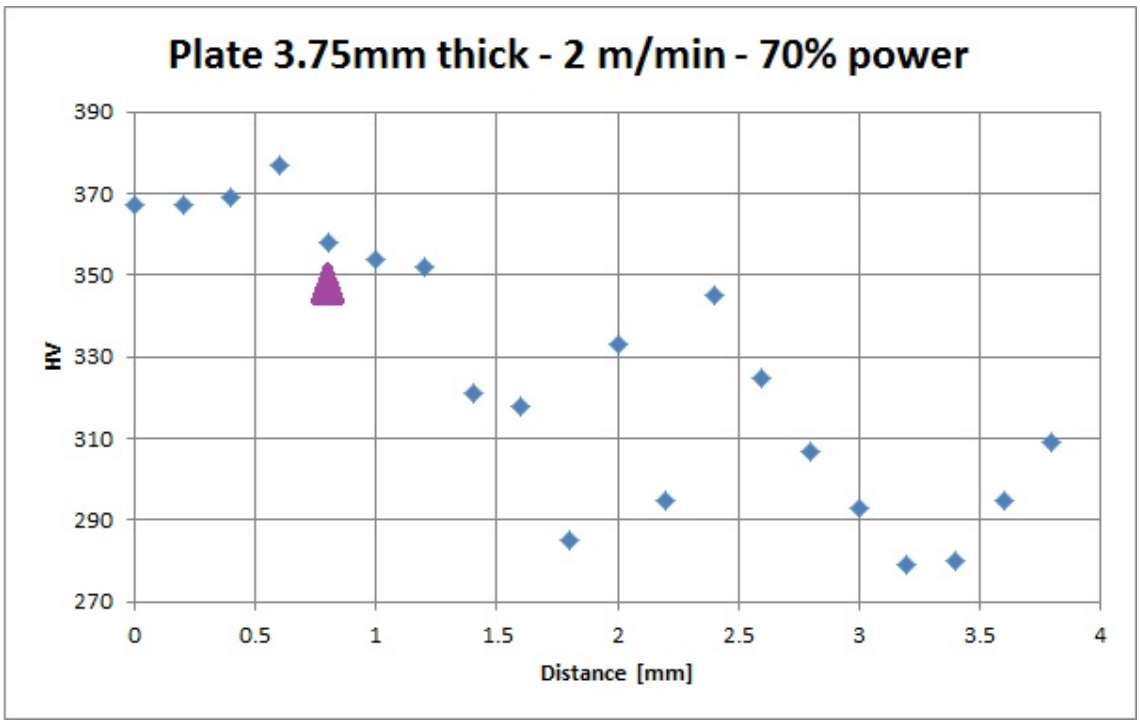

b)

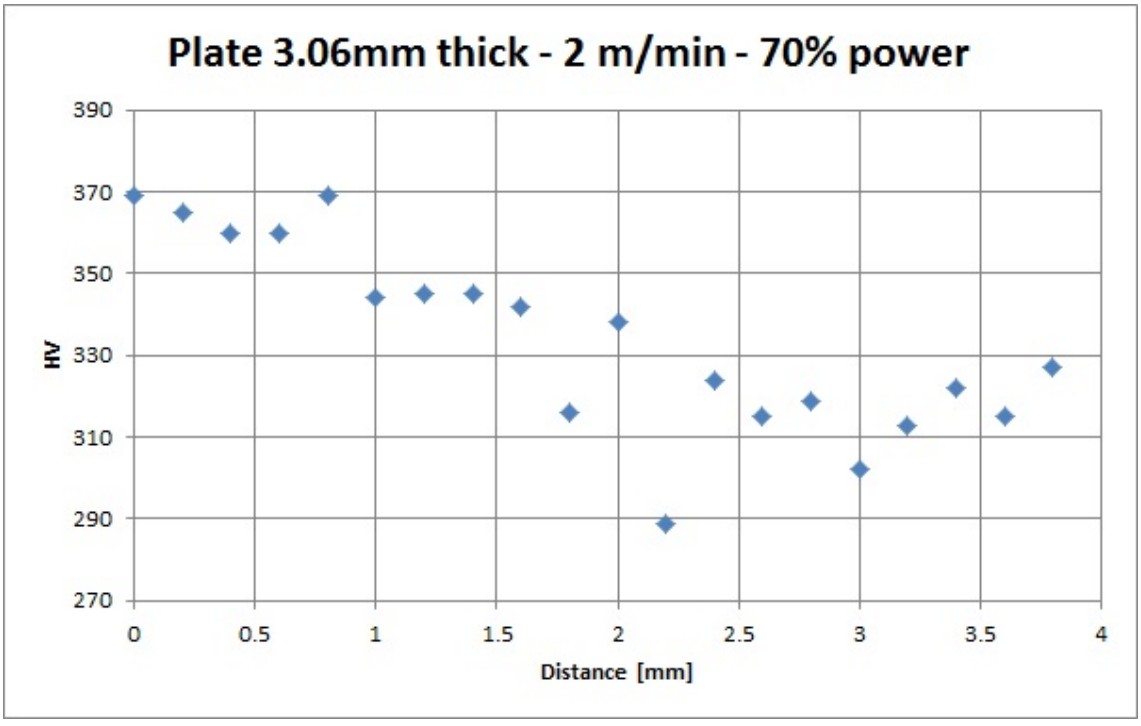

Figure 3.64.: Micro hardness measurements graphs of the Ti-6Al-4V plate 3.75 mm (a) and 3.06 mm (b) thick. In both cases the welding operative parameters were set at 2 m/min and 70% power. The triangle makes reference to the indent in the HAZ/bulk material interface, represented by a triangle also in pictures 3.63

a) 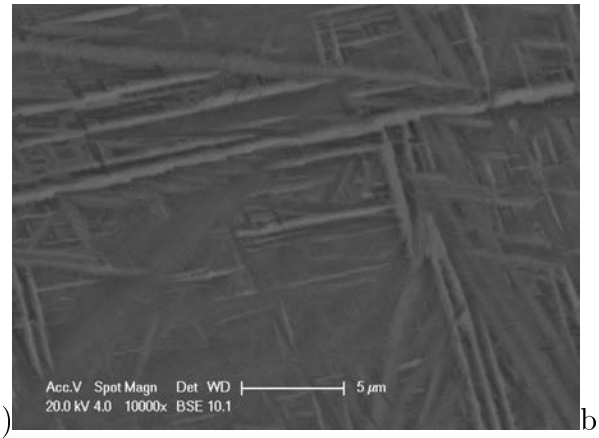

b) 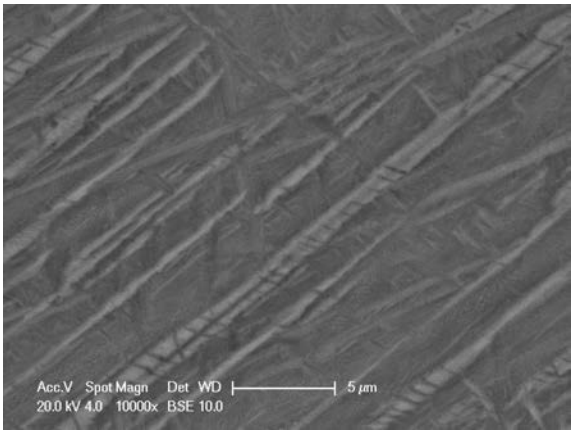

Figure 3.65.: High magnification BEI micrographs of the microstructure developed in the fusion zone of the Ti-6Al-4V plates with initial lamellar microstructure welded. a) 3.75 mm thick plate welded at 2 m/min, 70% power; b) 3.06 mm thick plate welded at 2 m/min, 70% power

driven by the same cooling rate.

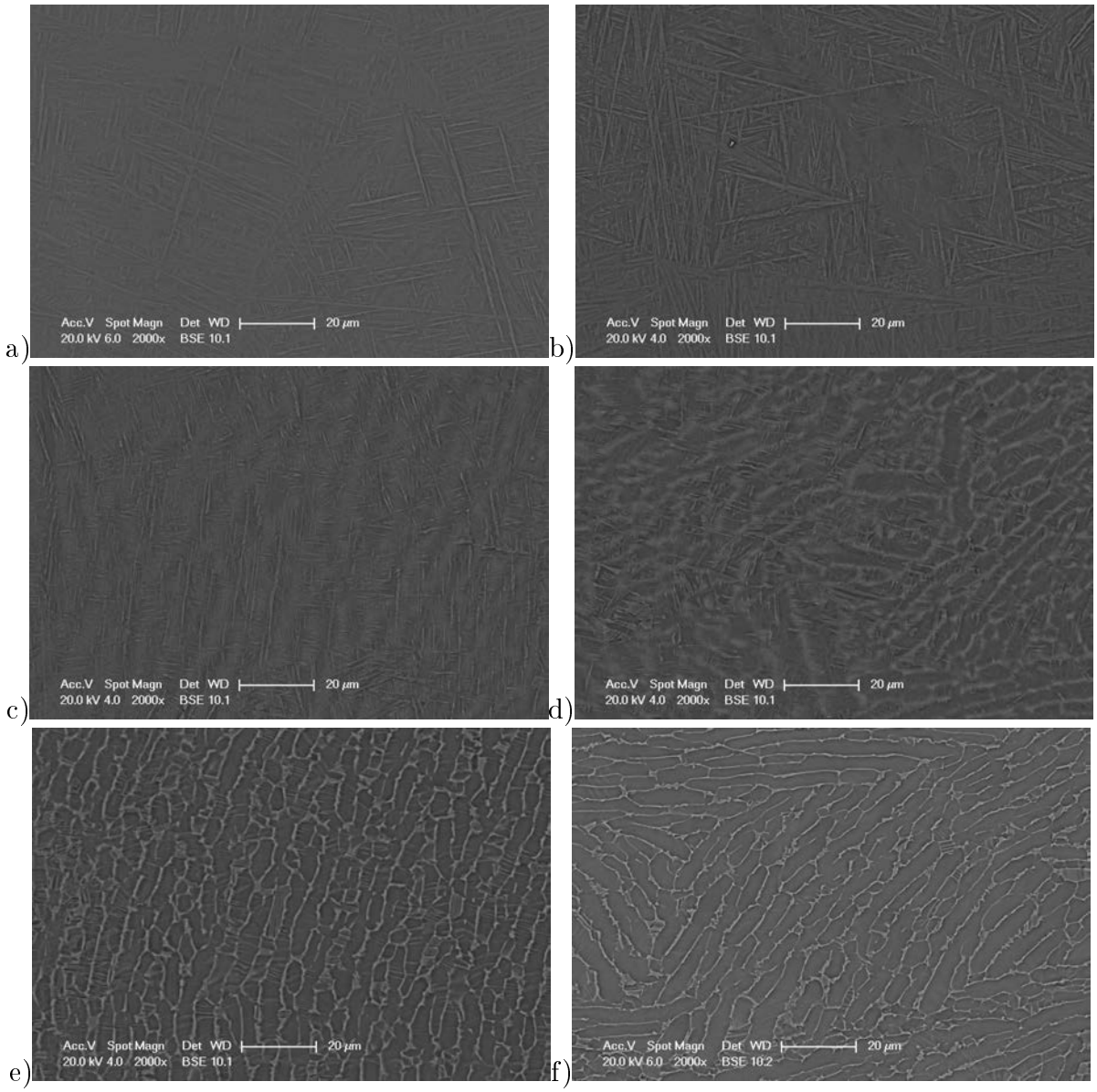

Figure 3.66.: BEI micrographs of the Ti-6Al-4V plate 3.75mm thick with initial lamellar microstructure welded at 2 m/min 70% power. Making reference to the row of indentations of figure 3.63-a and considering as 1^{st} point the first indent starting from the centre of the weld pool: a) 1^{st} point, b) 3^{rd} point, c) 4^{th} point, d) 6^{th} point, e) 8^{th} point, f) 10^{th} point

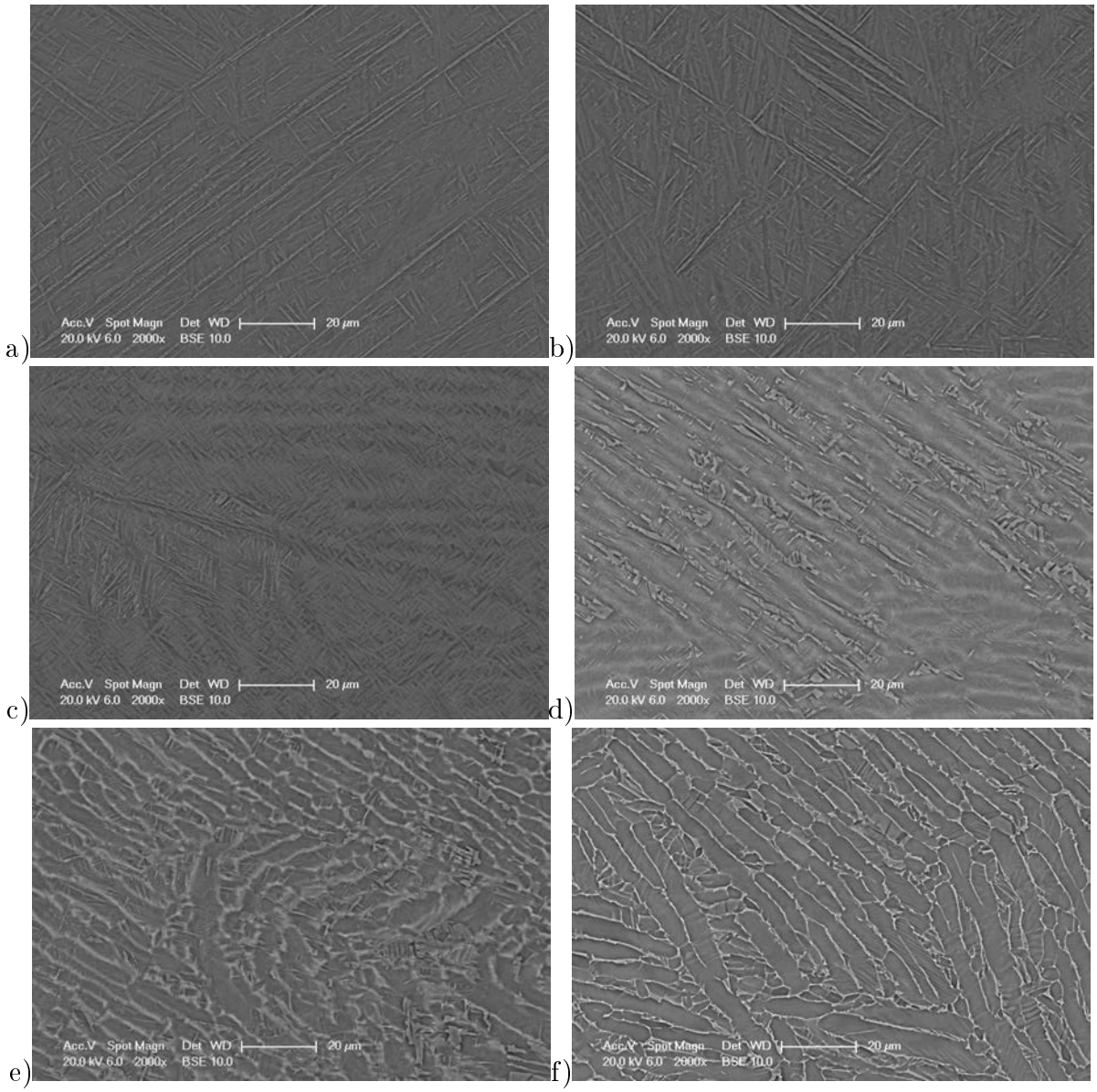

Figure 3.67.: BEI micrographs of the Ti-6Al-4V plate 3.06mm thick with initial lamellar microstructure welded at 2 m/min 70% power. Making reference to the row of indentations of figure 3.63-b and considering as 1^{st} point the first indent starting from the centre of the weld pool: a) 1^{st} point, b) 3^{rd} point, c) 4^{th} point, d) 6^{th} point, e) 8^{th} point, f) 11^{th} point

a)

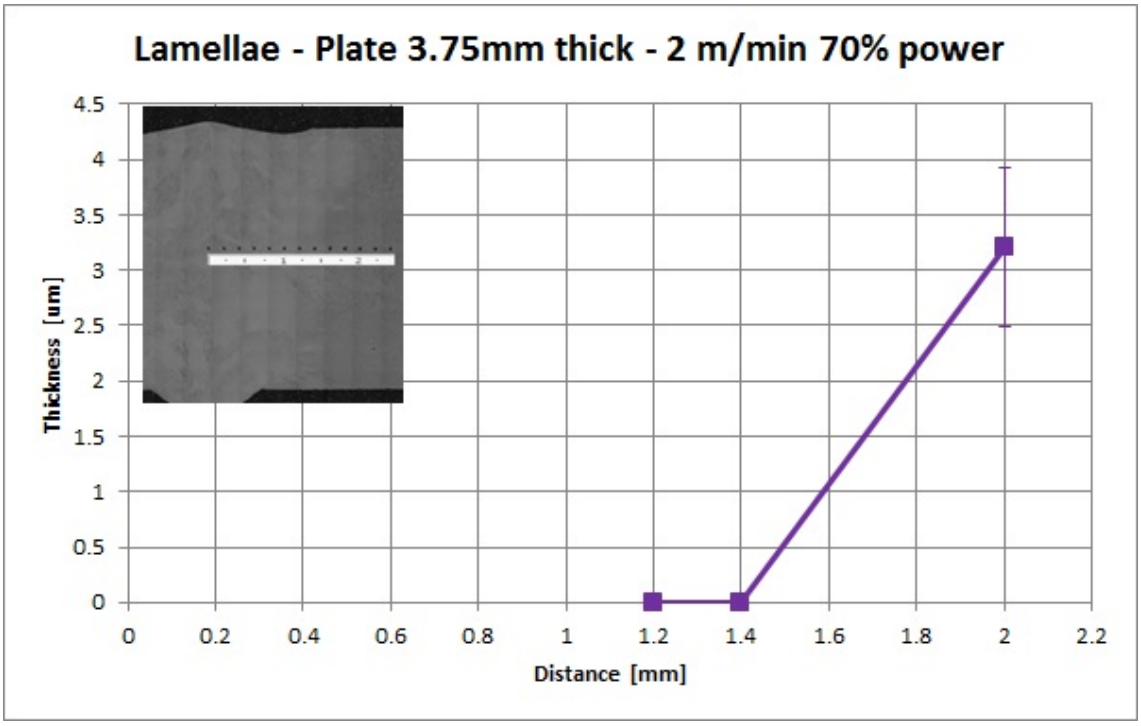

b)

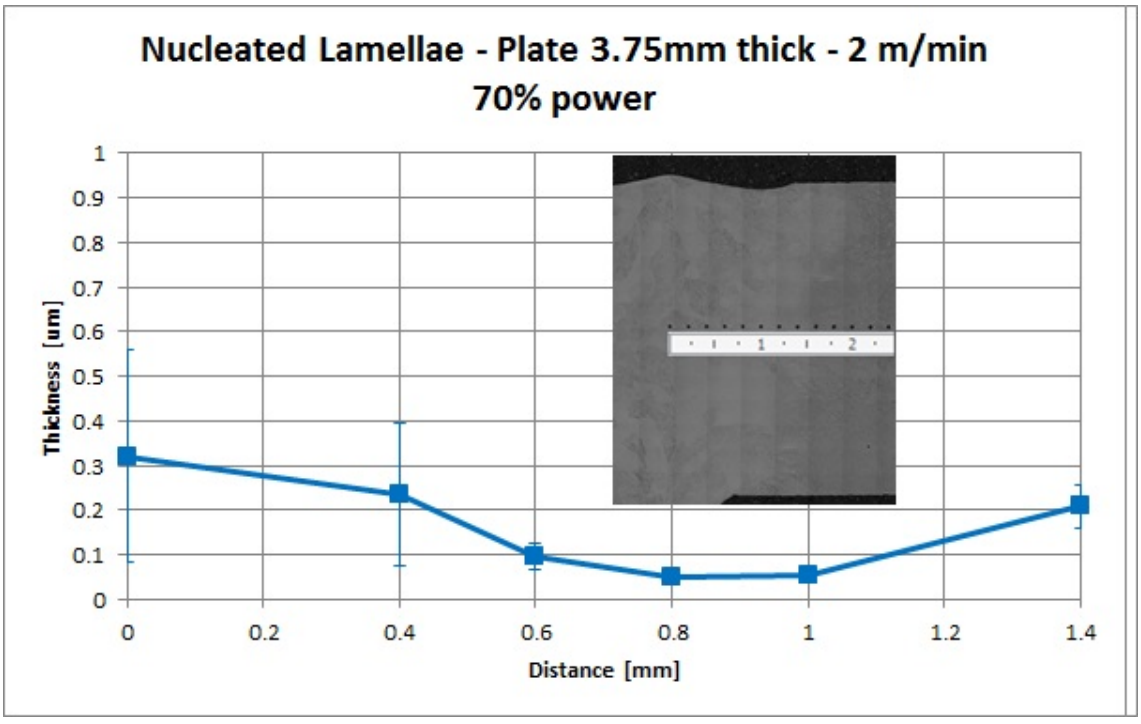

Figure 3.68.: Graphs showing a) the lamellae thickness of the original microstructure and b) the thickness of new lamellae nucleated during welding of the Ti-6Al-4V plate with initial lamellar microstructure 3.75 mm thick welded at 2.0 m/min and 70% power. The distance makes reference to the ruler reported in the pictures

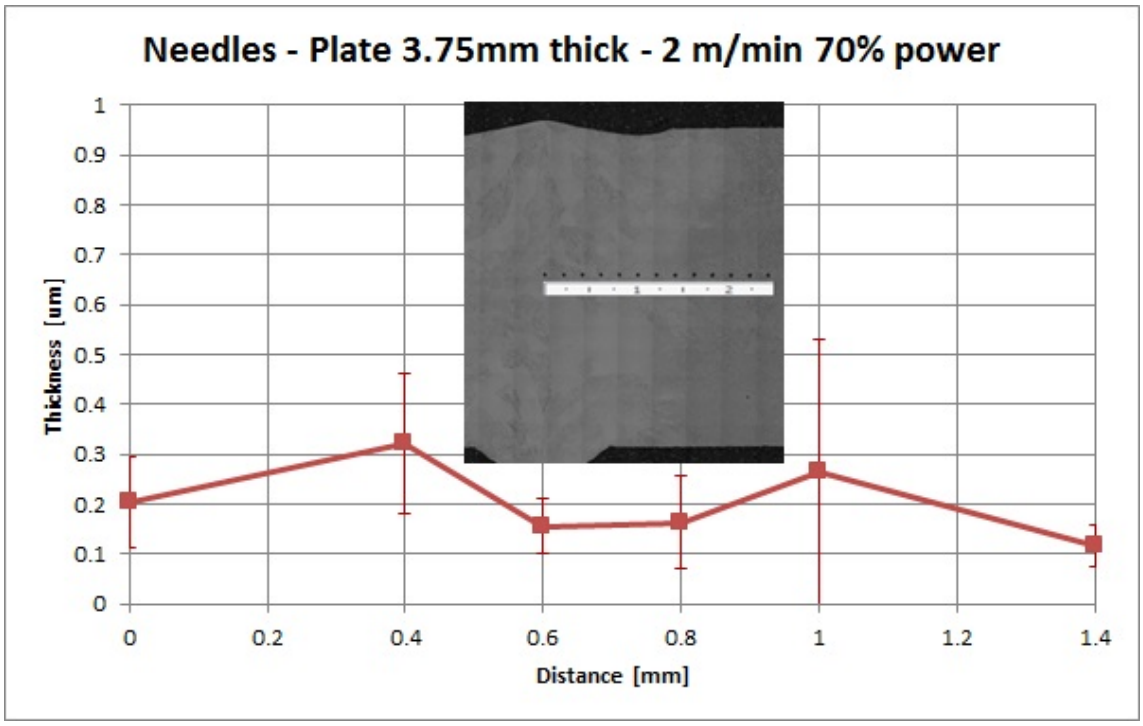

Figure 3.69.: Graph showing the needles thickness of the martensitic microstructure formed during welding of the Ti-6Al-4V plate with initial lamellar microstructure 3.75 mm thick welded at 2.0 m/min and 70% power. The distance makes reference to the ruler reported in the picture

a)

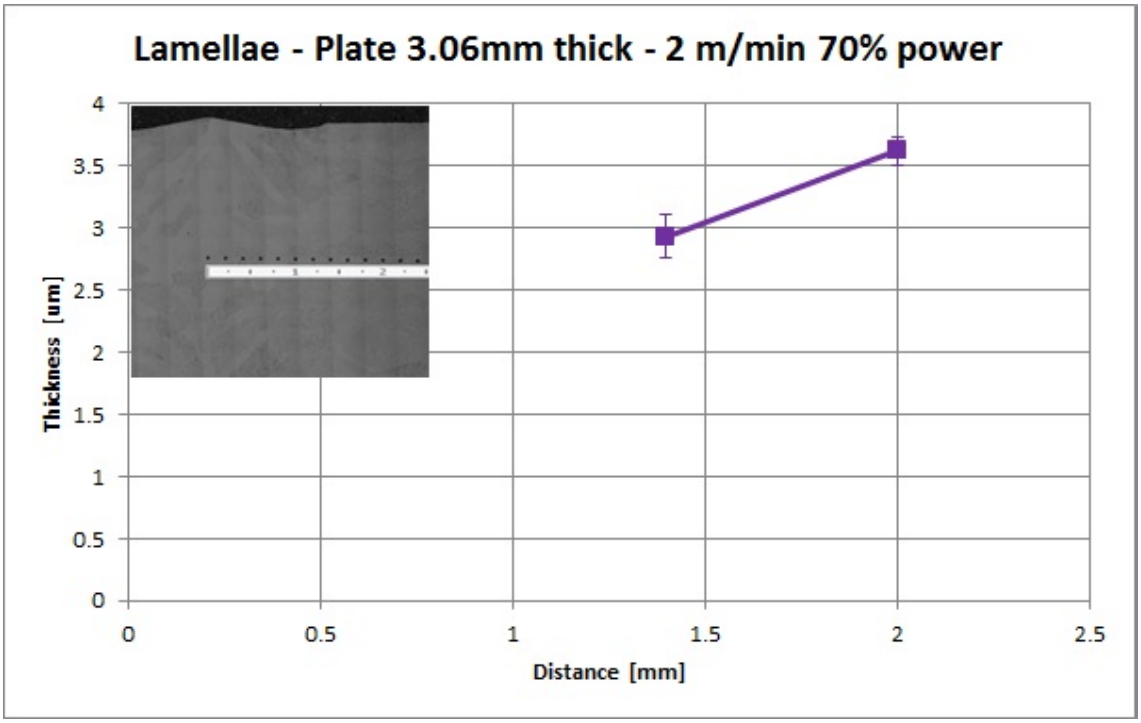

b)

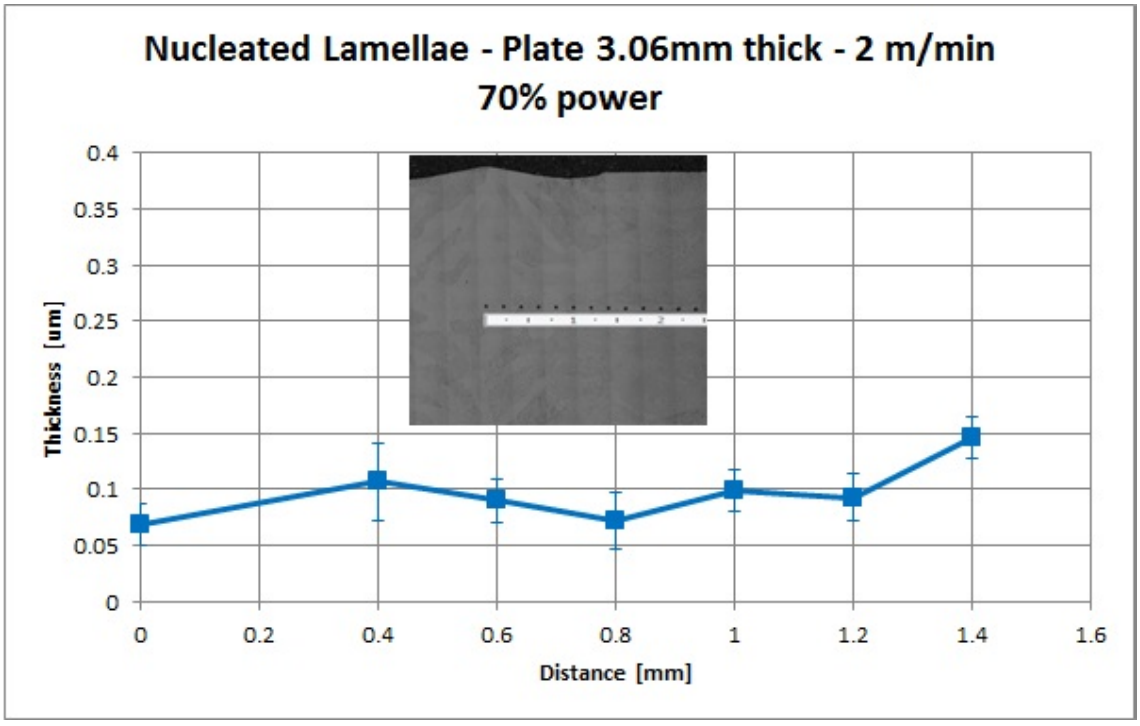

Figure 3.70.: Graphs showing a) the lamellae thickness of the original microstructure and b) the thickness of new lamellae nucleated during welding of the Ti-6Al-4V plate with initial lamellar microstructure 3.06 mm thick welded at 2.0 m/min and 70% power. The distance makes reference to the ruler reported in the pictures

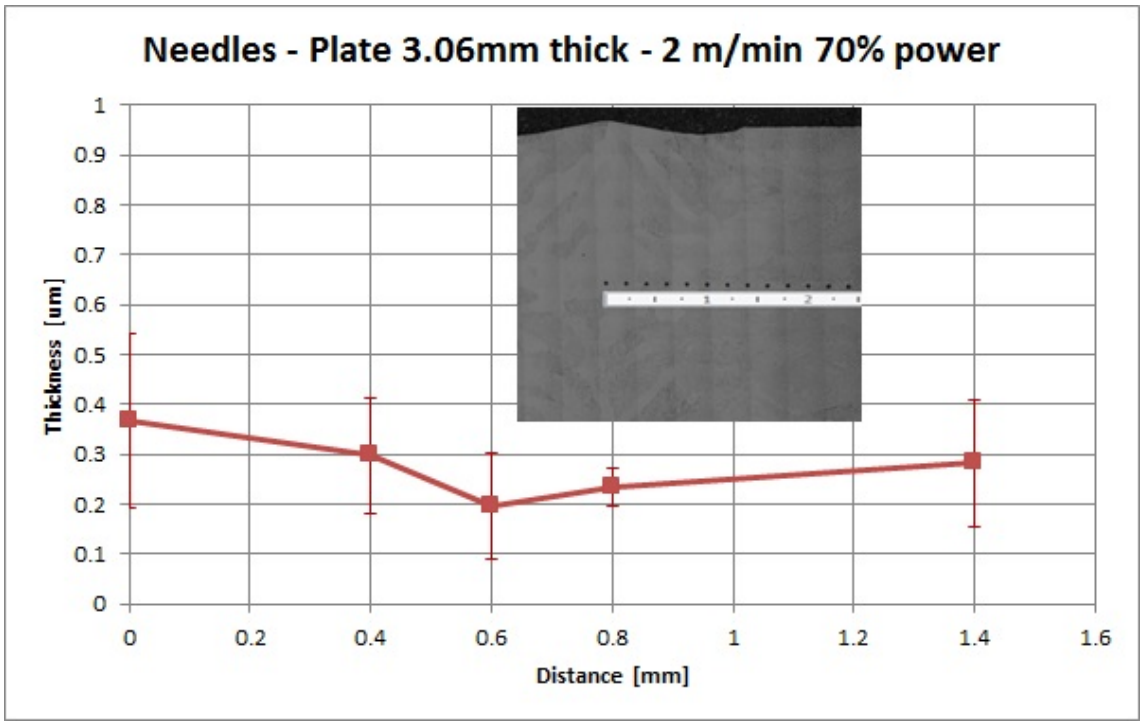

Figure 3.71.: Graph showing the needle thickness of the martensitic microstructure formed during welding of the Ti-6Al-4V plate with initial lamellar microstructure 3.06 mm thick welded at 2.0 m/min and 70% power. The distance makes reference to the ruler reported in the picture

3.5.3 Chemical analysis

Besides being microstructurally investigated at the locations adjacent to the micro hardness indents, the samples were also been microanalysed by X-EDS and the wt% composition trends of Aluminium and Vanadium plotted as a function of the distance (graphs in figure 3.72, 3.73 and 3.74).

The main observation from these results is the relatively small variation in composition of the alpha phase with respect to the beta phase, in particular for Vanadium. This could be indicative both of a slow diffusivity within the alpha precipitates and of a high diffusivity in the beta matrix during heat treatment, in particular in this case, for welding. Based on these observations, the numerical model will make some simplifying assumptions for the description of the diffusing process.

3.5.3.1 Plates with equiaxed microstructure

In graphs of figure 3.72 and figure 3.73 the chemical composition in term of weight percent of Aluminium and Vanadium is reported as a function of the distance from the weld line, for the plates with initial equiaxed microstructure. In both cases, as already mentioned, it is noticeable the high variation in Vanadium content of the beta phase. Due to the high speed of the welding process, the chemical composition along the material did not have time to homogenise and the chemical composition of the phases present in the parent microstructure was still noticeable after the formation of new morphological features (see micrographs in figure 3.57-d, 3.58-d, 3.59-d, in particular white segregation related to the original beta phase distribution), as alpha lamellae or martensitic needles. The appearance of this phenomenon is identified in the charts by the line reporting "local segregation".

3.5.3.2 Plates with lamellar microstructure

In figure 3.74 the chemical compositions in term of weight percent of Aluminium and Vanadium are reported as a function of the distance from the weld line, for the plates with initial lamellar microstructure. Also in these cases it is noticeable the high variation

a)

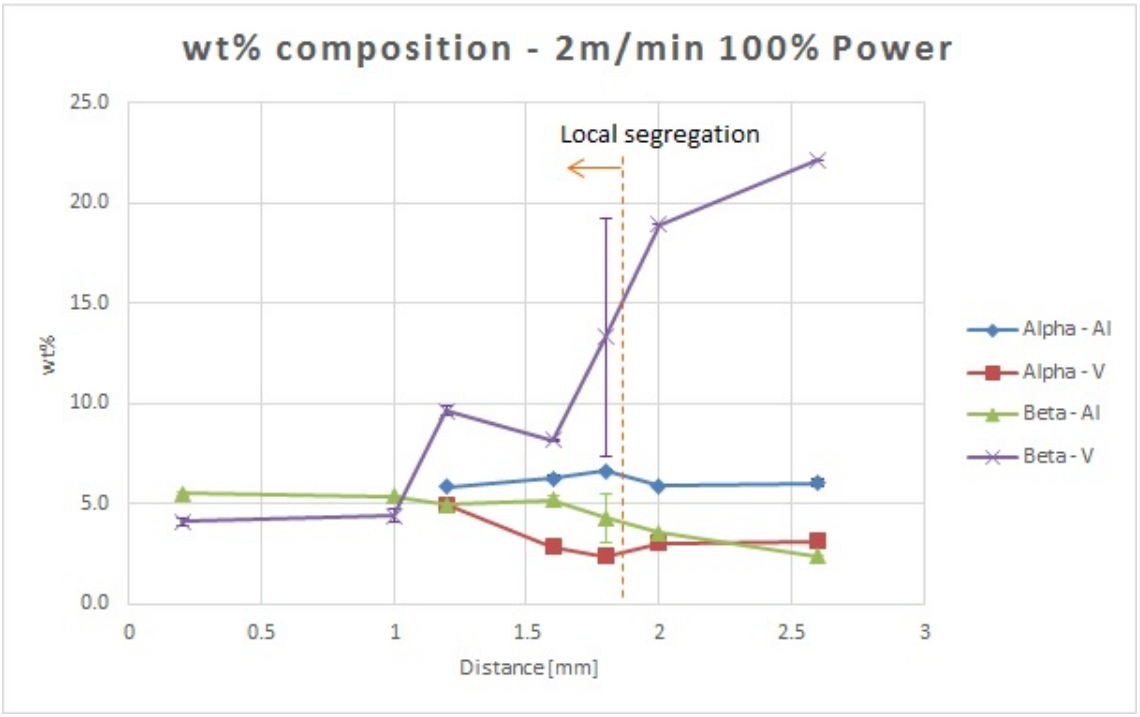

b)

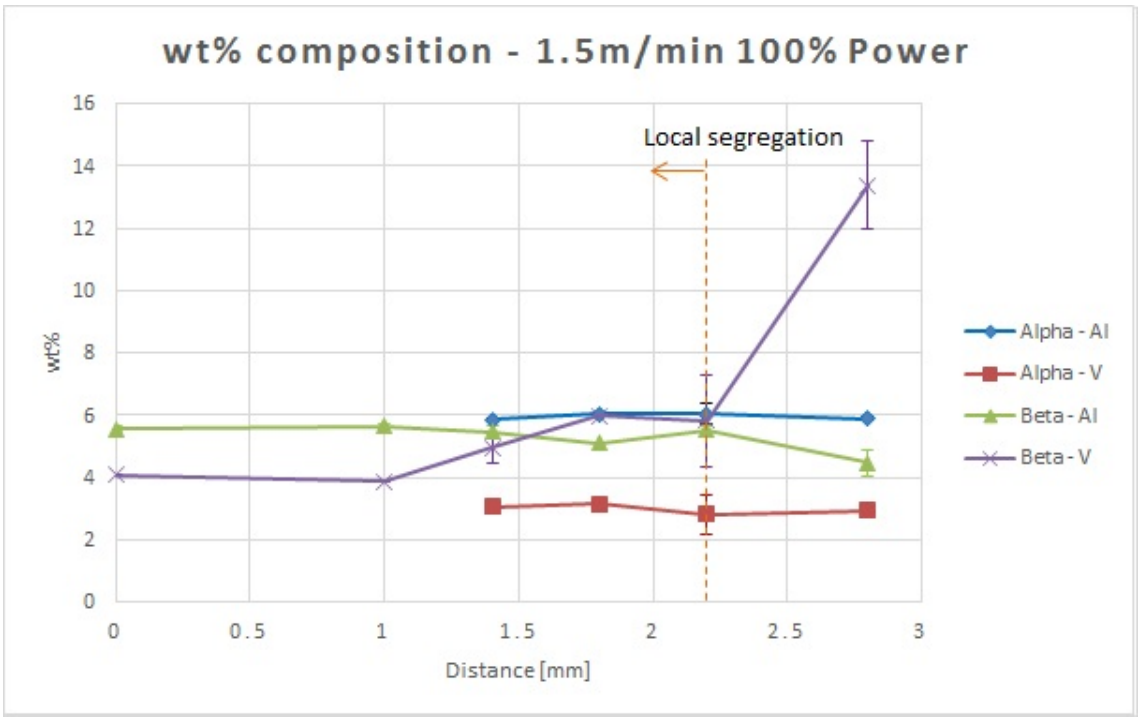

Figure 3.72.: Graphs showing the wt% of Al and V as a function of the distance from the weldline (figure 3.60 and figure 3.61) for the Ti-6Al-4V plates 5 mm thick with initial equiaxed microstructure. a) Plate welded at 2.0 m/min and 70% power, b) plate welded at 1.5 m/min and 100% power. For some points the errors bars are so small that they are not visible. The orange dotted line indicates where the original microstructure of the material dissolves but it is possible to notice still a local segregation related to the initial phases distribution

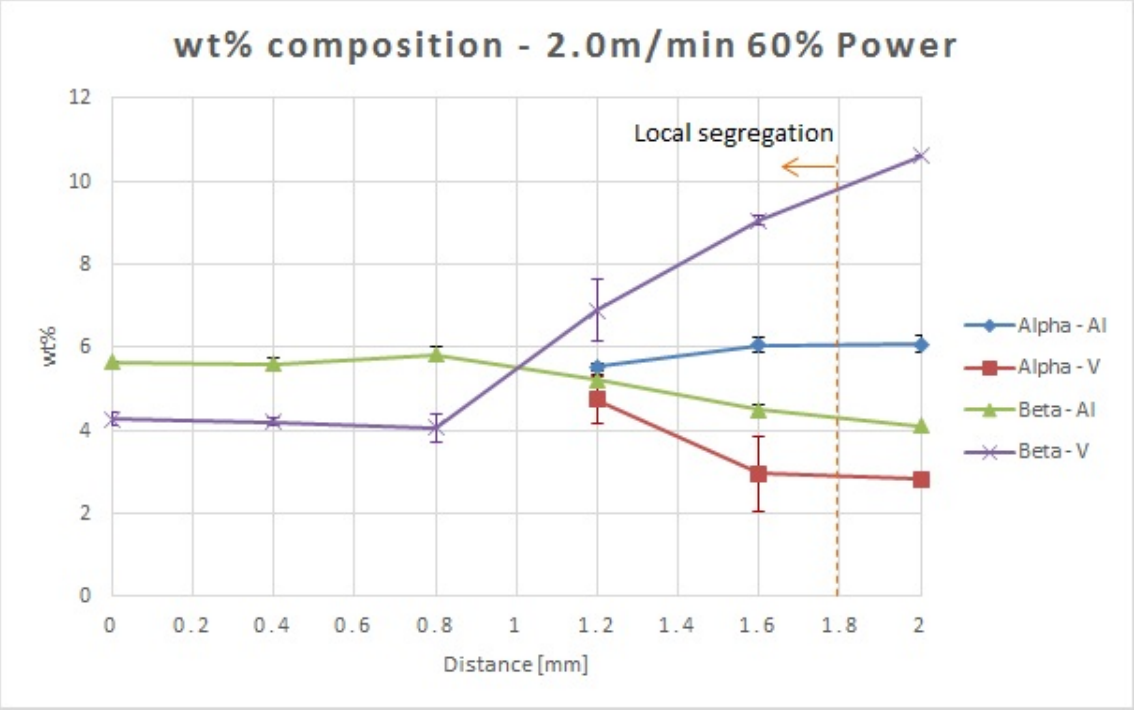

Figure 3.73.: Graph showing the wt% of Al and V as a function of the distance from the weldline (figure 3.62), starting from the first indent in the centre of the weld pool, for the Ti-6Al-4V plate 2 mm thick with initial equiaxed microstructure. The orange dotted line indicates where the original microstructure of the material dissolves but it is possible to notice still a local segregation related to the initial phases distribution

in Vanadium content of the beta phase. Due to the high speed of the welding process, the chemical composition along the material did not have time to homogenise and the chemical composition of the phases present in the original material was still noticeable after the formation of new morphological features (see figure 3.66-d, 3.67-d, in particular white segregation related to the original beta phase distribution), as alpha lamellae or martensitic needles. The appearing of this phenomenon is identified in the charts by the line reporting "local segregation".

a)

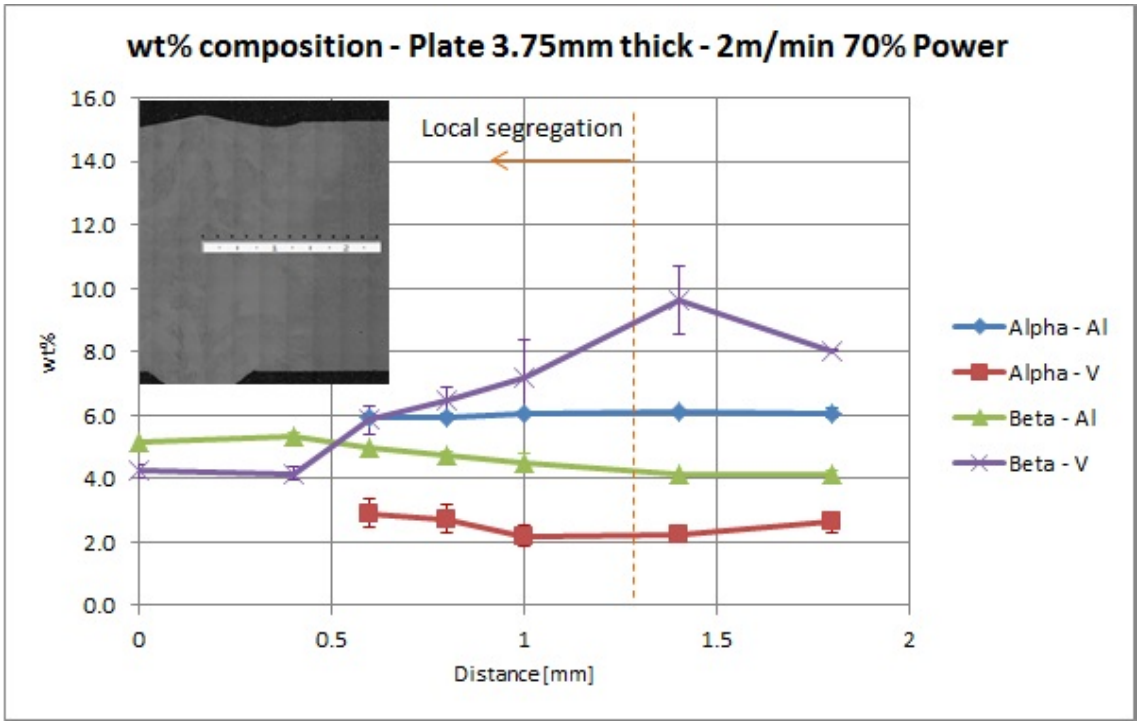

b)

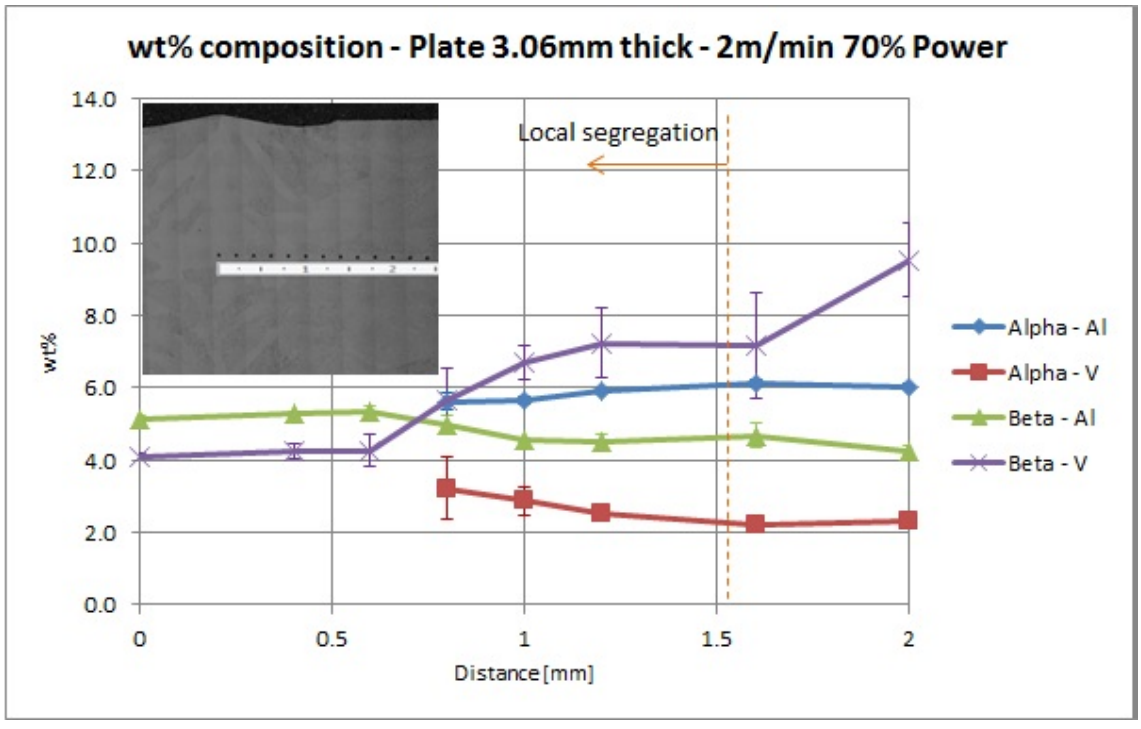

Figure 3.74.: Graphs showing the wt% of Al and V as a function of the distance from the weldline (figure 3.68 and figure 3.70) for the Ti-6Al-4V plates 3.75 mm a) and 3.06 mm b) thick with initial lamellar microstructure. For some points the errors bars are so small that are not visible. The orange dotted line indicates where the original microstructure of the material dissolves but it is possible to notice still a local segregation related to the initial phases distribution

3.5.4 Deformation measurement

Deflection measurement of the plates with initial lamellar morphology were carried out before and after welding, by a laser scanner Keyence LJ V7080.

The deformations are shown in the graphs of figure 3.75 and they are relative to the longitudinal centre line of the plates on their bottom side (the opposite side to the application of the heat source).

The central spikes in the measurements after welding are due to the Ti-6Al-4V melting and solidifying in the bottom part of the weld pool (figure 3.63).

The maximum deformation registered in both cases corresponds with the weld trajectory (not considering the spikes) and they are about 0.22 mm for the plate 3.75 mm thick and 0.14 mm for the plate 3.06 mm thick.

The results obtained by these measurements were meant to validate the numerical predictions of a welding simulation in case the mechanical model described in section 4.7 would have been successfully implemented in the commercial software Visual-Weld.

3.6 Summary

In conclusion, the main results observed in the experiments described previously in this chapter are listed below.

3.6.1 Heating rate

Alpha particles dissolution The alpha particles dissolve, during heating, as the heat treatment becomes faster, has no time to occur completely because it is limited by the speed of the diffusion process. As a consequence, the chemical field coupled to the distribution of the alpha and beta phases does not have time to reach the equilibrium conditions.

Using BEI analysis, in samples tested at sufficient high temperatures, it is possible to see the inhomogeneous chemical distribution above mentioned, resulting in ghost shapes, memory of the parent microstructure, containing martensite. This indicates that before

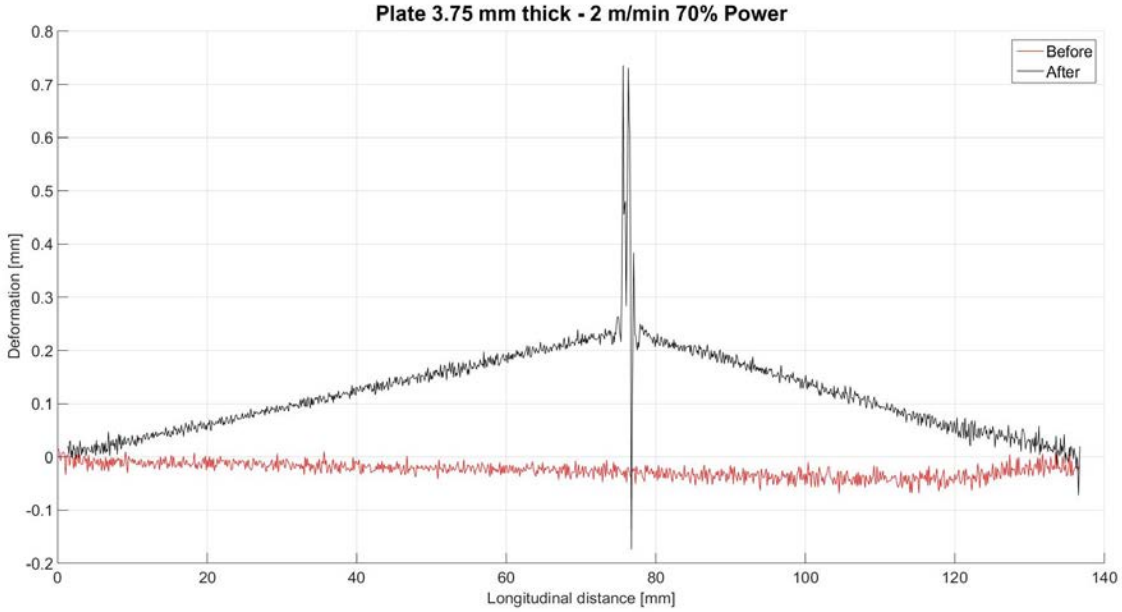

a)

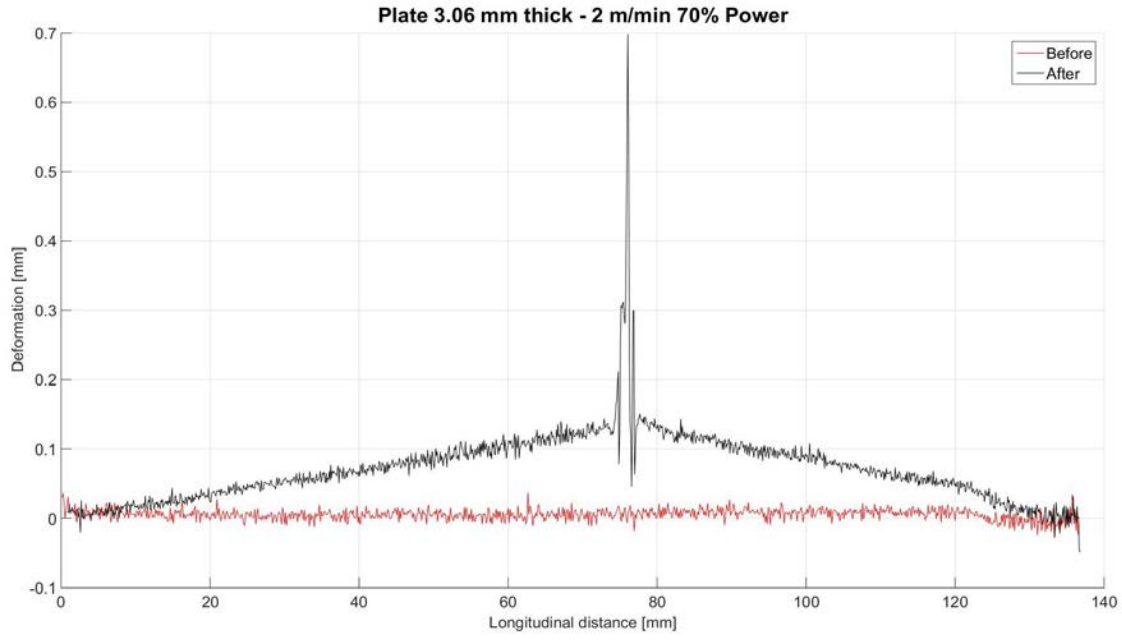

b)

Figure 3.75.: Deformation of the Ti-6Al-4V plates with initial lamellar morphology, before and after welding. The deformation shown is relative to the longitudinal centre line of the plates in their bottom side. The graph a) shows the deformation of the plate 3.75 mm thick, whilst the graph b) shows the deformation of the plate 3.06 mm thick

the water quenching, the material transformed from HCP to BCC thus, even if the chemical diffusion process does not have time to dissolve entirely the parent alpha precipitates, transforming from HCP to BCC occurs as soon as the thermodynamic conditions allow the transformation. In case of fast heat treatments, precipitate dissolution modelling that assumes disappearing of the alpha phase only when the particle dimension becomes null would make wrong predictions.

Experimental measurement of the volume fraction of the alpha and martensitic phase, for fast heat treatments, results particularly difficult, for the overlapping of ghost shapes above mentioned and martensitic needles. In this work, when martensite was observed, alpha phase was considered to be completely disappeared.

Beta grain growth The nucleation temperature of beta grains shows a shift toward higher values as the heating rate becomes faster, as expected from the literature. Moreover, between nucleation temperature of beta grains and beta transus temperature, there is a gap in temperature that seems to increase with the heating rate.

At high temperatures (>1100 °C) beta grain growth shows an asymptotic trend toward constant values. This can be explained by mechanical impingement of highly misoriented beta grains, that requires longer times and/or higher temperatures to let grains merge together.

Beta transus temperature The equilibrium beta transus temperature for the material tested can be located around $973 \pm 3\,°C$, with the considerations above mentioned for fast heating rates.

3.6.2 Cooling rate

The experiments carried out suggest that continuous cooling from above the beta transus temperature to ambient temperature has a relatively small effect on the lamellae growth, compared to the dimension of the beta grains in which lamellae nucleate.

Even if the amount of data points collected is not very high, the fact that thicker lamellae

have been measured for faster cooling rates is a first indication that the diffusion process is not the main driving factor in these kind of thermal loads. Plotting the lamellae thickness as a function of the beta grains where they nucleate, makes explicit how a greater beta grain volume allows grow of thicker lamellae, probably because being more statistically spaced thus having availability of more solute for their growth.

3.6.3 Welding tests

Observations done for the Gleeble tests are confirmed in welding tests: thicker lamellae seem to be associated with larger beta grains, thus thicker lamellae were measured closer to the heat source.

Similar lamellae thickness, in different plates, returned similar hardness measurements.

Close to the interface between the bulk material and the heat affected zone a drop in hardness is registered, probably associated with releasing of the residual stresses in the parent material caused by the rising of temperature during welding. This increase of temperature was not high enough to observe appreciable microstructural changes, but probably was sufficient to decrease the dislocation density in this portion of material.

The chemical composition of the beta matrix has a notable variation in Vanadium with respect to the Aluminium, suggesting that the former element is the controlling factor in the diffusion process for particle growth and dissolution.

The maximum deformation registered for the plates with an initial lamellar morphology is approximately 0.22 mm and 0.14 mm for the plate 3.75 mm and 3.05 mm thick respectively.

CHAPTER 4

Numerical modelling

4.1 Introduction

In this chapter, the physically and experimentally based models developed to describe the evolution of the microstructure of Ti-6Al-4V for the temperatures and temperature rates involved in a welding process are presented. The models described have been coded in the commercial welding simulation software Visual-Weld and welding simulation results for some cases are compared with the corresponding experimental data obtained for the same operating conditions, material and workpiece geometries.

The choice to adopt physically or experimentally based models was driven by the complexity of the phenomena investigated and by the level of understanding reached in literature to describe them.

A diffusion based model has been adopted to describe the microstructure evolution in the $\alpha + \beta$ field, as this approach had already been shown to be successful in forging applications, even though the thermal loads involved in this kind of process are much simpler. Also, the numerical implementation of such a model in Visual-Weld, adopting reasonable simplifications, was possible and gave run times close to the currently used approach in the welding simulation software (section 2.4.2), thus allowing this solution to be effective for industrial applications.

For the description of the microstructure evolution of the material in the beta field and molten zone (beta grain nucleation and coarsening) and for cooling from temperatures above the beta transus temperature (possible formation of martensite and alpha lamellae), no physically based reasonable solutions were found in the literature that use sufficiently simple models that could be implemented in welding simulations and still return comparable running times to the conventional approach used in Visual-Weld. Examples of the complexity and relative approaches to physically describe these phenomena have been investigated in [95, 96], where surface roughness and melted material fluid dynamics affect the heat flow, solidification and the beta grains columnar shape. Also, in the literature there are examples of martensitic transformation modelling that adopt the phase field approach [97, 98], but the computational power available nowadays is sufficient to simulate only a few microns of material volume. Following these considerations, empirical approaches were used for the beta grain and martensitic modelling based on the experimental data presented in chapther 3.

4.2 Alpha + Beta field

The kinetics of the growth and shrinkage of equiaxed and lamellar alpha in the $\alpha + \beta$ field has been modelled using a single element diffusion analysis of an isolated particle in an infinite matrix [39], but adapted to a finite matrix case where the system overall solute concentration is constant [71].

For an infinitesimal time step, the two equations describing the solute flux in a particle are [39, 67]:

1. Field equation

$$D\nabla^2 C = \frac{\partial C}{\partial t} \tag{4.1}$$

2. Flux balance

$$(C_P - C_I)\frac{dR}{dt} = D\left.\frac{\partial C}{\partial r}\right|_{r=R} \tag{4.2}$$

Where D represents the interdiffusion coefficient considered independent of composition for the time dt, C the solute concentration, t the time, R the radius of the particle, C_P the solute concentration in the matrix-particle interface at the particle side and C_I the solute concentration in the matrix-particle interface at the matrix side.

Assuming that the diffusion process is driven mainly by a single diffusing element that acts as limiting element, is a simplification that for both Ti-6Al-4V and other alloys, has been successfully adopted in literature [40, 30, 99]. In the experimental chapter (section 3.5.2) it has already been shown that actually in Ti-6Al-4V, Vanadium is the element having the most noticeable variation in composition in the matrix during the dissolution of alpha particles, indicating that this is the element with the highest mass transfer during the diffusing process. This hypothesis was then adopted and further validated by comparing the numerical prediction of the model presented in the current paragraph with experimental measurement.

When possible, the exact solutions of the field equation (eq. 4.1) and flux balance (eq. 4.2) have been used, otherwise simplified conditions have been applied to get a solvable analytical solution. In figure 4.1, all the terms of the equations 4.1 and 4.2 are schematised, together with the solute concentration field assumed for growth (figure 4.1-a) and dissolution (figure 4.1-b) of the diffusion driving element. During growth, the precipitate depletes the matrix immediately ahead of its interface [100, 101], since solute is needed to increase the particle dimensions. Contrarily, during shrinkage, the precipitate rejects solute, that moves toward the matrix, resulting in a gradual decrease in the solute distribution from the particle to the matrix [101].

Assuming incoherent diffusion controlled growth, local equilibrium at the interface can be assumed [94], C_I is then considered to be the equilibrium concentration of the matrix phase. C_P is considered as constant and equal to the value at the beginning of the heat treatment. This last hypothesis implies that a) the diffusion coefficient in the precipitate is small compared to the one in the matrix and/or b) the solute concentration in the precipitate is independent from the distance from the particle-matrix interface and

temperature [101].

Hypothesis a) cannot be fully verified by literature data as the diffusivity of Vanadium in the alpha phase was not found. But it can be considered reasonable if the order of magnitude of the Vanadium diffusivity in alpha Titanium is assumed to be similar to that for Aluminium reported in [102]. Semiatin et al [40] reported that the diffusivity of Aluminium in the beta phase is similar to that of Vanadium (equations 4.24 and 4.26). Accepting the previous hypothesis, an approximate comparison of impurity diffusion in the alpha and beta phases can be made. In the alpha phase the impurity diffusion goes from $10^{-9}(\mu m^2/s)$ to $10^{-5}(\mu m^2/s)$ passing from 950 K to 1150 K, for the same range of temperatures in the beta phase the diffusivity goes from $6 \times 10^{-4}(\mu m^2/s)$ to $2.5 \times 10^{-2}(\mu m^2/s)$. The diffusivity in the beta phase seems, in the worst case, at least 3 order of magnitude faster than in the alpha phase.

Hypothesis b) is supported by the small variation in concentration of Vanadium and Aluminium measured experimentally in the alpha phase composition reported in section 3.5.2 with respect to that in the beta phase. In this case, the concentrations were measured at different distances from the welding heat source, thus a wide range of temperatures were involved, and the variation in composition in the alpha phase was very small compared to the difference seen in the beta phase.

Thus assuming that the hypotheses mentioned above are valid, the following boundary conditions can be applied for the solution of equations 4.1 and 4.2:

$$\begin{aligned} C(r = R, t) &= C_I \qquad 0 < t \leq \infty \\ C(r, t = 0) &= C_M \qquad r \geq R \\ C(r = \infty, t) &= C_M \qquad 0 \leq t \leq \infty \end{aligned} \tag{4.3}$$

Where C_M is the solute concentration in the matrix (figure 4.1).

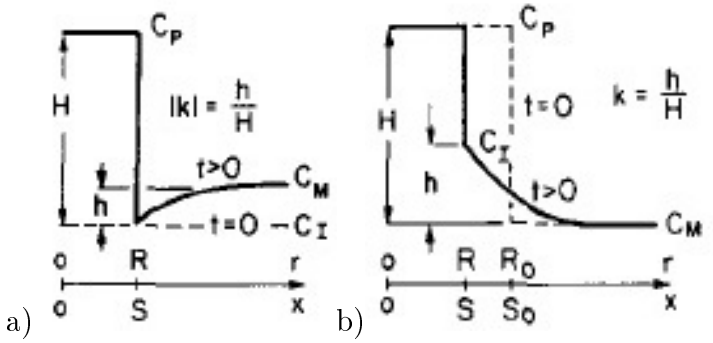

Figure 4.1.: Schematic representation of the concentration field during growth a) and shrinkage b) [39]

4.2.1 Spherical particles

4.2.1.1 Growth

The exact solution of equations 4.1 and 4.2, when applying the boundary conditions in equation 4.3 and using spherical coordinates, expresses the concentration field and the radius variation in time as [40, 39]:

$$C(r,t) - C_M = \frac{2\lambda(C_I - C_M)}{\exp(-\lambda^2) - \lambda(\pi)^{1/2} erfc(\lambda)} \times \left[\frac{(Dt)^{1/2}}{r} \exp\left(-\frac{r^2}{4Dt}\right) - \frac{1}{2}(\pi)^{1/2} erfc\left(\frac{r}{2(Dt)^{1/2}}\right)\right] \quad (4.4)$$

$$\frac{dR}{dt} = 2\lambda^2 D/R \quad (4.5)$$

where λ is a function of the supersaturation Ω:

$$\lambda^2 \exp\left(\lambda^2\right)\left[\left(\exp\left(-\lambda^2\right)\right) - \left(\lambda\pi^{1/2} erfc\left(\lambda\right)\right)\right] = \frac{\Omega}{2} \quad (4.6)$$

$$erfc(\lambda) = \frac{2}{\sqrt{\pi}} \int_{\lambda}^{\infty} e^{-t^2} dt \quad (4.7)$$

$$\Omega = \frac{C_M - C_I}{C_P - C_I} \tag{4.8}$$

Since λ cannot be computed directly, a fitting algorithm was used to give λ as a function of the independent variable Ω. In this work a code has been written in the commercial software Matlab. Figure 4.2 shows λ for of a range of supersaturation Ω values, from 0 to 1. At $\Omega = 1$ λ tends asymptotically to infinity.

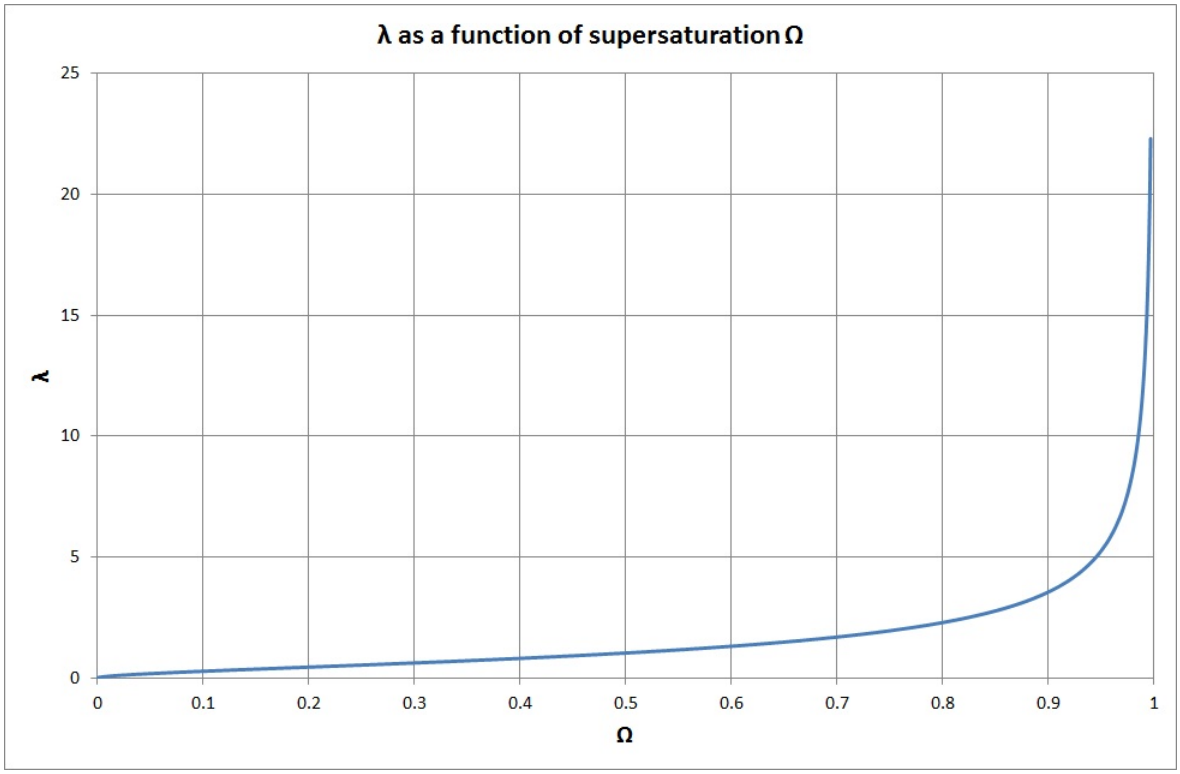

Figure 4.2.: Graph showing the parameter λ as a function of Ω of equations 4.6 and 4.8

The solute concentration in the matrix C_M is computed taking into consideration the soft impingement on the far-field composition, using a mass balance, where the overall solute concentration of the alloy (C_0) is given by the sum of the solute concentration in the alpha phase (C_α) and in the matrix:

$$C_0 = f_\alpha C_\alpha + (1 - f_\alpha) C_M \tag{4.9}$$

From the equation 4.9, the solute concentration in the matrix as a function of the phase

fraction of the precipitate (f_α) can be expressed:

$$C_M = \frac{C_0 - f_\alpha C_\alpha}{1 - f_\alpha} \tag{4.10}$$

In equation 4.10 the precipitate composition (C_α) is considered equal to C_P, in agreement with the initial hypothesis, and the phase fraction of the precipitate f_α is considered proportional to its initial value ($f_{\alpha 0}$) multiplied by the cube of the ratio between the current radius of the particle and its original dimension (R_0) [30]:

$$f_\alpha = f_{\alpha 0} \left(\frac{R}{R_0} \right)^3 \tag{4.11}$$

The assumptions involved for the calculation of C_M in equation 4.10 neglect the precise solute concentration in the region adjacent to the precipitate (figure 4.1). This simplification introduces an acceptable under prediction of the volume fraction of primary alpha transformed of $0.5 - 1.5\%$ [30]. Phase field calculations [103] support this hypothesis, in particular for long annealing times.

The interdiffusion coefficient D, was determined as a function of the composition and temperature at each delta time dt, using Darken's equation for a binary system [94]:

$$D = F(X_B D_A^* + X_A D_B^*) \tag{4.12}$$

This assumption has been made considering the diffusion process to be driven by only one element such as Aluminium or Vanadium diffusing in a Titanium matrix, in an analogous way to the growth model. Much recent work in the literature has adopted this procedure, and has obtained good predictions when compared with experimental results [40, 30, 71]. In equation 4.12 D_A^* and D_B^* are the intrinsic diffusion coefficients of the binary system of A and B elements, where in case of the current work A can be represented by Vanadium or Aluminium and B is Titanium.

The term F of the equation 4.12 is the thermodynamic factor, i.e.

$$F = \frac{X_A X_B}{\Upsilon T} \frac{d^2 G}{dX^2} \tag{4.13}$$

where X represents the mole fraction of the element A or B (as in equation 4.12), Υ is the gas constant, T the temperature in Kelvin and $\frac{d^2G}{dX^2}$ the second derivative of the Gibbs free energy (see paragraph 4.2.3).

4.2.1.2 Shrinkage

Since for the physical reasons discussed in [39], the exact solution of equations 4.1 and 4.2 for a dissolving sphere is not possible, a stationary interface $\left(\frac{\partial R}{\partial t} = 0\right)$ is assumed, as suggested in [39, 104] as being a reasonable approximation. As observed in [101], the stationary interface approximation can describe the kinetics satisfactorily when the supersaturation is within 0.3 such that the growth rate is not particularly high. Equations 4.14 and 4.15 describe respectively the concentration field around the particle and its shrinkage rate.

$$C(r,t) - C_M = \left\{ \left[\left(C_I - C_M\right) R \right] / r \right\} erfc \left[\left(r - R\right) / 2 \left(Dt\right)^{1/2} \right] \tag{4.14}$$

$$\frac{dR}{dt} = \frac{\Omega D}{4R} + \frac{\Omega}{4} \sqrt{\frac{D}{\pi t}} \tag{4.15}$$

All the terms have been already explained previously. The complementary error function (erfc) has the form of equation 4.7.

4.2.2 Lamellar particles

4.2.2.1 Growth

The lamellar particles growth has been modelled using the solution proposed in [105, 67, 68] for an ellipsoidal shape, whose aspect ratio between minor and major axis remains constant. In [30] it has been stated that this solution gives better results with respect to a

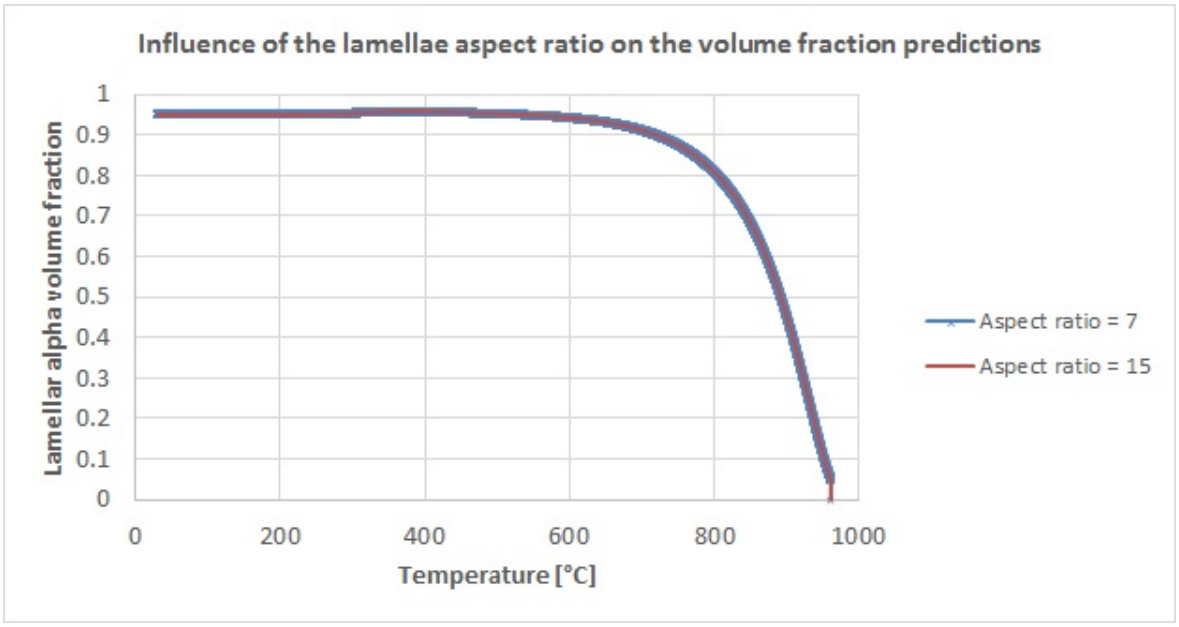

Figure 4.3.: Graph showing the influence of the lamellar aspect ratio to the volume fraction predictions for a Ti-6Al-4V alloy with an initial mean lamellae thickness of 3.0 μm, subjected to a hypothetical heating rate of 60 °C/s,

semi-infinite plate solution, where the growth of the particle seems to be underestimated.

This approach does not consider the initial stage of the growth of lamellar particles, where usually after nucleation a lengthening phase follows [68] until lamellae mechanically impinge on themselves. Since nucleation is out of scope for this model, the assumption of a constant aspect ratio is assumed to be reasonable for the description of growth and shrinkage in the $\alpha + \beta$ field.

Nucleation and lengthening could be considered using a further analytical model as in [72] or an experimental/phenomenological approach could be used.

Moreover the experimental measurements (figure 3.26) show that the aspect ratio change are relatively small as the lamellae thinning occurs. Consequently a sensitivity analysis of the numerical model to this variation was conducted, confirming that the changes involved have little appreciable effect on the final predictions (figure 4.3).

The ellipsoidal approach describes the half length of the major (Y) and minor axis (X) of the ellipsoid representing the lamellar particle by, respectively, the equations 4.16 and 4.17:

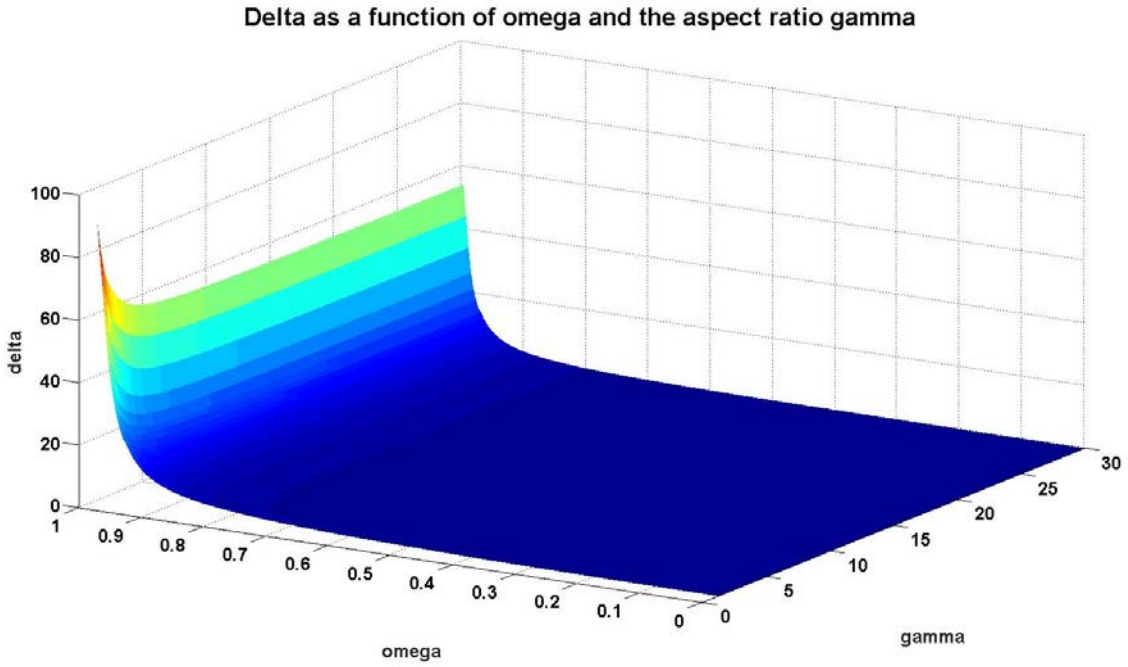

Figure 4.4.: Graph showing delta (δ) as a function of omega (Ω) and aspect ratio gamma (Γ) of equation 4.18

$$Y = 2\Gamma \left(\delta D t\right)^{1/2} \tag{4.16}$$

$$X = 2 \left(\delta D t\right)^{1/2} \tag{4.17}$$

Where Γ is the aspect ratio given by Y/X.

The dimensionless growth rate parameter δ is determined from equation 4.18, where Ω is the supersaturation (equation 4.8).

$$\Omega = \exp \delta \left[\delta^{3/2} \Gamma^2\right] \int_{u=\delta}^{u=\infty} \frac{\exp\left(-u\right) du}{\left\{\delta \left(\Gamma^2 - 1\right) + u\right\} u^{1/2}} \tag{4.18}$$

The solution of equation 4.18 has been computed using the commercial software package Matlab to obtain $\delta\left(\Omega\right)$ and its behaviour is shown in figure 4.4.

The volume of the ellipsoid, considering equations 4.16 and 4.17 is then determined from equation 4.19.

$$\frac{dV_e}{dt} = 8\pi\Gamma^2\delta DX \tag{4.19}$$

4.2.2.2 Shrinkage

To model the thinning of lamellar particles, the calculations have been based on diffusional shrinkage of a semi-infinite plane [39]. The exact solution of the concentration field is represented in equation 4.20 whilst the thickness of the plate is described by equation 4.21, where λ_1 and λ are described by the equations 4.22 and 4.23.

$$C(x,t) - C_M = (C_I - C_M)\frac{erfc\left[(x - S_0)/2(Dt)^{1/2}\right]}{erfc(-\lambda)} \tag{4.20}$$

$$S = S_0 - \lambda_1 (Dt)^{1/2} \tag{4.21}$$

$$\lambda_1 = \lambda/2 \tag{4.22}$$

$$(\pi)^{1/2}\lambda e^{\lambda^2} erfc(-\lambda) = \Omega/2 \tag{4.23}$$

4.2.3 Input data

The intrinsic diffusion coefficients have been expressed as Arrhenius equations [40]:

$$D_V^{\beta}(\mu m^2/s) = 10^5 \exp(-17460/T(K)) \tag{4.24}$$

$$D_{Ti}^{\beta}(\mu m^2/s) = 2x10^4 \exp(-15000/T(K)) \tag{4.25}$$

$$D_{Al}^{\beta}(\mu m^2/s) = 1.2x10^5 \exp(-18040/T(K)) \tag{4.26}$$

Where β means that the diffusivity of the elements is considered in the beta Titanium matrix.

For the calculation of $\frac{d^2G}{dX^2}$, the Gibbs free energy formulation in a beta matrix for a Ti-Al-V ternary system has been used (eq. 4.27) [106]. The Gibbs free energy total contribution is represented by the sum of the Gibbs free energy of a mechanical mixture of the constituents of the phase (eq. 4.28), the entropy of mixing for an ideal solution (eq. 4.29) and the excess term (eq. 4.30) [107] :

$$G^{\beta} = G^{0} + G^{ideal} + G^{xs} \tag{4.27}$$

$$G^{0} = X_{Al}G0_{Al}^{BCC} + X_{Ti}G0_{Ti}^{BCC} + X_{V}G0_{V}^{BCC} \tag{4.28}$$

$$G^{ideal} = \Upsilon T \left(X_{Al} \ln X_{Al} + X_{Ti} \ln X_{Ti} + X_{V} \ln X_{V}\right) \tag{4.29}$$

$$\begin{aligned} G^{xs} = {} & X_{Al}X_{Ti}\left(-125485 + 36.8394T\right) + X_{Al}X_{V}\left[\left(-95000 + 20T\right) + \left(-6000\right)\left(X_{Al} - X_{V}\right)\right] \\ & + X_{Ti}X_{V}\left[\left(10500 - 1.5T\right) + 2000\left(X_{Ti} - X_{V}\right) + 1000(X_{Ti} - X_{V})^{2}\right] \\ & + X_{Al}X_{Ti}X_{V}\left[X_{Al}\left(116976.3 - 9.067T\right) + X_{Ti}\left(-175169 + 59T\right) + X_{V}\left(31107.3 - 42.316T\right)\right] \end{aligned} \tag{4.30}$$

Where X_x is the mole fraction of the element x at the temperature considered, $G0_x^{BCC}$ is the Gibbs free energy of the pure element x [108], T is the temperature in Kelvin. With only considering a ternary system, the effect of other elements in the actual alloy, on the Gibbs free energy, like O, Fe, C, etc., has not been considered and consequently their mole fraction contribution, as predicted by Thermocalc®, was added to the Ti mol fraction, to get the unity sum of the Ti, Al and V mol fractions. This simplification, for the case under examination, was considered sufficiently precise as the errors in the prediction of the

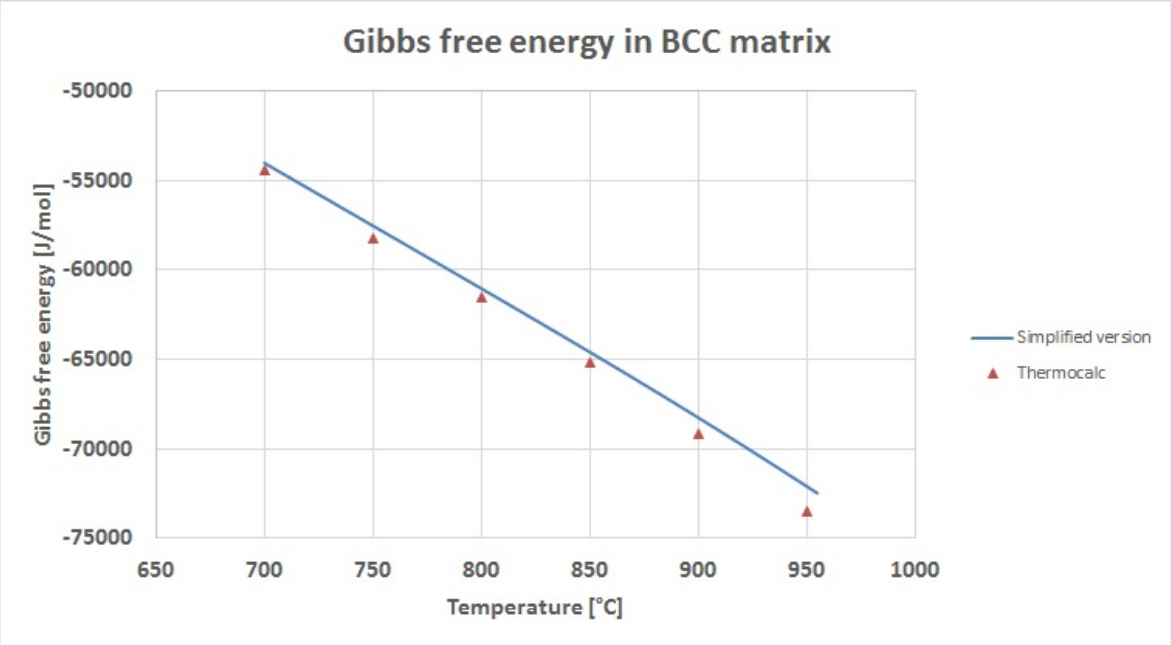

Figure 4.5.: Gibbs free energy calculated both by a simplified equation for a Ti-Al-V ternary system and using the actual composition by the Thermocalc database

actual Gibbs free energy were within 2%. These were compensated by the simplification of the model and shorter running times when compared with the use of an interface with Thermocalc® to get the actual Gibbs free energy values. Figure 4.5 shows a comparison of the Gibbs free energy obtained using both the simplified ternary system solution and the actual alloy composition from Thermocalc®, both referred to the beta matrix (BCC structure). Furthermore, the small sensitivity noticed of the diffusion growth model to the variation of the thermodynamic factor (equation 4.13) justify the adoption of this approach: when going from $F = 2$ to $F = 4$ the variation in the final phase proportion predicted is less than 3%.

All the considerations for the calculation of the interdiffusion coefficient D were considered valid for all the models presented in this work.

Even though the current model is thought to work only in the $\alpha + \beta$ field, the fast heat cycles experienced in welding could bring the alpha precipitates to liquation temperatures. Also, the transformation to liquid of the alpha precipitate and its local precipitate-matrix interface, is assumed to occur suddenly [109]. To check if the material has reached the

melting temperature in these regions, the Gibbs free energy equations for alpha (equations 4.31, 4.32, 4.33 and 4.34) and liquid (equations 4.35, 4.36, 4.37 and 4.38) are used [106, 110].

$$G^{\alpha} = G^{0} + G^{ideal} + G^{xs} \tag{4.31}$$

$$G^{0} = X_{Al} G0_{Al}^{HCP} + X_{Ti} G0_{Ti}^{HCP} + X_{V} G0_{V}^{HCP} \tag{4.32}$$

$$G^{ideal} = \Upsilon T \left(X_{Al} \ln X_{Al} + X_{Ti} \ln X_{Ti} + X_{V} \ln X_{V} \right) \tag{4.33}$$

$$\begin{aligned} G^{xs} = {} & X_{Al} X_{Ti} \left[(-123789 + 33.209T) + (16034.9 - 12.1827T) \left(X_{Al} - X_{Ti} \right) \right] + \\ & X_{Al} X_{V} \left[(-95000 + 20T) + (-6000) \left(X_{Al} - X_{V} \right) \right] + X_{Ti} X_{V} \left[16500 \right] + \\ & X_{Al} X_{Ti} X_{V} \left[X_{Al} \left(109690.9 - 97.06T \right) + X_{Ti} \left(-81024 + 38.06T \right) + X_{V} \left(104295.8 - 96.27T \right) \right] \end{aligned} \tag{4.34}$$

$$G^{liq} = G^{0} + G^{ideal} + G^{xs} \tag{4.35}$$

$$G^{0} = X_{Al} G0_{Al}^{liq} + X_{Ti} G0_{Ti}^{liq} + X_{V} G0_{V}^{liq} \tag{4.36}$$

$$G^{ideal} = \Upsilon T \left(X_{Al} \ln X_{Al} + X_{Ti} \ln X_{Ti} + X_{V} \ln X_{V} \right) \tag{4.37}$$

$$\begin{aligned} G^{xs} = {} & X_{Al} X_{Ti} \left[(-105404 + 36.1159T) + (7950.8) \left(X_{Al} - X_{Ti} \right) \right] + \\ & X_{Al} X_{V} \left[(-50725 + 9T) + (-15000 + 8T) \left(X_{Al} - X_{V} \right) \right] + X_{Ti} X_{V} \left[(1400) + 4100 \left(X_{Ti} - X_{V} \right) \right] \\ & + X_{Al} X_{Ti} X_{V} \left[X_{Al} \left(-11000 \right) + X_{Ti} \left(-15000 \right) + X_{V} \left(-10000 \right) \right] \end{aligned} \tag{4.38}$$

4.2.4 Results and discussion

The models presented previously, for spherical and lamellar particles, are adopted depending on the type of particle already existing in the microstructure under examination. No nucleation/formation of new particles is considered. The sign of the supersaturation determines if growth (positive sign) or shrinkage (negative sign) occurs.

Spherical and lamellar particles are treated as isolated with an independent supersaturation [30] if both are present in the material.

4.2.4.1 Interdiffusion coefficient

The intrinsic diffusion coefficients reported in equations 4.24, 4.25 and 4.26 are corrected by the thermodynamic factor (eq. 4.13). The resulting interdiffusion coefficient is dependent on the temperature and concentration of the beta matrix at the precipitate/matrix interface, it is then not possible to get a unique value for a specific temperature. An example of the magnitude of the intrinsic diffusion and interdiffusion coefficients, for an hypothetical heat treatment consisting of cooling down the material at $11°C/min$ starting from $955°C$ is reported in figure 4.6. In this case, the effect of the concentration of the elements on the diffusivity is very important for the Aluminium whose value is almost tripled for high temperatures, whilst the Vanadium one is a little reduced.

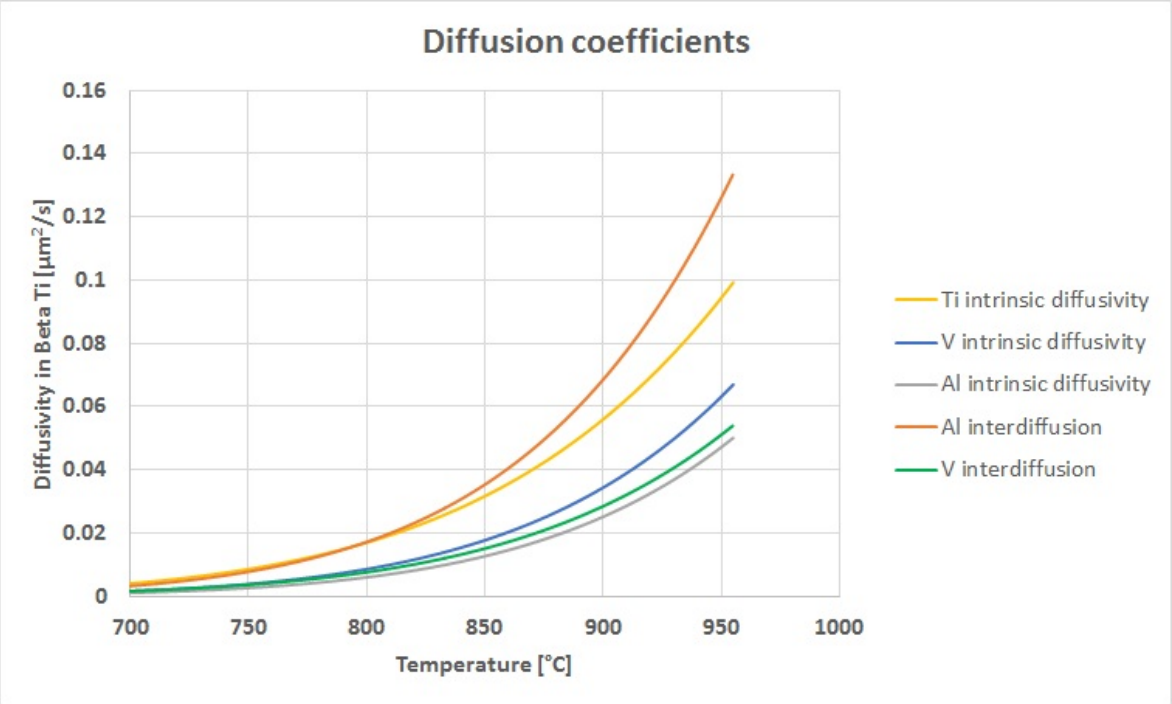

Figure 4.6.: Ti-6Al-4V intrinsic diffusion coefficients for Vanadium, Aluminium and Titanium and interdiffusion coefficients considering either Al as diffusing element (Al interdiffusion) or Vanadium (V interdiffusion)

4.2.4.2 Spherical precipitates growth

Existing data from literatur [40, 30] for the study of the spherical particle growth was used to validate the model. This allowed the experimental characterization carried out in this project to instead focus on the study of the lamellar microstructure for which no literature data was available.

The material conditions measured at the beginning of the heat treatments were used as initial conditions for the numerical model: initial average radius of the spherical particles 4.5 μm, initial phase fraction of spherical particles 0.27, material composition (in weight percent) of 6.4 Aluminium, 4.2 Vanadium, 0.14 Iron, 0.19 Oxygen, 0.016 Carbon, 0.004 Hydrogen, 0.005 Nitrogen and the balance Titanium. The alpha phase fraction of 0.27 was obtained by soaking the material at 955°C for 1 hour then water quenching it.

The heat treatments tested consisted of cooling at 3 different cooling rates (11, 42 and 194 °C/min) starting from a soaking temperature of 955°C after a 20 min hold.

The C_P value in equation 4.8 has been set as the equilibrium concentration of the diffusing element in the alpha phase, at the starting temperature of the heat treatment, and it was kept constant during the heat treatment (see section 3.6). This assumption gives negative values of the supersaturation for the first stage of the heat treatments (figure 4.8, 4.9 and 4.10) because the initial α phase fraction (0.27) is higher than the equilibrium value for $955°C$ and, consequently, the particle tends initially to reduce its dimension. The initial soaking of $20min$ before the heat treatments (the authors of the work in [40] sustain it is equivalent to one of $60\,min$ from the effects on the microstructure) is probably not enough to obtain the equilibrium microstructure at $955°C$. A composition of the particle (C_P) corresponding to the equilibrium value at about $900°C$ would not give the initial shrinkage but, since [40] does not report the actual initial value of C_P, the original solution presented has been preferred. A comparison with a hypothetical model where negative supersaturation values give just null shrinkage has been made. In this manner the impact of the different particle dimensions and relative solute concentrations has been evaluated on the final phase fraction predicted. In figure 4.7 this solution is compared with the model describing both growth and shrinkage, considering either Al or V as the diffusing element. Since after a different initial evolution, the phase fraction predicted is the same for both cases, the relative small variation in solute concentration, and relative possible resulting initial shrinkage at the first stage of the heat treatment is considered as not having a big impact on the predictions and model validation.

In figure 4.8, 4.9 and 4.10, the effect of different cooling rates ($11°C/min$, $42°C/min$, $194°C/min$) on the kinetics of growth has been investigated, starting from a peak temperature of $955°C$ and considering either Vanadium or Aluminium as the diffusing element. The numerical model, when compared with experimental results, describes the phase fraction evolution well, in particular for Vanadium as the diffusing element. The past work in [111] and the experimental tests presented in chapter 3 confirm that Vanadium is the limiting element in diffusion driven processes in Ti-6Al-4V.

The effect of the estimation of a different initial diameter of the particle size ($\pm 0.5\,\mu m$)

on the alpha phase proportion kinetic is represented in figure 4.11, for the case of a cooling rate of $11°C/min$ and Vanadium as the diffusing element. Such small variations in the particle size are plausible both for microstructural variations within the material [27] and instrument/measurement tolerance, but their impact on the growth kinetics seems modest: for the case considered, a variation of $\pm 12\%$ on the diameter of the particle returns a variation on the alpha phase growth of $\pm 3\%$.

An interesting observation, is the smaller growth rate shown when Aluminium is considered to be the diffusing element instead of Vanadium, even though its interdifusion coefficient is higher (figure 4.6). This is due to the smaller supersaturation related to Aluminium, since it has a lower difference in concentration between the alpha and beta phases than Vanadium (figure 3.72 and 3.73), this in turn, is related exponentially to the growth rate of the particle by the λ term (equation 4.5) (fig. 4.12 and 4.13).

Figure 4.14 shows an example of the trend in the matrix of the Vanadium concentration during particle growth, for the case of cooling down from $955°C$ at $42°C/min$. The Vanadium concentration of the alpha precipitate is fixed at 0.0129, the element equilibrium concentration in alpha phase at 955 °C. The difference of concentration acts as the driving force to let the particle grow, after a short time where it shrinks, since the Vanadium concentration in the matrix is higher than in the precipitate. These trends are in agreement with the experimental data reported in figures 3.60, 3.61, 3.62, 3.72 and 3.73 relative to the equiaxed microstructure: as the precipitate grows the Vanadium concentration in the matrix tends to increase since the alpha phase fraction, rich in Aluminium, increases leaving less volume to the Vanadium.

In figures 4.15, 4.16 and 4.17 some meaningful timings relevant to welding from figure 4.14 are shown. After an initial shrinkage, at the 17^{th} second the particle grows since the Vanadium concentration in the matrix is higher than in the precipitate.

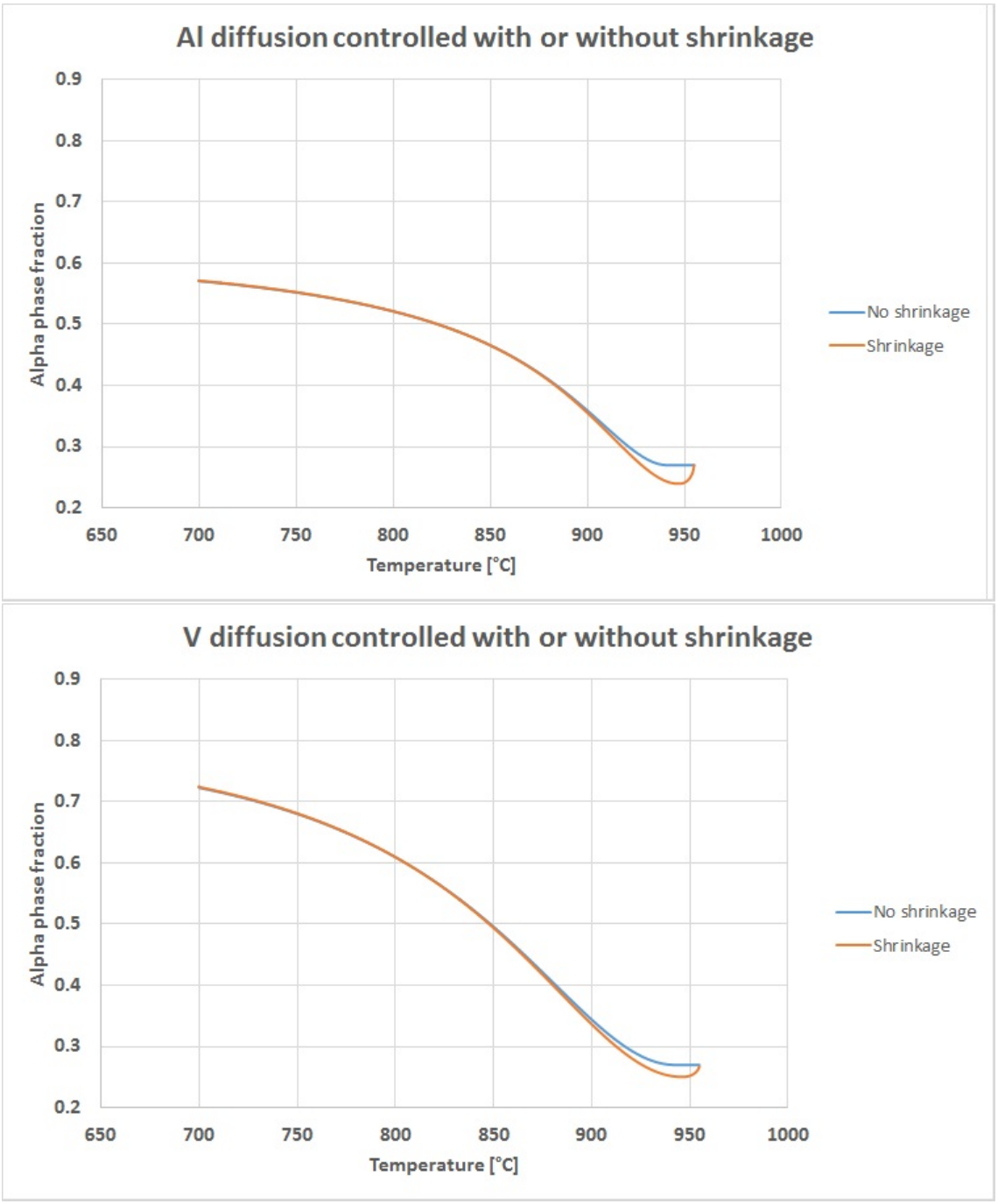

Figure 4.7.: Comparison of the equiaxed particle growth results obtained with or without shrinkage, and with diffusion controlled by either Al or V. Cooling from $955°C$ at cooling rate of $11°C/min$. Equiaxed microstructure

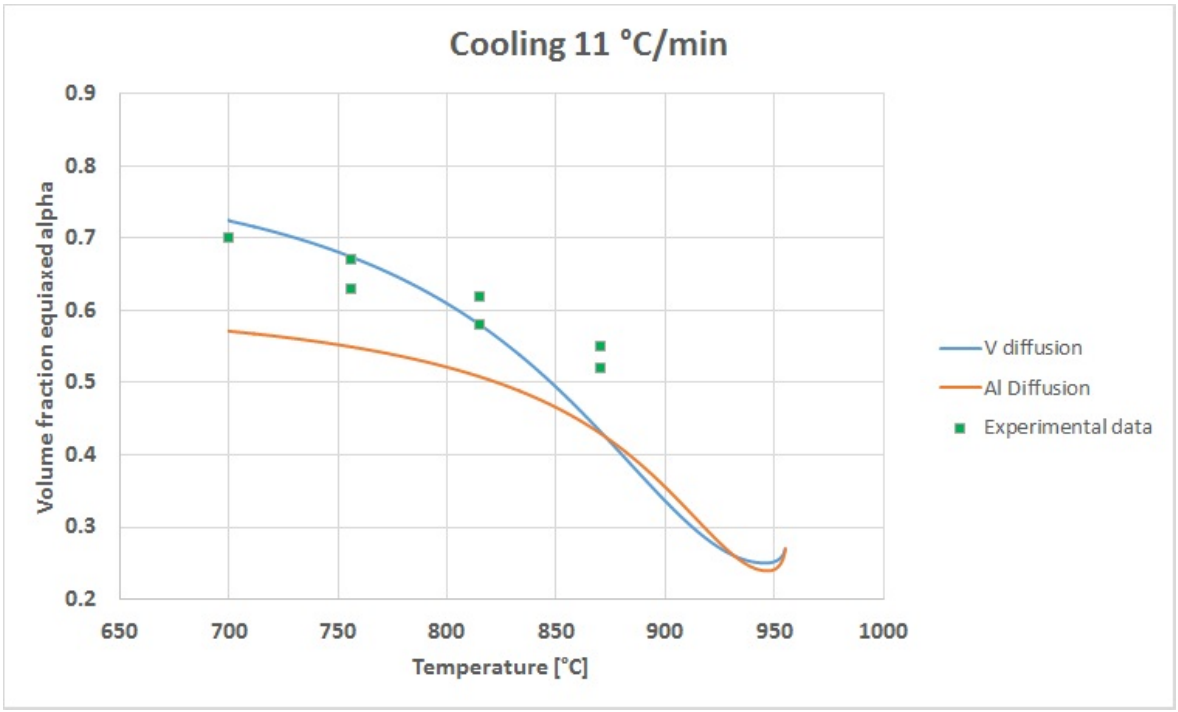

Figure 4.8.: Comparison between numerical (Al vs V diffusing elements) and experimental data [40] for a heat treatment consisting of a cooling at $11°C/min$ starting from $955°C$. Equiaxed microstructure with initial spherical particle size $4.5\,\mu m$

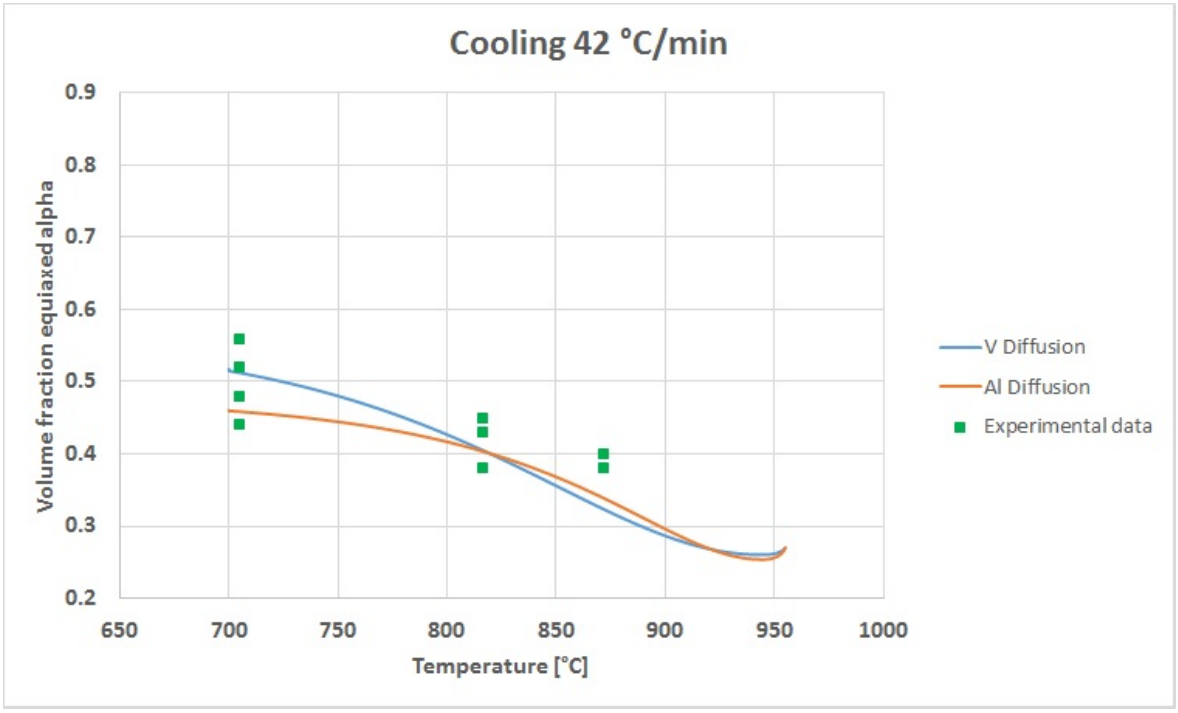

Figure 4.9.: Comparison between numerical (Al vs V diffusing elements) and experimental data [40] for a heat treatment consisting of a cooling at $11°C/min$ starting from $955°C$. Equiaxed microstructure with initial spherical particle size $4.5\,\mu m$

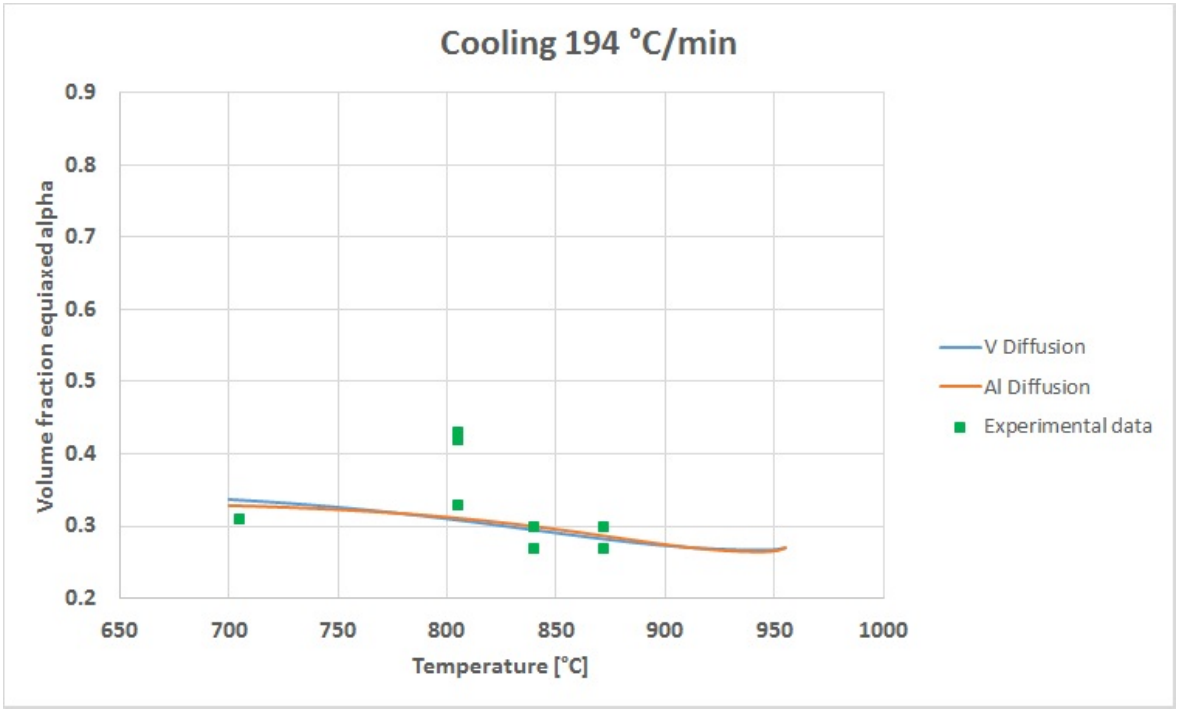

Figure 4.10.: Comparison between numerical (Al vs V diffusing elements) and experimental data [40] for a heat treatment consisting of a cooling at $11°C/min$ starting from $955°C$. Equiaxed microstructure with initial spherical particle size $4.5\ \mu m$

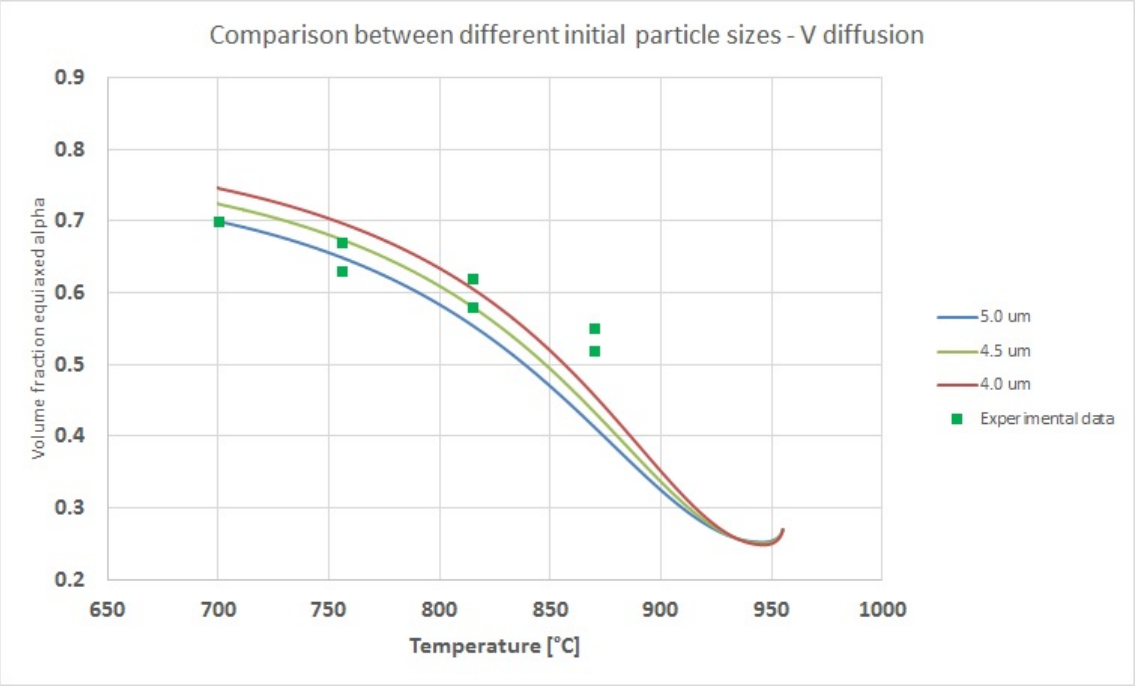

Figure 4.11.: Comparison between the different growth kinetics of an equiaxed microstructure resulting from an initial different spherical particle size. Soaking temperature 955°C then cooling at 11°C/min. Vanadium considered as diffusing element

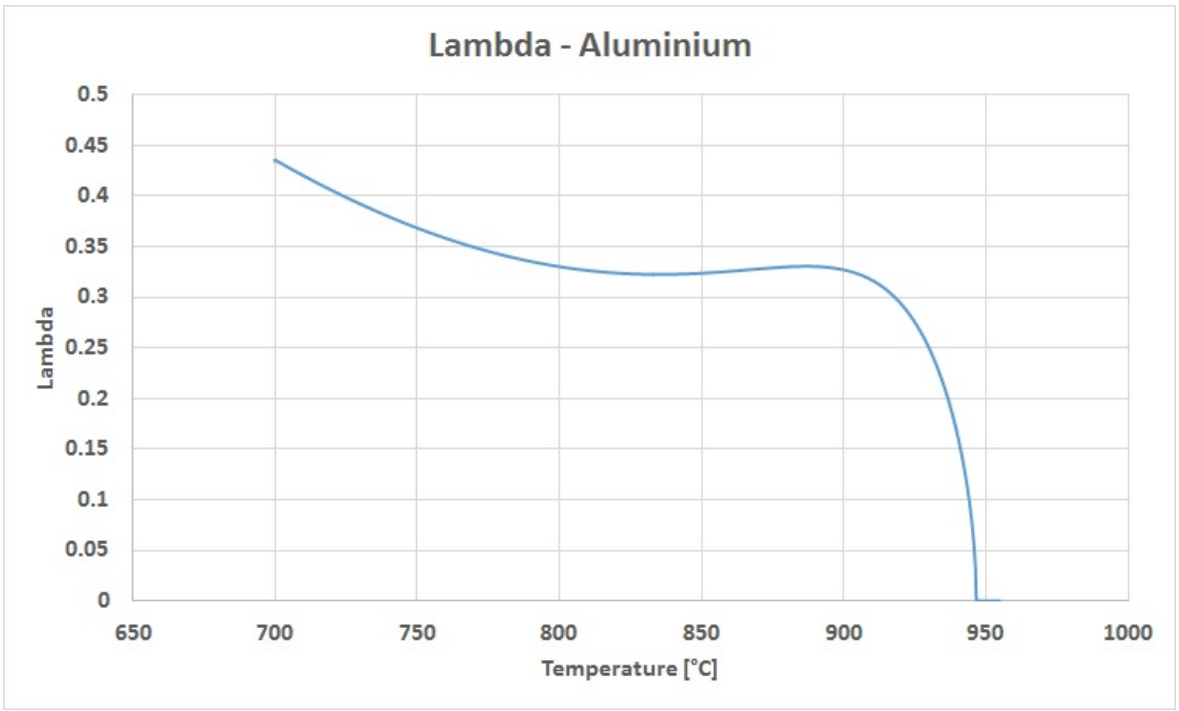

Figure 4.12.: Lambda as a function of temperature considering Aluminium as the diffusing element. Heat treatment consisting of a cooling at 11°C/min starting from a soaking temperature of 955°C. Equiaxed microstructure with initial spherical particle size 4.5 μm

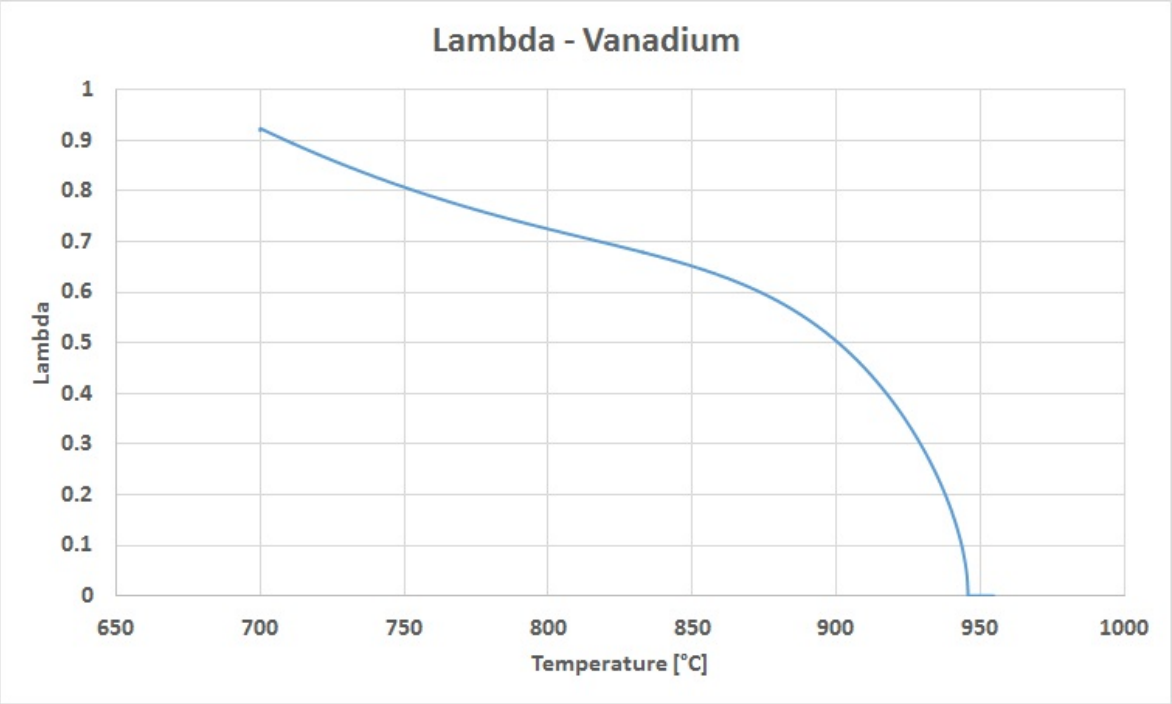

Figure 4.13.: Lambda as a function of temperature considering Vanadium as diffusing element. Heat treatment consisting of a cooling at $11°C/min$ starting from a soaking temperature of $955°C$. Equiaxed microstructure with initial spherical particle size $4.5\,\mu m$

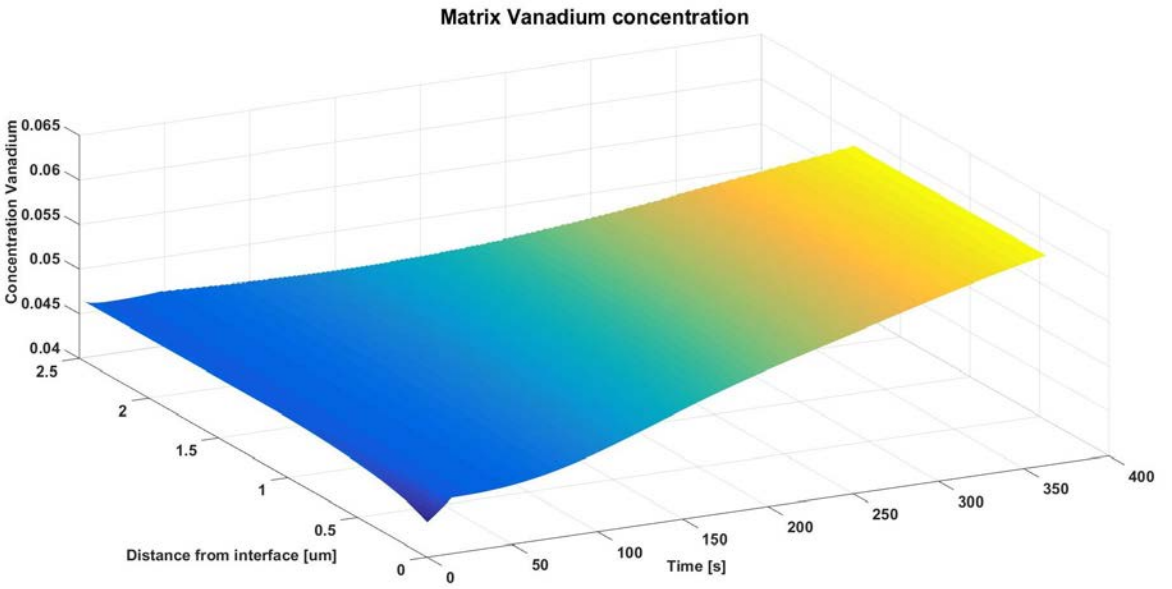

Figure 4.14.: Matrix Vanadium concentration for the growth of spherical alpha precipitate as a function of the time and distance from the particle interface (initial particle radius $4.5\,\mu m$) for the heat treatment consisting of cooling at $42°C/min$ starting from $955\,°C$ (case of figure 4.9)

a)

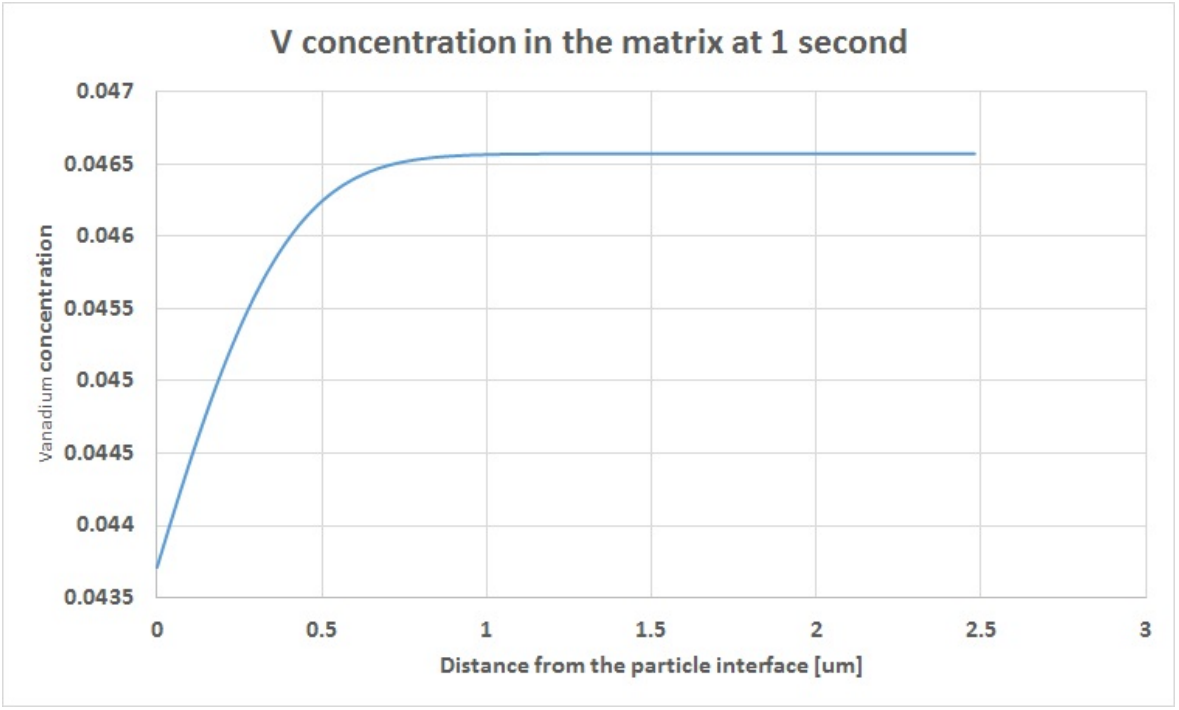

b)

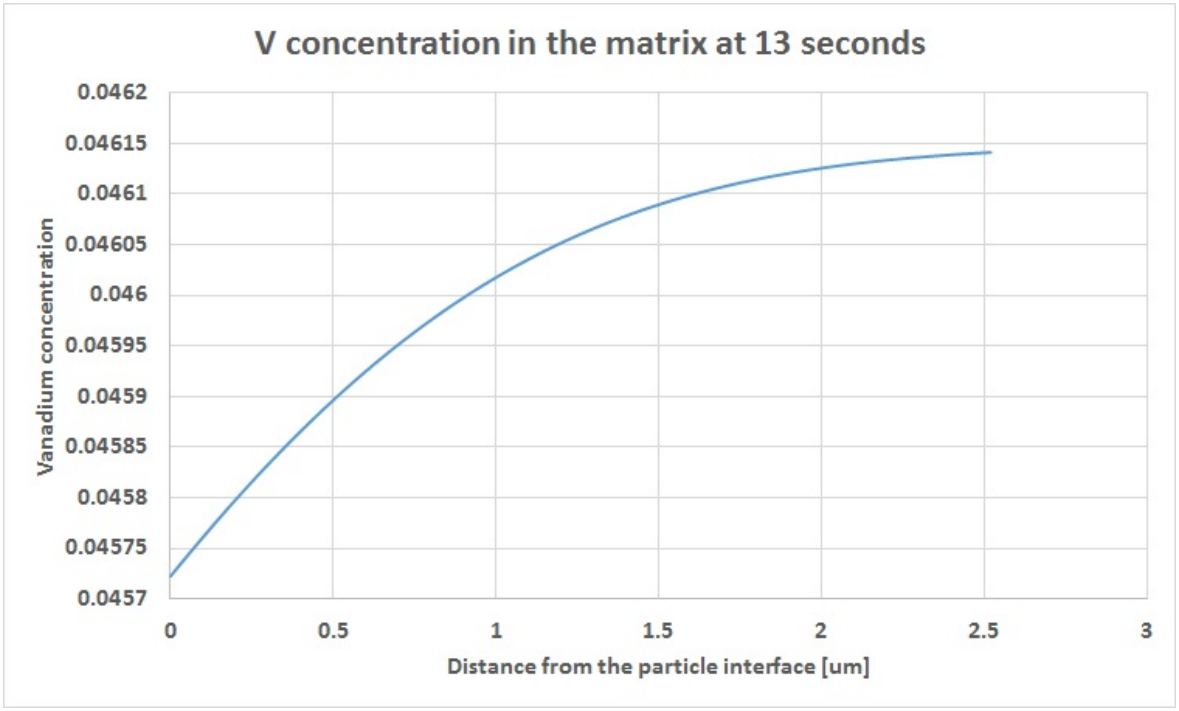

Figure 4.15.: Vanadium concentration in the matrix as a function of the distance from the precipitate interface at 1 and 13 seconds (figure a and figure b respectively) from the beginning of the heat treatment reported in figure 4.14, corresponding respectively to 954 °C and 945.9 °C

a)

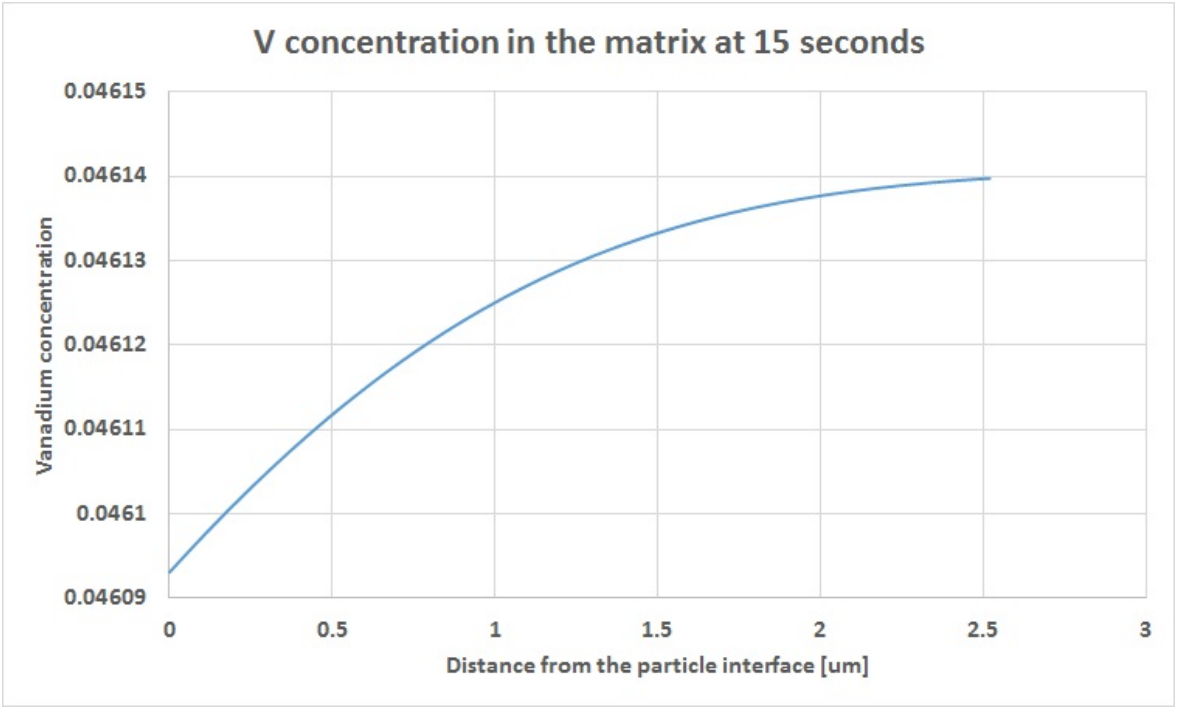

b)

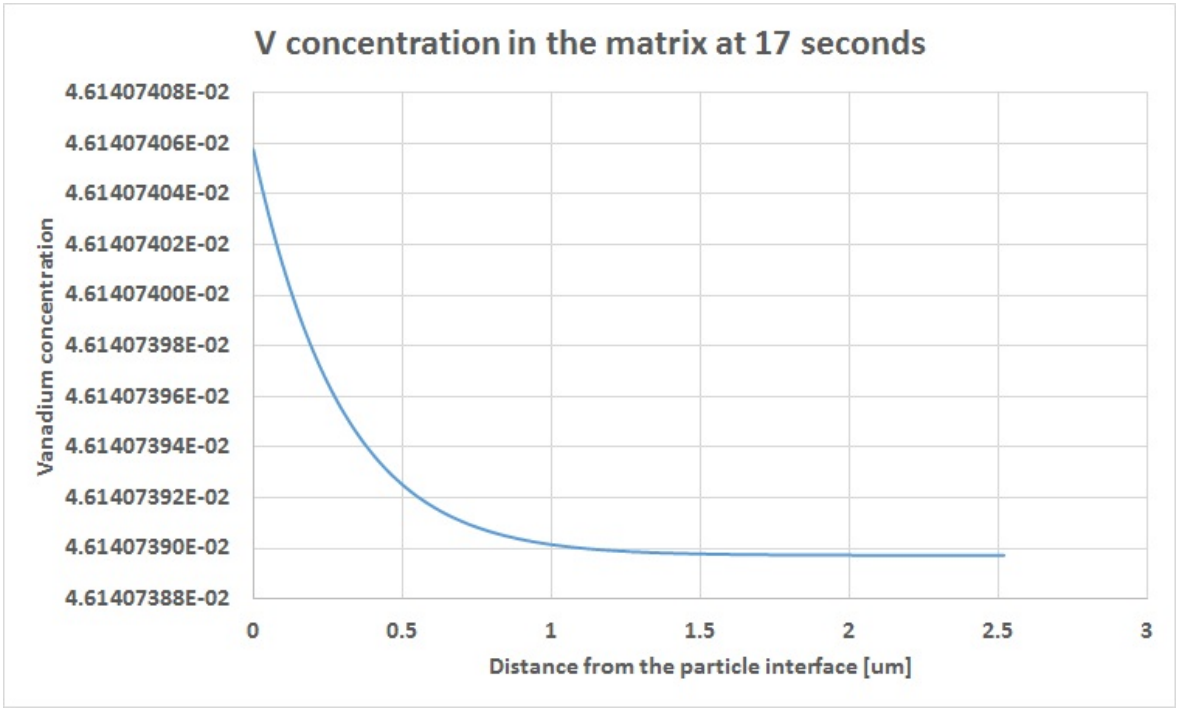

Figure 4.16.: Vanadium concentration in the matrix as a function of the distance from the precipitate interface at 15 and 17 (figure a and figure b respectively) seconds from the beginning of the heat treatment reported in figure 4.14, corresponding respectively to 944.5 °C and 943 °C. It is possible to notice the inversion of the Vanadium concentration field that makes the precipitate grow after an initial dissolution

a)

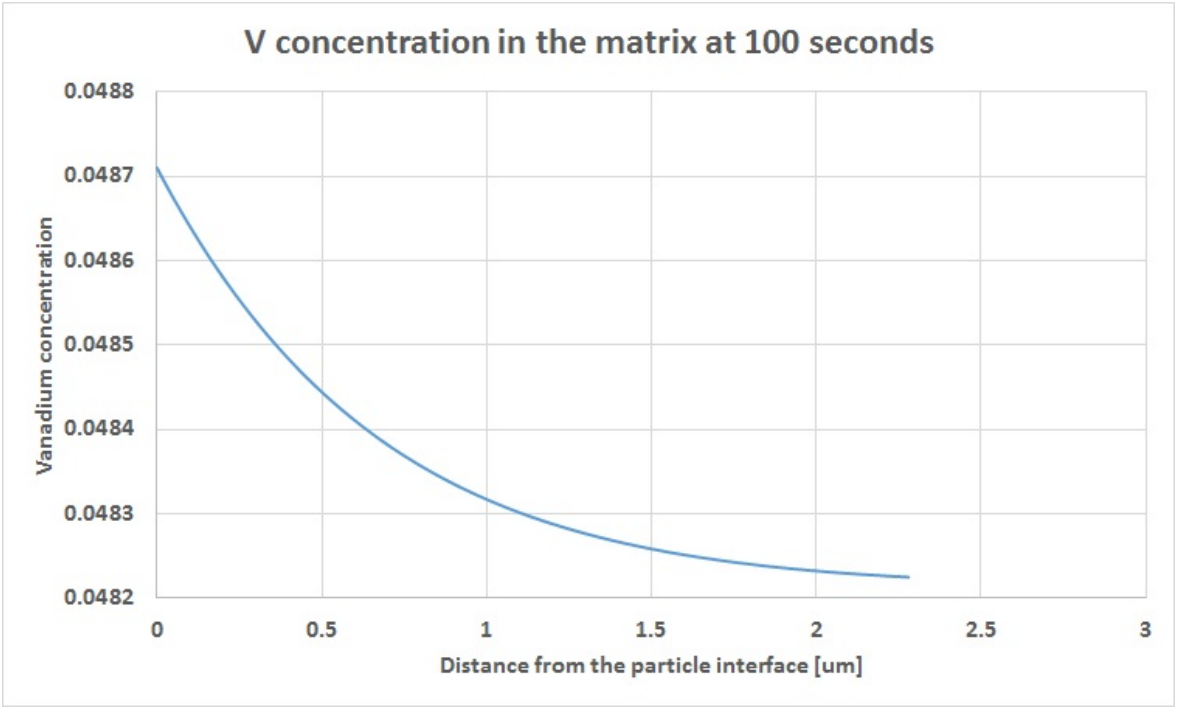

b)

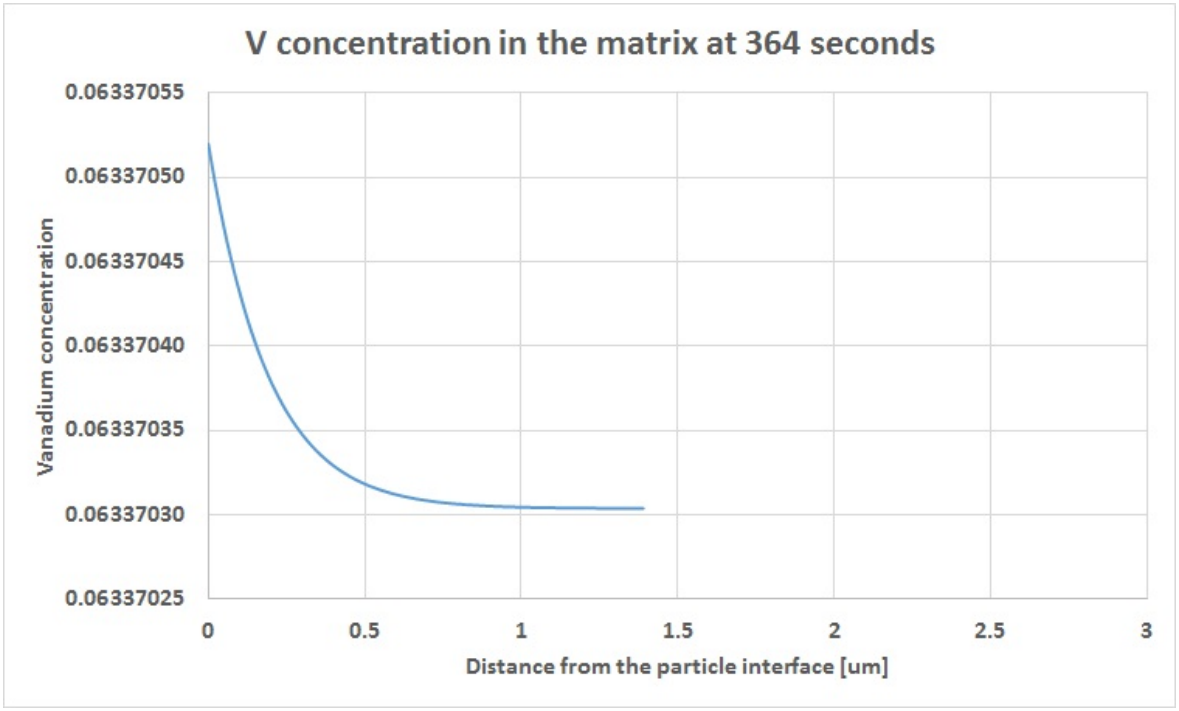

Figure 4.17.: Vanadium concentration in the matrix as a function of the distance from the precipitate interface at 100 and 364 (figure a and figure b respectively) seconds from the beginning of the heat treatment reported in figure 4.14, corresponding respectively to 885 °C and 700 °C

4.2.4.3 Lamellar precipitates dissolution

For the validation of the numerical model used to describe the evolution of the lamellar microstructure (see section 4.2.2), the experimental data reported in section 3.4.3 have been used and for clarity briefly listed below:

- aspect ratio 7.0
- initial lamellae thickness 3.0 μm
- initial alpha lamellar phase fraction 0.95
- mean Vanadium composition in the lamellar microstructure 2.47%
- mean Aluminium composition in the lamellar microstructure 5.495%
- overall Vanadium concentration 4.0479% in the material, as per the experimental measurements.

Since the model that describes the lamellar microstructure evolution showed very low sensitivity to small variations in the lamellae aspect ratio (figure 4.3), a value of 7 was assumed to be constant for the entire thermal treatments tested.

For the experimental data reported, only one sample was tested for each thermal condition. Thus for the volume fraction measurement the standard deviations error bar could not be computed, whilst for the lamellae thickness, since many particles were measured in the same specimen, the standard deviation is available.

Figure 4.18 reports the comparison between the numerical model predictions considering Vanadium as diffusing element and the experimental measurements carried out for samples tested at the heating rate of 5 °C/s. Figures 4.19 and 4.20 report respectively the comparisons for the heating rate of 50 °C/s and 500 °C/s. As shown, for temperatures close to the complete dissolution of lamellae, and for fast heating rates, the model would tend asymptotically to 0 in predicting the alpha lamellae thickness or phase fraction, this is because of the low supersaturation at this stage of the transformation that slows down

the shrinkage rate (section 4.2.2.2) and, for the very short times at fast heating rates, this results in dissolution happening at still relatively high temperatures. As shown in section 3.4.3, the diffusion process at fast heating rates does not allow sufficient time to dissolve completely the alpha phase but, it has also been shown that even though the local segregation is still visible in the SEM investigation, the switch in crystallographic structure from HCP to BCC occurs anyway, when the temperature passes the beta transus temperature of the material composition at the heating rate considered. For this purpose, the dissolution model presented in this section has been integrated with an experimental equation to predict the beta transus temperature as a function of the temperature rate (shown in section 4.3), to determine when the alpha phase is completely transformed in beta phase. This explains the sudden drop to 0 of the lamellae thickness and phase fraction shown in figure 4.18, 4.19 and 4.20.

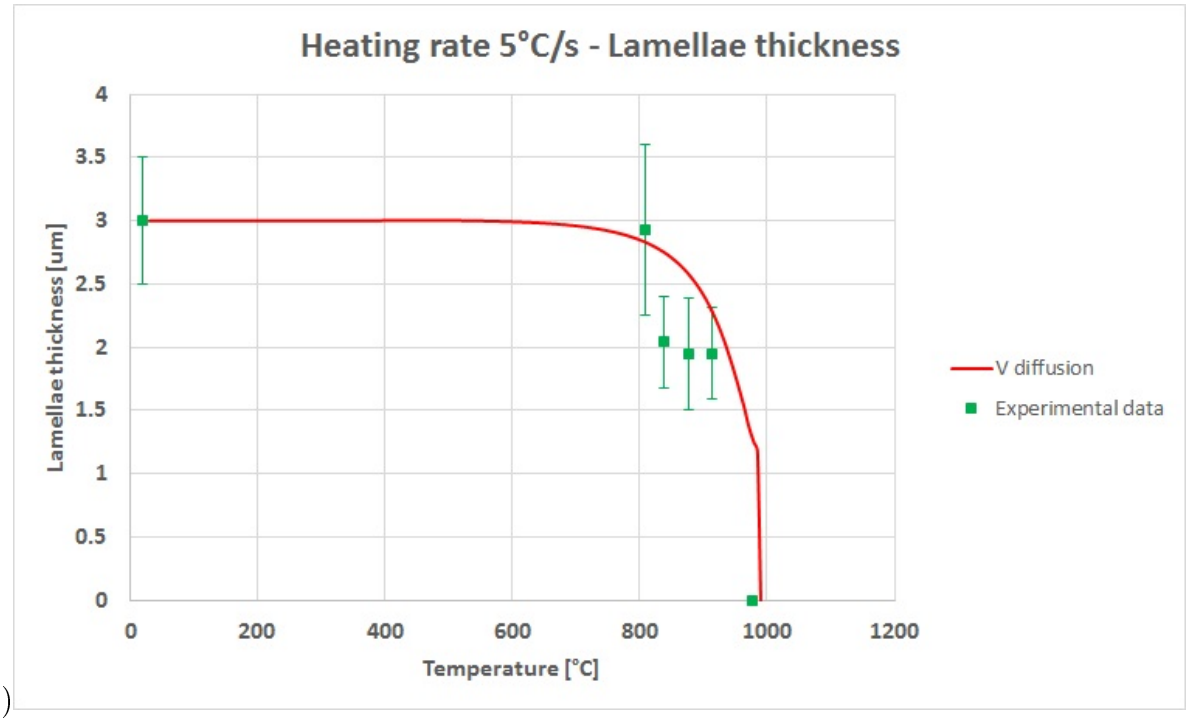

a)

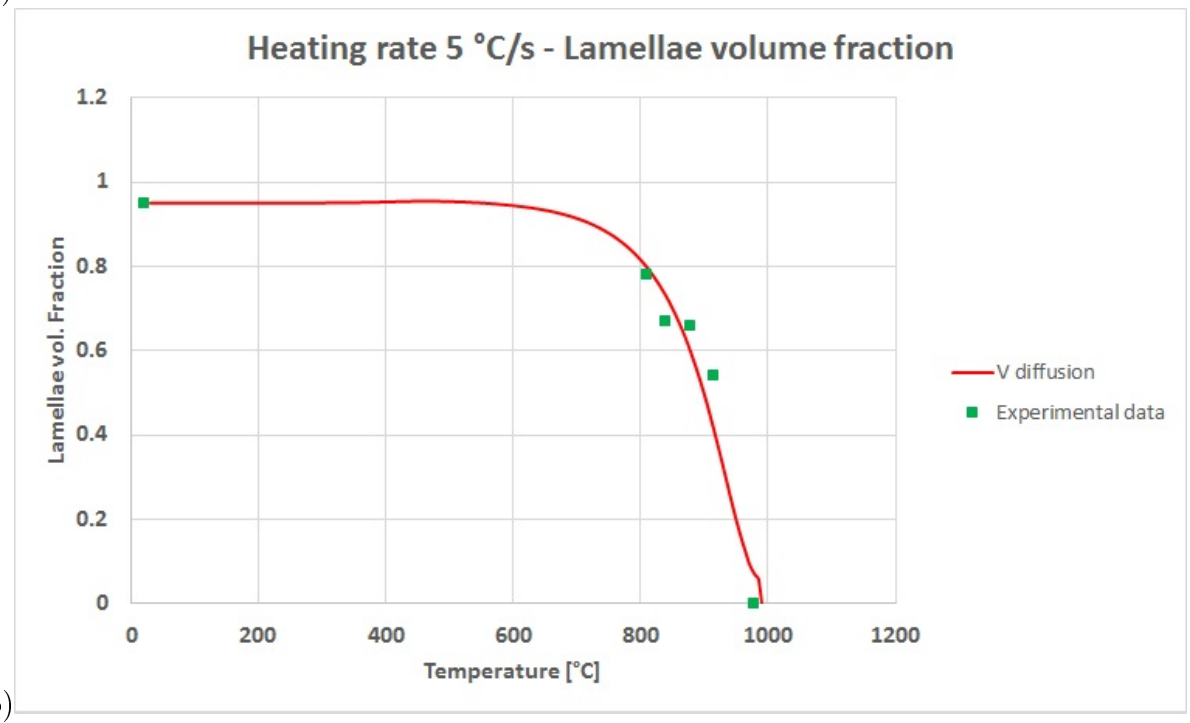

b)

Figure 4.18.: Lamellar microstructure comparisons between the numerical model considering Vanadium as diffusing element and the experimental measurements at the heating rate of 5 °C/s. a) Lamellae thickness, b) volume fraction lamellar microstructure

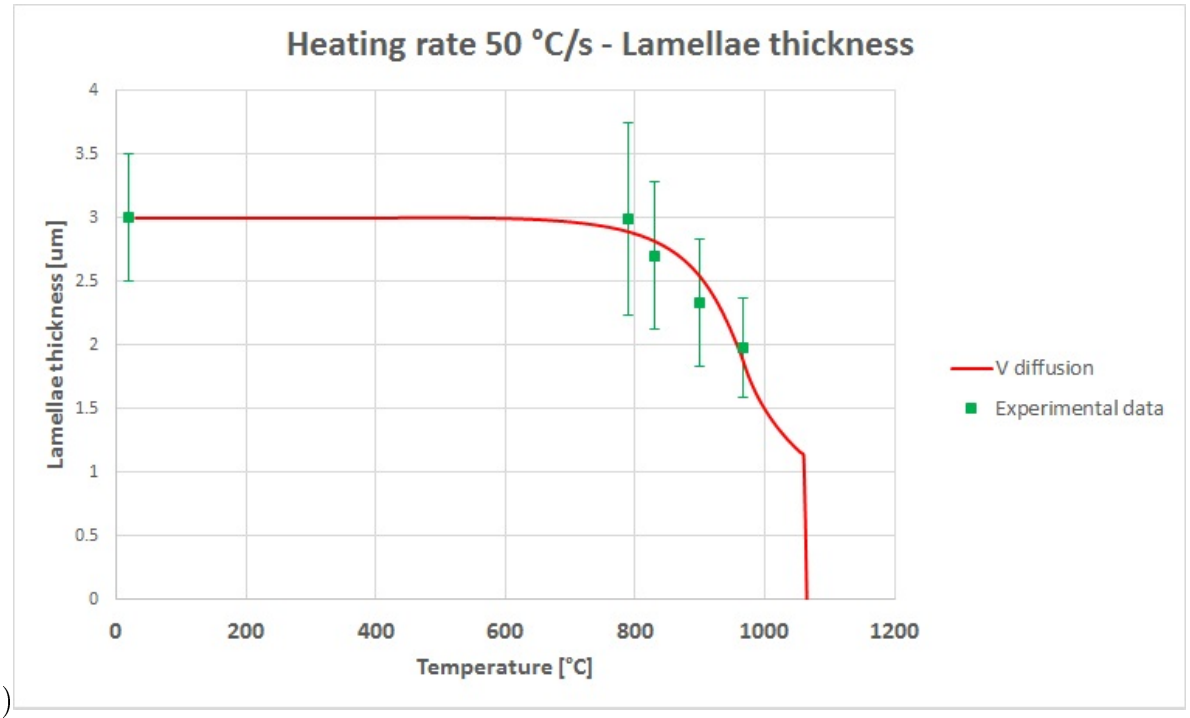

a)

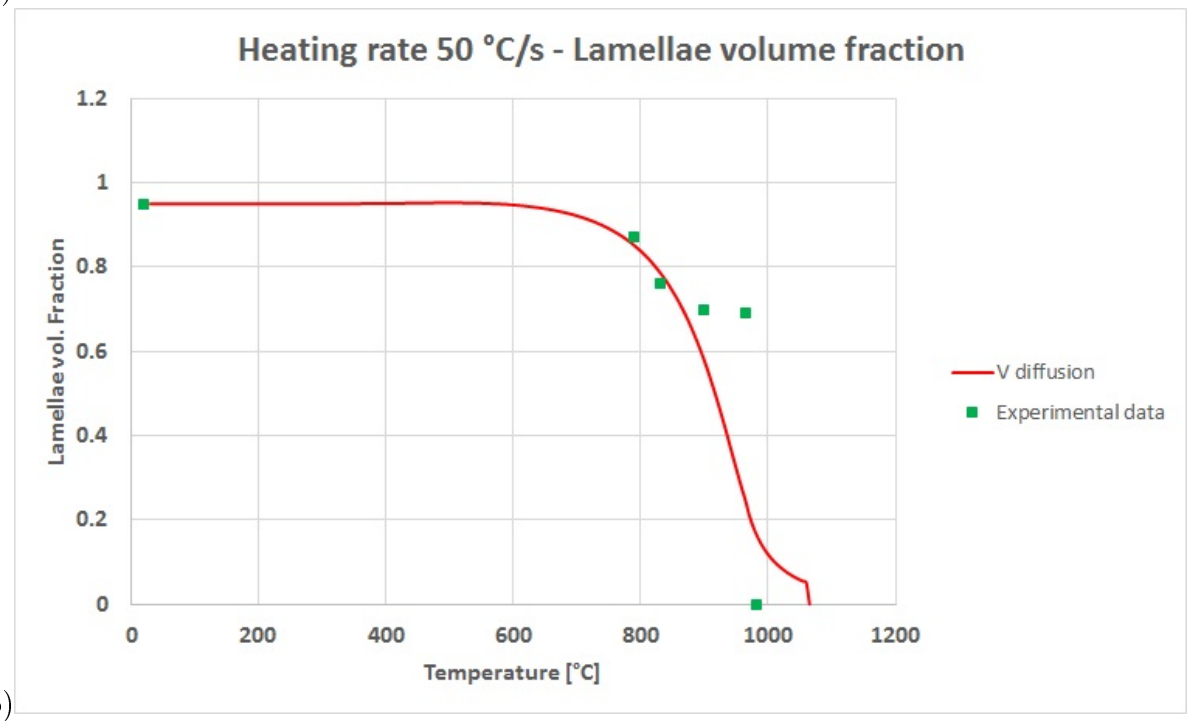

b)

Figure 4.19.: Lamellar microstructure comparisons between the numerical model considering Vanadium as diffusing element and the experimental measurements at the heating rate of 50 °C/s. a) Lamellae thickness, b) volume fraction lamellar microstructure

a)

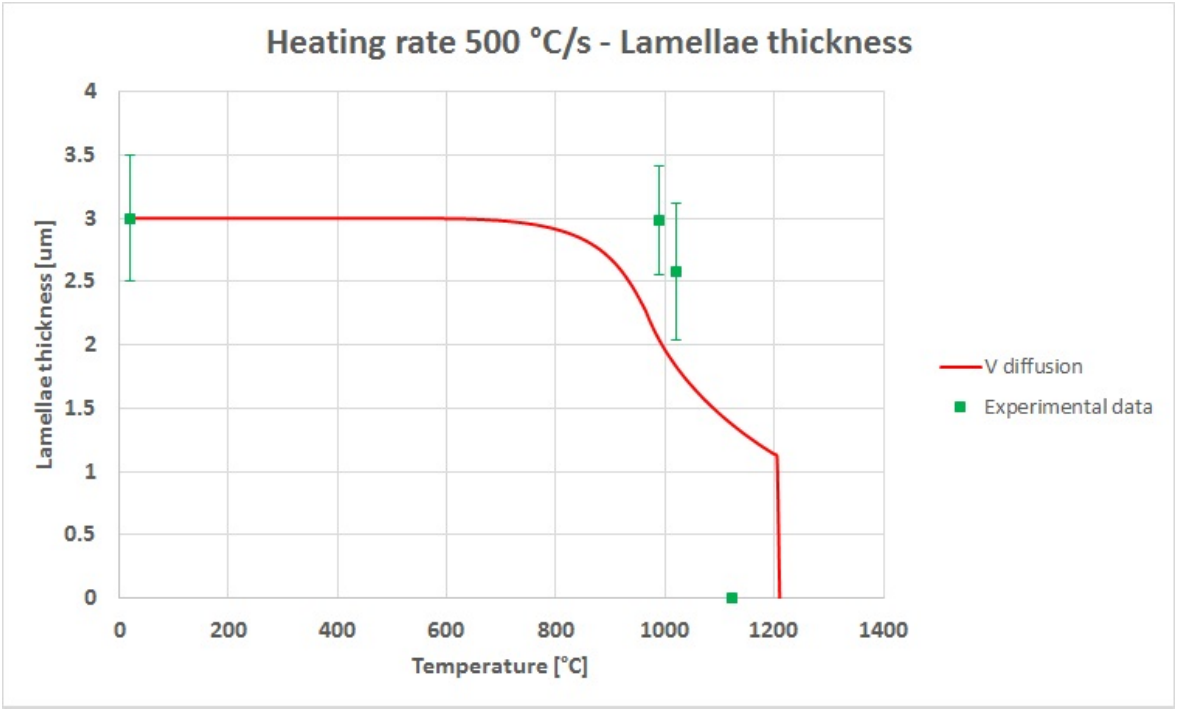

b)

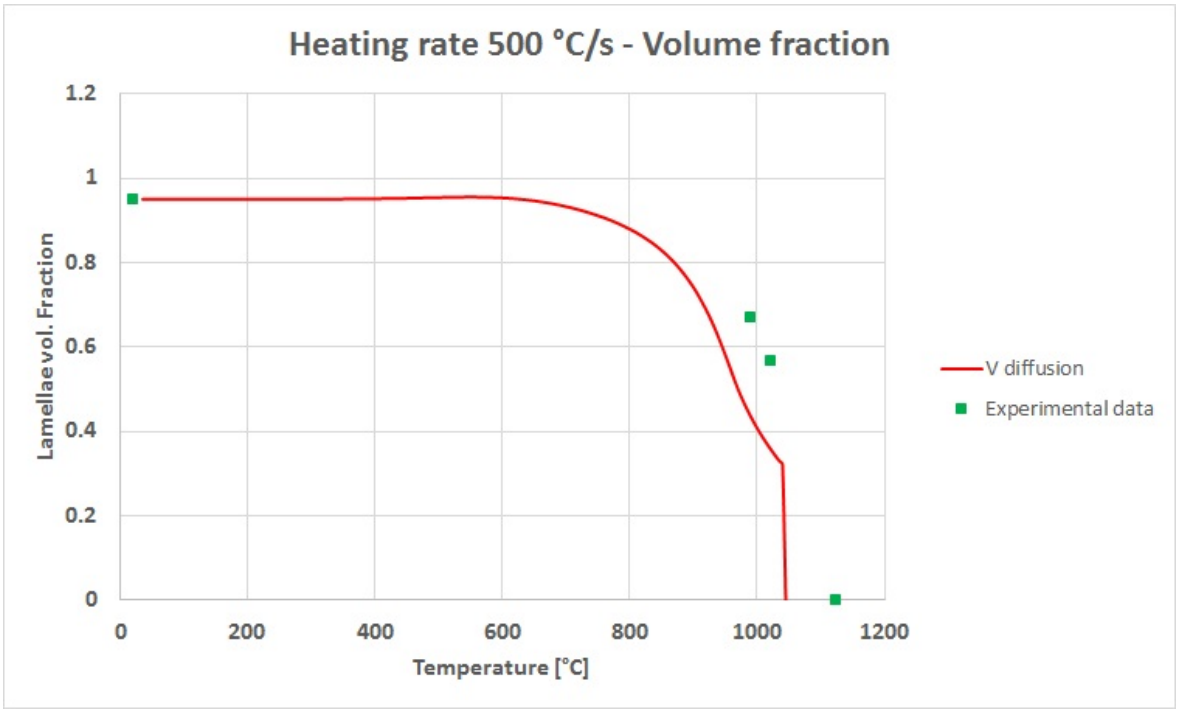

Figure 4.20.: Lamellar microstructure comparisons between the numerical model considering Vanadium as diffusing element and the experimental measurements at the heating rate of 500 °C/s. a) Lamellae thickness, b) volume fraction lamellar microstructure

4.3 Beta grain growth

For the description of the beta phase microstructure evolution above the beta transus, the phenomenological solution proposed in [73, 66] has been modified. In this approach, the beta grain dimensions data obtained from isothermal heat treatments are fitted to equation 2.5, reported again below for clarity.

$$d^n - d_0^n = A \times t \times \exp(-Q/\Upsilon T) \tag{4.39}$$

As written in section 2.3.6.3, this method was also adopted to describe the beta grain growth in Ti-6Al-4V for constant heating rate heat treatments, using the differential form of equation 2.6. Since the work only showed good agreement between experiments and numerical predictions for relatively low temperatures, a correction term to equation 4.39 has been applied to match the asymptotic trend shown by the grain growth. This correction factor was introduced for numerical purposes and has no particular physical meaning. The inverse tangent function was used to provide an asymptotic trend to equation 4.39, that otherwise would predict exponential behaviours for non constant times and temperatures. The new equation obtained is shown below:

$$d^n - d_0^n = A \times t \times \exp(-Q/(\Upsilon T_2)) \tag{4.40}$$

where

$$T_2 = atan\left(-\frac{T}{B}\right) * \frac{B}{atan(1)} \tag{4.41}$$

Where T_2 represents the correction factor and B a constant to be fitted to the experimental data.

The experimental data obtained in this work, shown in figure 3.41, together with some estimated data points at low and high temperatures (1600 °C) have been used to fit the

equation parameters B, Q and A in temperature ranges of interest for this work (figure 4.21). The author desires to point out that experimental tests at temperatures higher than 1250-1300 °C were planned but, for a technical problem at the testing machine, experiments could not be carried out in time for the end of this project.

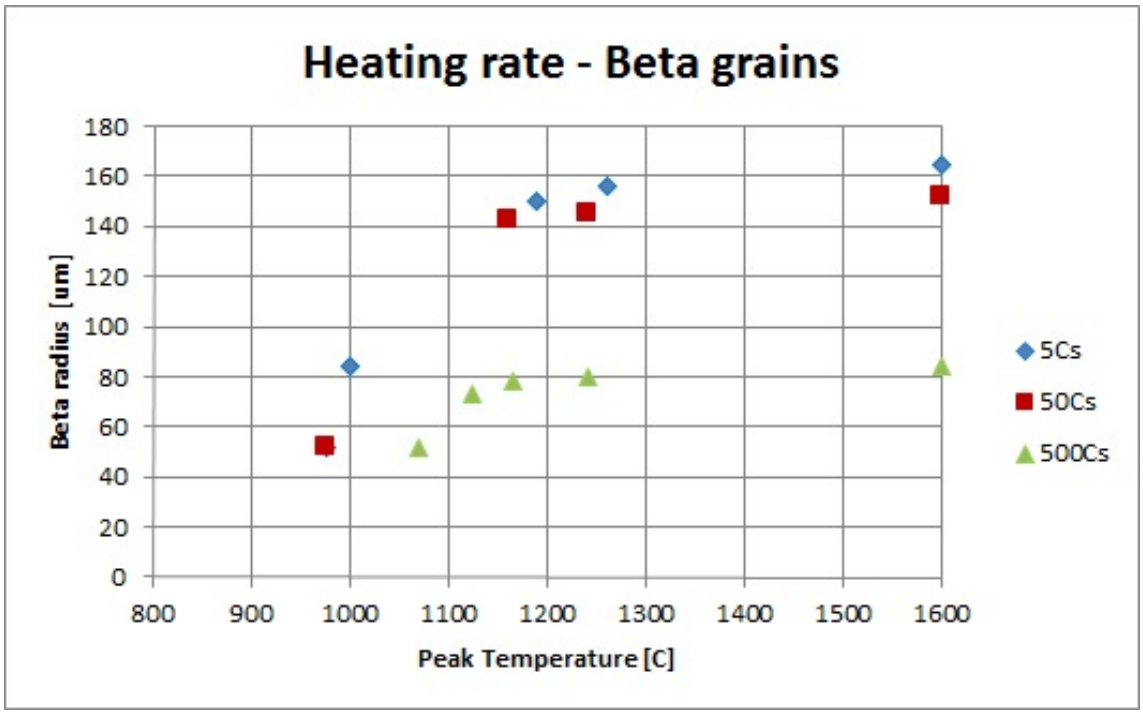

Figure 4.21.: Beta grain dimension data used for the calculation of the grain growth equation parameters. They are the same as figure 3.41 with estimated points at 1600 °C

The set of parameters obtained fitting the equation 4.40 to the data points of figure 4.21 is reported in the table 4.1 and the relative grain growth predictions for the same heating rates of the experiments shown in figure 4.22.

n	A	Q	M
	$[\mu m^n/s]$	[J/mol]	
8	8.688x10^9	203,810	1140

Table 4.1.: Parameters obtained from the current work by fitting equation 4.39 to the experimental results shown in figure 3.41

Since equation 4.40 needs implicitly to know at which temperature beta grains start to nucleate, the numerical approach presented in [61], based on isochronal conditions applied

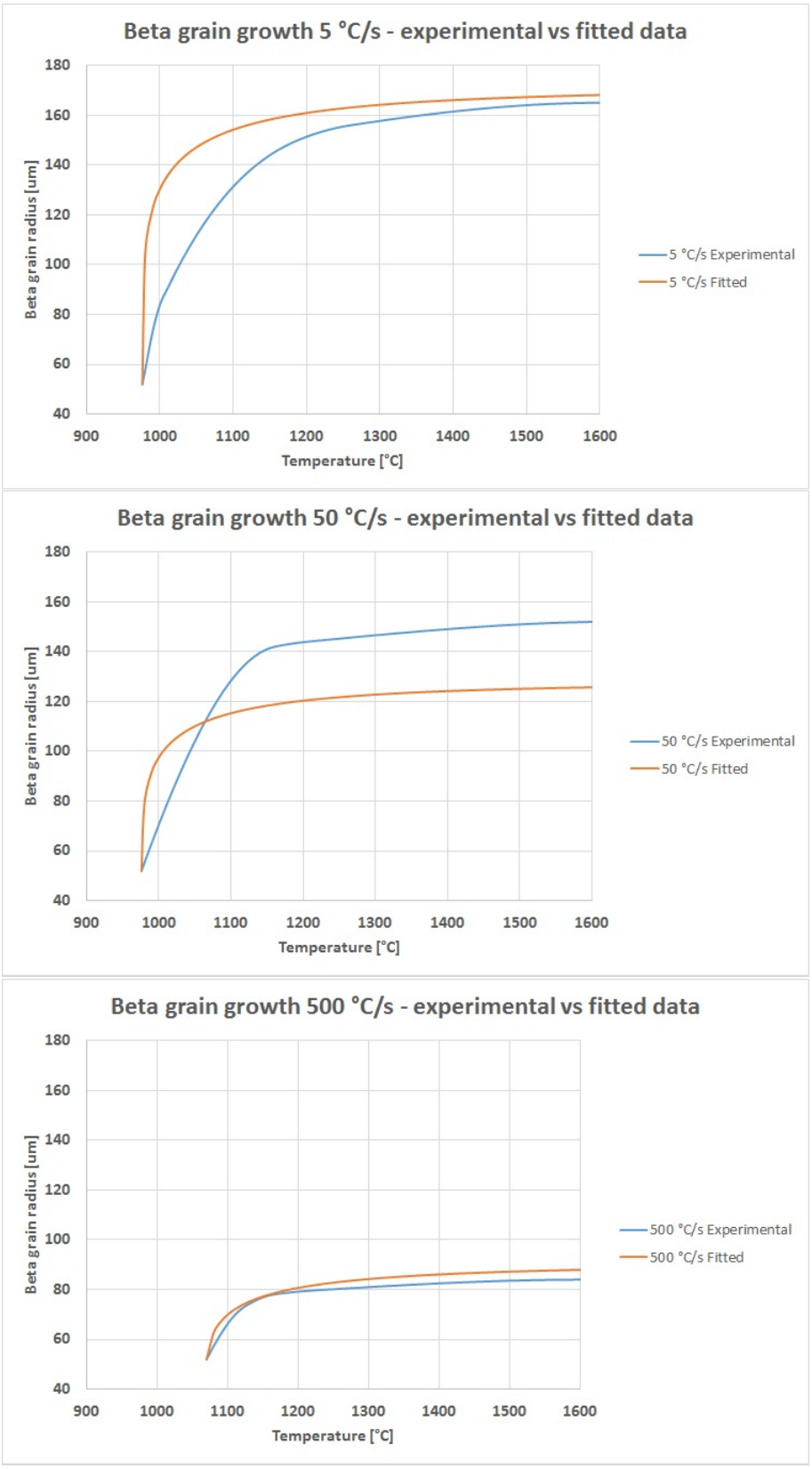

Figure 4.22.: Comparison between experimental data and numerical model prediction of the beta grain growth at different heating rates

to the JMA equation 4.42 has been used, returning equation 4.44.

$$f = 1 - exp(-\eta^p) \tag{4.42}$$

$$\eta = kt = k_0 t\, exp\left(-\frac{E}{\Upsilon T}\right) \tag{4.43}$$

$$\ln \frac{T_{\beta\phi}^2}{\Phi} = \ln \frac{E}{\Upsilon k_0} + \frac{E}{\Upsilon T_{\beta\phi}} + \frac{J}{n^2}\frac{\Upsilon T_{\beta\phi}^2}{E} \tag{4.44}$$

With k_0 pre exponential factor, E activation energy of the phase transformation considered, Υ gas constant, T temperature in Kelvin, Φ temperature rate, J constant, p exponential factor, $T_{\beta\phi}$ the beta transus temperature at a specific temperature rate ϕ.

Once equation 4.44 has been fitted to the beta transus temperatures at different heating rates for a Ti-6Al-4V alloy of known chemical composition, it is possible to predict the beta transus temperature at a desired heating rate and, by applying an empirical relationship with the alpha or beta stabilizer elements in a Ti-6Al-4V alloy, it is possible to predict the beta transus temperature for the desired chemical composition.

The relationship used to describe the effect of the alloying elements was obtained by running simulations of Ti-6Al-4V with different chemical compositions in the commercial software JMatPro and quantifying their effect on the beta transus temperature. From equations 4.45 and 4.46 the equivalent Aluminium and Vanadium content for a specific alloy are calculated, thereafter multiplying the values obtained by 20 for Al_{eq} and -20 for V_{eq} the total effect on the variation of the beta transus temperature with respect to the reference alloy can be calculated (equation 4.47).

$$Al_{eq\,new\,alloy} = Al + 10\,O + 40\,N \tag{4.45}$$

$$V_{eq\,new\,alloy} = V + 66\,H + 1.25\,Fe \tag{4.46}$$

$$\Delta T_{\beta} = (Al_{eq\,reference\,alloy} - Al_{eq\,new\,alloy})\,20 - (V_{eq\,reference\,alloy} - V_{eq\,new\,alloy})\,20 \quad (4.47)$$

4.3.1 Results and discussion

In figure 4.23 the data obtained for the alloy experimentally studied in section 3.4 for which the beta transus temperatures were known in ranges of heating rates from 5 K/s to 500 K/s is shown. The predictions of the beta transus for heating rates faster than 500 K/s were made by applying equation 4.44, whilst the beta transus temperatures for the other two representative alloys, one with more alpha stabilisers and one with more beta stabilisers, were made using equations 4.45, 4.46 and 4.47.

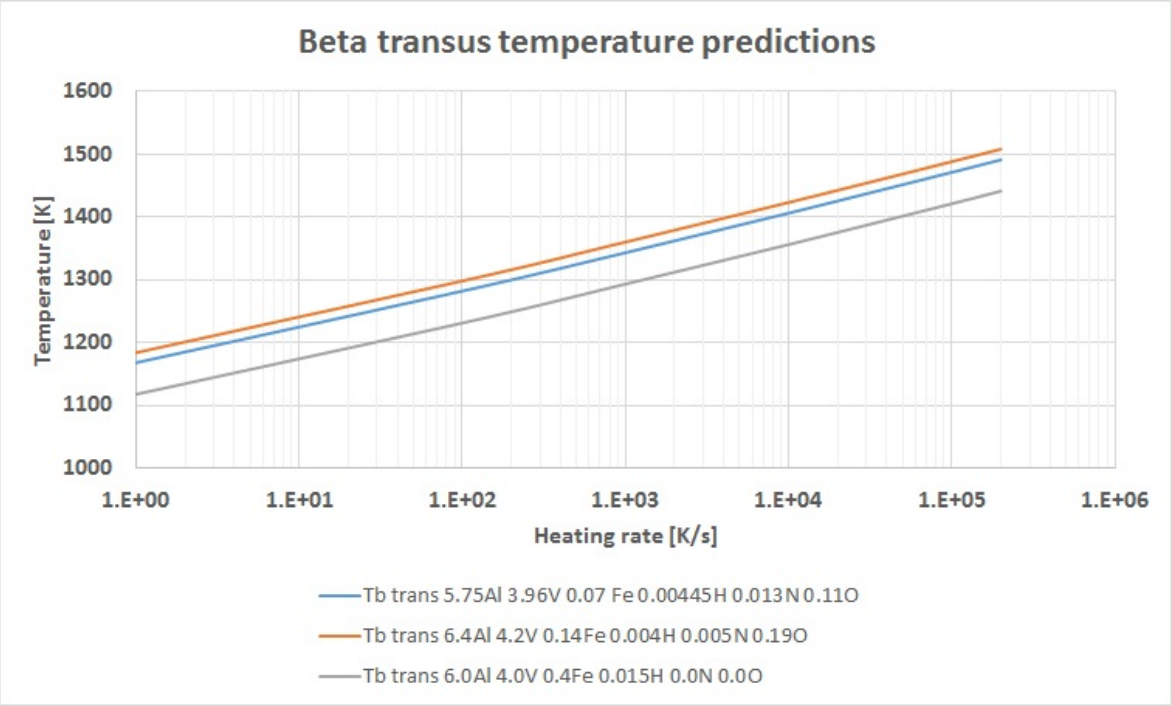

Figure 4.23.: Beta transus temperature predictions as a function of the heating rate and chemical composition

Once the beta transus temperature is known, for the alloy desired, equation 4.40 can be applied to get predictions on the beta grain growth evolution as a function of the heating rate, as for example, figure 4.24 shows.

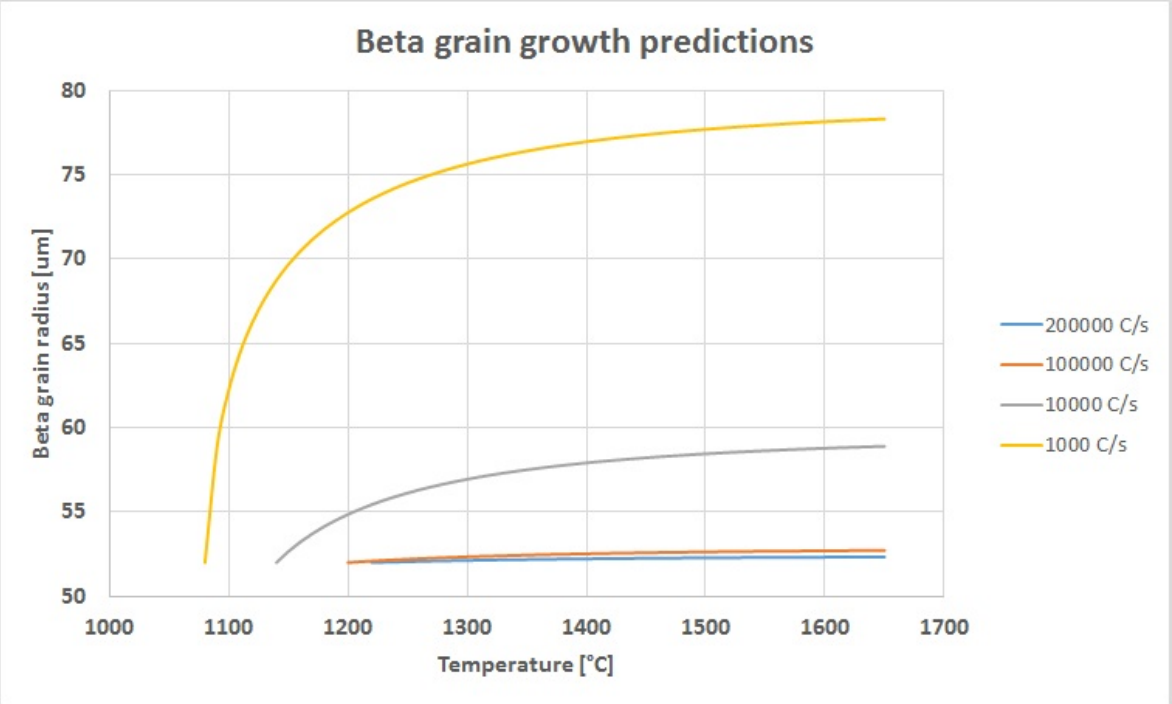

Figure 4.24.: Beta grain growth predictions as a function of temperature and heating rates

The predictions of beta grain growth have been done using a phenomenological equation widely used in literature, for ease of use.

A physically based approach would have been necessary to describe nucleation and growth competition of the beta grains. As a field this is still not well developed in the literature in the form of analytical expressions, requiring more experiments to set the parameters for the nucleation equations. The fast heating rates involved in welding would not have allowed model validation as facilities to apply the extreme thermal treatments to the material are not readily available.

By the approach used in this work, the model can still predict the beta transus temperature as a function of the alloy chemical composition and temperature rate, even if it is necessary to carry out experiments to set the initial beta grain size for the beta transus temperature of the alloy considered.

Thus although equation 4.40 is not able to self adapt to different alloy chemical compositions, the disadvantages brought from its adoption were considered to be well balanced by the advantages obtained. Furthermore it has been possible to set a model able to

predict reasonable beta grain growth values for extremely fast heating rates from a small number of experiments.

4.4 Lamellae nucleation

As mentioned at the beginning of this chapter (section 4.1), the alpha lamellae nucleation and growth, cooling down from the beta field, has been described by an experimental equation (equation 4.48).

$$Lamellae\,thickness\,[\mu m] = \phi \times -0.0013 + 0.0787 \times \ln(d) \tag{4.48}$$

Where ϕ represents the cooling rate of the heat treatment and d the mean beta grain size diameter $[\mu m]$ in which lamellae nucleate and grow.

The parameters of the equation 4.48 were obtained by fitting to the experimental data, adding some estimated points to the ones collected experimentally in this work, to provide a sufficiently wide range of beta grain dimensions to let the fitting algorithm work properly (figure 3.28-a vs figure 4.25).

4.4.1 Results and discussion

The trends obtained from the equation 4.48, for cooling rates ranging from 5 °C/s to 300 °C/s are compared with the experimental data in figure 4.25. For faster cooling rates and the same beta grain dimensions, the lamellae thickness obtained at the end of the heat treatment is thinner than the one obtained at a slower cooling rate. This can be related to the shorter time the lamellae have to grow at the faster cooling rates. Also, for the same cooling rate, the bigger is the beta grain where lamellae nucleate and grow, then the thicker the lamellae are at the end of the thermal process as, already discussed and reported in section 3.4.4, a larger beta grain volume allows nucleation of lamellae statistically more widely spaced and, as result, they hypothetically will impinge on themselves at a later stage in the diffusional growth process.

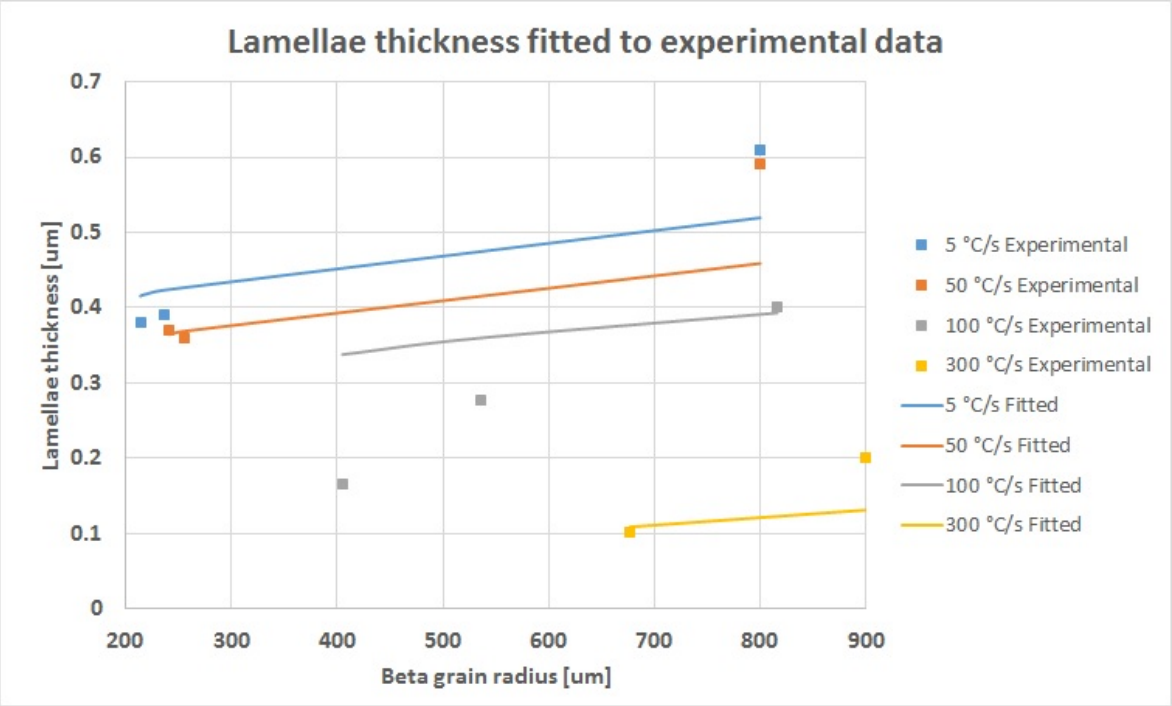

Figure 4.25.: Graph showing the experimental data compared to the predictions obtained applying the equation 4.48

Applying equation 4.48 to a series of beta grain radius, going from 0 to 900 µm, the lamellae thickness predicted, for cooling rates of 5 °C/s, 100 °C/s and 300 °C/s, are shown in figure 4.26. Even though this approach is not physically based, the lamellae trends predicted seem to reflect how the real behaviour (section 4.2.2), with a initial faster lengthening and minimal growth in thickness until mechanically impingement of the lamellae, than a slower thickening stage follows.

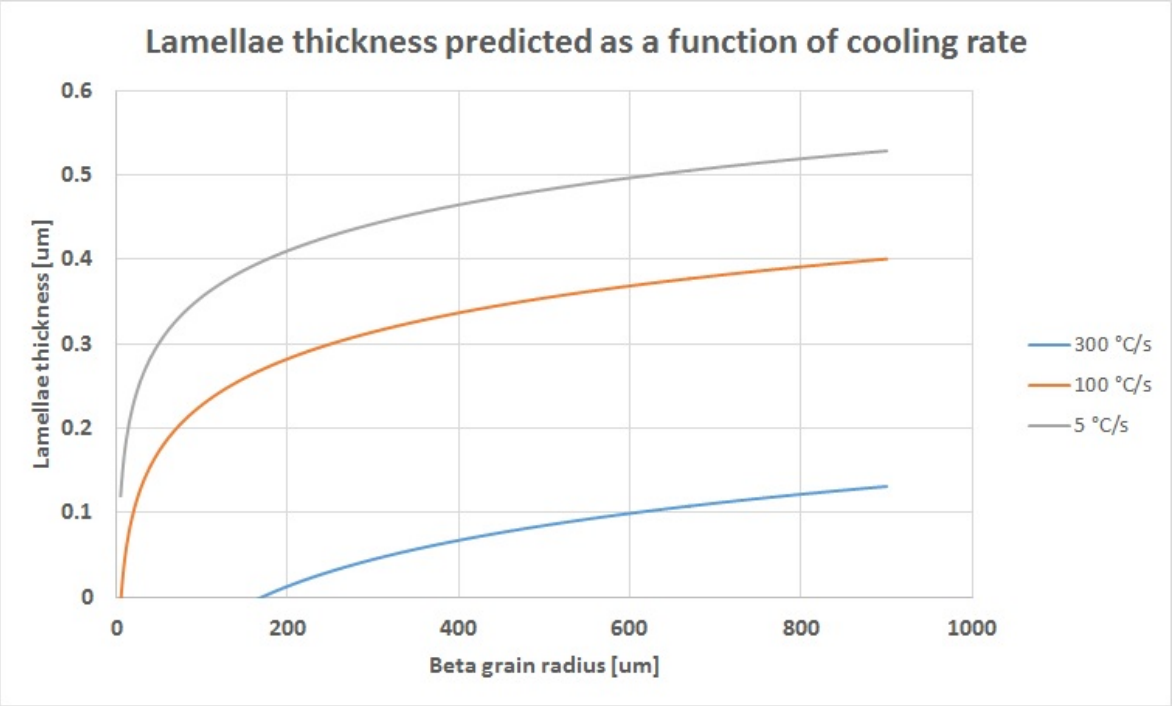

Figure 4.26.: Lamellae thickness predicted as a function of the cooling rate and beta grain radius

4.5 Martensitic model

The martensitic phase fraction evolution has been described as a function of the cooling rate by fitting an equation to the experimental data collected in section 3.4.4 and shown in figure 3.32. This model is based on the hypothesis that on cooling the material from temperatures above beta transus, the beta phase fraction not transformed to alpha phase is entirely transformed to martensite, as the cooling rates considered are fast enough to convert the residual beta phase into martensite.

$$\alpha'_{vol\ fraction} = \left(2.6245 - \arctan\left(\frac{dT}{dt} - 64.9971\right)\right) \times 20.4014 \tag{4.49}$$

The comparison between the experimental measurements of the martensitic phase fraction and the numerical predictions from the fitting equation 4.49, reported in figure 4.27, shows a good matching between the two trends.

The coarsening of the martensitic needles has been described by another equation based

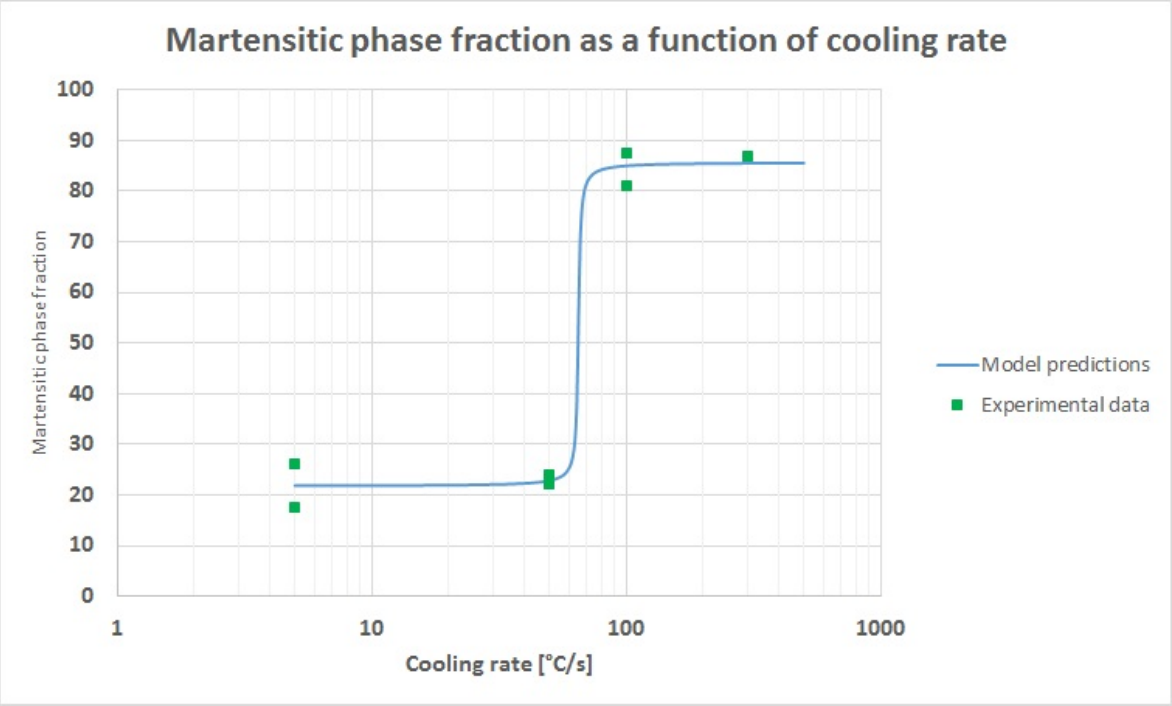

Figure 4.27.: Martensitic phase fraction as a function of cooling rate. Comparison between model predictions and experimental data

on the experimental data described in section 3.4.4. A logarithmic relationship with cooling seems to fit very well in this case. The results obtained by applying the fitting equation 4.50 compared with the experimental data are shown in figure 4.28.

$$Needle\,thickness = 0.0857 \ln\left(\frac{dT}{dt}\right) - 0.1136 \tag{4.50}$$

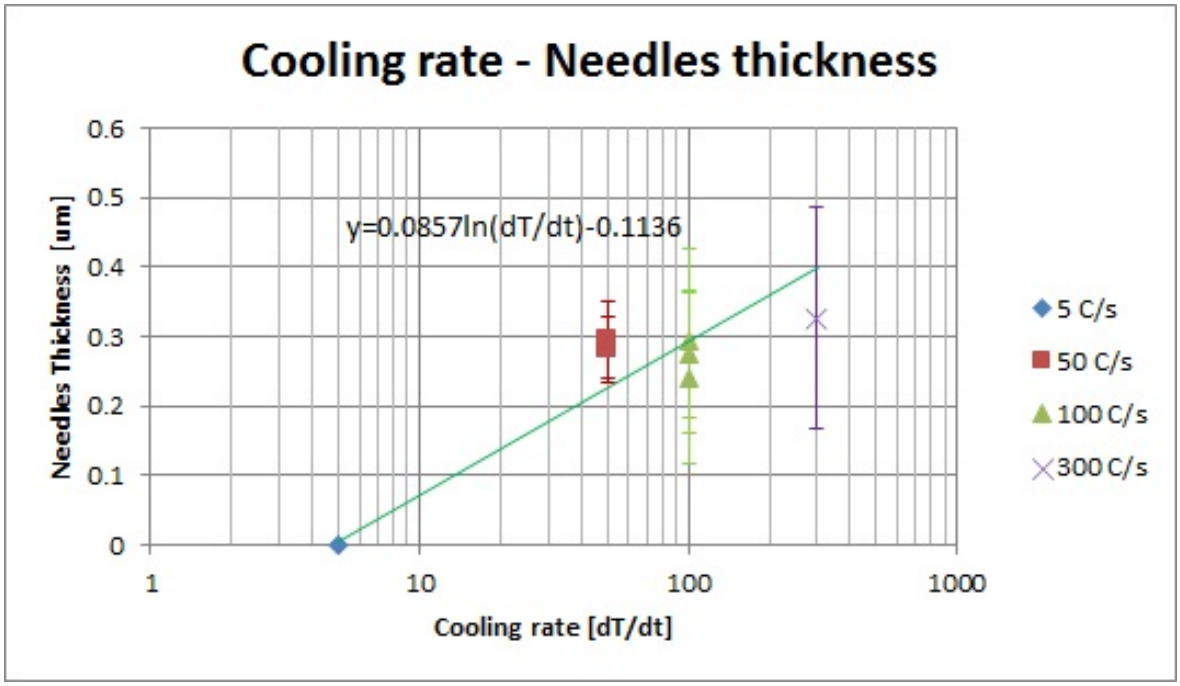

Figure 4.28.: Needle thickness as a function of the cooling rate. Experimental data (points) and interpolating function (green line)

4.5.1 Results and discussion

Since in literature there was no alternative solution to the phase field approach for the modelling of the martensitic microstructure evolution, which was considered too complex to be adopted in this work, where acceptable running times represent an important final objective, an experimental approach has been used.

Fitting equations have been coded to model both the martensitic volume fraction and needles thickness as a function of the cooling rate, obtaining a good match with experimental data. In particular, the martensitic volume fraction is well fitted by an arctangent function with the knee between 50 and 100 °C/s, while the needles thickness is well described by a logarithmic function.

4.6 Welding simulations

The numerical microstructure models developed and described previously in this chapter have been coded in subroutines for the commercial software Visual-Weld, to run welding

simulations able to predict the microstructural evolution of the material during the joining process. To validate the predictions of the welding simulations, the results have been compared with the data obtained from the experimental welding tests described in detail in section 3.5.

4.6.1 Workpieces and operative conditions

The different initial microstructures, chemical compositions of the material and geometries of the workpieces tested are summarised hereinafter.

Chemical compositions

- Plate 1 Equiaxed - Al 5.82, V 4.00, Fe 0.06, H 0.00963, N 0.010, O 0.063, Ti bal
- Plate 1 and 2 Lamellar - Al 5.75, V 3.96, Fe 0.07, H 0.00445, N 0.013, O 0.11, Ti bal

Plates tested geometry

- Plate 1 Equiaxed -46.95 $\times$ 151.5 $\times$ 2.00 mm^3
- Plate 1 Lamellar - 47.30 $\times$ 136.965 $\times$ 3.76 mm^3
- Plate 2 Lamellar - 47.31 $\times$ 137.05 $\times$ 3.06 mm^3

Operative parameters

- Plate 1 Equiaxed - 60% power, welding speed 2m/min
- Plate 1 amd 2 Lamellar - 70% power, welding speed 2m/min

4.6.2 Thermal material properties

The material thermal properties, used for the numerical simulations, are based on the mean values of thermal conductivity, specific heat and density obtained from several literature sources (private communication from prof Jeffery Brooks).

Making reference to the beta transus of the different materials, the thermal properties due to phase change have been consequently shifted to coincide with the transition area.

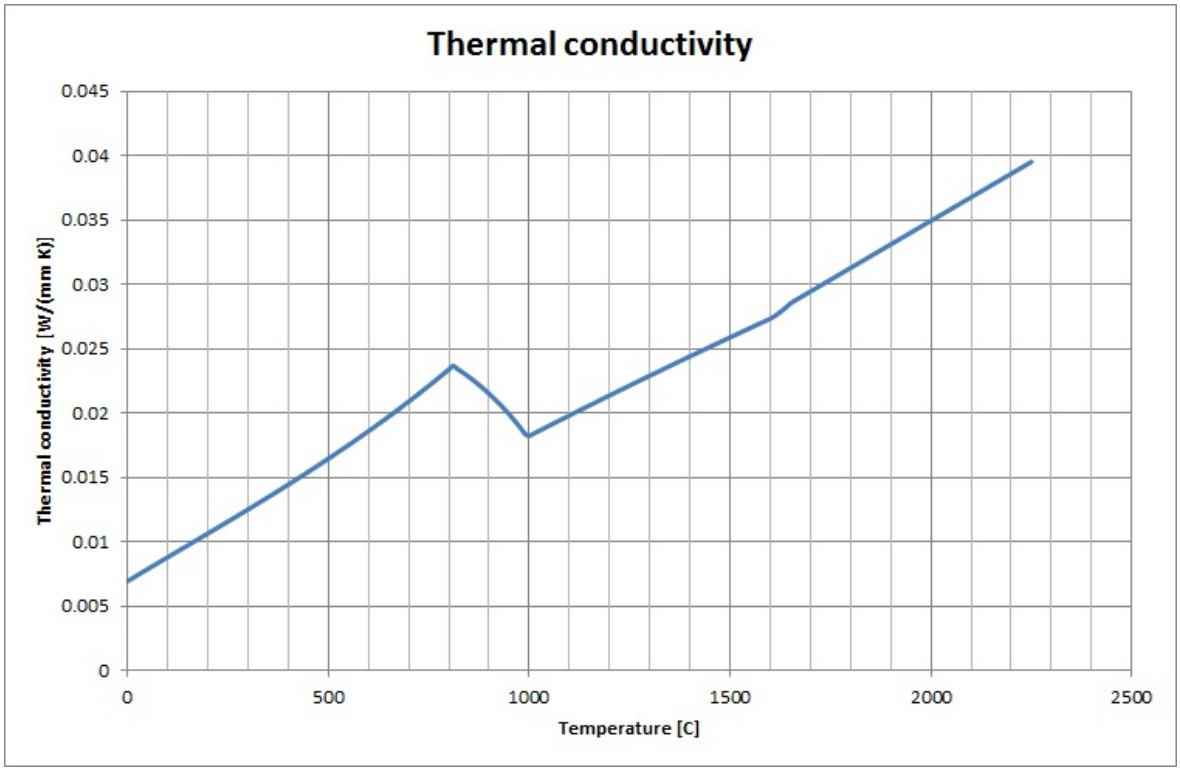

Figure 4.29.: Graph showing the Ti-6Al-4V thermal conductivity as a function of temperature used for the numerical simulations in Visual-Weld

In figures 4.29, 4.30 and 4.31 the thermal conductivity, specific heat and density used for the numerical simulations are shown, with the dimensions required by Visual-Weld.

In figure 4.30, it is possible to notice how the specific heat corresponding with the liquidus temperature has been scaled over a wider range of temperatures, keeping constant the area representing the latent heat of melting, this was needed to get stability of the numerical simulations and reduce running times.

4.6.3 Model mesh

The mesh used for the welding simulations was made of 201,520 quad linear elements, with a higher density close to area of the weld pool, to decrease the temperature gradient along the elements subjected to very high variations of temperature in space and time. Far from the weld pool, the number of elements along the thickness of the model was kept to 6, as this value is the limit at which linear elements can correctly represent bending of thin plates (figure D.6, D.7 and D.8). In figure 4.32 and 4.33 an entire view of the mesh

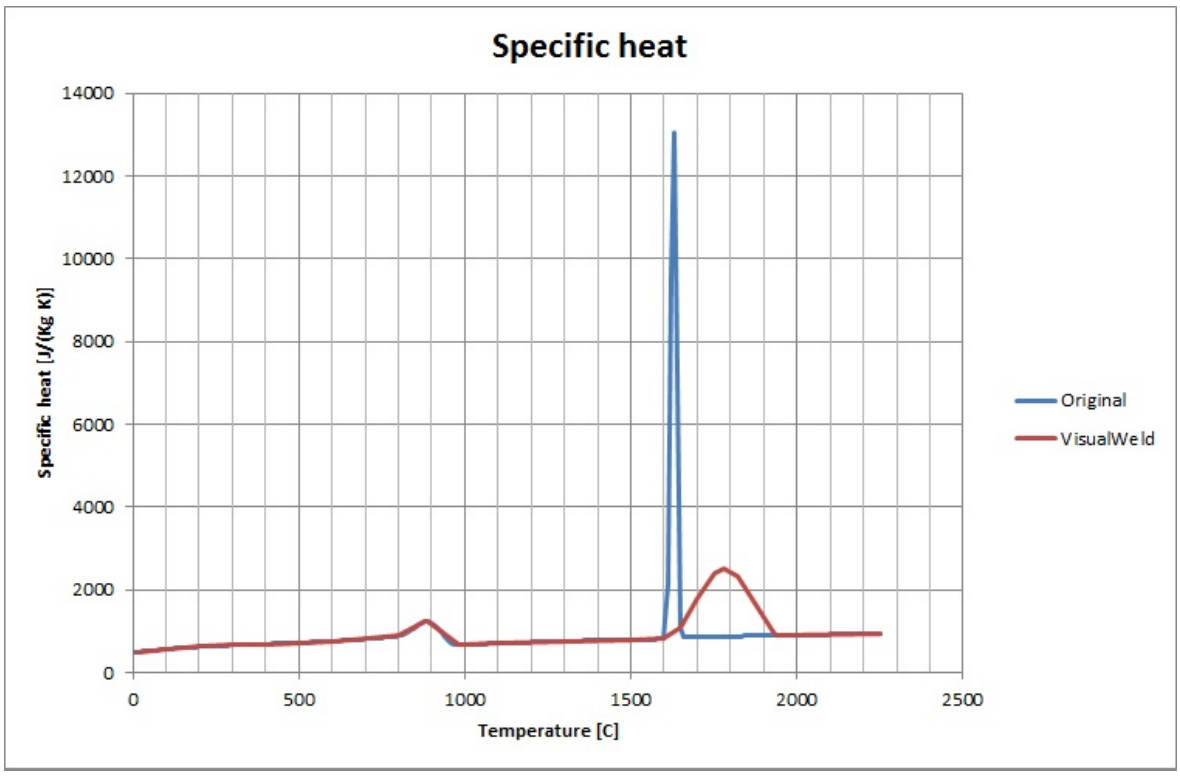

Figure 4.30.: Graph showing the Ti-6Al-4V specific heat as a function of the temperature used for the numerical simulations in Visual-Weld. Since the variation of this dimension, in correspondence of the liquidus temperature, was too high for the numerical convergence of the numerical simulations, the latent heat of melting has been spread out on a wider range of temperatures

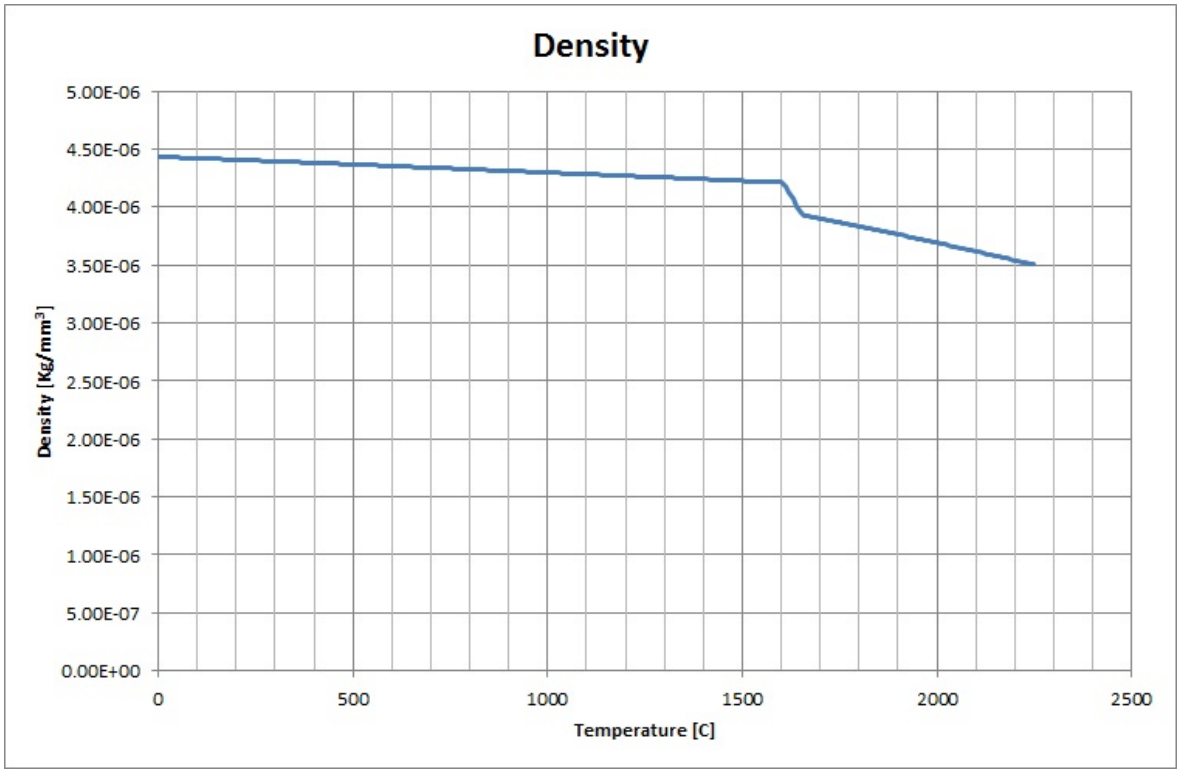

Figure 4.31.: Graph showing the Ti-6Al-4V density as a function of the temperature used for the numerical simulations in Visual-Weld

of the model and a zoom close to the weld trajectory are shown respectively.

The mesh used for the welding simulation of the plate with equiaxed microstructure was less fine in the weld pool area as, for this case, mechanical simulations were not run. A finer mesh allows a reduction in the stress gradient along each mesh element, caused by temperature gradient and the variation of the microstructure during the welding process.

4.6.4 Boundary conditions

The plates were clamped only on the left side as they were in the experiments.

All the external surfaces were set as in contact with air at 40 °C, as the temperature measured at the end of the welding tests. In reality this temperature changes during the welding tests but, as a simplification, it has been assumed constant.

The convection coefficient has been assumed as a function of temperature, as shown in figure 4.34.

The emissivity has been assumed constant and equal to 0.8.

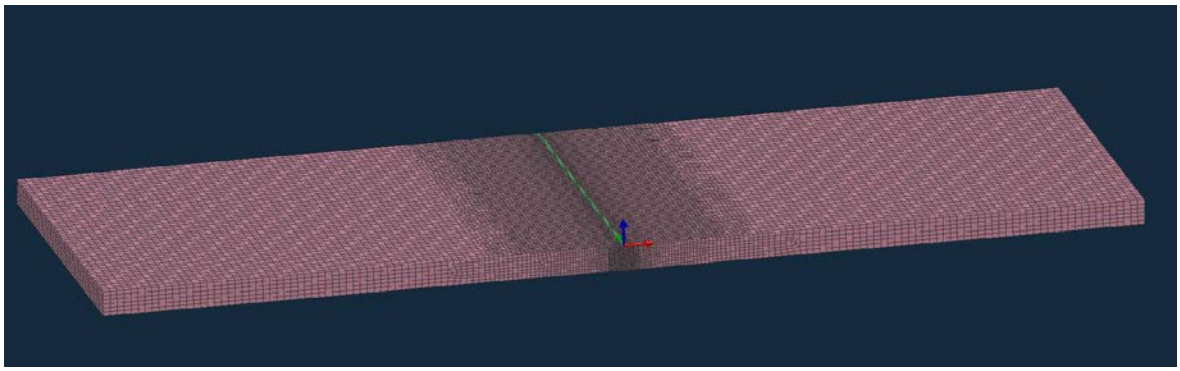

Figure 4.32.: Mesh used for the welding simulations in Visual-Weld, made of 201,520 quad linear elements

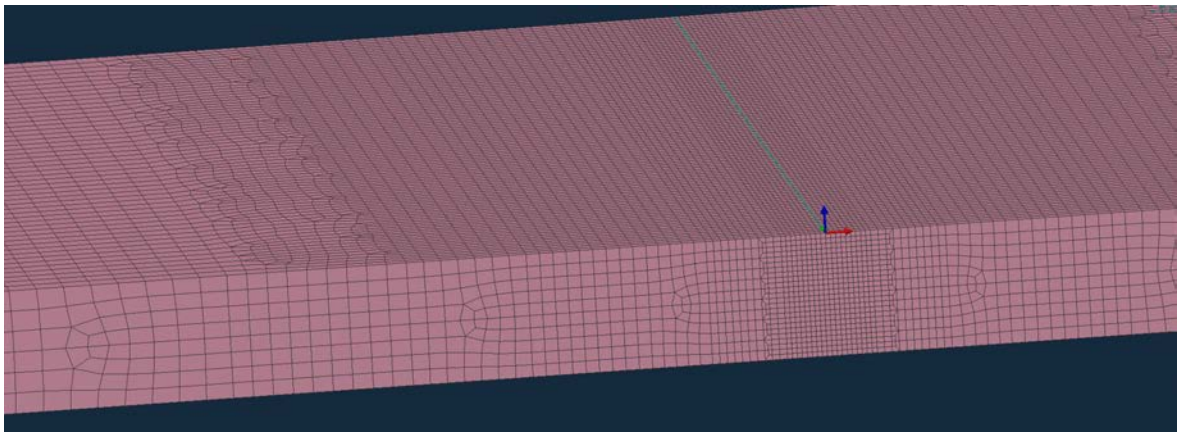

Figure 4.33.: Zoom close to the weld trajectory (green line) of the mesh shown in figure 4.32. Along the thickness, close to the weld line, 24 elements have been used, passing then progressively to 6 going farther from it

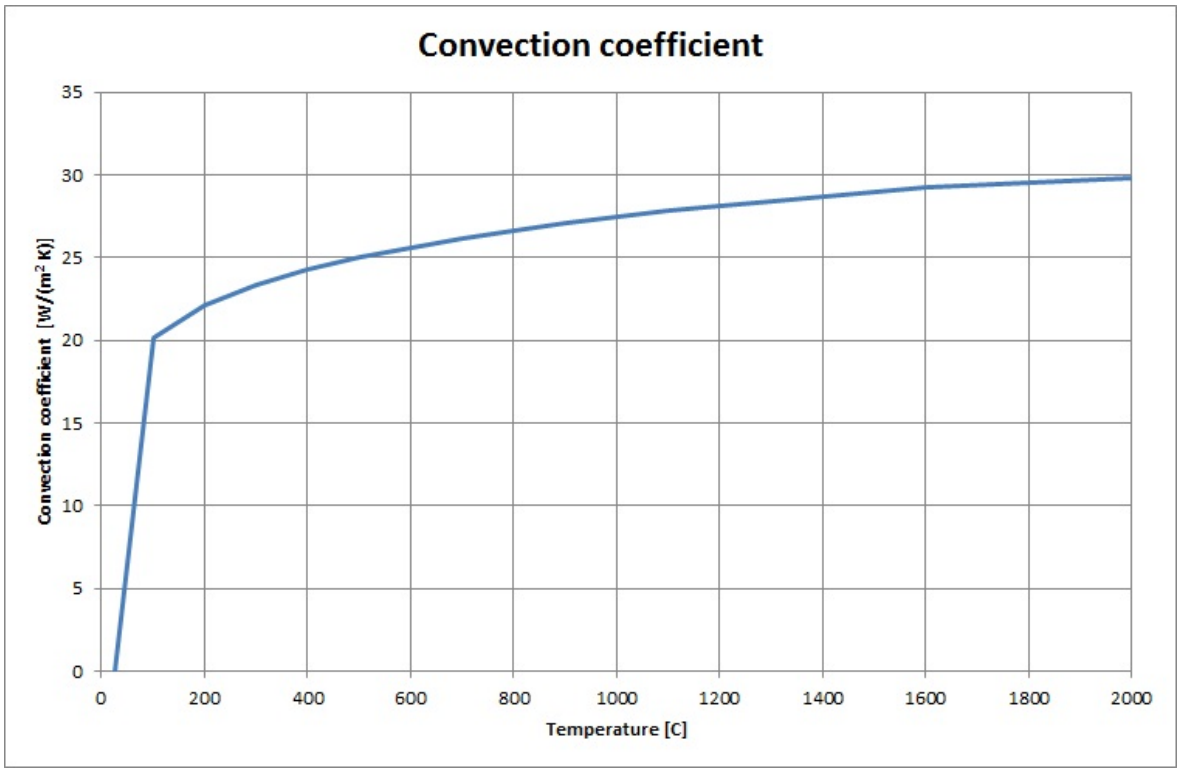

Figure 4.34.: Convection coefficient as a function of the difference of temperature between the workpiece and ambient temperature assumed at 20 ^{o}C (private communication from prof Jeffery Brooks)

4.6.5 Weld pool shape

As described in the paragraph 2.2.2, by adopting the classical approach of computational welding mechanics, the determination of the weld pool shape is a fundamental requirement to get reliable predictions from a welding simulation.

The welding experiments were executed before the numerical simulations, the plates welded were then sectioned and the weld pool shapes measured, in particular the fusion zone width as a function of the depth.

The fusion zone dimensions of the numerical models were matched to the real ones, by adapting the numerical models heat source shapes (paragraph 2.2.3). In particular, in this work, a specific heat source has been coded [112], since the ones described in paragraph 2.2.3 were not suitable for matching the weld pool geometries measured experimentally. The heat source was a modified three-dimensional conical heat source (figure 2.3), where the heat intensity decay, instead of being described by a polynomial function was defined using tabular data as a function of the weld depth.

To establish the boundaries of the fusion zone in the real case, pictures at high magnifications have been checked and, when "ghost shapes" of the original chemical segregation disappeared, giving rise to a well defined lamellar/martensitic structure, the material was considered to have reached the melting temperature (see for example pictures 3.66 b and c).

4.6.5.1 Equiaxed microstructure

In figure 4.35 a section of the experimental and numerical model, after welding, of the plate 2 mm thick with equiaxed microstructure, is shown. Temperatures above the melting temperature are represented by the grey colour, showing the fusion zone of the weld pool.

In figure 4.36 the fusion zones widths of the experimental and numerical case are compared for some some depths. The numerical fusion zone is in overall good agreement with the experimental one, staying within a tolerance of about 0.1 mm.

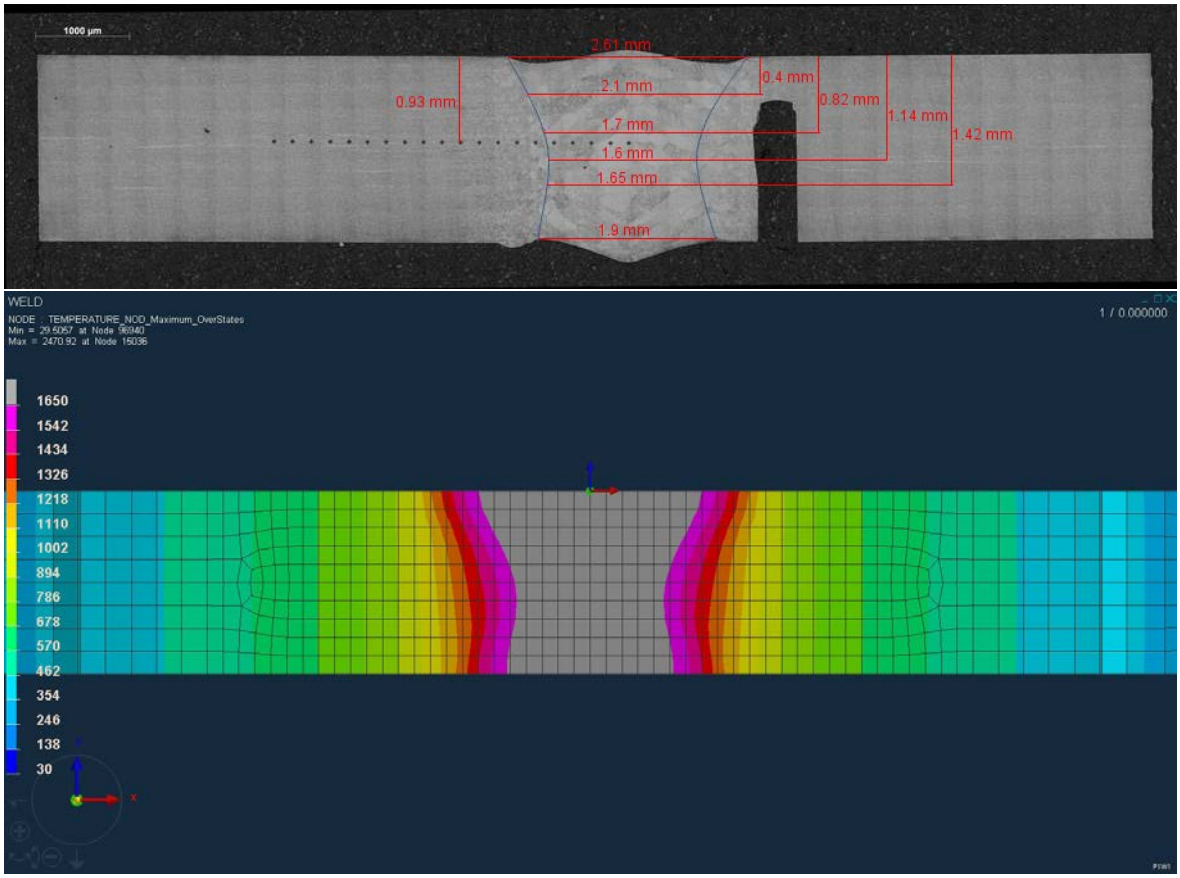

Figure 4.35.: Experimental (top) and numerical (bottom) weld pool fusion zones for the Ti-6Al-4V plate with initial equiaxed microstructure 2.00 mm thick, welded with a speed of 2 m/min and 60% power (2.4 kW). The fusion zone is bounded in the micrograph by blue lines. In the FE model, the grey colour shows locations where the maximum temperature during the welding simulation passed 1650 °C (melting temperature), representing thus the fusion zone. In the micrograph, depths and widths used for the fitting of the numerical heat source parameters are shown

Figure 4.36.: Comparison of the weld pool shape between numerical and experiment results of the Ti-6Al-4V plate 2 mm thick with initial equiaxed microstructure (figure 4.35). Only one half is shown as the shape of the weld pool is assumed to be symmetric

4.6.5.2 Lamellar microstructure

In figure 4.37 and 4.38 a section of the weld pool shape and the fusion zone width measurements as a function of some depth values are shown for the 3.76 mm thick plate with lamellar microstructure.

In figure 4.39 and 4.40 the ones for the 3.06 mm thick plate are instead shown.

In both cases, the numerical model was considered to describe accurately the shape of the real weld pool as the boundaries of the model/real case matched within about 0.1 mm.

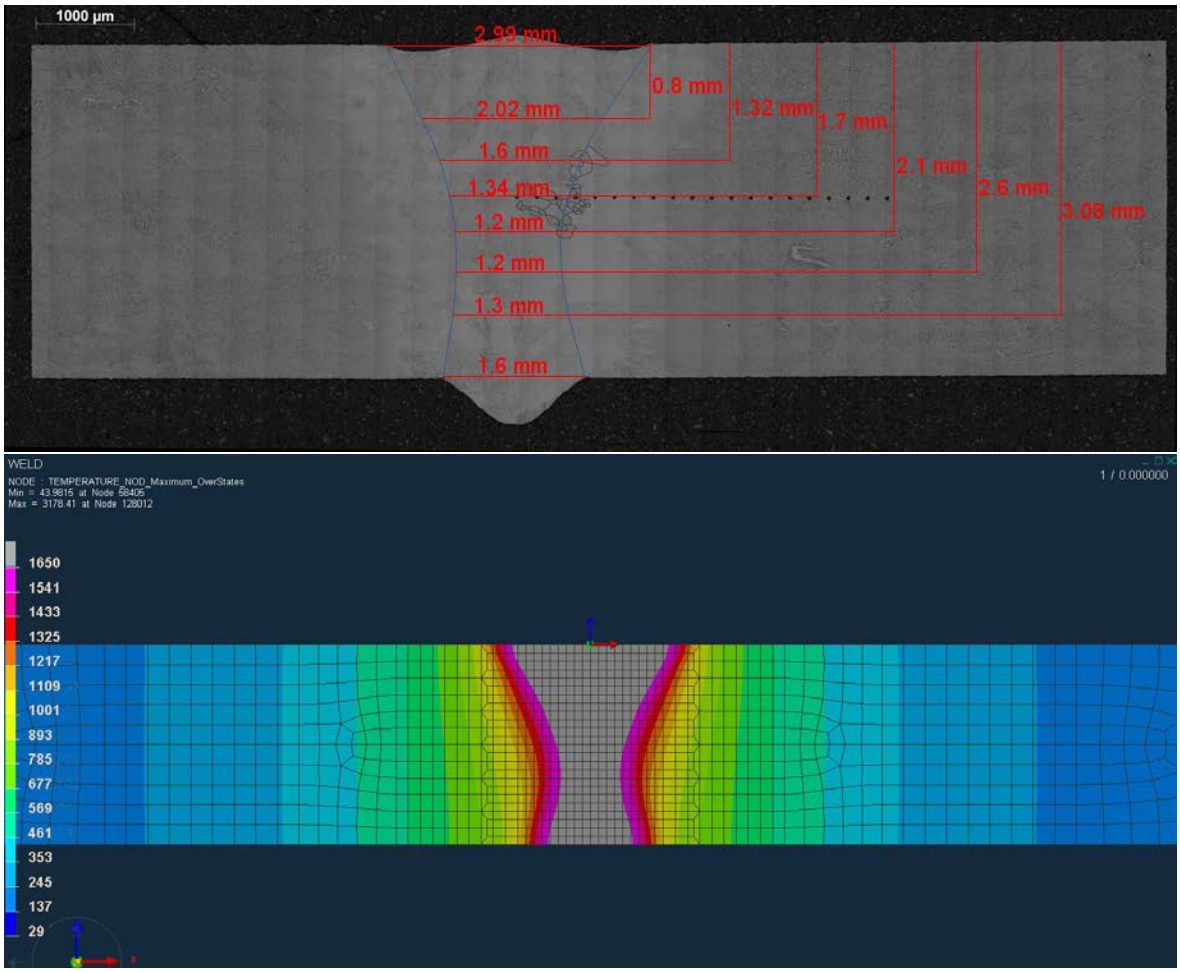

Figure 4.37.: Experimental (top) and numerical (bottom) weld pool fusion zones for the Ti-6Al-4V plate with lamellar microstructure 3.76 mm thick, welded with a speed of 2 m/min and 70% power (2.8 kW). The fusion zone is bounded in the micrograph by blue lines. In the FE model, the grey colour shows locations where the maximum temperature during the welding simulation passed 1650 °C (melting temperature), represents thus the fusion zone. In the micrograph, depths and widths used for the fitting of the numerical heat source parameters are shown. At half depth of the weld pool, also the beta grains around the heat affected zone are highlighted

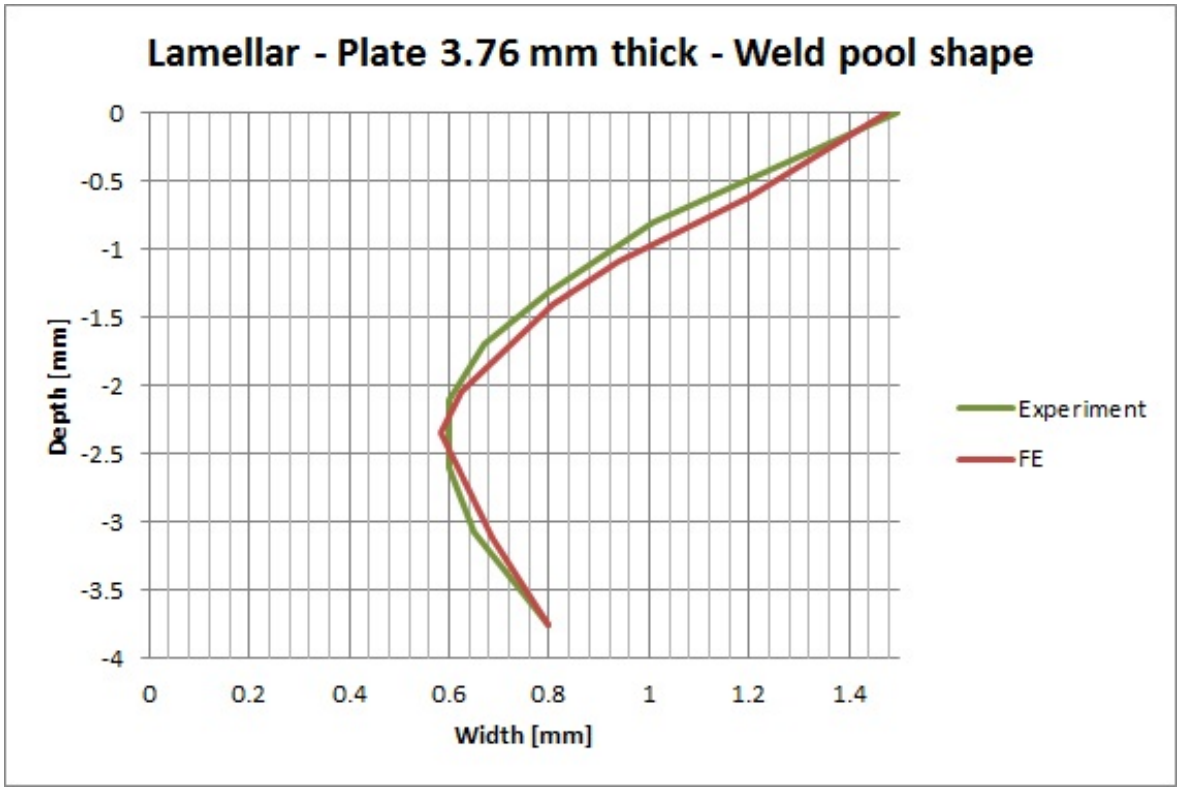

Figure 4.38.: Comparison of the weld pool shape between numerical and experiment results of the Ti-6Al-4V plate 3.76 mm thick with lamellar microstructure (figure 4.37). Only one half is shown as the shape of the weld pool is assumed to be symmetric

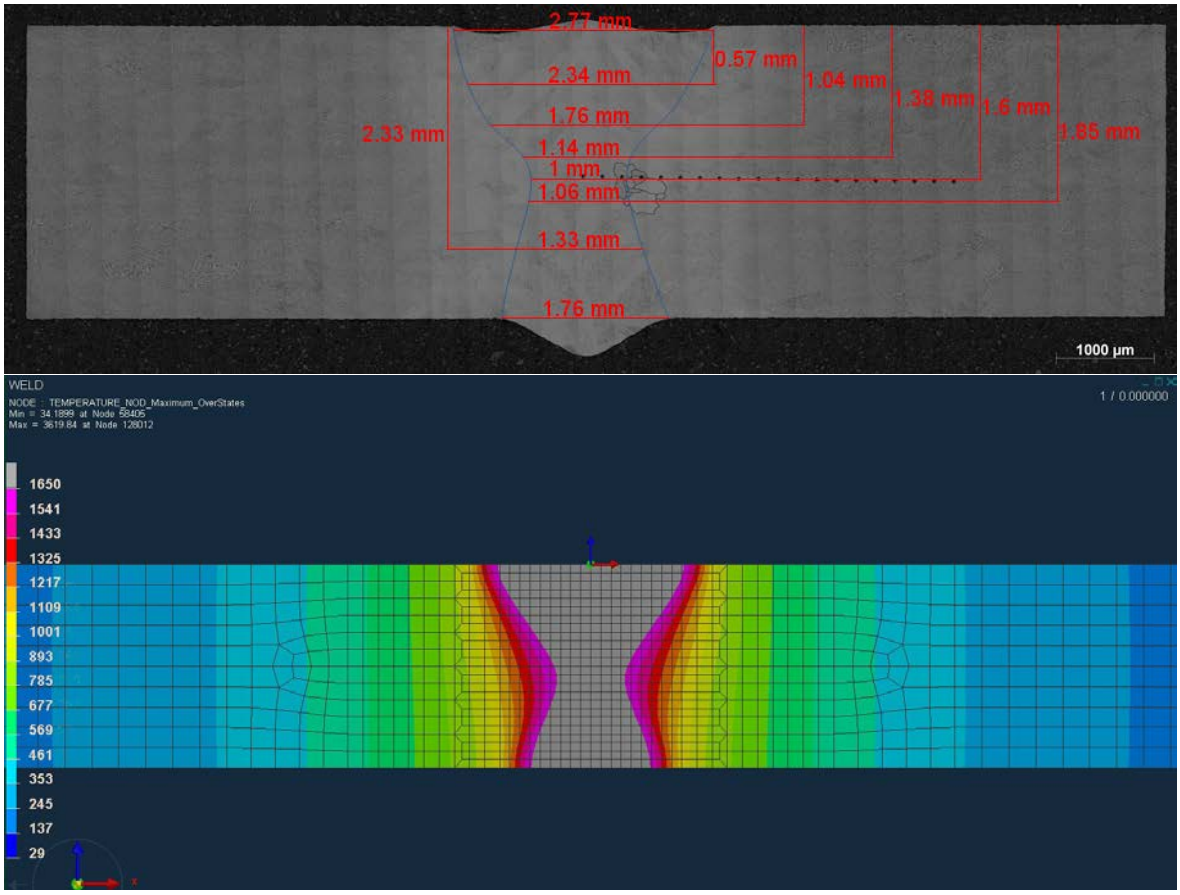

Figure 4.39.: Experimental (top) and numerical (bottom) weld pool fusion zones for the Ti-6Al-4V plate with lamellar microstructure 3.06 mm thick, welded with a speed of 2 m/min and 70% power (2.8 kW). The fusion zone is bounded in the micrograph by blue lines. In the FE model, the grey colour shows locations where the maximum temperature during the welding simulation passed 1650 °C (melting temperature), and represents the fusion zone of the numerical model. In the micrograph (top), depths and widths used for the fitting of the numerical heat source parameters are shown. At half depth of the weld pool, also the beta grains around the heat affected zone are highlighted

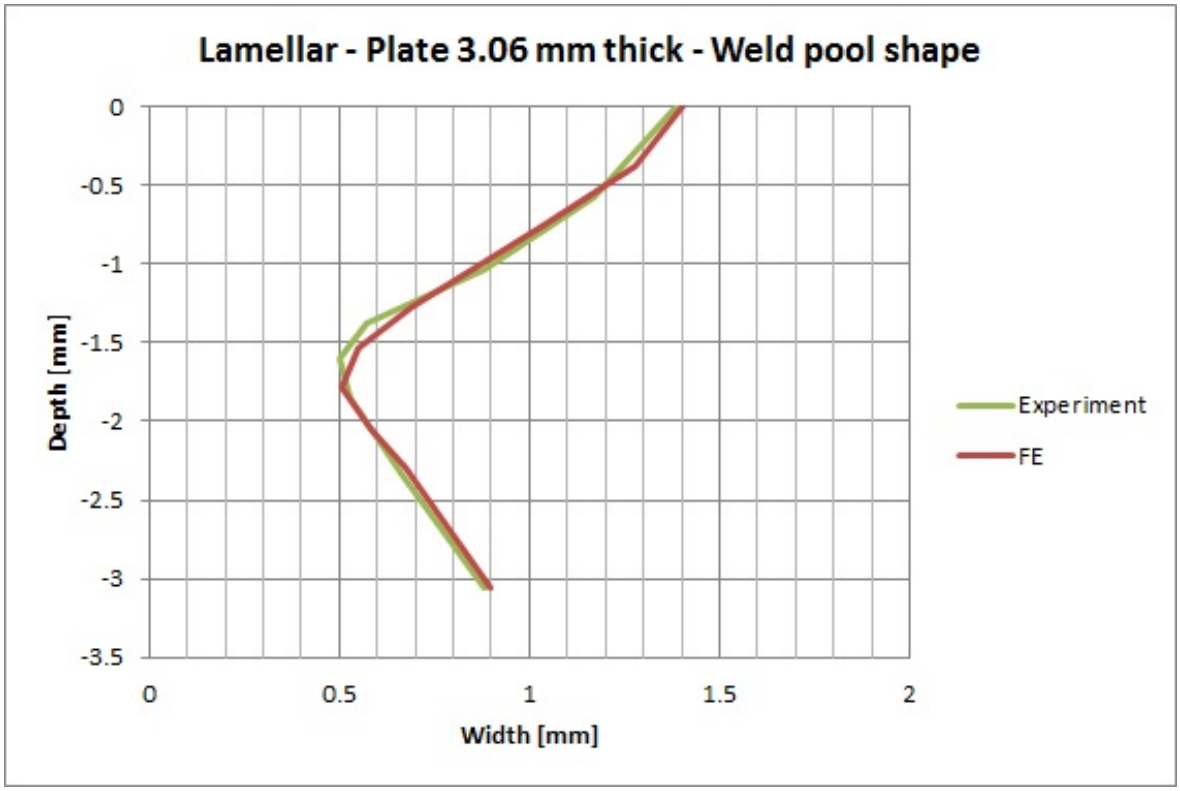

Figure 4.40.: Comparison of the weld pool shape between numerical and experiment results of the Ti-6Al-4V plate 3.06 mm thick with lamellar microstructure (figure 4.39). Only one half is shown as the shape of the weld pool is assumed to be symmetric

4.6.6 Implementation in Visual-Weld

The implementation in the commercial software Visual-Weld of the microstructural numerical models presented in sections 4.2, 4.3, 4.4 and 4.5 is shown schematically in the chart of figure 4.41, in which it is possible to see also the flow of the algorithm. The diffusion based model represented by the block "Diffusion based model lamellae/equiaxed microstructure" in figure 4.41 is then described more in detail by the flow chart shown in figure 4.42.

The algorithm is solved each time step of the welding simulation, for each integration point of the mesh.

As outputs, visible in the post processor, the following variables are saved for each time step and integration point: equiaxed alpha phase, lamellar alpha phase, beta phase,

martensitic phases, equiaxed alpha mean radius, lamellar alpha thickness, needle thickness and beta grain radius.

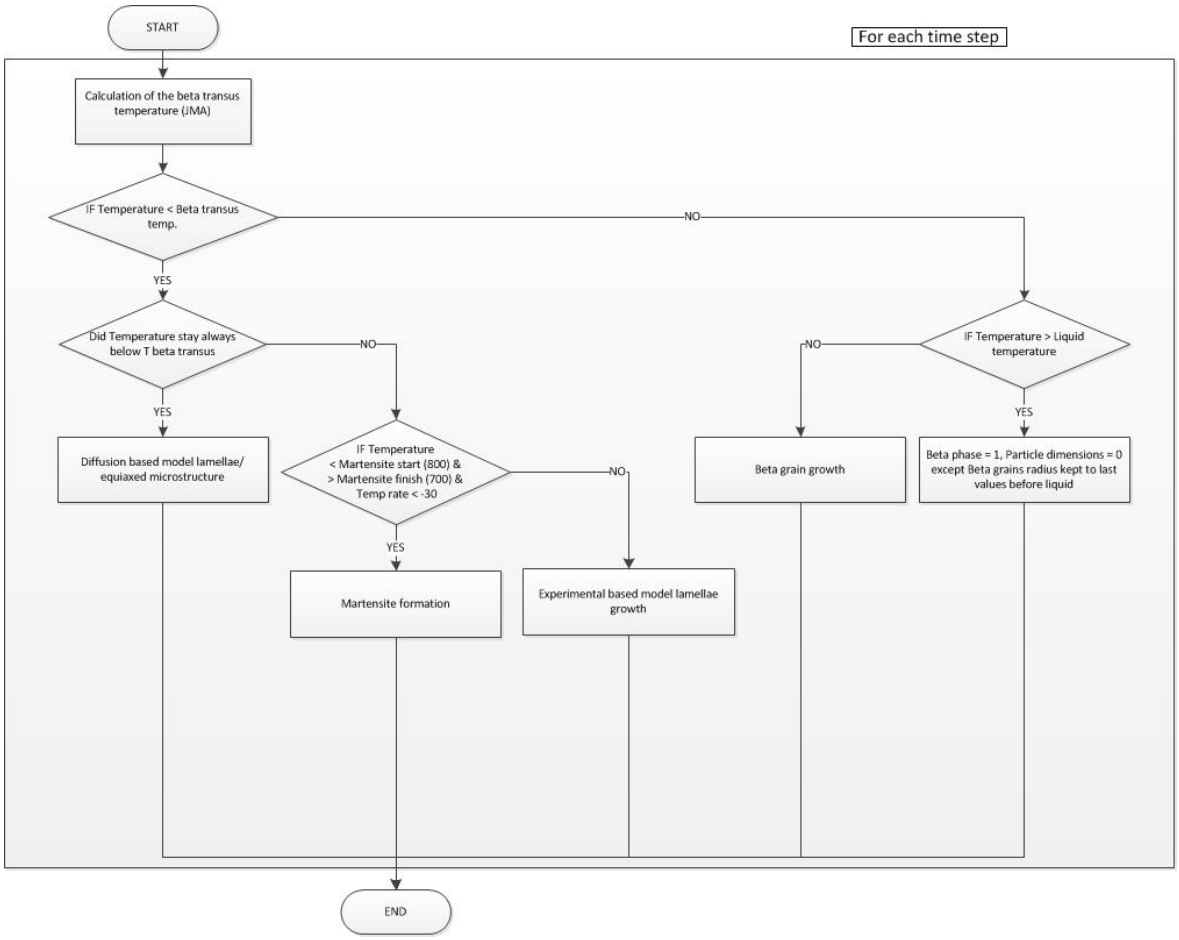

Figure 4.41.: Comprehensive numerical model flow chart for the description of the microstructure evolution in welding simulations

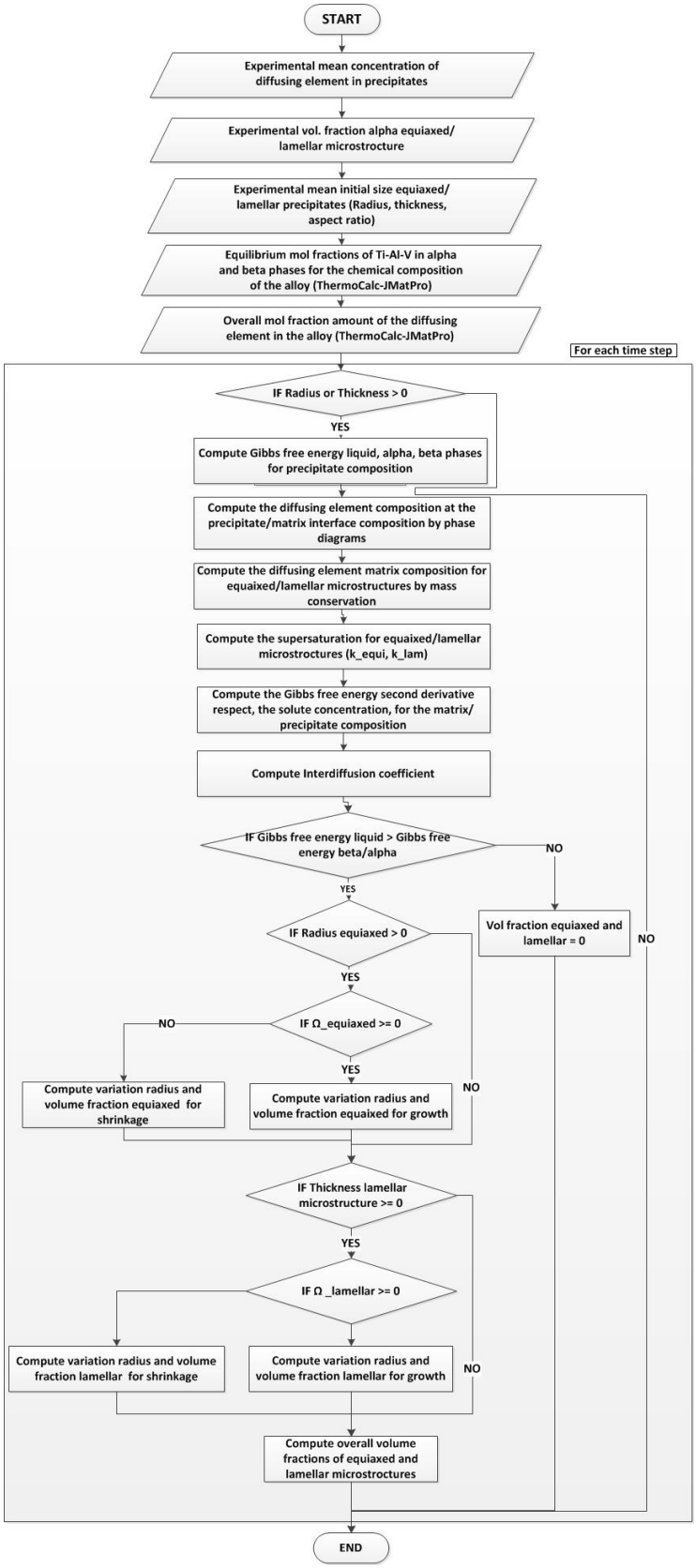

Figure 4.42.: Diffusion based model flow chart for the description of the alpha particle growth/shrinkage

4.6.7 Thermal comparison with experiments

In this section the temperature comparison between experiments and numerical predictions, at different distances from the weld lines of the welding tests conducted on the plates tested, is shown.

The temperatures measured in the numerical simulations were relatively sensitive to the thermal properties adopted to model the material behaviour and, in a smaller part, also to the temperature surrounding the workpieces and the convective coefficient. Due to time limitations, it was not possible in this work to investigate in detail the variations of each of these factors, thus the fixed values described in section 4.6.2 and 4.6.4 were assumed.

4.6.7.1 Equiaxed microstructure

In figure 4.43 the temperature comparison between experiments and numerical predictions, at different distances from the weld lines of the welding tests conducted on plates with initial equiaxed microstructures, is shown.

The temperatures reported for the numerical model make reference approximatively to the same positions where the thermocouples used for the experiments were located, compatible with the locations of the mesh nodes of the numerical model. The depth of the holes where the thermocouples were inserted was 1.5 mm, since the closest nodes of the mesh at this distance were at 1.4 mm and 1.6 mm, the first depth was used.

A good match with of the numerical results to the experimental ones was obtained, in particular for the closest distances to the weld line, where the temperatures are high enough to affect the material microstructure in the typical timings involved during welding.

The difference of temperature between experimental and numerical results, measured at 20 mm far from the weld line, can be explained by the higher impact that the convection coefficient has at lower temperature. To verify this hypothesis, further measurements and investigation on the variation of the heat flow dispersion during the cooling stage of

welding, should be carried out.

Considering the complexity of the problem to be modelled, the relatively good match with the temperatures between numerical models and experimental ones confirms the adoption of reasonable boundary conditions and material properties.

4.6.7.2 Lamellar microstructure

In figure 4.44 and 4.45 the temperature comparisons between experiments and numerical predictions, at different distances from the weld lines of the welding tests conducted on plates with initial lamellar microstructures, are shown.

The temperatures reported for the numerical model make reference approximatively to the same positions where the thermocouples used for the experiments were located, compatible with the locations of the mesh nodes of the numerical model. The depth of the holes where the thermocouples were inserted was 2.5 mm, since the closest nodes of the mesh at this distance were at 2.55 mm and 2.42 mm, the first depth was used.

In both cases a good match with the numerical results to the experimental ones was obtained, in particular for the closest distances to the weld line, where the temperatures are high enough to affect the material microstructure in the typical timings involved during welding.

The slightly lower temperatures measured in the numerical model with respect to the ones measured experimentally, can be explained both by the higher thermal dissipation given by the thermocouples wires with respect to the numerical model where they are not present, and to the higher thermal inertia given by the ceramic insulation used in the sensors to isolate the anode, cathode and sleeve from each other.

As for the equiaxed microstructure case, considering the complexity of the problem to be modelled, the relatively good matching of the temperatures between numerical models and experimental ones confirm the adoption of reasonable boundary conditions and material properties.

a)

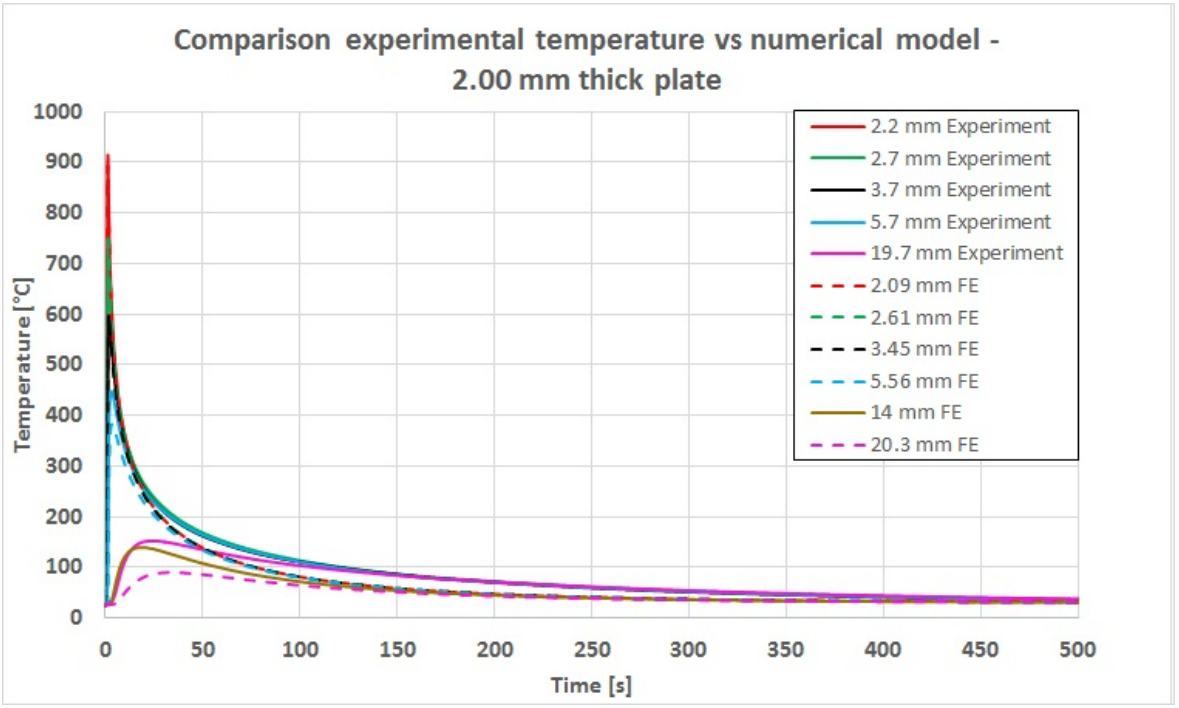

b)

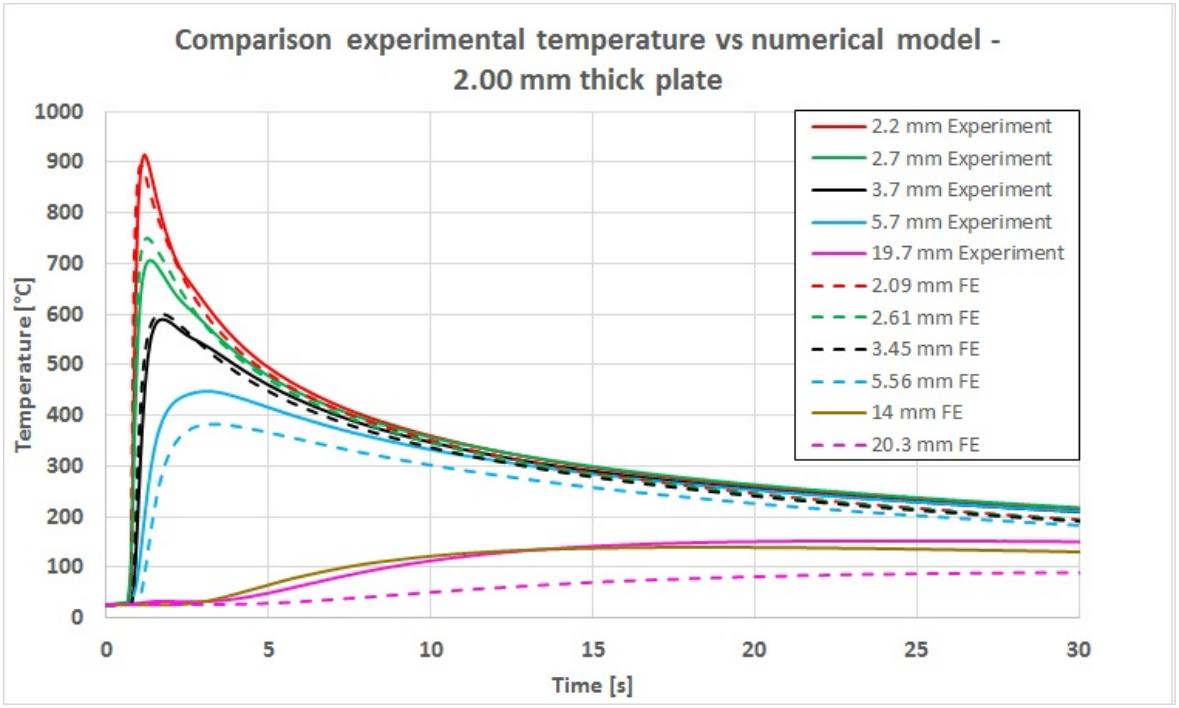

Figure 4.43.: Comparison between experimental measured temperatures and numerical results, for the Ti-6Al-4V plate with initial equiaxed microstructure and 2.00 mm thick. In a) and b) the same trends are reported but with different x scales. The different lines make reference to the temperatures measured at a series of distances from the weld line, in the experimental and numerical case

a)

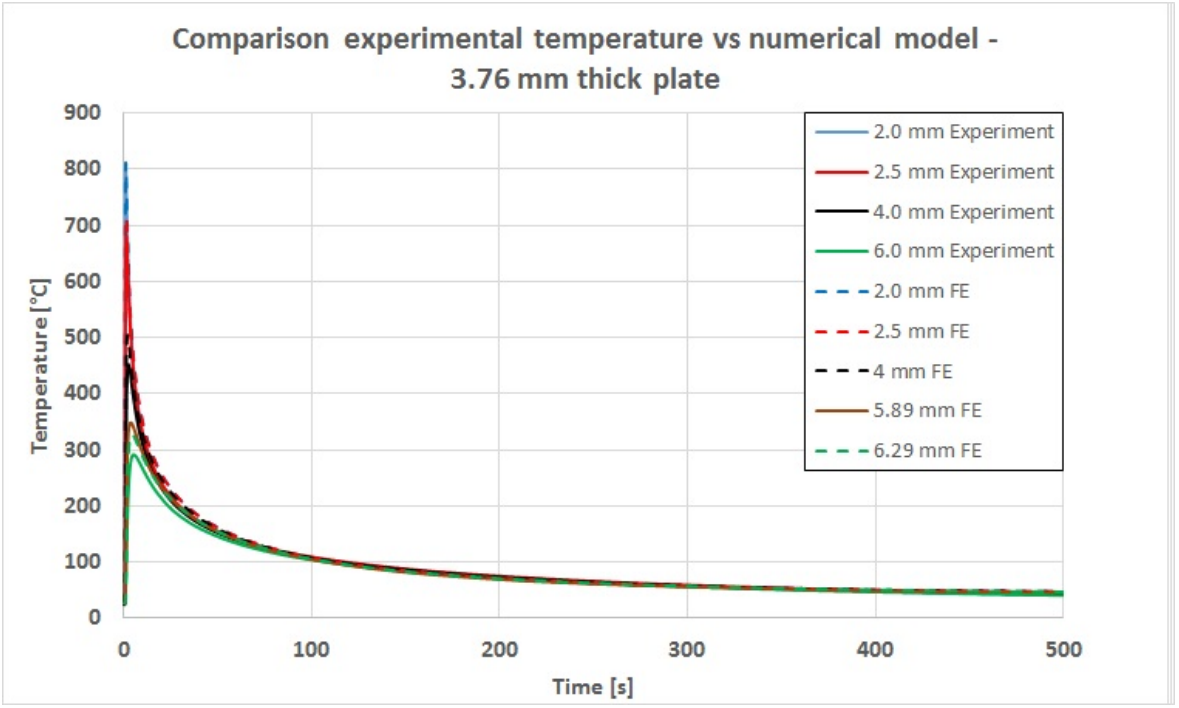

b)

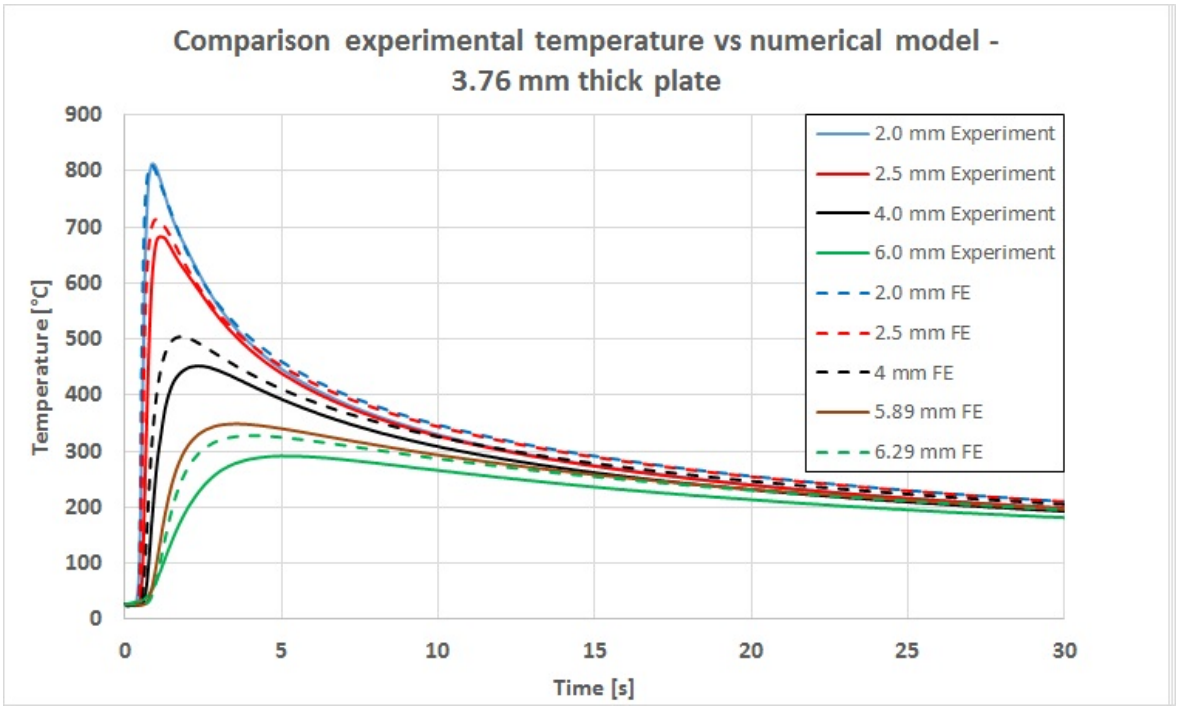

Figure 4.44.: Comparison between experimental measured temperatures and numerical ones, for the Ti-6Al-4V plate with initial lamellar microstructure and 3.76 mm thick. In a) and b) the same trends are reported but with different x scales. The different lines make reference to the temperatures measured at a series of distances from the weld line, in the experimental and numerical case

a)

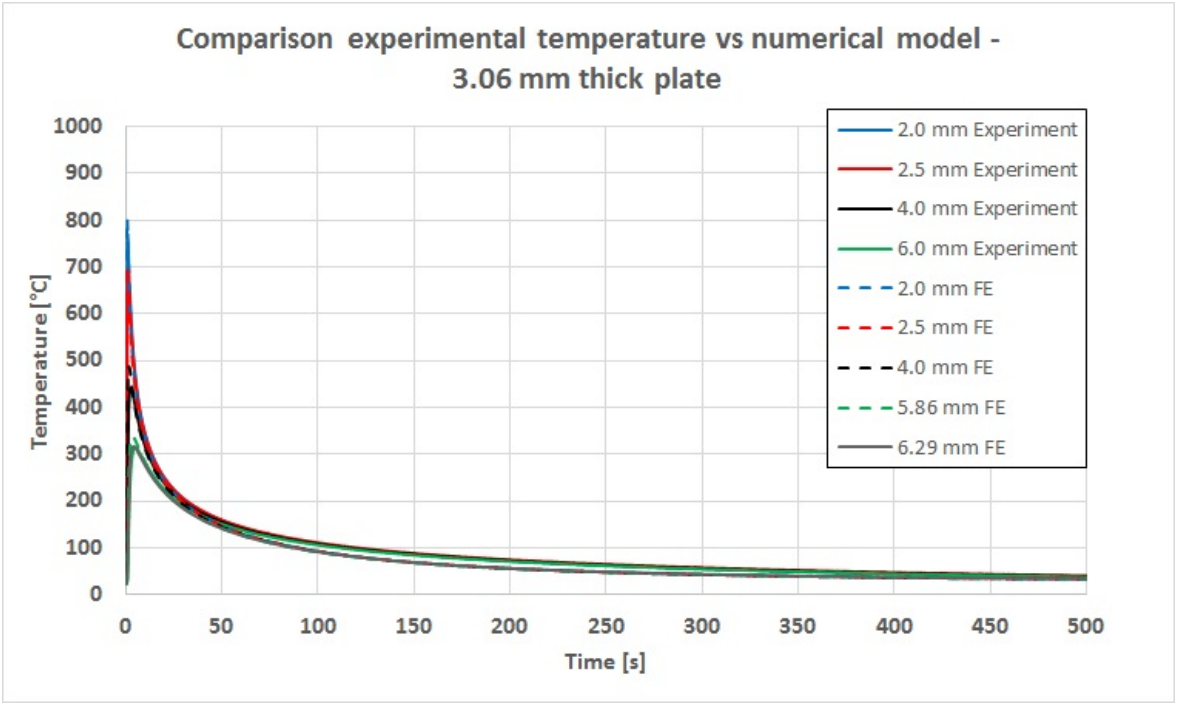

b)

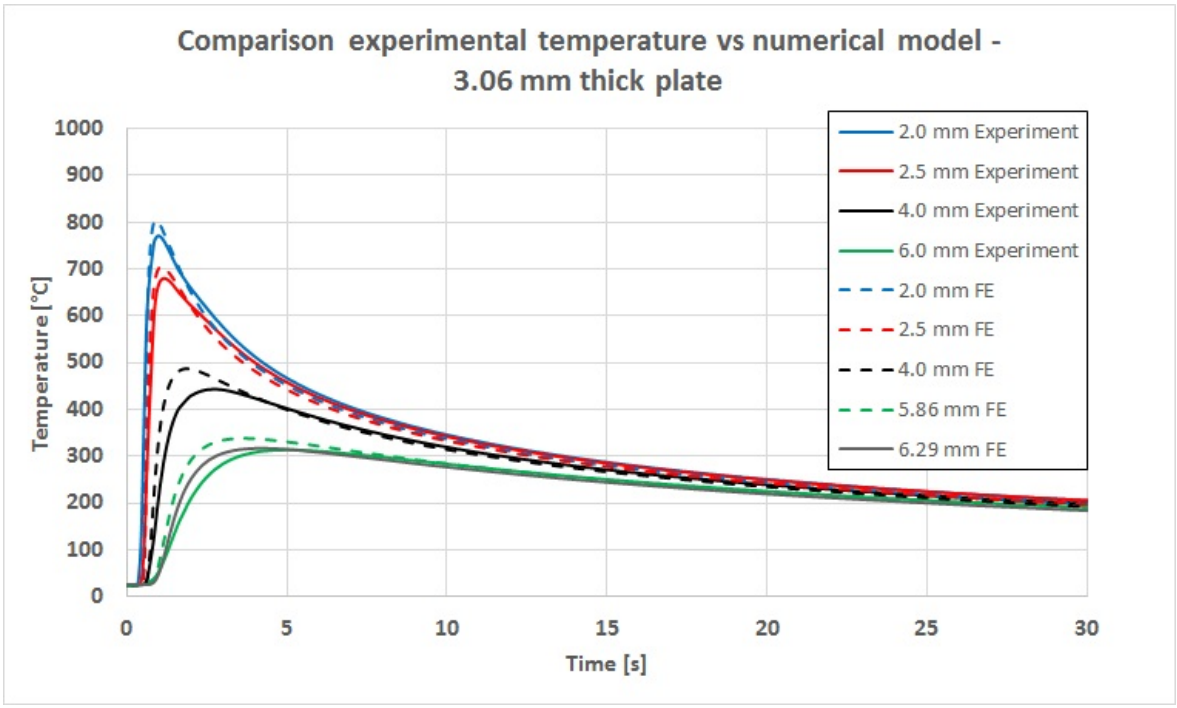

Figure 4.45.: Comparison between experimental measured temperatures and numerical ones, for the Ti-6Al-4V plate with initial lamellar microstructure and 3.06 mm thick. In a) and b) the same trends are reported but with different x scales. The different lines make reference to the temperatures measured at a series of distances from the weld line, in the experimental and numerical case

4.6.8 Microstructure comparison with experiments

In this paragraph a comparison between the microstructural morphologies, particle dimensions and phase proportions, between numerical predictions and experimental measurements is carried out.

As already pointed out in the chapter 3, the experimental measurement of microstructural features was not always easy, particularly when many typology of phases and particles were present in the same image analysed at the SEM. Sometimes, the welding numerical simulations were used to understand what thermal load a specific portion of material was subjected to, thus helping in qualifying the microstructure studied.

4.6.8.1 Equiaxed microstructure

In figure 4.46 experimental and numerical measurements of the mean radius of the equiaxed alpha phase for the plate with initial equiaxed microstructures are shown as a function of the distance from the weld line. A good match between numerical and experimental results was obtained, capturing the location where the alpha particles dissolve.

In figure 4.47 experimental and numerical measurements of the mean martensitic needles thickness for the plate with initial equiaxed microstructures are shown as a function of the distance from the weld line. A relatively good matching between numerical and experimental results was obtained even though the numerical model reports martensitic needles till a distance from the weld line of 3.0 mm. Since BEI images were taken only up to a distance of 1.7 mm, the possible formation of needles beyond this location was not possible to be verified.

In figure 4.48 the comparison between the numerical prediction and experimental measurements of the beta grains radius in the heat affected zone is shown. The numerical model seems to over predict where the area of beta grains with a specific dimension is, with an error of about 0.3 - 0.4 mm. Since the beta grain nucleation temperature for this material was not investigated experimentally, the same temperature of the material with an initial lamellar microstructure was assumed (figure 4.56). Consequently, these results suggest

Figure 4.46.: Ti-6Al-4V plate 2.0 mm thick with initial equiaxed microstructure. Comparison between the mean alpha equiaxed radius predicted by the numerical model and the one experimentally measured for different distances from the weld line

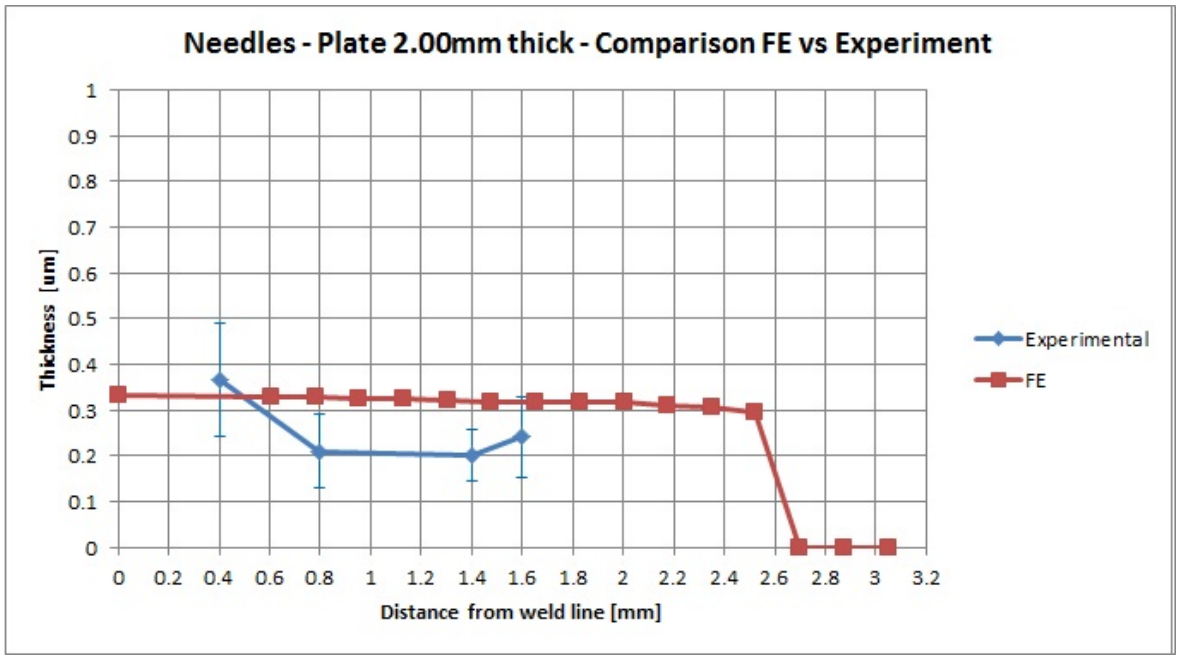

Figure 4.47.: Ti-6Al-4V plate 2.0 mm thick with initial equiaxed microstructure. Comparison between the mean martensitic needle thickness predicted by the numerical model and the one experimentally measured for different distances from the weld line

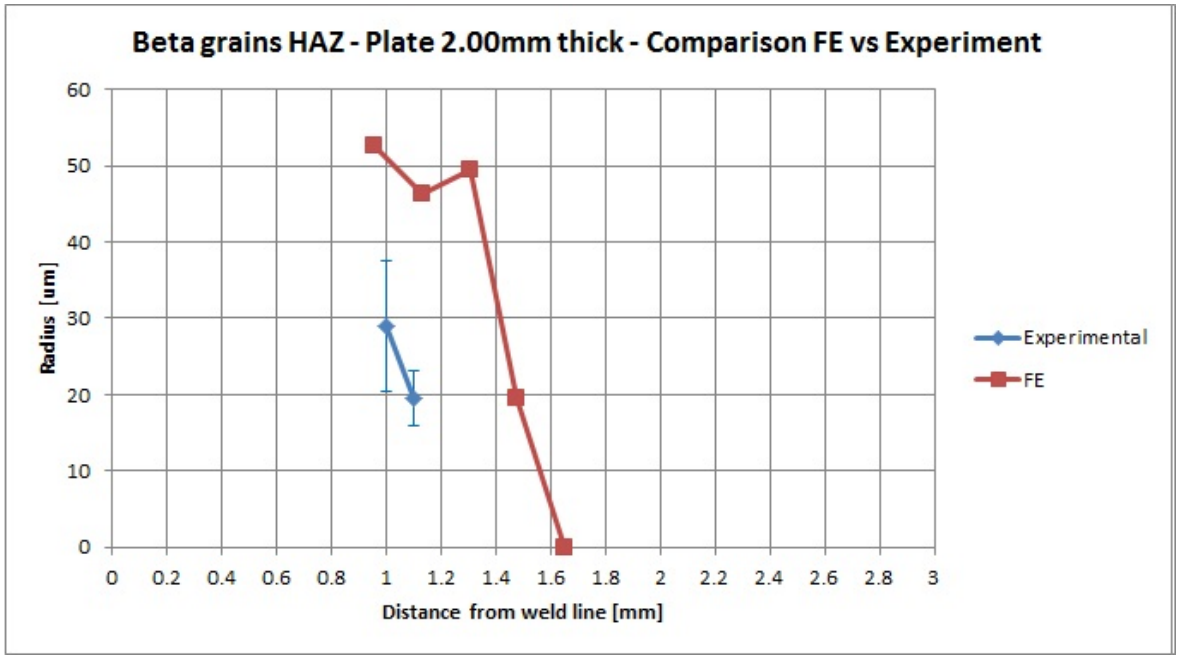

Figure 4.48.: Ti-6Al-4V plate 2.0 mm thick with initial equiaxed microstructure. Comparison between the mean beta grain radius predicted by the numerical model and the one experimentally measured for different distances from the weld line

that the nucleation temperature of the material with initial equiaxed microstructure is higher than the lamellar one.

Figure 4.49, 4.50 and 4.51 show the comparison between the equiaxed alpha, martensitic and beta phase proportions respectively. The numerical predictions match reasonably well the experimental results, compatible with the availability of BEI images up to 2.0 mm far from the weld line. The beta phase fraction prediction, even if the small scale of the y axis seems to amplify the difference with the experimental measurements, is still within the errors of the other charts.

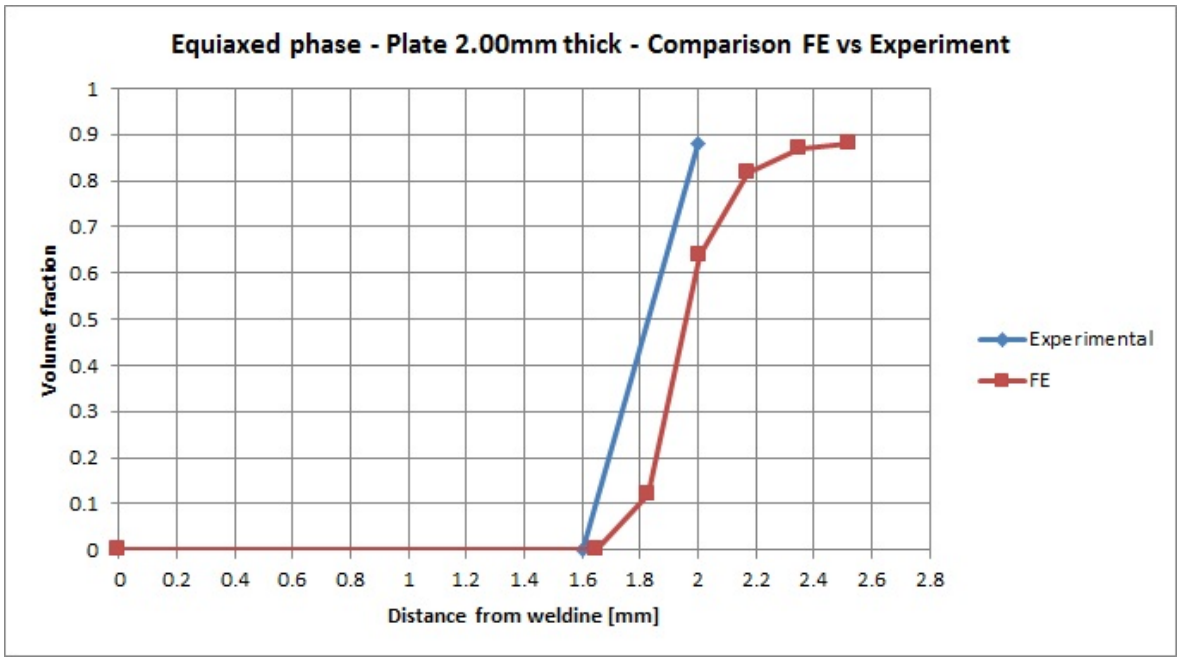

Figure 4.49.: Ti-6Al-4V plate 2.0 mm thick with initial equiaxed microstructure. Comparison between the equiaxed phase proportion predicted by the numerical model and the one experimentally measured for different distances from the weld line

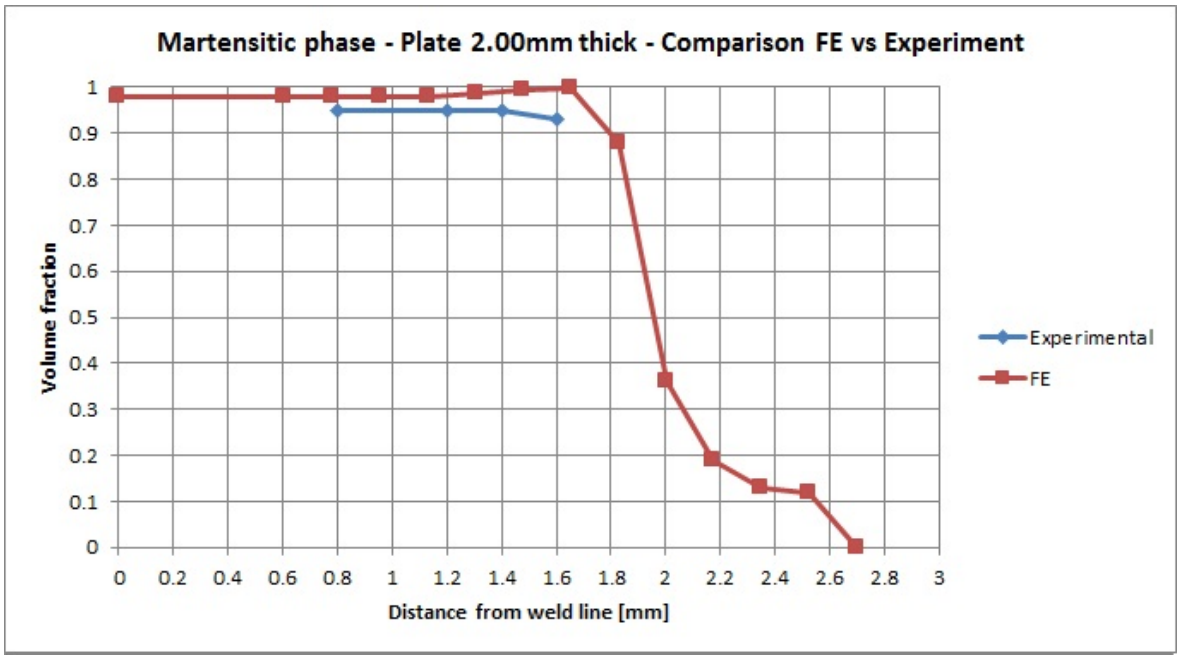

Figure 4.50.: Ti-6Al-4V plate 2.0 mm thick with initial equiaxed microstructure. Comparison between the martensitic phase predicted by the numerical model and the one experimentally measured for different distances from the weld line

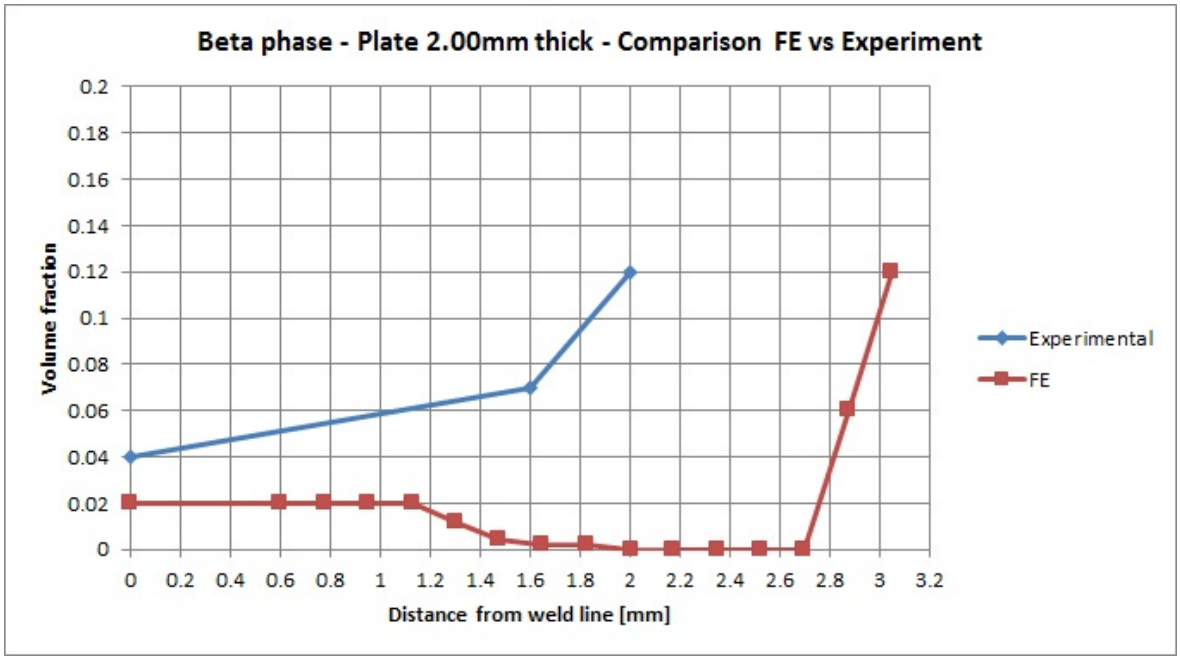

Figure 4.51.: Ti-6Al-4V plate 2.0 mm thick with initial equiaxed microstructure. Comparison between the beta phase proportion predicted by the numerical model and the one experimentally measured for different distances from the weld line

4.6.8.2 Lamellar microstructure

In figure 4.52 experimental and numerical measurements of the mean alpha lamellar thickness for the plates with initial lamellar microstructures are shown as a function of the distance from the weld line. The mean lamellar thickness of the original microstructure and the thickness of nucleated lamellae are reported in different colours as they are recognizable experimentally. When no lamellae were identified looking at the SEM pictures, empty spaces were left in the charts.

Considering the possible errors in the positioning of the different measurements taken by SEM analysis, measurement of the weld pool fusion zone dimensions and the tolerance of about 0.1 mm in matching the numerical weld pool fusion zone to the experimental one, a good match between numerical and experimental results was obtained, capturing the transition between disappearing of the original lamellae and nucleation of new ones.

In figure 4.53 the comparison between numerical and experimental measurements of the

a)

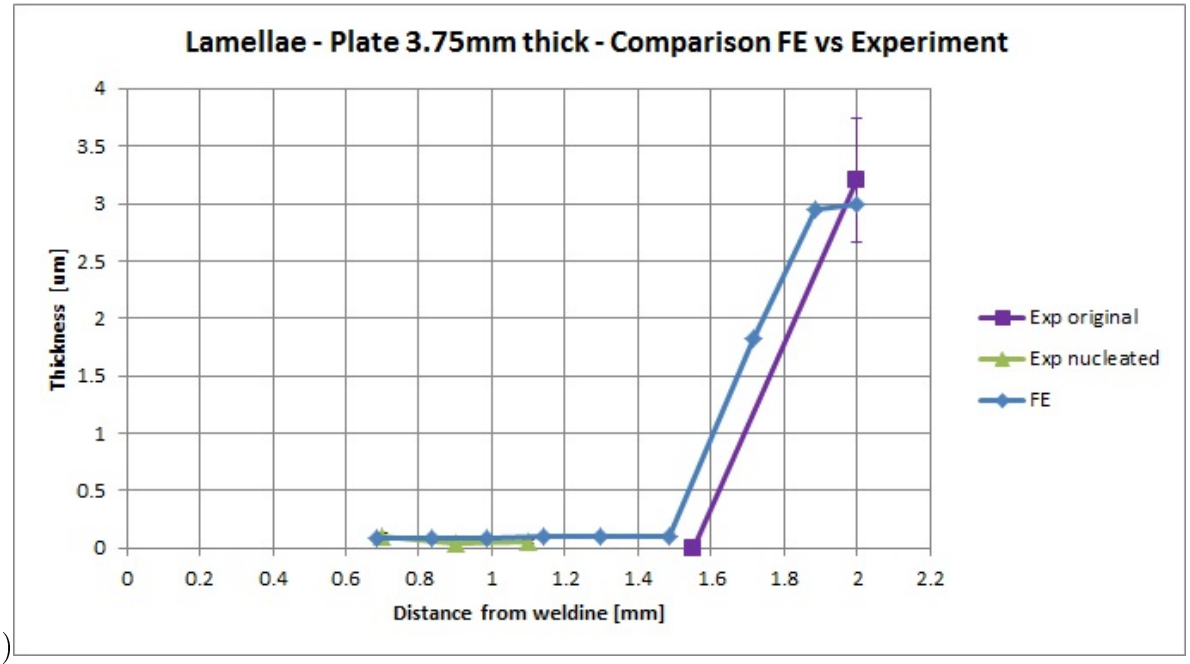

b)

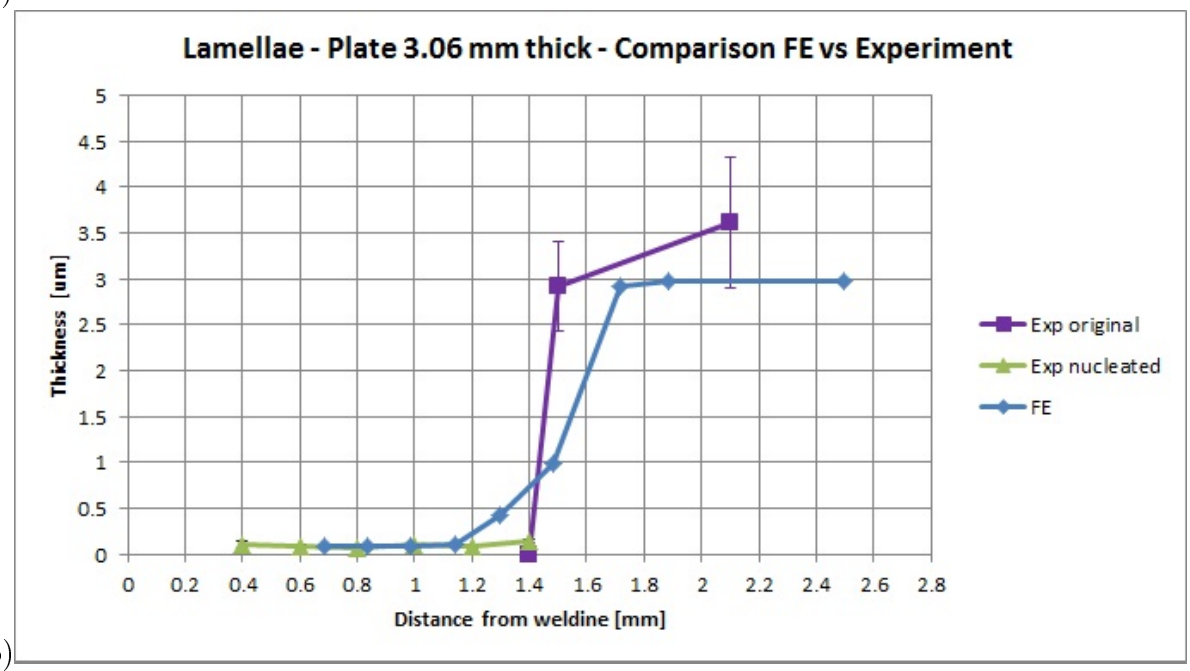

Figure 4.52.: Ti-6Al-4V plates with initial lamellar microstructure, a) 3.75 mm thick and b) 3.06 mm thick. Comparison between the mean alpha lamellae thickness predicted by the numerical model and the one experimentally measured for different distances from the weld line

mean martensitic needles thickness is shown as a function of the distance from the weld line.

The numerical predictions are in reasonable agreement with the experimental measurements, except for the very far locations from the weld line, where the numerical model seems to over predict by about 0.5-1.0 mm the area where martensitic needles stop forming. This is in agreement with the results obtained in section 4.6.8.1 and it shows that the conditions for martensite formation adopted in the current model, deduced partially from the experiments (figure 3.32) for the cooling rate, and from literature (figure 2.24) for the temperatures range at which the transformation occurs, should to be investigated more in detail. Currently, the minimum cooling rate and the range of temperatures at which the transformation is supposed to happen are set at 30 ^{o}C/s and 700 - 800 ^{o}C respectively. The comparison between numerical and experimental results seems to suggest that either a higher minimum cooling rate or range of temperatures should be adopted.

In figure 4.54 the comparison between experimental and numerical measurements on the mean beta grain radius dimension in the heat affected zone at different distances from the weld line are shown.

For the numerical model results, two lines are reported, making reference to the beta grain growth obtained considering nucleation directly after the passage of the beta transus temperature (line identified by "FE" in figure 4.56) or considering a further step in temperature to allow nucleation of beta grains (line identified by "FE nucleation" in figure 4.56). Trends of the nucleation temperature and beta transus temperature used, as a function of the heating rate, are shown in figure 4.56. These trends were obtained applying the approach explained in section 4.3 to the experimental data presented in section 3.4.3. Precisely, the beta transus temperature was assumed to be passed when a martensitic microstructure was observed within parent alpha lamellae at the end of the heat treatments whilst, the lowest temperature at which beta grains were noticed, for a specific heating rate, was assumed as the nucleation temperature of the beta grains.

As expected, with nucleation at the beta transus, larger dimensions obtained together

a)

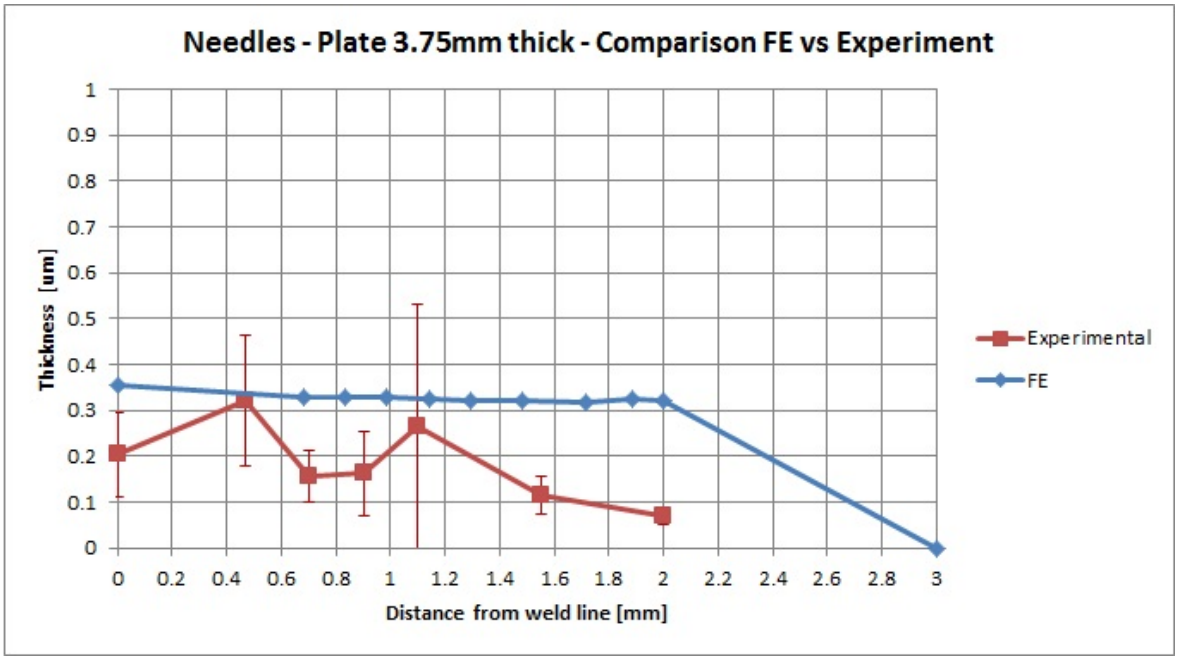

b)

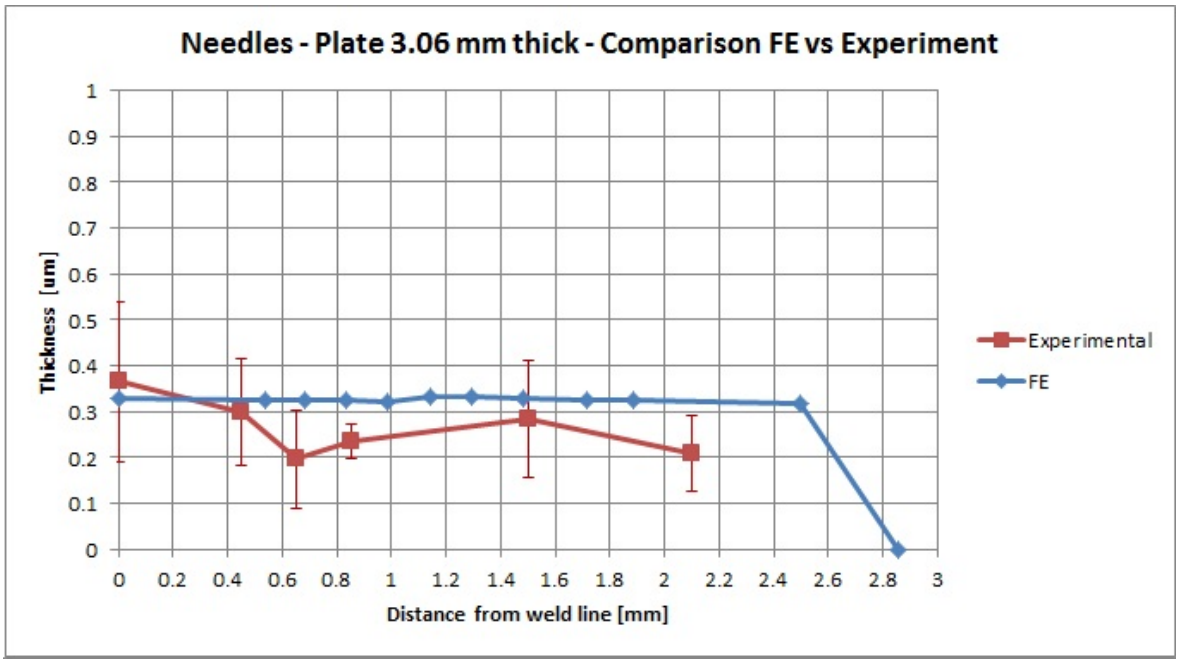

Figure 4.53.: Ti-6Al-4V plates with initial lamellar microstructure, a) 3.75 mm thick and b) 3.06 mm thick. Comparison between the mean martensitic needles thickness predicted by the numerical model and the one experimentally measured for different distances from the weld line

with nucleation at positions farther from the weldline, in respect to the case where nucleation starts at higher temperatures.

The peak in the beta grain dimension shown in figure 4.54-a at 1 mm distance from the weld line for the "FE nucleation" line, can be explained by a) the bigger area sampled experimentally ($\sim 0.2 \times 0.2\, mm^2$) than the corresponding numerical model mesh size of this location ($\sim 0.156 \times 0.156\, mm^2$), together with b) the relatively large dimension of the beta grains noticed experimentally around this area mixed with smaller ones (figure 4.55) and c) the slight wider weld pool size returned by the numerical model (figure 4.38). These factors could lead to the numerical model representing an area with a bigger beta grains size and, since the mesh elements are smaller than the area experimentally sampled, the mean value would not be lowered by other neighbouring smaller grains.

The trends of the lamellar phase shown in figure 4.57 are in good agreement with the experiments, as are the ones of the martensitic phase shown in figure 4.58, with the exception of positions very far from the weld line. As previously discussed, this overestimation could be due to conditions, for the martensitic transformation to occur, needing to be refined. Related to this result is the prediction of the beta phase, shown in figure 4.59, with an under prediction at far locations from the weld line, as the martensitic transformation still takes place.

a)

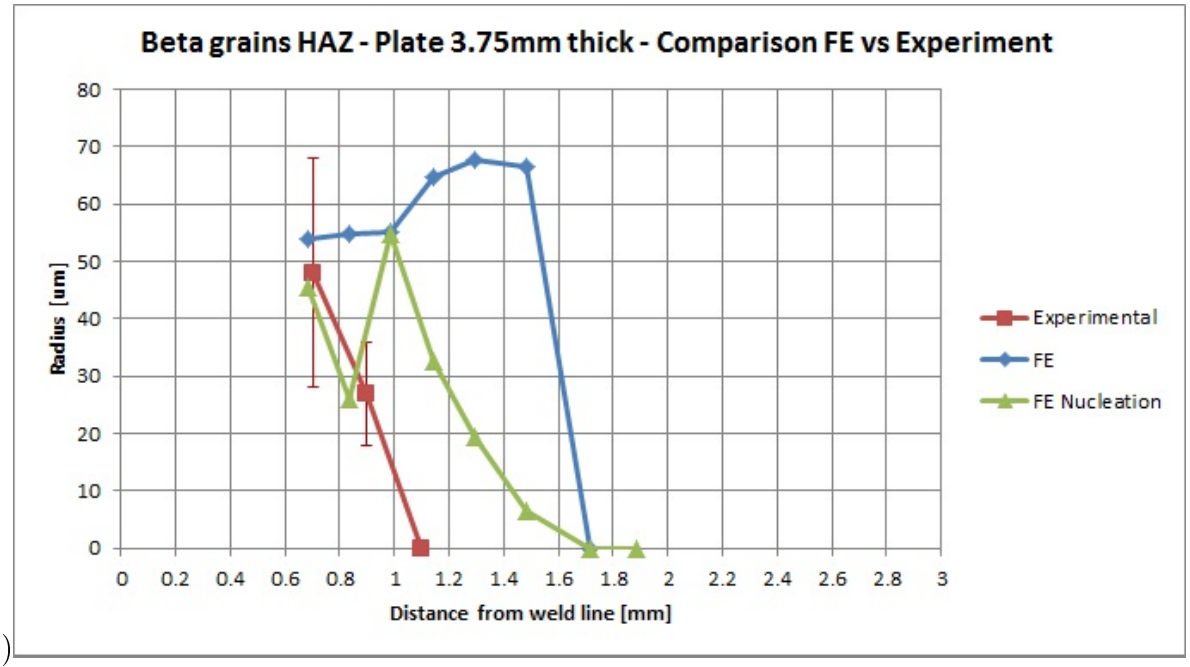

b)

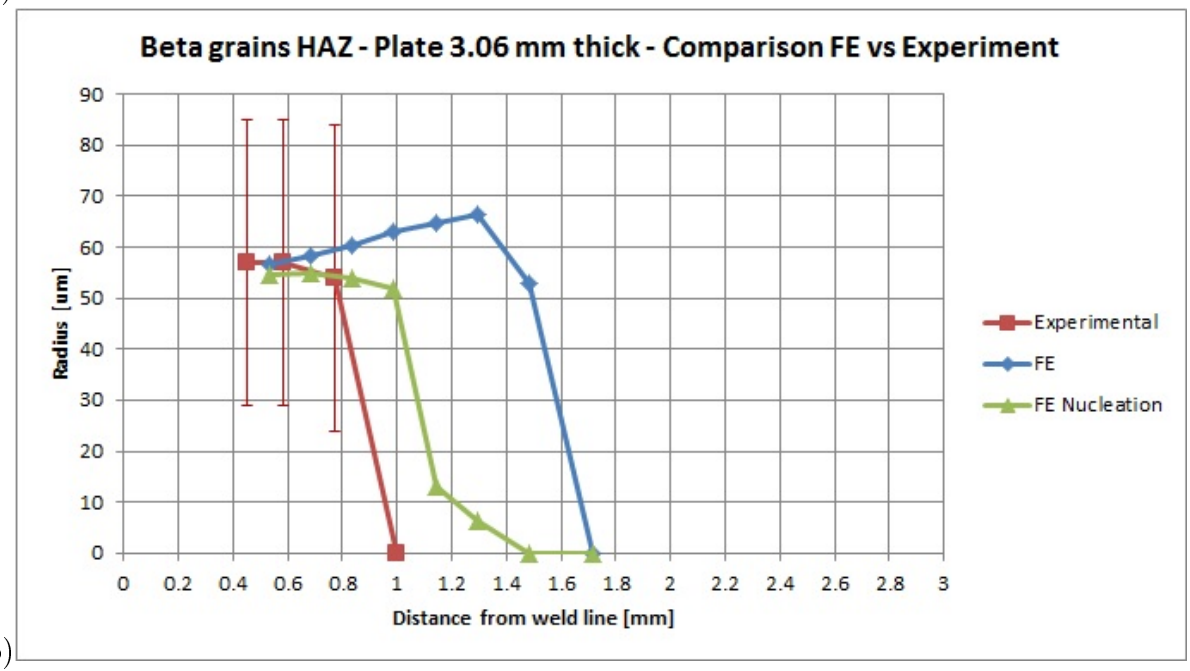

Figure 4.54.: Ti-6Al-4V plates with initial lamellar microstructure, a) 3.75 mm thick and b) 3.06 mm thick. Comparison between the mean beta grain dimension in the HAZ zone predicted by the numerical model and the one experimentally measured for different distances from the weld line

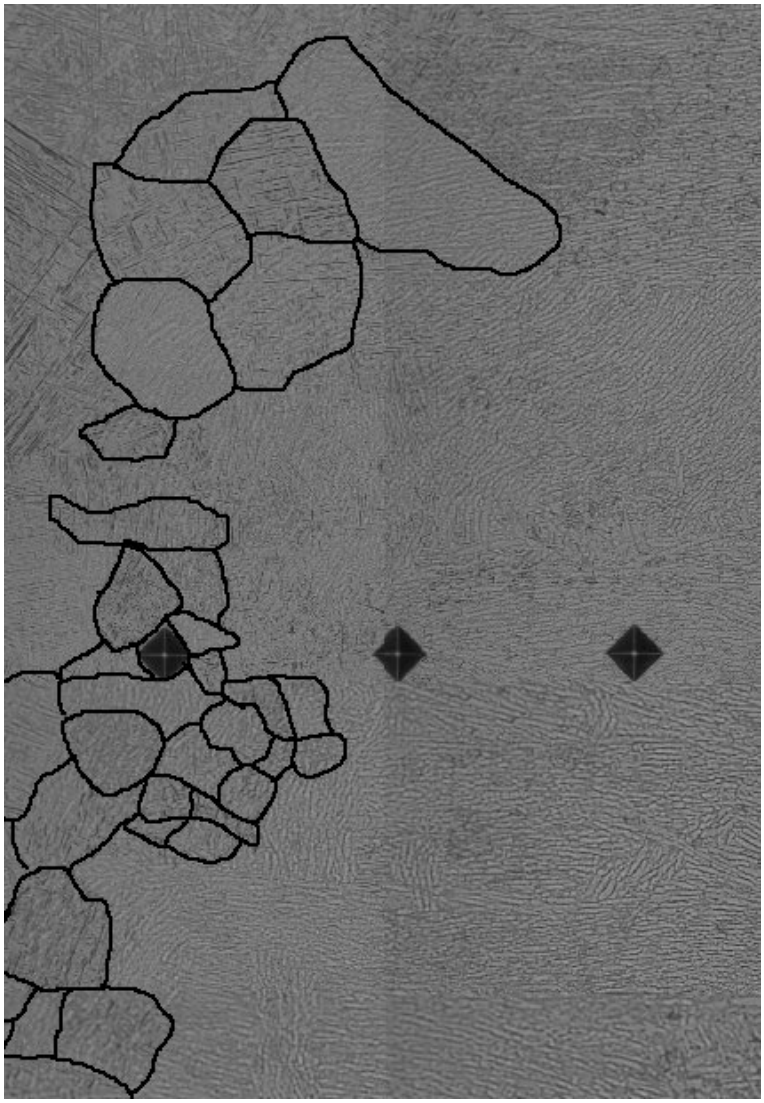

Figure 4.55.: Beta grain distribution in the location around 0.8 mm far from the weld line for the Ti-6Al-4V plate with initial lamellar microstructure and 3.75 mm thick

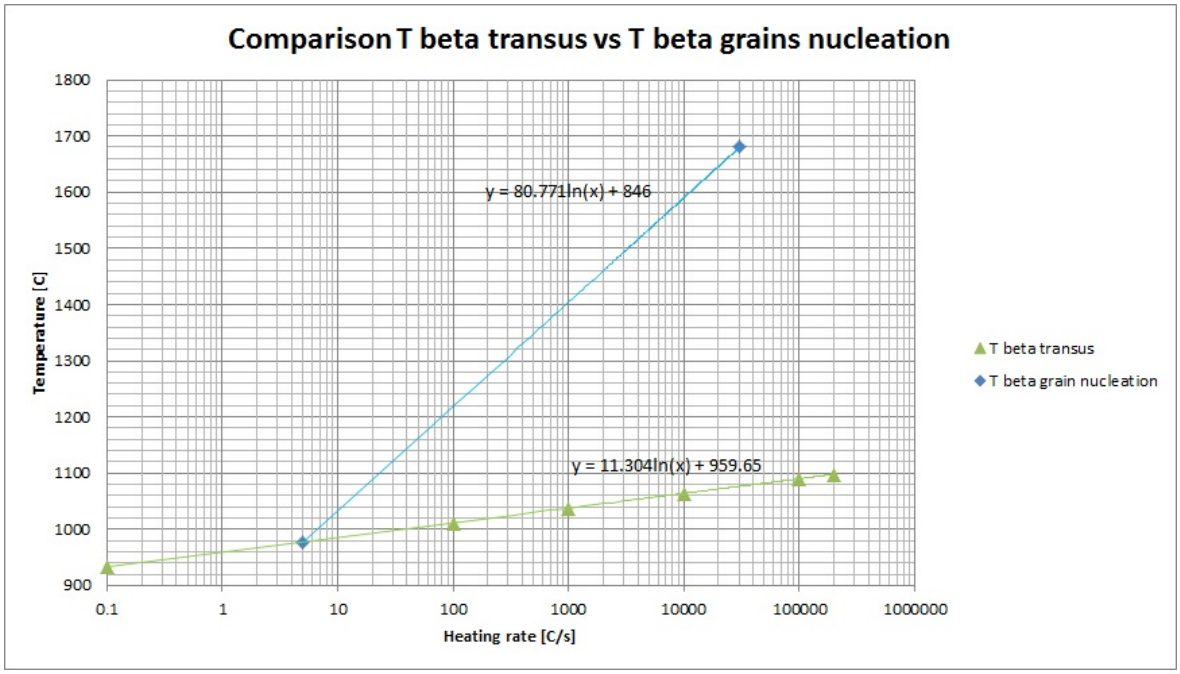

Figure 4.56.: Beta transus temperature and nucleation beta grains temperature as a function of the heating used for welding simulations of Ti-6Al-4V. The x axis represents the heating rate $\frac{dT}{dt}$

a)

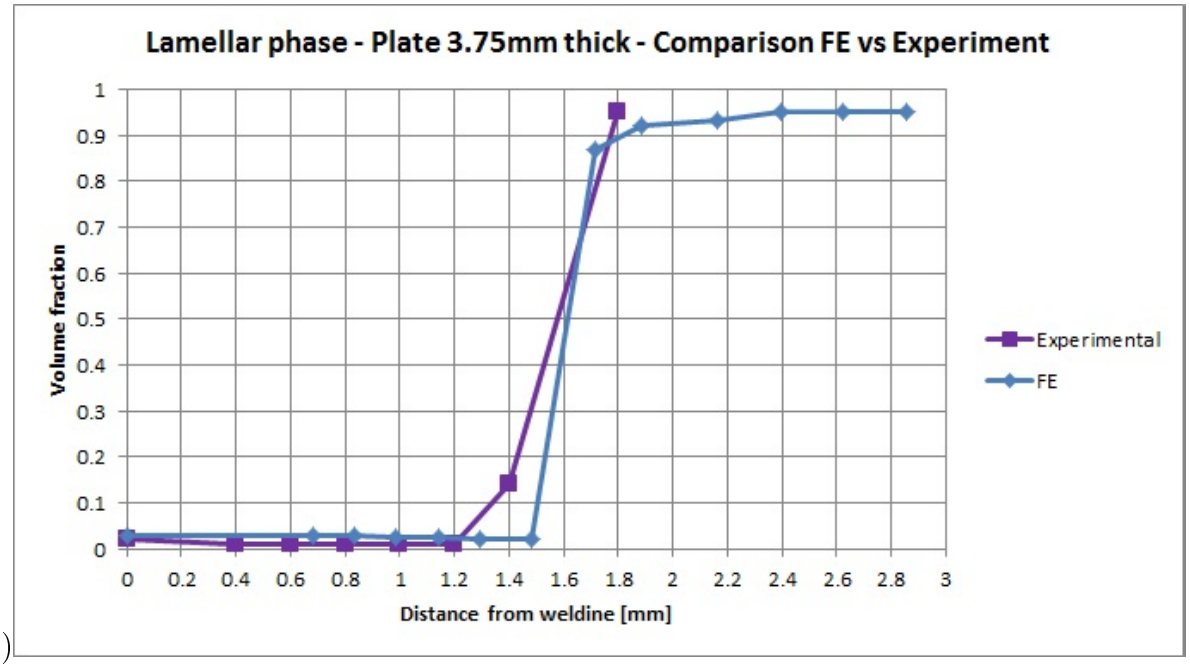

b)

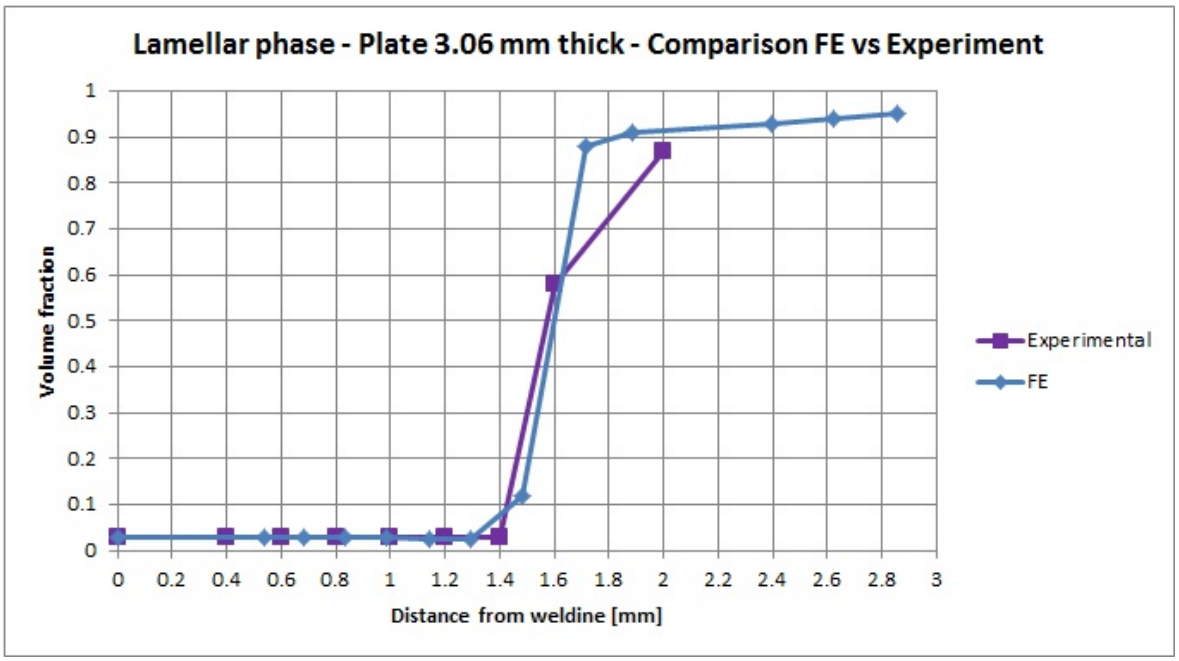

Figure 4.57.: Ti-6Al-4V plates with initial lamellar microstructure, a) 3.75 mm thick and b) 3.06 mm thick. Comparison between the alpha lamellar phase proportion predicted by the numerical model and the one experimentally measured for different distances from the weld line

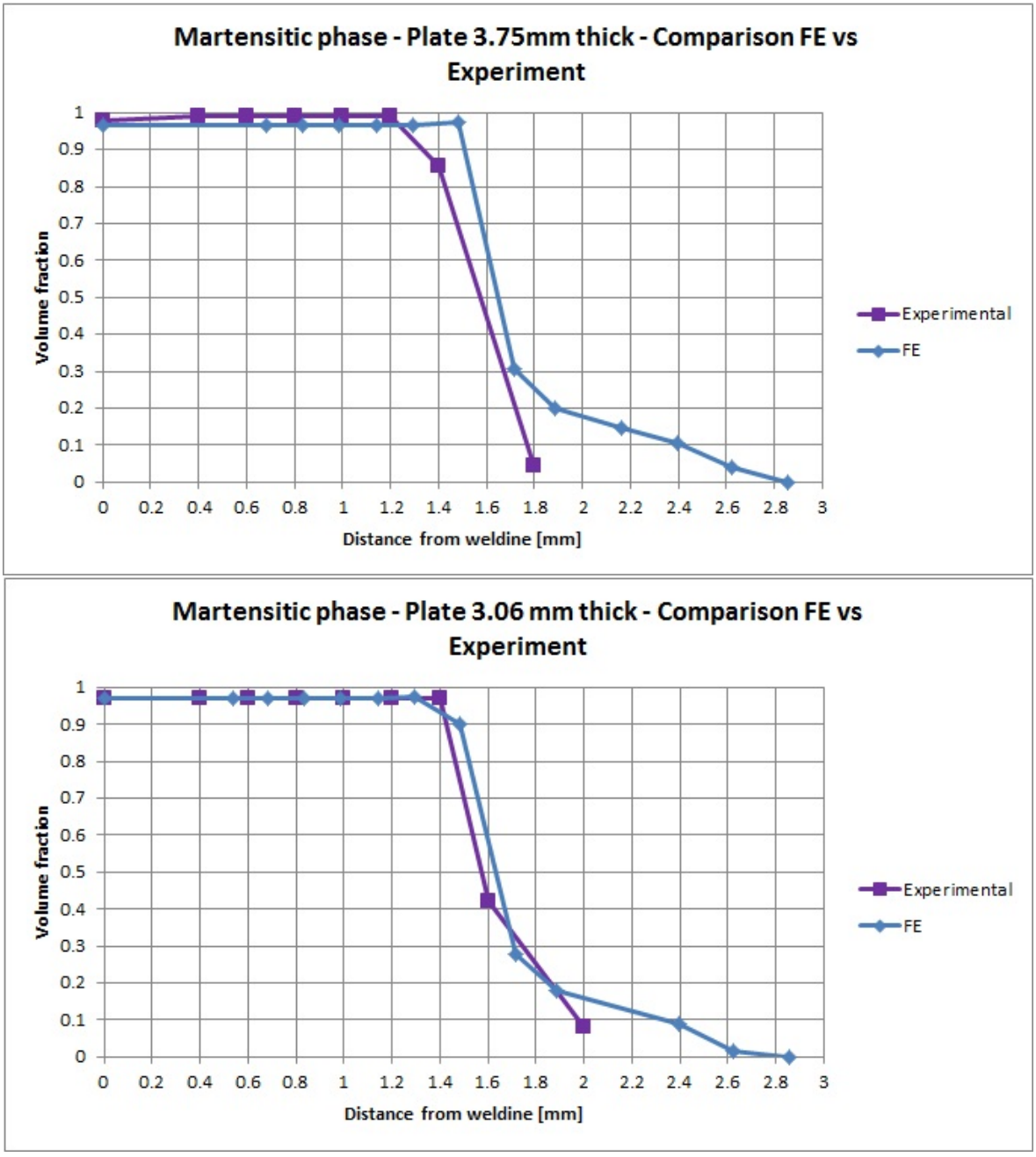

Figure 4.58.: Ti-6Al-4V plates with initial lamellar microstructure, a) 3.75 mm thick and b) 3.06 mm thick. Comparison between the martensitic phase proprtion predicted by the numerical model and the one experimentally measured for different distances from the weld line

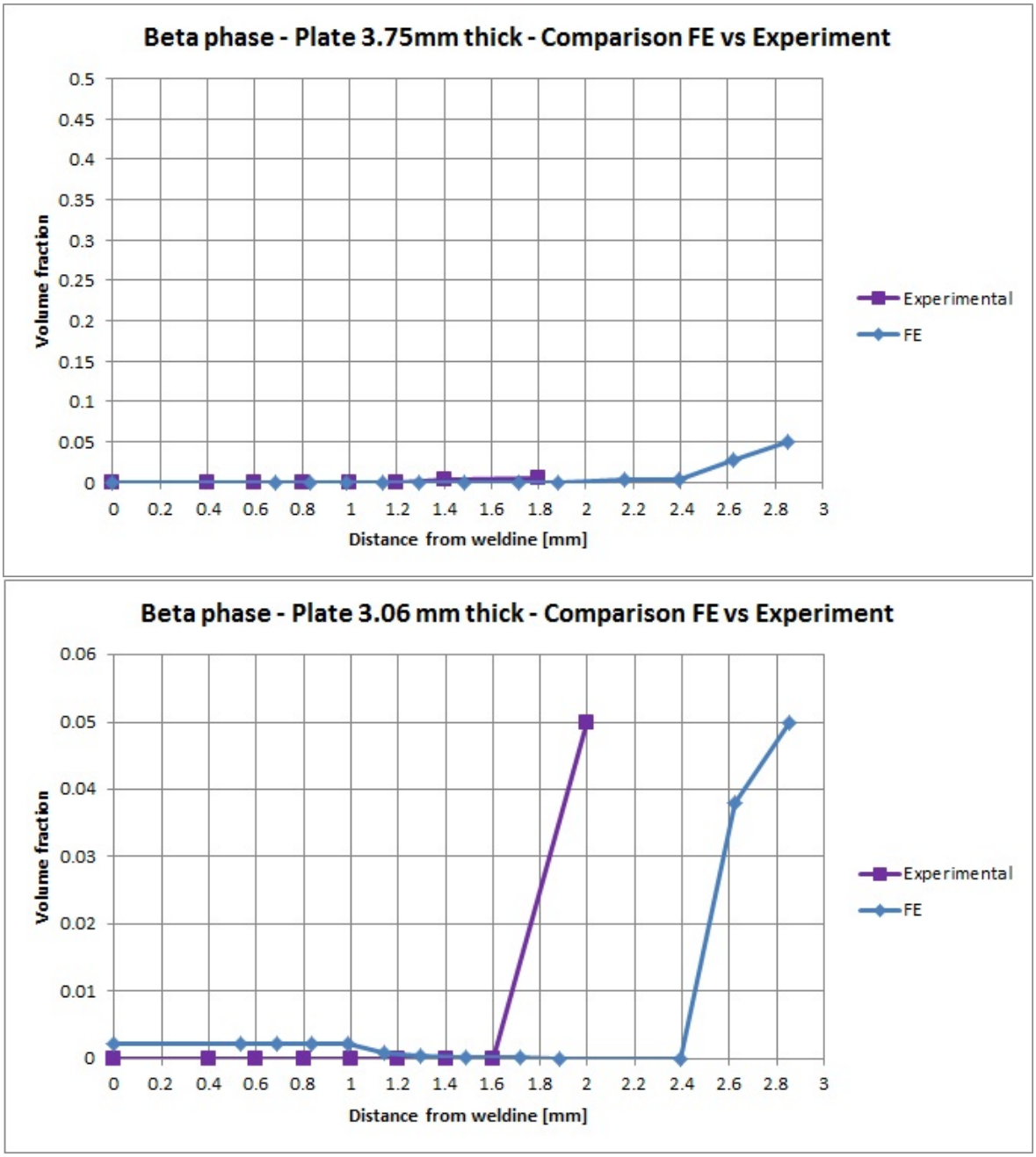

Figure 4.59.: Ti-6Al-4V plates with initial lamellar microstructure, a) 3.75 mm thick and b) 3.06 mm thick. Comparison between the beta phase proportion predicted by the numerical model and the one experimentally measured for different distances from the weld line

4.7 Mechanical model

The metallurgical model developed in this work can predict the evolution of the microstructure of the material during a welding process. In addition the mechanical models

in [113, 114] will allow the variation of the strength of the material when subjected to thermal treatments and mechanical loads to be investigated, with more accuracy than the current models the commerical software Visual-Weld in based on (chapter 2).

A preliminary set of equations based on the work presented in [113] and fully described in appendix E was gratefully accepted from the author to demonstrate the feasibility of coupling two phyisically based models, one metallurgical and one mechanical, for the description of the material behaviour. The author of this project did not develop this mechanical model and will therefore limit the discussion to a simple analysis of the potential of the approach, showing an example of the results that can be obtained.

The promise and advantage of such models is their capacity to adapt to different initial conditions of the material, such as microstructure and chemical composition. Thus eliminating the requirement for iteratively determining a new set of stress-strain curves and thus new experimental tests for each new variation. This allows the exploration of any combination of intial conditions of the material and process parameters to optimize the result desired, such as the final deformation, strength or ductility of a component subjected to a manufacturing process. A certain disadvantage of such physically based approaches is the complexity represented by the necessity to study and define appropriate physical equations to describe the phenomena under investigation. This results in more computational operations than is required when using simple tabular data, thus increasing inevitably the simulation running time. The developer of such models has to consider, when too complex models are obtained, reasonable simplifications to reduce the number of operations the computer has to cope with and, sometimes, to increase the stability of the model.

When the present work was carried out, the above mentioned mechanical model was still under development. Results of a preliminary version working in the $\alpha + \beta$ field of the material, for a lamellar microstructure, are shown in figure 4.62. As input data for the model, values sampled from a welding simulation are used, in particular phase proportions (alpha, beta and martensitic) and the particle dimensions (lamellae alpha and martensitic

needles) have been extracted at each time step to compute the mechanical stress induced as a function of the temperature and strain rate the material is subjected to. For this example, a constant strain rate of $0.0001\,s^{-1}$ has been applied to the model, for a duration of 800 seconds, giving a total strain of about 0.09. In figure 4.60 and 4.61 a zoom of the first 30 seconds of the results obtained from the welding simulation is shown to highlight the variation of phase proportions and particle sizes in correspondance with the temperature peak reached in the point sampled of the model.

In this project there was no time left for the validation of the results returned from the mechanical model, the chart shown is only for demonstrative purpose.

A first attempt to embed the code of the model into the commercial FE software VisualWeld was carried out. Results for simple heat treatments returned by this software were compared with the ones returned by the same mechanical model coded in the commercial software Matlab and were in agreement. Coupling of metallurgical and mechanical welding simulations was also feasible but the mechanical model showed to be still unstable when used in computation of welding simulations. A finer tuning and investigation of the behaviour of the model during welding processes is thus reccomended for future work.

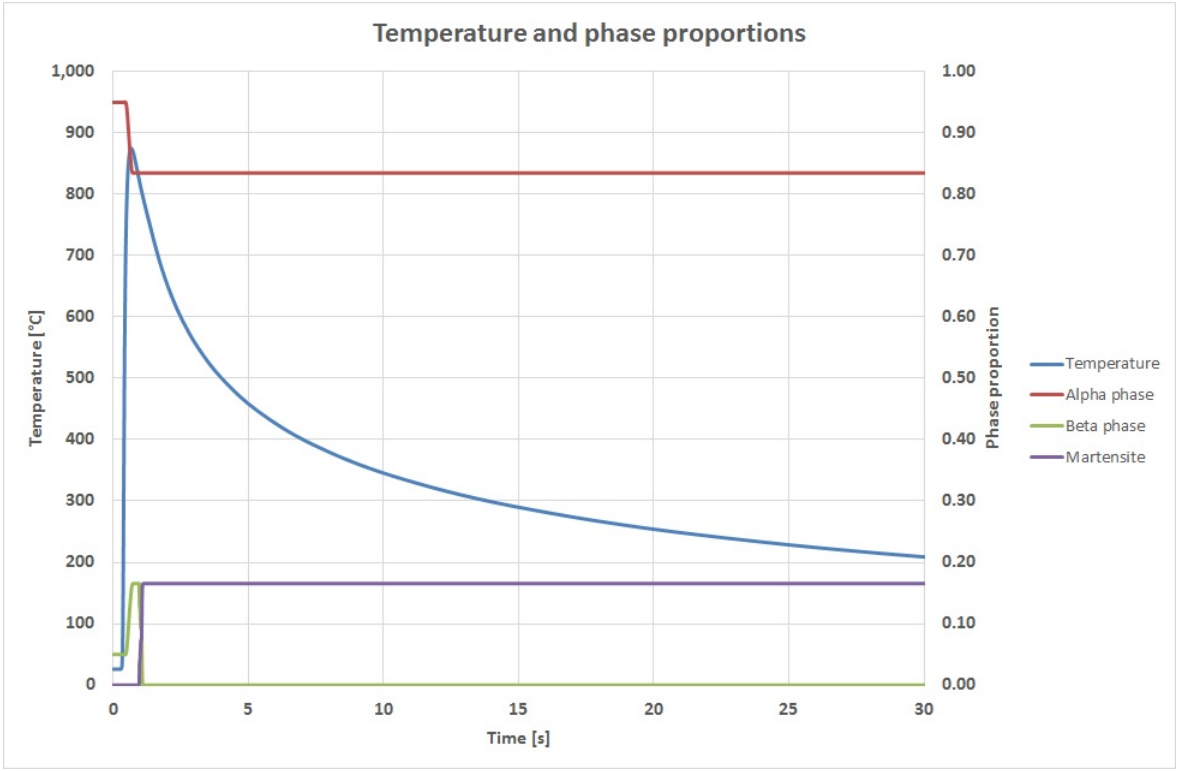

Figure 4.60.: Temperature and phase proportions used as input data for the prediction of the stress-strain curve shown in figure 4.62. In this figure the first 30 seconds of data obtained from a welding simulation with a total duration of 800 seconds are shown, to highlight the area of the chart where variations of phase proportions occur

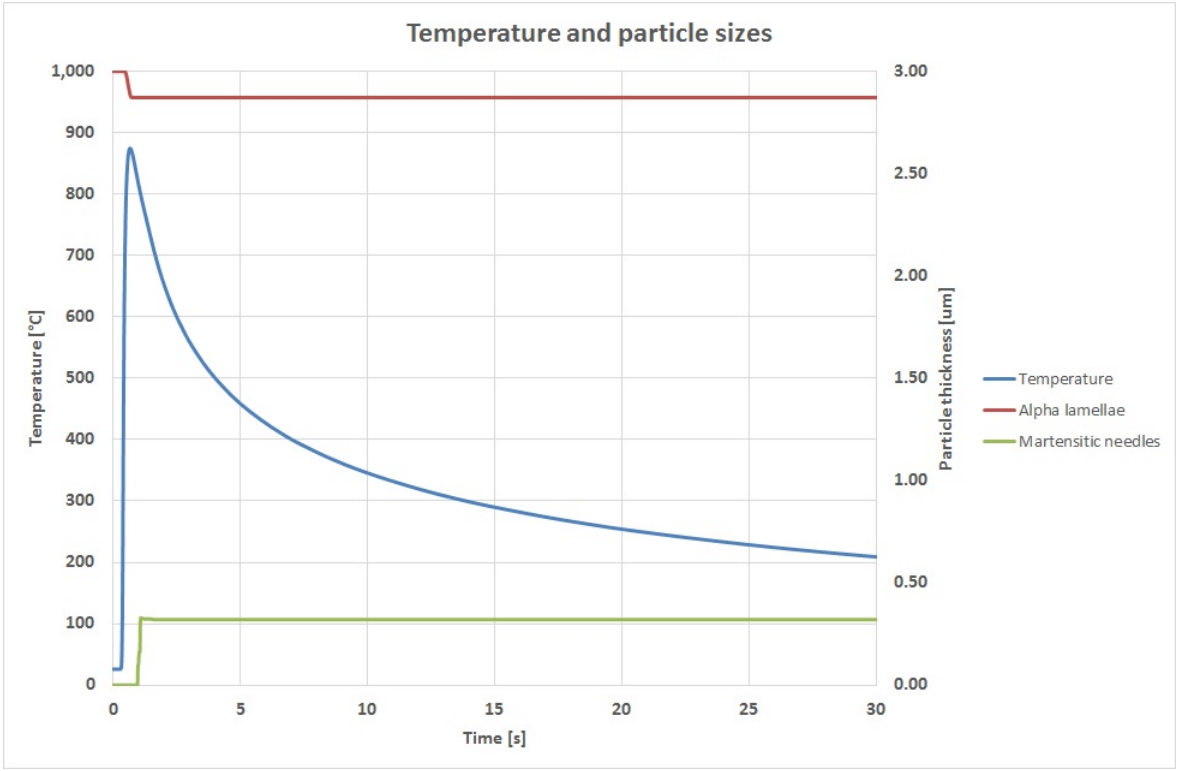

Figure 4.61.: Temperature and and particle sizes used as input for the prediction of the stress-strain curve shown in figure 4.62. In this figure the first 30 seconds of data obtained from a welding simulation with a total duration of 800 seconds are shown, to highlight the area of the chart where variations of particle sizes occur

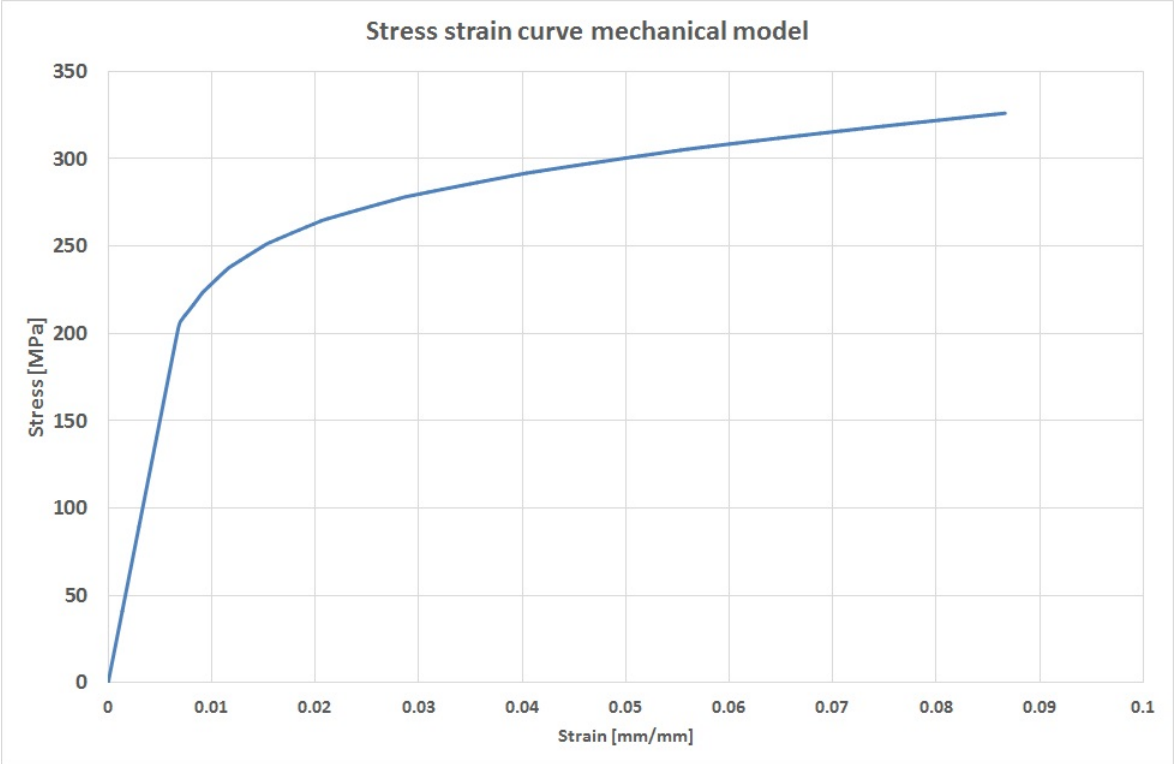

Figure 4.62.: Stress-strain curve predicted by the mechanical model for the temperature, phase proportions and particle sizes shown in figure 4.60, 4.61 and strain rate of 0.001 s^{-1}. The section relative to the first 30 seconds of computation covers strains up to 0.007

4.8 Summary

4.8.1 Diffusion based model

A diffusion based model has been developed and coded to describe growth and shrinkage of alpha equiaxed and lamellar microstructures for Ti-6Al-4V alloys in the $\alpha + \beta$ field.

The validation of the model has been carried out using data found from previous work published in literature in the case of the equiaxed microstructure, and by experiments in the case of the lamellar microstructure. In both cases the model returned predictions aligned with the experimental results.

When fast heat treatments were studied, the diffusion model showed a progressive temperature overestimation of the complete dissolution of the lamellar microstructure. In fact, from the experiments, a change in the crystallographic structure of the material,

from HCP to BCC, was noticed at temperatures lower than the ones predicted by the diffusion based model for complete dissolution of the alpha phase lamellae in the beta matrix. This can be explained by the material reaching a sufficiently high internal energy to allow a switch to the more stable crystallographic structure even with a non complete dissolution of the alpha phase. With this consideration, to determine the beta transus as a function of the heating rate, a JMA approach was adopted and applied to the diffusion based model, to establish when a complete transition from alpha to beta phase was obtained, independent of the state of the alpha phase dissolution reached.

With the integration of the diffusion and JMA models, a satisfactory prediction of the microstructural evolution at the different heat treatments tested was obtained.

4.8.2 Experimentally based models

For the following phenomena

- martensite formation
- beta grains nucleation, growth and coarsening both starting from state and liquid state
- lamellae nucleation and growth cooling down from above the beta transus temperature

No reasonable solutions were found in the literature to allow their physical modelling by relatively simple equations, suitable for adoption in industrial applications where short simulation running times are very important. Thus, phenomenological or experimental equations were adopted.

Satisfactory results were obtained using these models even though, when applied to a microstructure different to the one for which they were calibrated, a rise in the prediction errors could occur. But this limitation is in the intrinsic nature of this approach.

A reasonable solution to physically model the lamellae nucleation was found in the literature but there was no time to code, develop and validate such an approach.

The martensitic transformation seems to be over predicted at far locations from the weld line, suggesting that the conditions leading to this transformation should be investigated more in detail.

4.8.3 Welding models

Welding tests were carried out both on plates with an initial lamellar and an equiaxed microstructure. The samples welded were studied at different locations from the weld line, analysing the phase proportions and morphology evolution of the material microstructure. The results were then compared with the predictions of welding simulations run for the same conditions as the experiments and using the microstructural numerical models presented in this work. Considering the complexity of the phenomena described and the difficulty in experimentally quantifying the microstructure investigated, good agreement between experimental and numerical results was obtained.

The welding simulation run times obtained when adopting the models developed in this work were double those for the conventional approach adopted in the commercial software Visual-Weld, based on the phenomenological JMA approach.

The advantage of the solution proposed here, with respect to the JMA approach, is the capability to self adapt to different chemical compositions and initial microstructures of the material when predictions are made in the $\alpha + \beta$ field. Moreover, the microstructural evolution of the particle dimensions are predicted, which is important for mechanical strength prediction of Titanium alloys and also for possible future fatigue life modelling.

4.8.4 Mechanical model

A first attempt trying to couple the metallurgical model developed in this work with a mechanical physically based model able to describe the variation of the strength of the material as a function of temperature and microstructure was carried out.

The mechanical model is promising and currently still under development. A preliminary version has been coded in the commercial software Visual-Weld to interact with

results obtained from a metallurgical welding simulation computed using the diffusion based model presented in this work. The mechanical code showed still unstability and needed very small time steps, this did not allow any full weld model to be completed, but nonetheless it was possible to predict some stress-strain curves obtained by the interaction of the mechanical and metallurgical models.

CHAPTER 5

Summary

Ti-6Al-4V thermo-mechanical-metallurgical behaviour. During welding, a material is subjected to a very wide range of temperatures, highly varying as a function of time and space, inducing high stress gradients, significant changes in the microstructure and thermo-mechanical behaviour of the material. Modelling all these material property variations is complicated, particularly when coupling metallurgical and mechanical behaviour.

Some useful data and work found in the literature on the modelling of the material behaviour at different temperatures, stresses and with different microstructures have been analysed and presented. Many works have been carried out on the modelling of Ti-6Al-4V behaviour, adopting different approaches and levels of precision in the description of different phenomena, however little work has been carried out applying these solutions to welding simulations.

In an attempt to improve this situation, considering as a final objective the necessity to develop an industrially applicable model, with acceptable simulation running times, a solution had to be chosen between five fundamentally different ways in which the material behaviour can be modelled. These progressively become more accurate but also more time consuming:

1. usage of pure numerical data, usually in tabular form, as functions of temperature

and strain rate;

2. empirical equations without any physical meaning but able to describe the behaviour of the material in a continuous domain as functions of different variables, like temperature and strain rate;

3. relations between some particular significant properties of the material and its behaviour, like phase distribution and microstructure morphology;

4. internal constitutive equations describing actual physical phenomena in the material;

5. calculations based on the actual crystal physics.

Another important aspect of these choices was the progressively more accurate and specific data required by the solutions going toward more and more physically based predictions.

The fourth option is currently not able to return results in a reasonable computation time, if implemented in a FE code to simulate cases such as described in this work.

It was thus reasonable to develop a compromise solution between options 2, 3 and 4, describing the evolution of the morphology of the material as functions of lamellae/grains thicknesses, volume fractions of phases, temperature, strains and, then using a physically based relationhip, incorporate the morphology changes into the model for the strength of the material.

Previous to this work, the simulation of Ti-6Al-4V behaviour during welding processes was based on the description of the evolution of metallurgical phases by the JMA phenomenological equation, coupled to the mechanical behaviour by a rule of mixtures, in which the stress-strain curve of each phase, at a specific temperature, gave a contribution proportional to the relative amount of the phase in the material.

The capacity to predict residual stresses in the material or the ability to work with different thermal histories of the microstructure was unclear and it was believed that a model referring to the evolution of the microstructure could describe more accurately the material behaviour during welding, without increasing excessively the computational cost of a numerical simulation.

To adapt the microstructural model to the wide range of temperatures and conditions encountered in a welding process, different approaches were adopted, based on the type of microstructure evolving into the material and the solutions available in literature:

1. a single particle diffusion based approach was developed for the metallurgical modelling of the microstructure evolution in the $\alpha + \beta$ field

2. an experimental approach was adopted to model the beta grain growth in the beta field, nucleation and growth of alpha lamellae and martensitic formation of needles during cooling from temperatures above the beta transus temperature

3. a preliminary dislocation based approach was adopted for the mechanical behaviour modelling, which was able to predict the strength of the material as a function of the state of the microstructure.

The Gibbs free energy required to compute the diffusivity of the diffusing species was obtained from the Gibbs free energy analytical expression for a ternary system Ti-Al-V [106, 110]. This solution was within 2.5% of the Gibbs free energy calculated by Thermocalc® for the actual alloy composition. This difference was considered satisfactory as the effect on the prediction of the numerical models was small. The work in literature used discrete values of the Gibbs free energy at different temperatures and compositions in the form of tabular data, which required new values every time the alloy changed; in the solution developed in this work, the Gibbs free energy equation is based on the equilibrium element composition, returning values as a function of the chemical composition and temperature obtained during the solution of the diffusion based model and does not need new Gibbs free energy values to be input when the chemical composition of the alloy changes.

The validation of the diffusion based model was made using literature data for the equiaxed microstructure, and by conducting experiments at heating rates close to the ones involved in a welding process for the lamellar microstructure (5-500 °C/s). Welding

experiments considering either initially equiaxed or lamellar microstructures allowed a further validation of the model, with typical thermal loads generated during welding.

Studying the evolution of lamellar microstructure at fast heating rates, the diffusion kinetics seemed to prevent complete dissolution of the alpha precipitates when reaching the beta transus temperature, leaving typical "ghost shapes", observable by SEM-BEI, memory of the parent microstructure and relative chemical composition. When this microstructure was rapidly cooled down, martensite formed, confirming that the parent alpha phase had transformed to beta phase, even if the alpha stabilised chemical field was still not completely dissolved. This phenomenon had not been reported in any literature source investigated and thus would deserve further study to understand if the diffusion based process, in these situations, becomes a displacive transformation, more similar to the martensitic transformation. Since this phenomenon could not be predicted by the diffusion based model, a JMA approach was used to establish when, at temperatures close to the beta transus temperature, a complete transformation of the alpha phase to the beta phase occurred.

The validation of model 1), for a material starting with an initial lamellar microstructure, was made by an experimental characterization studying the effect of different thermal loads on the material. The validation of the model, when an initial equiaxed microstructure was present in the material, used literature results.

For model 2), experimental characterization was used to obtain the trends of the microstructure evolution which was then modelled by fitting the data to empirical equations.

The model 3) was based on the work published in [113] and is still under development but nonetheless it has been possible to run some tests to evaluate the feasibility of coupling the microstructure models with the flow stress evolution.

The metallurgical model provided a good matching between the numerical and experimental results obtained, with the capability of the diffusion based model to self adapt to different chemical compositions of the material and initial microstructures, with no need of any fitting parameters. The models developed were coded into the commercial

software Visual-Weld and validated running welding simulations with the same conditions of the experimental welding tests described in chapter 3 (reassumed in table 5.1). Good matching between phase proportions, lamellae thickness and alpha and beta grain size was obtained for all the cases investigated. The experimental approach used to describe the beta grain size and beta phase proportion evolution showed the highest discrepancy with the experimental measurements. Screenshots of the results obtained by running the FE welding simulations, described in detail and validated against experimental data in chapter 4, are shown:

- in figure 5.1, figure 5.2 and figure 5.3 for the plate 1;
- in figure 5.4, figure 5.5 and figure 5.6 for the plate 2;
- in figure 5.7, figure 5.8 and figure 5.9 for the plate 3.

To run welding simulations using the numerical models developed and coded into Visual-Weld, the user needs to input the chemical composition, the mean size of the α precipitates and the phase proportions in the initial microstructure of the component studied. At the end of the computation, the user can check the evolution of the microstructure (phase proportions and particle sizes) into the component during the welding process and optimize the process in case standards are not respected. Computational run times were increased by a factor of two when compared with a conventional simulation, meeting the requirements for acceptable computational efficiency.

The results of the metallurgical model when passed as input data to the mechanical model will allow FE simulations that consider the effect of the variation of the thermal loads on the evolution of the microstructure and mechanical strength of the material. This combined approach will require some further validation against experiments.

Plate	Microstructure	Dimension plate $[mm]$	Power [%]	Welding speed $[m/min]$
1	Equiaxed	$46.95 \times 151.5 \times 2.00$	60	2.0
2	Lamellar	$47.30 \times 136.965 \times 3.76$	70	2.0
3	Lamellar	$47.31 \times 137.05 \times 3.06$	70	2.0

Plate	Chemical composition
1	Al 5.82, V 4.00, Fe 0.06, H 0.00963, N 0.010, O 0.063, Ti bal
2	Al 5.75, V 3.96, Fe 0.07, H 0.00445, N 0.013, O 0.11, Ti bal
3	Al 5.75, V 3.96, Fe 0.07, H 0.00445, N 0.013, O 0.11, Ti bal

Table 5.1.: Welding test parameters used to run FE welding simulations. Experimental welding tests with the same conditions were carried out to validate the numerical models (chapter 3). Ti-6l-4V plates with two different initial microstructures, chemical compositions and different thicknesses were welded, using a welding speed of $2.0\,m/min$. The welding input power was set as percentage of the maximum power ($4\,kW$) of the welding machine used

Weld sequence optimization (appendix D). An algorithm for the determination of a initial DOE table was established. A surrogate model adopted from literature was improved and provided reasonable optimization of the component final deformation.

Further investigations are necessary to validate and possibly improve the model. The numerical models adopted for this work returned very small final deformations, comparable to the convergence tolerance of the numerical simulation. Models with higher deformations are suggested to stay far from the convergence tolerance and for easier experimental measurement.

The material data adopted for running the simulations of this part of work were in the form of tabular thermo-mechanical properties as a function of temperature.

As described in chapter 2, when using this approach is not possible to describe the variation of the behaviour of the material in function of its microstructure evolution and, at the same time, by the usage of discrete tabular data, the FE solver could be required to calculate properties of the material by interpolating between sudden variations of the input data.

Currently, the influence of the heat source on previous welds is taken in to consideration just from the stresses induced by thermal load without considering any metallurgical effect.

Conversely when adopting more complex solutions, the computation time necessary for

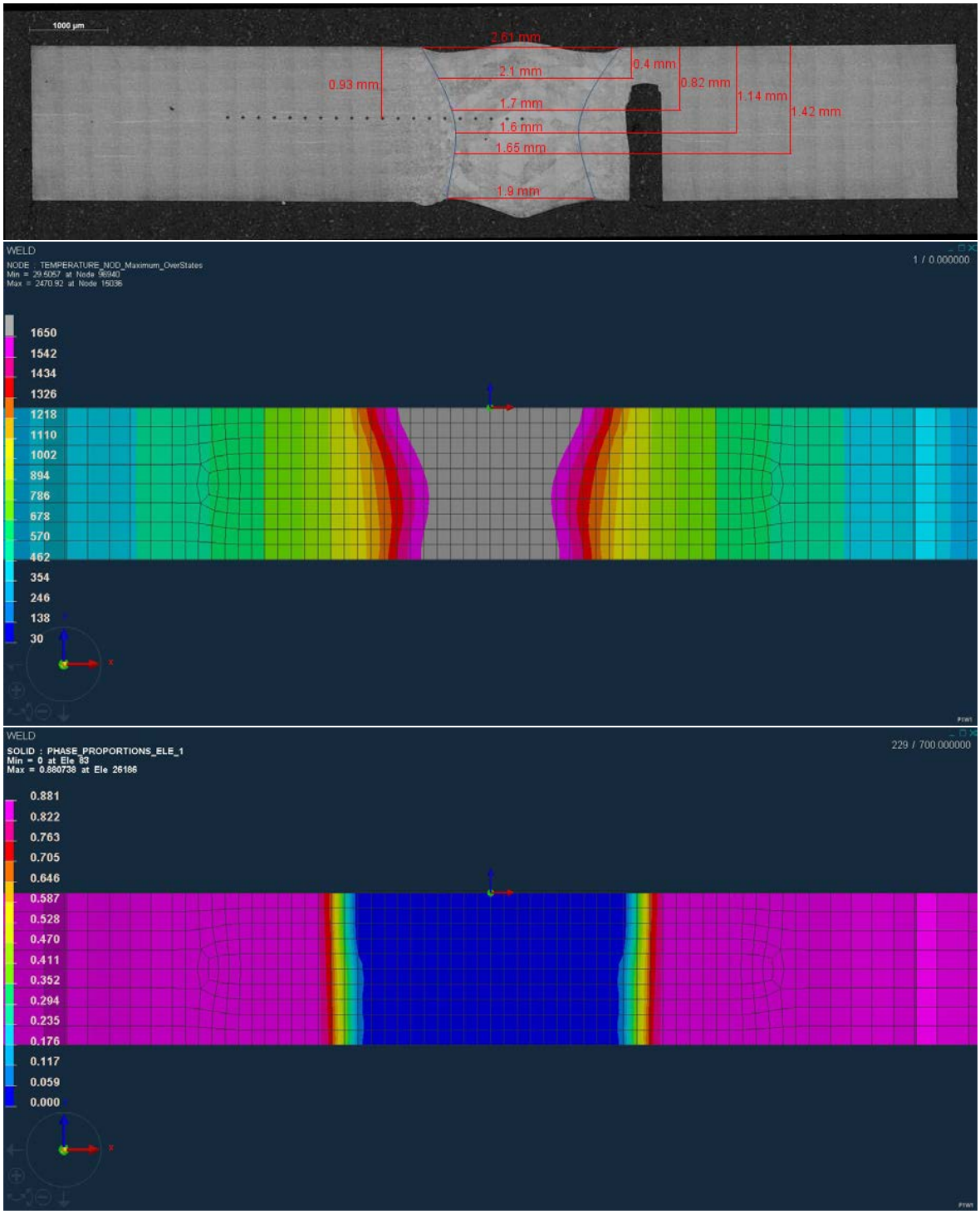

Figure 5.1.: Experimental (top) and numerical (centre) weld pool fusion zones for the 2 mm thick Ti-6Al-4V plate with initial equiaxed microstructure, welded with a speed of 2 m/min and 60% power (plate 1 in table 5.1). The fusion zone is bounded in the micrograph by blue lines whilst it is identified by the grey color in the FE model (see figure 4.36 for dimensional comparison). The bottom picture shows the α equiaxed phase proportion obtained for the same section of material, at the end of the FE simulation

Figure 5.2.: β phase proportion (top), martensitic phase proportion (centre) and radius $[\mu m]$ of the α equiaxed microstructure (bottom) obtained running the FE welding simulation with conditions described in figure 5.1 (plate 1 in table 5.1)

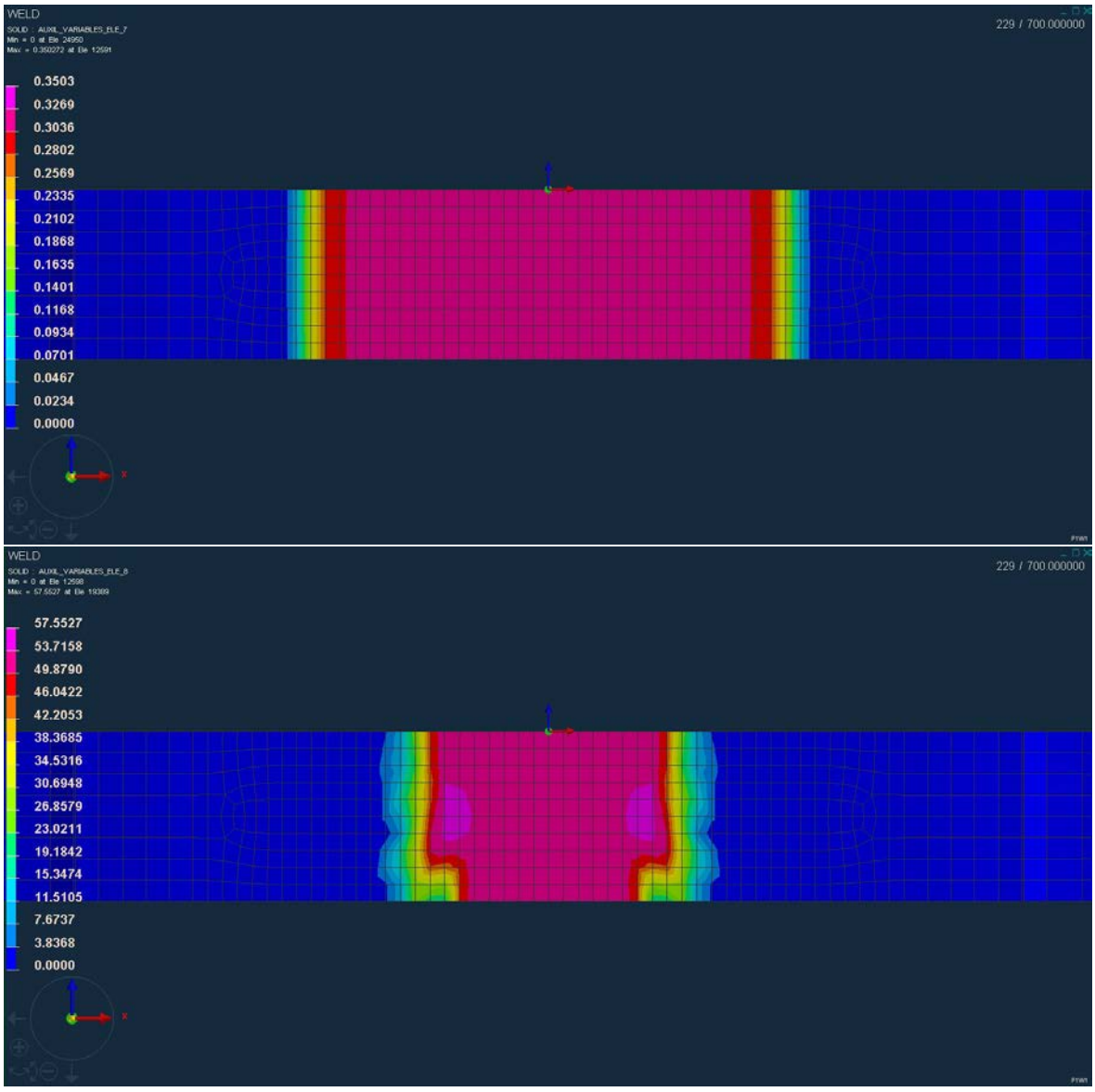

Figure 5.3.: Martensitic needles thickness [μm] (top) and beta grain radius [μm] obtained running the FE welding simulation with conditions described in figure 5.1 (plate 1 in table 5.1)

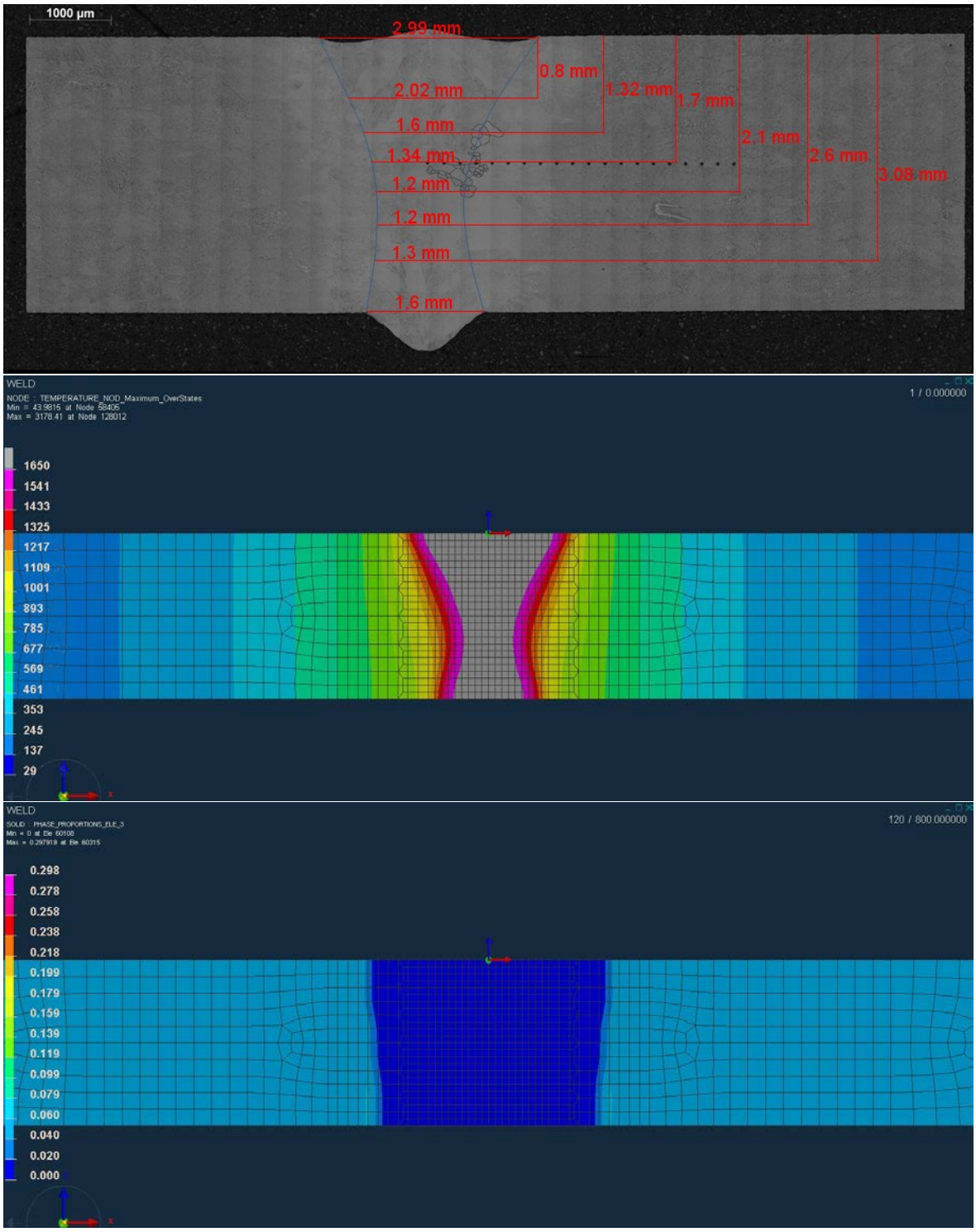

Figure 5.4.: Experimental (top) and numerical (centre) weld pool fusion zones for the 3.76 mm thick Ti-6Al-4V plate with initial lamellar microstructure, welded with a speed of 2.0 m/min and 70% power (plate 2 in table 5.1). The fusion zone is bounded in the micrograph by blue lines whilst it is identified by the grey color in the FE model (see figure 4.38 for dimensional comparison). The bottom picture shows the β phase proportion obtained for the same section of material, at the end of the FE simulation

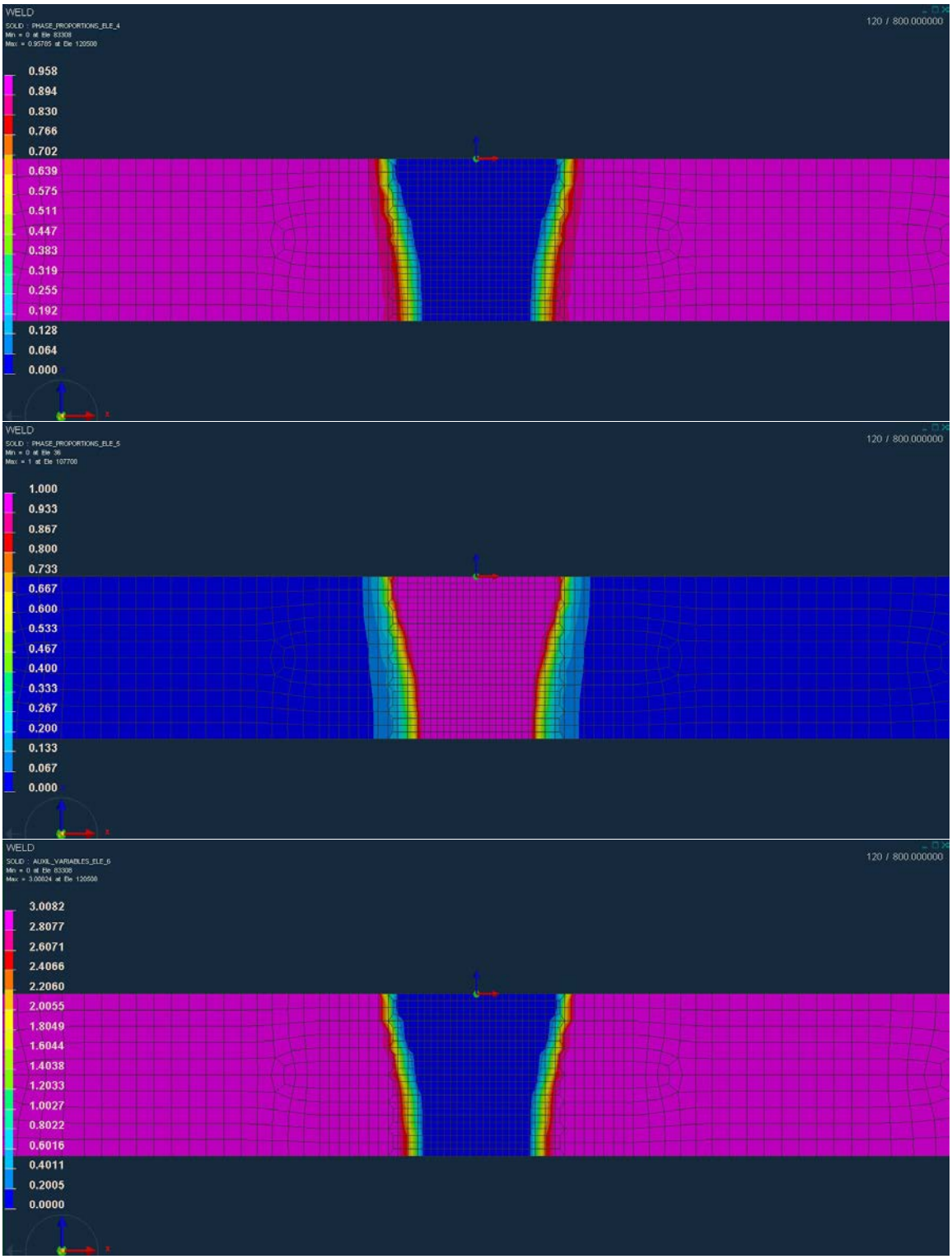

Figure 5.5.: Lamellar α phase proportion (top), martensitic phase proportion (centre) and lamellar thickness $[\mu m]$ of the alpha lamellar microstructure (bottom) obtained running the FE welding simulation with conditions described in figure 5.4 (plate 2 in table 5.1)

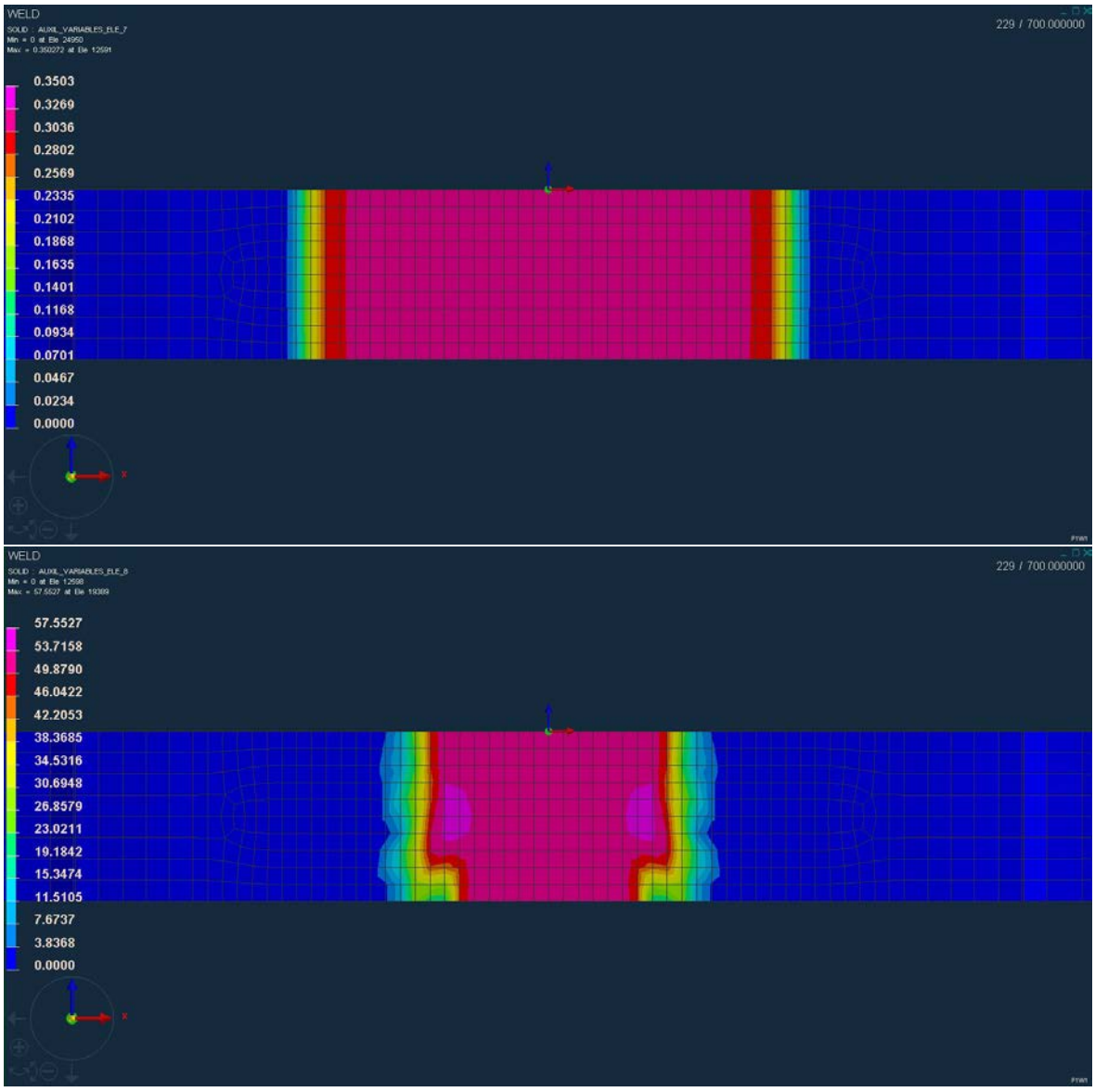

Figure 5.6.: Martensitic needles thickness [μm] (top) and beta grain radius [μm] obtained running the FE welding simulation with conditions described in figure 5.4 (plate 2 in table 5.1)

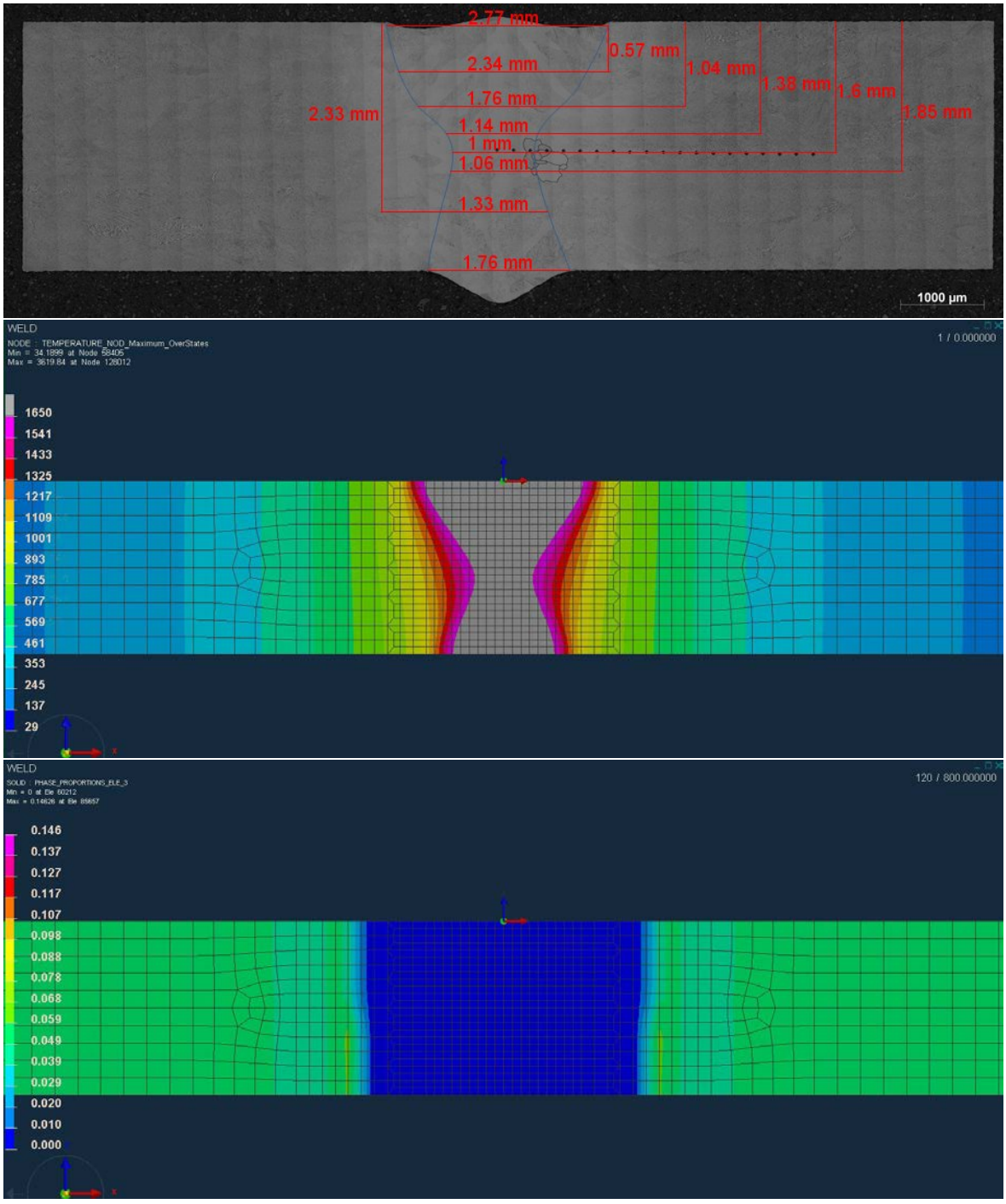

Figure 5.7.: Experimental (top) and numerical (centre) weld pool fusion zones for the 3.06 mm thick Ti-6Al-4V plate with initial lamellar microstructure, welded with a speed of 2.0 m/min and 70% power (plate 3 in table 5.1). The fusion zone is bounded in the micrograph by blue lines whilst it is identified by the grey color in the FE model (see figure 4.40 for dimensional comparison). The bottom picture shows the β phase proportion obtained for the same section of material, at the end of the FE simulation

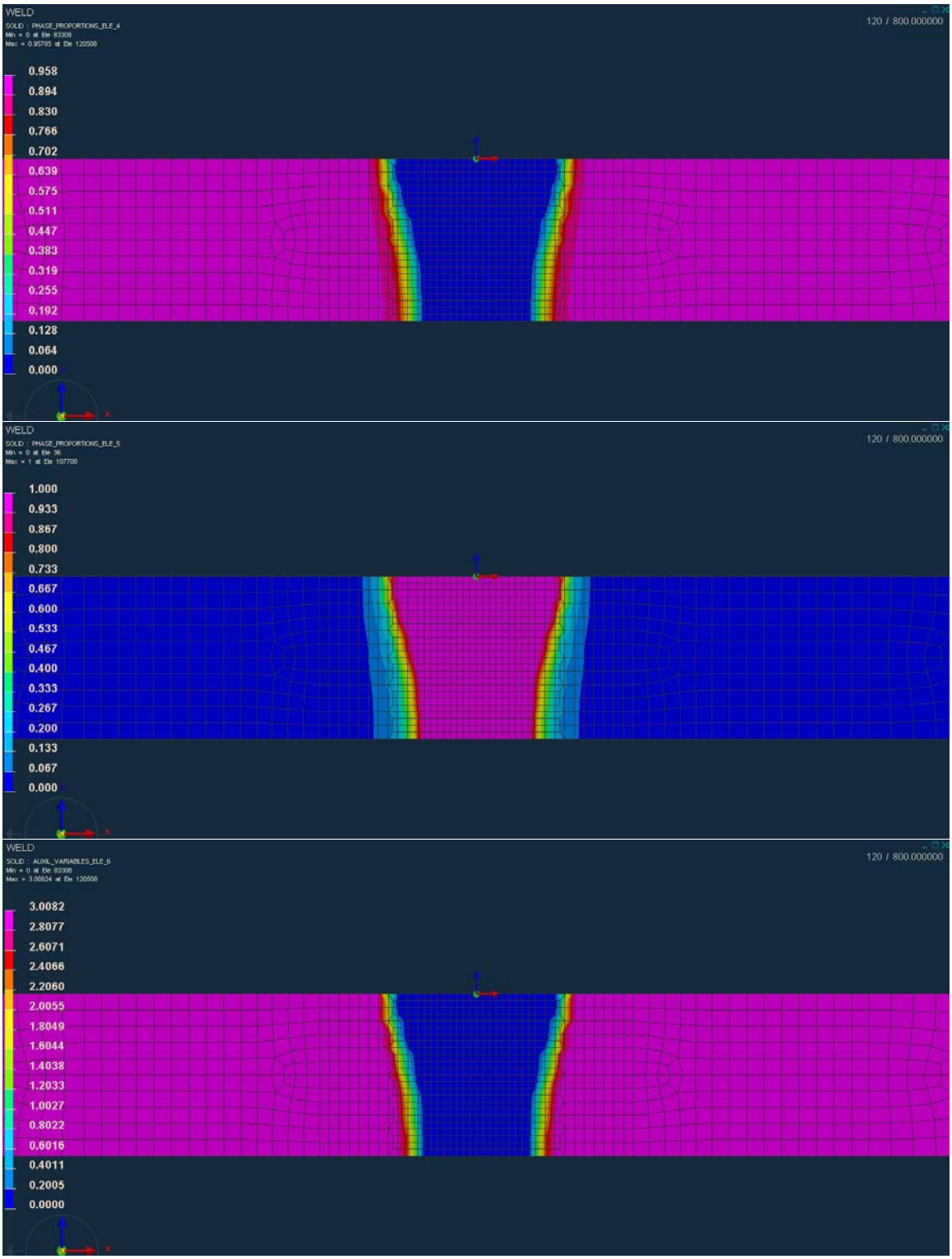

Figure 5.8.: Lamellar α phase proportion (top), martensitic phase proportion (centre) and lamellar thickness $[\mu m]$ of the alpha lamellar microstructure (bottom) obtained running the FE welding simulation with conditions described in figure 5.7 (plate 3 in table 5.1)

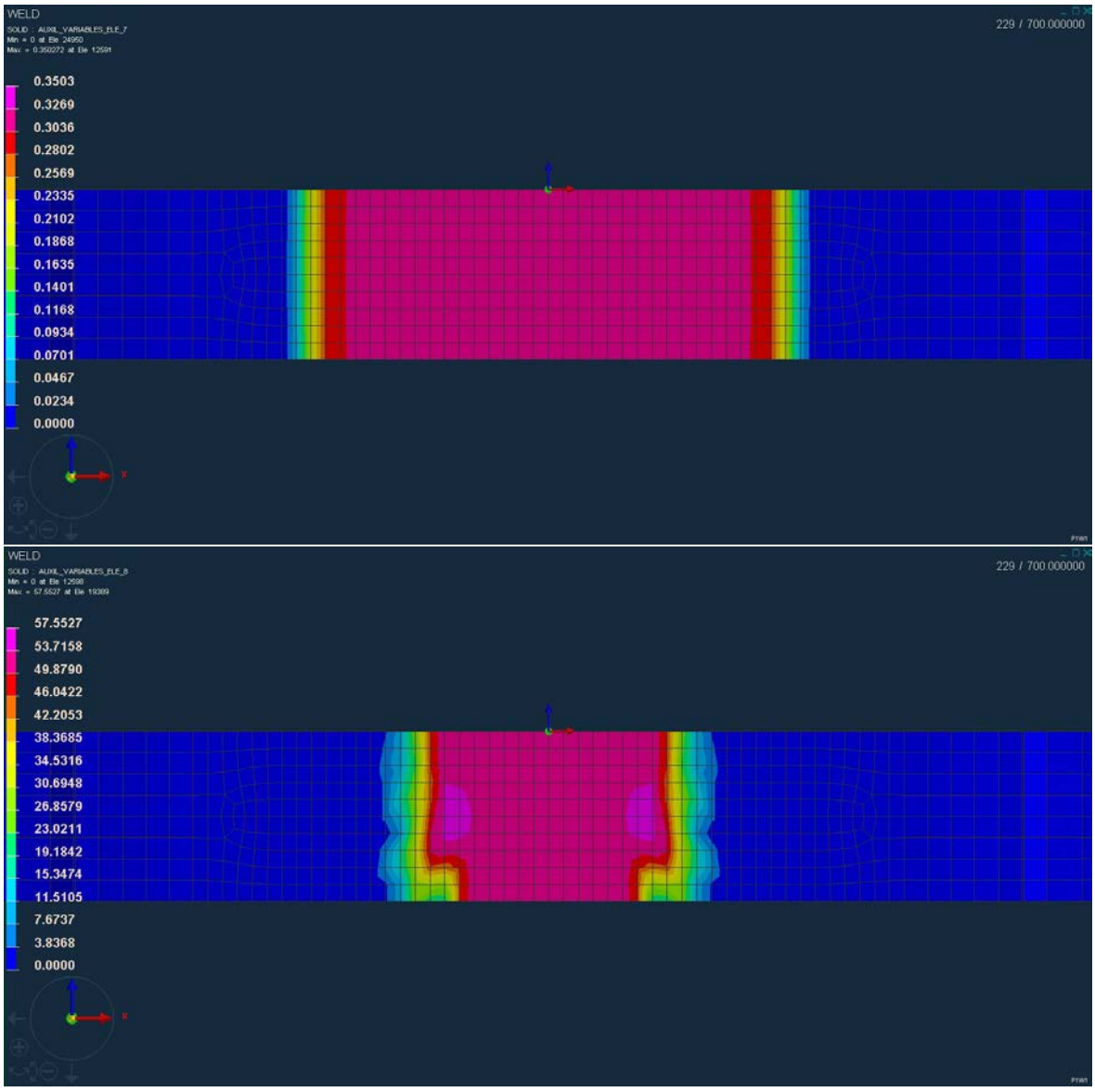

Figure 5.9.: Martensitic needles thickness [μm] (top) and beta grain radius [μm] obtained running the FE welding simulation with conditions described in figure 5.7 (plate 3 in table 5.1)

the execution of simulations increases. This consideration assumes particular importance when complex structures, big geometries or a process of optimization requires execution of many simulations, like in the case of the weld sequence optimization problem.

However run times are already considerable using thermo-mechanical tabular data, typically three days for a simulation.

CHAPTER 6

Conclusions

1. A model for the evolution of microstructure during welding of Ti-6Al-4V has been developed. The model has been coupled to a physically based constitutive equation for the prediction of flow stress evolution.

2. The microstructural models have been implemented in the ESI FE solver Visual-Weld and have met the requirement for acceptable computational efficiency such that run times are only increased by a factor of two when compared with a conventional simulation.

3. An innovative method for determining the Gibbs Free energies, needed to model the phase coarsening or dissolution, has been implemented which allows the model to accommodate a wide range of compositions in a computationally fast and robust way.

4. The changes in phase morphology that occur in welding have been quantified using a comprehensive set of experimental tests carried out at temperatures and heating rates relevant to welding. It was noted that at high heating rates not only the beta transus temperature increased but also the beta phase remains segregated in accordance with the original alpha-beta structure due to the short timescale preventing diffusion based homogenisation.

5. The fusion zone shapes obtained using a series of instrumented autogenous test welds were used to calibrate the heat source used in the models [112].

6. The microstructural model predictions were in good agreement with both literature data and the structural characterisation results obtained from the test welds produced.

7. The preliminary simulations carried out using the coupled metallurgical and microstructural model gave reasonable results and it is recommended that this approach is developed further in future work.

8. An instrumented test rig was designed and manufactured to facilitate the measurement of the distortion that occurs in welding (figure C.1).

9. An optimised welding sequence for a multipass weld was demonstrated using the approach developed in this work (described in appendix D).

CHAPTER 7

Future work

The work proposed for the future would be useful to fill the weak points, in the author's opinion, of the current study and to better understand some unclear phenomena revealed during this PhD.

- A physically based approach to describe nucleation and growth of alpha lamellar microstructure, cooling down from temperatures above the beta transus temperature, should be investigated and developed, instead of using the experimental approach adopted in this work. A promising recent publication [72] tried to cope with this phenomenon, obtaining good predictions, even when assuming the initial beta grain dimensions. The experimental approach presented in this work to describe the beta grain growth could be used as a first step and then left, when a reasonable physical solution becomes available.

- A physically based approach to describe the formation of martensitic needles should be developed to better describe the relation between their dimension with the heat treatment and/or other factors. In this case, no work was available in literature to describe this phenomenon, besides experimental or the phase field approach. A solution requiring shorter simulation times than the phase field is, however, suggested, otherwise the final objective to realize a solution for industrial applications will not be anymore feasible.

- Modelling of the beta grains nucleation cooling down from above the liquidus temperature is currently investigated in literature by coupling CFD and cellular automaton simulations. This approach, from the industrial application point of view, is unfeasible, as the interaction between the two simulations is still manual and the running times are too long to be considered for simulation of objects with industrial dimensions. A simplified numerical approach would be required, to describe the formation of the columnar beta grains in the weld pool area and, in the literature, some work is being carried out in this direction.

- More detailed characterization of the lamellae nucleation and growth, cooling down from temperatures above beta transus, should be carried out, both to get validation data for the numerical model presented and to understand better the relation with the beta grain dimensions. For this purpose, combinations of different material chemical composition, initial beta grain dimensions, starting temperatures and cooling rates followed by water quenching from different temperature are suggested. A similar approach could be used to study the martensitic microstructure evolution with the complication that the water quenching will form martensite not related to the cooling rate preceding it. Thin and short needles were also observed in material subjected to heat treatments that did not dissolve completely the initial microstructure (in this case lamellar), they were classified as martensitic by the the numerical model but an experimental investigation by TEM could be useful to validate this assumption.

- Further characterization of the beta grain growth should be carried out to understand the kinetics of the process, it would also be useful to establish and/or validate a physical based model to describe this phenomenon. In the experiments carried out in this work, nucleation of the beta grains was very difficult to observe. The grains looked as if they were already mechanically impinged on each other as soon as they nucleated. Moreover, as the heating rate increased, the first beta grains

observed were at progressively higher temperatures than the relative beta transus temperature, leaving a "gap" between complete dissolution of the alpha phase and formation of beta grains where no particles seemed to be present in the material. An investigation of this area, where local segregation of the previous alpha phase is still present, but where no particles seem to characterize the microstructure should be carried out, both from the metallurgical and mechanical (rather challenging) point of view.

- Temperature measurements within the weld pool, in different positions along the length and width, should be carried out for a better understanding of the phenomena occurring into it. This could help also the validation of CFD simulations.

- Further development of the mechanical model adopted in this work is necessary to validate its predictions for the Ti-6Al-4V alloys, improve its stability and allow faster FE welding computations.

- The surrogate model presented in the appendix could be tested and validated by models with higher final deformations, to avoid working within the small tolerance values set for the solver convergence and to allow easier experimental measurements. An approach using neural networks could also be attempted, even though the relation with mechanical phenomena caught by the current solution would be lost. The material model developed in this work could be used in welding simulations to take into consideration the different microstructure evolution for each sequence analysed.

- The contact problem presented in appendix would deserve a deeper experimental investigation, understanding when this problem has particular importance in the final deformation of the welded components. Currently, parts welded together are modelled as a single body, already before the application of the welding process. This does not reflect the reality, where instead the junction is formed progressively and during the welding process. In this work, different numerical approaches to take in consideration the progressive formation of the joint during welding were adopeted,

showing different final deformations between the conventional "single body" and the "two bodies" approach. Experiments are suggested to compare the deformation returned by welding a component machined as single piece and a component actually made of two different bodies that are joint together by welding. In the author opinion, more attention should be given to slim structures, where deflections and deformation at the interface of the butts are easier. In case experiments show a different deformation between the two cases, numerical models able to describe the formation of the junction during welding will be required.

Bibliography

[1] John P. Byrne. Conference Proceedings - 22nd Annual International Titanium Association.

[2] Justin Hale. Boeing 787 from the Ground Up. *AERO Magazine*, (4):17–23, 2006.

[3] MSM Aerospace. MSM aerospace fabricators.

[4] Thomas W. Eagar. Energy sources used for fusion welding. *Massachusetts Institute of Technology.*

[5] L. Karlsson, L.-E Lindgren, and M. Jonsson. *Mechanical effects of welding.* Springer-Verlag, 1991.

[6] M Salcudean, M. Choi, and R. Greif. A study of heat transfer during arc welding. *Heat Mass Transfer*, 29(2):215–225, 1986.

[7] John Goldak, Aditya Chakravarti, and Malcolm Bibby. A new finite element model for welding heat sources. *Metallurgical and materials transactions B*, 15(June):299–305, 1984.

[8] C.S. Wu, H. G. Wang, and Y. M. Zhang. A new heat source model for keyhole plasma arc welding in FEM analysis of the temperature profile. *Welding Journal*, (December):284–291, 2006.

[9] Komeil Kazemi and John a. Goldak. Numerical simulation of laser full penetration welding. *Computational Materials Science*, 44(3):841–849, 2009.

[10] Kenneth C. Mills. *Recommended values of thermophysical properties for selected commercial alloys.* Woodhead Publishing, 2002.

[11] D. Basak, R. a. Overfelt, and D. Wang. Measurement of specific heat capacity and electrical resistivity of industrial alloys using pulse heating techniques. *International Journal of Thermophysics*, 24(6):1721–1733, nov 2003.

[12] Rodney Boyer, Gerhard Welsch, and E.W. Collings. *Materials Properties Handbook - Titanium Alloys.* ASM International, 1994.

[13] Yannick Robert. *Simulation numérique du soudage du TA6V par laser YAG impulsionnel: caractérisation expérimentale er modélisation des aspects thermomécanique associées à ce procédé.* PhD thesis, Ecole des Mines de Paris, 2007.

[14] Jeffery Brooks. Private Communication.

[15] M. Boivineau, C. Cagran, D. Doytier, V. Eyraud, M. H. Nadal, B. Wilthan, and G. Pottlacher. Thermophysical properties of solid and liquid Ti-6Al-4V (TA6V) alloy. *International Journal of Thermophysics*, 27(2):507–529, mar 2006.

[16] Gerhard Welsch, Rodney Boyer, and E.W. Collings. *Materials properties handbook: titanium alloys.* ASM International, 1994.

[17] Robert Pederson. *Microstructure and phase transformation of Ti-6Al-4V.* PhD thesis, Lulea University of Technology, 2002.

[18] W Szkliniarz and G Smotka. Analysis of volume effects of phase transformation in titanium alloys. *Journal of Materials Processing Tech.*, 53(3):413–422, 1995.

[19] J. W. Elmer. Phase transformation dynamics during welding of Ti-6Al-4V. *Journal of Applied Physics*, 95(12):8327, 2004.

[20] B. Hocheid, R. Klima, C. Beauvais, M. Rapin, and C. Roux. Contribution à l'ètude des transformations de l'alliage de titane TA6V en conditions isothermes. *Mémoires Scientifique*, LXVII(9), 1970.

[21] L.E. Tanner. *Time-Temperature-Trasnformation diagrams of the titanium sheet-rolling-program alloys*. Columbus, 1959.

[22] F. Le Maitre. Etude des transformation en refroidissement continu de l'alliage de titane TA6V. *Revue de Métallurgie*, LXVII(9):563–574, 1970.

[23] R. Dabrowski. The kinetics of phase transformations during continuous cooling of Ti6Al4V alloy from the diphase $\alpha + \beta$ range. *Archives of Metallurgy and Materials*, 56(2):217–221, 2011.

[24] S Malinov, Z Guo, W Sha, and A Wilson. Differential Scanning Calorimetry Study and Computer Modeling of β to α Phase Transformation in a Ti-6Al-4V Alloy. 32(April), 2001.

[25] F J Gil, J M Manero, M P Ginebra, and J A Planell. The effect of cooling rate on the cyclic deformation of beta-annealed Ti-6Al-4V. *Materials & Design*, 349:150–155, 2003.

[26] R. Ding, Z.X. Guo, and A. Wilson. Microstructural evolution of a Ti-6Al-4V alloy during thermomechanical processing. *Materials Science and Engineering: A*, 327(2):233–245, 2002.

[27] T Searles, J Tiley, A Tanner, R Williams, B Rollins, E Lee, S Kar, R Banerjee, and H L Fraser. Rapid characterization of titanium microstructural features for specific modelling of mechanical properties. *Measurement Science and Technology*, 16(1):60–69, 2005.

[28] J Tiley, T Searles, E Lee, S Kar, R Banerjee, J.C Russ, and H.L Fraser. Quantification of microstructural features in α/β titanium alloys. *Materials Science and Engineering: A*, 372(1-2):191–198, 2004.

[29] J D Miller and S L Semiatin. Effect of the Size Distribution of Alpha Particles

on Microstructure Evolution during Heat Treatment of an Alpha/Beta Titanium Alloy. *Metallurgical and Materials Transactions A*, 36(January):259–262, 2005.

[30] S. L. Semiatin, T. M. Lehner, J. D. Miller, R. D. Doherty, and D. U. Furrer. Alpha/Beta Heat Treatment of a Titanium Alloy with a Nonuniform Microstructure. *Metallurgical and Materials Transactions A*, 38(4):910–921, 2007.

[31] S.L Semiatin and T.R Bieler. The effect of alpha platelet thickness on plastic flow during hot working of TI-6Al-4V with a transformed microstructure. *Acta Materialia*, 49(17):3565–3573, 2001.

[32] A. Squillace, U. Prisco, S. Ciliberto, and A. Astarita. Effect of welding parameters on morphology and mechanical properties of Ti-6Al-4V laser beam welded butt joints. *Journal of Materials Processing Technology*, 212(2):427–436, 2012.

[33] X. Cao and M. Jahazi. Effect of welding speed on butt joint quality of Ti-6Al-4V alloy welded using a high-power Nd:YAG laser. *Optics and Lasers in Engineering*, 47(11):1231–1241, 2009.

[34] Liu Chuan, Zhang Jianxun, and Niu Jing. Numerical and experimental analysis of residual stresses in full-penetration laser beam welding of Ti6Al4V Alloy. *Rare Metal Materials and Engineering*, 38(8):1317–1320, 2009.

[35] P. Wanjara, M. Brochu, and M. Jahazi. Ti-6Al-4V electron beam weld qualification using laser scanning confocal microscopy. *Materials Characterization*, 54(3):254–262, 2005.

[36] Roel Snieder. The role of nonlinearity in inverse problems. *Inverse Problems*, 14(3):387–404, 1998.

[37] Nestor V. Queipo, Raphael T. Haftka, Wei Shyy, Tushar Goel, Rajkumar Vaidyanathan, and P. Kevin Tucker. Surrogate-based analysis and optimization. *Progress in Aerospace Sciences*, 41(1):1–28, 2005.

[38] Jim Mabon, Wacek Swiech, Honghui Zhou, Matt Bresim, and Catalin Chiritescu. Scanning Electron Microscopy (SEM) and Focused Ion Beams (FIB) in Materials Research. *6th Advanced Materials Characterization Workshop*, 2014.

[39] Howard B. Aaron. Diffusion Limited Phase Transformations: A Comparison and Critical Evaluation of the Mathematical Approximations. *Journal of Applied Physics*, 41(11):4404, 1970.

[40] S L Semiatin, S L Knisley, P N Fagin, F Zhang, and D R Barker. Microstructure Evolution during Alpha-Beta Heat Treatment of Ti-6Al-4V. *Metallurgical and Materials Transactions A*, 34A(October):2377–2386, 2003.

[41] Jinkeun Oh, Nack J. Kim, Sunghak Lee, and Eui W. Lee. Correlation of fatigue properties and microstructure in investment cast Ti-6Al-4V welds. *Materials Science and Engineering: A*, 340(1-2):232–242, 2003.

[42] R R Boyer. An overview on the use of titanium in the aerospace industry. *Materials Science and Engineering: A*, 213:103–114, 1996.

[43] Patricio F Mendez and Thomas W Eagar. Welding processes for aeronautics. *Advance materials & processes*, (May):39–43, 2001.

[44] J. Blackburn. *Laser welding of metals for aerospace and other applications*. Woodhead Publishing Limited, 2011.

[45] R. Freeman. *New welding techniques for aerospace engineering*. Woodhead Publishing Limited, 2011.

[46] IPG Photonics. Benefits of laser welding. *FabShop Magazine Direct*, pages 27–31, 2015.

[47] Melvin Avrami. Kinetics of Phase Change. I General Theory. *The Journal of Chemical Physics*, 7(12):1103–1112, 1939.

[48] Melvin Avrami. Kinetics of Phase Change. II Transformation-Time Relations for Random Distribution of Nuclei. *The Journal of Chemical Physics*, 8(2):212–224, 1940.

[49] Melvin Avrami. Granulation, Phase Change, and Microstructure Kinetics of Phase Change. III. *The Journal of Chemical Physics*, 9(2):177–184, 1941.

[50] Esi-group. *Sysweld 2013 Reference Manual*. esi-group, 2012.

[51] ISO. ISO 4063:2009 Welding and allied processes – Nomenclature of processes and reference numbers.

[52] Rob Long. Electron Beam vs Laser Beam Welding, 2014.

[53] Tech Briefs. Laser Beam vs. Electron Beam Welding Which process works best for what?, 2011.

[54] John A. Goldak and Medhi Akhlaghi. *Computational welding mechanics*. Springer, 2010.

[55] Lars-Erik Lindgren. *Computational welding mechanics Thermomechanical and microstructural simulations*. Woodhead Publishing and Maney Publishing, 2007.

[56] Fang Hongyuan, Meng Qingguo, Xu Wenli, and Ji Shude. New general double ellipsoid heat source model. *Science and Technology of Welding and Joining*, 10(3):361–368, 2005.

[57] N. Siva Shanmugam, G. Buvanashekaran, and K. Sankaranarayanasamy. Some studies on weld bead geometries for laser spot welding process using finite element analysis. *Materials & Design*, 34:412–426, 2012.

[58] Richard Turner, Jianglin Huang, Mark Ward, Matteo Villa, and Roger C Reed. On the Modelling of a Pulsed TIG Weld process in a Nickel Superalloy. *Material Science Forum*, 762:531–537, 2013.

[59] Øystein Grong. *Metallurgical modelling of welding (2nd edition)*. Maney Publishing, 1997.

[60] Robert E. Reed-Hill. *Physical Metallurgy Principles*. D. Van Nostrand Company, 1973.

[61] E J Mittemeijer, A V A N Gent, and P J V A N D E R Schaaf. Analysis of Transformation Kinetics by Nonisothermal Dilatometry. *Metallurgical Transactions A*, 17(August):1441–1445, 1986.

[62] A. Suárez, M.J. Tobar, A. Yáñez, I. Pérez, J. Sampedro, V. Amigó, and J.J. Candel. Modeling of phase transformations of Ti6Al4V during laser metal deposition. *Physics Procedia*, 12:666–673, 2011.

[63] A. Longuet, Y. Robert, E. Aeby-Gautier, B. Appolaire, J.F. Mariage, C. Colin, and G. Cailletaud. A multiphase mechanical model for Ti-6Al-4V: Application to the modeling of laser assisted processing. *Computational Materials Science*, 46(3):761–766, 2009.

[64] Y. Fan, P. Cheng, Y. L. Yao, Z. Yang, and K. Egland. Effect of phase transformations on laser forming of Ti-6Al-4V alloy. *Journal of Applied Physics*, 98(1):013518, 2005.

[65] D.P. Koistinen and R.E. Marburger. A general equation prescribing the extent of the austenite-martensite transformation in pure iron-carbon alloys and plain carbon steels. *Acta Metallurgica*, 7(1):59–60, 1959.

[66] G. Shen, D. Furrer, and J. Rollins. Microstructural development in a titanium alloy. *Advances in the Science and Technology of Titanium Alloy Processing*, 1997.

[67] Frank S. Ham. Theory of diffusion-limited precipitation. *Journal of Physics and Chemistry of Solids*, 6:335–351, 1958.

[68] M. Ferrante and R. D. Doherty. Inluence of interfacial properties on the kinetics of precipitation and precipitate coarsening in aluminium-silver alloys. *Acta Metallurgica*, 27(10):1603–1614, 1979.

[69] K. E. Rajab and R. D. Doherty. Kinetics of growth and coarsening of faceted hexagonal precipitates in an FCC matrix - I Experimental observations. *Acta Metallurgica*, 37(10):2709–2722, 1989.

[70] R.D. Doherty and K. E. Rajab. Kinetics of growth and coarsening of faceted hexagonal precipitates in an FCC matrix - II Analysis. *Acta Metallurgica*, 37(10):2723–2731, 1989.

[71] H. R. Shercliff and O Grong. Microstructural modelling in metals processing. *Progress in Material Science*, 47:163–282, 2002.

[72] A. Rostamian and A. Jacot. A numerical model for the description of the lamellar and massive phase transformations in TiAl alloys. *Intermetallics*, 16(10):1227–1236, 2008.

[73] J C Soper, Materials Directorate, and Wright-patterson Air Force Base. Short-Time Beta Grain Growth Conventional Kinetics Alloy. *Acta Metallurgica*, 44(5):1979–1986, 1996.

[74] O. M. Ivasishin, S. L. Semiatin, P. E. Markovsky, S. V. Shevchenko, and S. V. Ulshin. Grain growth and texture evolution in Ti-6Al-4V during beta annealing under continuous heating conditions. *Materials Science and Engineering: A*, 337(1-2):88–96, 2002.

[75] M. Vanderhasten, L. Rabet, and B. Verlinden. Ti-6Al-4V: Deformation map and modelisation of tensile behaviour. *Materials & Design*, 29(6):1090–1098, jan 2008.

[76] Mohammad Sima and Tugrul Özel. Modified material constitutive models for serrated chip formation simulations and experimental validation in machining of ti-

tanium alloy Ti-6Al-4V. *International Journal of Machine Tools and Manufacture*, 50(11):943–960, 2010.

[77] S L Semiatin, T R Bieler, and I Introduction. Effect of Texture and Slip Mode on the Anisotropy of Plastic Flow and Flow Softening during Hot Working of Ti-6Al-4V. *Metallurgical and Materials Transactions A*, 32A(July):1787, 2001.

[78] A Majorell, S Srivatsa, and R.C Picu. Mechanical behavior of Ti-6Al-4V at high and moderate temperatures-Part I: Experimental results. *Materials Science and Engineering: A*, 326(2):297–305, 2002.

[79] R.C. Picu and A. Majorell. Mechanical behavior of Ti-6Al-4V at high and moderate temperatures-Part II: constitutive modeling. *Materials Science and Engineering: A*, 326(2):306–316, 2002.

[80] Jeoung Han Kim, S.L Semiatin, and Chong Soo Lee. Constitutive analysis of the high-temperature deformation of Ti-6Al-4V with a transformed microstructure. *Acta Materialia*, 51(18):5613–5626, 2003.

[81] T A E Kwon Ha and Young W O N Chang. An internal variable theory of structural superplasticity. *Acta Materialia*, 46(8):2741–2749, 1998.

[82] X.G. Fan and H. Yang. Internal-state-variable based self-consistent constitutive modeling for hot working of two-phase titanium alloys coupling microstructure evolution. *International Journal of Plasticity*, 27(11):1833–1852, 2011.

[83] Shaogang Wang and Xinqiang Wu. Investigation on the microstructure and mechanical properties of Ti-6Al-4V alloy joints with electron beam welding. *Materials & Design*, 36:663–670, 2012.

[84] Timothy W. Simpson, John J. Korte, Timothy M. Mauery, and Farrokh Mistree. Kriging models for global approximation in simulation-based multidisciplinary design optimization. *AIAA Journal*, 39(12):2233–2241, 2001.

[85] Chung Hyoung-Seog and Alonso AJuan J. Comparison of approximation models with merit functions for design optimization comparison of approximation models with merit functions for design optimization. In *Proceedings of the eigthth AIAA/USAF/NASA/ISSMO symposium on multidisciplinary analysis and optimization*, Long Beach, CA, 2000.

[86] R Jin, W Chen, and T W Simpson. Comparative studies of metamodelling techniques under multiple modelling criteria. (1998):1–13, 2001.

[87] Jerome Sacks, William J. Welch, Toby J. Mitchell, and Henry P. Wynn. Design and analysis of computer experiments. *Statistical Science. ® www.jstor.org*, 4:409–435, 1989.

[88] Andrew J. Booker, Dennis J.E., Paul D. Frank, David B. Serafini, and Virginia Torczon. Optimization using surrogate objective on a helicopter test example. Technical report, Center for research on parallel computation, 1997.

[89] Man Mohan, K Madavan, and W Huber. Improving the unsteady aerodynamic performance of transonic turbines using neural networks. *NASA*, (September), 1999.

[90] Nilay Papila, Wei Shyy, Lisa W Griffin, Daniel J Dorney, and Lisa Griffins. Shape optimization of supersonic turbines using response surface and neural network methods. *AIAA Journal*, 2001.

[91] Wei Shyy, Nilay Papila, Rajkumar Vaidyanathan, and Kevin Tucker. Global design optimization for aerodynamics and rocket propulsion components. *Progress in Aerospace Sciences*, 37(1):59–118, 2001.

[92] Thaddeus B. Massalski. *Binary alloy phase diagrams*. 1990.

[93] T. Ahmed and H.J. Rack. Phase transformations during cooling in α+β titanium alloys. *Materials Science and Engineering: A*, 243(1-2):206–211, mar 1998.

[94] D.A. Porter and K.E. Easteriling. *Phase transformations in metals and alloys.* Chapman & Hall, London, 2009.

[95] C. Panwisawas, C.L. Qiu, Y. Sovani, J.W. Brooks, M.M. Attallah, and H.C. Basoalto. On the role of thermal fluid dynamics into the evolution of porosity during selective laser melting. *Scripta Materialia*, 105:14–17, 2015.

[96] C. Panwisawas, Y. Sovani, R. Turner, B. Perumal, Ward R.P., J.W. Brooks, and H.C. Basoalto. A Multi-scale, Multi-physics Approach to Modelling of Fusion Welding in Titanium Alloys. In *The 3rd World Congress on Integrated Computational Materials Engineering (ICME 2015)*, 2015.

[97] Tae Wook Heo and Long-Qing Chen. Phase-field modeling of displacive phase transformations in elastically anisotropic and inhomogeneous polycrystals. *Acta Materialia*, 76:68–81, sep 2014.

[98] Yuan Zhong and Ting Zhu. Phase-field modeling of martensitic microstructure in NiTi shape memory alloys. *Acta Materialia*, 75:337–347, 2014.

[99] S. Zhu, H. Yang, L.G. Guo, and X.G. Fan. Effect of cooling rate on microstructure evolution during α/β heat treatment of TA15 titanium alloy. *Materials Characterization*, 70:101–110, 2012.

[100] Qing Chen, Ning Ma, Kaisheng Wu, and Yunzhi Wang. Quantitative phase field modeling of diffusion-controlled precipitate growth and dissolution in Ti-Al-V. *Scripta Materialia*, 50(4):471–476, 2004.

[101] Howard B. Aaron and Gerald R. Kotler. Second phase dissolution. *Metallurgical Transactions*, 2:393–408, 1971.

[102] Y Mishin and Chr Herzig. OVERVIEW NO. 136 DIFFUSION IN THE Ti - Al SYSTEM. *Acta Materialia*, 48(3):589–623, 2000.

[103] Y Wang, N Ma, Q Chen, F Zhang, S Chen, and Y A Chang. Predicting Phase Equilibrium , Phase Transformation , and Microstructure Evolution in Titanium Alloys. *JOM*, 57(September), 2005.

[104] M J Whelan. On the Kinetics of Precipitate Dissolution. *Metal Science Journal*, 3(4):95–97, 1969.

[105] G Horvay and J. W. Cahn. Dendritic and spheroidal. *Acta Metallurgica*, 9:695–705, 1961.

[106] H. Wang, N. Warnken, and R.C. Reed. Thermodynamic and kinetic modeling of bcc phase in the Ti-Al-V ternary system. *Materials Science and Engineering: A*, 528(2):622–630, 2010.

[107] Ursula R. Kattner. The thermodynamic modeling of multicomponent phase equilibria. *Jom*, 49(12):14–19, 1997.

[108] A. T. Dinsdale. SGTE DATA FOR PURE ELEMENTS A T. *CALPHAD*, 15(4):317–425, 1991.

[109] F. Tancret. Thermo-Calc and Dictra simulation of constitutional liquation of gamma prime during welding of Ni base superalloys. *Computational Materials Science*, 41(1):13–19, 2007.

[110] H. Wang, N. Warnken, and R.C. Reed. Thermodynamic assessment of the ordered B2 phase in the Ti-V-Cr-Al quaternary system. *Calphad*, 35(2):204–208, 2011.

[111] I. Katzarov, S. Malinov, and W. Sha. Finite element modeling of the morphology of β to α phase transformation in Ti-6Al-4V alloy. *Metallurgical and Materials Transactions A*, 33(4):1027–1040, 2002.

[112] R P Turner, M Villa, Y Sovani, C Panwisawas, B Perumal, R M Ward, J W Brooks, and H C Basoalto. An Improved Method of Capturing the Surface Boundary of a Ti-

6Al-4V Fusion Weld Bead for Finite Element Modeling. *Metallurgical and Materials Transactions B*, 2015.

[113] H Basoalto and P L Blackwell. Slip induced strain rate sensitivity for superplastic material. *11th International conference on Superplasticity in Advanced Materials*, 2012.

[114] B. F. Dyson. Microstructure based creep constitutive model for precipitation strengthened alloys: theory and application. *Materials Science and Technology*, 25(2):213–220, 2009.

[115] R. A. Matula. Electrical resistivity of copper, gold, palladium and silver.pdf. *Journal of Physical and Chemical Reference Data*, 8(4):1147–1298, 1979.

[116] R. W. Powell, C. Y. Ho, and P. E. Liley. Thermal conductivity of selected materials.pdf. *National Standard Reference Data Series*, 1966.

APPENDIX A

Gleeble numerical model

To estimate the thermal gradients present in the specimens tested by the Gleeble machine electrical-thermal simulations have been run in the FE software DEFORM. These simulations rather than simulating accurately the physics behind the testing process, were used particularly to understand the temperature distribution along the specimens and through the thickness, during hypothetical heating and cooling in the Gleeble machine.

The results of these simulations were used to decide the sample diameter that could be used in the heat treatments to ensure an acceptable temperature variation between the surface and the centre, for a fixed x coordinate (see figure A.1). For the microstructural study, a wide section was desirable to ensure a higher amount of measurements, but if this meant an effective different heat treatment across the section because of a big variation of temperature, the microstructure studied could not be related to one specific thermal load, thus losing significance for this work.

Two different numerical models have been used (figure A.1), since two different kinds of Gleeble tests were carried out (figure 3.16, 3.15): when faster heating rates were needed, tensile tests were adopted, otherwise compression tests were preferred (section 3.4).

The Gleeble components thermal properties were taken from JMatPro for the Titanium material and from literature for the electrical and thermal conductivity of Copper [115, 116]. Specimen and hexagonal bolts have been set as Titanium components, whilst the

a)

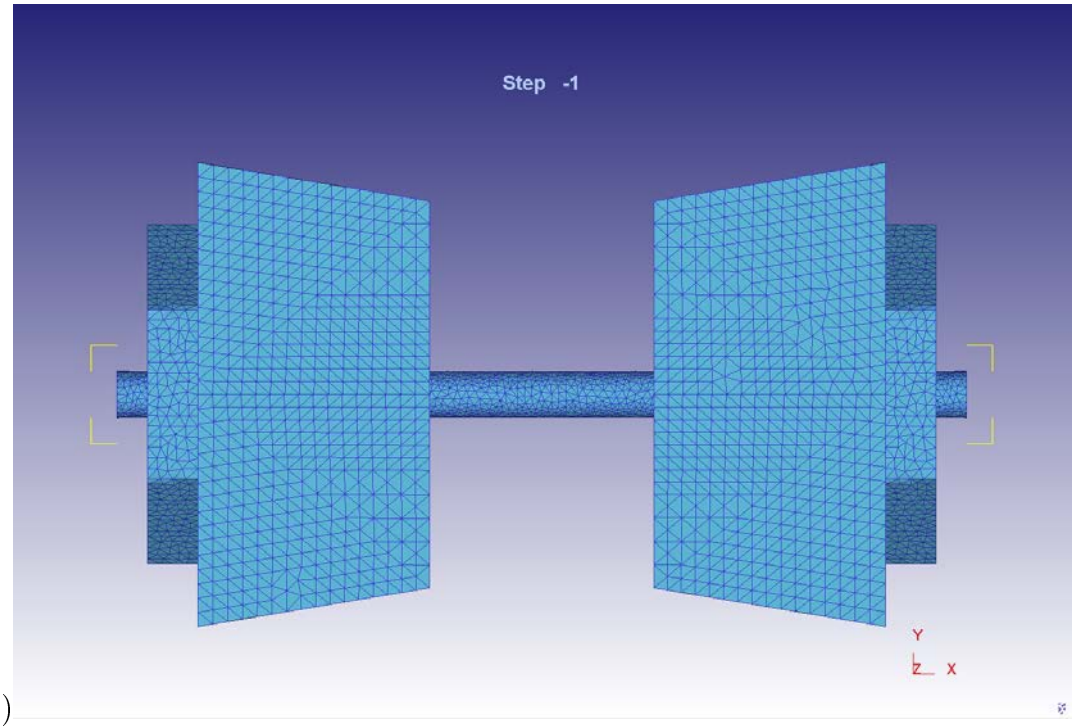

b)

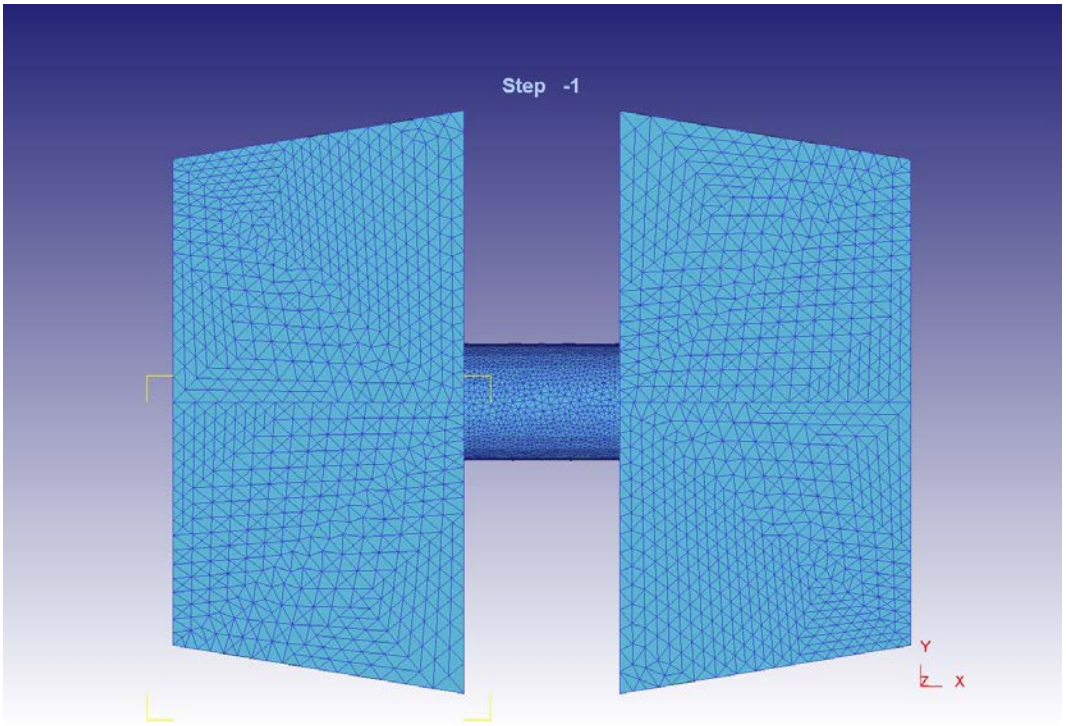

Figure A.1.: DEFORM a) tensile numerical model and b) compression numerical model

holders have been set as Copper parts.

The geometry of the model used to simulate the tensile tests reflected the geometry of the real assembly while the geometry of the compression model was a simplification of the real case. In the real compression assembly, the specimen was in contact with Tungsten cylinders placed within the Copper holders. These parts have not been modelled since they were considered not to be important, in the determination of the gradient of temperature developed across the thickness of the samples, or in relation also to the complexity of the geometry to be modelled.

The heat losses were represented in the models by convection and radiation. The first one was a function of temperature (private communication) while the second used an emissivity of 0.7.

A voltage potential was applied between the right and left side of the Copper holders, such that the specimens were heated up by the Joule effect and the temperature distribution could be investigated. Since the current DEFORM version does not allow a voltage potential to be set as a function of the time, a constant value was used to get heating similar to the experimental tests for the range of temperature of interest.

The points sampled for the tensile model are shown in figure A.2 and A.3, respectively for the transverse and longitudinal directions. The relative temperatures measured are reported in figure A.4 and A.5. The points in figure A.2 were representative of the temperature across the specimen section, whilst the points represented in figure A.3 show the longitudinal temperature trends.

Since in the real tensile experiments, temperatures were acquired at 3 different locations along the samples (figure 3.13), the model temperatures were recorded at the centre of the specimen and at about 8 mm far from it. This allowed an assessment of any significant temperature variations in the middle of the samples, with respect to the surface, in correspondence with the actual thermocouples locations.

Simulations were run for a voltage potential of 1V and 2V, to check how the temperature distribution changed with increasing heating rate: the first voltage potential returned

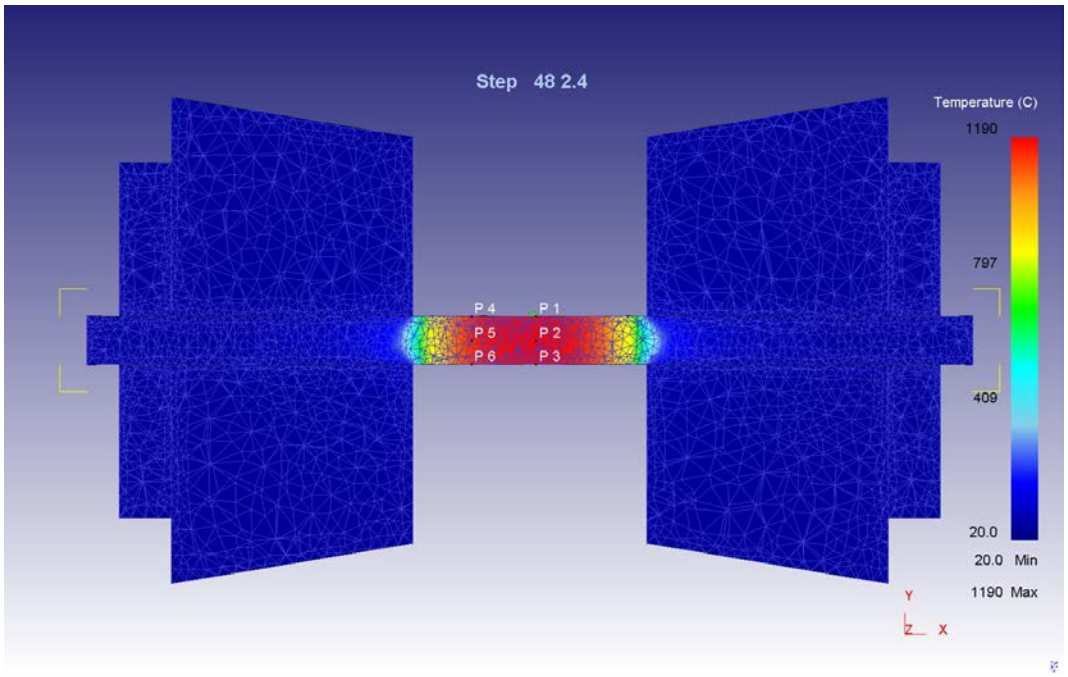

Figure A.2.: To evaluate the temperature distribution across the thickness of the Ti-6Al-4V tensile samples, points in two different sections were sampled. P1, P2 and P3 were sampled in the centre of the sample and P4, P5 and P6 were sampled at 8 mm far from the centre

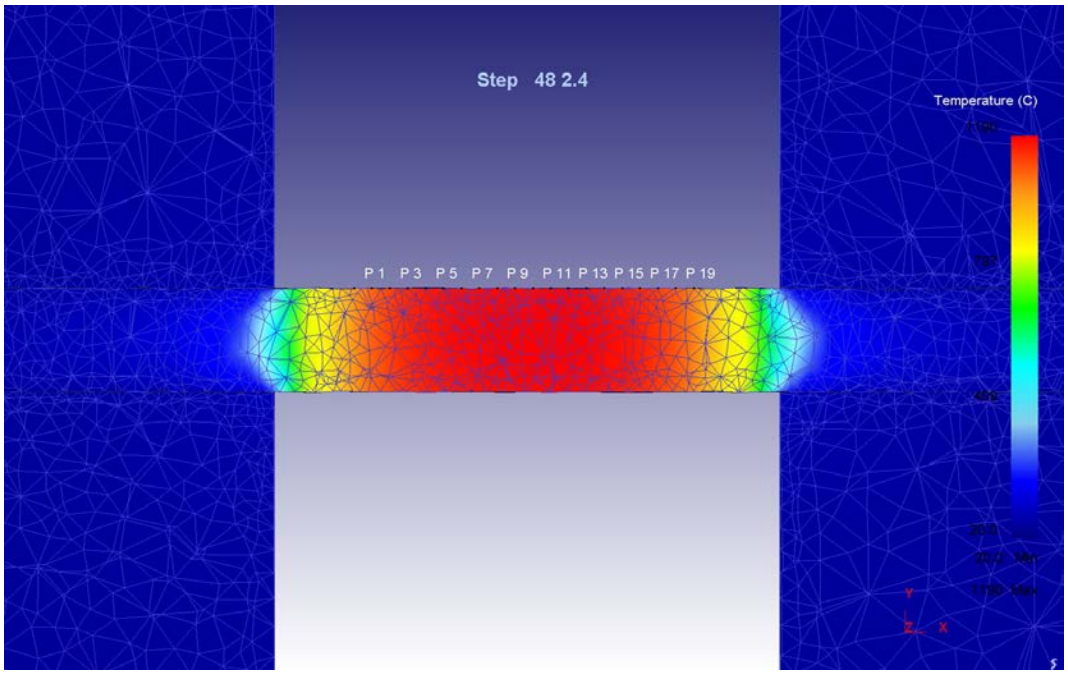

Figure A.3.: To evaluate the temperature distribution along the longitudinal direction of Ti-6Al-4V tensile samples, points from P1 to P19 were sampled

a)

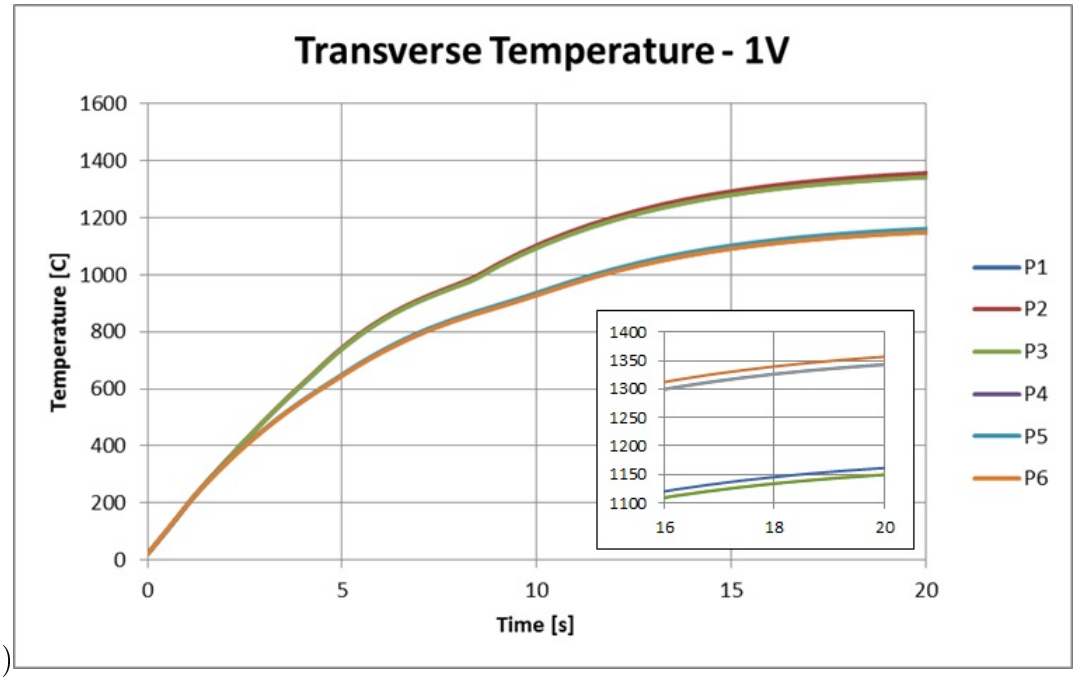

b)

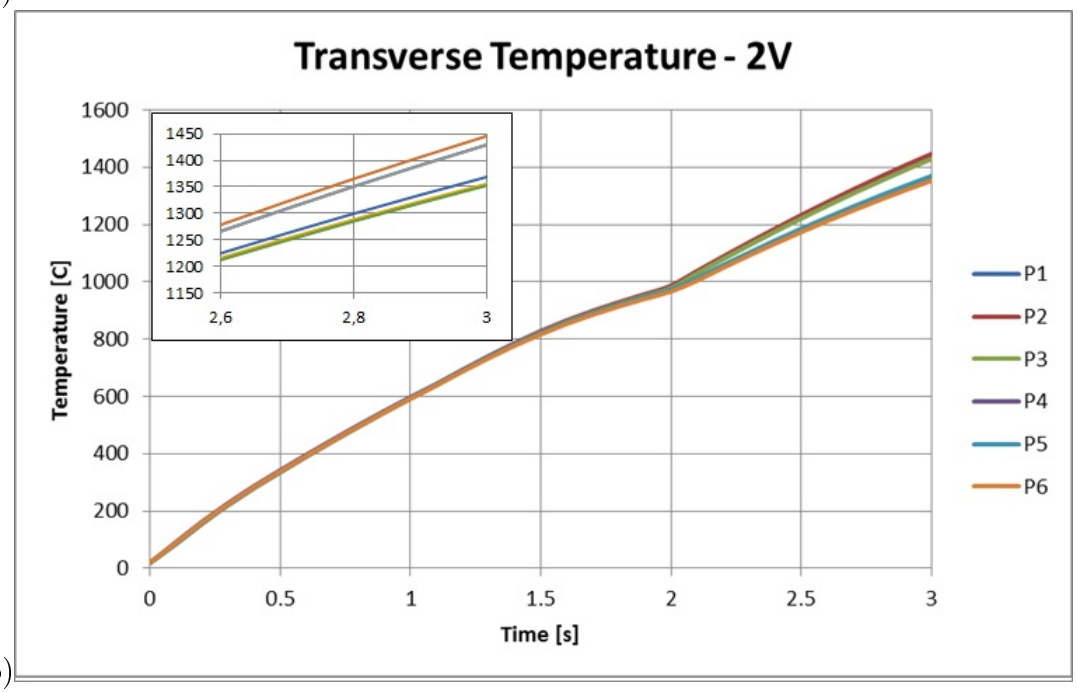

Figure A.4.: Temperature trends along the thickness of the Ti-6Al-4V tensile Gleeble samples, applying a voltage potential of 1V (a) and 2V (b). Temperatures relative to the points P1, P2 and P3 are all in the upper group of lines, vice versa for points P4, P5 and P6. See figure A.2 for locations of the points P1, P2, P3, P4, P5 and P6

a)

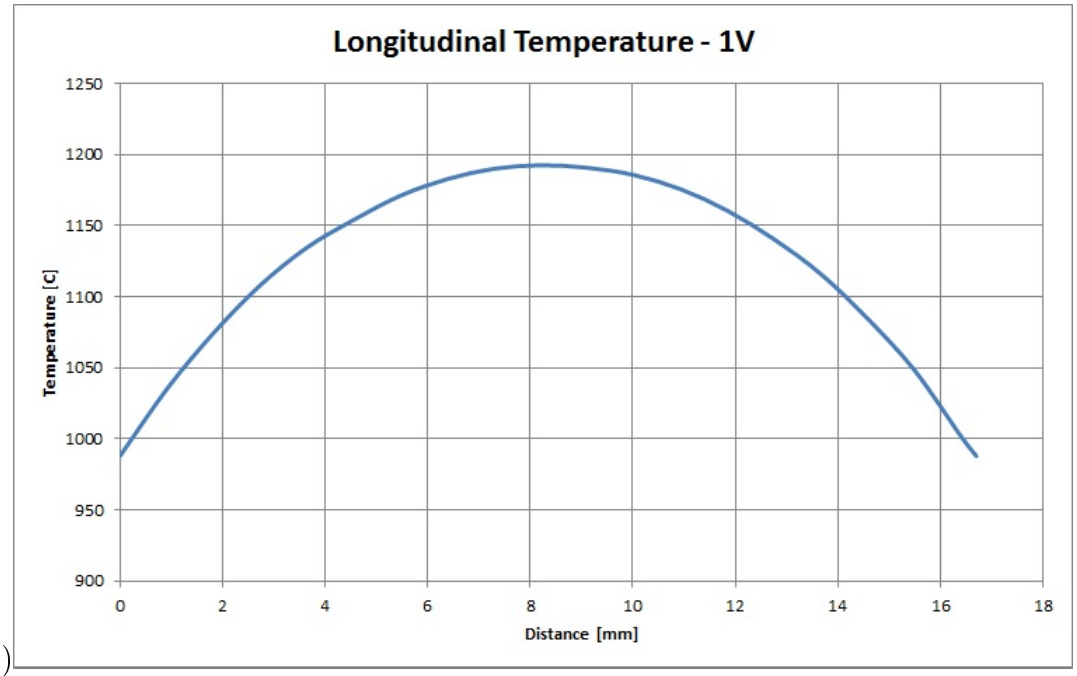

b)

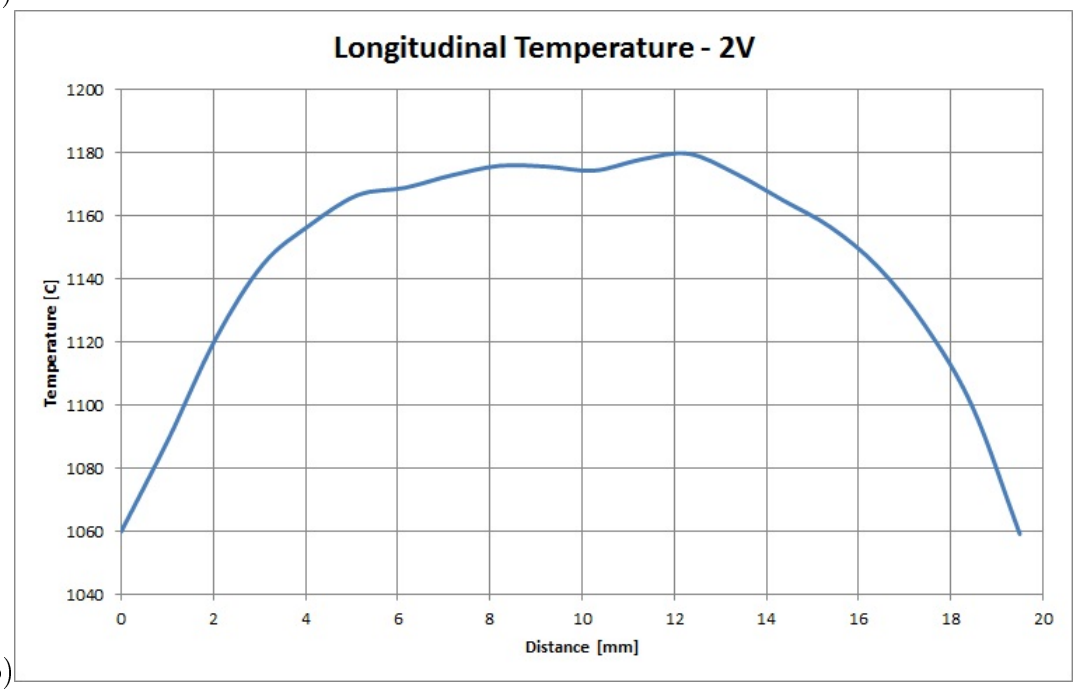

Figure A.5.: Temperature trends along the longitudinal direction of the Ti-6Al-4V tensile Gleeble samples, applying a voltage potential of 1V (a) and 2V (b). The trends are not symmetrical because of a not a perfectly symmetrical mesh. See figure A.3 for location of the sampled points: distance 0 is relative to the point P1

a heating rate of about 60 °C/s, the second voltage potential returned a heating rate approximatively of 360 °C/s. Results of the first test are shown in figure A.4-a, results of the second case are shown in figure A.4-b. The maximum difference of temperature recorded, between surface and centre, for the 1V case was 14 °C, whilst for the 2V case was 11 °C.

Considering the results obtained, the variation of temperature across the sections of the sample was considered to be satisfactory and falling within errors of termocouples measurements and numerical models predictions, so the tensile specimens were machined with a diameter of 6 mm. The other diameter option was 12 mm but, the temperature gradient across the sections would have been definitely higher than 14 °C, so this option was discarded.

In figure A.5-a and A.5-b the representative temperature trends along the longitudinal direction of the samples are shown. Even though a longitudinal temperature gradient would affect the evolution of the microstructure of the material, for this work it has been assumed that every section of the sample had a microstructure affected only by the local temperature. This permitted, for the real tests, the study of 3 different heat treatments per specimen by sectioning at 3 different distances from the centre thus allowing a reduction in cost and time for the machining and experimental setting up and testing. Also, when the specimens were sectioned, the tip of the thermocouples was still attached to them, reducing errors in extracting samples in correspondance of actual thermal treatment measured.

For completeness, in figure A.6 the temperature trends across the thickness of the tensile sample during cooling is reported. As during heating the temperature difference between surface and centre of the same section is maximum of around 15 °C.

To check the temperature along the thickness of the compression samples another model was made as figure A.7 shows. Contrary to the previous case, only the points P1, P2 and P3 have been sampled across the specimen thickness as, in the real case, only one temperature was acquired, in the centre of the specimen. A series of points linearly connecting Ps and Pe have been sampled to check also the longitudinal temperature

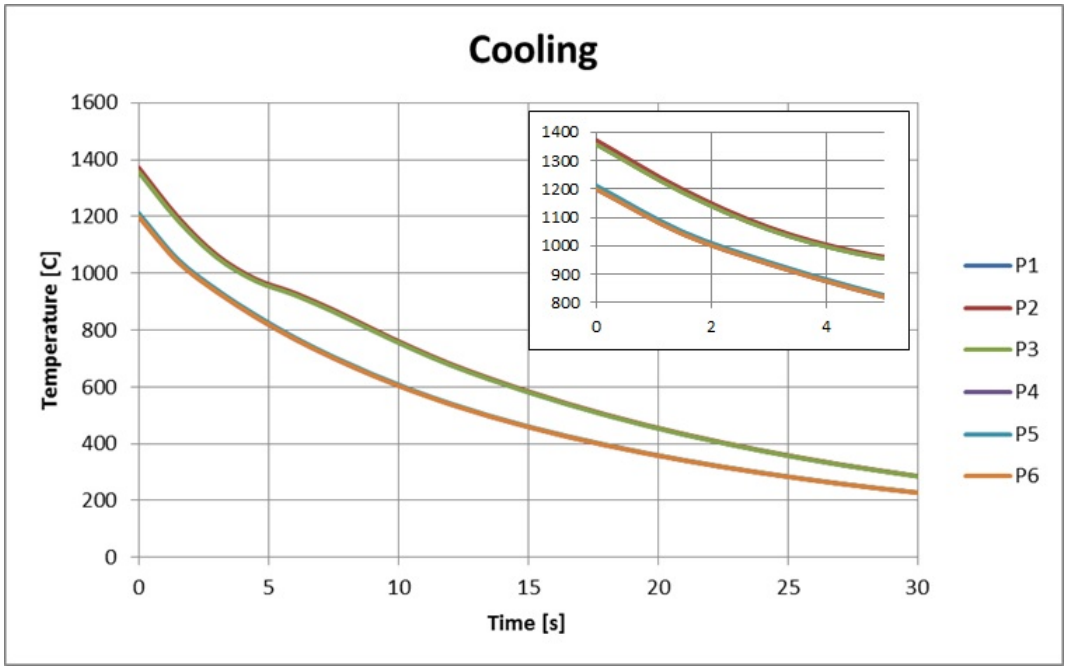

Figure A.6.: Modelled temperature trends across the thickness of the Ti-6Al-4V tensile Gleeble samples, during cooling. Temperatures relative to the points P1, P2 and P3 are all in the upper group of lines, vice versa for points P4, P5 and P6. See figure A.2 for locations of the points P1, P2, P3, P4, P5 and P6

distribution (figure A.7). The results are shown in figure A.8 and A.9. At the maximum temperature, the difference in temperature between surface and centre of the specimen was 26 °C, still acceptable, considering also that as the temperature decreases, this difference becomes smaller: around the beta transus it is 20 °C and these samples were used to study the microstructure evolution for temperatures below the beta transus temperature after soaking in the beta field. For completeness the longitudinal temperature is also reported but as stated before not taken in particular consideration.

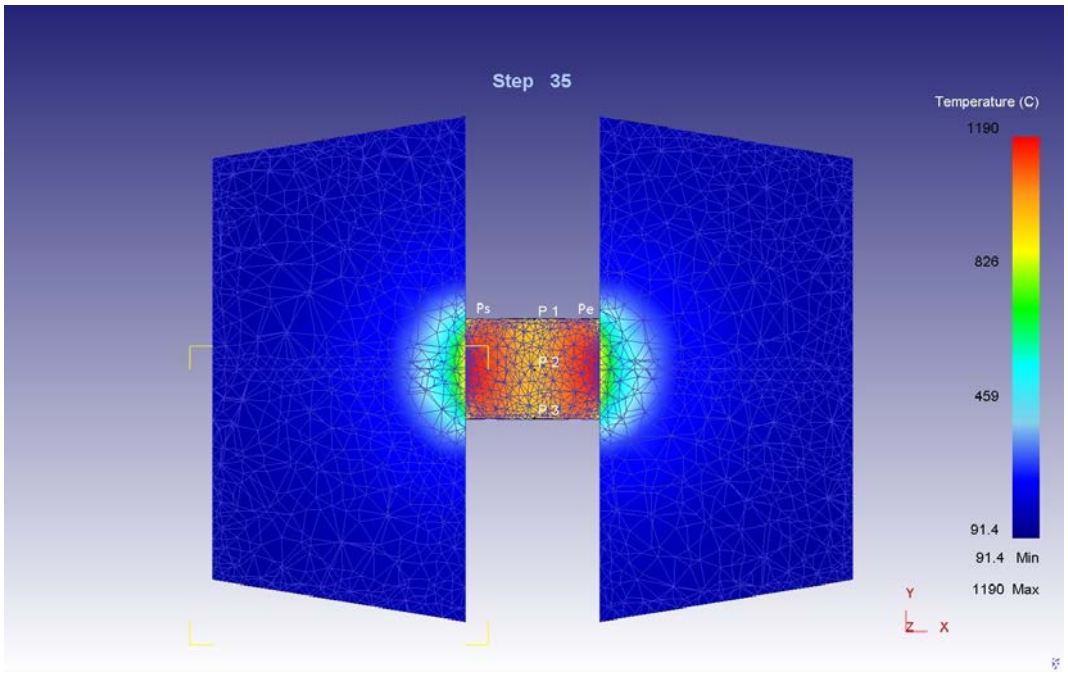

Figure A.7.: Section view of the Gleeble compression model. To evaluate the temperature distribution across the thickness of the tensile samples, the points P1, P2 and P3 were sampled in the centre of the sample

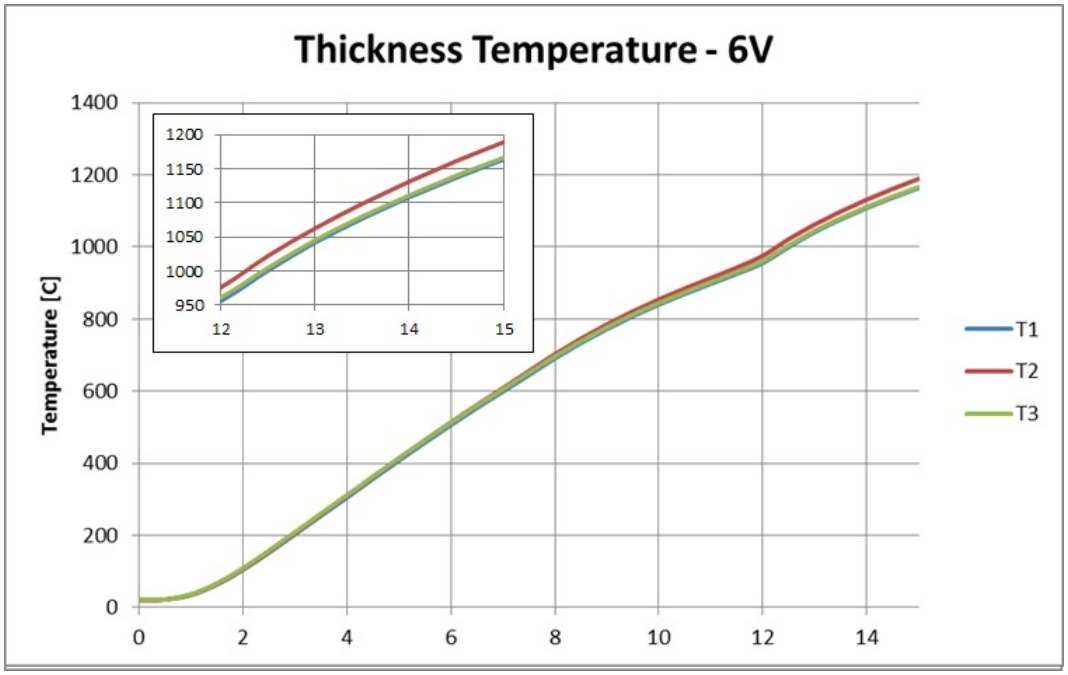

Figure A.8.: Modelled temperature distribution across the thickness of the compression sample. The points at which the temperatures make reference are the ones shown in figure A.7

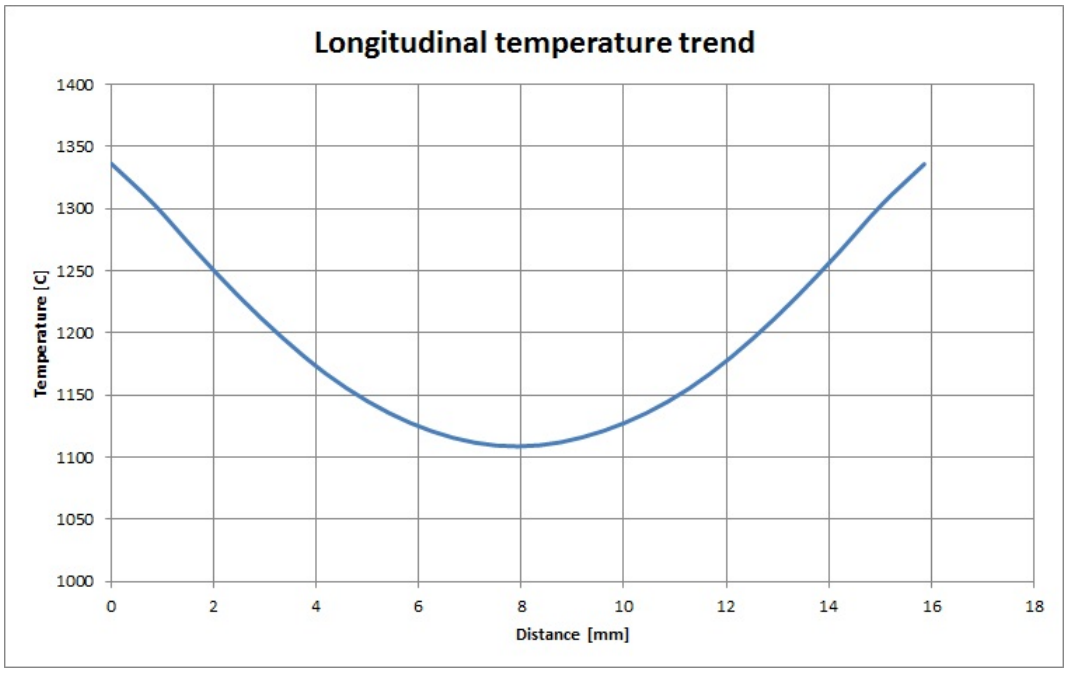

Figure A.9.: Longitudinal temperature distribution in the modelled numerical compression sample

APPENDIX B

Montages

B.1 Heating rate 5 °C/s

Figure B.1.: Montage of the sections taken at the optical microscope for the sample tested at a heating rate of 5 °C/s till 1260 °C then water quenched. The irregular surface close to the vertical hole is due to the spot welding of thermocouples in that area

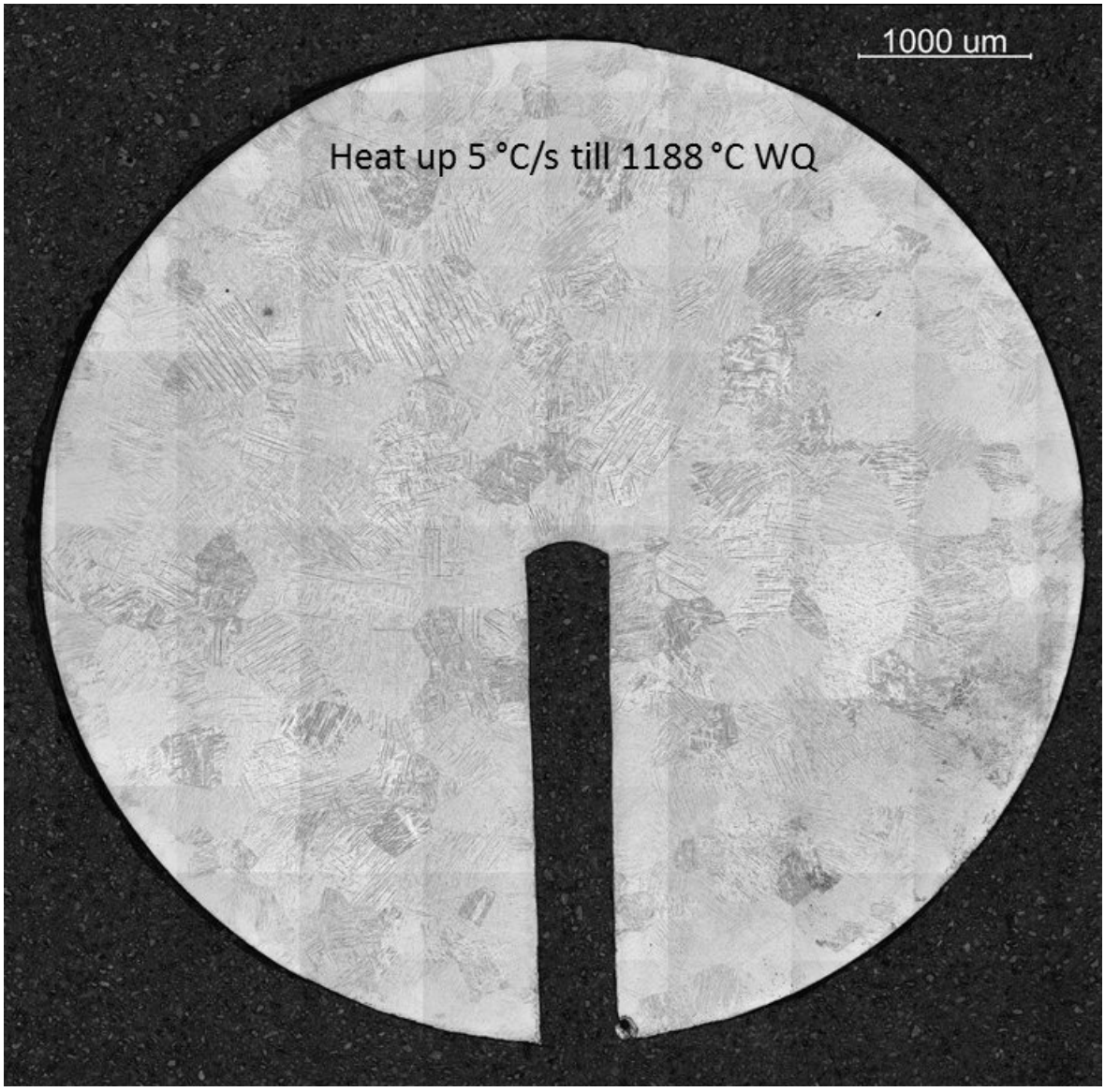

Figure B.2.: Montage of the sections taken at the optical microscope for the sample tested at a heating rate of 5 °C/s till 1188 °C then water quenched

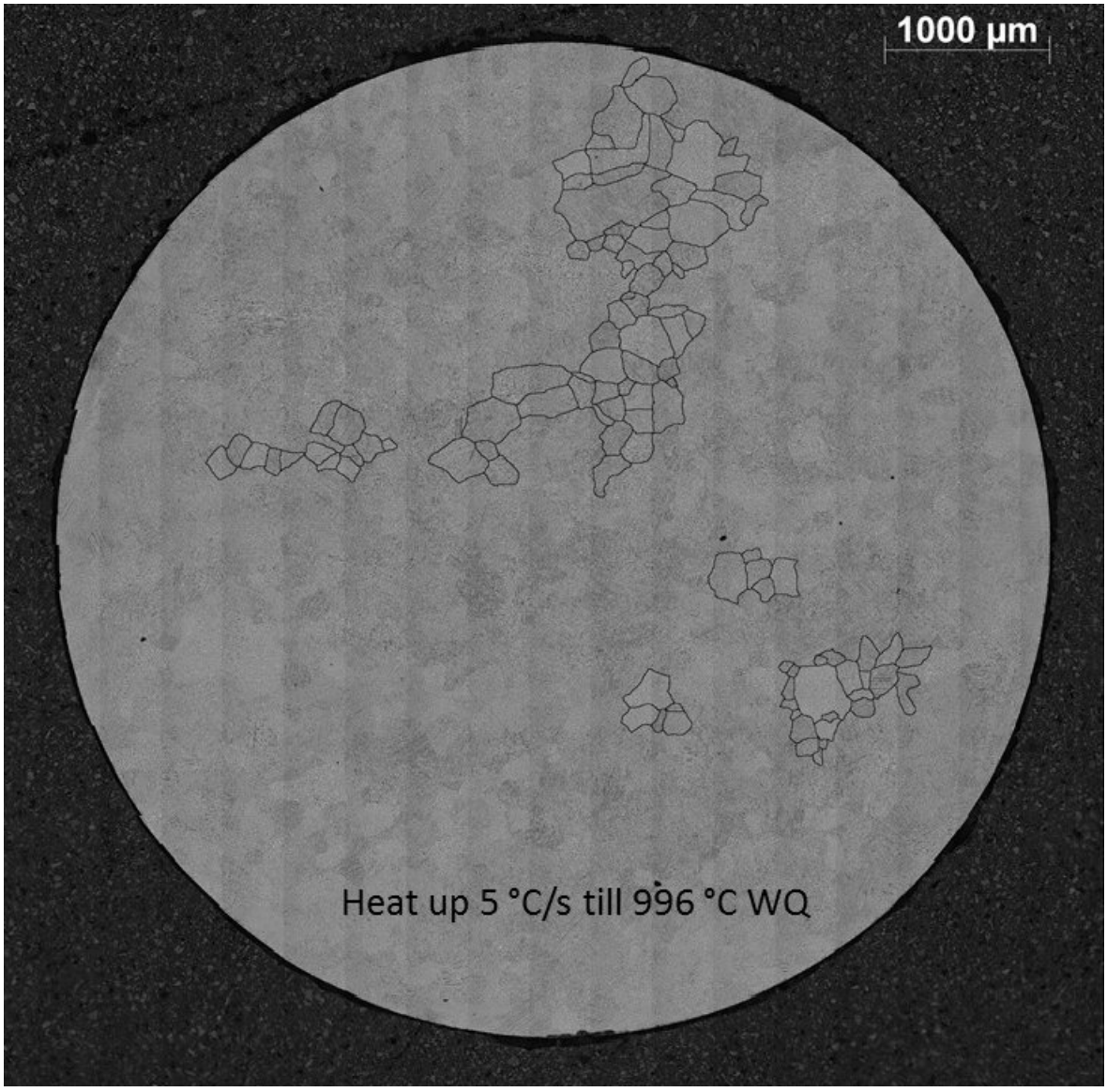

Figure B.3.: Montage of the sections taken at the optical microscope for the sample tested at a heating rate of 5 °C/s till 996 °C then water quenched. At this peak temperature, and magnification, the original morphology is not visible anymore (figure B.4) as beta grains have taken is place

Figure B.4.: Montage of the sections taken at the optical microscope for the sample tested at a heating rate of 5 °C/s till 996 °C then water quenched. At this peak temperature the original morphology is still visible, with elongated parent beta grains where lamellae are grown

B.2 Heating rate 50 °C/s

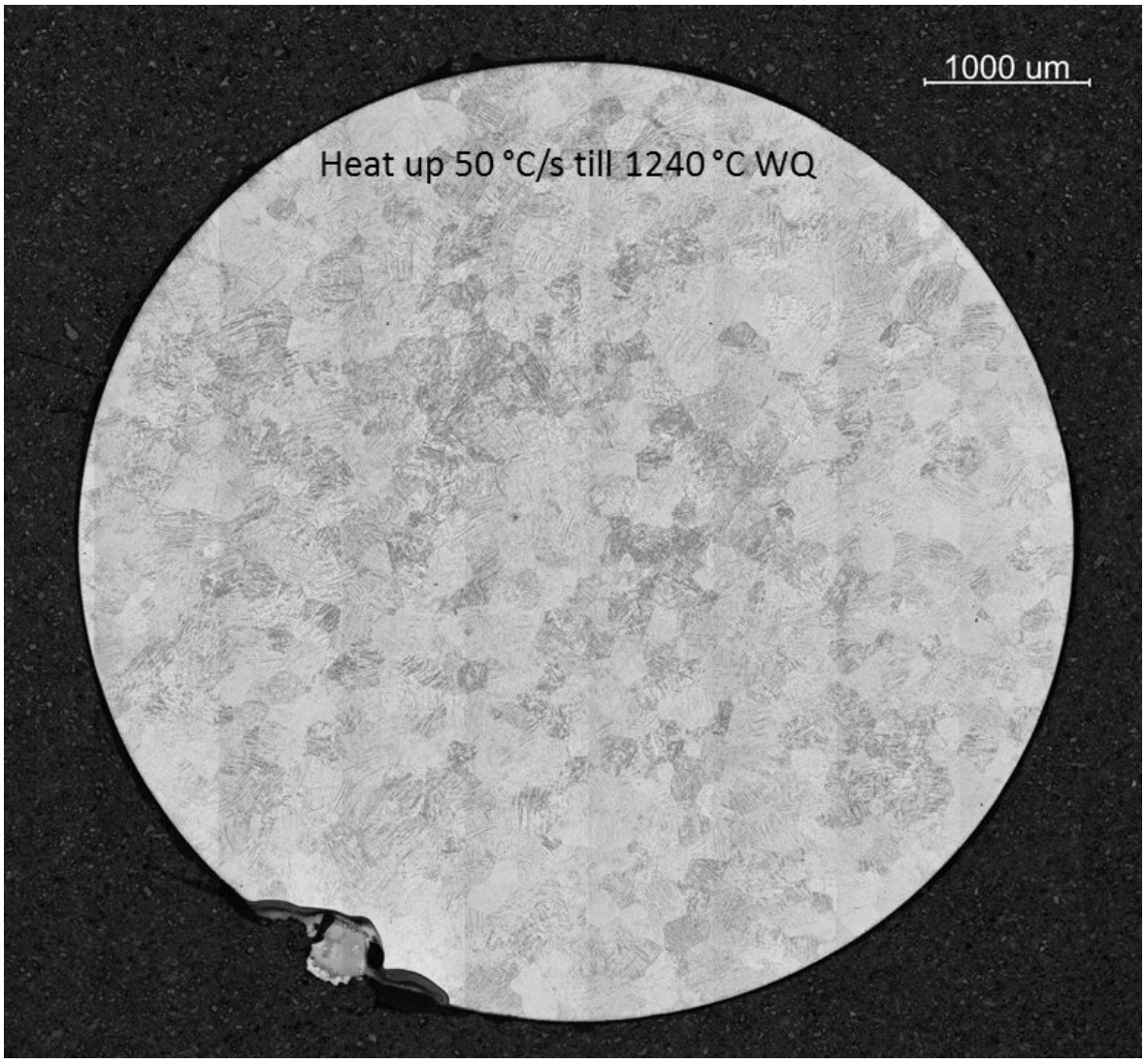

Figure B.5.: Montage of the sections taken at the optical microscope for the sample tested at a heating rate of 50 °C/s till 1240 °C then water quenched

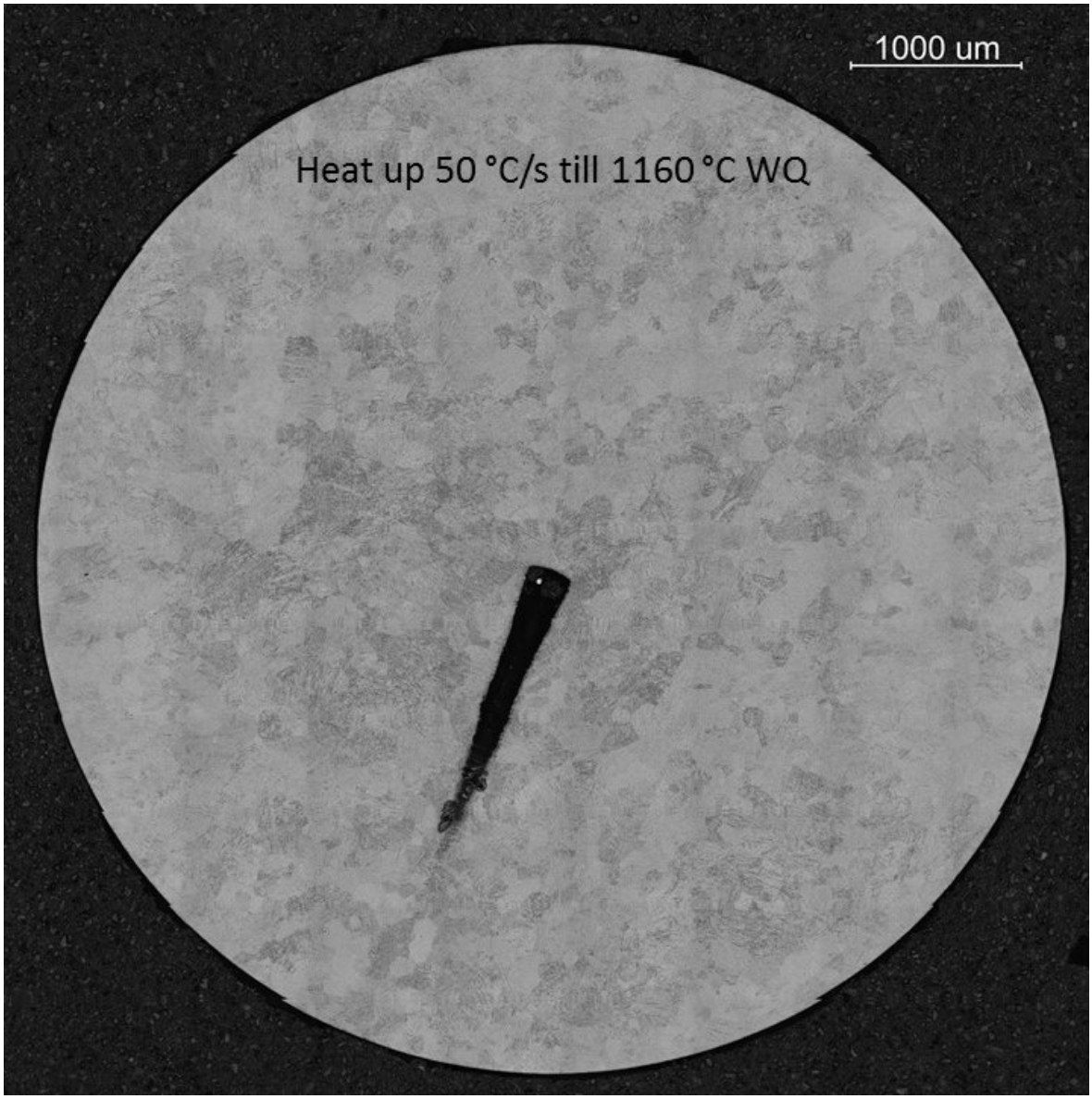

Figure B.6.: Montage of the sections taken at the optical microscope for the sample tested at a heating rate of 50 °C/s till 1160 °C then water quenched

B.3 Heating rate 500 °C/s

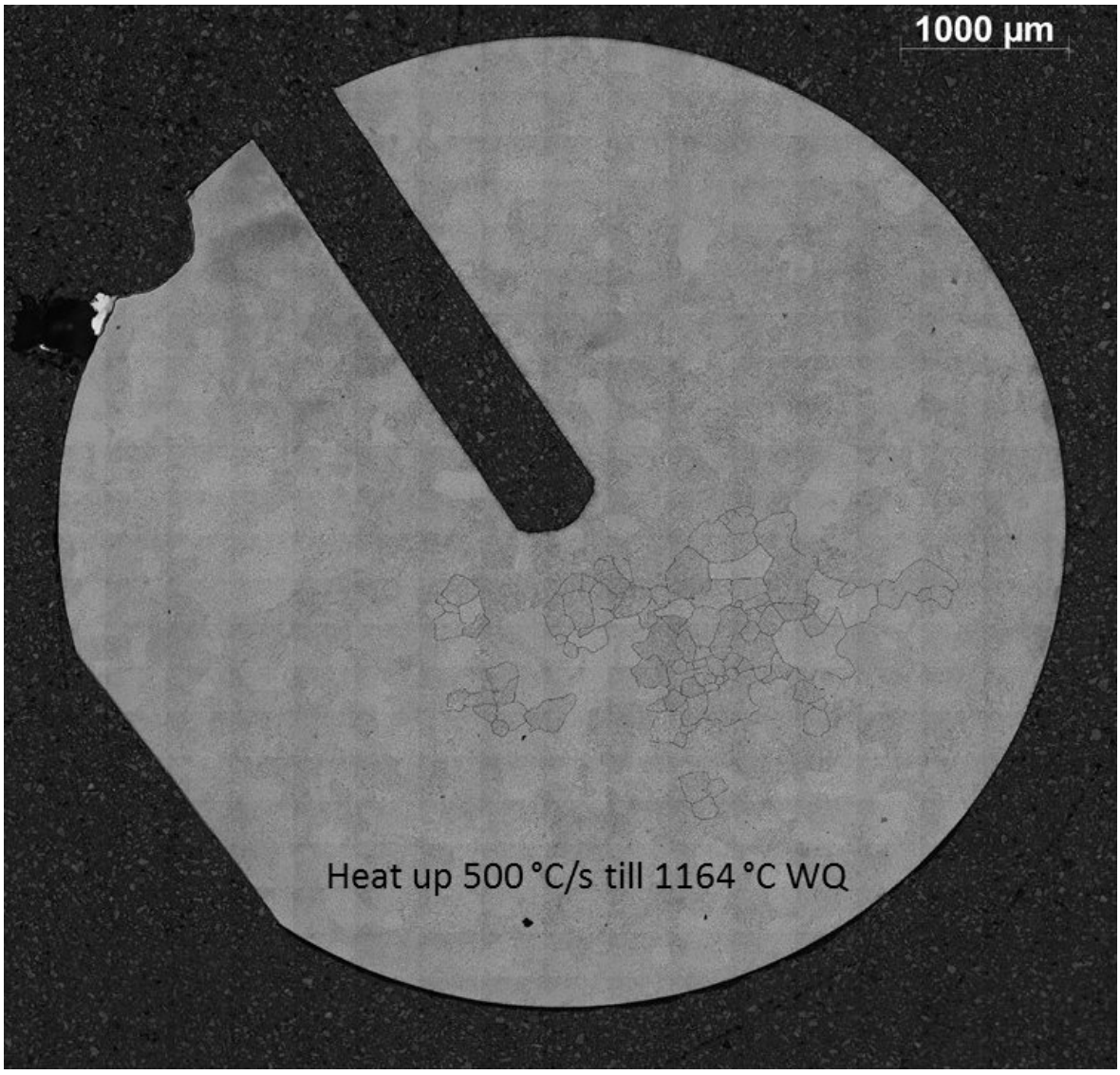

Figure B.7.: Montage of the sections taken at the optical microscope for the sample tested at a heating rate of 500 °C/s till 1164 °C then water quenched

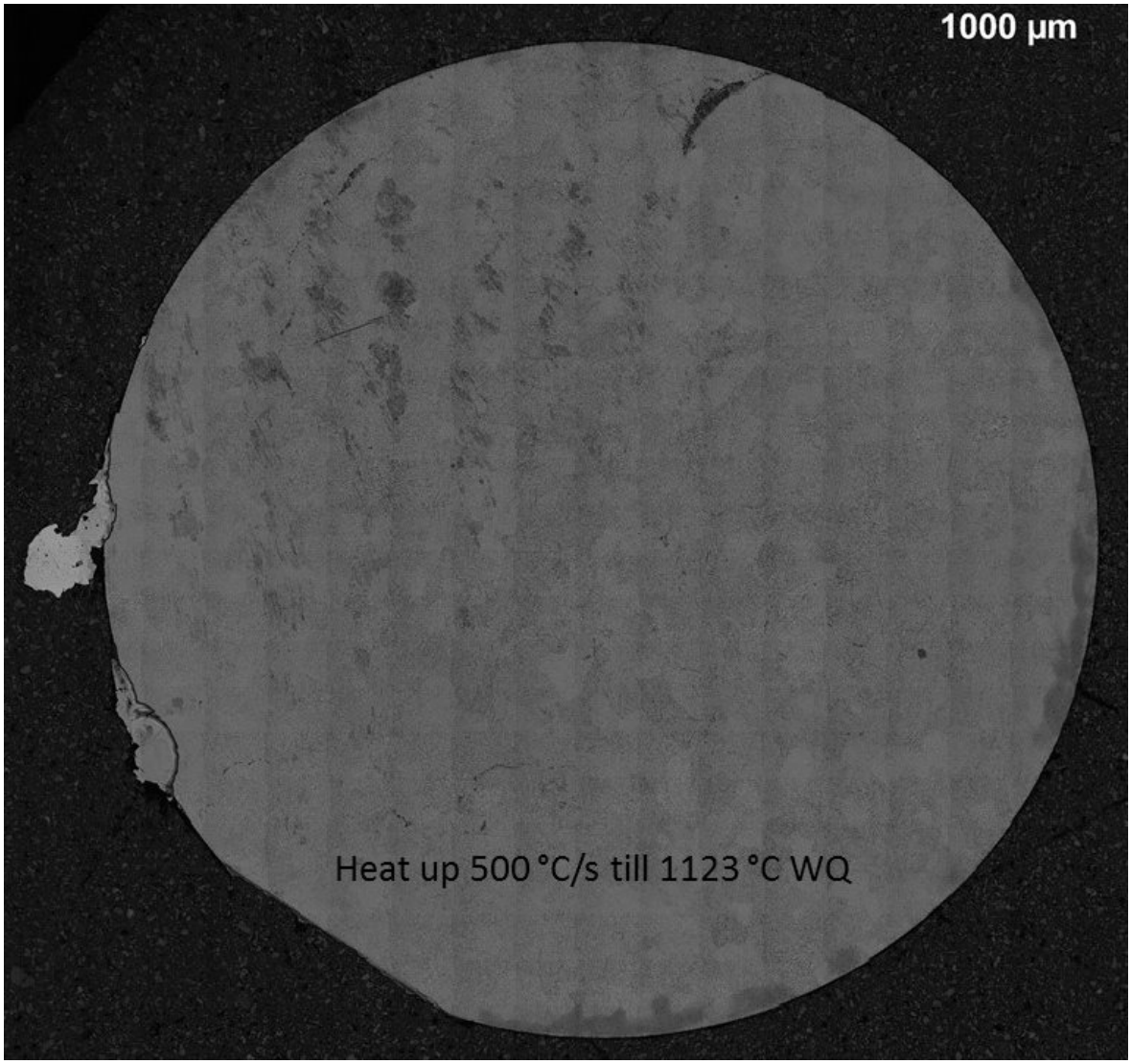

Figure B.8.: Montage of the sections taken at the optical microscope for the sample tested at a heating rate of 500 °C/s till 1123 °C then water quenched

APPENDIX C

Contact in welding

During the first year of the project, part of the time was spent getting information on the actual behaviour of two butts joined by welding and comparing it to the predictions of a numerical model.

Currently, in the commercial software Visual-Weld, the actual junction of two workpieces during a welding process is not simulated, as they are modelled already as a single part. This could introduce errors in the deformation predictions that could become important when a) more components are welded together, b) uncontrolled preloads are used to clamp the workpieces and c) thin structures, which are more prone to deflect, are joined.

The work carried out on this topic, consisted in the design and machining of the welding assembly for the experimental validation and some preliminary FE analysis to investigate the problem from a numerical point of view.

C.1 Welding jig

To experimentally clamp the workpiece in a way analagous to that usually practised in numerical simulations, by either a) clamping both sides of the component in all the degrees of freedom or b) fully clamping one side and imposing a displacement to the other side, two jigs (figure C.1) were realized to be fixed on a vice (figure 3.44). In this way it was

possible to keep the components to be welded aligned and, possibly, apply an external displacement or load to them. Furthermore, a spacer was designed to avoid possible movement of the clamps due to the stresses induced in the component during and after welding. This, as mentioned, was to replicate as best as possible the clamping conditions imposed in numerical simulations.

The workpiece considered in this stage is made of two plates to be joined together. After the welding test, the plate on the left side would be unclamped by removing the cover of the left jig and the deformation along Z and X directions can be measured by the laser sensors 1 and 3 respectively.

The laser sensor 2, protected by a ceramic plate, measures the relative displacement of the butt joint during the welding process, along the Z direction.

Part of the assembly was used also for the welding tests carried out for the study of the microstructure evolution of Ti-6Al-4V (figure 3.44).

C.2 Numerical modelling

The work carried out on the numerical side was focussed on finding a solution for the actual behaviour of two parts welded together and to compare the prediction of this approach to the conventional one, and then validate and/or improve the model by comparison with experimental tests.

The most realistic but complicated approach would be a) to update, every time step, the nodes of the mesh corresponding to the part of the model that, during welding, merge together, with relative change in the stiffness matrix and, b) at the same time, the contact between the two butts should also be modelled. Since Visual-Weld offered some solutions for describing the contact problem, and as this was easier from the modelling implementation point of view, for this phase of the work the ESI approach was preferred, to get possible indications for future developments.

By mixing Visual-Weld built-in functionalities, two solutions were set up:

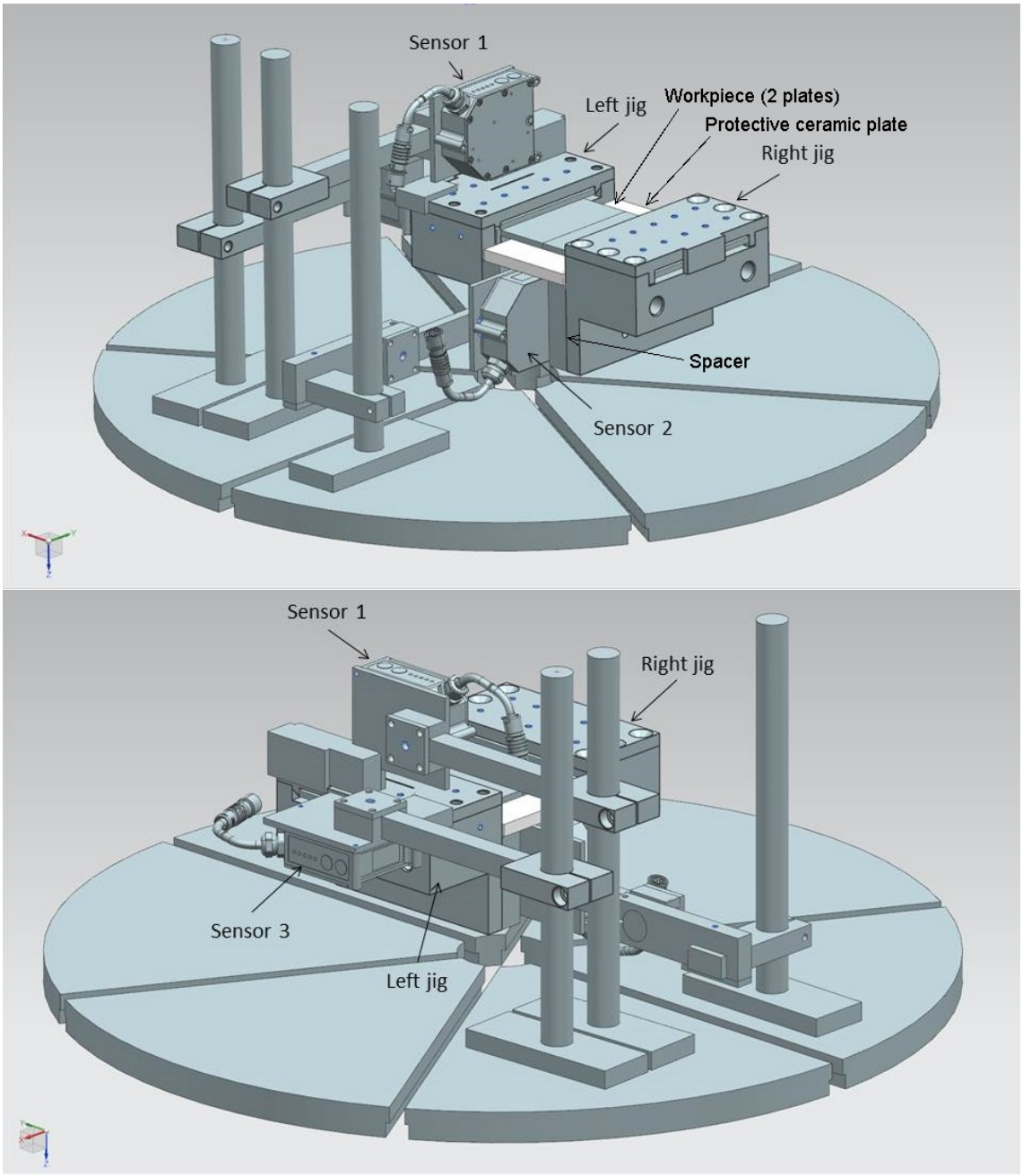

Figure C.1.: Welding assembly designed for displacement measurements during and after a welding test. The two pictures show views from two opposite sides.

- Chewing gum + contact elements
- Chewing gum + contact springs elements

Chewing gum elements are elements of the model with:

- very low Young's modulus (e.g. 1000 MPa)
- relatively low yield stress to avoid convergence problems (e.g. linearly scaled from 280 MPa at T_{amb} to 10 MPa at 1500 ^{o}C)
- thermal conductivity and specific heat set based on the actual conditions of the contact, e.g. air properties if there is a gap between the butts or, as in this work, the material of the component welded properties if the parts welded are pushed against each other
- thermal strains equal to zero
- capacity to switch to the material properties of the components welded when the melting temperature is reached

Contact elements are the usual contact properties set for elements of a model that can be in touch with each other, slide relatively to each other if the tangential force is high enough and a maximum interpenetration above which normal forces are transmitted is allowed.

Contact spring elements are 1D elements whose:

- stiffness can be updated every time step to the mean stiffness of the elements they connect
- stiffness can be switched off and on when specific temperatures are reached
- stiffness in compression and tension can be set differently
- tangential stiffness is zero

C.2.1 Chewing gum + contact elements (low preloads)

This approach consists in modelling the contact area both using chewing gum and contact elements (figure C.2).

By this technique it is possible to describe the relative sliding and loss of contact of the components not yet welded, as the chewing elements are very soft and the contact elements do not apply any resistance in tension. At the same time, by using contact elements it is possible to avoid squeezing the chewing gum when compressive loads are applied. Obviously, the more chewing gum elements are used, the higher will be the squeezing when compression is applied before welding but, also, the higher will be the stiffness of the joint when the parts have been welded.

This approach would be indicated when not too high compressive pre-loads are applied to the structure before and during welding and, instead, relative tangential sliding is supposed to occur. In this case, contact elements will avoid unrealistic inter penetration of the two butts (allowed instead by the chewing gum elements) and will describe friction as well as detachments. High compressive pre-loads would rise unrealistically the stresses the contact elements are subjected to, imposing a higher local displacement than the real case. The application of the heat source would cancel the local stresses of the elements, as above melting temperature the elements are made "stress-free", but the local displacement of the nodes would remain, introducing errors in the numerical predictions.

C.2.2 Chewing gum + contact spring elements (high preloads)

This approach consists in modelling the contact area using chewing gum and contact spring elements (figure C.3).

By this technique it is possible to describe the loss of contact of the components not yet welded and the real stiffness of the area of contact, as the contact spring elements have the mean stiffness of the material they connect at their side and do not apply any resistance in tension and tangential direction. Using contact spring elements it is also possible to avoid squeezing of the chewing gum when compressive loads are applied.

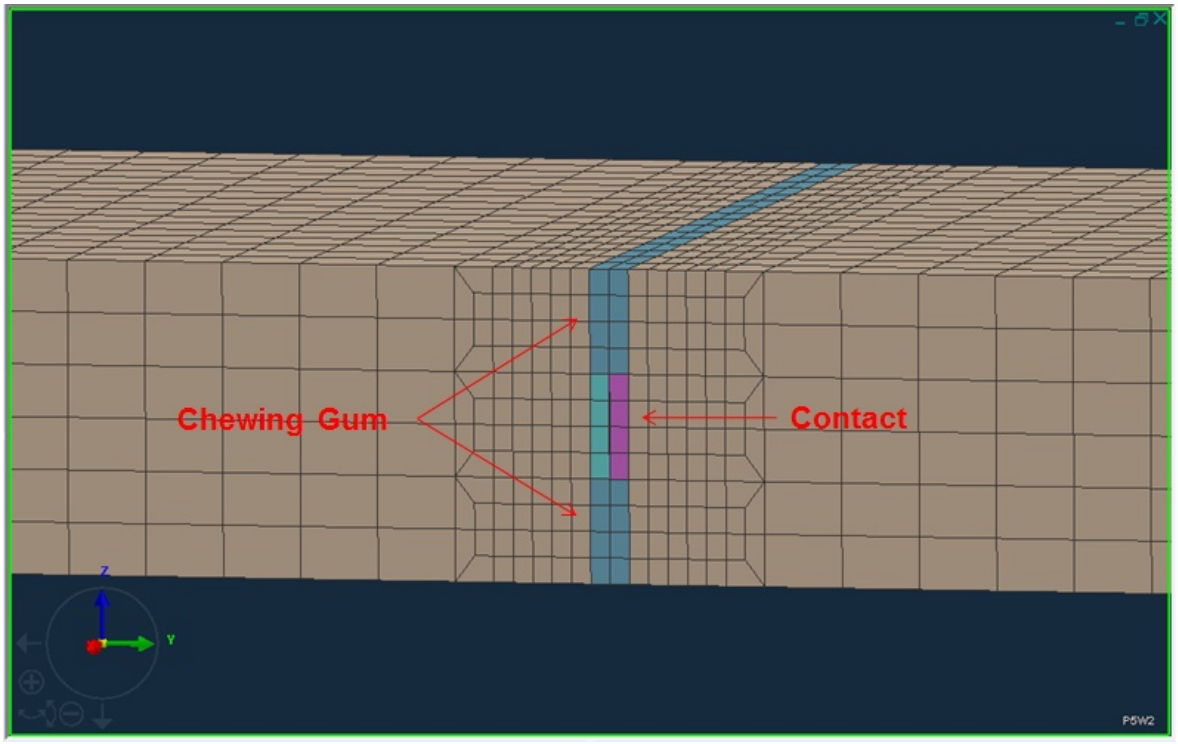

Figure C.2.: Chewing gum + contact elements adopted to model the contact of two butts to be welded

This approach would be indicated when high compressive pre-loads are applied to the structure before and during welding and, relative tangential sliding is supposed to be not relevant.

When a specific temperature is reached, the stiffness of the spring contact elements is removed whilst the chewing gum is switched to the real material properties, simulating the creation of a joint.

C.2.3 Preliminary results

The model used for the first numerical investigation is shown in figure C.4.

The left side of the model was completely clamped in all directions, whilst a displacement of 0.2 mm was applied to the right side along the Y direction avoiding, instead, movements in the X and Z directions.

Two points were sampled, one on the side of the application of the displacement and one close to the area where the heat source is applied and the junction is created, in the

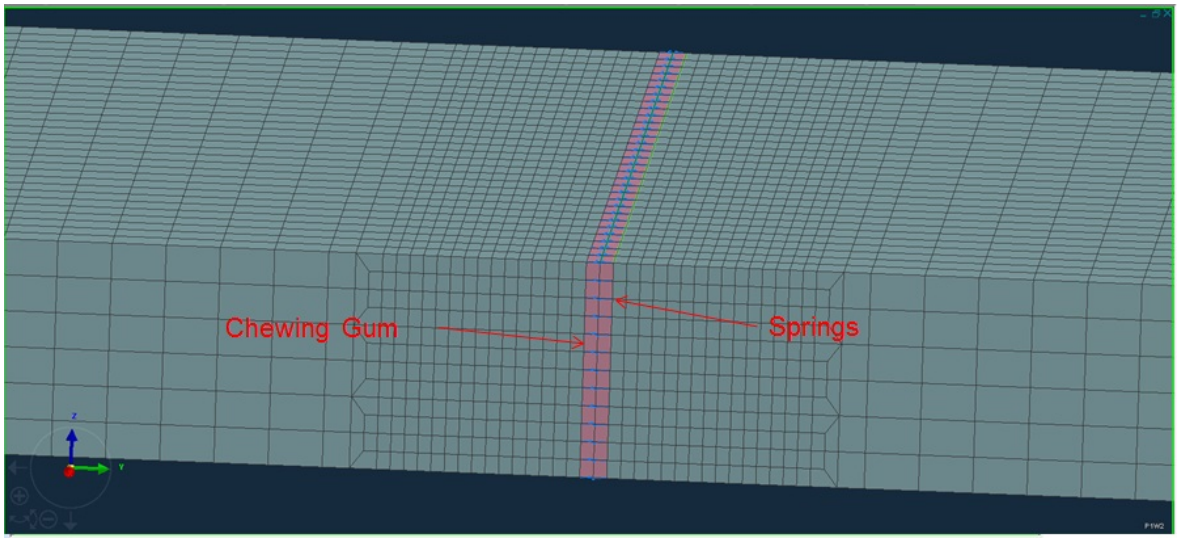

Figure C.3.: Chewing gum + contact spring elements adopted to model the contact of two butts to be welded. The spring contact elements are represented by blue lines connecting the sides of the chewing gum section

opposite side to the application of the displacement. This last point was to check how the forces passed through the junction. For comparison, values obtained running a weld simulation with only chewing gum elements in the junction was also run.

Looking at the displacements sampled in the right side of the model (figure C.5), relative to the Y direction, after the unclamping of the right side at 100 seconds, as expected the model adopting only chewing gum elements shows a higher shrinkage due to the squeezing during the preload, whilst the model without a description of the junction shows almost no variation, since the possible expansion at the interface of the butts is avoided by having a part actually already joined. The cases with spring contact elements + chewing gum and contact elements + chewing gum show the tendency of the component to increase its original length. This could be due to the expansion of the material during welding that pushes the two butts one against the other.

The displacement along the Z direction toward positive values is related to the "butterfly" shape usually observed after welding of plates. The higher amount of movement registered for the solution with contact spring elements + chewing gum could again be related to the higher freedom left to the butts during welding.

Figure C.6 shows identical behaviour of the plate after unclamping, except for the

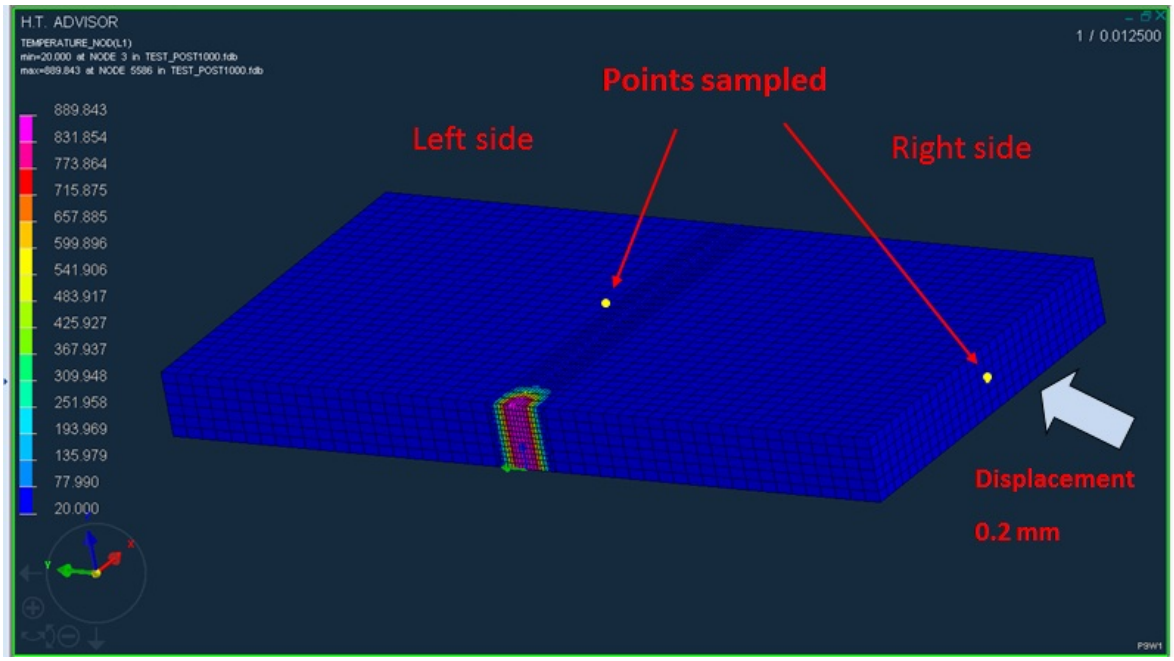

Figure C.4.: Model used for the first numerical investigation on the response of the different techniques adopted to model the contact of the butts

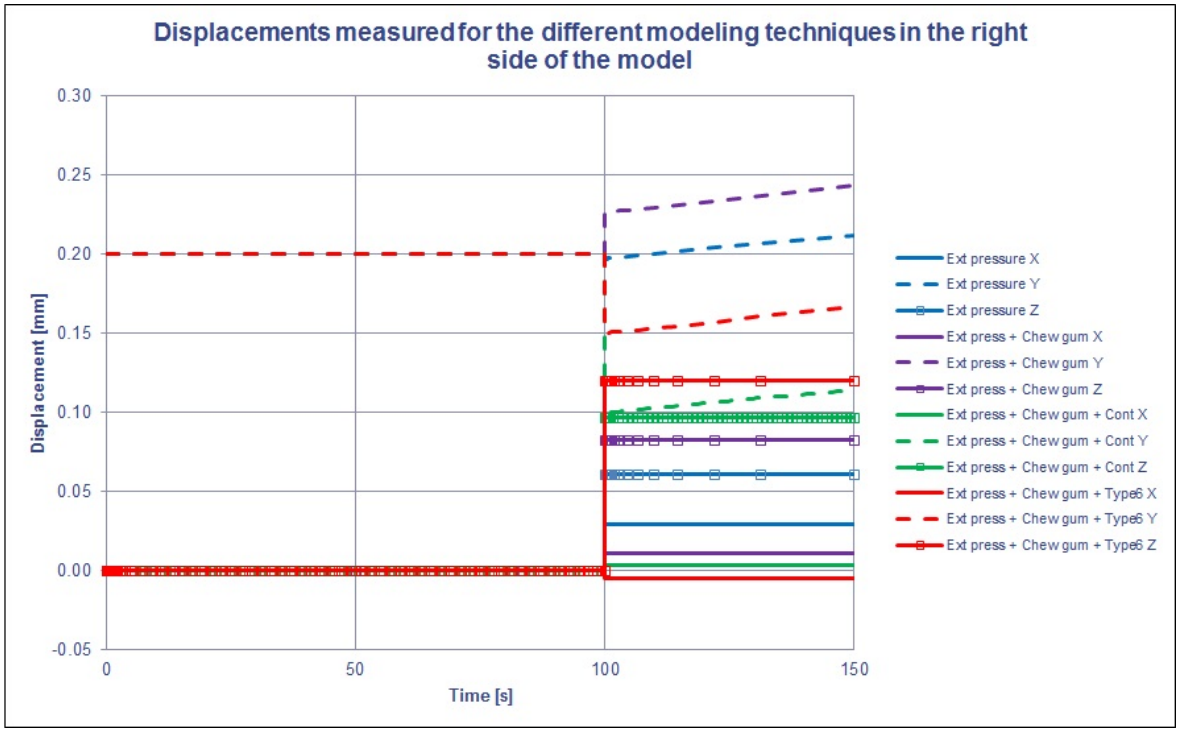

Figure C.5.: Displacements sampled in the right side of the model shown in figure C.4. Type 6 represents the nomenclature for spring contact elements used in Visual-Weld whilst "Cont" is for contact elements. The blue data are relative to the case where the junction is not modelled

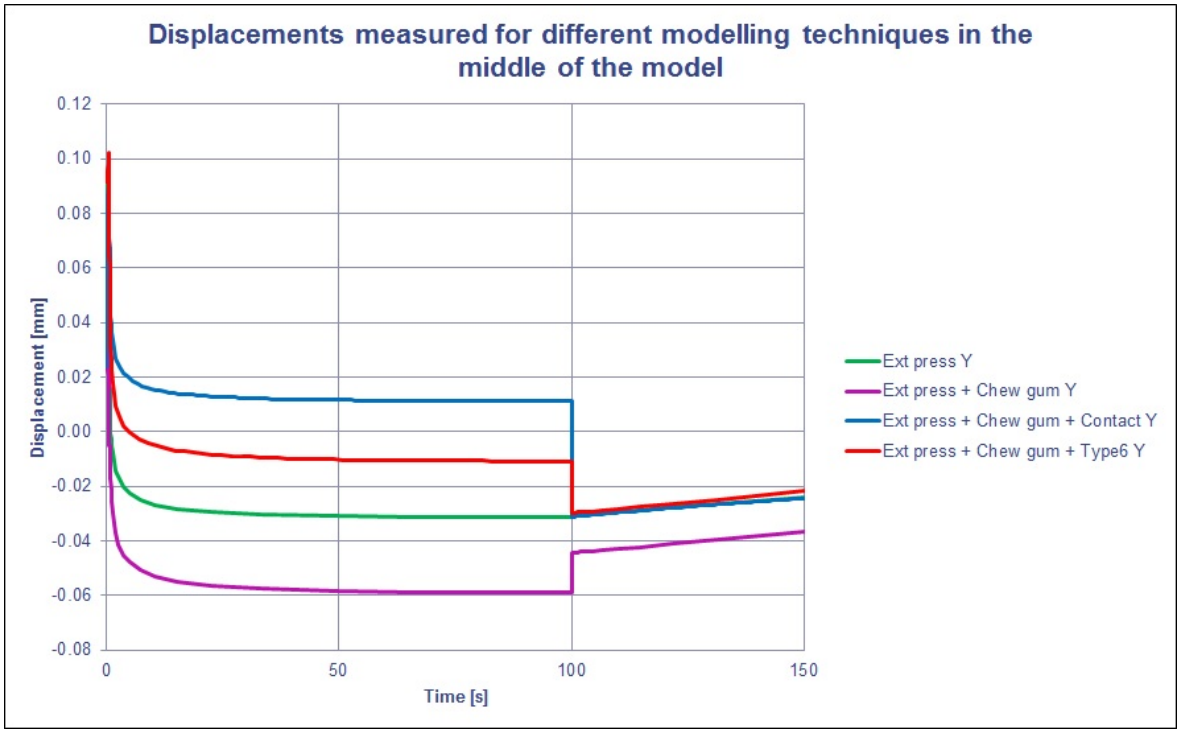

Figure C.6.: Displacements sampled in the centre of the model shown in figure C.4. "Type 6" represents the nomenclature for spring contact elements used in VisualWeld whilst "Contact" is for contact elements. At 100 seconds the right side of the model is unclamped

solution where only chewing elements are used, as the junction is easily prone to squeezing and hence can absorb the deformation imposed from the right side of the plate. The left side of the junction is thus free to deform and expand during welding, resulting in the overall length of the left component slightly increasing.

C.3 Conclusions

Initial numerical simulations were run to investigate the numerical predictions returned by models describing the contact of butts welded together, rather than considering them already as a single part.

Modelling the contact between the parts welded seems to result in different final deformations of the components that, even when absolute values are low, can result in 50% variations between the different solutions.

Experimental investigation is needed to understand better this phenomenon and to validate possible numerical models as, probably, this problem could become more important when more components of the same structure have to be welded together and/or thin parts, that are more prone to deflect, are joined.

APPENDIX D

Weld sequence optimization

D.1 Introduction

During the first year of the PhD, an investigation of the weld sequence optimization was carried out, in an attempt to understand the problem and to establish an initial approach to a solution.

In industrial applications, when two parts have to be joined together by welding, it is quite common to have weld paths constituted of many sub-welds and it is also normal to join several parts together involving a still higher number of welds. As a first approximation, it is possible to say that these processes require as much time and material as the number of welds increases. Also it is very important to understand and predict how systems result in distortion at the end of a welding process to reduce costs and waste of components, it is also an important requirement to optimize the order of the welds, finding the weld sequence that returns the best results in terms, for example, of final deformation or residual stress.

The computational time needed to evaluate all the possible combinations of welds involved in joining a mechanical system (e.g. by FE analysis) could become very high: the usage of a surrogate model could thus be useful in trying to simplify this burden.

To approach this kind of problem, an optimization of a sequence of sub-welds used to

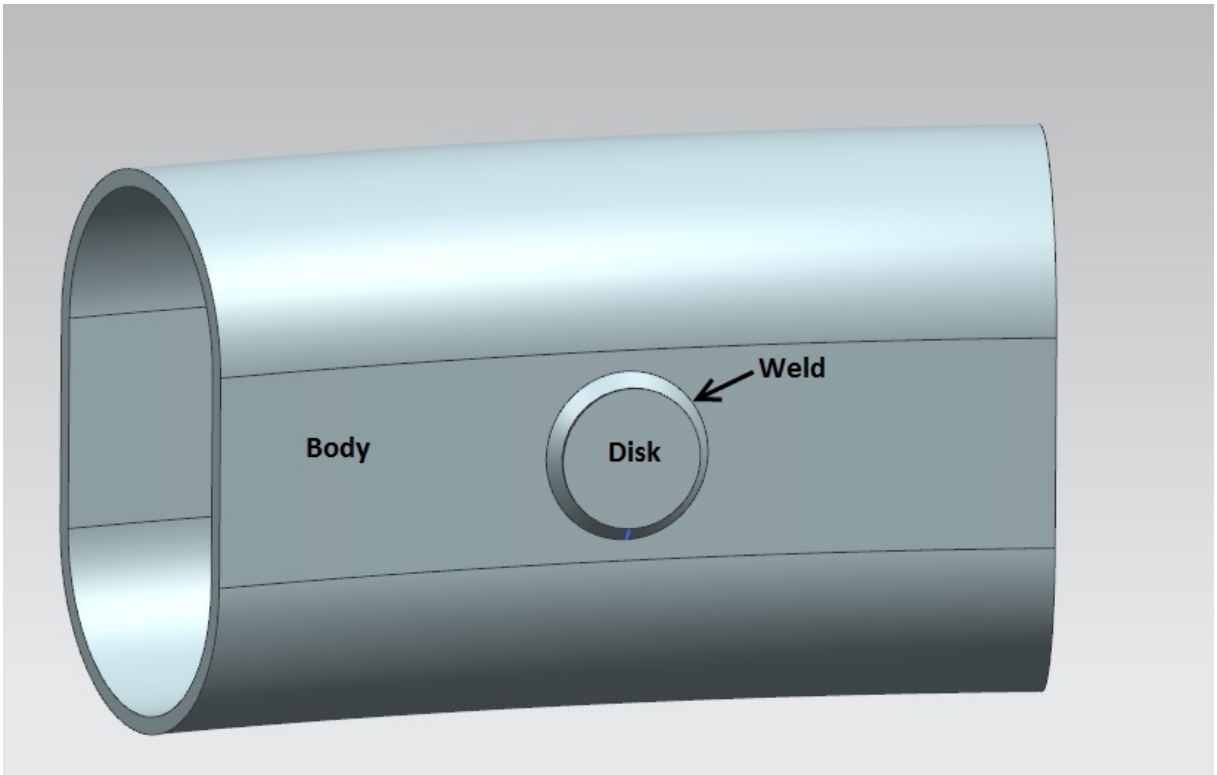

Figure D.1.: Drawing of the model considered for the weld sequence optimization study

joint the parts showed in figure D.1 was studied: a disk has to be joined to a main body with a toroidal form using a sequence of 4 sub-welds made by a TIG process.

D.2 Overview

The objective of the study was to optimize the weld path used to attach the disk to the body shown in figure D.1, choosing the sequence of four sub-welds between those shown in figure D.2 that deform the body the least amount possible at the point highlighted in figure D.2.

The model was meshed following a mesh sensitivity study, in which the least number of elements through the thickness of the body, that did not modify the deformation prediction of the simulation, was determined. This was to reduce the computational time required for running the simulations.

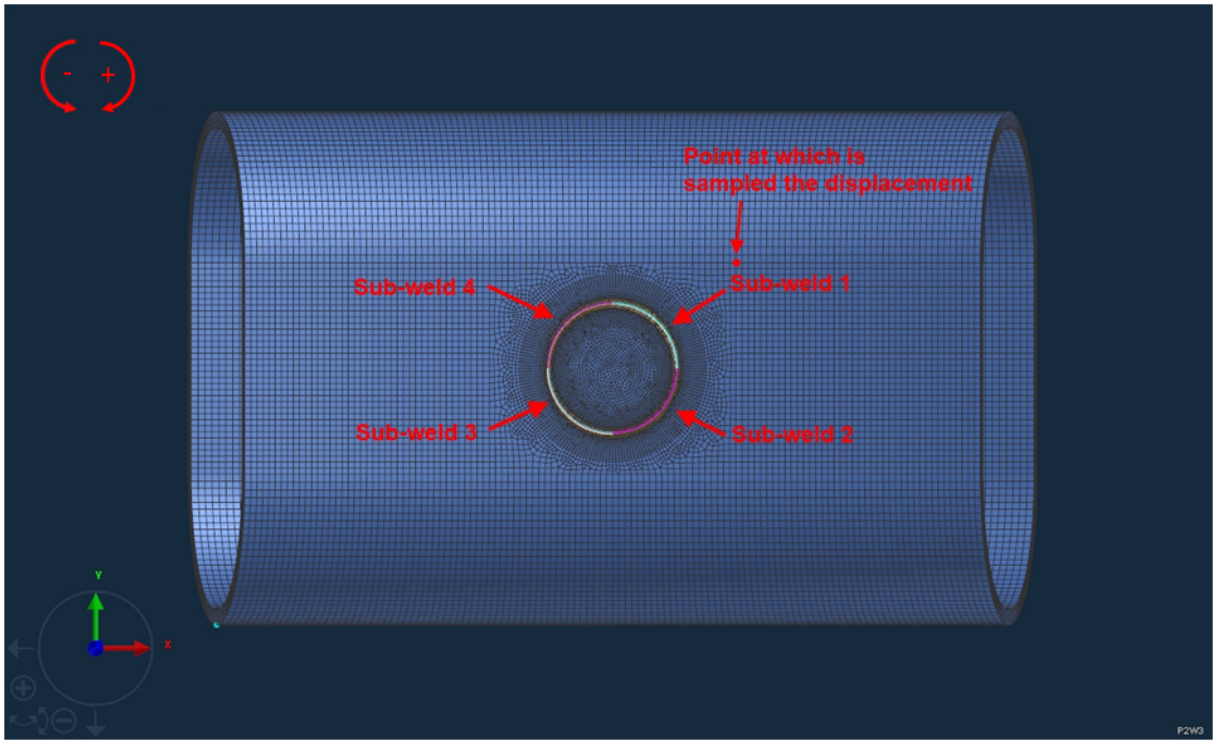

Figure D.2.: Mesh of the model studied for the weld sequence optimization. The 4 sub-welds constituent the weld sequence to be optimized are shown. For each of them it is possible to choose the direction, clockwise direction is identified by the positive sign vice versa for the anti-clockwise direction

Close to the weld path, since there were high temperature and deformation gradients, a high mesh density was localized and kept unchanged during the mesh sensitivity study whilst, farther away, the number of elements through the body thickness was changed, going from 2 to 6, to analyse the effect on the deformation predictions of the model (figure D.3 and D.4).

Results of the mesh sensitivity study, obtained running simulations with the same welds path but using different mesh densities, as described previously, are shown in figure D.6 and D.7, reporting the displacement along X, Y and Z directions measured in the point highlighted in figure D.5.

The displacement measured at the end of the simulations along the Z direction, as a function of the number of elements through the body thickness, is shown in figure D.8, and considered as the main deformation to be optimized. From these data it is possible to observe a pronounced asymptotic trend of the deformation around 5 and 6 elements, the choice was thus for 5 elements along the body thickness, with the purpose of shorter running times possible, with the smallest effect on the distortion prediction introduced by the mesh.

A complete FE analysis for the case shown, with the mesh optimized, took about 3.5 days to be solved. Assuming that the results of all possible sub-welds orders are evaluated, it would have taken (384 x 3.5)/(number of contemporaneous simulations launched) days. This procedure would have allowed the identification of the best theoretical solution but obviously it was not practically feasible, a compromise was thus needed to reduce the number of simulations to obtain a reasonably good optimization of the weld sequence. For this purpose a surrogate model was investigated and is presented in the next sections.

The work consisted of developing three main programs:

1. algorithm for the determination of the initial design of experiment (DOE) table;

2. algorithm for the automatic creation of all the files necessary to run FE analysis on the sequences proposed in the DOE table (1);

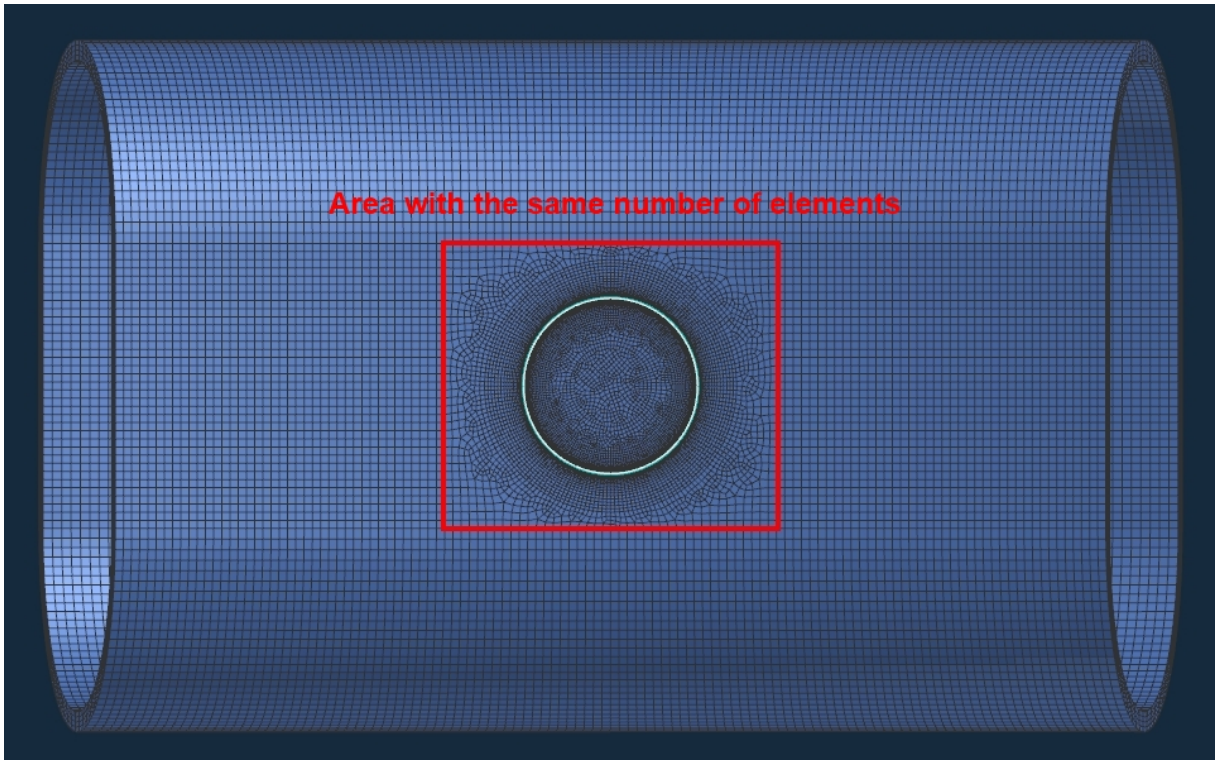

Figure D.3.: Model mesh. The area where the number of elements is not changed during the mesh sensitivity study is highlighted by the red square

3. algorithm for the prediction of the best sequence(s) with respect to some conditions specified by the user, using evaluations of results obtained in the previous points and on possible further FE analysis.

D.3 DOE algorithm

This phase of the work, and the relative algorithm, has the important function of determining the *minimum number* (saving time) of *significant* (getting useful information for the surrogate model) sequences that should be evaluated, using FE analysis, to extract data for a first evaluation and optimization.

To identify the welds (or sub-welds) constituting the sequence, in this work numbers are used (figure D.2); since it is possible to decide also the direction of the welds, the sign ("+" or "-") is used to discriminate between respectively the clockwise and the anti-clockwise direction. The temporal order of a sequence is identified by reading numbers from the

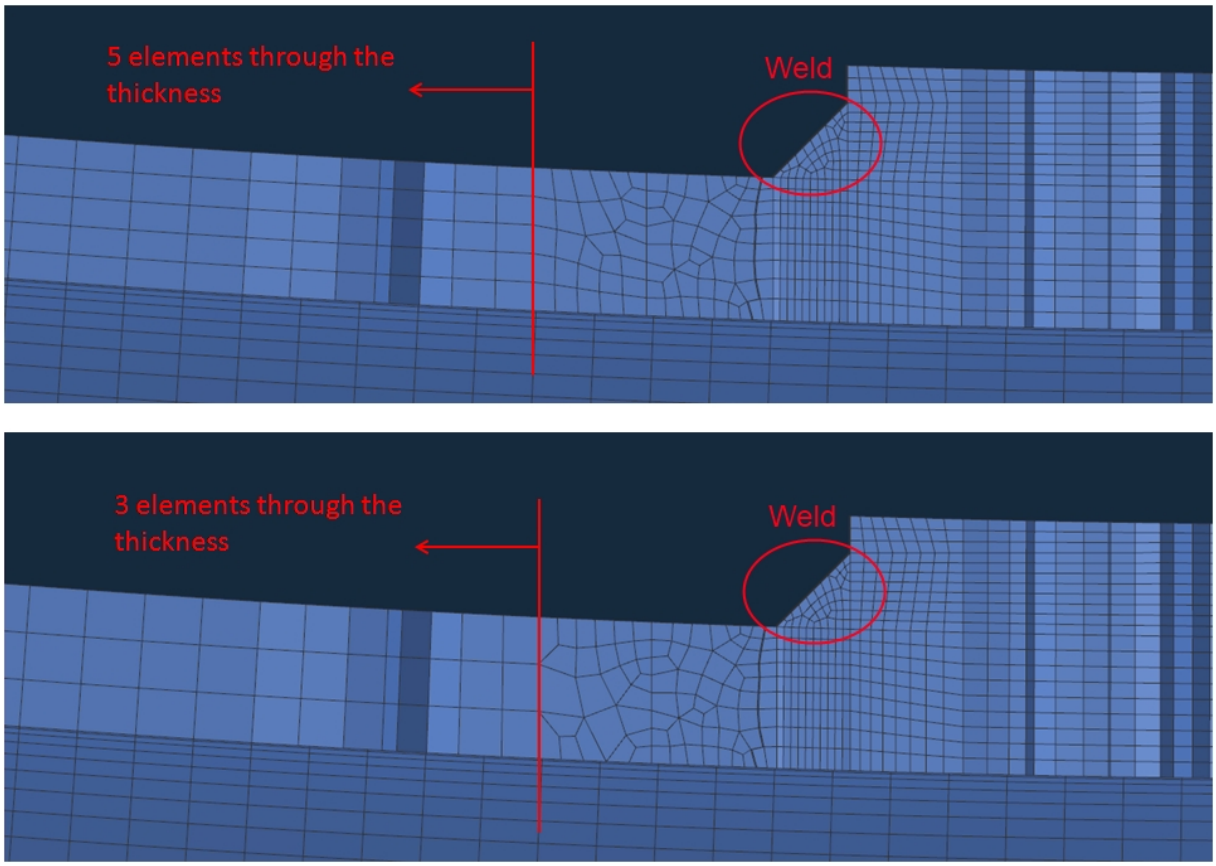

Figure D.4.: Section view of figure D.3: in the right side of the red line the mesh density is kept constant whilst in the left side the number of elements through the thickness of the body is changed for the mesh sensitivity study

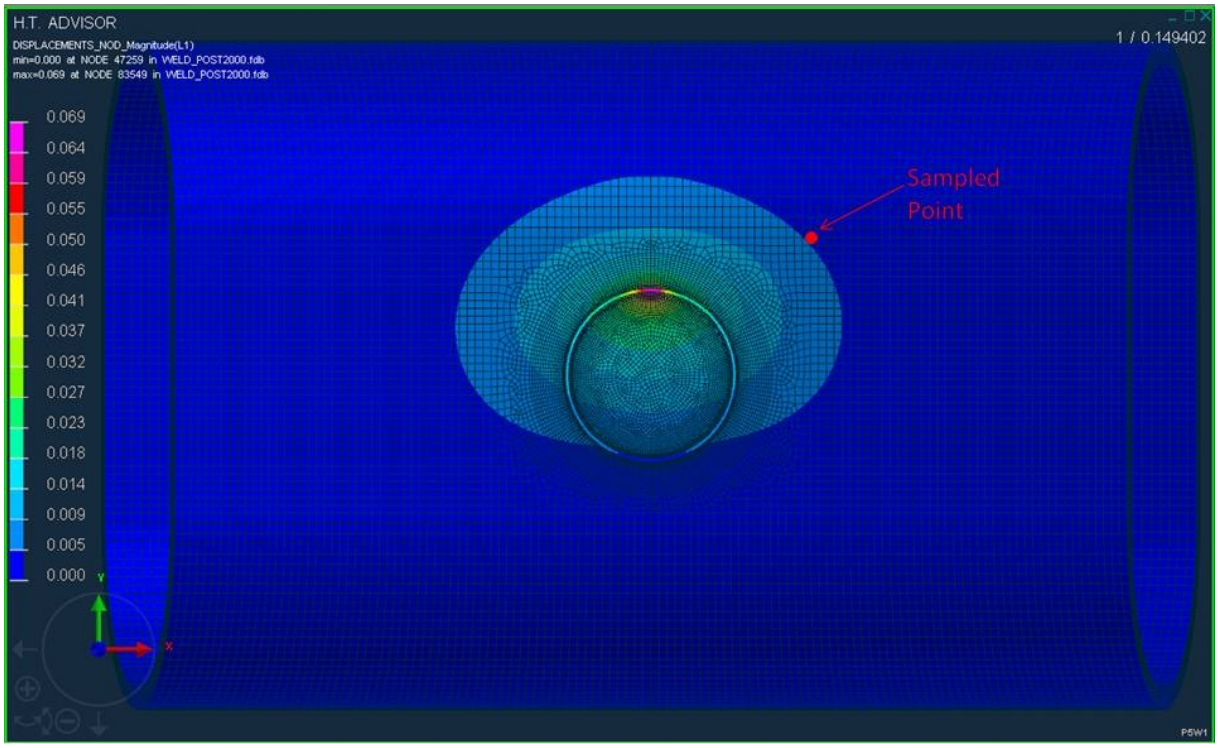

Figure D.5.: Point sampled for the mechanical analysis. The coordinate system used for the displacement measurement is shown in the bottom left side

right to the left (the first number on the right is the first weld occurring).

The algorithm searches the minimum number of random sequences that:

- give all welds coupled with all other possible previous ones, in temporal order;
- distribute as best as possible, every weld for every possible position inside a sequence.

In table D.1 a simple example of a good list of sequences, for an hypothetical case of welds identified by 1-2-3-4, is shown.

1	2	3	4
3	1	4	2
2	4	1	3
4	3	2	1

Table D.1.: Example of a minimum number of sequences for a case of 4 welds in which it is possible to choose only one direction (+). The two condition "all welds coupled with all other welds" and "good distribution of every weld in every position" are satisfied

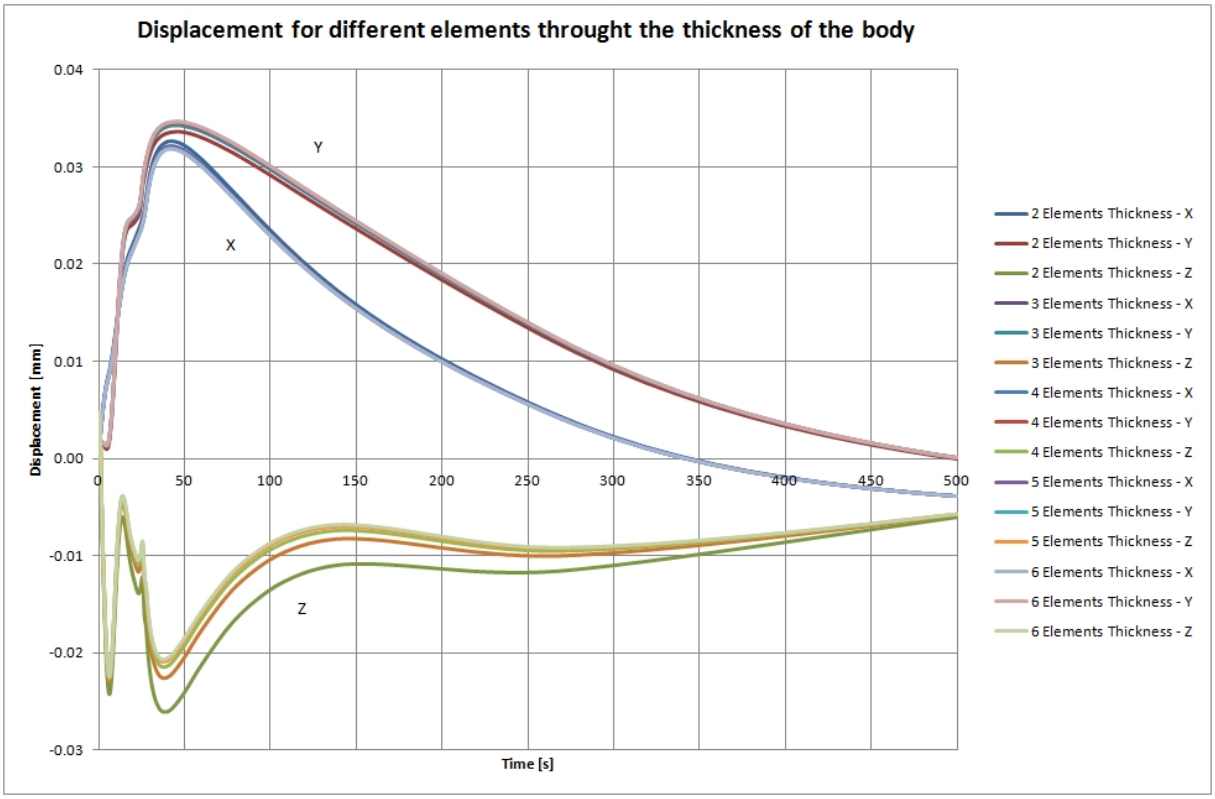

Figure D.6.: Mesh sensitivity study: displacements along X-Y-Z directions measured in the point highlighted in figure D.5 changing the number of elements through the thickness (figure D.4)

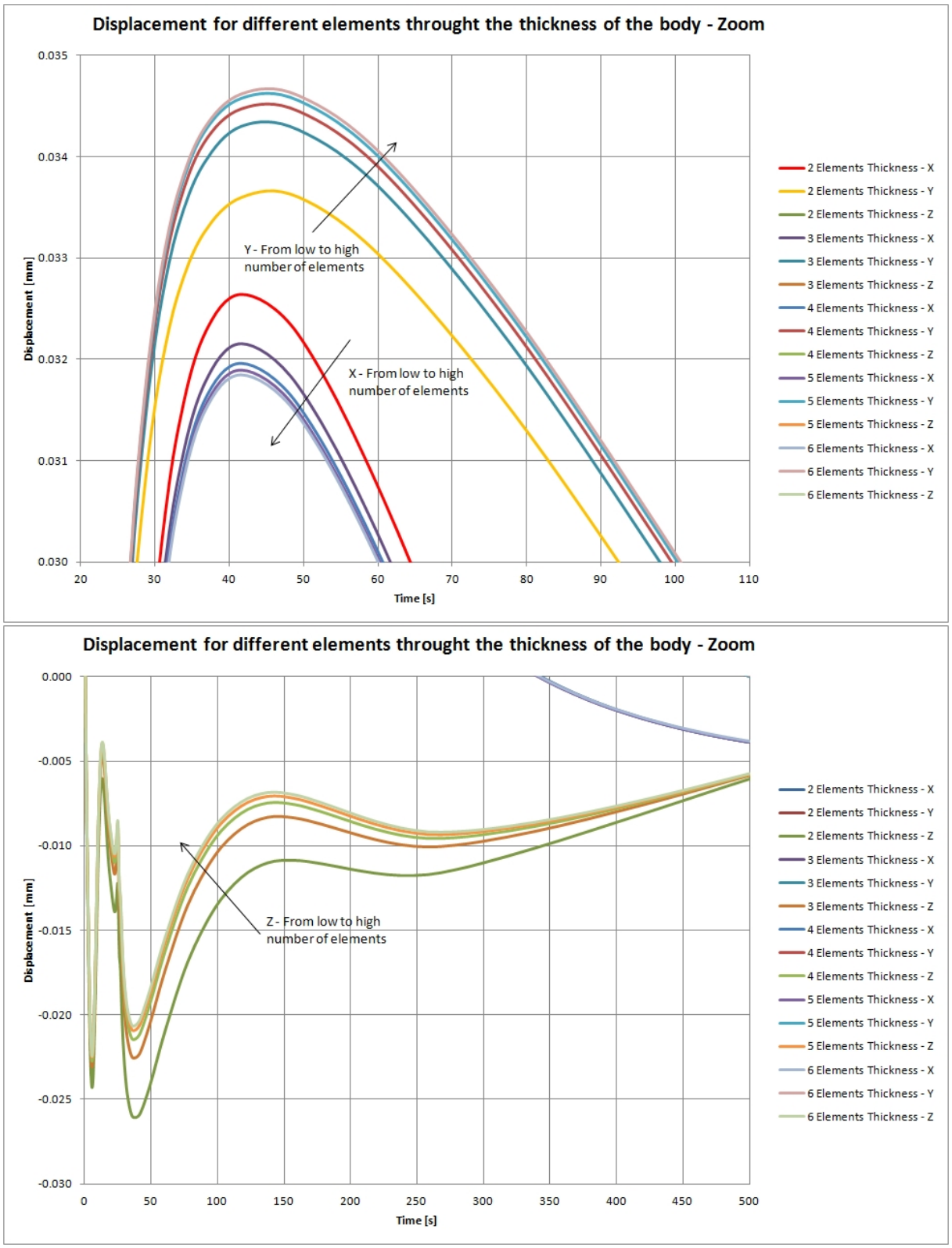

Figure D.7.: Mesh sensitivity study: zoom of the chart reported in figure D.6

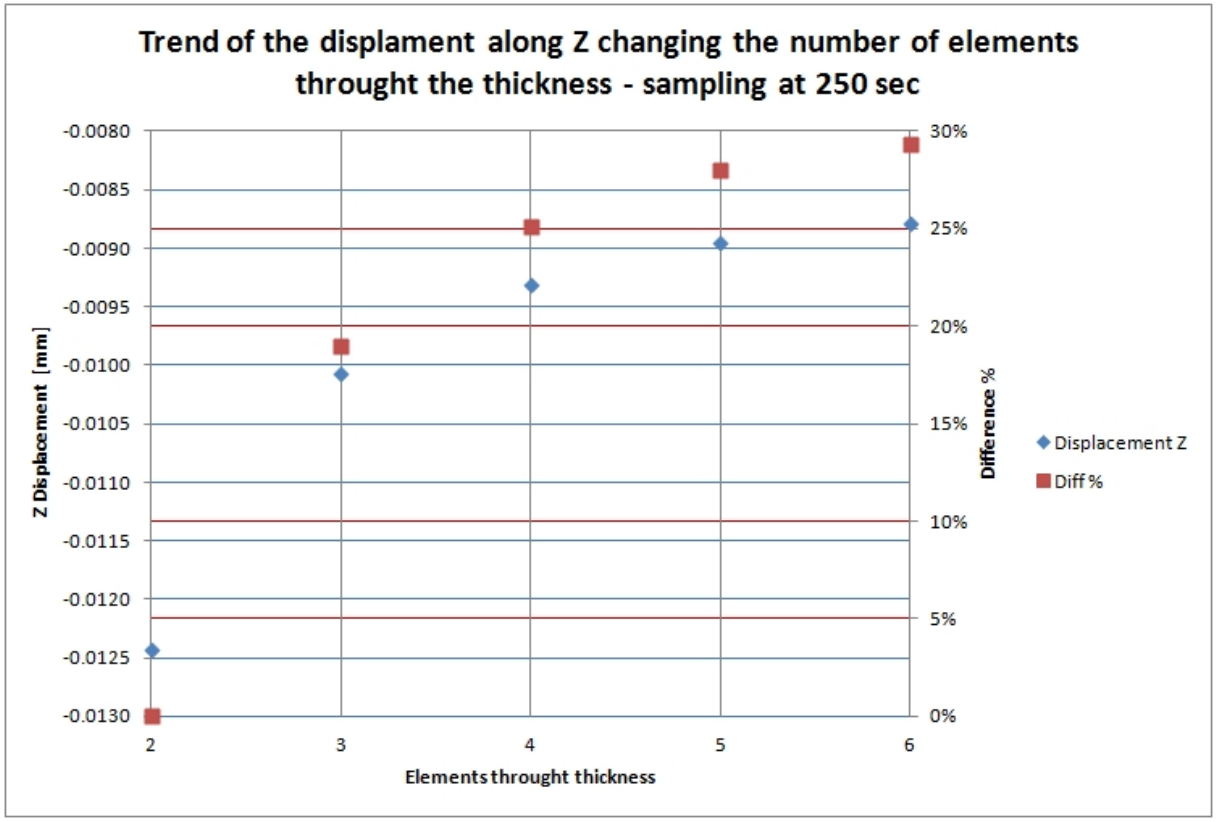

Figure D.8.: Mesh sensitivity study. Light blue rhombus represent the trend of the displacement along the z coordinate at 250 s as a function of the number of elements through the thickness. Red squares represent the difference percentage between the various displacements, referred to the value registered for the case with 2 elements through the thickness

The two above conditions for the determination of the initial DOE table are desired because, besides the numerical reason for having a good data dispersion, they also have a thermo-mechanical meaning:

1. it is important to know the effect of any weld on all the possible next ones both for the high effect on the temperature distribution and obviously for the change in the system global stiffness;

2. it is important to have data for every possible position occupied by every weld inside a sequence because this is related to how many parts have already been joined, thus changing the global system stiffness; obviously this is a not very correct statement because in two different sequences a weld can occupy the same position but if the previous welds are different the global stiffness will be different. This is a simplification necessary to have a DOE table not too big; obviously the surrogate model should keep in consideration these phenomena.

In figure D.9 the flow chart of the algorithm is shown.

In figure D.10 and D.11 two screen shoots of the algorithm output for the sequence of four welds represented in figure D.2 are shown.

In figure D.10 it is possible to see that without optimization, 384 combinations (384 FE analysis) would be necessary to be analysed whilst, using the algorithm presented in this section, it is possible to begin the optimization of the problem by analysing 17 sequences. The distribution of every weld in each sequence suggested is also shown, in this case there are almost 2 occurrences for every weld and every position: within the red rectangle, the amount of occurrences for the weld shown in the left side of the rows, for each position, is reported.

In figure D.11, in the black rectangle, the list of all the couples of welds, within the list of sequences suggested by the algorithm, is shown. In this case, every weld is preceded by all the other possible welds, exactly once.

Once the initial DOE table is defined, all the FE analysis relative to the sequences

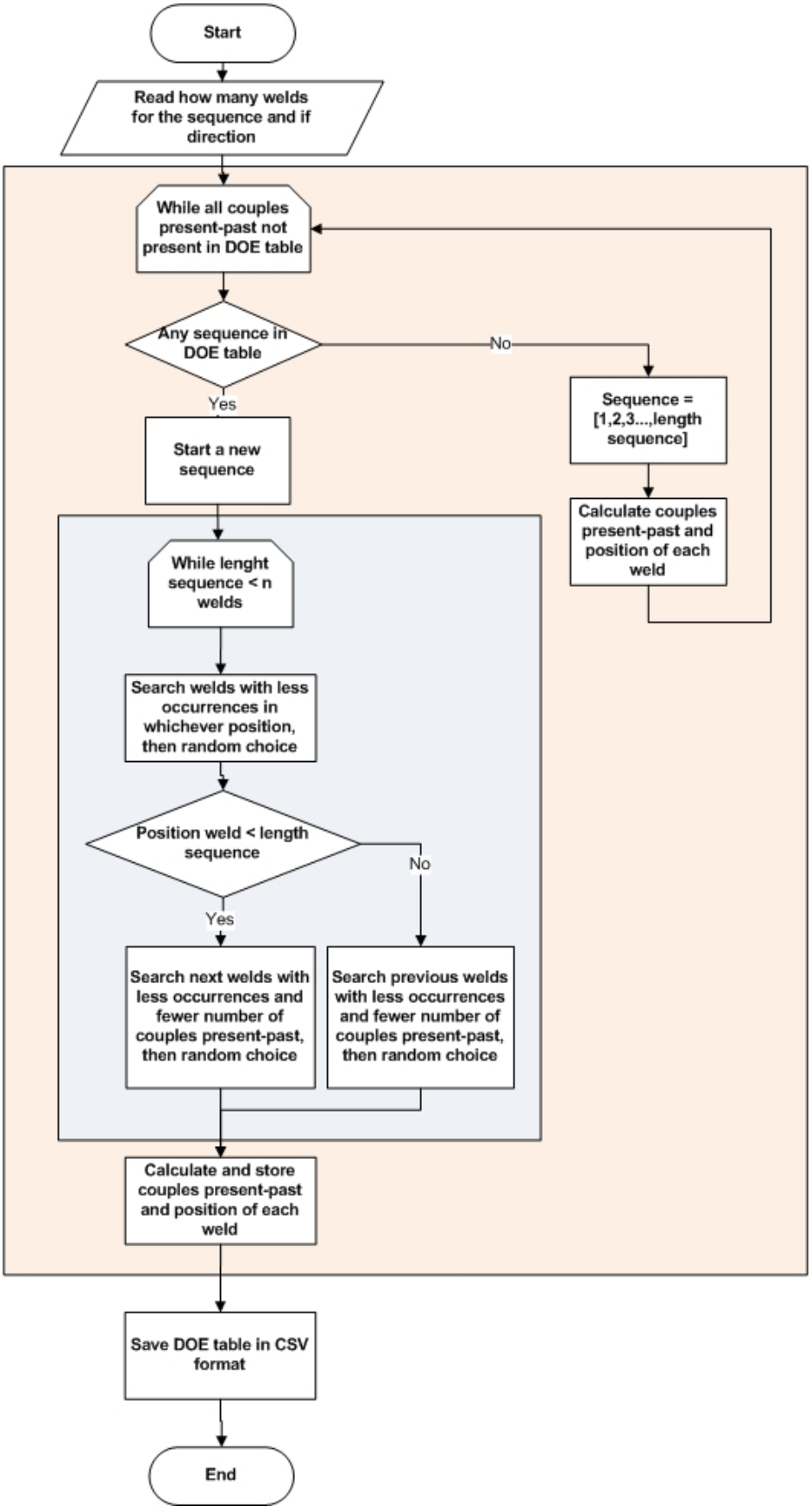

Figure D.9.: Flow chart of the 1^{st} algorithm

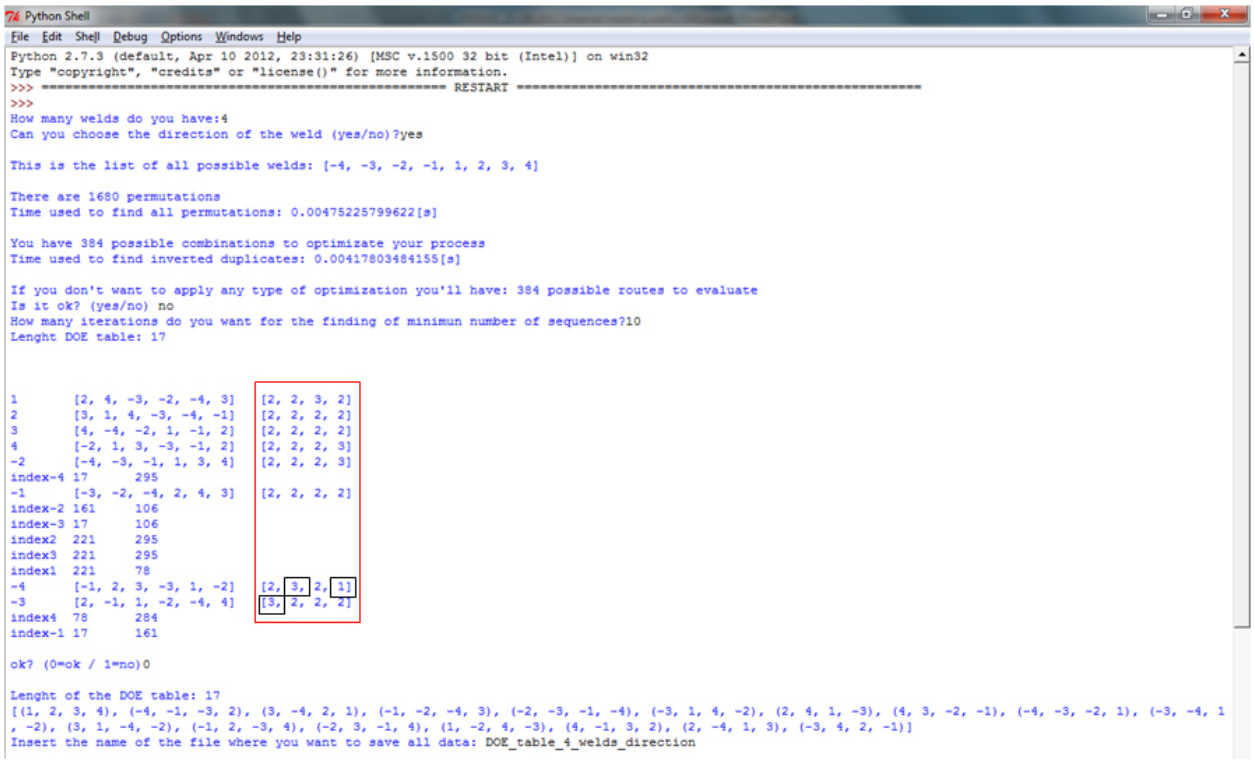

Figure D.10.: First screen shot of the DOE algorithm used to get an initial list of sequences to analyse, in particular this case would be useful to study the system shown in figure D.2 . In the red rectangle, the number of occurences for the weld shown at the left side of each row, for each position withn the sequences, is reported

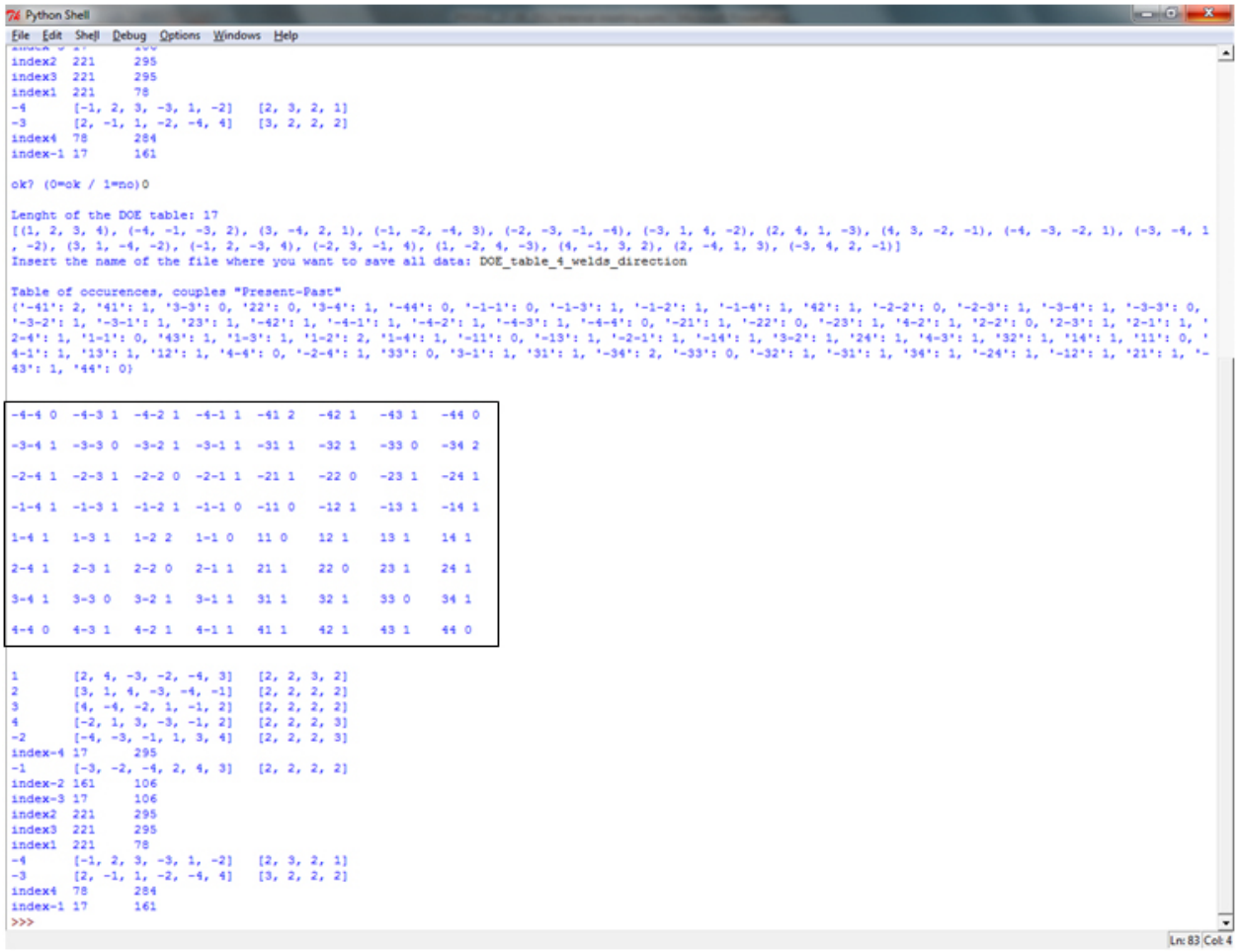

Figure D.11.: Second screen shoot of the DOE algorithm. In the black rectangle, the couples of all the welds formed within the list of sequences suggested by the DOE algorithm if figure D.10 is shown D.10

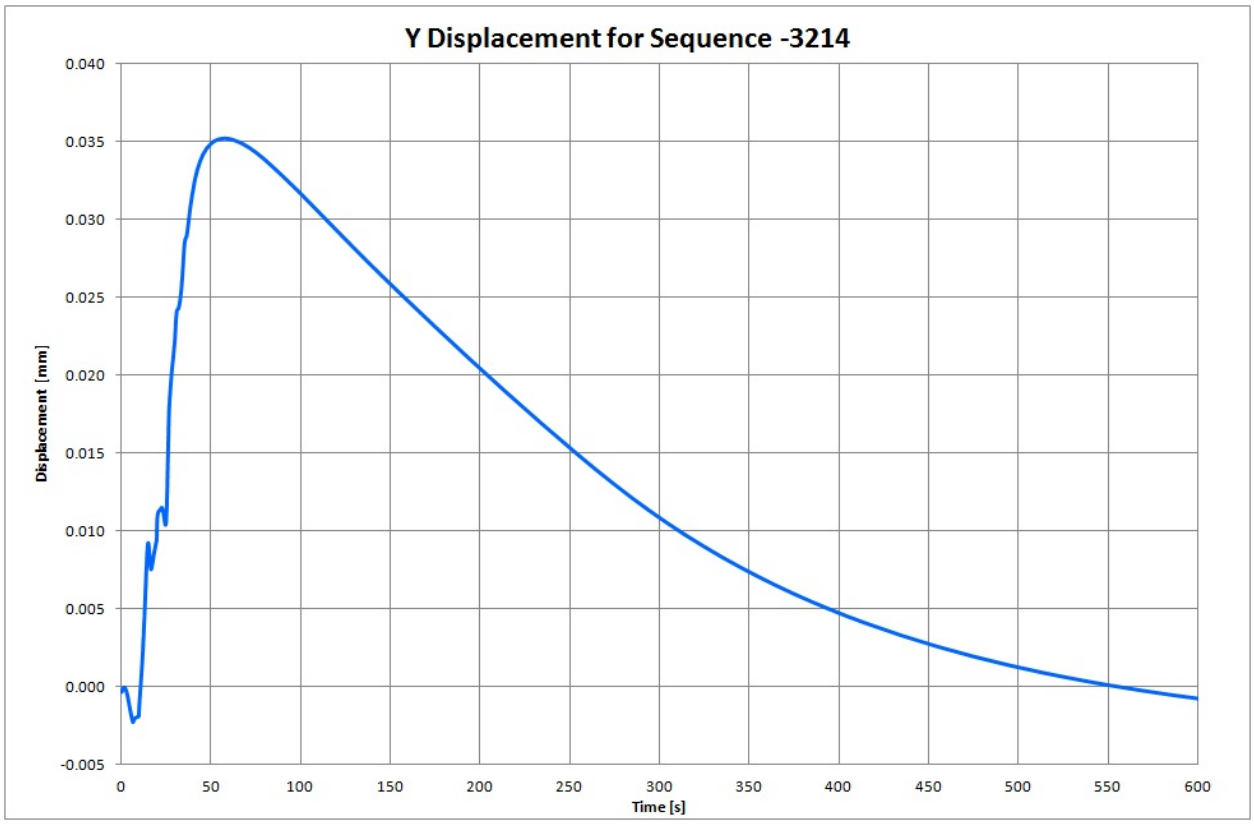

Figure D.12.: Displacement measured along Y direction for the sequence -3,2,1,4 in the point shown in figure D.5

suggested have to be run, then the data relative to the dimension to be optimized have to be extracted, stored in a file (comma delimited format) that is going to be used by the 3^{rd} algorithm of the surrogate model.

In figure D.12 the displacement measured along the Y direction for the sequence -3,2,1,4 is shown; the data sampled are the Δdisplacement between each weld within the sequence (at 0, 10, 20, 30 and 40 seconds) and the one due to the cooling (between 40 and 600 seconds). In table D.2 the results obtained from carrying out the FE analysis on the sequences proposed in figure D.10 are shown.

D.4 Surrogate model

In this section, the surrogate model used to find the optimum weld sequence, from using the data obtained running the simulations of the sequences suggested from the algorithm

Sequences	DISPLACEMENT [mm]				Cooling [mm]		Final Def [mm]
-4-2-3-1	0.009110	0.016784	0.000858	0.007698	-0.035627		-0.001177
-3-2-41	0.005539	0.014758	0.008639	0.006863	-0.034926		0.000874
-4-123	0.010086	0.013162	0.010504	-0.000752	-0.033710		-0.000710
-2-134	0.012874	0.004522	0.002650	0.006455	-0.027138		-0.000638
-2314	0.012973	0.008361	0.000311	0.006455	-0.028285		-0.000185
412-3	0.009644	0.012665	0.011322	-0.001860	-0.032488		-0.000718
2-4-31	0.015006	0.010075	0.001655	0.006863	-0.035723		-0.002123
1-24-3	0.006907	0.011196	0.008207	-0.001860	-0.025184		-0.000734
3-21-4	0.007410	0.016681	0.000932	0.007777	-0.032582		0.000218
3-142	0.003573	-0.002045	0.014507	0.014865	-0.028298		0.002602
213-4	0.019212	0.000709	0.001502	0.007777	-0.030504		-0.001304
-1-423	0.011595	0.010053	0.010504	-0.000752	-0.029750		0.001650
-34-1-2	0.003893	0.006341	0.008861	0.014445	-0.034061		-0.000521
1-324	0.003383	-0.007614	0.021077	0.006455	-0.021180		0.002120
-4321	0.003990	0.002899	0.020698	0.006863	-0.036380		-0.001930
431-2	0.006079	0.003591	0.008685	0.014445	-0.034517		-0.001717
4-2-3-1	0.009860	0.016783	0.000858	0.007698	-0.036369		-0.001169
-14-23	0.009413	0.011889	-0.000752	-0.000752	-0.029153		-0.009354
32-4-1	0.001471	0.017257	0.008879	0.007698	-0.034052		0.001253
31-4-2	0.005455	-0.003704	0.015104	0.014445	-0.029035		0.002265
3-24-1	0.005011	0.014205	0.006805	0.007698	-0.032808		0.000911

Table D.2.: Results obtained running a FE analysis on the list of sequences shown in figure D.10. Starting from the first column on the left the following information is reported: the sequence analyzed, the Δdisplacement measured for each weld into the sequence and due to the cooling and finally the final deformation obtained by the algebraic sum of the previous contributions. Saving the table as format "csv", these data can be readable by the 3^{rd} algorithm

in section D.3 (identified hereinafter as initFEdata), is described.

This program, by searching the data passed to it, tries to predict the weld sequence that returns the smallest deformation at the end of the simulation, between all the possible sequences.

The final deformation of a sequence is assumed to be given by the algebraic sum of the effect of each weld plus the effect due to the cooling (table D.2).

The effect of each constituent weld of a sequence is calculated finding, in the initFEdata, the weld satisfying one or some of the following characteristics. The following definitions are made with respect to an hypothetical weld (identified hereinafter as WELD) belonging to a SEQUENCE:

- a weld into the initFEdata that is in the same position of the WELD is called of 1^{st} *type*, otherwise 2^{nd} *type*;
- the number of consecutive welds found in a sequence of initFEdata, in the same order of the SEQUENCE, is identified by *order;*
- the number of consecutive welds found in a sequence of initFEdata, in the same order of the SEQUENCE but neglecting the sign, is identified by *parents.*

To understand using a practical case, supposing we have to predict the distortion of the sequence (1,2,3,4,6,5) having data from FE analysis of the sequence (1,2-3,4,-5,6), there are:

- an occurrence of 1^{st}type, 2^{nd} order and 4 parents $\rightarrow$ 1
- an occurrence of 1^{st} type, 1^{st}order, with 3 parents $\rightarrow$ 2
- an occurrence of 1^{st} type, 1^{st}order $\rightarrow$ 4
- an occurrence of 2^{nd} *type,* 1^{st}order $\rightarrow$ 6

The program, for the estimation of the final displacement of every possible sequence, searches into the initFEdata the welds with the highest order and parents giving preced-

ence to the ones of 1st type. In the case of two welds with the same properties, the mean is calculated.

It is possible to load new FE results whenever they are available and the algorithm will update the predictions with the new data.

In figure D.13 the flow chart of the surrogate model algorithm is shown .

In figure D.14 a screen shot of how the program interface is reported .

In figure D.15 the displacements measured for the sequence proposed by the surrogate model is shown: the direction optimized is Y, the final displacement is 0.009 mm (last row of the table D.2) .

Even though the displacement obtained by the sequence suggested by the surrogate model is not the best one compared to the results obtained for the other sequences run to collect the initFEdata (table D.2), it is possible to appreciate a good level of optimization of the final deformation.

Further improvements have been evaluated to improve predictions and to propose new sequences based on results obtained and the uncertainty of the predictions related to some welds for which not satisfactory data were found in initFEdata.

However, the displacement to be optimized was already so small and falling within the displacement convergence tolerance of the numerical simulations that, in the author's opinion, it did not represent a valid case for further validation of the algorithm. Another model was tested but the final displacements were again too small falling within the convergence displacement tolerance of the simulations. Further work was not able to define a system which returned sufficient deformation to asses the method and consequently the work was stopped.

D.5 Conclusions

A preliminary surrogate model was developed to optimize the order of welds to be applied to a structure, so as to get the smallest possible deformation at a specific point.

To collect the information necessary for predicting the right weld order to minimize

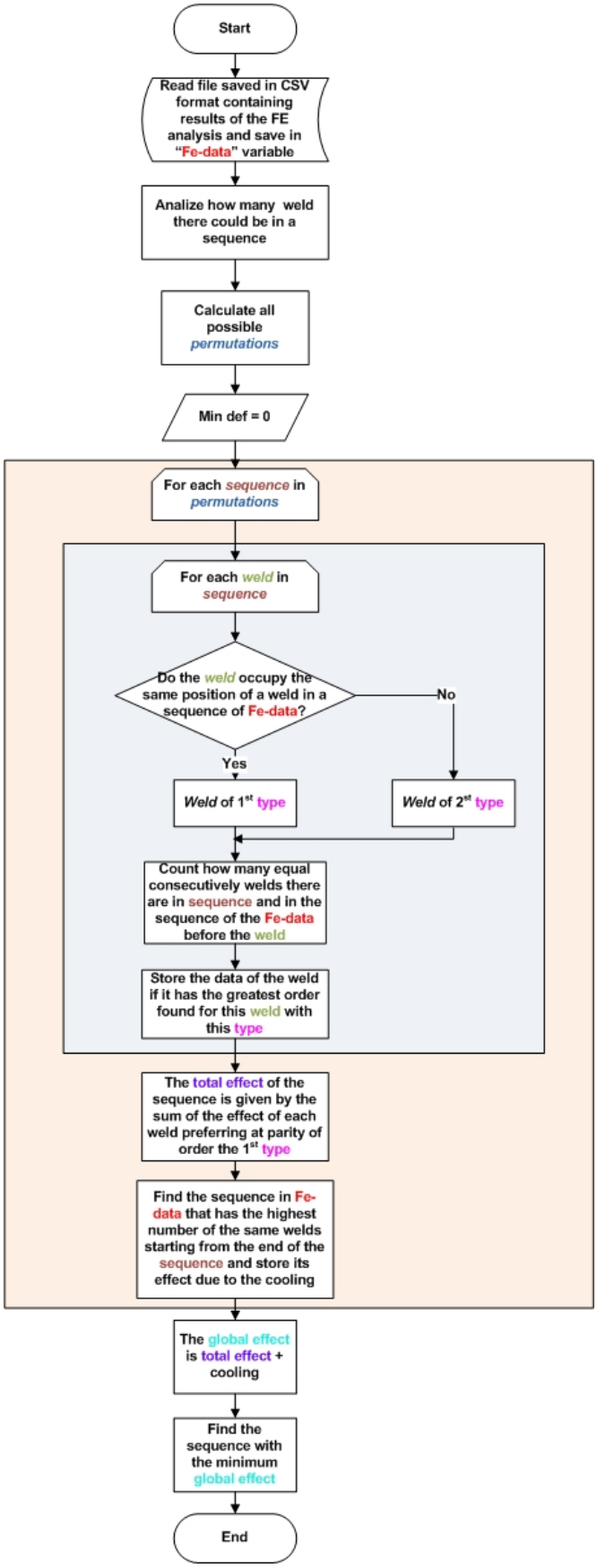

Figure D.13.: Flow chart of the 3^{rd} algorithm

```
Insert the name of the file where are stored all results of the sequences analyzed (extensione included, use a
comma delimited format!): sequence.csv

--------------------------------------------------------------------------------

Sequences evaluated: 384

Optimal sequence: (3, -2, 4, -1)

Elements of 1st type with order, relative mean deformation and parents: {3: (2, 0.0074099999999999999, 2), 4: (
1, 0.0082070000000000008, 1), -1: (1, 0.007698, 1), -2: (2, 0.011195999999999999, 2)}

Elements of 2nd type with order and relative mean deformation and parents: {3: (1, 0.0028988769999999998, 2), 4
: (2, 0.0063409540000000002, 2), -1: (1, 0.0074990433750000002, 1), -2: (1, 0.014064634749999999, 1)}

Deformation due to the welds: 0.032644954
Deformation due to the cooling: -0.032582
Total deformation: 6.2954e-05
```

Figure D.14.: Screen shoot of the program for the calculation of the distortion using the surrogate model

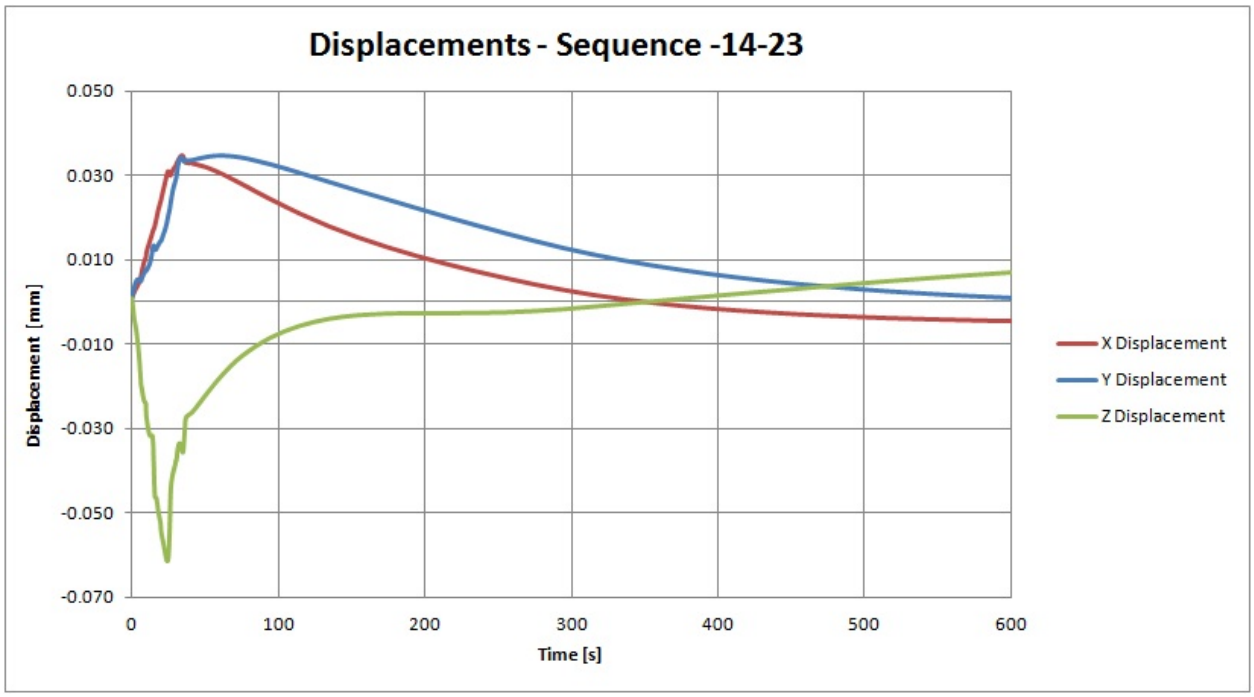

Figure D.15.: Results obtained doing a FE analysis for the sequence suggested by the program reported in figure D.14

the deformation, the optimization required the least number of numerical simulations as possible, as the running time of a welding simulation could be considerable. In this case, a single simulation required 3 days to be computed.

Three algorithms were written with this scope, trying also to minimise the amount of time sent by the user doing repetitive tasks, as when several cases of the same simulation have to be run.

In the first algorithm, a DOE table is suggested to the user, from which a series of simulations on the structure are analysed, using different weld sequences, to compute data for the optimization.

The second algorithm helps the user run the simulations more quickly by not passing through the simulation file generation process.

For each simulation of the DOE computed, the user has to measure the variation of deformation given by each weld to the structure, and also the deformation during the final cooling. These values have to be stored in a file with a comma separated value format (csv).

The third algorithm, reads the deformation results stored in the csv file and makes a prediction on which weld sequence minimises the final deformation of the structure.

The work showed the capacity to optimize the deformation of the structure, but the result obtained for the weld sequence suggested was higher than some final deformations obtained from running simulations of the DOE table. These deformations were however below the deformation tolerance set for the solver convergence of the numerical simulations ($<$0.001 mm). This deformation was considered to be rather small for containing simulation running times and also for possible experimental measurements ($<$1 μm).

Another structure was investigated in an attempt to obtain bigger final deformations but unfortunately, the simulations again showed very small distortions, below the tolerance value mentioned.

At this point the work was stopped. The framework was set for further improvements and case studies, where bigger deformations were involved.

APPENDIX E

Mechanical model

The physically based mechanical model used to describe the strength evolution of the material, as a funciton of temperature and microstructure, is based on the Kocks Mecking theory and further developed in [113, 114].

In this chapter the constitutive equations on which the model is based on are presented. As the terms used in the equations have been kept unchanged from the ones of the papers they made reference to, and since some of the symbols were already used in the nomenclature of this thesis, the reader is advised to consider the terms of this appendix as stand alone.

The shear strain rate in a material can be described by:

$$\dot{\gamma} = b\rho_m v_g \tag{E.1}$$

where $\dot{\gamma}$ represents the shear strain rate, b the burger vector, ρ_m the mean dislocation density and v_g the mean gliding disclocations velocity.

The mean dislocations density rate can be writtes as the sum of the rate of dislocations generated ($\dot{\rho_m^+}$) and dislocations annihilated ($\dot{\rho_m^-}$):

$$\dot{\rho_m} = \dot{\rho_m^+} - \dot{\rho_m^-} \tag{E.2}$$

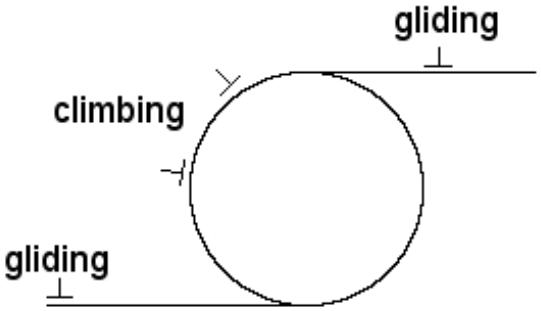

Figure E.1.: Dislocations glide until they find an obstacle. At this point they climb it until they can return to their gliding direction

The mean dislocation density can also be expressed as the sum of the gliding (ρ_g) and climbing (ρ_c) dislocations (figure E.1):

$$\rho_m = \rho_g + \rho_c \tag{E.3}$$

Since it can be shown that the shear rate is driven mainly by the gliding dislocation:

$$\dot{\gamma} = b\rho_g v_g \tag{E.4}$$

To express the gliding dislocations evolution, the dislocations that meet an obstacle are defined as "trapped" (-) whilst the dislocations that have just passed an obstacle are called "generated" (+):

$$\dot{\rho_g} = \dot{\rho_g^+} - \dot{\rho_g^-} \tag{E.5}$$

Now, the gliding dislocations generated can be described as a function of the number of climbing dislocations (ρ_c) and the probability (P^+) and the frequency (Γ^+) that they escape from an obstacle:

$$\dot{\rho_g^+} = \dot{\rho_c} P^+ \Gamma^+ \tag{E.6}$$

The trapped dislocation can, instead, be expressed as a function of the number of gliding dislocations (ρ_c), the velocity of gliding (v_g) and the mean free path the gliding dislocations have between an obstacle and another one (λ_m):

$$\rho_g^- = \rho_c \frac{v_g}{\lambda_m} \tag{E.7}$$

Adding equation E.6 to equation E.7, the rate of dislocations generated can be written as:

$$\dot{\rho_g} = \rho_c P^+ \Gamma^+ - \rho_c \frac{v_g}{\lambda_m} \tag{E.8}$$

The solution of equation E.8 is:

$$\rho_g = \rho_c P^+ \Gamma^+ \frac{v_g}{\lambda_m} \left(1 - \exp\left(-\frac{v_g}{\lambda_m} t\right)\right) \tag{E.9}$$

Equation E.9, considering that λ_m increases faster than v_g with increasing the shear rate, can be simplified in:

$$v_g \rho_g = \rho_c P^+ \Gamma^+ \lambda_m \tag{E.10}$$

Putting equation E.10 in equation E.4:

$$\dot{\gamma} = b \rho_c P^+ \Gamma^+ \lambda_m \tag{E.11}$$

Dyson, in [114], defined the frequency of escpaing of dislocations from an obstacle as

$$\Gamma^+ = \frac{c_j D_v}{b^2} \left\{ \exp\left(\frac{\tau b^2 \lambda_p}{kT}\right) - 1 \right\} \tag{E.12}$$

and the probability of a dislocation escaping from an obstacle as

$$P^+ = \phi \frac{b}{r_p} \tag{E.13}$$

Where k is the Boltzman constant, T the temperature, $c_j$the jogs concentration, D_v the diffusivity and λ_p the pinning spacing, ϕ the volume fraction, r_p the radius of the obstacle.

Putting equation E.12 and E.13 in equation E.11

$$\dot{\gamma} = b\rho_c\lambda_m\phi\frac{b}{r_p}\frac{c_j D_v}{b^2}\left\{\exp\left(\frac{\tau b^2\lambda_p}{kT}\right) - 1\right\} \tag{E.14}$$

Considering positive and negative jogs the function exponential can be transformed into the sinh function

$$\dot{\gamma} = \rho_c\lambda_m\phi_p\frac{c_j D_v}{r_p}\left\{\sinh\left(\frac{\tau b^2\lambda_p}{kT}\right)\right\} \tag{E.15}$$

Dyson in [114] proposes that $\lambda_m = \lambda_p$ (where λ_p is pinning distance) and, considering a square lattice spacing, λ_p can be expressed as

$$\lambda_p = \sqrt[2]{\frac{2}{3}}r_p\left(\sqrt{\frac{\pi}{4\phi_p}} - 1\right) \tag{E.16}$$

r_p, λ_p and ϕ_p are parameters related to the microstructure and they can be seen as related:

$$\frac{\lambda_m}{r_p} = \frac{\lambda_p}{r_p} = \sqrt[2]{\frac{2}{3}}r_p\left(\sqrt{\frac{\pi}{4\phi_p}} - 1\right) = F\left(\phi_p\right) \tag{E.17}$$

Putting equation E.17 in equation E.15:

$$\dot{\gamma} = \rho_c\phi_p\sqrt[2]{\frac{2}{3}}r_p\left(\sqrt{\frac{\pi}{4\phi_p}} - 1\right)c_j D_v\left\{\sinh\left(\frac{\tau b^2\lambda_p}{kT}\right)\right\} \tag{E.18}$$

If the particles are supposed to not deform plastically, the macroscopic rate is related geometrically to the shear rate by

$$\dot{\varepsilon^p_{matrix}} = \frac{\dot{\gamma}}{M} \tag{E.19}$$

Where M is the Taylor factor and ε^p_{matrix} is the plastic strain in the matrix. The overall

plastic strain can be expressed:

$$\dot{\varepsilon^p} = \phi_m \varepsilon^p_{matrix} = (1 - \phi_p) \frac{\dot{\gamma}}{M} \tag{E.20}$$

Putting equation E.20 in equation E.18:

$$\dot{\varepsilon^p} = \frac{\phi_p (1 - \phi_p) F(\phi_p) \rho_c c_j}{M} D_v \left\{ \sinh \left(\frac{\tau b^2 \lambda_p}{kT} \right) \right\} \tag{E.21}$$

Considering that, for most of the time, the dislocations climb, equation E.3 can be approximated as $\rho_c \sim \rho_m$ and considering $\dot{\varepsilon} = \frac{\dot{\gamma}}{M}$ and $\tau = \frac{\sigma}{M}$

$$\dot{\varepsilon^p} = \frac{\phi_p (1 - \phi_p) F(\phi_p) \rho_m c_j}{M} D_v \left\{ \sinh \left(\frac{\sigma_m b^2 \lambda_p}{MkT} \right) \right\} \tag{E.22}$$

Where τ has been considered equiavelent to the shear stress applied to the matrix τ_m.

Applying the compatibility condition, the plastic stresses at the interface between particle and matrix are the same. To change the stress applied at the interface to the stress aplied to the particle and the matrix, a backstress is used (figure E.2):

$$\sigma_m = \sigma - \sigma_k \tag{E.23}$$

Thus equation E.22 becomes

$$\dot{\varepsilon^p} = \frac{\phi_p (1 - \phi_p) F(\phi_p) \rho_m c_j}{M} D_v \left\{ \sinh \left(\frac{(\sigma - \sigma_k) b^2 \lambda_p}{MkT} \right) \right\} \tag{E.24}$$

The backstress is defined as

$$\sigma_k = \phi_p E \left(1 - \frac{\sigma_k}{H^* \sigma} \right) \dot{e^p} \tag{E.25}$$

Where H^* is a function of the particle volume fraction and geometry, for spherical ones it is

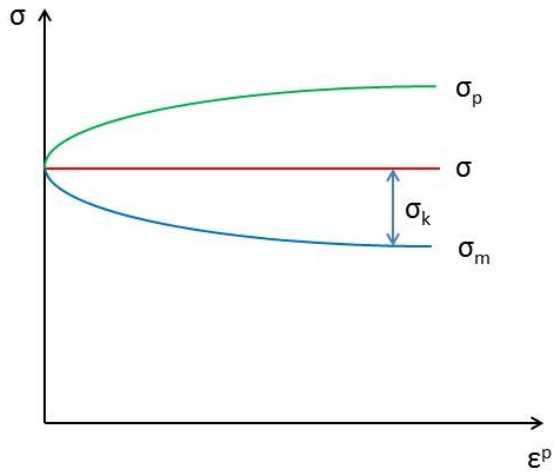

Figure E.2.: The backstress allows the stress calculated at the interface between particle-matrix to be related to the stress applied to the matrix or to the particle

$$H^* = \frac{2\phi_p}{1 + 2\phi_P} \tag{E.26}$$

Equations E.24, E.25 and E.26 are the constitutive equations on which the mechanical model is based, in particular, for the FE implementation, a set of equations for the alpha phase and one for the beta phase have been used, as reported below, with the "alpha" or "beta" subscripts indicating dimensions relative to the alpha or beta phase respectively. Martensitic phase was considered as alpha phase.

Effective stress on the alpha phase

$$\sigma^{eff}_{alpha} = \sigma_{alpha} - \sigma_{k\,alpha} - G_{alpha} b_{alpha} \sqrt{\rho_{m\,alpha}} \tag{E.27}$$

Plastic strain rate on the alpha phase

$$\dot{\varepsilon^p_{alpha}} = \frac{\phi_{alpha}\rho_{m\,alpha}}{M^2_{alpha}} D_{v\,alpha} \frac{\sigma^{eff}_{alpha}}{G_{alpha}} \left(\frac{\lambda_{alpha}}{b_{alphs}}\right)^2 \left\{ exp\left(\frac{\left(\sigma^{eff}_{alpha}\right) b^2 \lambda_{alpha}}{MkT} \right) \right\} \tag{E.28}$$

Backstress on the alpha phase

$$\dot{\sigma_{k\,alpha}} = \phi_{beta} E_{alpha} \left(1 - \frac{\sigma_{k\,alpha}}{H^* \sigma_{alpha}}\right) \dot{\varepsilon^p_{alpha}} \tag{E.29}$$

$$H^* = \frac{2\phi_{hard}}{1 + 2\phi_{hard}} \tag{E.30}$$

Where ϕ_{hard} is the volume of hard particle in the material considered, thus the ones offering higher resistance to the stress applied.

Mean dislocation density rate in alpha phase

$$\dot{\rho_{m\,alpha}} = \frac{M_{alpha}}{b_{alpha} d_{alpha}} \left(\frac{2}{\sqrt{3}\rho_{m\,alpha} d^2_{alpha}} + \eta_{alpha}\right) \dot{\varepsilon^p_{alpha}} - \frac{\rho_{m\,alpha} D_{v\,alpha} \sigma^{eff}_{alpha} b^3_{alpha}}{2\pi\left(1 - \upsilon_{alpha}\right) M_{alpha} kT} \tag{E.31}$$

Effective stress on the beta phase

$$\sigma^{eff}_{beta} = \sigma_{beta} - \sigma_{k\,beta} - G_{beta} b_{beta} \sqrt{\rho_{m\,beta}} \tag{E.32}$$

Plastic strain rate on the beta phase

$$\dot{\varepsilon^p_{beta}} = \frac{\phi_{beta} \rho_{m\,beta}}{M^2_{beta} C_{beta}} D_{v\,beta} \frac{\sigma^{eff}_{beta}}{G_{beta}} \left(\frac{\lambda_{beta}}{b_{beta}}\right)^2 \left\{ exp\left(\frac{\left(\sigma^{eff}_{beta}\right) b^2 \lambda_{beta}}{MkTC_{beta}}\right)\right\} \tag{E.33}$$

Backstress on the beta

$$\dot{\sigma_{k\,beta}} = \phi_{alpha} E_{beta} \left(1 - \frac{\sigma_{k\,beta}}{H^* \sigma_{beta}}\right) \dot{\varepsilon^p_{beta}} \tag{E.34}$$

Mean dislocation density rate in beta phase

$$\dot{\rho_{m\,beta}} = \frac{M_{beta}}{b_{beta} d_{beta}} \left(\frac{2}{\sqrt{3}\rho_{m\,beta} d^2_{beta}}\right) \dot{\varepsilon^p_{beta}} - \frac{\rho_{m\,beta} D_{v\,beta} \sigma^{eff}_{beta} b^3_{beta}}{2\pi\left(1 - \nu_{beta}\right) MkT} \tag{E.35}$$

Where d_{beta} is the mean beta grains size.

$$C_{beta} = 1 + 0.1\frac{l_{alpha}}{w_{beta}} \tag{E.36}$$

Where l_{alpha} is the mean length of alpha particles and w_b is the mean thicknes of beta lamellae.

Total plastic strain

$$\dot{\epsilon^p_{total}} = \phi_{alpha}\dot{\varepsilon^p_{alpha}} + \phi_{beta}\dot{\varepsilon^p_{beta}} \tag{E.37}$$

Parameters used for the equations

$D_{v\,alpha} = 1^{-3}\exp\left(-\frac{320000}{RT}\right)\left[\frac{m^2}{s}\right]$

$D_{v\,beta} = 1^{-6}\exp\left(-\frac{240000}{RT}\right)\left[\frac{m^2}{s}\right]$

$\nu_{alpha} = \nu_{beta} = 0.4$

$E = 105 - 0.05461T + 0.00001263T^2 - 1.25 \times 10^{-8}T^3$

$G_{alpha} = G_{beta} = 0.5\frac{E}{1+\nu}\,[Pa]$

$b_{alpha} = b_{beta} = 2.54 \times 10^{-10}\,[m]$

$M_{alpha} = 2.54$

$M_{beta} = 3.1$

$\lambda_{alpha} = \lambda_{beta} = 60 \times 10^{-9}\,[m]$

$d_{alpha} = w_{alpha} = lamellae\,thickness\,[m]$

$d_{beta} = 100 \times 10^{-6}\,[m]$

$w_{beta} = 1 \times 10^{-6}\,[m]$

$l_{alpha} = 10^{-6}\,[m]$

Initial conditions

$\rho_{m\,alpha} = \rho_{m\,beta} = 0$

$\varepsilon^p_{alpha} = \varepsilon^p_{beta} = 0$

$\sigma_{k\,beta} = \sigma_{k\,alpha} = 0$